NATIONAL TECHNICAL UNIVERSITY OF ATHENS
SCHOOL OF MECHANICAL ENGINEERING
SECTION OF MANUFACTURING TECHNOLOGY

Study of the powder deposition in laser powder bed fusion additive manufacturing processes

DOCTOR OF PHILOSOPHY THESIS

Author
AVRAMPOS PANAGIOTIS

Supervisor
Prof. G.-C. VOSNIAKOS

Athens, July 2024

NATIONAL TECHNICAL UNIVERSITY OF ATHENS
SCHOOL OF MECHANICAL ENGINEERING
SECTION OF MANUFACTURING TECHNOLOGY

Study of the powder deposition in laser powder bed fusion additive manufacturing processes

DOCTOR OF PHILOSOPHY THESIS

AVRAMPOS PANAGIOTIS

Evaluation committee

Assoc. Prof. P. Benardos (Mech. Eng., NTUA, Advisory Committee)
Prof. C. Charitidis (Chem. Eng., NTUA)
Prof. S. Kourkoulis (App. Math. And Phys. Sciences, NTUA)
Emer. Prof. D. Manolakos (Mech. Eng., NTUA, Advisory Committee)
Prof. N. Michailidis (Mech. Eng., AUTH)
Assoc. Prof. P. Stavropoulos (Mech. Eng., UPATRAS)
Prof. G.-C. Vosniakos (Mech. Eng., NTUA, Supervisor)

Athens, July 2024

This doctoral thesis has been financially supported by the four-year scholarship, contributed from the Special Account for Research Funding (E.L.K.E) of National Technical University of Athens (N.T.U.A.)

ΕΘΝΙΚΟ ΜΕΤΣΟΒΙΟ
ΠΟΛΥΤΕΧΝΕΙΟ
ΕΙΔΙΚΟΣ ΛΟΓΑΡΙΑΣΜΟΣ
ΚΟΝΔΥΛΙΩΝ ΕΡΕΥΝΑΣ

Acknowledgments – Ευχαριστίες

Όταν ξεκινούσα αυτό το ταξίδι προς την απόκτηση ενός διδακτορικού τίτλου σπουδών, δεν μπορούσα να φανταστώ πόσο συναρπαστική και συνάμα επίπονη διαδικασία θα ήταν. Κατά τη διάρκεια αυτής απέκτησα γνώσεις, δημιούργησα σχέσεις και φιλίες που θα με ακολουθούν μια ζωή και καλλιέργησα άλλες που ήταν ήδη σημαντικές για εμένα.

Πρωτίστως, θα ήθελα να ευχαριστήσω τους γονείς μου, Γιάννη και Παρασκευή, που, ο καθένας με τον τρόπο τους, στάθηκαν αρωγοί σε αυτή μου την προσπάθεια. Ο πατέρας μου αποτέλεσε έμπνευση και πηγή δημιουργικότητας, μεταλαμπαδεύοντάς μου γνώσεις και εμπειρία, ενώ η μητέρα μου ήταν πάντοτε ένα κύμα θέλησης ικανό να κινήσει κάθε εμπόδιο που θα έβρισκα στο δρόμο μου ώστε να με βοηθήσει.

Εν συνεχεία, ο κύριος Βοσνιάκος, με τον οποίο συνεργαστήκαμε αρμονικά επί σειρά ετών, με βοήθησε με την καθοδήγησή του, την άρτια γνώση της μηχανολογίας που διαθέτει και με βοήθησε ώστε να εξελιχθώ σε έναν ικανό μηχανολόγο ο οποίος διαθέτει τα απαραίτητα εφόδια επί των οποίων θα βασίσει την μελλοντική του καριέρα.

Επίσης, ο κύριος Μανωλάκος, με τη φύσει ευγενική του προσωπικότητα αποτέλεσε έναν άνθρωπο – στήριγμα για εμένα, διαθέσιμο ανά πάσα στιγμή για να βοηθήσει με όποιον τρόπο μπορούσε.

Οφείλω επίσης να ευχαριστήσω το Γιώργο Παπαζέτη, το Μανώλη Σταθάτο και όλους τους υπόλοιπους υποψήφιους διδάκτορες με τους οποίους συνεργάστηκα κατά περίοδο. Η αλληλεπίδρασή μας κατέστησε την επίπονη αυτή διαδικασία πολύ πιο ευχάριστη και η ανταλλαγή ιδεών και γνώσεων μεταξύ μας με εξέλιξε τόσο ως άτομο, όσο και ως μηχανικό.

Κατόπιν, θερμές ευχαριστίες επιθυμώ να δώσω στον Νίκο Μελισσά, τον Κώστα Κερασιώτη και σε όλο το τεχνικό προσωπικό του εργαστηρίου Τεχνολογίας των κατεργασιών για τη συνεισφορά τους και την αρωγή τους σε κατασκευαστικά θέματα, καθώς και για τη διάθεσή τους να βοηθήσουν αγόγγυστα, όποτε και αν τους ζητήθηκε.

Επιπρόσθετα, θέλω να ευχαριστήσω τον φίλο μου, Σωτήρη, με τον οποίο ξεκινήσαμε μία πορεία από το πρώτο έτος και χτίσαμε μία στενή φιλία που διαρκεί μέχρι και

σήμερα, στηρίζοντας ο ένας τον άλλο σε κάθε δυσκολία που παρουσιάστηκε, ακόμα και εξ' αποστάσεως.

Κλείνοντας, άφησα το σημαντικότερο για το τέλος. Οφείλω να ευχαριστήσω την κοπέλα μου, Κωνσταντίνα, που εμφανίστηκε σε μία περίοδο της ζωής μου που όλα έδειχναν μαύρα και αποτέλεσε την κινητήριο δύναμη για όλα όσα ακολούθησαν. Χωρίς την αγάπη και την εμπιστοσύνη της, ίσως να μην έγραφα αυτές τις γραμμές τώρα. Της εκφράζω την αγάπη μου και την ευγνωμοσύνη μου για την ανεκτίμητη συνεισφορά της στην επίτευξη αυτού του στόχου – ορόσημο για εμένα.

Abstract

During the 40 years since the conception of Additive Manufacturing, Powder Bed Fusion processes have been a very important sub-category of AM, mostly due to their ability to produce metal parts of promising quality. Extensive research has been performed in order to ascend PBF processes from their initial prototype-developing status to fully industrial, large-production processes. However, despite the efforts being made, due to their high complexity, PBF processes still have not reached their potential. This work aims to contribute in this direction, and more specifically, to powder deposition. The aspect of powder deposition is of paramount importance to all PBF processes, since the quality of the deposited layer is directly connected to the mechanical properties of the finished part.

The *first chapter* of this thesis presents an overview of AM processes, their historical background and the development status of PBF processes.

The *second chapter* provides a thorough analysis of the connection between powder spreading process parameters, powder layer quality and finished part quality in terms of mechanical properties. The process parameters of powder deposition are recorded and possible ways that each one affects the other are identified. Then, the quality criteria of the deposited powder layer are identified, and methods of monitoring them, both in-line and off-line, are presented. The ways in which the process parameters are deemed to affect the layer quality criteria are presented too. Subsequently, the mechanical properties that serve as quality criteria of the finished part are analyzed. Finally, the ways in which the powder layer quality criteria are deemed to affect the finished part quality criteria are explained. Extensive use of tables has been made, in order to simplify the navigation and make it easier for future researchers to use this literature review as general guidelines for optimizing the powder spreading process in their projects.

The *third chapter* presents a robust statistical analysis and comparison of all the powder deposition methods found in literature via Analytic Hierarchy Process. The comparison is performed by defining criteria and grading each method based on its performance with regard to each specific criterion as compared to the other methods. The importance of each criterion is subjective and the weights can be altered based on each researcher's

priorities. The comparison proved that mechanical deposition is preferable with regards to other, innovative methods. Then, a prototype Powder Deposition/Recoating System is designed. The innovative design is divided in two groups, the doser/sieving group and the recoating group. Each of these groups is compared via AHP to the respective group of a commonly used powder deposition system embedded in a commercial SLM machine. The criteria based on which the comparisons will be performed are defined in advance. The AHP comparison proved the superiority of the suggested design.

The *fourth chapter* of this thesis presents the modelling of powder in Discrete Element Method (DEM) simulations and the optimization of doctor-blade facilitated, vibration-assisted mechanical spreading via Taguchi DoE and subsequent ANOVA. Initially, a method to model particle size distribution given by D_{90}, D_{50} and D_{10} via a lognormal distribution is presented. Then, the available contact models are presented and the best-suited one is selected by Tabor parameter comparison. It is proven that Hertz-Mindlin with JKR is the most suitable model. Modelled powder rheological behaviour is evaluated via cross-check between experiments and simulations using the angle of repose and angle of avalanche tests. The simulations that followed examined the spreading conditions (spreading speed, vibrational frequency and amplitude of the blade and relief angle of the blade) by specific layer quality criteria (layer thickness deviation, surface coverage ratio, surface roughness and true packing density) and proved that vibration assists deposited layer evenness and homogeneity. Weighted means analysis of the surface roughness, surface coverage ratio and layer thickness deviation proved that the surficial skewness and kurtosis can serve as equivalent layer quality indicators, for layers created by spherical powder particles. It was proven that the lower the deposition recoating speed, the better the surface quality. True packing density was found to remain constant despite the change of parameter levels.

The *fifth chapter* of this thesis evaluated the sieving process via DEM simulations of the same powder as the one modelled in the fourth chapter. The sieving was evaluated by the duration of the linear phase, the mass flow during this phase and the mass sieved during this phase. The sieving parameters were the frequency and amplitude of the sieve's vibration, the taper angle of the sieve's apertures and the level of the powder inside the sieve prior to sieving. The level combinations that maximize powder flow, linearity duration and mass deposited during linearity were identified. Then, the effect of different aperture shapes was evaluated for these optimum level combinations.

Finally, the quality of the deposited powder layer via sieving alone, in a recoater-less powder deposition process, was examined. It was proven that it is possible, by calibrating the amount of powder fed into the sieve and the sieving parameters, to achieve level quality superior to that of the vibration-less doctor blade powder spreading, but still inferior to the vibration-assisted doctor blade powder spreading.

The *sixth chapter* of this thesis presents a novel method for the deposition of multi-material powder layers based on the dual contour-gauge design. The method is mathematically defined and the problem is solved numerically via a C-code. The results are presented schematically for a layer of 5 border curves that define material transitions within the mosaic-patterned layer. The method's viability is proven via an experimental jig and DEM simulations. The simulations used the sieving and spreading optimized parameters that were defined in the fourth and fifth chapter of this thesis. Both experiment and simulation achieved very good approximation of the borders of the developed pattern. The DEM simulations achieved good layer evenness and homogeneity, comparable to the vibration-assisted, doctor blade powder deposition.

Overall conclusions and suggestions for future work are presented in the *seventh chapter*.

Πίνακας περιεχομένων

List Of Tables

List of Figures

1 Introduction

1.1 Additive Manufacturing

Additive Manufacturing (AM), is a term that encompasses every manufacturing process that is based on the principle of developing a three-dimensional object by gradually adding material into it, contrariwise to subtractive manufacturing. Nowadays, AM is used as a "blanket" term for every process based on layer-wise object building strategies. The first approach was made in May 1981 by Dr. Hideo Kodama [1], who combined elements from 3D scanning and 3D topographical maps in order to create the "prototyping machine". Since then, many other attempts have been made and the field of AM has turned into one of the most rapidly evolving in the new century.

According to ISO/ASTM 52900 [2], additive manufacturing is divided into seven key technologies:

1. Binder Jetting (BJT), which produces parts by selectively depositing a binding agent over a powder bed.
2. Directed Energy Deposition (DED), which produces parts by pushing powder or wire through a nozzle and melting it via an intensely focused energy source (usually a laser) at the point of deposition.
3. Material Extrusion (MEX), which produces parts by layering extrusions of molten thermoplastic filament, continuously deposited at specific locations, where it cools and solidifies.
4. Material Jetting (MJT), which produces parts via selectively depositing and UV-light curing a liquid photopolymer onto the build platform either continuously or on demand.
5. Powder Bed Fusion (PBF), which produces parts by using an energy force to selectively melt or sinter powdered material which has been deposited on a fabrication table.

6. Sheet Lamination (SHL), which produces parts by stacking very thin sheets of material and laminating them together through ultrasonic welding, bonding, or brazing.
7. VAT Photopolymerization (VPP), which produces parts by selectively exposing photopolymer liquid resins in a vat to UV light.

Initially, the niche of AM processes was their ability to develop parts containing complex geometries, such as internal cavities and overhangs, which conventional/subtractive manufacturing was incapable of creating. Hence, AM made it possible to minimize the number of parts in assemblies, developing more robust constructions with fewer failure-prone areas.

AM are traditionally superior and more cost-efficient in terms of low to medium volume production, mainly due to their straightforward, tool-less function. Furthermore, the wide variety of materials they can utilize, ranging from powder to liquid and solid, provides the potential for creating Functionally-Graded Materials [3]. They are also more time-efficient, since they can develop complex parts directly from a 3D CAD file with a single machine setup, in contrast to conventional machining, where multiple setups and various part holding ways might be necessary to develop a single part. Fewer part holding changes throughout the process also increases part dimensional accuracy [4]. Finally, AM processes give the potential of applying low-waste engineering, since, in most cases, the materials are easily recyclable or even, readily reusable.

Despite the fast evolution that additive manufacturing technologies have undergone, the challenges encountered in order to turn them from rapid prototyping means to high-production industrial manufacturing processes have not been eliminated yet. The limited speed at which layers are built, the high cost for developing large structures and the high energy needed to power AM machines during large production cycles, in combination with part quality issues, such as the staircase effect, which is the trademark defect of AM-produced parts, still need to be addressed and tackled effectively. However, the rise of renewable energy sources, process hybridization with subtractive machining and even 4D printing, i.e., AM where the developed parts can adapt to outside parameters such as stress, moisture, pressure, etc. offer numerous possibilities [3].

1.2 Powder Bed Fusion - based Additive Manufacturing

The present thesis focuses on Powder Bed Fusion-based Additive Manufacturing (PBF). PBF processes include [5]–[8]:

1. Selective Laser Sintering (SLS)
2. Selective Laser Melting (SLM)
3. Direct Metal Laser Sintering (DMLS)
4. Selective Heat Sintering (SHS)
5. Electron Beam Melting (EBM)
6. Selective Laser Reactive Sintering (SLRS) or High-Speed Sintering (HSS)

All of these processes include the development of an even, homogeneous powder bed of a pre-defined thickness. Then, the only process aspects that differ are the particle consolidation method and the power source.

SLS partially melts polymer powders via a CO_2 laser beam, while SLM/DMLS melt completely/partially metal powders, most commonly using Nd:YAG laser beams. Furthermore, SLM/DMLS are forced to create void in the fabrication chamber, and then fill it with inert gas, in order to prevent oxidation of the powder, which is not an issue with polymer powders which are used in SLS.

EBM is similar to SLM, the only difference being the power source (electron beam instead of laser beam). Similarly, SHS is comparable to SLS, the difference being again the power source (thermal printhead instead of laser beam). However, thermal printheads are cheaper compared to laser sources, therefore SHS demands a smaller initial budget to get ready to print objects.

SLRS/HSS combine BJT with PBF; firstly, an inkjet printhead selectively deposits a radiation-absorbing material (RAM) onto the powder bed. Then, an infrared lamp irradiates the entire surface. BJT is not classified as a PBF fusion, since, despite involving powder bed deposition, it does not involve partial or total melting and subsequent fusion of the particles via a power source.

All PBF processes implement substrate heating in order to pre-heat the powder and reduce residual stress and part deformation/bending.

A common advantage of PBF processes is that they provide the capability of building complex structures, such as closed cavities and overhangs with minimal or no support build at all, since the previous powder layers provide enough support, unless materials of very high density are used.

Table 1.1 summarizes the differences among the aforementioned PBF processes, as well as their date of invention and their inventors.

Table 1.1: PBF process categorization.

PBF Process	Acronym	Power Source	Material	Melting level of grain	Consolidation method	Inventors	Invention date
Selective Laser Sintering	SLS	Laser beam	Polymer	Partial	Re-solidification	Carl Deckard, University of Texas, USA [4]	1984
Selective Laser Melting	SLM	Laser beam	Metal	Complete	Re-solidification	Dieter Schwarze and Matthias Fockele, Fraunhofer Institute ILT, Aachen, Germany [9]	1995
Direct Metal Laser Sintering	DMLS	Laser beam	Metal	Partial	Re-solidification		
Selective Heat Sintering	SHS	Thermal printhead	Polymer	Partial	Re-solidification	Frederik Tjellesen and Anders Hartmann, Blueprinter™, Denmark [10]	2011
Electron Beam Melting	EBM	Electron beam	Metal	Complete	Re-solidification	Arcam AB Corporation, Sweden [11]	1997
Selective Laser Reactive Sintering/ High-Speed Sintering	SLRS/HSS	Laser beam	Si, ZrO_2, Cr, Cr_2O_3	Partial	Re-solidification, with simultaneous chemical conversion of solid precursors	Neil Hopkinson, Loughborough University, UK [12]	2003

1.3 Scope

It has been 40 years since the invention of Powder Bed Fusion (SLS, 1984) and, like every newly emerged technology, it was initially touted as “revolutionary”. The Gartner Hype Cycle is a tool developed to trace whether a technology is mature enough to be effective for industrial use or not. It consists of 5 stages:

1. Innovation Trigger: A technological breakthrough that only recently was made known to public, however it does not yet have any practical application.
2. Peak of Inflated Expectations: Some successful case studies increase the hype, while failures are sometimes concealed.
3. Trough of Disillusionment: Slow advancement makes the technology seem like a failure, causing the funding and company interest to decrease.
4. Slope of Enlightenment: Maturity and realistic industrial applications are studied; funding begins to return.
5. Plateau of Productivity: Realistic public expectations create a healthy environment for widespread utilization.

Table 1.2 shows the maturity development of PBF processes.

Table 1.2: Gartner Hype Cycle stages for Powder Bed Fusion processes.

	Innovation Trigger	Peak of Inflated Expectations	Trough of Disillusionment	Slope of Enlightment	Plateau of Productivity
Date	1984-2010 (approx.)	2017	2018-2020 (approx.)	2020 (approx.)-present	(not yet reached, rapidly approaching)
References	[4], [13]	[14]	[15]	[16]	[16]

Nowadays, in 2024, the PBF processes are rapidly maturing, reaching the stage at which realistic industrial applications are being developed and companies such as Siemens and BMW stably invest and develop large AM centres [16]. Hence, there are still areas of research to optimize PBF processes till they reach their potential.

1.3.1 Contribution and Progressive Motivation of Work

The current thesis focuses on a specific aspect of the PBF processes; powder deposition. Powder deposition is of paramount importance, since the quality of the powder bed is one of the parameters that drastically affect the quality of the finished products in terms of mechanical properties, such as surface roughness, tensile strength, hardness, brittleness, density, etc. [8]

Table 1.3 presents a categorization of Laser-Based PBF process parameters.

Table 1.3: LB-PBF process parameter categorization.

LB-PBF process parameters			
Laser-related	***Scan-related***	***Powder-related***	***Temperature-related***
Laser power	Scanning speed	Particle size and distribution	Powder bed temperature (heated table)
Wavelength	Scanning pattern	Particle shape	Powder feeder temperature
Spot size	Scanning spacing	Powder bed packing density	Temperature uniformity
Pulse duration		Layer thickness	
Pulse frequency		Material properties	

It is easy to notice how many process parameters exist; PBF processes are highly complex, and the process parameters are interacting with each other, affecting the end-product in unexpected ways. This work focuses on powder deposition, since it has been the least analysed category of process parameters in literature.

The starting point of this work (*Chapter 2*) was to create a literature review of powder deposition for PBF processes, as there was an identified gap in literature. The developed literature review provides a systematic method of connecting PBF powder-related process parameters to the powder layer quality criteria and, ultimately, to the finished part's quality criteria. Initially, every parameter that affects the powder deposition process was identified. Secondly, quality criteria for the non-sintered/melted powder layer were defined, as well as ways to monitor these. Finally, the quality criteria that characterize the finished part and its mechanical properties were identified. The relation

between process parameters, spread powder layer quality and finished part quality was ultimately established sequentially. This illuminated the topic of powder bed recoating and untangled the perplexed relations between its aspects, creating a guide which researchers can refer to for any powder-deposition issue that potentially arises.

This review provided the foundation for the innovative work that follows in the next Chapters.

The powder deposition process begins with the powder deposition/recoating system (PDS/PRS) itself. In *Chapter 3*, Analytic Hierarchy Process (AHP) was used to compare various powder deposition methods with each other, based on specific criteria. This provided a quantifiable basis that proved how mechanical powder deposition is indeed superior to other methods. Furthermore, a prototype PDS was designed and its functionality and features were compared to benchmark PDS, again via AHP. No similar work was found in literature where a systematic statistical method was implemented to optimize the design of a PDS. The quality of the designed PDS in terms of surface roughness and layer thickness accuracy was evaluated via 3D-white light scanning of the powder layers and extraction of layer profiles via the point cloud that was created via the scanning. This created a robust method to evaluate every PDS design based on its performance with regard to the common industrial standard, which is flexible enough, since the criteria grading is subjective and can be varied based on each researcher's goals and needs.

The powder deposition via a vertically vibrating doctor blade was then modelled in a DEM simulation environment (EDEM, by Altair) and simulated for various values of recoating speed, vibration amplitude and frequency and blade sharpness (*Chapter 4*). The simulations were run after Taguchi DoE in order to systematically organise and minimize the number of trials. The produced layer was evaluated by the criteria that were defined in the literature review via the exported by the simulation environment result file. It was proven that skewness (Ssk) and kurtosis (Sku) are indicative of the powder layer quality, corresponding to different weighted means of the predefined quality criteria. This enables researchers to easily evaluate layer quality by only examining one surficial parameter instead of numerous parameters, turning an arduous simultaneous optimization task into a trivial single optimization one. Furthermore, the positive effect of a vibrating doctor blade recoater was proven, an aspect that had not been examined in literature to the author's knowledge.

The powder sieving method was also modelled in the same DEM environment and simulated, also using a Taguchi DoE for the same reasons (*Chapter 5*). The sieving process parameters were the sieve's vertical oscillation amplitude and frequency, loaded powder amount and sieve aperture taper angle. Sieving has not been examined in literature as a powder deposition means, or as a means to filter out agglomerates and larger particles to ensure higher powder bed quality. In this work it has been proven that, by proper calibration of the aforementioned sieving parameters, it is even possible to deposit PBF-ready powder layers at comparable quality to the ones spread by a non-vibrating doctor blade, which would vastly increase the powder deposition speed and reduce the total manufacturing time.

The motivation for *Chapter 6* was the identified gap in multi-material deposition methods, i.e., in methods of creating single layers that include various powder types in a mosaic-type layer. The lack of efficient ways of powder border definition in combination with the fact that the few methods that exist are patent-locked or nozzle-based, lead to either poor surface quality or very slow deposition. A method based on a dual contour-gauge system was proposed. In advance to the design of the system, G-codes that perform the segmentation of the multi-material surface in many uni-material surfaces were written and tested. The design of a jig evaluated experimentally the applicability of the method, providing good approximation of the preset border curves and acceptable layer quality, even by sieving deposition. A DEM simulation was used, utilizing the optimized spreading and sieving settings that were defined in the previous two chapters. This proved the capabilities of the method, opening the path for actual system implementation and experimental testing.

1.4 Thesis Structure

Section 1.3.1 provided the motivational and innovative framework of this work. Following the description above, this thesis is divided as follows:

In *Chapter 1*, a brief introduction about AM and specifically about PBF processes is provided, along with the work's scope, contribution and progressive motivation.

In *Chapter 2*, a detailed literature review focused on the powder layer spreading aimed for PBF processes is provided. The analysis is divided in the powder deposition process

parameters, powder layer quality criteria and finished part quality criteria and sequentially connects these three categories.

Chapter 3 provides an AHP based comparison of the powder deposition methods that exist. Then, the design and manufacturing of a prototype PDS is presented and the design is, again via AHP, compared to a common, industrially-utilized PDS.

Chapter 4 presents the work done on DEM simulations of powder spreading. The simulations examine a vertically vibrating doctor blade recoater. Surface layer quality criteria are mathematically defined and numerically calculated via simulation-extracted files. The results in terms of spreading parameter optimization are presented via Taguchi DoE and subsequent ANOVA.

Chapter 5 presents the work done on DEM simulations of powder sieving. The simulations examine a vertically vibrating sieve of various aperture shapes. The results in terms of sieving parameter optimization are presented via Taguchi DoE and subsequent ANOVA. Then, the sieving process is examined as a powder deposition method to produce PBF-ready layers via the layer quality criteria defined in *Chapter 4*. The results are presented in comparison to the vibration-assisted doctor blade spreading.

Chapter 6 presents a novel method for the deposition of multi-material powder layers based on the dual-contour gauge design. The layer division into many uni-material layers is mathematically defined and numerically calculated. The viability of the dual contour gauge system is examined via experiments on a manufactured jig and via DEM simulations using the optimized spreading and sieving parameters defined in *Chapter 4* and *Chapter 5* respectively. The results are presented and method viability is proven.

Finally, *Chapter 7* summarizes the work's achievements, findings, breakthroughs and limitations, making suggestions for improvements and future work.

2 Literature Review

One of the most important aspects of Powder Bed Fusion (PBF) processes is the powder layer spreading. The powder layer needs to be applied in such a way that its evenness and homogeneity is ensured. This, in turn, will ensure that no inconsistencies or defects of the non-sintered powder layers, internal or superficial, will be inherited to the finished part, which would negatively affect its mechanical properties and dimensional accuracy causing drastic quality deterioration. This chapter [8] aims to address the powder recoating process parameters, intrinsic and extrinsic, that affect the non-sintered powder layer quality and, ultimately, the finished part quality. The non-sintered layer's quality and the finished part's quality are examined via certain powder layer quality indicators (PLQIs) and finished part quality indicators (FPQIs) respectively. This work systematically identifies and records the connections between process parameters on one hand and PLQIs and FPQIs on the other hand. Moreover, the multiple ways and corresponding methods found in literature in which the powder layer quality can be quantified are presented with the advantages and disadvantages of each one. Finally, gaps in literature are revealed and suggestions for future work to focus on are made.

2.1 Powder Bed Fusion (PBF) Processes

In Powder Bed Additive Manufacturing processes, alternatively termed Powder Bed Fusion (PBF) processes, a 3-dimensional part is built sequentially, layer after layer. First, a thin layer of powder is applied onto the top surface of a downwards moving fabrication piston. The thickness of this layer typically varies between 30 and 150μm. Afterwards, a properly controlled and concentrated energy force, e.g., a laser or electron beam, follows a certain space filling path to sinter or melt the powder at the areas that are pre-defined by the slicing software. This solidifies the powder and creates the bulk material of the finished part. Alternatively, a nozzle distributes a binding liquid (binder) onto the deposited powder layer following the path that the slicing software defines.

Then, the fabrication piston moves downwards by a height equal to the layer thickness and another layer of powder is applied on top of the previous one. Non-sintered/non-melted (or non-fused) powder acts as support material, and the same process of powder solidification follows. When every layer scan is completed, the finished product is removed from the powder chamber and the non-fused powder, also known as "cake", is removed via suction techniques.

Table 2.1: Powder Bed Fusion Processes.

Process	Acronym	Power source/method	Powder type	Melting level of grain
Selective Laser Sintering	SLS	Laser beam	Polymer	Partial
Selective Laser Melting	SLM	Laser beam	Metal	Complete
Direct Metal Laser Sintering	DMLS	Laser beam	Metal	Partial
Selective Heat Sintering	SHS	Thermal printhead	Polymer	Partial
Electron Beam Melting	EBM	Electron beam	Metal	Complete
3-Dimensional Printing or 3D Inkjet Powder or Binder Jet Printing	3DP/ 3DIJPP (BJP)	None (Drop-on-Demand or Continuous-Jet printheads)	Any	None (Liquid binder)
Selective Laser Reactive Sintering	SLRS	Laser Beam	Si, ZrO_2, Cr, Cr_2O_3	Partial, with simultaneous chemical conversion of solid precursors

There are various types of PBF processes. The categorization is based on the type of power source/method used, the powder type that is used and the achieved melting level of the powder grains. If the powder particles are fully melted, the process is termed "melting", while, if they are only partially melted and the fusing happens via the bottleneck effect, the process is termed "sintering". Finally, if a liquid binder is used, there is no power source and the fusion happens via the solidification of the binder that creates "bridges" between the particles. Hence, there are seven subcategories of PBF processes [17], [18], [19], [7], [20], [21], see *Table 2.1*.

When it comes to PBF processes, most often research focuses on the interaction of the laser beam with the powder material in order to produce the finished part. Either experimentally, or via simulations, the result is recorded and, afterwards, some kind of control is applied to the laser beam parameters, the scanning speed or the scanning pattern, in order to optimize the result and achieve the desired finished part properties.

However, far less research effort has been expended on the powder bed itself. The common aspect among all the aforementioned PBF subcategories is the necessity of spreading even and homogeneous powder layers in order to manufacture a high-quality finished part. The powder spreading process is not easy to fully understand due to its high level of complexity.

This review identified five main topics and the respective subtopics that need to be analyzed in order to fully understand the state of the art of the powder spreading process, as follows:

1. Process parameters
    1.1. Powder material
    1.2. Particle size distribution (PSD)
    1.3. Particle shape (2D-3D analysis, circularity, convexity, elongation, etc.)
    1.4. Recoater material
    1.5. Recoater shape
    1.6. Recoating strategy (i.e., recoating process parameters and setup/spreading pattern)
    1.7. Nominal, effective and actual layer thickness
    1.8. Environmental parameters (temperature, humidity, etc.)
2. The importance of powder flowability
3. Powder layer quality indicators
    3.1. Surface roughness-S.R. and S.R. distribution
    3.2. Packing density-P.D. (also known as powder compaction level) and P.D. distribution
    3.3. Appearance of surface defects (e.g., cracks, separations, cavities)
    3.4. Accuracy of achieving the desired layer thickness

4. Methods of measuring powder layer quality indicators
5. Finished product quality indicators

    5.1. Density/porosity percentage
    5.2. Tensile strength/elongation at break
    5.3. Hardness
    5.4. Surface roughness
    5.5. Dimensional accuracy
    5.6. Appearance of superficial or internal defects

The following sections constitute a review treatise of each one of the aforementioned five main topics.

2.2 Powder Spreading Process Parameters

Powder Bed Fusion processes are complex, complexity lying in different aspects. Most research papers focus on the interaction between the material and the source of power that performs the sintering/melting of the powder particles. In many works, the powder layer is modelled as a bulk material of density equal to a weighted mean of the bulk density of the powder's raw material and the air. However, the process of recoating/powder layer deposition is of paramount importance, since the layer quality is directly connected to the finished part's quality, so such a simplification is not adequate to simulate reality. In the next sections, not only the importance of each process parameter itself is established, but also the interconnections between the process parameters are identified pairwise and documented in individual Tables based on literature and the authors' deductions. Each one of these Tables (*Table 2.3* to *Table 2.10*) follows at the end of the Section in which the respective process parameter is discussed.

2.2.1 Powder Material

Arguably one of the most important parameters of the powder bed recoating process is the powder material itself, since it defines the intrinsic material properties and characteristics, like bulk density, hardness and Young's modulus and shear modulus of the powder particles, etc. Tiwari et al. (2015) identify 5 categories of materials suitable

for Selective Laser Sintering (SLS), which is one among the seven PBF processes mentioned in *Table 2.1*. These categories are polymers, ceramics, metals, composites and bio-materials [22]. *Table 2.2* records which powder materials, PSDs and particle shapes are found in various PBF processes in many recent works. Singh et al. (2017) present the commercial machine manufacturers and material providers of all the PBF processes that appear on *Table 2.1* [23].

Table 2.2: Material, particle size distribution and particle shape found in literature.

Reference	Material	Particle size distribution	Particle shape	Process
Ferreto et al. (2021) [24]	Fe-Mn-Si alloy (**M**)	d_{50}=29.7μm, d∈(10,50)μm	Spherical (mostly)	LPBF-SLM
Rouzé l'Alzit et al. (2021) [25]	Cu-doped HAP (**CER**, **BM**)	d<5μm (est. by film layer thickness)	Non-spherical (concluded by photo)	LPBF-SLS
Ullsperger et al. (2021) [26]	Al-Si alloys (**M**)	d_{50}=35μm, (d_{10}=16μm, d_{90}=56μm)	Approximately spherical	LPBF-SLM
Pramanik et al. (2021) [27]	Fe-Co alloys (**M**)	Gaussian, d_{50}=38μm, d∈(10,100)μm	Spherical	LPBF-SLM
Soundarapandiyan et al. (2021) [28]	Ti6Al4V (**M**)	$d_{v,10}$=45μm, $d_{v,50}$=69μm, $d_{v,90}$=105μm (virgin) $d_{r,10}$=47μm, $d_{r,50}$=71μm, $d_{r,90}$=107μm (recycled)	Spherical with few satellites, elongations, irregularly shaped particles and particles with open porosities	EBM
Bae et al. (2020) [29]	Al_2O_3(alumina)/ Glass (**COM**)	$d_{50,\ Alumina}$≈1μm $d_{50,\ Glass}$=15μm, $d_{max,\ Glass}$=50μm (opt. mix ratio Glass:Alumina= 70:30)	Irregular, highly angular (glass frit, concluded by photo) Not mentioned (Alumina powder)	LPBF-SLS
Xianglong et al. (2021) [30]	Stainless steel 316L (**M**)	d_{10}=20μm, d_{50}=29μm, d_{90}=45μm	Spherical (produced via gas atomization)	LPBF-SLM
Sofia et al. (2018) [31]	Limestone-soda glass beads (L-S) & ceramic powder (CP) (**CER**)	(6 bimodal mixtures) Sauter mean diameter $d_{i,1}$ and $d_{i,2}$ (in μm) couples	Spherical (glass beads) & irregular with sharp edges (ceramic material)	LPBF-SLS

		(27,160) (L-S), (86,184) (L-S), (27,184) (L-S), (48,184) (L-S), (22.5,104.2) (CP), (51,104.2) (CP)		
Sofia et al. (2018) [32]	Limestone-soda glass beads (**CER**)	(Examined d_{50} between 16 and 184μm)- Optimum product strength at d_{50}=48μm	Spherical	LPBF-SLS
Ziółkowski et al. (2021) [33]	Inconel 718 (**M**)	d_{10}=19.62μm, d_{50}=34.6μm, d_{90}=55.23μm	Mostly spherical (few satellites and irregularly shaped particles)	LPBF-SLM
Gu et al. (2019) [34]	Poly- (ethylene terephthalate) (PET) (**P**)	$d_{f,10}$=23μm, $d_{f,50}$=46μm, $d_{f,90}$=89μm (fresh) $d_{h\text{-}a,10}$=25μm, $d_{h\text{-}a,50}$=49μm, $d_{h\text{-}a,90}$=93μm (heat-aged)	Irregular, “like potatoes and carrots” (similar for fresh and heat-aged powder)	LPBF-SLS
Tan et al. (2021) [35]	PA12 and glass fibres (**COM**)	$d_{50,\ PA12}\approx$50μm d_{fibre}=8μm, $L_{fibre}\in$[80,120]μm	PA12: Complex, non-spherical Fibres: Spherocylindrical shape	LPBF-SLS

(**Note:** **P**=Polymers, **M**=Metals, **CER**=Ceramics, **COM**=Composites, **BM**=Bio-materials.)

The ratio of virgin/recycled powder used for the process also affects the composition of the powder, since recycled powder has been affected by both the mechanical interactions during the spreading stage and the heat during the printing stage and the concentration of each ingredient in the particles has changed (increased O, slightly decreased Al, V) [36], [37]. Moreover, reused powder has a narrower PSD (less satellites and fines, so an increased D_{10} too) ([28], [38]), slightly decreased sphericity (even though there are studies that contradict this, e.g. [28]) but significantly lower roundness (particles getting bumps by the collisions during previous uses) and most of the humidity has been dissipated by the heat of the previous cycles, factors that increase flowability.

However, evaluating the effect of powder reuse exceeds the purpose of this chapter, since it has been reported in other sources [36], [37]. In alloys, the concentration change might be an effect of evaporation of a metal during the heating of the particle, which leads to the lowering of the concentration of this metal in the used powder. *Table 2.3* presents the interconnections between the powder material and the other process parameters of powder deposition for PBF processes.

Table 2.3: Interconnections between powder material and the other process parameters for PBF.

	1. Powder material
2. PSD	***Polymers:*** d_{50}=50-90μm ***Metal:*** d_{50}=20-100μm ***Ceramic:*** d_{50}=40-60μm ***Composites:*** $d_{50,matrix}$=(same as in the matrix material's category) $d_{50,reinforcement} \leq 0.1 \cdot d_{50,matrix}$ $d_{50} \approx$20μm (avg.) ***Bio-material:*** $d_{50} \approx$20μm (avg.) [22], [29]
3. Particle shape	**Polymers:** Mostly irregular, with rounded edges **Metal:** Mostly spherical, few satellites and irregular ones **Ceramic:** Sometimes spherical (e.g., glass beads), others irregular and highly angular (e.g., glass frit)
4. Recoater material	Any combination is viable. **Metal recoaters**: not suitable for **ferromagnetic powders**. Similarly, the combination of recoater-powder materials that can both get electrostatically charged is to be avoided.
5. Recoater shape	This relationship has not been studied in literature.
6. Recoating strategy	This relationship has not been studied in literature.
7. Layer thickness	The connection can be made via the connection between the **1-2** and **2-7** boxes (Typical PSD for each material and layer thickness limitations due to PSD respectively)
8. Environmental parameters	Different materials require different preheating and chamber conditions (e.g., **metals** require **less humidity** and **no oxygen**, to avoid oxidation and chemisorption). **Polymers** get **tribocharged** and their cohesion↑ in very low humidity (RH<20%).

2.2.1.1 Polymers

Polymers are widely used in SLS and SHS processes. Additionally, they have been among the first materials that have been used in SLS, since Nylon 11 (also known as Polyamide-PA 11) has been in use since 1993 [22]. The particle size (d_{50}) of polymer

powders for PBF processes ranges between 50 and 90μm [22]. Kruth et al. (2009) provide two categorizations of polymers, the first based on their structure (thermoplastics -either (semi-)crystalline or amorphous- and thermosets) and the second on their applications [39]. They also provide details about the main binding mechanisms encountered in polymers during SLS and SLM, by using Differential Scanning Calorimetry techniques (DSC) to establish how suitable they are for PBF processes. However, they do not focus on the intrinsic properties that define the spreadability and flowability of each powder material. Bourell et al. (2017) mostly identify semi-crystalline polymers, like PA11, PA12 and polypropylene, as suitable for PBF, with the exception of a few amorphous ones, like polystyrene. Additionally, they stress the importance of powder flowability for the quality of the finished part [40]. Leigh et al. (2020) provide a complete list of polymer materials used in PBF processes, with emphasis on mechanical properties, post-processing, finishing and potential defects of the finished parts [41]. However, they do not examine how the powder rheological characteristics and spreadability of powder affect the finished parts' properties, or which factors they depend on.

2.2.1.2 Ceramics

Ceramics, like limestone-soda glass, calcium phosphate, silicon carbide, silica, zirconia and alumina have been used for decades in PBF processes. PBF processes and AM in general has been really important in the effort to develop ceramic parts of arbitrarily complex shapes, since this task has proved itself to be extremely challenging with other manufacturing methods [42]. Ceramic materials are widely used to make engine and propulsion components in aerospace, automobile and energy applications, either as thermal insulation (thermal coat barriers-TBC) or as structural materials. Also, they are used in dentistry and even in electronic components such as fuel cells, solar cells and microchips [43]. The reason that they have such a wide range of fields in which they are used is their mechanical strength and hardness, their thermal and chemical stability as well as their viable thermal, optical, electrical and magnetic performance [42]. However, the very high melting temperatures make it very difficult to produce ceramic parts by PBF processes, especially by solely employing SLS, SLM or EBM techniques without a binding material that melts at a lower temperature in order to create bridging between the ceramic particles. Also, it has been proven that the density of ceramic PBF-

manufactured parts is quite low [44] (reversely, the porosity is high), unless some infiltration follows the initial solidification stage, during which a green part is composed. These factors, combined with the high shrinkage, due to the high temperature gradient show why 3DP (BJP) is more promising for the 3D printing of ceramic parts [43]. Furthermore, ceramics (especially glass fibers or glass beads) are used as part in composite mixtures, with metals or polymers being the counterpart of the composite mixture. Chen et al. (2019) have provided a good report on the current state-of-the-art and challenges that the 3D printing of ceramics faces, for each different category of AM [42].

2.2.1.3 Metals

Metals and their alloys are widely used in PBF processes, especially SLM and EBM since they can easily melt completely and enhance their mechanical properties during the cooling-solidification process, while forming dense, low-porosity parts at the same time. The fact that the cooling rate and heating-cooling pattern followed can define the microstructure and vary the mechanical properties of a metal as the manufacturer sees fit for each application makes metals extremely versatile all-purpose materials. More specifically, the grain microstructure of metal parts made by PBF depends on the temperature gradient and the solidification interface velocity [45]. Various metals have been employed in PBF processes, like aluminum alloys (e.g., Al6063 and Al3003), titanium alloys (e.g., Ti-6Al-4V), stainless steel, tungsten, etc. The challenge in powder layer spreading for metal PBF is to ensure that the powder bed is of high quality and not causing defects, since the smallest defects can drastically affect the cooling rate or temperature gradient, hence the microstructure of the finished part.

2.2.1.4 Composites

Composites are materials who are formed by combining two or more materials of different properties, without dissolving or blending them into each other. Puttegowda et al. (2018) define composites as material structures consisting of two materials that can be macroscopically identified and assist each other into creating a superior structure [46]. Composites have been employed in almost every kind of industry, aiming to exploit their superior properties to common materials, like metals, polymers, ceramics, etc. Composites typically consist of the matrix material, which must be homogeneous

and completely continuous, and the reinforcement, which must be evenly distributed inside the matrix in order for the composite to be developed.

Industries must be able to develop parts from composites in any shape, regardless of the complexity. This is the reason why AM, and especially PBF processes are a very promising field for the manufacturing of composite parts. In literature there are already many works towards this direction. Shishkovsky et al. (2018) developed functionally graded nickel-TiC composite structures by increasing the TiC concentration in the NiCrSiB matrix [47]. In their work, SLM was used, the matrix powder particles had a 60-80μm size dispersion and the TiC particles were of cubic shape with a side ranging between 40 and 60nm. Chueh et al. (2020) developed an ultrasound-assisted nozzle recoating system and method to perform multi-material PBF of polymer-metal or polymer-ceramic composites, using PA11 as polymer (matrix) and Cu10Sn (metal alloy) or Al_2O_3 (ceramic) and soda-lime glass (ceramic) powders [48]. Their excellent work combines novelty in the new field of multi-material powder deposition and PBF, which is expected to open new horizons for additive manufacturing, and the field of composites. Zhang et al. (2020) developed metal-glass functionally graded composite materials via multi-material SLM [49]. Bae et al. (2020) developed a composite material for PBF by combining Al_2O_3 (ceramic powder of $d_{50}\approx1\mu m$) with a low-melting-point glass powder of $d_{50}=15\mu m$ and $d_{max}=50\mu m$ [29], which agrees with the particle size distribution suggested by Tiwari et al. (2015) [22]. Finally, the work on composites is not only limited in experimental and theoretical background, since Tan et al. (2021) evaluated the packing quality of a polymer (PA12)/ glass fibre composite where the fibres had a sphero-cylinder shape (elongated, spherical ending cylinders). They studied the angle of repose experimentally and via DEM simulation to calibrate the inputs of the simulation, then they ran roller recoating powder layer spreading simulations via a DEM model [35].

2.2.1.5 Bio-Materials

Bio-materials is a special material category. Despite being composed by materials that can be classified under the four aforementioned categories, there is the distinct difference between their functionality. Bio-materials are termed “bio” because they provide characteristics like mechanical strength, lightness, porosity etc. that enables them to be used in order to build parts that can be implanted into living organisms to

facilitate some biological process. According to Kam Leong, “a biomaterial is now defined as a substance that has been engineered to take a form which, alone or as part of a complex system, is used to direct, by control of interactions with components of living systems, the course of any therapeutic or diagnostic procedure” (Kam Leong, Biomaterials, 2021) [50]. Bio-materials might be used to develop implants or medical devices to enhance or repair some damage caused to the tissue of a living body, hence improving the quality of life and prolonging life expectancy [51]. Hudecki et al. (2019) offer an extensive review of the categories under which the bio-materials can get classified, presenting various examples of metals/alloys, biopolymers, ceramics and bio-composites. They also present the basic properties a material must have in order to be eligible to be used as a bio-material [51]. Nouri et al. (2021) provide a review of the additive manufacturing of load-bearing biomaterials. They point out that, in the field of bio-materials, SLS focuses on the processing of polymers, ceramics and their composites, while SLM and DMLS are mainly used to develop parts made of metals and their alloys [52]. Barui et al. (2019) examine the use of BJP to manufacture parts from bio-materials, focusing on Ti-6Al-4V [21]. Bose et al. (2018) and Harun et al. (2018) provide invaluable detailed information on every single aspect of the additive manufacturing of bio-materials, ranging from the required powder size distribution, average particle size and optimum material for each different AM process, to the microstructure and mechanical properties of the developed parts [53], [54].

Bio-materials are mentioned here for reasons of completeness and clarity; however, a more detailed review exceeds the purpose of this review.

2.2.2 Particle Size Distribution (PSD)

Dobson et al. (2021) point out that the percentage of fine particulate within the powder directly affects its flowability. More specifically, there is a threshold of fine particulate percentage, above which the powder is no longer spreadable via a doctor blade. This is because, the smaller the particle size, the greater the effect of cohesive forces between the particles and the adhesive forces between the particles and the recoater. Van der Waals forces overcome the effect of gravitational forces, preventing the powder from forming a homogeneous, even layer onto the substrate. Dobson et al. (2021) noticed that 17-4 PH stainless steel powder with approximately 30% of powder volume having

particle diameter <15μm was spread successfully. However, when that percentage increased to 55% it was impossible to spread an acceptable for LPBF-SLM layer [55].

In order to evaluate the PSD's effect on the powder flowability and spreadability, it is necessary to divide it into some parameters. A PSD might be unimodal, bimodal or even multimodal, meaning that the volume distribution function diagram has one, two or many peaks. It has been found that a bimodal PSD positively affects the packing density of the layer, since the fine particles gather in the gaps between the coarse particles, essentially diminishing the big gaps and drastically reducing the porosity of the layer. Karapatis et al. (2002) [56] and Spierings et al. (2009) [57] defined some relations between the fine and coarse particle sizes and the layer actual thickness that need to apply in order to ensure that the increased quantity of fines will not have a negative impact on the flowability and have negative effects on the layer surface roughness and packing density instead. More specifically, the requirements they have set are the following (*Equations (2.1)* to *(2.3)*):

$$t_{eff} > D_{90}, \text{ typically, } \frac{t_{eff}}{D_{90}} \approx 1.5 \quad (2.1)$$

$$\frac{D_{50}}{D_{10}} \in [1.4,2.5], \text{ with } D_{10} \geq 5\mu m \quad (2.2)$$

$$\frac{D_{90}}{D_{10}} \in [2, 5], \text{ typically } \frac{D_{90}}{D_{10}} \approx 5 \quad (2.3)$$

These requirements set a reasonably narrow PSD for unimodal powders, meaning that, in general, narrow PSD promote good flow. This does not mean that bimodal powders or powders with a wider PSD cannot flow well enough to form a uniform, even and homogeneous layer, it just means that some compensation must be applied because they lack in flowability due to the cohesive forces that the fine particles introduce, since they function as satellites for the coarse ones, decreasing the mobility of the grains. For bimodal powders, the requirements take the form shown in *Equations (2.4)* to *(2.6)*, while each one of the two separate PSDs must comply to the requirements of the unimodal powders:

$$t_{eff} > D_{90,coarse}, \text{ typically: } \frac{t_{eff}}{D_{90,coarse}} \approx 1.5 \quad (2.4)$$

$$\frac{D_{50,coarse}}{D_{50,fine}} \geq 10, \text{ with } D_{10,fine} \geq 5\mu m \quad (2.5)$$

$$\frac{m_{coarse}}{m_{fine}} \approx \frac{7}{3} \quad (2.6)$$

Additionally, powders with a wider PSD are more prone to developing agglomerates and clusters, causing voids on the powder bed, or even lines caused by the dragging of the agglomerate by the recoater.

Table 2.4: Interconnections between particle size distribution and the other process parameters for PBF.

	2. PSD
1. Powder material	**See *Table 2.3*.**
3. Particle shape	Sphericity↑ ⇒ Flowability↑. The smaller the particles, the higher the possibility that they are less spherical [58].
4. Recoater material	**Finer particles** and PSDs with **smaller D_{10} value** should be spread with **recoaters made by materials with smaller surface energy**, to **minimize adhesion** forces and stickiness. Polymers>ceramics>metals is the order from the most to the least favourable recoater material.
5. Recoater shape	Powders with narrow PSD show better flowability, but particles with wider PSD (lower d_{10}, same d_{90}) or bimodal powders can offer better packing density, as long as they are spread evenly. **Wider PSD and bimodal powders are more cohesive**, so recoaters of **higher compressive force are preferable** (round blade>roller>vertical blade).
6. Recoating strategy	Powders with **wide PSDs** are more **prone to segregation** during recoating. A sieve should be used to refresh the powder in front of the recoater. **Sieve/Doctor blade/roller assembly** offers **optimal** packing density and roughness **consistency along the powder bed** [59].
7. Layer thickness	$t_{eff}>\Delta H=t_{nom}$ $t_{act}\neq t_{nom}$ (To define t_{act}, middle line must be found, based on roughness) $t_{eff}\geq d_{max}$ $\left({}^{t_{eff}}/_{D_{90}}\right) \cong 1.5$ [57].
8. Environmental parameters	Moisture absorption $\xrightarrow{Particle\ swelling}$ Size↑⇒Necessity for t_{nom} to ↑ Similar for adsorption, during which the particle diameter effectively ↑, due to the surface attachment of water molecules.

Weaver et al. (2021) suggest that, even though it is known that a smaller particle size increases adhesive and cohesive forces, reducing flowability and deteriorating the

quality of the powder layer in terms of packing density and roughness, in order to make connections between finished part's quality and PSD it is necessary to control the morphology, shape and chemistry tighter. They suggest that it would be valuable to create different PSD samples by the same batch of powder before running comparative experiments, and ensuring the powder layers that will be created are identical in terms of powder layer quality indicators [60]. *Table 2.4* presents the interconnections between the particle size distribution and the other process parameters of powder deposition for PBF processes.

2.2.3 Particle Shape

The shape of particles affects the flowability of the powder. It has been proven that higher sphericity and roundness promote good powder flow because of less particle interlocking and the sphere's natural ability to roll smoothly, causing less unpredictable collisions compared to irregularly shaped particles [61]. Also, irregularly shaped particles are more prone to adsorption, which means that an increase in relative humidity will make such powders more cohesive compared to powder with almost spherical particles.

Sphericity (Ψ) is calculated as shown in *Equation (2.7)*:

$$\Psi = \frac{S_n}{S} = \frac{\sqrt[3]{36\pi V^2}}{S} \qquad (2.7)$$

Where S_n is the nominal surface area, i.e., the surface area of a sphere that has the same volume as the particle that is being examined, and S, V are the particle's actual surface area and volume respectively. The 2D equivalent of sphericity is the circularity (C), which is defined as in *Equation (2.8)*:

$$C = \frac{4\pi S}{P^2} \qquad (2.8)$$

Where S is the surface and P is the perimeter of the 2D trace of the particle. Both the sphericity and circularity range from 1, for spherical/circular shapes, to 0, for elongated shapes.

While sphericity is a good indicator of how closely a 3D particle's surface approaches the surface sphere of the same volume, it is not enough to estimate how closely the

shape of the particle approaches the shape of a sphere as well. For this reason, roundness (R) is defined. 2-dimensional roundness (R) is defined as the ratio of the average radius of curvature of the corners of the object's silhouette to the radius of the maximum inscribed circle, as shown in *Equation (2.9)*

$$R = \frac{\sum_{i=1}^{n} r_i}{n \cdot r_{max}} \qquad (2.9)$$

Where n is the number of corners of the maximum particle's 2D trace and r_{max} is the radius of the maximum inscribed circle. However, roundness is a 3D property, and it can be calculated by defining the oriented bounding box (OBB) and its reference ellipsoid via principal component analysis (PCA). Then, the 3D roundness can be calculated as in *Equation (2.10)*:

$$R = \frac{V}{S\sqrt[3]{abc}} \qquad (2.10)$$

Where a, b, c the principal axis lengths of the reference ellipsoid, V and S are the volume and surface area of the particle respectively. Cruz-Matías et al. (2019) also devised a method to calculate 3D-roundness via extreme vertices modeling of the particle, method that saves computational time and has equal accuracy as the aforementioned method [62].

Sphericity and roundness are enough to determine the particle shape's relevance to the optimum, perfect spherical shape. However, it has been observed that, in most research papers found in literature, the authors use the term "sphericity" abstractly to describe both how spherical a particle is volume-wise and how smooth and round a particle is, which is causing misinterpretations of the findings and the authors' deductions. This should be addressed and a commonly accepted terminology should be followed, in order for the findings to be presented in a uniform manner.

It is undoubtedly easier to develop DEM models for the simulation of powder spreading based on spherical particles. However, this simplification does not always lead to realistic results, as powders sometimes include irregular shapes, or it is even possible that particles of some materials are purposefully alternatively shaped (e.g., spherocylindrical glass fibres [35]). The most common method of modelling irregularly-shaped particles is to combine a number of spheres together by defining the

coordinates of their centres and the distances between their centres, so as to create a new particle [35]. In many works this has been a method of creating particles with highly angular shapes. The point of such studies is to approximate the real particle shape as closely as possible in order to resemble the actual powder. Nasato et al. (2020) used X-ray computed tomography (3D) and SEM imaging (2D) in order to acquire the shape data of particles and then represented them with multi-sphere models. However, their choice to use 2D particle traces obtained via SEM in order to create a 3D model of particles is controversial, since the reconstruction of a 3D object based on 2D data induces unwanted uncertainty into the simulations and might cause non-realistic results [40]. There are also studies that optimize this process by managing to achieve acceptable resemblance of powder particle models with the real particles by using a minimum of spheres [63], which do not necessarily only have contact points with each other, but might overlap to create a complex shape with the minimum amount of spheres [64]. This is incredibly important, since, even though it is easy to use a large number of spheres to combine them together and develop the model of the real particle with high dimensional accuracy, the more the spheres, the more the computational cost, hence the more time necessary for the simulation to run to completion.

It has been proved that powder reuse affects both the PSD and the particle shape. Soundarapandiyan et al. (2021) showed via SEM analysis and by introducing certain criteria to categorize a 2D-trace of a particle as spherical, satellite, irregular or fine, that recycled powder has improved sphericity, better flowability (due to less satellites and fines) and better packing behaviour (less cohesion overall, since sphericity was higher and fines/satellites were less) [28]. However, the oxygen content of the particles also increased by 25% between virgin and 10-times-recycled Ti6Al4V powder. However, it is possible that, in the reused powder, sphericity increased slightly, but the roundness of particles dropped significantly, as stated by Ghods et al. (2020) [38]. In general, during powder reuse, the particles tend to collide with each other, the substrate and the recoater, losing their roundness and smoothness. However, sphericity is generally not greatly affected.

Sutton et al. (2017) provide a review of powder characterization techniques commonly used in AM, as well as a review of 2D shape factors (circularity, elongation, aspect ratio, dispersion, roundness, flatness, perimeter to area ratio) used for particle shape

characterization and of the manufacturing methods used to create powders for AM (water/gas/plasma/centrifugal atomization, PREP) [61].

Finally, the less spherical powder particles show higher sensitivity to layer thickness variations, which negatively affects the powder bed layer quality [58]. *Table 2.5* presents the interconnections between the particle shape and the other process parameters of powder deposition for PBF processes.

Table 2.5: Interconnections between particle shape and the other process parameters for PBF.

	3. Particle shape
1. Powder material	**See *Table 2.3*.**
2. PSD	**See *Table 2.4*.**
4. Recoater material	**Harder blade recoaters** or **rollers** opted for **less spherical particles**, since the higher compressive forces are necessary to overcome the powder cohesion. Important to select **non-stick materials for recoaters**.
5. Recoater shape	**Harder blade recoaters, rounded blades** or **rollers** opted for **less spherical particles**, since the higher compressive forces are necessary to overcome the powder cohesion.
6. Recoating strategy	Sphericity↓⇒ Powder cohesion↑ ⇒ **Controlled ultrasound or micro-vibrative excitation** needs to be applied on recoater for **better compaction of the irregularly shaped particles** to promote better spatial arrangement.
7. Layer thickness	**Average particle diameter** is **not enough to set the minimum t_{act}** for **irregularly shaped particles**. The largest length of the D_{90}-sized particles needs to be measured, since it can orientate in the gap between recoater and substrate and block it, or get dragged and create defects, or just reduce flowability and even distribution of flow and compressive/shear forces.
8. Environmental parameters	**Sphericity**↓$\overset{RH=ct}{\Longrightarrow}$ Adsorption↑⇒ Powder cohesion↑⇒Layer quality↓ In order to use less spherical particles of the same powder, the **RH** needs to be lowered in order to keep cohesiveness at the same level (or increase **temperature** to achieve adsorption compensation via desorption)

2.2.4 Recoater Material

Shamsdini et al. (2021) examined the effect of using different material recoating blades, one of high hardness, made of ceramic material (ZrO_2) and one softer, made of carbon fibre brush. They proved that, even though yield and ultimate tensile strength of the samples made of brush (LPBF-Brush) and the ones made of ceramic recoater (LPBF-Ceramic) are almost the same, the LPBF-Brush samples lack severely in ductility and strain hardening [65]. Both samples are almost fully dense beneath the top 2-3 mm. It is suggested that the hard recoater might be able to apply more pressure in order to increase packing density, but the soft recoater applies the powder more gently, enabling the motion of the finer particles [65]. However, this suggestion needs validation through simulations and experiments. Furthermore, LPBF-Brush samples show the emergence of micro-voids that engulf unmelted powder, leading to a higher martensitic fraction and a lower austenitic fraction, with the austenitic regions being non-continuous, which negatively affects the ductility. However, the reason of the micro-void emergence is not explained in the article [65]. Daňa et al. (2019) examined the effect of different recoated materials based on their compliance on the dimensional accuracy of the finished part, based on the fact that, the harder the blade's material, the more vibration it inflicts on the part that is getting build if it collides accidentally with some solidified protrusion of the previous layer. A hard recoater inflicts vibrations, and creates a tiny gap bilaterally of the solidified protrusion. This creates an unevenness of the new powder layer, leading to dimensional inaccuracies of the finished part. In some cases, this collision can even distort or slightly move the solidified part, leading to improper relative position of the layers, which again leads to dimensional inaccuracies. Instead, more compliant recoating blades minimize or even eliminate this vibration, ensuring the dimensional accuracy of the finished part [66].

Wohlfart (2020) has made some significant observations about the material of recoater (doctor blades) and when a hard (made of HSS or ceramic) and soft (carbon fibre, silicon or nitryle butadiene rubber-NBR) recoater should be preferred [67]. The harder recoaters provide higher powder compaction, as well as higher repeatability and consistency in terms of powder layer thickness. They also can remove spatter from the powder bed, effectively "cleaning" the contaminated area and preventing layer surface defects. They show superior wear resistance, are more expensive, but last longer than

softer recoaters. However, due to their rigidity, if the previous layer has formed any protrusions during its solidification, the contact with the blade will either destroy the recoater, or move the part slightly, causing dimensional inaccuracies [67], [68]. Also, due to the high friction forces, it is impossible to use a hard recoater when high aspect ratio parts are being built, since this could bend the part and cause dimensional inaccuracies. This issue could partly be solved via selecting the proper part orientation for building. Also, in case of a magnetizable powder material such as ferromagnetic powders, a hard recoater can only be ceramic, since steel would force the particles to stick on the blade.

Table 2.6: Interconnections between recoater material and the other process parameters for PBF.

	4. Recoater material
1. Powder material	**See *Table 2.3*.**
2. PSD	**See *Table 2.4*.**
3. Particle shape	**See *Table 2.5*.**
5. Recoater shape	**Rollers:** Stainless steel (e.g., 316L) **Doctor blades:** Stainless steel, ceramics or compliant polymers
6. Recoating strategy	Useful to examine recoater material-spreading translational speed for various recoater shapes and patterns. No such work exists to the knowledge of the authors.
7. Layer thickness	Harder recoaters⇒ compression↑ $\xrightarrow{friction\uparrow}$ unwanted vibrations to powder layer and surface defects, the effect of which is more detrimental the smaller the t_{act}.
8. Environmental parameters	Temperature↑ $\xrightarrow{thermal\ expansion}$ **metal (steel or aluminium) and polymer recoaters expand more** than ceramic ones, which affects the accuracy of achieving the t_{act} that is preset by the slicer (post compensation). Humidity↑ $\xrightarrow{adsorption}$ Powder **cohesion**↑⇒ Opt for recoaters made of materials with lower surface energy to minimize adhesion of powder on recoater (polymers>ceramics>metals order from the most to the least preferable) [69].

On the other side, the main advantage of a soft recoater is the fact that it can build fragile geometries and large aspect ratio parts more easily, since the friction forces are much smaller due to its compliance and there is less risk for the part or blade to break. Also, it is less possible to create vibrations that will be transferred into the powder layer

in the form of waviness, due to the friction forces. Finally, it will not break or create dimensional inaccuracies in the case of collision with a solidified protrusion of the previous layer, thanks to its compliance [67].

Table 2.6 presents the interconnections between the recoater material and the other process parameters of powder deposition for PBF processes.

2.2.5 Recoater Shape

Haeri et al. (2017) have proved by DEM simulations that, under the same operating conditions (translational velocity of the recoater, layer thickness) and for the same powder, a counter-rotating roller outperforms a doctor blade, due to the "inadequate contact of a blade with the bed, which causes particle dragging and degrades the bed quality" (Haeri et al., 2017) [70]. Zhang et al. (2020) examined the counter-rotating roller as a means for powder spreading and deduced that, as the cylinder diameter increases, the compression powder zone increases, hence the packing density of the layer is increased [71]. However, this only applies to a certain limit, because, if the compressive force becomes too strong and the layer thickness does not increase to distribute this increased force into a larger volume, then the powder layer breaks and entire crust pieces get dragged along the surface by the roller, destroying the layer. Budding et al. (2013) proved that, for the examined powder and spreading patterns, the optimal setting was a counter rotating pattern with a roller of 22 mm diameter (the alternative was a 12mm diameter) [72]. Furthermore, it has been proven, that inclined recoaters apply more compressive force onto the applied layer, which can lead to higher packing density, but only if the deposition remains smooth and without particle burst or jamming phenomena [73].

Haeri (2017) examined different profile shapes for vertical blade spreaders and how the profile effects the result of the deposited powder layer. He used DEM simulations with rod-like particles of 10^{-4} m diameter (D_{sph}) first, and a super-elliptic profile (see *Equation (2.11)*, recoater spreads along the y-axis) was used to define the blade's profile.

$$\left|\frac{y}{a_s}\right|^{n_s} + \left|\frac{z}{b_s}\right|^{n_s} = 1 \qquad (2.11)$$

He deduced that, for a vertical blade (zero inclination) and a gap between the blade and the substrate equal to $5D_{sph}$, to ensure homogenous speed profile of the flow, the optimum parameters were $n_s = 5.0, a_s = 100D_{sph}, b_s = 10D_{sph}$. For these values, the recoating result was compared to a counter-rotating roller spreading result with the same translational velocity and gap. For these DEM simulations, realistic multi-sphere particle models were used. Even though the same trend is observed (increasing translational speed reduces packing density and increases surface roughness of the deposited layer), the surface roughness achieved by the optimized blade is smaller than the one achieved by the counter-rotating roller and the packing density achieved via the blade is higher than the one achieved via the roller with an exception for very low translational velocities. Furthermore, the blade-achieved packing density is much less affected by the increase in translational velocity than the roller-achieved, which might be an effect of the particle burst phenomenon, which intensifies for a counter-rotating roller at high velocities, and diminishes the positive effect of the high compressive force. The super-elliptic profile blade is a similar case with the round blade, meaning that -contrariwise to the counter-rotating roller- despite of the high compressive force that it applies onto the layer, it causes zero particle motion conflict in the compaction region, so it is immune to particle burst phenomenon [64], [73].

Wang et al. (2021) [73] examined various shapes of recoaters by employing DEM simulations. More specifically, they examined the inclined blade, declined blade, vertical blade, wide blade, counter-rotating roller and round blade. They came to some interesting conclusions. Specifically:

1. In terms of deposited particle volume, the order from the highest (optimum) to the lowest is round blade > inclined blade > roller, but for larger nominal thickness it can be roller > inclined blade.

2. In terms of transmitting contact forces to the underlying part, the order for the highest to the lowest is round blade > roller > inclined blade > vertical blade. Let us note that, on the one hand high contact forces in the compaction zone are promoting higher packing density and, on the other hand, they are transmitting higher forces onto the building part via friction, increasing the risk of deformation or moving it slightly, causing dimensional errors. It becomes clear

that a golden means must be found to ensure high packing density and prevent any risks for finished part defects.

3. In order of how affected they are from particle burst phenomenon, the order from the one most affected to the least affected (optimum) is roller > inclined blade > vertical blade > round blade.

4. Round blade system has the smallest particle size segregation and roller system has the largest. The segregation highly depends on the degree of particle mixing in the powder pile during recoating, which is promoted by the roller's counter-clockwise rotation.

Table 2.7 presents the interconnections between the recoater shape and the other process parameters of powder deposition for PBF processes.

Table 2.7: Interconnections between recoater shape and the other process parameters for PBF.

	5. Recoater shape
1. Powder material	**See *Table 2.3*.**
2. PSD	**See *Table 2.4*.**
3. Particle shape	**See *Table 2.5*.**
4. Recoater material	**See *Table 2.6*.**
6. Recoating strategy	**Patterns:** Doctor blade (DB, sole, various profile shapes and inclination angles) Roller (R, sole, CW or CCW, or CCW and CW in return) DB&R (CW or CCW) Many different translational and rotating speed combinations
7. Layer thickness	**Roller diameter**↑⇒ Layer Compression↑ up to a certain breaking limit for every **layer thickness** (for every t_{eff}, there is a $D_{r,max}$). Potentially a similar relation applies for an **inclined blade**, since the inclination applies compaction (max. inclination for layer thickness).
8. Environmental parameters	For both high (e.g., roller) or low compressive forces (e.g., doctor blade), a very high or very low relative humidity negatively affects the flowability and compressibility of powder. **Optimum RH** around 45%. Temperature not evaluated in literature.

2.2.6 Recoating Process Parameters and Setup/Spreading Pattern

The recoating process parameters here strictly refer to the setup of the powder deposition system. The main parameters are the recoater's translational velocity (important regardless of recoater shape and general geometrical characteristics), the recoater's angular speed (in the case of a roller), the recoater's direction of rotation (clockwise or counter-clockwise, again, in the case of a roller) and the doctor blade's angle of inclination.

Based on the setup of the powder deposition system (PDS) of each machine, there are various different spreading patterns, term also found in many works as "recoating strategies". The most common strategies are listed here. There are more strategies that can be devised, relying on recoaters of different shapes (like rounded blade [73], which was tested and proved to outperform roller in DEM simulations), but there has been found no experimental work that actually put these to the test to verify the simulation results.

1. Counter-clockwise roller (CCW) (with or without sieve [59])
2. Clockwise roller (with or without sieve [59])
3. Doctor blade (with or without sieve [59])
4. Doctor blade and CCW roller (with or without sieve [59])
5. Doctor blade and CW roller (with or without sieve [59])
6. Doctor blade and CCW roller on forward move of PDS, then tiny z-axis positive move by the fabrication piston and CCW roller on backward move of the PDS (CCW works as front-rotating when the PDS moves from the right to the left of the table)

To the authors' knowledge, up to date, no concentrated, comparative study of all the possible recoating strategies has been written, to identify which one provides better results and at which conditions (in terms of process parameters *2.2.1* to *2.2.8*).

Budding et al. (2013) examined experimentally different setups of powder spreading. Namely, they examined deposition via a doctor blade, a counter-rotating roller, a

forward-rotating roller and a combination of a doctor blade followed by a forward-rotating roller [72]. They proved that the front rolling (CW) roller strategy almost always leads to layer surface separations, destroying the layer, due to the very high compressive forces. It is possible to work only for further compression of the already deposited powder layer (see strategy #6) and at very low translational speeds. Zhang et al. (2020) developed a DEM simulation to examine the dynamics and results achieved by a roller that rotates CCW. They examined the effect on factors such as the roller diameter, the translational and rolling velocity of the roller and the nominal layer thickness [71]. They found that the translational velocity is the most important factor, since, if it increases beyond a limit, it is not possible for the powder layer to maintain a low surface roughness and good packing density. Depending on the particle burst phenomenon, caused by the motion conflict of particles between the recoater and the substrate, the increased translational velocity, especially in the case of a CCW roller, causes highly inhomogeneous surface, at a point that even the obtained layer thickness is highly different in comparison to the expected effective layer thickness [73].

Table 2.8: Interconnections between recoating strategy and the other parameters for PBF.

	6. Recoating strategy
1. Powder material	**See *Table 2.3*.**
2. PSD	**See *Table 2.4*.**
3. Particle shape	**See *Table 2.5*.**
4. Recoater material	**See *Table 2.6*.**
5. Recoater shape	**See *Table 2.7*.**
7. Layer thickness	**Spreading patterns** can incorporate **thickness manipulation**: e.g., CCW roller or blade spreading at (t_{act}+dt), then in return, CW the compaction roller, at a t_{act} thickness. **Spreading translational velocity** and $\mathbf{t_{act}}$ compensate for each other in terms of packing density (if $t_{act}\downarrow$, u_{trans} must also ↓ to achieve same layer quality)
8. Environmental parameters	Humidity$\uparrow \xrightarrow{adsorption}$ Powder **cohesion**↑⇒ Spreading translational velocity must↓ to compensate and maintain layer quality.

Table 2.8 presents the interconnections between the recoating strategy and the other process parameters of powder deposition for PBF processes.

2.2.7 Nominal, Effective and Actual Layer Thickness

When the first powder layer in a PBF process is deposited onto the downwards-moving fabrication piston, the expected layer thickness is equal to the vertical distance between the top surface of the piston and the surface that is defined by the lowest edge of the recoater as it moves along the x-axis (generatrix of a roller or bottom edge of a doctor blade), which will be referred to as the "top surface of the powder layer" from now on. The second layer will be deposited onto the first powder layer, after the piston moves downwards by ΔH. *ΔH* is the nominal layer thickness (t_{nom}), and it is equal to the downwards displacement of the fabrication piston between two subsequent powder layers. However, powder has some specific rheological characteristics that, in combination with the recoater geometry and motion, define the way that powder will be spread onto the substrate, be it the surface of the piston or the previous powder layer. More specifically, based on friction-motion phenomena between the powder particles and the substrate, the top surface of the powder layer is not a perfectly level plane, but it has some roughness, and depending on the spreading parameters and powder characteristics, it might even show some inconsistencies, like craters, peaks and waviness [71], .

After the sintering/melting of the n^{th} layer has been completed, the piston lowers by the nominal thickness, in order for the recoater to spread the $(n+1)^{th}$ powder layer. However, when the particles of the previous layer melted, the molten material fills the voids between the particles, reducing the porosity of the layer. It is even possible that infiltration phenomena will appear, where the molten material infiltrates the nearby non-sintered powder to some extent. Also, during the consolidation of the molten material, some further shrinkage is demonstrated. These phenomena make the top surface of the n^{th} powder layer to be lower compared to where it was before the melting/sintering process took part. The layer height that is measured between the top surface of the n^{th} powder layer after the shrinkage has taken place, and the top of the $(n+1)^{th}$ powder layer before the shrinkage has taken place is termed effective layer thickness (t_{eff}). Jacob et al. (2018) have attributed the difference between effective and nominal layer thickness to melting and consolidation shrinkage of the layer [74]. They defined the *Equations* that calculate the effective layer thickness, as follows:

$$t_{eff,n+1} = t_{eff,n} + \left(t_{shrink,n} - t_{shrink,n-1}\right) \quad (2.12)$$

$$t_{shrink,n} = t_{eff,n} \cdot (1 - \varphi_n) \quad (2.13)$$

Where φ_n is the packing density of the nth layer.

It is necessary, in order to ensure that all layers have a powder of the same PSD, that

$$d_{90} < t_{act,min} = t_{nom} \quad (2.14)$$

For every single layer, from the first one to the last one deposited, the maximum particle size must be approximately smaller than the effective layer thickness, otherwise the largest particles will be dragged by the recoater along the substrate, creating grooves into the newly deposited powder layer, as reported by Utela et al. (2008) in their review over 3DP [19], [75]. Even if they do not cause grooving, if larger particles get dragged away, then the layer will only consist of finer particles, meaning that the deposited powder's PSD will be different than the powder's actual PSD, inserting error between the layers. However, the same principle must be applied on powder layers deposited for every PBF process.

Table 2.9: Interconnections between layer thickness and the other process parameters for PBF.

	7. Layer thickness
1. Powder material	**See *Table 2.3*.**
2. PSD	**See *Table 2.4*.**
3. Particle shape	**See *Table 2.5*.**
4. Recoater material	**See *Table 2.6*.**
5. Recoater shape	**See *Table 2.7*.**
6. Recoating strategy	**See *Table 2.8*.**
8. Environmental parameters	**Humidity**↑ $\xrightarrow{adsorption}$ Powder **cohesion**↑⇒ Layer quality ↓ for the same layer thickness. **Layer thickness** must ↑ to retain the same layer quality standards

Shamsdini et al. (2020) examined the effect of increasing the (nominal) layer thickness from 40μm to 50μm in order to increase the production rate by reducing the time per part. They proved that, for small increases of the layer thickness, even though such a change can affect the microstructure, it is possible to achieve similar mechanical

properties (almost same tensile strength and elongation at break and slightly lower hardness for samples made with higher layer thickness). This is possible even by using the same power/laser-related process parameters (laser scanning speed, laser power, hatch spacing), if they are selected cautiously [76].

Table 2.9 presents the interconnections between the layer thickness and the other process parameters of powder deposition for PBF processes.

2.2.8 Environmental Parameters

An aspect that has not been investigated by many researchers, is the effect of environmental factors on powder rheological characteristics and in the powder spreading process in general. While it has been proved that the temperature of the building chamber, the fabrication plate and the humidity play a major role in the thermal process of sintering or melting and solidification of the powder, few have examined how these factors affect the powder spreading process and what is the connection between these and the rest of the process parameters.

When it comes to humidity, relative humidity shows how much water in vapour form there is in the atmosphere or in this case, in a closed chamber. The vaporized water molecules may come in contact with the powder particles. If this happens, depending on the hygroscopic properties of the material, the water molecules can be absorbed or adsorbed by the particle, which drastically affects its mechanical and rheological characteristics. As mentioned, humidity can affect particles in two ways, via absorption or adsorption. During the former, the particle absorbs the water molecules, being "soaked up" by them, resulting in a uniform concentration of water molecules throughout the entire volume of the particle. Contrariwise, during the latter, the water molecules latch on the outer surface of the particle, surrounding it rather than permeating inside its volume. The higher the relative humidity (RH) of the chamber, the more water molecules will be absorbed and adsorbed by the powder particles.

The water absorption coefficient depends mostly on the material. Other materials (called "hygroscopic", like polymers such as PA6, a type of nylon) can absorb bigger amounts of moisture, and others, like most metals, smaller ones. Moisture absorption is directly connected to the porosity of the powder particles. The more pores a particle has, the more water molecules will get trapped in them. Strømme et al. (2000) proved

that porous glass particles have both a higher absorption rate and capacity compared to solid glass beads despite being of the same material, thanks to the higher porosity they had throughout their volume [77]. Powder particles absorb moisture both by capillary imbibition and swelling. The capillary imbibition happens almost instantaneously, but swelling is a process that takes some time [78]. The swelling of the particles, which is caused by the absorption of moisture, is increasing their size and slightly altering their shape. This makes obvious that, in the case of powder with high moisture absorptivity, it is necessary to keep the RH low, because the size distribution might be altered if the particles absorb enough moisture. The water adsorption on the other hand depends on many parameters besides the material. One of them is temperature. The coefficient of adsorption is inversely proportional to the temperature, meaning that, the higher the temperature, the smaller the amount of water molecules that will be adsorbed by a powder particle. This is explained since it is an exothermic process. However, this only applies to physical adsorption, which is the only case of adsorption that can appear during the powder spreading process, since temperature is too low to trigger chemisorption between oxygen and metallic powders (which might happen during the thermal processing stage of PBF processes). Furthermore, the less spherical a particle is, the larger its outer surface, meaning that the more prone it is to adsorb many water vapour molecules. The same applies if particles have high porosity, since it creates cavities where the water molecules can latch onto the particle. Additionally, if a powder has very fine particles, or many satellites, it means that the fraction of surface/volume is drastically increased for a given amount (mass) of powder. That's why finely powders are more affected by adsorption.

Lefebvre et al. (2019) proved that adsorption happens rapidly and it affects the powder's flowability under low flow stresses (like these observed with a blade recoater), but there is no significant effect on the flowability under high compressive forces (like when a roller recoater is deployed) [79], possibly because the high compressive forces are overwhelming the capillary forces developed between the liquid interparticle cross-links that are created by the water molecules that are adsorbed by the particles [80]. However, since the powder feedstock is initially stored in a silo or a storing piston, it can create many liquid bonds and create agglomerates that either have to be dried out or at least sieved out prior to the recoating, or they have to be broken via the dispensing or recoating system, which faces many difficulties. Reused powder is even more prone

to adsorption compared to virgin powder, because during the work cycles the particles' sphericity lowers and more satellites and fine particles are created, increasing the total surface to volume ratio of the powder. Furthermore, Rescaglio et al. (2017) proved that it is more difficult for a powder to reach a desired tap density via compression when the relative humidity is either too high, due to the liquid bonds and capillary attraction, or too low, because the electrostatic charges become prevalent and increase the powder cohesion [81]. Hence, extreme values of relative humidity can affect negatively the powder flowability in both high and low compressive forces.

Finally, with regard to temperature, it has been shown that the cohesion of powders is affected by temperature. Even though there are plenty articles examining the flowability of a powder, the tests are mainly run at ambient temperatures, even though it is common knowledge in the field of AM that the fabrication piston and the chamber get preheated, in order to minimize the residual stresses and the crack formation and achieve a denser finished part with enhanced mechanical properties [82], [83], [84] [85]. However, some work suggests that the preheating can also have negative results in terms of mechanical strength and hardness [86], so it is important to carefully select the preheating method and the temperature range of both the chamber and the building plate. The preheating temperature is selected based on the glass transition temperature for polymer powders (calculated via Differential Scanning Calorimetry-DSC), and the melting point for alloys and metallic powders. More specifically, the preheating of polymers happens at a temperature slightly lower than glass transition [87], and the preheating temperature for metals and alloys commonly stands at about one fourth to half of the melting temperature [84], [82], [86], even though preheating temperatures at even one tenth of the melting temperature have been used (e.g., for Ti-6Al-4V) [84]. Especially at very high temperatures, many researchers have proved that the difference compared with the storage temperature contributed in a change of the powder's flowability, attributed mainly to the difference in powder cohesion [88]. However, it has not been possible to establish a univocal connection between the temperature and the powder's rheological properties, leading to the conclusion that other parameters, such as the powder material and the kind of the test and experimental apparatus used to take measurements affect the results [88].

Table 2.10: Interconnections between environmental parameters and the other process parameters for PBF.

	8. Environmental parameters
1. Powder material	**See *Table 2.3*.**
2. PSD	**See *Table 2.4*.**
3. Particle shape	**See *Table 2.5*.**
4. Recoater material	**See *Table 2.6*.**
5. Recoater shape	**See *Table 2.7*.**
6. Recoating strategy	**See *Table 2.8*.**
7. Layer thickness	**See *Table 2.9*.**

The evaluation of powder's flowability has been performed via various experimental methods and simulations. However, most of these experiments and simulations evaluate the spreadability and rheological properties of the powder in ambient temperature, while this is not the case in PBF processes. It is of paramount importance to develop experiments and DEM simulations that will take under consideration the preheating temperature of the process and how it affects the temperature distribution inside a powder layer in order to accurately predict the result of the powder spreading process. The work of Ruggi et al. (2020) and van der Eynde et al. (2017) are useful towards this direction [88], [89]. The former utilized a custom-made apparatus to measure powder flowability in elevated temperatures and proved that the use of Bond granular number is more characteristic of how well a powder flows in powder layer spreading for PBF processes compared to densification-related tests, such as the Jenike shear test [88]. The latter expanded a custom blade-based powder spreader setup in order to measure temperature with infrared ceramic heaters coupled with PID control loop to maintain constant powder bed temperature. Their device can measure the packing density via measuring the weight of the powder layer and dividing with the layer thickness, and make the connection with the temperature, making it a very useful experimental setup to draw data on the process [89].

Table 2.10 presents the interconnections between the environmental parameters and the other process parameters of powder deposition for PBF processes.

2.3 The Importance of Powder Flowability

Powder flowability, i.e., how easily a powder flows, behaving as a fluid, serves as the connecting link between the process parameters (*Sections 2.2.1* to 2.2.8) and the powder layer quality indicators (*Sections 2.4.1* to *2.4.4*). This is because powder flowability is directly affecting powder spreadability. However, "flowability is not an inherent material property" (Budding et al., 2013) [72]. Flowability is rather, the result of various geometrical and physical properties of the powder examined and its particles, combined with environmental parameters and even the method of measurement [79].

In literature, there are "external variables" defined that affect the way a powder behaves. These are consolidation, aeration, flow (shear) rate, moisture, electrostatic charge and storage time [80]. In the case of powder layer spreading for PBF, the variables that are involved are flow rate, moisture, storage time and, in some cases (e.g., polymer powders) electrostatic charge.

Particle size distribution, particle shape and powder material directly affect powder flowability. It has been stated in literature that "for powders of narrow particle size distribution the most spherical and larger the particles, the better their flow behaviour" (Grossin et al., page 4, 2021 [90]). Furthermore, material is also of crucial importance, since, in the case of polymers, particles get some triboelectric charge during the recoating process, which affects the flowability [91], [79], [81]. Hesse et al. (2019) developed a method to measure the electrostatic current build-up on polymer powder particles during spreading for LPBF-SLS, proving that the charging is significantly enhanced for aged powder material, which potentially affects the flowability of powder mixtures with high reused powder ratio [91]. This does not happen in the case of metals, since the triboelectric charge diminishes rapidly due to the high electrical conductivity of the material. Rescaglio et al. (2017) proved via rotating drum experiments that the increase of powder cohesion caused by the effect of static charges is prevalent in low relative humidity content (below 20%), while the cohesion increase caused by liquid bonds due to adsorption appears at a RH above 50%. The combination of tribocharging and capillary forces contribute to having a minimum of powder cohesion for an RH values approximately equal to 45% [81].

The way in which environmental parameters (temperature, pressure and humidity) affect powder flowability has been examined in *Section 2.2.8*. For fine powders, the small particle size means that the powder flowability is already affected by van der Waals forces, which are not negligible compared to gravitational forces anymore. If this fact gets combined with the liquid interparticle capillary bonds created by the adsorbed water molecules, it is evident that the flowability gets reduced even more.

There are many ways in the form of experiments and devices used to quantify a powder's flowability. Kulkarni et al. (2010) provide a review of the methods used to measure a powder's flowability, including Hall flow tests, density-based flow measuring techniques, flow function-annular shear tester and wall friction angle [92]. Many researchers that have run DEM simulations of the powder spreading process for various different process parameter combinations have used flowability measurement tests to ensure that the property settings used in their powder model (properties such as Young's modulus, rolling and static friction coefficient, etc.) define a powder that behaves exactly like the real one in terms of flowability. The most common combination is the avalanche angle and repose angle. The avalanche angle is measured when the powder is placed in a rolling cylinder, forcing the powder to form an angle with the horizontal plane as it is tipped over by the cylinder's motion. The profile of the powder while the cylinder is rolling at a stable angular velocity and the avalanche angle depend on the powder's cohesiveness and flowability. The angle of repose is the angle that is formed if you pour a powder on a level, horizontal surface. The avalanche angle experiment is the "dynamic" flow test, and the angle of repose experiment is termed "static" flow test. The combination of these two and the accurate comparison of them with a simulation that recreates these experiments is enough to ensure that a powder model closely resembles the real powder [71]. The authors reckon that this is enough since the avalanche angle experiment suggests the powder to both gravitational, cohesive and shear forces inflicted by the wall of the cylinder till a dynamic equilibrium state is reached (if possible), whereas the repose angle experiment only examines the powder's cohesion in respect with the gravitational forces, letting the powder reaches a static equilibrium state. The combination fully recreates every kind of force and motion the powder can potentially be submitted into.

However, in order for a DEM simulation to adequately resemble reality, it is important to define the static and rolling friction coefficients between the particles and the

substrate, as well as between the particles and the recoater and between the particles themselves. Escano et al. (2018) developed a method of measuring the dynamic angle of repose not during an experiment of pouring powder on a level surface, but instead during the powder spreading itself, using high-speed X-ray imaging. This is more accurate compared to the common angle of repose experiment, since it shows how the angle of repose evolves dynamically and how the spreading parameters affect it. They also examined the dynamics of powder clusters, which severely affect the surface quality, both in terms of surface roughness and layer defects. Additionally, they examined the dynamics of single particles, measuring by definition the kinetic friction coefficient between the particles and different substrate materials. However, they could in a similar manner measure the interparticle friction coefficient, by laying a second layer over the previous one and using a similar, adjusted for rough surface substrate, method [93].

2.4 Powder Layer Quality Indicators (PLQIs)

In various studies, the deposited powder layer quality is evaluated by measuring the *powder compaction level* of the layer (in many works termed also as *powder packing density*), the *surface roughness* of the layer, the *appearance of surface defects* (e.g. cracks, separations and cavities) on the deposited layer and the *accuracy of achieving the desired layer thickness*, since the nominal layer thickness, which is equal to the downwards displacement of the fabrication piston is not equal to the actual layer thickness. An even and homogeneous powder layer must have uniform powder packing density throughout its surface, while maintaining relatively small surface roughness and small error between actual and nominal (theoretical) layer thickness. *Table 2.11* presents how the process parameters (*Sections 2.2.1* to *2.2.8*) affect the powder layer quality indicators.

2.4.1 Surface Roughness (SR) and Surface Roughness Distribution (SRD)

Surface roughness of the deposited unsintered/unmelted powder layer is the most reliable quality indicator and the easiest one to use for evaluation of the result of the powder spreading process.

Surface roughness of the deposited powder layer must be kept as low as possible, since an increased roughness value means that the laser/electron beam will strike the layer at a different height, slightly affecting the focus and the energy transfer onto the layer. Even if the change of focus is negligible and has no effect on the thermal phenomena, if the roughness is large, this will be translated into a large roughness of the consolidated layer. Large surface roughness values in successive powder layers mean that the roughness of the consolidated layers will stack up and take the form of error in the vertical dimension of the part, finishing in dimensional inaccuracies (worst case scenario) or bad surface quality (best case scenario).

In various literature sources it has been proven that, not only the powder layer surface roughness can be used as a measure of the powder packing density, since the two properties demonstrate correlation, but also it is directly connected to the finished part's quality. In general, the surface roughness increases with the increase of the powder's cohesiveness [94]. Even though Meier et al. (2018) proved this in the case of a doctor blade recoater, it is safe to assume that a decrease of the powder's flowability due to the increase of cohesive forces would have a negative impact on the surface roughness regardless of the type of the recoater.

It is also shown that, a compliant doctor blade promotes lower SR levels compares to hard, rigid ones, which increase the transfer of unwanted friction-oriented vibrations to the deposited powder layer [95], [96], [67].

It is important to notice that, most of the research articles so far, run experiments or simulations of powder deposition on the fabrication piston's solid and level top surface. They then measure the powder layer quality indicators. This method means that they only evaluate the first layer deposited during the powder deposition process in a PBF manufacturing process, while, the rule is that every other powder is deposited on the previous layer, which is a matrix of consolidated via fusion and unfused powder. The

surface onto which the powder is deposited is a crucial parameter and, in order to come to safe conclusions that will apply throughout the part's 3D building process, it is important to take this under consideration. Xiang et al. (2021) proved how important it is for homogeneous and even powder spreading that the substrate has sufficient layer thickness. They showed that, when the substrate's surface roughness increased from 0 to 9μm, the layer's PD increased at an exponential trend, but when it increased from 9 to 12μm, PD remained unaffected. On the other hand, when the substrate's SR increased from 0 to 6μm, the applied powder layer's surface roughness increased linearly, and when it increased even more, from 6 to 12μm, powder layer's SR increased linearly but at a significantly lower (almost negligible) rate [97]. This leads us to the conclusion that there is a sweet spot at which the consequent deposited powder layers only marginally increase their surface roughness (or not at all), while their packing density is at an optimum. This value in this work is at approximately 9μm of SR.

2.4.2 Packing Density (PD) or Powder Compaction Level (PCL) and Packing Density Distribution (PDD)

It has been proven that the packing density (φ) of the powder layer is directly affecting the density and of the finished part, since it affects its porosity. If the powder compaction level highly varies between points of the powder bed with different coordinates, then the finished part's density will not be uniform throughout its volume, which might render the part unusable, depending on its application.

Research has shown that, in order to maximize PD of a layer, bimodal or multimodal powder mixtures have been used. In this case, the smaller particles fill the interstitial voids that get developed between the larger particles. It is proven that maximum PD is achieved with a size ratio of over 1:10 (coarse: fine particles) and a weight ratio 7:3 (large: small particles) [90].

Shanjani et al. (2008) [98] examined the physics behind the powder spreading with a counter-rotating roller. They proved that, the smaller the compacted layer thickness, the higher its relative density, hence the higher the powder compaction level. However, layer compaction also depends on the accumulation of powder in front of the cylinder. The larger the densification zone, the more compacted the powder layer gets. However, regardless of the kind of recoater, packing density decreases with recoater travel

distance. This is caused by an evolving particle diameter distribution, arising from preferential deposition of finer, gap-filling particles, effect known as segregation [96], [99].

Jacob et al. (2018) established that there is a connection between effective layer thickness and powder layer density (PLD), stating that, the greater the packing density of the powder layer, the smaller the difference between the nominal and the effective layer thickness, and vice versa [74].

Furthermore, it has been shown by Penny et al. (2021) that, for high values of the normalized layer thickness ($t_{norm}=t_{eff}/D_{50}$), the packing density φ follows an *Equation* of the form:

$$\varphi = \alpha\left(1 - e^{-\beta t_{norm}}\right) \qquad (2.15)$$

Where α and β are free parameters, depending on the powder material and characteristics. For 15-45 μm highly spherical particles of Ti-6Al-4V (D_{10}=23.4, D_{50}=31.5 and D_{90}=43.4μm), α and β are equal to 0.5 and 0.3 respectively. An increase of the normalized layer thickness causes an increase of the packing density according to the aforementioned formula [96]. Among α and β, the former represents the packing density of a theoretical layer of infinite size, while the latter is purely flowability-related.

2.4.3 Appearance of Surface Defects (e.g., Cracks, Separations, Cavities)

Layer surface roughness is a good means of detecting powder layer defects, such as cracking, waviness or concentration/dragging of agglomerations. Layer defects like the aforementioned ones must be detected and eliminated, since the error they create gets inherited to the next layers, and it can even act additively, via stacking up of successive layer defects, resulting to poor finished part surface roughness or even to dimensional inaccuracy. Wycisk et al. (2014) suggest that surface and bonding defects in the middle layers increase the possibility of crack initiation [100]. Bonding defects in the middle layers can be caused by a random surface defect, such as a cavity or a high roughness peak of the unmelted powder layer. This would cause the effective thickness of the next layer to be increased locally, potentially leading to the creation of a pore.

Most times, the surface defects are caused by powder agglomerates, i.e., clusters of particles, usually consisted by a core of larger particles merged via interparticle cohesive forces with many smaller ones (fines). These clusters appear more readily when the percentage of fines in the powder sample becomes higher or when the PSD becomes smaller ("moves" towards the left of the distribution diagram). Very high preheating temperatures, near glass transition for polymers (SLS) or melting for metals (SLM) and increased relative humidity (RH) are factors that increase powder cohesion as well. These clusters can get dragged along the substrate via the recoater, creating grooves, or cause the "jamming" of powder deposition by "blocking" the gap between the recoater and the substrate, causing void areas on the new layer, rendering it non-suitable for the continuation of the PBF process [101], [102].

2.4.4 Accuracy of Achieving the Desired Layer Thickness

In PBF processes, the actual post-sintering/melting layer thickness is slightly less compared to the powder layer thickness. This happens because of denudation, partial vaporization/sublimation that occurs in the meltpool, spattering and infiltration of the liquid phase of the material (molten material) through the interparticle pores and cavities towards the lower layers of the part. This difference is less significant in SLS, due to the partial, less violent melting, and more prominent in SLM/EBM. The difference between effective and nominal layer thickness and its connection with layer packing density has been covered in *Section 2.2.7* [74]. This fact makes the need for layer thickness control and/or compensation imperative to achieve high dimensional accuracy of the finished part. More specifically, if the slicing software creates horizontal sections of t_f of the finished part, the recoating system will need to apply powder layers of $t_p>t_f$ thickness in order to achieve acceptable dimensional accuracy. Hence, a relation of $t_p=a\cdot t_f$ must be calculated, where $a>1$. However, depending on layer number, potential existence of overhangs and thin walls, and, in general, with variance of the scanning space-filling curve used by the power beam to melt/sinter the powder, this number might need to vary from layer to layer. Additionally, based on powder recoating method, the expected theoretical (also known as nominal) powder layer thickness might be slightly different from the actual powder layer thickness, mostly due to the dynamics of the powder in cases where a roller or doctor blade performs very fast layer spreading, if particle burst phenomenon emerges, due to the particle motion

conflict in the compaction region (between recoater and substrate) [73]. So, monitoring in situ the actual powder layer thickness is necessary to apply the right amount of compensation for the finished part's layer thickness to be just as designed and not less.

It has been made clear that the differences between nominal, effective and actual powder layer thickness and their connection with the thickness of the consolidated layer must be taken under consideration during the slicing process of the part, since the thickness of the finished part's slices that the slicing software produces might not be equal to the necessary vertical displacement of the fabrication piston, which could lead to severe dimensional inaccuracies.

2.5 Methods of Measuring Powder Layer Quality Indicators (PLQIs)

Layer evenness and homogeneity usually get estimated by measuring the properties mentioned in the previous section. This mostly happens via optical methods, since they are non-invasive and they do not destruct the applied layer, allowing for the manufacturing process to continue and detect the connection of these with the finished part's quality.

Pasalopoulos et al. (2021) have used white light 3D scanning in order to get a depiction of the powder layer as a cloud of points in 3 dimensions. Then, they calculated the surface roughness along vertical intersection planes of the surface, and the layer thickness, as the vertical average distance between two consecutive scanned layers. The fabrication piston has embedded weight sensors at various positions, creating a powder weight distribution. Combining this with a numerical calculation of the volume between two successive layers makes it possible to obtain a powder packing density distribution on the surface of the powder bed [103]. Similarly, many other researchers have been based on high precision metrology relied on structured light and fringe projection profilometry techniques ([104], [105], [87], [88], [89], [90]) just like in [103]. The differences between these works lie on the way (mathematical models, statistical analysis, etc.) the acquired data is used to calculate the powder layer quality indicators. Lin et al. (2019) calculated the surface roughness of the powder layer optically, by photographing the layer and then applying greyscale filters on the image taken. The greyscaled image was then binarized by appropriate selection of a threshold value and

the black-and-white pixel distribution was compared to a binarized image of an "ideal layer", to estimate the layer quality [106]. Beitz et al. (2019) implemented an intrusive method in which a sample was taken by an insert rig from an experimental setup based on a laboratory scale. The sample was examined by X-ray Micro-Tomography and Laser Scanning Microscopy methods to image the surface and extract roughness data [107]. Ali et al. (2018) suggested a methodology of measuring the packing density of layers deposited in SLS. They used a pipette to apply droplets of UV-curable polymer onto the layer that was under examination. The liquid permeated the non-sintered layer and then, UV light was emitted to solidify it, taking a sample of the engulfed powder particles. The samples were nano-CT scanned and the packing density was measured [99]. Jacob et al. (2016) SLS-printed closed cylindrical containers, in order to isolate powder samples from the powder bed. The packing density was measured as a fraction of the weighted trapped powder to the internal volume of the hollow cylinder [108]. Similarly, Choi et al. (2017) evaluated the powder layer density by manufacturing via SLM a cubic container with an internal volume of 1000 mm^3 with the internal dimensions (10×10×10) mm. This container stored an amount of non-melted powder during the manufacturing process. The weight of the powder divided by the internal volume of the container gave the packing density of the powder [109]. Lhuissier et al. (2020) developed a custom-designed build chamber with a rotating rake and a piston-like cylindrical build plate in order to isolate a sample of the powder layer. Then, they used 3D X-ray microtomography in order to evaluate the sample both prior and after the fusion of the powder [110]. Le et al. (2021) have developed a method called "powder bed scanner technology". It provides particle-level resolution images of the entire powder layer as it is recoated. A custom-made platform is used, which consists of an interchangeable recoater a contact image sensor (CIS) and the substrate which can adapt its height to provide optimum focus to the CIS. The system can accurately extract profiles of the layer by slight variations of the focus of the CIS, translating the blurriness into z-axis height values via image analysis [84].

More novel techniques, like spatial mapping of the powder layer via transmission X-ray imaging verified by DEM simulation and experiments [96] and a digital, pixel-characterization-based approach that relies on the spatial discretization of the working space [111] to measure PD, SR and identify pore defects have also been proposed, but they have not been widely used so far, even though the results look very promising.

Table 2.12 classifies and compares the aforementioned works that focused on powder layer quality evaluation methods, by presenting which powder layer quality indicators the proposed methods can monitor and whether they are destructive or not. Additionally, it is examined whether, in the case of non-destructive methods, the cause some delay to the 3D printing process in order to acquire and process the data or not. *Table 2.12* reveals the strong points and the disadvantages of each method.

Table 2.11: Connection between process parameters and powder layer quality indicators.

Process parameters / Powder layer quality indicators	**Surface Roughness (SR) and Surface Roughness Distribution (SRD)** ***(Section 2.4.1)***	**Packing density (PD) or powder compaction level (PCL) and Packing density distribution (PDD)** ***(Section 2.4.2)***	**Appearance of Surface Defects (e.g., Cracks, Separations, Cavities)** ***(Section 2.4.3)***	**Accuracy of Achieving the Desired Layer Thickness** ***(Section 2.4.4)***
Powder Material ***(Section 2.2.1)***	Differences on SR achieved by different materials depend on friction coefficients (static and rolling) between particles and recoater, substrate and adhesion on substrate and recoater (given that all other process parameters remain the same between the experiments) [94], [112].	Same as in Powder material-SR connection. Otherwise, the differences in particle shape between materials can affect the PD (sphericity↑ ⇒ PD↑)	Polymer powders more prone to develop surface defects on layers due to: 1) Adhesion on recoater 2) Increased cohesion due to tribo-charging 3) Higher water absorptivity and adsorptivity (due to lower sphericity)	Depends on cohesion coefficient of powder (based on material) and PD. No such research has been found to the knowledge of the authors.
Particle Size Distribution (PSD) ***(Section 2.2.2)***	A wider PSD (with lower D_{10}) ⇒ SR ↑, because Very small sizes ⇒ cohesion ↑ ⇒ flowability ↓ ⇒ SR ↑ [94]. A wider PSD (with same D_{10}) ⇒ SR ↓, because Larger sizes ⇒ cohesion ↓ ⇒ flowability ↑ ⇒ SR ↓	A wider PSD (with smaller D_{10}) ⇒ PD ↑, since the fine particles fill the cavities between the larger ones, creating a denser layer (provided that powder flowability is ensured by the limitations in par. B [56]) Bimodal PSD's also increase PD (size ratio big/small peak of PSD ~7-10) [94].	A wider PSD (with lower D_{10}) ⇒ more surface defects, because Very small sizes ⇒ cohesion ↑ ⇒ flowability↓	Wider PSD (with smaller D_{10}) ⇒ PD ↑ ⇒ $(t_{eff}\text{-}t_{nom})\downarrow$ ⇒ Accuracy of achieving the desired layer thickness ↑ (SR also ↑, but the positive influence of the PD outweighs the negative influence of SR on the accuracy)

Particle Shape (2D-3D analysis, circularity, convexity, elongation, etc.) ***(Section 2.2.3)***	Sphericity↓⇒ Cohesive forces↑ due to interlocking, adsorptivity, etc. ⇒ SR↑	Sphericity↑⇒PD↑, due to less interparticle friction and higher mobility.	Sphericity↑⇒ Less tendency to form agglomerates due to less Surface/Volume ratio, which means less adsorptivity and less interlocking forces ⇒ Surface defects' possibility↓	Sphericity↓ $\xrightarrow{SR\uparrow, PD\downarrow}$ (t_{eff}-t_{nom})↑⇒ repeatability and dimensional accuracy↓
Recoater Material ***(Section 2.2.4)***	**Harder recoater**⇒Segregation more intense due to rigidity⇒**SR↑**	**Harder recoater ⇒ PD↑**	**Harder recoater⇒Waviness is more often** (uncontrolled vibrations)	**Harder recoater**⇒Higher accuracy of desired layer thickness⇒**Higher repeatability and dimensional accuracy** of finished part
Recoater Shape ***(Section 2.2.5)***	**Rounded blade** provides optimal quality (minimum SR), due to the **zero possibility of burst phenomenon** and **large powder compression zone**, combination neither the blade/inclined blade nor the roller provide [73].	A roller recoater outperforms a blade recoater if every other recoating process parameter is held the same between the 2 experiments. However, the **rounded blade** outperforms both [73].	**Roller:** Separation of crust-like pieces if the minimum layer thickness is subceeded for the given roller diameter. Particle burst phenomenon for small t_{nom} values [73]. **Blade:** Waviness if uncontrolled vibrations of the recoater are inserted. **Both:** Lines if agglomerations are dragged along the surface.	Under the same process parameters, the recoaters that apply the **largest compressing force** (e.g., roller and rounded blade) can slightly drag the solidified part via the increased friction, causing **dimensional inaccuracies**.
Recoating Process Parameters and Setup/Spreading Pattern ***(Section 2.2.6)***	Translational velocity of recoater↑ ⇒ SR↑.	Doctor blade's inclination↑ ⇒ PD↑. Translational velocity of recoater↑ ⇒ PD↓. No sieve in front of roller/blade⇒Powder segregation becomes visible ⇒ PD decreasing the further the spot of the feeding bin [59].	Translational velocity of roller↑ ⇒ Particle burst phenomenon intensifies ⇒ Layer gaps and inhomogeneity↑ [73]. For CW Roller⇒ frequent separations and gaps.	Any settings that increase SR and decrease PD cause decrease of accuracy. (e.g., translational velocity of recoater, lack of sieve)
Nominal, Effective and Actual Layer Thickness ***(Section 2.2.7)***	An actual thickness close to the maximum powder particle diameter causes a high roughness value. Higher thickness values diminish this effect. (Necessary to	(t_{eff}-t_{nom})↑ ⇔ PD↓ Ambiguity for connection between t and PD	Almost no gaps for a fully developed particle flow below the blade, which is achieved for $t_{nom,\ min}$=4D_{90}. [101]	First layer has a t_{nom} thickness. After spreading approximately 6-10 layers, t_{eff} is reached [56], [57].

	t_{act}>>D_{90}. If $t_{act.}$~D_{90}⇒ SR↑)			
Environmental Parameters (Temperature, Humidity, etc.) ***(Section 2.2.8)***	Humidity↑⇒ Flowability↓ (in general) ⇒ SR↑ Temperature↑(~T_g for polymers or T_m for other powders) ↑⇒ Flowability↓ (in general) ⇒ SR↑	Humidity↑⇒ Flowability↓ (in general) ⇒ PD↓ Temperature↑(~T_g for polymers or T_m for other powders) ↑⇒ Flowability↓ (in general) ⇒ PD↓	Humidity↑⇒ Flowability↓ (in general) ⇒ More surface defects Temperature↑(~T_g for polymers or T_m for other powders) ↑⇒ Flowability↓ (in general) ⇒ More surface defects	Humidity↑⇒ Flowability↓ (in general) ⇒ SR↑ & PD↓⇒ SR↑ & (t_{eff}-t_{nom})↑ ⇒ Accuracy↓

(**Note:** Based on references and author's observations.)

Table 2.12: Methods of evaluating the powder layer's evenness and homogeneity found in literature.

Method	Packing Density	Surface Roughness	Defects	Thickness Accuracy	Degree of Invasiveness	Reference
3D white light scanning	✓	✓	✓	✓	ND-D	Pasalopoulos et al. (2020) [103]
Camera vision binarized layer imaging	✗	✓	✓	✗	ND-D	Lin et al. (2019) [106]
Lab-scale experimental setup/insert rig (sample taking) X-ray Micro-Tomography/Laser Scanning Microscopy (sample evaluation)	✗	✓	✓ (only on sample)	✗	D	Beitz et al. (2019) [107]
UV-curable polymer as binder (sample taking) Nano-computing tomography (sample evaluation)	✓	✓	✓ (only on sample)	✓	D	Ali et al. (2018) [99]
SLS-printed closed containers in the shape of a hollow cylinder with conical lid (sample taking) Density=weight of the trapped powder divided by the internal volume of the hollow container (sample evaluation)	✓	✗	✗	✗	D	Jacob et al. (2016) [108]

Custom designed build chamber with piston-like build plate (sample taking) 3D X-ray microtomography (sample evaluation)	✓	✓	✓	✓	ND-D (Very small objects only for experimentation)	Lhuissier et al. (2020) [110]
10x10x10 (1000 mm^3 internal volume) containers built via SLM (sample taking) Powder samples weighed by electronic scale and packing density calculated by division with container volume	✓	✗	✗	✗	D	Choi et al. (2017) [109]
Custom-made platform (interchangeable recoater, contact image sensor (CIS) and substrate)	✓ (estimation by surface particle density)	✓	✓	✓	ND-ZD	Le et al. (2021) [95]
High precision metrology based on structured light, CCD or CMOS camera-evaluation of measurements with structure function analysis	✗	✓	✓	✗	ND-D	Kalms et al. (2019) [104], Kalms et al. (2020) [105]
3D measurement of powder bed via fringe projection profilometry technique	✗	✓	✓	✓	ND-D	Liu et al. (2020) [113], Zhang et al. (2016) [114], Land et al. (2015) [115]
Vision sensing methods (3D surface topography (fringe image projection) via enhanced phase measuring profilometry (EPMP) and 3D contour data of fused area)	✗	✓	✓	✓	ND-D	Li et al. (2018) [116]
Spatial mapping of the powder layer via transmission X-ray imaging	✓(estimated)	✓	✓	✓	ND-D	Penny et al. (2021) [96]
Digital, pixel-characterization-	✓	✓	✓	✗	ND-D	He et al. (2020) [111]

based approach that relies on the spatial discretization of the working space						

(**Note:** Degree of Invasiveness (it has 3 values based on whether the method destroys or not the applied powder layer(s) and, in the case it does not destroy the layer(s), whether it delays the additive manufacturing process or not) = 1) (**ND-ZD**) Non-destructive, zero delay; 2) (**ND-D**) Non-destructive, delay; or 3) (**D**) Destructive).

2.6 Finished Product Quality Indicators (FPQIs)

Many researchers have focused on the finished part of the PBF processes with regard to its predetermined mechanical property standards that determine its quality. Only by ensuring the homogeneity and evenness of the powder bed by having complete control of the process parameters of powder spreading it is possible to control the finished part's properties. The most common finished part's properties that get measured by researchers are density/porosity, mechanical strength (yield, tensile, elongation at break), hardness, surface roughness and dimensional accuracy, as well as the appearance of superficial or internal defects, like protrusions, pores or cavities [61]. This work will attempt to connect these quality indicators with the unfused powder layer's quality indicators and, ultimately, with the powder spreading process parameters. However, it should be taken under consideration that the finished product's quality indicators also rely heavily on the powder fusion process parameters, such as the hatch spacing, scan speed, power of the laser/electron beam, etc. This is why it is incredibly difficult to connect the differences of the finished part's quality to a specific quality indicator of the powder bed, unless an experiment that maintains the powder fusion parameters constant is designed and the researchers only alter the powder spreading parameters, in order to come to safe conclusions, which is a task that, to the authors' knowledge, has not been done in any research to date. *Table 2.13* presents the connection between the powder layer quality indicators and the finished part quality indicators, as observed by the authors and recorded in literature.

2.6.1 Density/Porosity Percentage

Spierings et al. (2011) proved that PSD affects the finished part's density. More specifically, in order to achieve greater density, as well as lower surface roughness

(*Section 2.6.4*) and enhanced mechanical strength (*Section 2.6.2*), in SLM of 316L, it is necessary to include a larger amount of fine particles in the powder [117]. Also, the size of big particles must stay limited and well below the effective layer thickness, to ensure that the powder layer's roughness will remain within acceptable levels.

It has been mentioned in *Sections 2.2.7* and *2.4.2* that, changing the layer thickness affects the packing density of the unmelted layer. This has been proved in the case of a counter-rotating roller (recoater) with a PA12-glass fibre composite (irregular PA12 with elongated spherocylindrical glass particles) (Tan et al., 2021) and for a doctor blade (recoater) with SS316L near spherical particles (Xiang et al., 2021) [35], [97]. More specifically, in both the aforementioned studies, increasing the layer thickness had a positive effect, increasing the packing density as well. Chen et al. (2019) also came to the same conclusion, for SS316L spherical particles with a blade recoater. They explained this by referring to the static and dynamic "wall effect" [118]. However, other researchers, like Shanjani et al. (2008), Budding et al. (2013) and Mostafaei et al. (2021) mention that a smaller layer thickness has a better packing density as a result, all of them having examined the counter-rotating roller as a recoater [5], [72], [27]. It is possible that both the two contradictory views are correct, and that there is some other aspect of this complex process that is the root of this difference, however this needs to be thoroughly investigated. It is speculated that, the cause of this difference is: (i) the particle shape in the case of the PA12-glass fibre composite, since the elongated spherocylindrical glass fibre particles add a whole new complexity to the simulation and it is possible that the correct rolling and sliding friction coefficient values were not estimated properly, as well as the surface energy, factor that affects adhesion and cohesion forces, and (ii) in the vertical blade recoater, which does not really compress the powder unless it is stimulated by some vibration, meaning that it mostly alters the layer height and the compaction level mostly depends on the PSD, the substrate roughness and the particle shape [20], [97]. In any case, in order to reach safe conclusions, a comparative study is necessary, in which the secondary process parameters, such as powder material, PSD, particle shape, recoater material and shape, recoating process parameters and setup/spreading pattern and environmental parameters will be rendered as non-factors by being held stable throughout the series of experiments. It is also important to run an experiment not only to check via angle of repose and angle of avalanche that the correct friction and cohesion/adhesion inputs

have been selected, but to run experimentally the powder layer spreading as well and compare it with the result of the DEM simulation, since many researchers have pointed out that the shear tests and flowability experiments do not perfectly correlate with the powder spreadability for the spreading method that is under examination at all times [88].

Even though better packing density of the powder layer means generally more dense finished parts, with less and smaller pores, sometimes this is not the case. This is, because, by increasing the nominal layer thickness, the effective layer thickness is increased much more, making it sometimes impossible for the laser beam or the source of power to penetrate all the way to the substrate and perform the fusion between the current and the previous layers. This leads to the creation of pores in the finished part, within which unmelted/unsintered particles get trapped [119]. To the knowledge of the authors, no researchers have identified this contradiction, where, even though a powder layer with better compaction level is produced, the finished part has poorer properties in terms of density/porosity, because the positive effect of the increased compaction level has been negatively overcompensated by another factor, the penetration depth of the beam with regard to the effective layer thickness.

2.6.2 Yield Strength/ Tensile Strength/ Elongation at Break

Ultimate tensile strength (UTS) is the maximum tensile load a material can withstand prior to fracture, while yield strength is the tensile load a material can withstand before it gets subjected to plastic deformation. Elongation at break (a measure of ductility) is the ratio between changed (final) length and initial length after breakage of the test specimen. Yield strength, UTS and elongation at break are properties that serve as finished part's quality indicators, and they can vary based on differences of powder spreading process parameters, powder bed quality indicators and fusion process parameters, such as hatch spacing, scan speed, laser power, etc.

Leicht et al. (2021) showed that increasing the t_{nom} from 20μm to 80μm can increase the productivity without having a negative effect on the UTS at all. However, the yield strength and elongation at break dropped by 15% and 30% respectively when the nominal layer thickness increased from 20 to 80μm [120]. The authors though, used a powder of PSD between 20 and 53μm, which means that all particles are larger than the

nominal layer thickness, so during the spreading of the first layers, and while the t_{act} had not reached the t_{eff} value yet, the recoater was only spreading a layer consisting of fine particles, meaning a much higher layer density, so the results are having an inherent error due to difference in the deposited powder's PSD in each layer. To achieve reliable results, it is necessary to ensure that $d_{90}<t_{act,min}=t_{nom}$.

Ali et al. (2017) showed that the temperature gradient and cooling rate are factors that greatly affect the crystallographic microstructure of steel during SLM. They controlled these factors by pre-heating the chamber and bed at various temperatures, from 100 to approximately 900ºC. This, in turn, affects the UTS, yield strength, ductility and Vickers hardness (see *Section 2.6.3*) of the produced part. However, they did not evaluate any powder spreading parameters or powder layer quality indicators to develop a connection to the microstructure of the finished parts [84].

Soundarapandiyan et al. (2021) examined the effect of powder recycling on the UTS, YS, elongation at break, Charpy impact energy and hardness. They deduced that, even though the three last showed no difference, YS and UTD increased marginally when recycled powder was used. They attributed this to the increased oxygen amount in the reused Ti6Al4V powder, however, they did not run statistical analysis to define the importance of the powder bed's packing density on these results, even though they also saw that fatigue life drastically decreased when reused powder was used, due to finished part internal defects caused by powder bed voids [28].

Spierings et al. (2011) report that fine particles melt easily and promote high finished part density and tensile strength, while bigger particles promote higher breaking elongation [117]. This leads to the conclusion that PSD must be chosen in order to comply with these contradictory observations, taking under consideration the desired finished part properties.

2.6.3 Hardness

Hardness is an important finished part quality criterion, since it enables a part to resist plastic deformation, penetration, indentation and scratching. Hence, a high hardness value increases resistance to wear by friction or erosion (e.g., by water, oil or steam). The most widely used methods of measuring hardness is by indentation tests, like in Brinell, Rockwell and Vickers tests. These tests differ mainly on the shape of the

indenter (square-based pyramid for Vickers test, ball indenter for Brinell test), but on the indenter's material as well. The hardness is calculated based on the depth and shape of the indentation left on the specimen.

In PBF processes, hardness is directly connected with the crystalline microstructure of the part, which is achieved by the heating-cooling pattern that is followed during the process. Preheating, and laser power density play a major role, but it has been proven that layer thickness' effect is equally important.

A highly porous powder bed means that the energy provided to the layer will find higher resistance transferring to nearby positions of the laser spot. This is because, the heat transfer by conduction coefficient of the layer is a weighted mean value of the conductivity of the powder's bulk material and the conductivity of air, with the weights been defined by the porosity (inversely, the packing density) of the deposited layer. The more porous it is, the more the percentage of air in the layer, and the lower the thermal conductivity. This highly affects the heating and cooling pattern that will be followed locally, hence the crystalline microstructure of the finished part. In general, slower cooling leads to lower hardness values. Additionally, it has been proven that low packing density of the deposited layer leads to lower density values of the finished part, with more mores distributed in its volume. The higher the porosity of the finished part, the lower its hardness, since the indenter during the testing penetrates more easily into the part, due to the micropores collapsing under the preloading or loading stages of the test [121]. Ziri et al. (2021) also showed that, since porosity can be connected to the PSD, a narrow PSD with medium average diameter (D_{50}=29μm and D_{90}=41μm) is preferable to achieve high hardness compared to very coarse or very fine powders [121]. The same was confirmed by Balbaa et al. (2021), where a very fine powder, with an average diameter of less than 10μm, hence with much lower flowability, produced powder layers with much lower PD. This led to much higher finished part porosity and, consequently, to much lower finished part hardness. The part's micro-hardness was also lower for the finer powder, which was caused by the micro-cracks, since micro-hardness does not depend on the porosity, like macro-hardness [122].

Nadiyadi et al. (2021) showed by factorial experiments that, among layer thickness, laser power and laser scan speed, the layer thickness has the biggest impact on finished part's hardness. They deduced that a small layer thickness requires less amount of

power to create parts with sufficient hardness, while thicker layers need more energy to melt at a sufficient depth, which creates more violent melting phenomena, hence increasing finished part porosity via keyholing and denudation, leading to lower hardness [123]. Large layer surface roughness means high variation of powder layer thickness, which can have a negative effect on hardness by the mechanism explained above as well.

2.6.4 Surface Roughness

Spierings et al. (2011) have recorded better surface quality with a PSD that included more fines [117]. This is attributed to the fines filling the gaps between the larger particles. However, an excessive number of fines can cause reduced flowability and spreadability due to increased cohesion, and have the opposite results than the desired. Azar et al. (2021) [124] have reported that an increased value of the surface roughness of the finished part deteriorates the fatigue performance of the as-built Ti-6Al-4V material, as proved by the studies of Wycisk et al. (2014) [100]. This might the case regardless of the material, but it has not been investigated thoroughly.

Large particles, especially irregularly-shaped ones, tend to increase the finished part's surface roughness [122]. More specifically, Balbaa et al. (2021) report an increase in the range of 5-73% for parts made with coarse powder compared to parts made by finer powder, depending on the laser scanning speed [122]. Also, an increase in layer thickness tends to increase the finished part's surface roughness, but only if the layer thicknesses in comparison are below the powder's maximum particle size. This happens because, if the $d_{90}>t_{nom}$, then what actually happens is a preferential deposition of a "finer" PSD, which gets coarser as the layer thickness increases, hence decreasing the PD of the layer (in the case that all powders exhibit good flowability and the cohesive forces do not hinder the deposition) [61].

Apart from the horizontal finished part's surface roughness, the vertical is also important. This value gets larger with the increase of the effective layer thickness, due to the stair stepping effect [103].

2.6.5 Dimensional Accuracy

Azar et al. (2021) provide a diagrammatic connection between dimensional accuracy and surface roughness of the finished part for PBF of metals. They also compare the curve with other manufacturing technologies, such as polishing, machining, forging and sand-casting [124].

Brika et al. (2020) compared the parts made by SLM of three different powder batches of Ti-6Al-4V alloy (made by 3 different methods so that their shape was different, but their PSD was approximately the same). They showed that the most spherical powder has a better flowability and the most efficient particle packing, leading to denser powder beds and created finished parts with superior density (see *Section 2.6.1*), surface finish (see *Section 2.6.4*) and dimensional accuracy. A larger amount of fines negatively affects the aforementioned properties due to the increased cohesive forces [58]. Balbaa et al. (2021) also reached the same conclusion by comparing a fine powder with 75% more cohesion that created layers of 30% less PD than a coarser powder. The finer powder led to the construction of parts with lower dimensional accuracy in both the X-Y plane, and along the building direction (height-Z axis) proving the effect of PSD, which affects in turn powder flowability, and then packing density, surface roughness and dimensional accuracy of the finished part. The lower dimensional accuracy in the X-Y plane is caused mainly by the fine powder's high adhesion, which causes unmelted, or partially melted particles to stick on the sides of the part, while the lower dimensional accuracy along the Z-axis is caused by the tendency of the fine powder's particles to form agglomerates which, in turn, either drastically increase the deposited layer's surface area roughness, or inherit defects to the following layers, which stack and magnify the dimensional errors [122].

It is also obvious that the layer thickness affects the dimensional accuracy because of the stair stepping effect. The larger the layer thickness, the bigger the loss of dimensional accuracy and surface quality (see *Section 2.6.4*) [103].

2.6.6 Appearance of Superficial or Internal Defects

Soundarapandiyan et al. (2021) compared the fatigue life of specimens made by EBM of Ti6Al4V virgin and 10-times-reused powder. They found that the specimens made by reused powder had approximately 25-30% decreased fatigue life, which they attributed to the increase in lack-of-fusion internal defects in recycled builds. They traced these defects back to the voids formed in the powder bed, due to the reduced number of fines and the presence of some irregular, high aspect ratio (elongated) particles that exist in the reused powder [28]**.**

Balbaa et al. (2021) proved that highly cohesive, very fine powders, of average size less than 10 μm, create micro-cracks, which can drastically reduce the part's micro-hardness. Furthermore, the presence of pores in the finished part's volume can drastically reduce the macro-hardness as well, since the indenter penetrates the part more easily [122].

Powder agglomerations that form by particles of very cohesive powders can be dragged onto the powder bed and form powder layer defects, as explained in *Section 2.4.3*. In general, every defect caused on the powder layer can be inherited to the finished part as well. Additionally, low packing density increases the finished part's porosity, so, every setting of the process parameters that causes low packing density of the non-fused layer can lead to internal defects of the finished part.

It is important to always consider the difference between effective and nominal layer thickness and never calibrate the power of a laser/electron beam assuming that the nominal layer thickness is the actual one. In the first case, the beam might not be strong enough to melt deep enough to consolidate the $(n+1)^{th}$ layer with the n^{th} layer, creating pores. In the second case, the power of the beam might be too large for the actual layer thickness, creating violent melting phenomena, causing spattering that will contaminate the powder bed, increasing the surface roughness of the finished part or even causing dimensional inaccuracies, since spatter can even disturb the recoater during the spreading of the next powder layer. Furthermore, violent melting can even cause keyholes, which are internal defects that deteriorate the mechanical properties of the finished part and increase its porosity [125], [126]–[128].

Table 2.13: Connection between powder layer quality indicators (PLQI) and finished part quality indicators (FPQI).

(**Note:** Based on references and author's observations.)

PLQIs\FPQIs	Density/ porosity percentage	Yield strength/ Tensile strength/ elongation at break	Hardness	Surface roughness	Dimensional accuracy	Appearance of superficial or internal defects
Surface roughness (SR)	SR↑⇒ Porosity↑	SR↑⇒ Tensile strength/Yield strength↓ (Connection with elongation at break not examined to authors' knowledge)	The connection has not been examined in any research to the authors' knowledge.	Powder layer SR↑⇒ Finished part's SR↑	SR↑⇒ Dimensional accuracy↓	SR↑⇒ Superficial/internal defects↑
Packing density (PD)	PD↑⇒Porosity↓	PD↑⇒ Tensile strength/Yield strength↑ (Connection with elongation at break not examined to authors' knowledge)	The connection has not been examined in any research to the authors' knowledge.	PD↑⇒ Surface Roughness↓	PD↑⇒ Dimensional accuracy↑	PD↑⇒ Superficial/internal defects↓
Appearance of surface defects	The appearance of surface defects like cracks due to very high compression by the recoater, grooving by dragging of powder agglomerations, or gaps and cavities by an extremely cohesive powder or a very high recoater translational velocity render the powder layer not suitable for PBF, hence completing these boxes would be of no meaning.					
Accuracy of achieving the desired layer thickness	$t_{act}>t_{desired}$⇒ Possible partial layer melting⇒ Porosity↑	$t_{act}>t_{desired}$⇒ Possible partial layer melting⇒ Improper bonding between layers⇒ Tensile strength along the building direction↓	$t_{act}<t_{desired}$⇒ Possible remelting of previous layer⇒ different crystallic structure (in steel powders)⇒ Change in hardness depending on heating-cooling pattern (austenite-martensite percentage)	$t_{act}<t_{desired}$ ⇒ Possible spatter/keyhole due to the larger energy distributed to a smaller amount of powder⇒ surface roughness↓ due to droplets contaminating the powder bed	$(t_{eff}-t_{nom})↑$⇒ Dimensional accuracy↓	$t_{act}>t_{desired}$⇒ Possible partial layer melting⇒ Internal pores $t_{act}<t_{desired}$⇒ Possible remelting of previous layer⇒ different crystallic structure of the remelted metal.

Note on *Table 2.13*:

1. $t_{act}>t_{desired}$ can happen if the researchers omit to take under consideration the shrinkage of the powder layer due to denudation, spattering, infiltration of the molten material in the porosity of the powder that acts as support.

2. $t_{act}<t_{desired}$ can happen if the researchers overestimate the powder layer shrinkage (possibly by underestimating the powder layer packing density), hence they calculate a larger (t_{eff}-t_{nom}) value than the real one.

2.7 Discussion

This chapter manages to illuminate many of the aspects of the powder spreading process for PBF, as well as identifying the relations between process parameters, powder layer quality indicators (PLQI) and finished part quality indicators (FPQI). Many gaps in literature have been identified as well. *Table 2.3* shows that there has been no established connection between the powder material and the recoater's shape or the recoating strategy. Even though all kinds of powders can be spread regardless of the recoater's shape and the strategy that is used, it has been proven that not every recoater shape and strategy is equally effective and achieves high standards of PLQIs. Researchers should aim to cover this knowledge gap. Furthermore, *Table 2.8* shows that, to the authors' knowledge, no connection has been established between the recoating strategy and the recoater's material. More specifically, it is not clear whether certain recoating strategy aspects, such as the translational velocity of the blade or roller, or the purposeful vibration of the recoater would lead to different results in terms of PLQIs if the recoater was made by different materials (e.g., less elastic, harder, more rigid materials, etc.). This is a knowledge gap that should be examined by researchers in order to optimize the process.

Table 2.14, *Table 2.15* and *Table 2.16* provide a categorization of some important articles that focus on the powder spreading/recoating for PBF processes. The process parameters, powder layer quality indicators and finished product's quality indicators that each paper focuses on are shown in *Table 2.14*, *Table 2.15* and *Table 2.16* respectively.

It is important to note that most works use experiments, as seen in *Table 2.14*, even if it is solely to calculate the value of a property necessary to set up a simulation, to validate the result of a simulation, or to properly calibrate a simulation before running it. This is because of the very high complexity level that the powder spreading process possesses, which makes it impossible to simulate without making (plenty) assumptions.

When it comes to the process parameters, some interesting conclusions can be extracted by *Table 2.14*. First, in terms of material, most works focus on metals and significantly fewer articles focus on polymers, ceramics or composites. This reflects the superior mechanical properties that metals provide and their capability to cover a wide range of applications. At the same time, ceramics and especially composites are still at a prenatal stage when it comes to PBF processes and need much more research till they can be widely used. Secondly, most articles examine primarily layer thickness, particle shape and PSD and secondarily recoating strategies, but few works focus on recoater shape and material, even though there are plenty of various recoaters and materials that offer different capabilities. This field turns out to be more industry than academically-examined. Finally, almost no works examine, or even refer to the environmental parameters, such as humidity and temperature during the recoating process, regardless of the fact that they have proven connection with powders flowability and spreadability. This should be immediately remedied. The authors suggest that a protocol gets developed in order to define standard acceptable limits for humidity and temperature and that every powder spreading-related work must refer to this protocol to ensure the validity and trustworthiness of their results.

In terms of PLQIs, as shown on *Table 2.15*, most articles examine the surface roughness and the packing density, while fewer works focus on surface defects of the layer and the accuracy of achieving the desired layer thickness. In most works the difference between nominal, effective and actual layer thickness is not even considered. It has been noted that, even though there are works that examine powder flowability, not many of them are directly connecting it to the other PLQIs. Also, even though there are plenty of methods to accurately measure the PLQIs, most of them are either destructive, or non-destructive, but with significant delay added to the process, which means that they would significantly lower the productivity if they were to be applied on industrial production PBF machines. This is deduced by *Table 2.12*. Hence, a solid non-invasive method of adequate speed and accuracy that can be applied in-line must be developed

in order to prevent the manufacturing of defective parts or even identify when a new powder layer should be scraped off and re-applied, which cannot be done so far.

When it comes to the FPQIs, as shown in *Table 2.16*, the most works focus on density/porosity and yield/tensile strength and ductility of the part. Fewer works focus on the hardness and microhardness, dimensional accuracy and surface roughness. Finally, all the articles that examine microstructure in the form of internal and superficial defects do it as a means to explain reduced density and mechanical strength, and they rarely focus on finding the connection between PLQIs and the internal or superficial defects of the finished part and the defects' morphology. This is something that should be addressed in a way to determine reversely which kind of non-sintered powder layer defect causes which finished part defect (e.g., could a crack cause a pore and to what extent the shape of the crack could define the size and shape of the pore?).

In order to delve into the topic of FPQIs and their connection with PLQIs, it is important to note that very few works currently address the connection between non-melted powder layer quality and the late-stage processes, i.e., the processes that take place when the laser beam interacts with the powder particles. When this happens, various phenomena take place. Particles partly sublimate, causing vapour jets to create disturbances in both the melt pool and the non-melted powder particles. This can create all kinds of spatter (e.g., solid or liquid spatter) [127], [128]. Recoil pressure and laser radiation pressure can also induce phenomena such as spatter creation and denudation. It has been proven that radiation pressure is comparable to aerodynamic forces and grain weight in terms of magnitude [129]. Layer packing density or, inversely, the powder layer porosity, plays a significant role in terms of spatter generation, since it measures the volume of air cavities that exist within the layer. If these ducts/"tunnels" between the powder particles are of substantial size, then the vapour jets might escape without creating solid spatter. However, the smaller the packing density, the less the laser beam scattering that will take place internally, i.e. inside the non-melted layer, and that means that the actual laser absorptivity value will be decreased. Indeed, there are various works that prove that smaller particle size distributions are promoting the absorptivity value due to increased internal scattering of the beam [130]. However, a higher amount of fines is proven to increase powder cohesion and make it very difficult to spread an even layer with high packing density. This means that, although a smaller packing density value will lead to less violent phenomena and decrease the risk of

spatter creation, it will also reduce the ability of the powder layer to melt completely and effectively, increasing the risk of partial melting and internal porosity/defects. The trade-off relationship between these two needs to be experimentally addressed in order to optimize the process without risking sacrificing the finished part's quality by either the former or the latter.

Also, the effect of radiation pressure on a whole powder layer has not been thoroughly examined, even though its significance has been proven, so it is not possible to conclude how it is affected by certain PLQIs. Additionally, Guo et al. (2018) proved that, based on environmental pressure and by tuning layer thickness one can minimize total (hot and cold) spatter. To be more specific, larger environmental pressure increases the amount of hot spatter but decreases the amount of total spatter. Also, reducing the effective layer thickness reduces spatter as well [131]. However, a reduction of the layer thickness without a simultaneous adjustment of the laser beam's power would mean that the penetration depth would affect the 2 or more previous layers, drastically increasing the residual stress and affecting the microstructure of the finished part [132]. This means that there is another trade-off in terms of quality, this time due to layer thickness.

In addition, when the laser beam interacts with the powder particles, the particles' begin melting from the outside, and their coalescence behaviour is affected by the size distribution and the shape of the powder grains [133]. Smaller particles melt more easily and function as adhesive material that will bond larger particles together. Also, elongated or irregular particles exhibit a vastly different behaviour compared to spherical ones. The layer's packing density affects the permeation of the liquid adhesive to the particles that are located deeper within the layer. However, no work exists to the authors' knowledge that systematically examines the relation between powder layer quality and the binary coalescence of particles, even though there are works that examine particle size and shape's effect on binary coalescence of powder grains.

Finally, as mentioned above, the packing density, directly affects the laser absorptivity by the layer. It is proven that the attenuation of the laser beam on the powder layer is up to four orders of magnitude less in comparison to the respective coefficients of the same bulk material as that of the powder. This means that the laser beam's penetration

depth is larger through a superposition of powder layers compared to what it would be if the beam was aimed to the solid, bulk material.

Table 2.14: Paper categorization based on the process parameter they focus on during the study.

Process parameters\ References		[134]	[63]	[95]	[117]	[70]	[35]	[120]	[72]	[65]	[66]	[76]	[74]	[71]	[88]	[135]	[79]
Powder material	Polymers		✓			✓									✓		
	Ceramics	✓												✓			
	Metals			✓	✓			✓		✓	✓	✓	✓			✓	✓
	Composites						✓		✓								
Particle size distribution (PSD)		✓	✗	✓	✓	✓	✓	✓	✓	✗	✗	✓	✓	✓	✓	✓	✓
Particle shape (2D-3D analysis, circularity, convexity, elongation, etc.)		✓	✓	✓	✗	✓	✓	✓	✓	✓	✗	✓	✓	✓	✓	✓	✓
Recoater material		✗	✗	✓	✗	✗	✓	✗	✗	✓	✓	✗	✓	✗	✗	✗	✗
Recoater shape		✓	✓	✓	✗	✓	✓	✗	✓	✓	✓	✗	✓	✓	✓	✗	✗
Recoating process parameters and setup/spreading pattern		✓	✓	✓	✓	✓	✓	✗	✓	✗	✗	✗	✗	✓	✗	✗	✗
Nominal and actual layer thickness		✓	✓	✓	✓	✓	✓	✓	✓	✓	✓	✓	✓	✓	✗	✓	✗
Environmental parameters (temperature, humidity, etc.)		✗	✗	✓	✗	✗	✗	✗	✗	✗	✗	✗	✓	✗	✓	✓	✓
Experimental (E), simulation (S), or analytical (A) work		E	E&S	E	E	E&S	E&S	E	E	E	E	E	E&A	S	E&A	E	E

(**Note:** ✓= simple mention of the parameter, but not studying its effect or kept constant, ✓= extensive study of its effect on the process, ✗= the parameter does not get mentioned in the study.)

This is easily explained based on scattering theory. The larger the average particle size of the powder, the bigger the penetration depth and the smaller the attenuation coefficient. Despite the fact that attenuation depends not only on particle size and shape (irregular particles increase the randomness of the scattering pattern), but also on the laser's wavelength and the material itself (bulk reflectivity and absorptivity), it is clear that the denser (or, equivalently, the less porous) the powder layer, the smaller the laser beam's penetration depth [136]. This observation, however, clashes against the point made that smaller particle size distributions increase laser absorptivity that was made in a previous Section. The authors tend to believe that the relation between the packing

density and the laser absorptivity is not a linear one, but a peak absorptivity value can be achieved for some value of the packing density of the non-sintered layer.

Table 2.15: Paper categorization based on the powder layer quality indicators they use to reach to conclusions in the paper.

Powder Layer Quality Indicators\References	[134]	[63]	[95]	[70]	[35]	[72]	[65]	[66]	[74]	[71]	[88]	[79]
Surface Roughness (SR)	✓	✓	✓	✓	✓	✓	✗	✗	✗	✗	✗	✗
Packing Density (PD)	✗	✓	✓	✓	✓	✓	✓	✗	✓	✓	✗	✗
Appearance of Surface Defects	✓	✗	✓	✗	✓	✓	✗	✓	✗	✓	✓	✗
Accuracy of Achieving the Desired Layer Thickness	✗	✗	✓	✗	✗	✗	✗	✗	✓	✗	✗	✗
(Flowability)	✗	✗	✗	✗	✗	✗	✗	✗	✗	✗	✓	✓

(**Note 1:** ✓= simple mention of the indicator, but not studying how it is affected, ✓= extensive study of how the indicator is affected in the process, ✗= the indicator does not get mentioned in the study; **Note 2:** Flowability is also examined here despite not being a PLQI, since it directly influences it.)

Table 2.16: Paper categorization based on the finished product quality indicators they use to reach to conclusions in the paper.

Finished Product Quality Indicators\References	[117]	[120]	[65]	[66]	[76]	[135]
Density/Porosity Percentage	✓	✓	✓	✓	✓	✗
Yield Strength/ Tensile Strength/ Elongation at Break	✓	✓	✓	✗	✓	✓
Hardness	✗	✗	✓	✗	✓	✗
Surface Roughness	✓	✗	✗	✓	✗	✗
Dimensional Accuracy	✗	✗	✗	✓	✗	✗
Appearance of Superficial or Internal Defects	✗	✓	✓	✓	✓	✗

(**Note:** ✓= simple mention of the indicator, but not studying how it is affected, ✓= extensive study of how the indicator is affected in the process, ✗= the indicator does not get mentioned in the study.)

After all, if the packing density approaches 100%, then the powder layer tends to behave as bulk solid material, which is proven to have a much higher reflectivity compared to any porous powder layer. However, this value of packing density that optimizes laser absorptivity has not been defined neither experimentally and analytically, nor via simulations, despite of its obvious importance in understanding the fundamentals of the PBF processes.

2.8 Conclusions and Suggestions for Future Work

This chapter initially categorizes the process parameters that affect powder deposition for Powder Bed Fusion manufacturing processes. Factors like powder material, PSD, particle shape, layer thickness, recoater shape and material, recoating strategy, as well as environmental factors like temperature and humidity were defined and the way in which they affect the process has been thoroughly described. The way in which the variation of one creates a variation in any one of the other process parameters has been examined and presented with the use of *Table 2.3* to *Table 2.10*.

The effect of the referred process parameters on the powder layer was made evident by examining four PLQIs, the surface roughness, packing density, appearance of defects and accuracy of achieving the desired layer thickness.

Finally, the effect of each one of the four PLQIs on the finished part quality was examined by defining 6 FPQIs, density, mechanical strength, hardness, roughness, dimensional accuracy and defects.

In this way, it was made possible to decode a highly complex process by breaking it down and identifying connections between process parameters and PLQIs at the first stage and PLQIs and FPQIs at the second stage. The highlights of the article can be summed up as:

1. The powder layer quality depends on the flowability that the powder exhibits during the spreading process, however there is no experimental test that can estimate accurately the powder flowability for every different spreading strategy. A combination of the angle of repose and avalanche tests can be enough to ensure agreement between experimental and simulation results.

2. Not enough attention is given to environmental factors. The authors suggest the development of a protocol that is to adhere to during powder deposition trials, in order for the results to be accurate and reliable between different works.

3. Powder layer quality evaluation happens mainly by optical methods, however no on-line implementation of the method is created, and the current computational speed remains a limitation. Unless this problem gets tackled, a way of predicting and preventing defected parts due to poor powder layer quality will remain a challenge for the industry.

4. The PP-PLQI-FPQI system (PP stands for process parameters) could be adopted by the entirety of the researching society in order to simplify and enhance our understanding of the powder deposition process for PBF. It is a robust, well-defined system that can be cross-used with factorial experiment methods (e.g., Taguchi experiments with ANOVA) to establish interactions and connections throughout the process in a systematic way that is less chaotic than the way in which the process is being examined to the present day.

5. A similar review focusing on the way in which the powder layer quality in combination with laser beam parameters (e.g., power, scanning speed, hatch spacing, wavelength, etc.) interact and affect the FPQIs is of paramount importance. The process' high complexity is preventing the researchers from analyzing the large number of parameters at once, so the method of breaking the process down into more easily observable and researched sub-processes is the only way to enhance the research community's knowledge and understanding on PBF processes. In this light FPQIs may be extended to include microstructure and residual stress distribution.

In the future, researchers should ultimately aim to develop a universally applicable method in which, based on the desired FPQI levels, the proper intrinsic and extrinsic process parameter levels are selected. It is also necessary that the recoating process is monitored to ensure a consistently high level of PLQIs. It is possible to alter the process parameters between layers in order to actively fine-tune the PLQIs and, ultimately, the FPQIs, which would provide the researchers the ability to develop functionally-graded finished parts, with mechanical properties varying within their volume. The development of such a manufacturing protocol would take PBF processes to a whole

different level. Even though it is an arduous task, considering the complexity of the process, the authors firmly believe that it is necessary in order for PBF processes to achieve their full potential.

3 *Design of Powder Deposition/ Recoating System (PDS/PRS)*

This chapter [59], [137] presents the methodological design and manufacturing of a prototype powder recoating system (PRS) for a custom Selective Laser Sintering (SLS) machine aimed at investigating/modeling and benchmarking the process as regards polymer powders. Firstly, available powder deposition methods are examined, namely: mechanical, electrostatic, vibrational, aerosol-assisted spray and tower nozzle deposition. The analytic hierarchy process (AHP) is used to systematically compare and rank them according to criteria like: calibration need, spreading speed, deposited surface quality, functional simplicity, control/automation ease, manufacturing ease and cost. Mechanical method is found to be the most advantageous. Then, a custom PRS utilizing a roller/blade combination is developed by providing engineering solutions for the individual functions that should be supported and divided into doser/siever and recoater groups. Each group is compared via AHP to the -widely adopted in industry- benchmark mechanical PRS and superiority of the Prototype is proven. The latter's detail design is subsequently presented.

3.1 Methods of Powder Deposition

Selective Laser Sintering (SLS) and Melting (SLM) are Powder Bed Fusion (PBF) additive manufacturing (AM) processes. Very thin layers of densely packed metal, polymer or composite powder are deposited and a 3D object is built by sintering or melting the powder layer, which is caused by a focused laser beam. Literature has proven the importance of a uniform and homogeneous powder layer for the finished product's mechanical properties. The quality of the deposited non-sintered powder layer is determined by its surface roughness, its density and the difference between its actual thickness and the expected, theoretical thickness [103], [71]. Even though the importance of powder spreading has been proven and discussed in many articles, there has been no comprehensive, comparative review covering the various powder

spreading methods materializing in corresponding powder recoating system (PRS) designs. Such methods can be divided into four categories.

Firstly, mechanical powder deposition systems solely depend on friction-based phenomena between a recoater and powder grains on a substrate [138]. A feeding slot [139] or a feeding bin/powder delivery piston are common features providing the necessary powder quantity, in combination with a method, most often a doctor blade and/or a roller, for spreading an even layer [72].

Secondly, there are electrostatic methods of powder deposition, such as the corona gun, the triboelectric gun [140] or the electrophotographic PRS [141]. Such systems work on the principle of attraction between particles with opposite electric charge. The powder particles are charged in various ways (corona gun, triboelectric gun, charging roller in electrophotography) and then deposited onto a grounded, metal surface. This surface might be the build platform of the SLS machine, in the case of the gun-using electrostatic deposition, or a charged carrier plate which will convey the powder to the build platform, in the case of electrophotographic powder deposition.

Thirdly, there are vibrational methods of powder deposition. They mostly involve a nozzle of a very small orifice, through which the powder cannot pass via gravitational forces alone, due to clogging. However, the powder is fluidized via vibrations or ultrasound stimulation leading to a highly consistent powder flow, hence very accurate powder quantity control. It has also been proven that properly tuned ultrasound can have a positive effect in subsequent powder compaction [142], [143].

The fourth category comprises more rarely encountered powder deposition methods that cannot be placed into one of the aforementioned three categories, such as aerosol assisted spray deposition (AASD), and gas-flow assisted methods such as tower nozzle and coaxial powder delivery. In AASD, the powder gets mixed with a fluid and then sprayed onto a surface to create the layer which needs to dry off before laser scanning [144], [145]. In the tower nozzle method, the powder gets propelled upwards through a nozzle via an air current, and then collides with a horizontal deflection cap that makes powder particles move in a radial direction. The powder then falls onto the deposition table via gravitational forces creating an even layer [146]. The coaxial powder system is implemented by a specially designed head that accommodates both the powder feeding systems, by means of gas flow, and the laser beam that melts the powder with

a properly embedded cooling system. However, this is mainly applicable to directed energy deposition (DED) rather than powder bed AM [147].

This chapter focuses on identifying the advantages and disadvantages of the aforementioned methods, and comparing them via AHP after defining specific criteria to determine their suitability for powder bed AM. As a result, a prototype PRS is designed and the design is divided into two groups, the doser/siever group and the recoating group covering the pertinent functions. Each of the groups is compared via AHP with the equivalent most common industrial/commercial PRS design, termed Benchmark PRS, proving the superiority of the former. The prototype is then manufactured and its function is preliminarily tested on a prototype SLS machine. In *Section 3.2* the main powder spreading methods are analyzed and their advantages and disadvantages are identified. In *Section 3.3*, these methods are compared via AHP. In *Section 3.4*, the Prototype PRS design is presented and compared to the Benchmark PRS via AHP. *Section 3.5* outlines the implementation of the Prototype PRS and briefly presents the results of preliminary functionality tests. Finally, *Section 3.6* summarizes conclusions of the study and defines future continuation of this work.

3.2 Analysis of Alternative PRS Methods

SLS/SLM requires the deposition of an even and homogeneous powder layer [148], on which the laser beam will subsequently follow the predetermined by the slicing software path to build the desired part. Mechanical powder deposition has been the most widespread in literature so far, since it is relatively fast, simple and provides acceptable powder layer quality [72]. However, the method undeniably relies heavily on powder characteristics [149] such as the particle sphericity and angularity and the particle size distribution [94], which affect directly powder flowability and spreadability [102], [150], since adhesive and cohesive forces will be developed during interaction of the recoater with the powder substrate. In this context it has to be noted that powder agglomerates caused by increased humidity may affect surface integrity during the spreading process, calling for sieving of the raw powder. There are many process parameters [71], [8], such as feed velocity of recoater, roller diameter, roller rotating speed and direction of rotation, profile shape and inclination angle of the doctor blade [64], as well as many different layer spreading patterns, e.g. only by roller, only by

doctor blade, or by combined action [72]. Thus, there can be an exponential increase in the complexity of the process, which however, guarantees near-optimal handling of different powder types following, for instance, factorial experiments.

Electrostatic powder deposition is applicable to polymer powders but not to metallic particles. An analogous process might be applicable for ferromagnetic alloy powders [151] that will take advantage of a magnetizing instead of electrostatically charging methods, however no such method has been described in literature to the authors' knowledge. The process is very fast and guarantees coverage of the surface, as long as the build table is grounded (for electrostatic deposition) or made by a ferromagnetic metal (for electromagnetic deposition). However, not every powder particle is of the same size, which means that the electric charge will vary [140]. In conclusion, not all particles will be attracted onto the build platform with the same force; hence it is difficult to calibrate this process in terms of evenness and homogeneity of the layer. Due to the electrostatic attraction phenomena in conjunction with gravitational and Van der Waals forces between the particles, it is difficult to determine accurately the trajectory of the particles [140], [152], [153] and connect the process parameters with the compaction level, surface roughness and layer thickness. Furthermore, the electrostatic charging parameters will have to be adjusted with every subsequent powder layer added, in order to achieve adequate attraction with increasing distance to the plate. Overall, the need for advanced control is imperative regarding desired quality and consistency standards and substantially increases complexity of the method.

Vibrational/ultrasound-assisted powder deposition usually involves a small orifice nozzle by which it becomes very time consuming to create a powder bed at the flowing rates achieved by a single nozzle, therefore it is considered more suitable in connection to DED [154]. However, vibration/ultrasound stimulation can be used for assisting homogeneous powder spreading and compaction. Furthermore, in the case of multi-material deposition, contribution of such methods can be significant, since they can administer small amounts of powder very accurately in terms of positional distribution. This could be highly useful in composite part manufacturing. However, such systems achieve very small flow rates, so it would be time consuming to spread a large layer. Furthermore, it would be challenging to isolate the stimulation or calibrate it and control its frequency so as to act only on the newly-deposited layer, without affecting the lower layers in terms of layer height and powder compaction. This means that modeling of

the powder's behaviour (e.g., via discrete element analysis) will be an absolute necessity in order to develop a control system that maintains high standards irrespective of powder type.

As regards the fourth category of powder deposition methods, coaxial powder delivery system is strictly designed for DED [147] but the other two methods are interesting and show promising results. In particular, the AASD method is very accurate and can successfully deposit layers of very small height, combining very low surface roughness with good powder compaction [144], [145], yet at a maximum thickness deposition rate of 150 μm/hour. In addition, many steps are involved in creating the solutions - precursors and suspensions, spraying them onto the substrate and then evaporating the liquid phase of the suspension, which makes it very tough to embed the process into a PRS. Known implementation examples refer to alumina or titanium dioxide powder in which case chemical reactions were involved; thus, the whole process must be extremely varied in order to achieve universality to be applied to a range of powder types. Moreover, a robust control system is necessary, since layer thickness and powder compaction are determined via many inter-related stages. As an alternative, the tower nozzle method is easy to use with any type of powder regardless of material, size distribution and shape [146]. Layer thickness is controlled by the air flow through the nozzle, but layers are not perfectly horizontal but profiled, thus leading to dimensional inaccuracy. Compaction rate control might only be possible by raising or lowering the tower nozzle, so that gravitational forces take effect before the inter-particle ones. The process is quite fast but part size is restricted by the tower nozzle position in the middle of the building platform.

3.3 Powder Spreading Method Comparison

In order to design a PRS in the context of SLS/SLM, the first step was to comparatively evaluate the candidate methods presented in *Section 3.2* together with their advantages and disadvantages. The tool employed to reach this decision is the Analytic Hierarchy Process (AHP), a multi-criteria decision making method that was originally developed by Saaty [155]. Details of the method can be found in [156], [157].

The alternatives are coded as *Alti* (i=1 to 5) as follows:

1. *Alt1:* Mechanical deposition
2. *Alt2:* Electrostatic deposition (or magnetic for ferromagnetic powders)
3. *Alt3:* Aerosol assisted spray deposition (AASD)
4. *Alt4:* Tower nozzle deposition
5. *Alt5:* Vibrational/ultrasound deposition

The criteria based on which the alternative methods are to be evaluated are coded as *Crj* (j=1 to 7) as follows:

1. *Cr1-Need for calibration*: How many aspects of the process need to be calibrated for it to run as planned with the desired result (e.g., for mechanical deposition, calibration of both roller and table).
2. *Cr2-Ease of automation and control for universal application*: How easy it is to develop a PRS that functions automatically and adapts to various powder types.
3. *Cr3-Simplicity of process*: How many stages (including preparatory ones) need to be executed (e.g., for mechanical deposition, prior sieving of the powder).
4. *Cr4-Quality of deposited surface*: This is quantified by layer thickness, surface roughness, powder compaction averaged throughout the layer and by the standard deviation of these properties.
5. *Cr5-Spreading speed*: The time needed for a full layer to be applied on the previous layer.
6. *Cr6-Manufacturing cost*: Monetary cost estimate of PRS design for the respective method.
7. *Cr7-Ease of manufacturing*: How easy it is to manufacture a PRS design for the respective method.

These were set based on the author's experience and general industrial and commercial design targets and goals for widespread production.

Next, the importance of each of these criteria is to be determined, i.e. the *priority vector values*. Thus, *Table 3.1* is completed based on a scale of relative importance. In particular, intensity of importance is assigned primarily odd values from 1 to 9 denoting: equal, weak, essential, demonstrated and absolute importance, respectively,

of one part over the other. Even values (2 to 8) can be used when a compromise is needed. If intensity of part A over part B equals to k, then intensity of B over A is its reciprocal, i.e. 1/k. The estimated values that appear in *Table 3.1* are based on the analysis provided in *Section 3.2*.

To check if the matrix is consistent, CI (Consistency Index) and CR (Consistency Ratio) are calculated as in *Equation (3.1)*, where λ_{max} is the maximum eigenvalue and n is the size of the table [157]. RCI (Random Consistency Index) depends on the size of the matrix. For n=7, RCI=1.32. In the case of *Table 3.1* the calculated consistency ratio does not exceed 10%, thus the matrix is consistent and results are trustworthy.

$$CR = \frac{CI}{RCI} = \frac{\lambda_{max} - n}{n - 1}\frac{1}{RCI} \qquad (3.1)$$

Table 3.1: Criteria judgment matrix for powder spreading method selection.

	Cr1	Cr2	Cr3	Cr4	Cr5	Cr6	Cr7	PVCr
Cr1	1	1/2	1/2	1/5	1/4	2	3	0.077
Cr2	2	1	1/2	1/3	1/3	2	2	0.097
Cr3	2	2	1	1/3	1/3	3	3	0.133
Cr4	5	3	3	1	3	4	5	0.352
Cr5	4	3	3	1/3	1	4	4	0.239
Cr6	1/2	1/2	1/3	1/4	1/4	1	2	0.058
Cr7	1/3	1/2	1/3	1/5	1/4	1/2	1	0.044
	$\boldsymbol{\lambda_{max} = 7.3709}$				$\boldsymbol{CR = 4.68\% < 10\%}$			

The eigenvector that corresponds to the maximum eigenvalue is the principal eigenvector. The priority vector (PV) is calculated by normalizing the latter, i.e. by dividing each of the vector's coordinates by the sum of its coordinates [157]. Based on the respective column of *Table 3.1*, the most important criterion is the deposited surface quality (Cr4, PV=35.2%) followed closely by the spreading speed (Cr5, PV=23.9%). The least impactful criteria were ease of manufacture (Cr7, PV=4.36%) and manufacturing cost (Cr6, PV=5.76%), mostly because manufacturing cost can be easily compensated for by the reliability and the capability of producing quality parts, while all methods, even the most difficult ones to implement, can produce PRS designs that are reasonably easy to manufacture.

Subsequently, the alternative judgment matrices for each criterion need to be formulated, by comparing pairwise each alternative method with all other methods for each criterion in turn [157]. Thus, 7 submatrices are developed. After every alternative judgment matrix is checked for consistency (by CR calculation noting that RCI=1.12 for n=5), the priority vectors are calculated as in the case of *Table 3.1*. The individual alternative judgment matrices are combined in *Table 3.2*.

Table 3.2: Judgment matrices for criteria Cr1 to Cr7 for powder spreading method selection.

	Cr1						Cr2						Cr3						Cr4					
Alt_j/Alt_i	**1**	**2**	**3**	**4**	**5**	**PV**	**1**	**2**	**3**	**4**	**5**	**PV**	**1**	**2**	**3**	**4**	**5**	**PV**	**1**	**2**	**3**	**4**	**5**	**PV**
1	1	5	5	1/2	3	.322	1	5	5	3	4	.473	1	3	5	1/2	2	.270	1	3	1	5	2	.317
2	1/5	1	2	1/4	2	.115	1/5	1	3	1/3	1/2	.095	1/3	1	4	1/4	1/3	.105	1/3	1	1/3	3	1/2	.115
3	1/5	1/2	1	1/5	1/3	.056	1/5	1/3	1	1/4	1/3	.054	1/5	1/4	1	1/5	1/4	.049	1	3	1	5	3	.349
4	2	4	5	1	3	.399	1/3	3	4	1	3	.247	2	4	5	1	2	.378	1/5	1/3	1/5	1	1/3	.055
5	1/3	1/2	3	1/3	1	.108	1/4	2	3	1/3	1	.133	1/2	3	4	1/2	1	.197	1/2	2	1/3	3	1	.164
λ_{max}	5.280						5.255						5.227						5.092					
CR(%)	6.25						5.69						5.07						2.06					

	Cr5						Cr6						Cr7						FP
Alt_j/Alt_i	**1**	**2**	**3**	**4**	**5**	**PV**	**1**	**2**	**3**	**4**	**5**	**PV**	**1**	**2**	**3**	**4**	**5**	**PV**	
1	1	2	5	3	4	.416	1	3	4	2	3	.388	1	3	5	1/3	3	.263	0.352
2	1/2	1	4	2	3	.261	1/3	1	2	1/3	1/2	.105	1/3	1	4	1/4	1/2	.106	0.146
3	1/5	1/4	1	1/4	1/2	.058	1/4	1/2	1	1/3	1/3	.070	1/5	1/4	1	1/5	1/4	.047	0.159
4	1/3	1/2	4	1	2	.169	1/2	3	3	1	3	.282	3	4	5	1	3	.437	0.201
5	1/4	1/3	2	1/2	1	.096	1/3	2	3	1/3	1	.154	1/3	2	4	1/3	1	.147	0.143
λ_{max}	5.095						5.190						5.323						
CR(%)	2.12						4.23						7.21						

Figure 3.1 and *Figure 3.2* present a comparison of the methods considered across all examined criteria. *Figure 3.1*, initially, presents graphically the criteria in terms of importance, as established by the AHP process. The most important criterion is by far the quality of the deposited surface, with a priority value of 35.2%, followed by the spreading speed, with a PV of 23.9%. The least important criteria are the ease of manufacturing and cost of manufacturing, with priority values of 4.4% and 5.8% respectively.

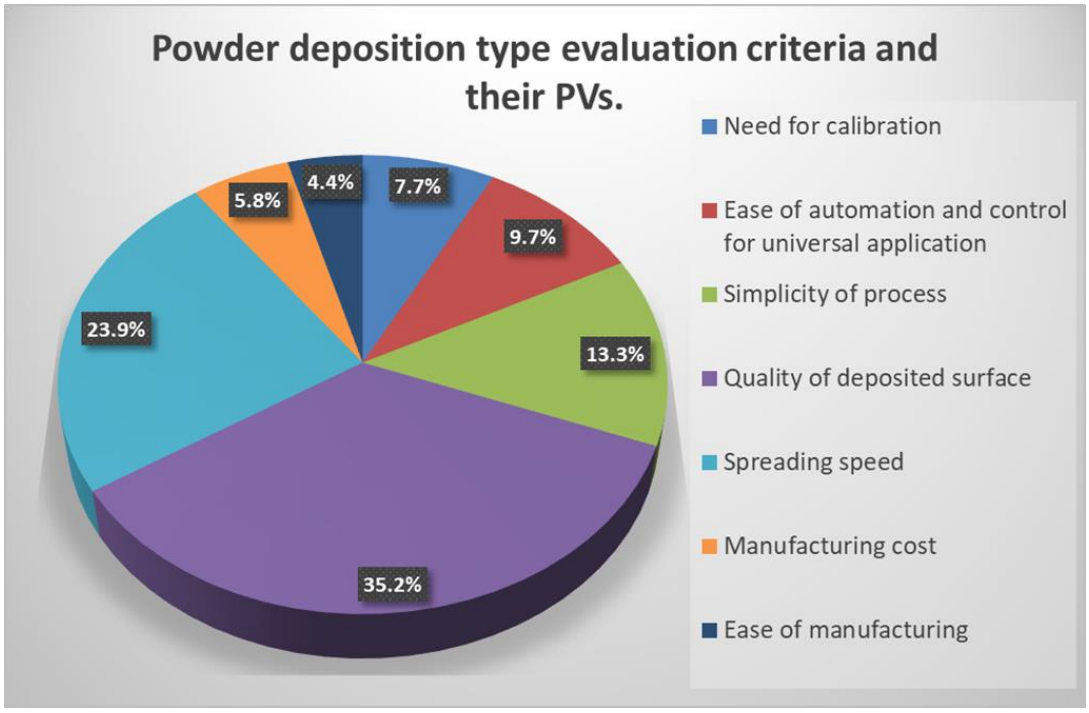

Figure 3.1: The 7 criteria for the evaluation of the 5 different powder deposition methods and their respective Priority Values.

Then, *Figure 3.2* presents how each of the 5 alternative powder deposition methods rank versus each other in terms of each of the 7 criteria, and in total. Mechanical deposition (Alt1) is among the two methods ranking highest, being first with regard to Cr2, Cr5 and Cr6, as presented in *Figure 3.2*. The overall consistency of the method makes it a highly reliable solution. It should be noted that AASD (Alt3) is not suggested despite of its superiority with regard to surface quality (Cr4), mostly due to its high complexity (Cr3) and low spreading speed (Cr5). Contrariwise, the tower nozzle method (Alt4) is not the best one despite being the easiest to calibrate (Cr1), simplest (Cr3) and easiest to manufacture (Cr7) due to its very low surface quality (Cr4), and more specifically to its failing to produce a perfectly horizontal layer. Electrostatic (Alt2) and vibrational (Alt5) deposition, in spite of being promising in terms of spreading speed and surface quality (i.e., the most impactful criteria) respectively, are too difficult to calibrate and control.

The final priority (FP_i) of i alternative (i=1 to 5) based on all 7 criteria (N=7) is calculated as follows:

$$FP_i = \sum_{j=1}^{N} PV_{ji} \cdot PVCr_j \qquad (3.2)$$

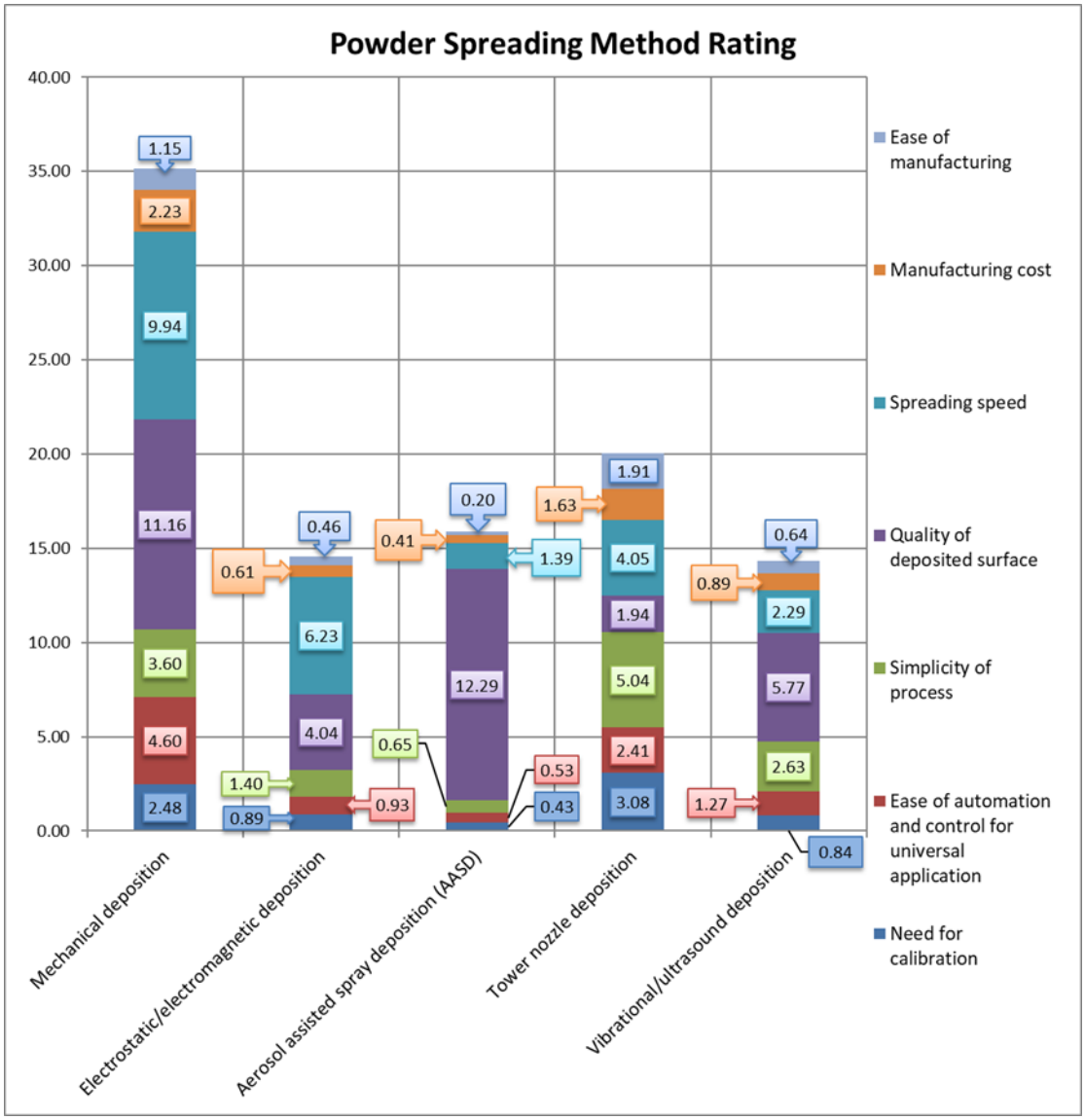

Figure 3.2: Powder spreading method rating. The height of the bar shows the total rating (PV) of each method, while each bar is broken down into 7 smaller ones, showing how each criterion contributes to the rating of the method.

According to FP column of *Table 3.2*, the best powder spreading method is mechanical deposition (Alt1, FP= 35.2%), with tower nozzle (Alt4, FP= 20.1%) being the closest alternative and the rest lying way behind it.

3.4 Custom Mechanical PRS Configuration and Comparison with Existing Benchmark

In most literature sources the laser beam parameters and the path that the beam follows on the powder layer have been examined as the main object of process optimization [158]. However, the powder layer quality, in terms of consistent thickness, powder compaction and surface roughness, is also of paramount importance and heavily affects the mechanical properties of the finished part [98],[159],[106]. In short, homogeneous powder layers of the desired thickness must be deposited. Powder layer homogeneity is examined via parameters which have been proven to affect quality of the final part, such as the degree of powder compaction [99], [108], surface roughness of the non-sintered layer [160] and layer thickness [161]. These have been extensively evaluated in *Chapter 2*.

Most commercial SLS systems come with their own powder recoating system (PRS) installed. However, even though these machines offer some freedom when it comes to sintering parameter selection, the control of the powder layer spreading is mostly limited to the layer thickness parameter. Hence, little space is allowed for researchers who desire to experiment with powder dynamics and rheology parameters to examine their effect on the quality of the deposited non-sintered powder layer. The limitations in controlling both powder spreading and laser beam parameters is the main reason why prototype, open-system SLS machines have been developed by researchers, to examine parameter correlations that could not have been examined in the closed, industrial SLS machines [162].

In order to achieve homogeneous, high quality powder layers, various custom mechanical powder deposition systems have been designed. When it comes to raw powder storage, the most common solution is the powder delivery piston, see *Figure 3.3*. However, this means that the powder that is stored must be properly sieved beforehand, so that is guaranteed to be clear of agglomerates and have the desired grain size distribution. Since humidity of the environment can cause agglomerate formation, the powder storing tank above the piston must be emptied and refilled regularly, otherwise the conditions of the raw powder can be considered neither stable nor known.

A PRS must provide the following functions: (a) accurate dosing of the appropriate volume of powder to spread on one layer, (b) sieving of the powder in order to break down agglomerates that might have been formed due to storage conditions, and (c) spreading of the powder to form a layer. Considering the different functions is necessary in order to enable reliable comparison of alternatives. In this case, a basic commercially available PRS design [163], [164], henceforth termed 'Benchmark PRS' will be compared to a Prototype PRS. The Benchmark PRS consists of a powder delivery piston supporting the raw material within a container, which moves upwards to provide the powder quantity that is to be spread, and a fabrication piston that moves downwards every time a new layer is to be deposited, see *Figure 3.3*. Commonly, either a roller or a doctor blade is used for recoating. Typical examples of the Benchmark PRS can be found for instance in [165], [166].

In the Prototype PRS, the above-mentioned functions materialize in the form of two PRS groups:

1. The *doser/sieving group*, which is responsible for administering exactly the necessary powder quantity and making sure to filter out oversized grains and agglomerates. It consists of the following subsystems: (i) Powder hopper/doser, (ii) Sieve.

2. The *recoating group*, which is responsible for spreading the powder evenly onto the building table, and consists of the following subsystems: (i) Doctor blade, (ii) Recoating cylinder (roller), (iii) PRS carriage and linear motion system.

3.4.1 Doser/Sieving Group Assessment

The two alternatives to compare are the Prototype PRS (Alt1), see *Figure 3.4*, and the Benchmark PRS (Alt2), see *Figure 3.3*.

As depicted in *Figure 3.4(a),* the Prototype PRS doser includes a hopper, where the powder is stored, and a doser drum. The latter possesses blind spherical indentations positioned on a helical pattern. Each of the indentations can store a certain amount of powder. While the cylinder rotates via the stepper motor, these indentations release the powder that is trapped inside them when they reach the lowest point of the cylinder, into the sieve, see *Figure 3.4(b)*. By controlling the angle of revolution of the doser's

stepper motor, it is possible to accurately control the powder amount deposited into the sieve. It becomes obvious that, depending on the angle of revolution of the doser drum, the powder amount administered into the sieve will be approximately equal to $(n \cdot V_{ind})$, where n is the number of indentations that released their powder content and V_{ind} is the volume of each indentation. By adjusting the speed at which the motor rotates and taking under consideration the packing density of the powder, powder inflow control is achieved (powder mass per unit time). These two controls combined optimize the time needed to refill the sieve between layers.

The powder is then sieved by the interchangeable mesh that is secured at the bottom of the siever, which is forced to a reciprocating motion via a cam, see *Figure 3.4(e)*. The complete assembly is shown in *Figure 3.4(b)*. Palindromic motion of a mesh is relied on in order to sieve the powder raw material. The mesh's interchangeability enables the selection of various mesh sizes to achieve the desired size distribution of powder particles. The palindromic motion of the sieve is provided by a stepper motor which defines the said cam, rotating in the groove of a connecting rod, see *Figure 3.4(f)*, thereby converting the rotary into an oscillatory linear motion. The sieve's rod is sliding inside bushings to minimize friction. While sieving, the granules that surpass the size limit as well as larger agglomerates of granules are withheld in the sieving tank. If these were deposited on the powder bed, they would be subsequently dragged along the powder layer by the doctor blade or roller, thereby creating deep grooves on the powder layer and ultimately rendering it useless. The sieved powder ends up on the powder bed compartment, accumulating in front of the doctor blade-roller setup that has been selected (see *Section 3.4.2*). It is possible to perform sieving before the PRS begins moving along the x-axis to spread the powder, which means a bigger height of the accumulated powder (hence, a higher compression level), or sieve throughout the PRS travel for a controlled powder deposition and smaller height of the accumulated powder. The rhythm at which the powder is deposited can be controlled by adjusting the speed of the sieve's stepper motor. Trial and error method in combination with a sieving simulation based on the used powder dynamics can be used to establish the desired speed for the proper powder quantity per time unit needed (see *Chapter 5*) for the process [167].

The sieved powder drops by gravity onto the building table, which moves downwards via a piston, thus delineating layer thickness. By comparison, as seen in *Figure 3.3*,

Benchmark PRS involves a powder delivery piston, which is the bottom envelope of the powder storage area (feeding bin). The upwards motion of this piston supplies the desired powder quantity which is then spread by the recoater onto the building table.

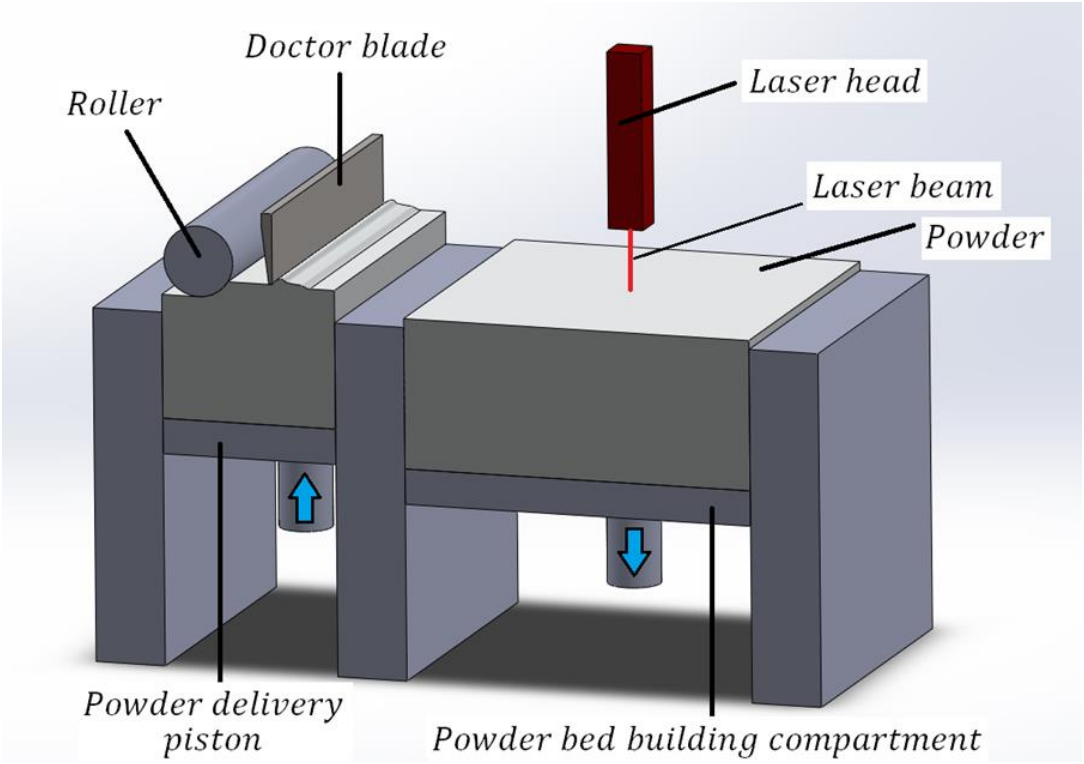

Figure 3.3: Common commercially available PRS design.

By using a hanging powder hopper instead of a feeding bin in the Prototype PRS, it is easy to install additional systems, such as humidity and temperature sensors in order to measure the environmental factors that actively affect the powder quality. According to these measurements, it is possible to fit a dehumidifier coupled with bulb heating or just control the laser beam of the SLS machine in such a way as to counter the effects of the humidity in the powder. Furthermore, it is possible to install a powder stirrer to safeguard powder quality, or a re-feeding conveyor belt in order to feed the non-sintered powder back into the hopper after a sintering cycle. The tank is fitted with a powder level gauge to monitor when it needs to be refilled. So far, this evaluation is performed visually by the machine handler, however it is possible to get automized via level sensors. This would also allow the user to automatically define a fresh/recycled powder ratio. Installing such auxiliary systems would be difficult in the Benchmark PRS, due to likely interference with the piston and the recoater.

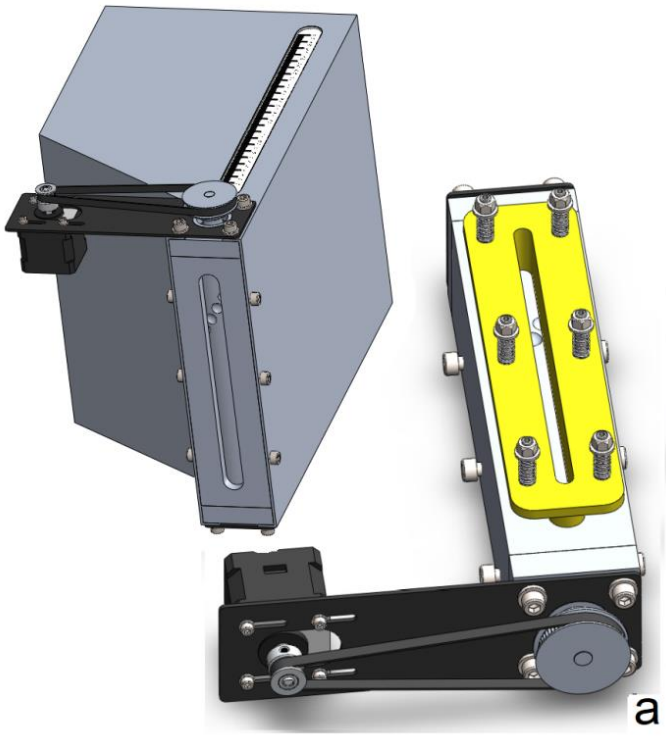

a

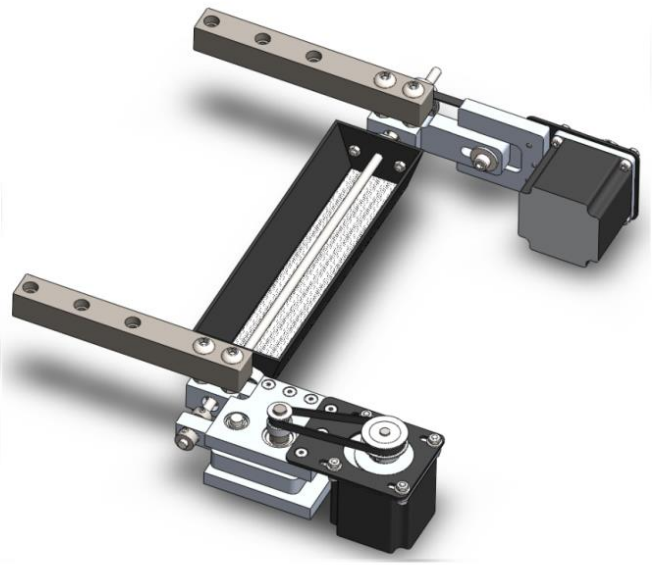

b

c

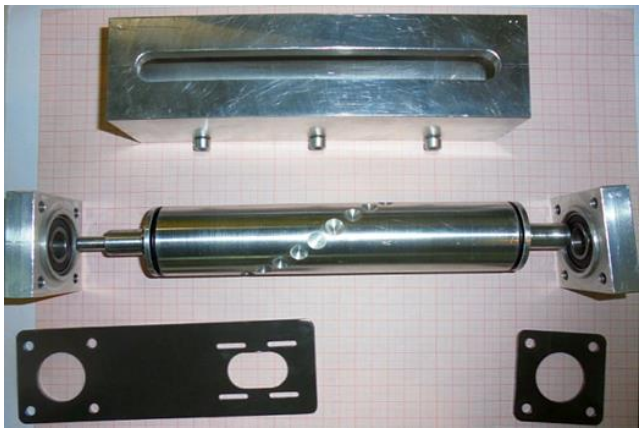

d

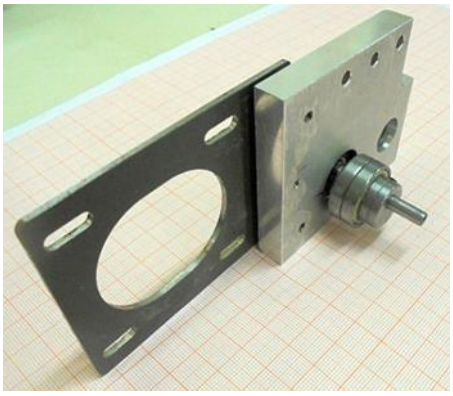

e

f

g

Figure 3.4: ***(a)*** CAD design of the hopper-doser subsystem; ***(b)*** CAD design of the siever subsystem; ***(c)*** Photo of the hopper-doser subsystem; ***(d)*** Photo of the doser's components; ***(e)*** Siever's cam; ***(f)*** Siever's connecting rod; ***(g)*** Siever's assembly.

Furthermore, the Prototype PRS design is highly accurate when it comes to administering the exact amount of powder that is necessary, hence promoting powder economy, as less powder will be forced to move over the table. In the Benchmark PRS, a lot of powder is pushed upwards, to ensure that the building table will be fully covered, the rest of the powder remaining in the machine's chamber, creating a powder cake of larger volume. This is considered as recycled powder because, due to thermal load, its properties will have deteriorated.

The doser's cylinder with its indentations initially breaks the larger powder agglomerates that might exist inside the raw material. Remaining agglomerates are retained in the siever, thereby preventing the recoater (roller or doctor blade) from dragging them along the layer and creating detrimental crevices.

The siever is equipped with an interchangeable mesh in order to achieve the maximum powder particle size that is necessary as it affects the minimum layer thickness desired. By using a superposition of different meshes, while controlling the reciprocating stimulation of the sieve and the recoater's feed velocity, it is possible to even control particle size distribution, although this is difficult in dry sieving conditions. On the contrary, in the Benchmark PRS, the only way to ensure no agglomerates are spread onto the build platform is to perform sieving of the powder prior to loading it into the feeding bin. The latter must be emptied and refilled on a regular basis to prevent creation of agglomerates due to humidity. Prototype PRS design is considered easier to manufacture, as it does not require sealing of a large surface perimeter against powder

penetration, which is the case in the Benchmark PRS. Moreover, every component of the Prototype PRS is relatively small rendering the required tolerances easier to achieve.

On the downside, the siever of the Prototype PRS design needs to be emptied by the tipping motor into a powder waste bin that is positioned past the end of the building table, if the accumulation of agglomerates hampers the sieving process due to clogging phenomena. In addition, it is necessary to properly calibrate its reciprocation speed, so that the deposited amount of powder per unit time is enough to perform layer spreading at the predetermined feed velocity of the recoater.

Taking the aforementioned analysis into consideration, AHP is conducted with the following 6 criteria:

1. *Cr1-Ease of manufacturing*: How complicated the manufacturing of the designed system is in terms of machining time and accuracy for it to be functional with a normal life expectancy.
2. *Cr2-Speed of layer spreading*: The time needed for the system to complete one full working cycle, corresponding to spreading of a single powder layer.
3. *Cr3-Ease of customization*: How easy it is for the system to accommodate extra utilities/devices, e.g., re-feeding of the initial powder storage tank, blade stirrer, dehumidifier, etc.
4. *Cr4-Reliability*: The probability that the system is hampered by errors that will force the process to stop or render the built part useless.
5. *Cr5-Powder economy*: The ability of the system to function by using the minimum amount of powder per working cycle or equivalently by creating the least amount of recycled powder.
6. *Cr6-Manufacturing cost*: The monetary cost of manufacturing and maintenance of the system.

Table 3.3 shows the criteria judgment matrix comparing the system administering powder, while *Table 3.4* shows the alternative judgment matrices for criteria Cr1 to Cr6. It should be noted with regard to *Equation (3.1)* that CRI=1.24 for n=6, whilst 2x2 matrices are consistent by default, i.e., CR does not need to be calculated.

Table 3.3: Criteria judgment matrix for powder doser/sieving group design.

	Cr1	Cr2	Cr3	Cr4	Cr5	Cr6	PVCr
Cr1	1	1/4	1/4	1/6	1/3	1/2	0.040
Cr2	4	1	1/3	1/5	2	4	0.134
Cr3	4	3	1	1/5	3	3	0.202
Cr4	6	5	5	1	4	5	0.470
Cr5	3	1/2	1/3	1/4	1	3	0.098
Cr6	2	1/4	1/3	1/5	1/3	1	0.056
	$\boldsymbol{\lambda_{max} = 6.5257}$				$\boldsymbol{CR = 8.48\% < 10\%}$		

Table 3.4: Alternative judgment matrices for criteria Cr1 to Cr6 for powder doser/sieving group design.

Alt_j/Alt_i	Cr1			Cr2			Cr3			Cr4			Cr5			Cr6			FP
	1	**2**	**PV**	**1**	**2**	**PV**	**1**	**2**	**PV**	**1**	**2**	**PV**	**1**	**2**	**PV**	**1**	**2**	**PV**	
1	1	2	.667	1	1/3	.25	1	4	.80	1	3	.75	1	2	.667	1	1	.50	0.668
2	1/2	1	.333	3	1	.75	1/4	1	.20	1/3	1	.25	1/2	1	.333	1	1	.50	0.332

Figure 3.5(a) depicts graphically the importance of the criteria for the evaluation of the doser/sieving groups. The most important criterion is by far the system's reliability, with a PV of 47%, followed by its ease of customization, with a PV of 20.2%. On the contrary, the least important criteria are the ease of manufacturing and the manufacturing cost with priority values of 4% and 5.6% respectively. *Figure 3.5(b)* compares the two alternatives across the different criteria according to AHP. The Benchmark PRS is only superior in terms of the doser/siever subsystem's contribution to the spreading speed (Cr2), while the Benchmark and Prototype PRSs entail equivalent manufacturing cost (Cr6), i.e., the same manufacturing processes (CNC lathe and CNC mill) and same cost of materials.

Contrariwise, the Prototype PRS is superior in terms of reliability (Cr4) and ease of customization (Cr3), which are the two most impactful criteria (46.96% and 20.24% respectively) that largely determine the overall result. This shows that the Prototype PRS is preferable, by reaching a Final Priority (FP) value of 66.8% in comparison to the 33.2% of the Benchmark PRS, see *Table 3.4*.

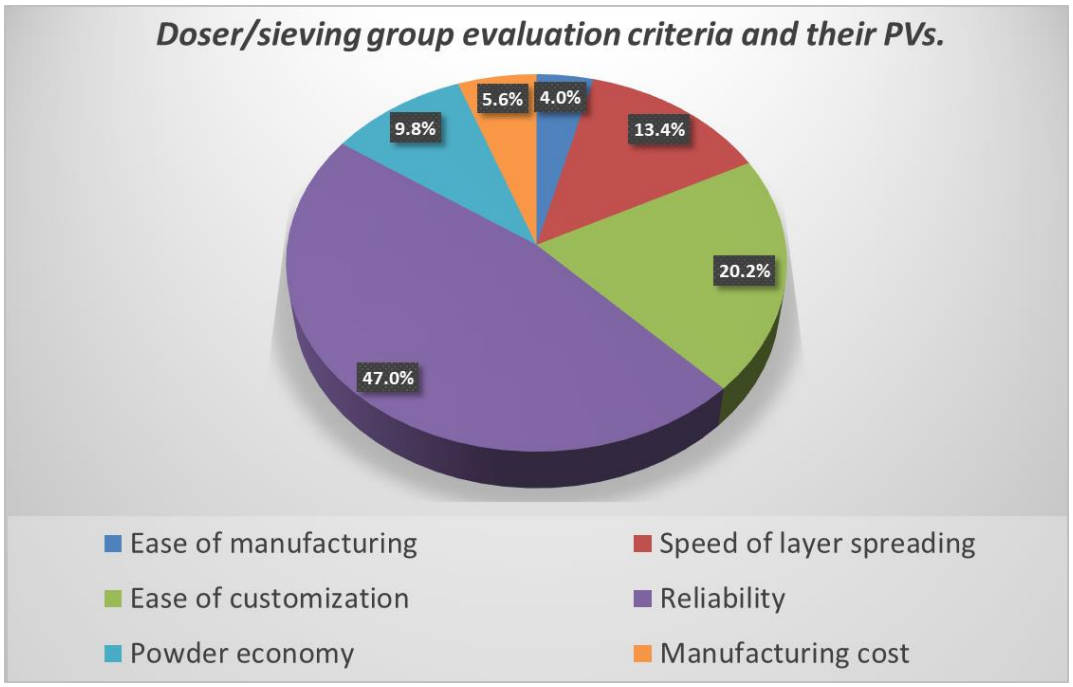

a

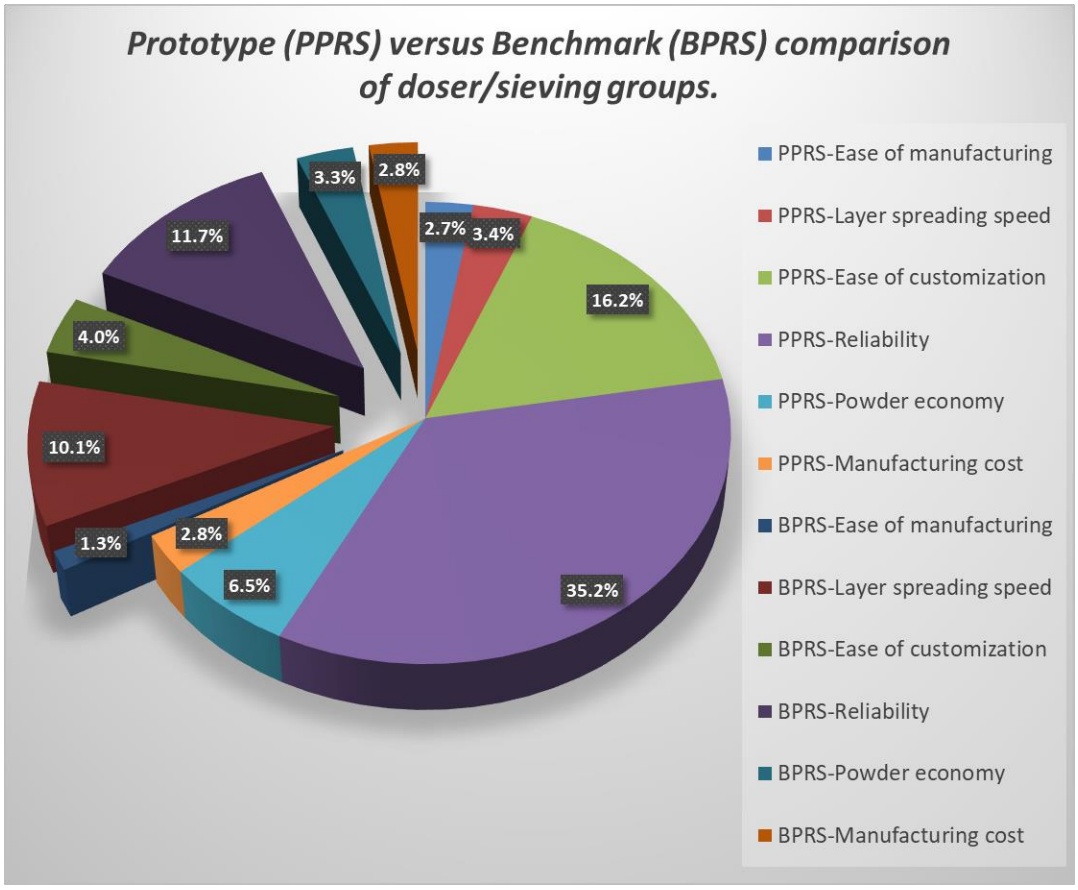

b

Figure 3.5: ***(a)*** The 6 criteria for the evaluation of the Prototype and the Benchmark PRS doser/sieving groups and their respective Priority Values; ***(b)*** $PV_{Al_i} \cdot PV_{Cr_j}$ versus Criteria for AHP evaluation of doser/sieving group (exploded view for BPRS, normal view for PPRS).

3.4.2 Recoating Group Assessment

The recoating group of the Prototype PRS is presented in *Figure 3.6* consisting of a doctor blade subassembly, a recoating cylinder subassembly and the PRS carriage and linear motion system subassembly. This is not substantially different from the Benchmark PRS, yet, because of the features explained next, it offers higher flexibility of experimentation.

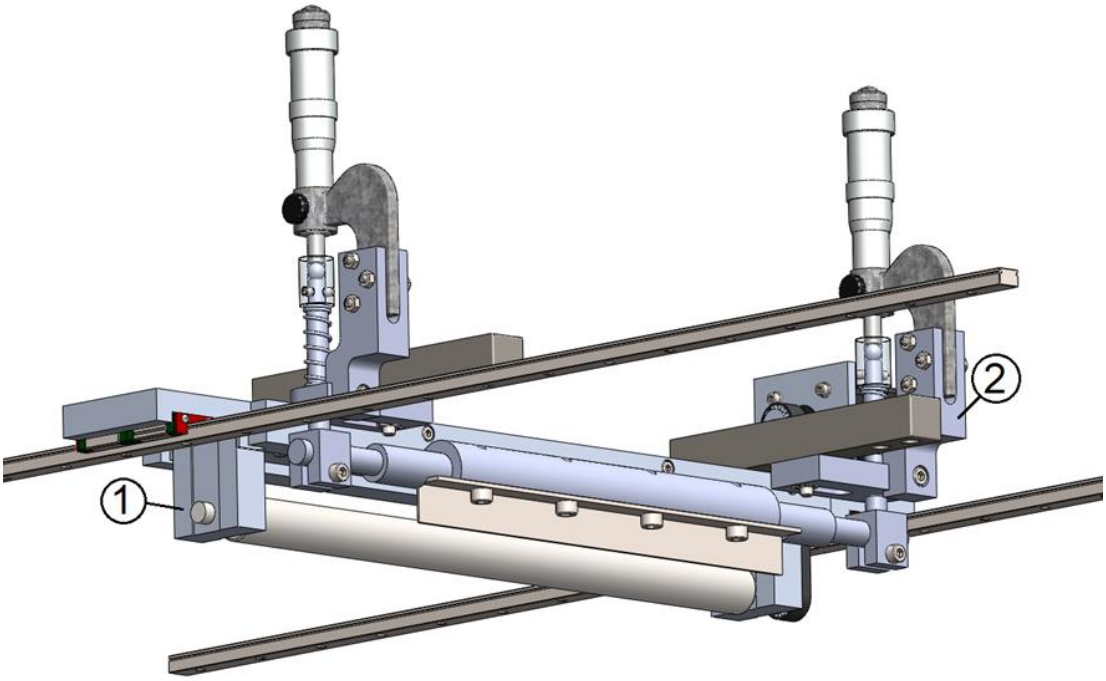

Figure 3.6: Prototype PRS recoating group consisting of roller subsystem (1) and doctor blade subsystem (2).

In particular, the doctor blade subassembly is calibrated via micrometer calipers to adjust layer height. Furthermore, the design allows blade inclination about y axis and a smaller one about z axis. Y axis is along the length of the doctor blade, while z axis is vertical, i.e., normal to the building table of the SLS machine. The range of the inclination allowed by the design is given in degrees in *Table 3.9* [59]. The doctor blade is interchangeable, see *Figure 3.6*, in order to evaluate different blade materials and profiles in terms of layer spreading quality. In addition, the recoater's control system allows for adjustment of the recoater's feed velocity and the roller's rotational speed and direction of rotation. In literature, the cooperation of a doctor blade with a forward-rotating roller is examined in order to add further compression to the powder and

increase the packing density of grains [72]. It is proven that this has a positive effect on mechanical properties of the finished part, such as density and tensile strength [168]. There are also systems which feature only a doctor blade for powder spreading [72]. The blades come in various geometrical shapes with particular advantages and disadvantages [169]. In order to experiment appropriately, it is necessary to be able to test doctor blades of different geometries and materials and at different inclinations. The aforementioned settings and their connection to layer quality have been examined in *Chapter 2*.

Furthermore, the Prototype PRS design can accurately determine the vertical distance between the doctor blade and the roller to establish that the layer is evenly pressed and acquires uniform powder compaction. The height of the powder accumulation in front of the roller is connected with the pressure that the roller applies onto the powder layer [170], i.e., powder compaction. A very large powder accumulation can even lead to inconsistency of the powder layer, e.g., cracking of powder "plates" due to the very large amounts of pressure developed between the roller and the powder layer [170], [71], rendering the layer useless for sintering/melting. In Benchmark PRS with a single roller powder accumulation gradually decreases. As the roller feeds on, a smaller powder amount is accumulated in front of it and the height of the powder hill decreases. This makes the compression force decrease, the compaction level of the powder bed decreases towards its end and the finished part's density differs along the layer [99]. In addition, the Benchmark PRS recoater does not allow calibration, let alone adjustment, of the powder spreading parameters. Instead, a single powder spreading pattern is followed with the same process parameter values irrespective of the powder material, particle size and shape.

Taking the aforementioned analysis into consideration, AHP is followed here, too, for assessing recoating group of the Prototype (Alt1) against the Benchmark (Alt2) PRS, using 6 criteria as follows:

1. *Cr1-Ease of manufacturing*: see Cr1 of doser/siever group in *Section 3.4.1*.
2. *Cr2-Manufacturing cost*: see Cr6 of doser/siever group in *Section 3.4.1*.
3. *Cr3-Experimentation value*: How much room for experimentation in research the design provides (e.g., alternative powder spreading patterns, ability to control the respective settings, etc.)

4. *Cr4-Speed of layer spreading*: see Cr2 of doser/siever group in *Section 3.4.1*.
5. *Cr5-Reliability*: see Cr4 of doser/siever group in *Section 3.4.1*.
6. *Cr6-Adaptability, ease of process monitoring and controllability*: How easy it is to apply means of process monitoring (e.g., sensors) and control mechanical and electrical aspects to optimize results.

Table 3.5 shows the criteria judgment matrix for the comparison of layer spreading, while *Table 3.6* shows the alternative judgment matrices for criteria Cr1 to Cr6.

Table 3.5: Criteria judgment matrix for powder recoating subsystem design.

	Cr1	Cr2	Cr3	Cr4	Cr5	Cr6	PVCr
Cr1	1	1/2	1/4	1/4	1/6	1/4	0.0414
Cr2	2	1	1/4	1/4	1/5	1/4	0.0546
Cr3	4	4	1	2	1/3	1	0.1802
Cr4	4	4	1/2	1	1/5	1/2	0.123
Cr5	6	5	3	5	1	3	0.4206
Cr6	4	4	1	2	1/3	1	0.1802
	$\boldsymbol{\lambda_{max} = 6.2723}$				$\boldsymbol{CR = 4.39\% < 10\%}$		

Table 3.6: Alternative judgment matrices for criteria Cr1 to Cr6 for powder recoating subsystem design.

	Cr1			Cr2			Cr3			Cr4			Cr5			Cr6			FP
Alt_j/Alt_i	**1**	**2**	**PV**	**1**	**2**	**PV**	**1**	**2**	**PV**	**1**	**2**	**PV**	**1**	**2**	**PV**	**1**	**2**	**PV**	
1	1	1/3	.25	1	1/2	.333	1	4	.80	1	1	.50	1	2	.667	1	3	.75	0.65
2	3	1	.75	2	1	.667	1/4	1	.20	1	1	.50	1/2	1	.333	1/3	1	.25	0.35

Figure 3.7(a) depicts graphically the importance of the criteria for the evaluation of the recoating groups. The most important criterion is by far the system's reliability, with a PV of 42.1%, followed by its adaptability and experimentation value, which score priority values of 18% each. On the contrary, the least important criteria are the ease of manufacturing and the manufacturing cost with priority values of 4.1% and 5.5% respectively.

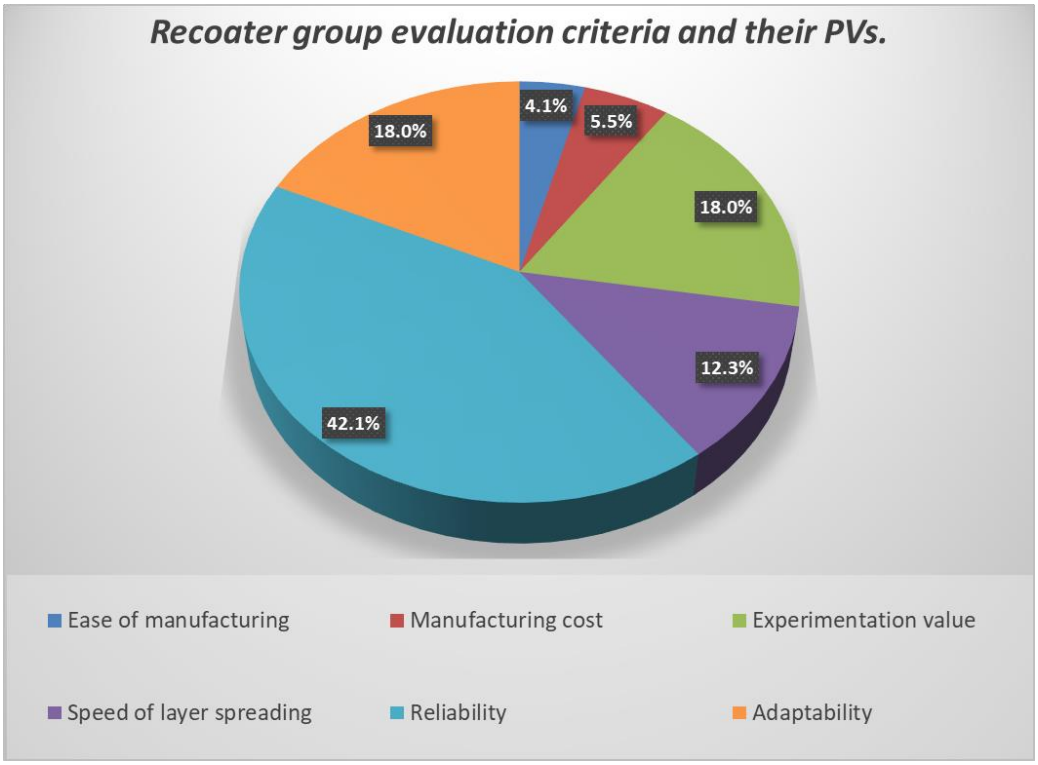

a

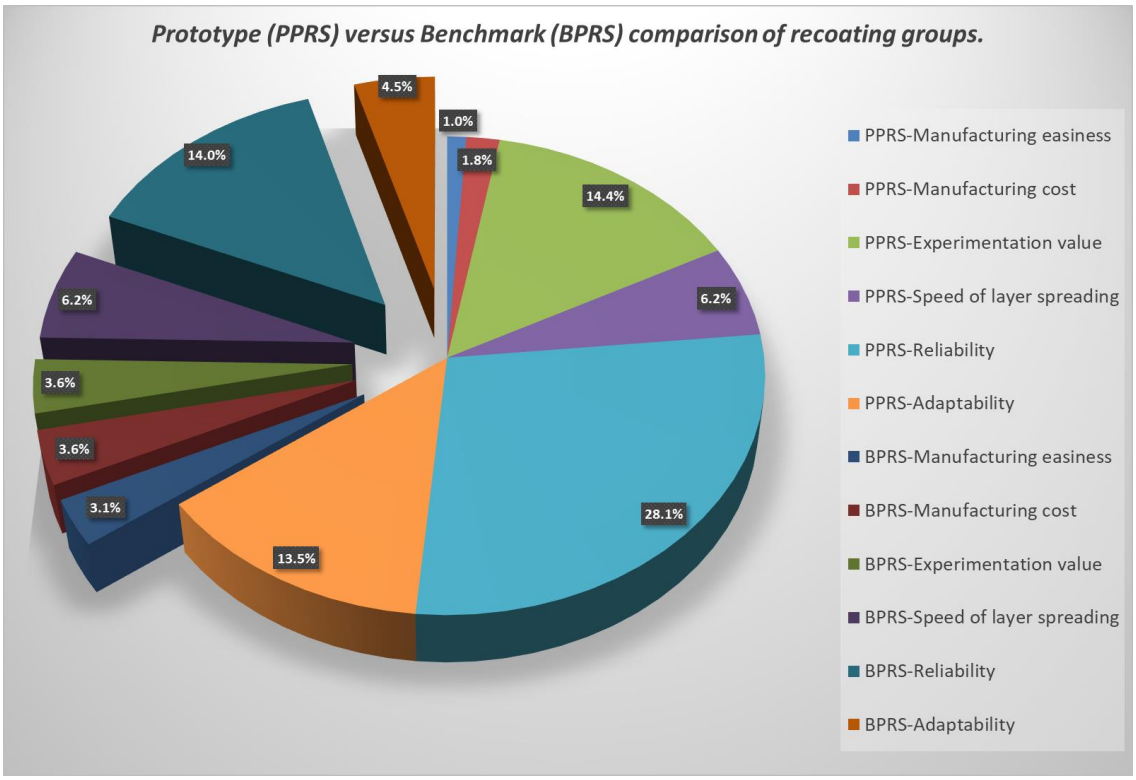

b

Figure 3.7: ***(a)*** Criteria PV comparison for recoater groups evaluation; ***(b)*** $PV_{Al_i} \cdot PV_{Cr_j}$ versus Criteria for AHP evaluation of recoater group.

(Note: exploded view for BPRS, normal view for PPRS).

Figure 3.7(b) presents the AHP comparison of the recoating subsystems for all applicable criteria. Even though the Benchmark PRS design is easier to manufacture (Cr1) and less expensive (Cr2) and the two designs are equivalent in terms of speed of layer spreading (Cr4), Prototype PRS is superior in terms of research value (Cr3) and reliability (Cr5), which outweigh the previous two criteria. Furthermore, it offers a user-friendly electronic platform to work on providing the ability to monitor surface quality and accordingly control process parameters to achieve a better result. The overall result shows superiority of the Prototype PRS, at a priority percentage of 64.99% in comparison to 35.01% of the Benchmark PRS design, see *Table 3.6*.

3.5 Implementation of Prototype PRS

3.5.1 Final Design and Specifications

The design of the prototype SLS/SLM machine on which the PRS is to be fitted is shown in *Figure 3.8* [171], [172], [173].

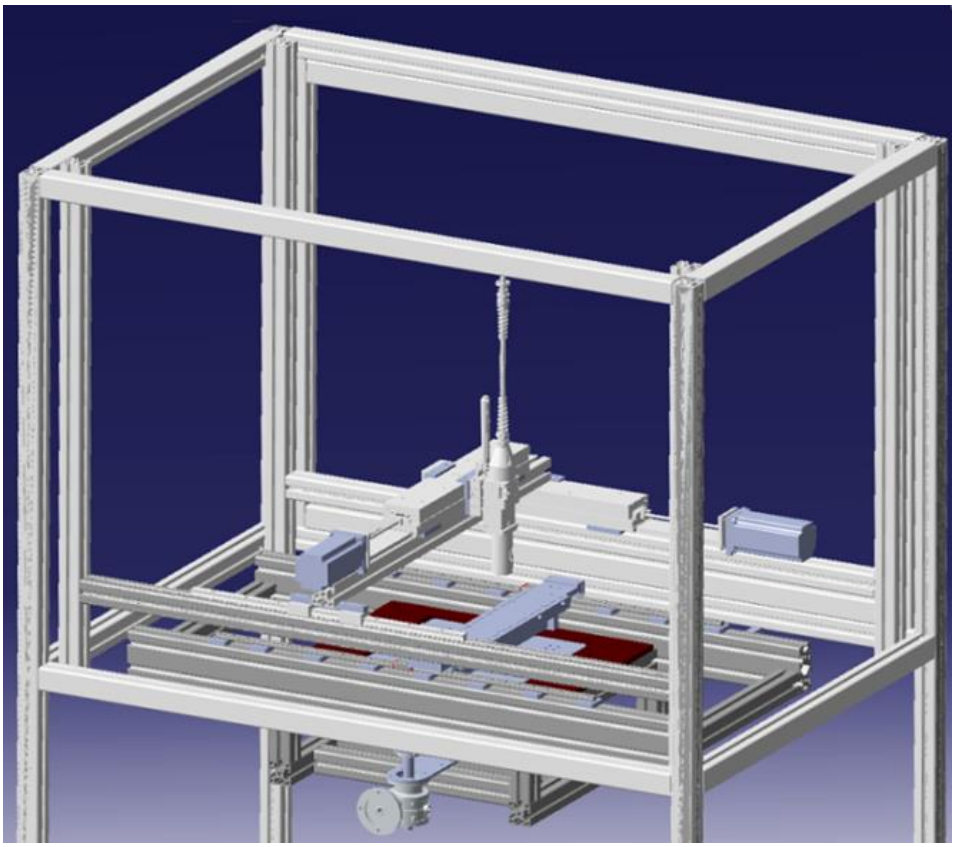

a

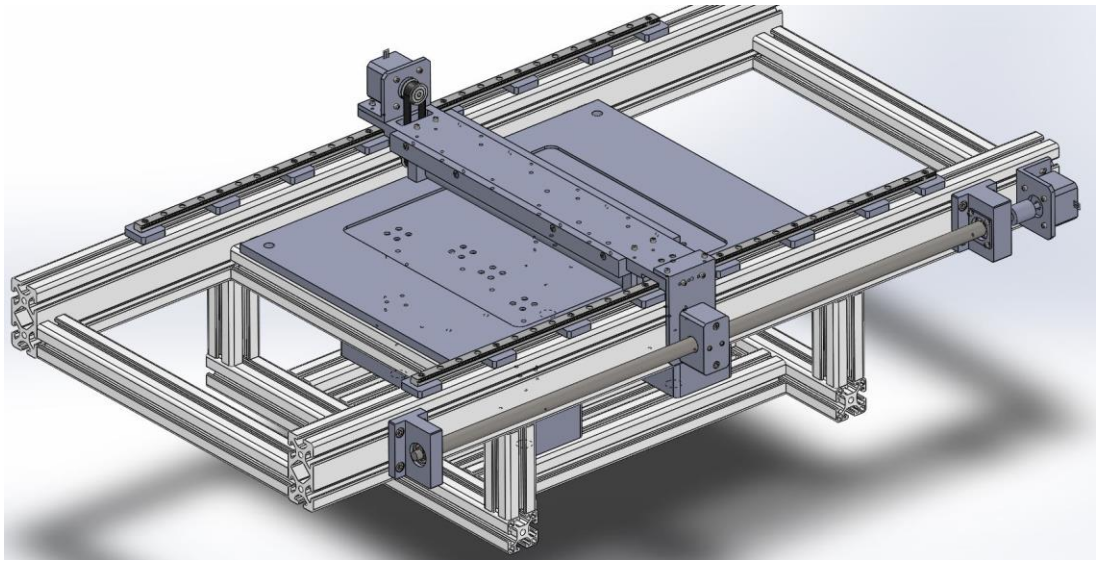

b

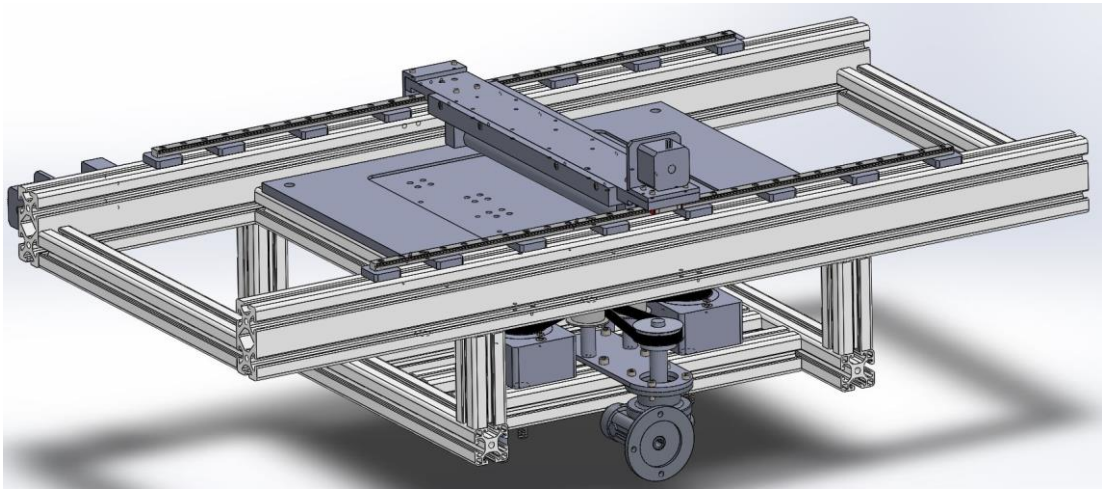

c

Figure 3.8: CAD model of SLS/SLM machine without PRS; ***(a)*** visible laser head and laser motion system; ***(b)*** only the build plate and the roller assembly of the PRS with its motion system; ***(c)*** visible vertical displacement system of the build plate.

The roller subassembly is presented in *Figure 3.9(a)* to *(d)*. The roller is among the most common methods of spreading and compacting an even, homogeneous powder layer, either in combination with a doctor blade or without one, enhancing density and mechanical properties of the sintered part. In the suggested PRS, the roller is an inox steel cylinder of 22 mm diameter, see *Figure 3.9(b)* and *(c)*, which is rotated via a stepper motor; see *Figure 3.9(d)*. Its direction of rotation (forward or backward) and rotational speed can be fully adjusted.

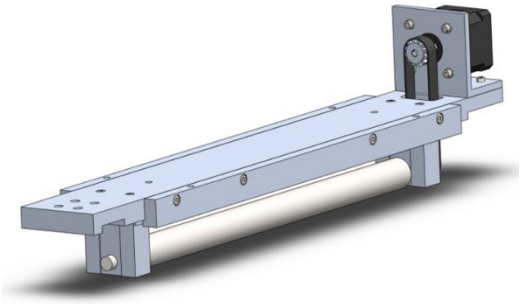

a

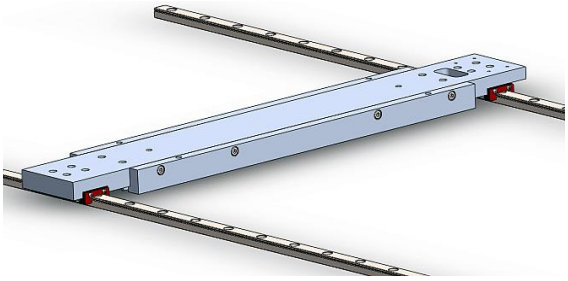

e

b

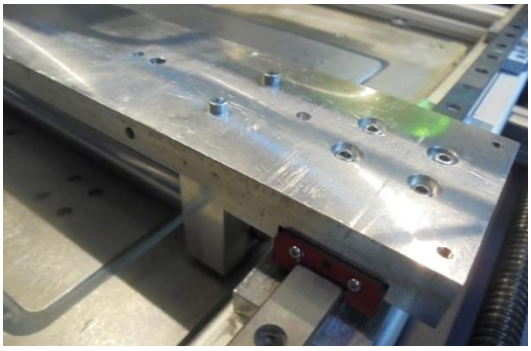

f

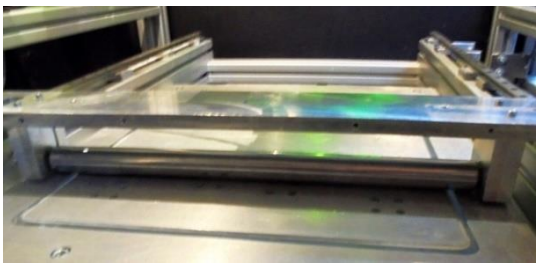

c

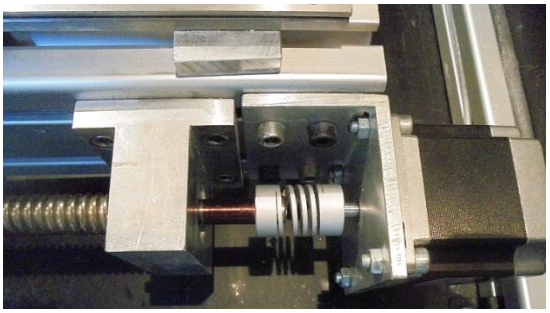

g

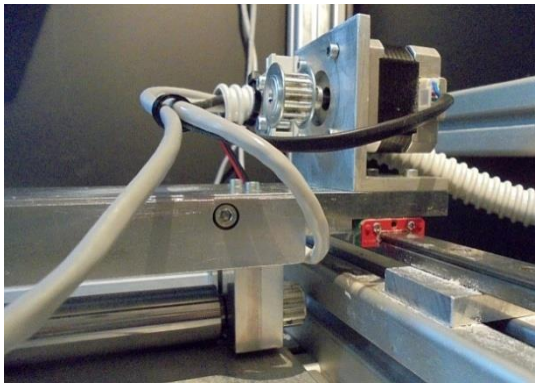

d

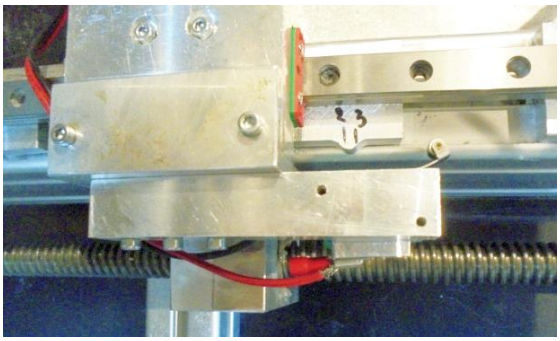

h

Figure 3.9: *Left column:* Roller: ***(a)*** 3D CAD drawing; ***(b)*** Unmounted roller; ***(c)*** Mounted roller; ***(d)*** Stepper motor; *Right column:* PRS carriage-linear motion system: ***(e)*** 3D CAD drawing; ***(f)*** Linear bearing-rail; ***(g)*** x-axis stepper motor; ***(h)*** Lead screw-nut housing and linear encoder-switch.

Figure 3.9(e) to *(h)* present the PRS carriage subassembly model. The carriage moves on slides using linear bearings, see *Figure 3.9(f)*. Motion in x-axis is provided by a stepper motor and a lead screw-nut housing; see *Figure 3.9(g)*.

Terminal limit switches are used to signal travel ends of the carriage. In *Figure 3.9(h)* a linear encoder plate is visible, with indications (2) and (3) declaring the positions at which the terminal switch will change value. In this way, the position of the carriage is monitored and controlled by an Arduino™ UNO microcontroller. The linear encoder consists of 4 such plates placed securely at specific points along the x-axis. This is necessary for the controller to know where the PRS is at each moment in order to control when every stepper motor begins and stops rotating. For example, when the PRS triggers the linear encoder switch at point (2) (see *Figure 3.9(h)*), the controller will stop the x-axis stepper motor and start the powder doser drum motor, since (2) signifies the x-coordinate at which the sieve is directly below the feeder tank.

Table 3.7 summarizes the main characteristics of the motors used in the PRS and their controllers. All motors are controlled via a single Arduino™ UNO microcontroller on which the "AccelStepper.h" library is loaded.

Table 3.7: PRS stepper motors and controllers (CW: Clockwise; CCW: Counter-Clockwise).

Task	Type	Holding torque (kg.cm)	Step (º)	Design speed (rpm)	Rated current (A/phase)	Rated Voltage (V)
Carriage motion	57BYGH420 (NEMA23)	9	1.8	50-300	2	3.6
Roller rotation	42BYGHW804 (NEMA 17)	4.8	1.8	20-100 (CW/CCW)	1.2	3.6
Sieve rotation	57BYGH420 (NEMA23)	9	1.8	50	2	3.6
Sieve vibration	57BYGH420 (NEMA23)	9	1.8	50-300	2	3.6
Doser rotation	42BYGHW804 (NEMA 17)	4.8	1.8	20-200	1.2	3.6

All motors used were bought from Wantai Motors. Each stepper motor is stepped via a separate DQ420MA driver of Wantai Motors. It should be noted that all of the custom-made parts are made from aluminum, apart from the stepper motor mounting brackets, which are made from iron, and the sieve, which was also made from a 1mm-thick iron sheet via bending.

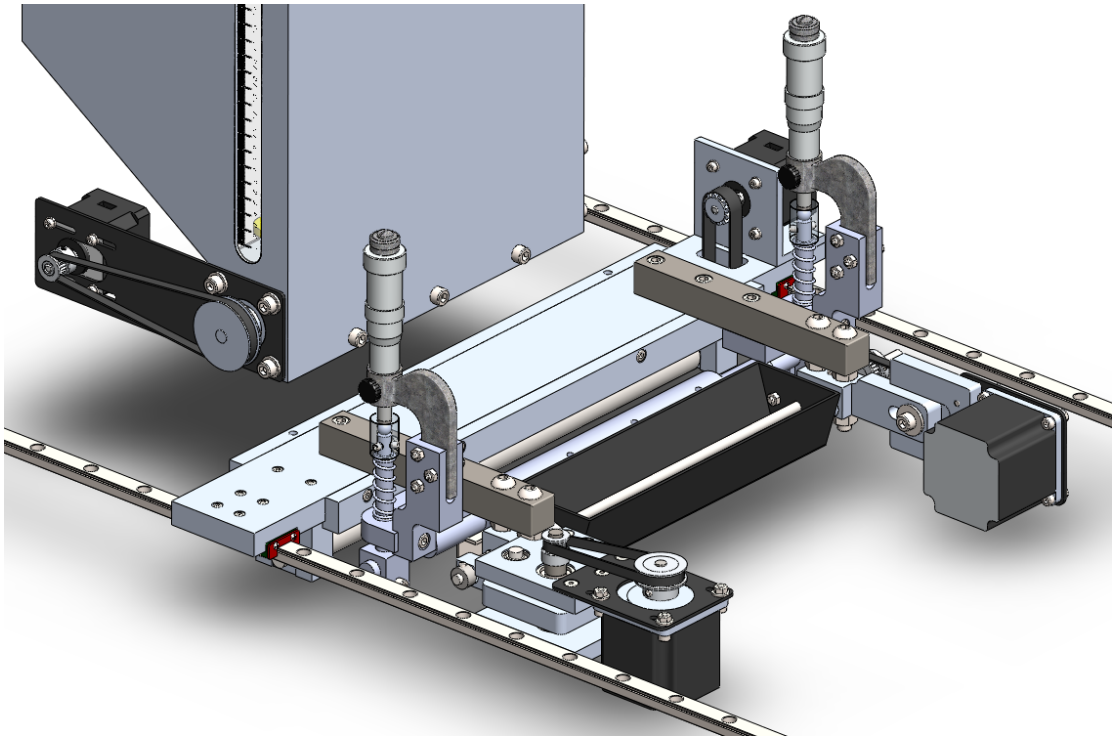

a

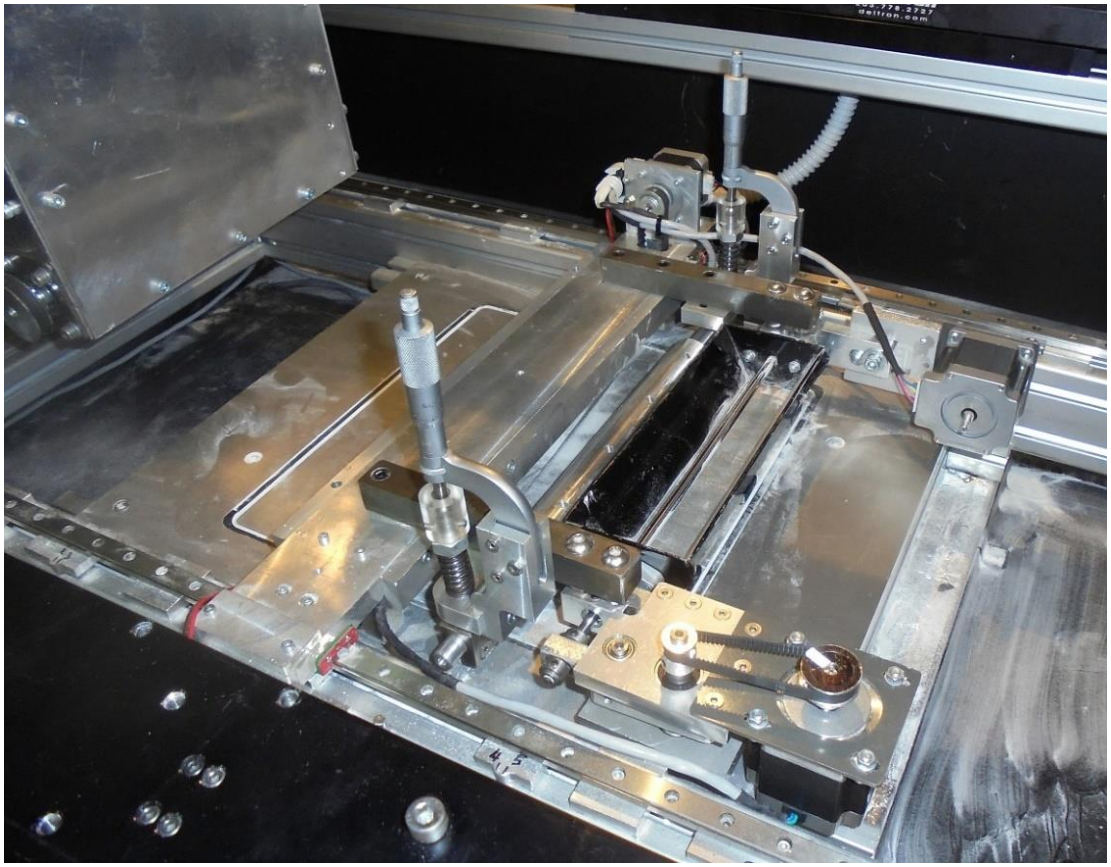

b

Figure 3.10: Prototype PRS ***(a)*** as designed, ***(b)*** as manufactured and assembled.

The Prototype PRS as configured in *Section 3.5* has been detail-designed as shown in *Figure 3.10(a)*. The Bill-of-Materials (*Section 8.1: Appendix A*) consists of 5 subassemblies and 107 part-codes amounting to 327 parts, of which 39 part-codes concern screws, nuts and washers amounting to 218 parts. An overview of the manufactured PRS is shown in *Figure 3.10(b)*. 44 parts were manufactured in-house on a CNC machining center (HAAS TM-1) and a CNC lathe, whereas the rest were bought in.

3.5.2 PRS Cycle Description

The assembled PRS is depicted in *Figure 3.10*. The PRS's functions are briefly described next.

First, the PRS base has been moved to the left limit switch along the x-axis. It then moves to the right and positions the sieve exactly below the aperture of the doser. Second, the doser's motor rotates the cylinder at a predefined angle and speed, in order to fill the sieve with the desired amount of raw material powder. Third, the doser motor stops and the PRS carriage starts moving to the right along the x-axis. When the linear encoder switch, see *Figure 3.9(h)*, reaches the specified point, i.e., the sieve is over the left edge of the powder bed compartment, the sieve motor begins to generate sieve vibrations. Fourth, while the whole assembly keeps moving to the right, the roller - doctor blade combination will apply the powder layer on the powder bed compartment following the selected settings regarding feed and rotary speed/direction. Fifth, when the linear encoder switch signals the terminal position, i.e., the full layer has been deposited, the PRS carriage will move to the left along x-axis. After the laser finishes sintering of the layer, the PRS cycle will be repeated. Minor adjustments of the process might be necessary between the first layer and subsequent layers. For example, in the first cycle, the empty sieve should be filled with a greater powder quantity than in subsequent cycles, where only the powder quantity deposited in the previous cycle should be replenished into the sieve. This means that more revolutions of the doser stepper motor should be coded for the first cycle. Also, after a fixed number of cycles, the sieve should be emptied to avoid blocking/clogging of the mesh openings by the increased number of trapped oversized agglomerates and grains. Hence, after every, e.g., 20 powder layers spread, the sieve should be emptied via the tipper stepper motor

at the defined position. It should be noted that, even though this is the current routine according to which the PRS is functioning, by adjusting the switch positions of the PRS carriage (see *Figure 3.9(h)*) and making appropriate changes in the microcontroller code, it is possible to run many different spreading routines (e.g., counter rotating cylinder to spread an initial layer, then in PRS return use forward-rotating cylinder for increased powder compression and packing density, etc.).

Table 3.8: PRS utilities by subsystem.

Subsystem	Utilities
Powder hopper/doser	Accurate and time-efficient powder quantity measurement. Initial breakage of agglomerates
Sieve	Particle/grain size distribution control. Interchangeable mesh. Containment of powder grain agglomerates.
Doctor blade	Interchangeable-removable. Rotation around y-axis and (smaller) around x-axis. Adjustable height with micrometer accuracy.
Roller	Removable. Adjustable rotation direction and speed.
PRS carriage /motion system	Adjustable speed. Monitored position for process planning-optimization.

Table 3.9: Range of adjustable PRS parameters.

Subsystem	Adjustable Parameter	Range
Powder doser	Angle of rotation (°)	(No maximum value)
	Speed (RPM)	(60 to 600)
Sieve	Interchangeable mesh	(Any mesh size)
	Palindromic speed (RPM)	(100 to 600)
Doctor blade	Interchangeable blade	(Any blade profile shape)
	Height in z-axis (mm)	(0 to 20)
	Inclination about y-axis (°)	(-50 to 50)
	Inclination about z-axis (°)	(-15 to 15)
Roller	Rotary speed (RPM)	(20 to 100)
	Rotational direction	(CW/FW or CCW/BW)
PRS carriage	Speed in x-axis (mm/sec)	(5 to 30) (can be multiplied)

A summary of the utilities associated with each subsystem is provided in *Table 3.8*. The range of the adjustable PRS parameter values can be found in *Table 3.9*.

3.5.3 Accuracy Assessment

The Prototype PRS design and its envisaged functionality were verified by preliminary tests conducted by spreading single layers of PA12 powder (DuraForm™ by 3D Systems) and measuring layer thickness using a white light scanner (IScan M300 by Imetrics™) [103]. A downwards displacement of the fabrication platform by 100 μm allowed a layer of equal thickness to be deposited by the PRS. The experiment was repeated three times and measurements were taken twice for each repetition for the sake of reliability. Resulting average layer thickness was 105.7 μm, standard deviation being 5.6 μm. These results are considered satisfactory taking into account that they were obtained without any prior particular calibration with respect to process parameters such as roller speed, recoater feed, powder particle size, sieving reciprocating speed etc [59].

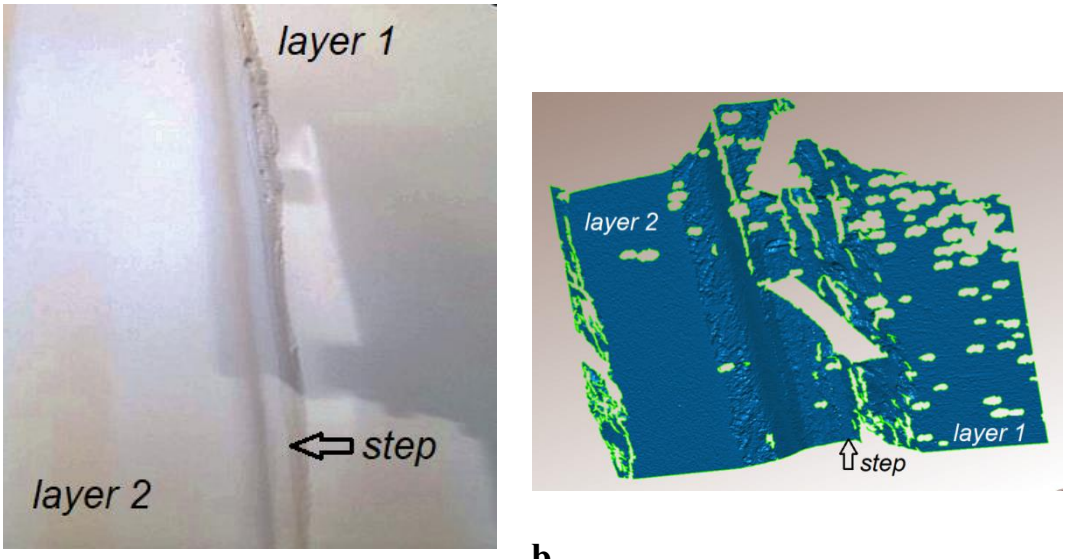

Figure 3.11: Stepped layers: ***(a)*** on powder bed, ***(b)*** as scanned.

More specifically, The PRS was setup so as to spread a layer of 0.1 mm thickness. On top of an existing layer a new layer was built but not along the full length of the former. Thus, the roller was programmed to stop half-way so that a step was formed between the new and the previous layer, see *Figure 3.11(a)*. This stepped layer was scanned by using IScan M300 by Imetric™, possessing a nominal accuracy of 8 μm (see *Table 3.10*

for specifications). The resulting point cloud was interpolated in the respective software, thereby constructing two best-fit planes corresponding to the previous and new layers, see *Figure 3.11(b)*.

Table 3.10: IScan M300 (V70 lenses) specifications.

Measurement volume (mm x mm)	Standoff distance (mm)	Point spacing (mm)	Noise (mm)	Accuracy (mm)
70x55	235	0.055	0.0025	0.008

Their distance was measured within the same software and compared to the nominal layer thickness of 100 μm. The results are shown in *Table 3.11*.

Table 3.11: Layer thickness deviation results (μm).

	Scan			
Layer	**1**	**2**	**3**	**Mean**
1	-1.20	-2.30	-3.00	-2.17
2	10.10	9.80	9.00	9.63
3	9.00	10.20	9.30	9.50

The mean absolute deviation in different areas within the first layer is lower than the measuring instrument's accuracy, thus it is low enough, but not really possible to assess. However, for the next two layers, mean deviation is about 10% and standard deviation is about 0.5 μm. These measurements are quire acceptable, because even though mean error may seem high, it can be adjusted by calibration since standard deviation is very low. Mean deviation in layer thickness is correlated to controllable parameters of the PRS, which is planned to be established by suitable experiments. Furthermore, the full PRS cycle typically takes ~47.5 secs, which is broken down as shown in *Table 3.12*.

The time needed for the PRS to move to doser, to build platform, to deposit a layer and to move to far-left all depend on the x-axis stepper motor, which currently imparts motion to the PRS via a lead screw-nut housing. These times could be vastly improved, if the motion system were replaced by a precision-belt-drive, see *Figure 3.12*.

Table 3.12: PRS cycle breakdown.

Phase	Typical duration (sec)	Min. duration (sec)
Movement to doser	7.5	5
Powder loading	3	2
Movement to build platform	3	2
Vibratory sieving	6	3
Layer deposition	24	18
Movement to far left (home)	4	3
TOTAL	47.5	33

Layer deposition and sieving might be performed simultaneously to control the degree of powder compaction; e.g., when only a roller is used it is necessary to control the height of the powder accumulation. Furthermore, it might be necessary to lower powder deposition time on purpose in order to examine its correlation with layer quality.

Figure 3.12: Alternative solution of linear motion guide.

In terms of functionality, the following observations were made: Good control of powder quantity deposited into the sieve is achieved. Also, the small openings on the doser cylinder break down large powder agglomerates, thereby assisting the sieving process. The linear encoder helps the system stop sieving before the PRS reaches the left end switch; thus, less powder is used per fabricated piece. The suggested roller-doctor blade system is very flexible and allows a number of parameter combinations. Also, the system is robust, user-friendly and can be controlled via the Arduino™ interface by simple program code adjustments. On the other hand, powder particles contaminate the working environment of the machine and potentially affect bearings and moving surfaces by clogging and increasing friction between them, creating a need for them to be replaced more often than they otherwise should, thus a better means of protection may prove necessary.

The Arduino code that controls the PRS can be found in *Appendix B (Section 8.2)*.

3.6 Conclusions and Future Work

This chapter covers an area that has been neglected in literature, as it comparatively evaluates multiple powder deposition methods not in an abstract way, but by using quantitative analysis in the form of the analytic hierarchy process (AHP). The criteria of method suitability have been determined in the context of developing an open SLS/SLM machine for the purpose of experimenting with process parameters. The alternatives have been documented and their pros and cons explained in order to support pairwise comparison in AHP. The most suitable method proved to be mechanical powder deposition.

In order to implement mechanical PRS, an improved solution to the solution that is commonly found in many commercially available SLS/SLM machines, i.e., the dual piston PRS, was sought. For a legitimate comparison it was necessary to first define the five functions supported by mechanical PRS. The Prototype PRS was broken down into two sub-groups each encompassing specific functions, namely the doser/sieving group, which is responsible for administering the correct amount of powder onto the building table, and the recoating group, which is responsible for spreading an even and homogeneous powder layer. AHP was run twice for evaluating these groups, quantitatively proving that both were clearly superior to the Benchmark PRS.

At this point, it would be beneficial to underline the fact that AHP, despite being a robust method of statistical analysis, relies itself on pairwise comparison. Be it the pairwise comparison to determine whether a criterion is more important than another one, or how well two different alternatives are rated with regard to a specific criterion, the number that is assigned as a result of this pairwise comparison unavoidably incorporates the subjective opinion of an expert about the topic. For example, the author considers the manufacturing cost to be a far less important criterion for the evaluation between powder deposition methods compared to the achievable surface quality, hence assigning to it a ¼ value, meaning that surface quality has a *strong* importance over manufacturing cost (*strong* being 4, rating between *weak* and *essential*, which are equal to 3 and 5 respectively). However, if a manufacturing company made a similar analysis, aimed towards developing a commercial PRS, they would also aim at the highest possible profit without hampering the quality of the finished product or making it too expensive, which would drastically limit the sales. So, it is possible that a different value would be assigned to the surface quality-manufacturing cost pair (e.g. 3, making surface quality a *weak* priority over manufacturing cost). So, it becomes apparent that, not only different expert opinions but also different goals of the people responsible for the AHP setup may have an impact on the methods' results. In order to take under consideration that inherent uncertainty [174] when it comes to human opinions, researchers have developed methods that compensate for this by adapting the original AHP and combining it with other methods. Some examples are the SMAA-AHP (Stochastic Multicriteria Acceptability Analysis) [175], [176] and the fuzzy-AHP methods [177], [178]. However, these methods are much more complex than simple AHP and, despite the fact that they are used widely, their superiority over the original AHP method is still being disputed [177].

The developed PRS was detail-designed consisting of 68 part-codes apart from screws, nuts and washers. 44 custom-designed parts were manufactured in-house and 283 were bought in as standard. The PRS has been preliminarily tested and the achieved layer thickness accuracy was found acceptable, see *Figure 3.13*.

The developed PRS is based on the feeding of a siever via a vertical silo in order to deposit powder onto the fabrication plate. This contradicts the most commonly-used feeding piston/bin assembly that features in most commercial SLS/SLM machines,

meaning that, in order to implement it in a commercial SLS machine the entire raw material-feeding method would have to be adjusted or even replaced.

Ongoing work involves layer quality assurance in terms of compaction, surface roughness and actual layer height on multiple points of the powder bed by experimentally establishing the influence of process parameters in a systematic statistically meaningful manner. Furthermore, the significant overlap among the alternative deposition methods throughout the criteria points to the possibility of combining methods into hybrid powder deposition systems [179], [180], [181], which is a direction that might be worth exploring.

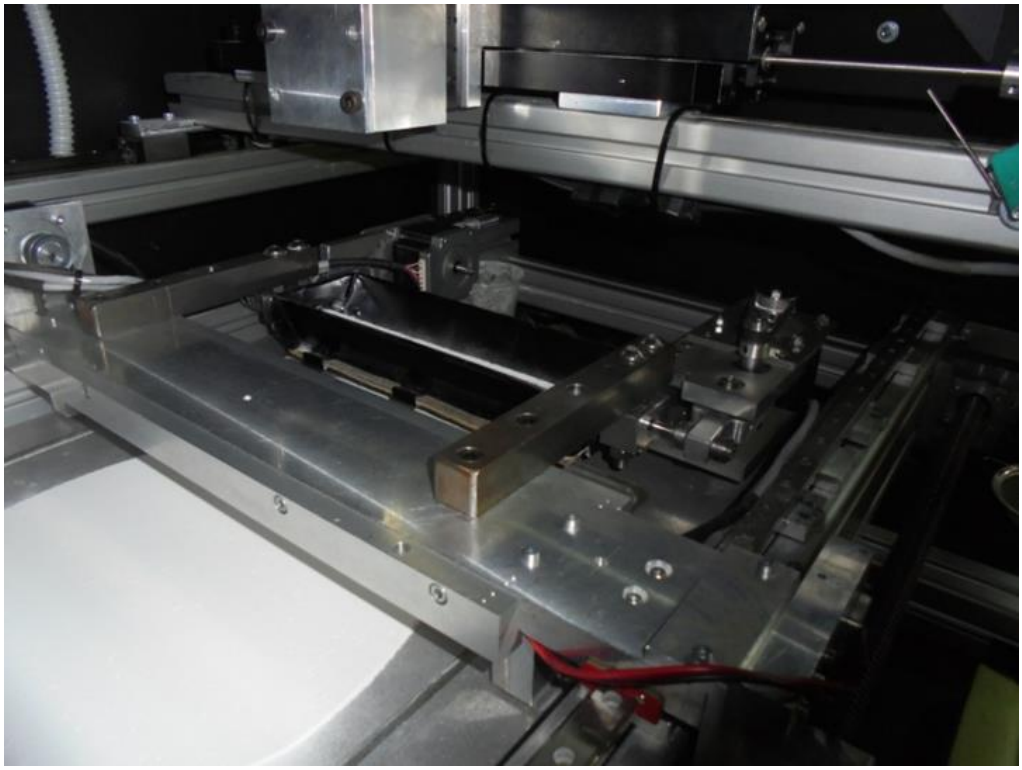

Figure 3.13: PRS while spreading a powder layer.

The development of this experimental apparatus was based on the proven importance of powder sieving in terms of ensuring powder layer quality and maintaining powder economy. However, sieving is a complicated process that must be calibrated. Feeding a much larger amount of powder than necessary into the sieve would cause the siever mesh to clog down due to the excess of large grains and agglomerates, while a smaller quantity would be insufficient for the layer to be thoroughly deposited in only one travel of the recoater. Hence, the author has worked on powder sieving simulations (see

Chapter 5), to examine how the vibrational parameters of the siever (frequency and amplitude of oscillation) with regard to the mesh size and the powder's geometrical and rheological characteristics affect sieving behaviour. The ultimate goal was to optimize powder consumption, deposited layer quality in terms of packing density and surface roughness. Sieving was also examined as a recoater-less powder deposition method, in order to maximize layer deposition speed.

In conclusion, the suggested and manufactured PRS design is low-cost, in-house built, user-friendly and provides full control of the powder layer spreading process by providing the appropriate utilities. The system's high degree of accessibility and adaptability means that in only a few minutes change over time an entirely different process setup can be materialized and experimented with. The PRS has been successfully tested and the quality of the deposited powder layer has been evaluated via 3D white light scanning, achieving a layer thickness error of less than 10 μm.

4 Powder Spreading Simulations

In order to evaluate mechanical powder spreading via a doctor blade, a Taguchi Design of Experiments (DoE) is implemented [182]. The tests were carried out via Discrete Element Method simulations in the EDEM software package, that was kindly provided by Altair™.

4.1 Powder Material Properties

The powder selected for the experiments was the SA-ZL-20 spherical alumina (Al_2O_3) powder provided by the manufacturing company Sinoenergy Group™. The datasheet of the powder can be seen in *Table 4.1*.

Table 4.1: Specifications of the powder used in the simulations.

Item		Unit	Typical Value
Particle size	D_{10}	µm	8.2
	D_{50}	µm	21
	D_{90}	µm	47.5
S.S.A.		m^2/g	0.19
E.C.		µs/cm	300
pH		-	8.5
Moisture		%	0.05
True Density		g/cm^3	3.8
Spheroidization		%	96
Chemical Composition	Al_2O_3	%	99.5
	Fe_2O_3	ppm	300
	Na_2O	ppm	3500
Ion content	Na^+	ppm	400

In order to accurately depict the specific powder in the EDEM™ software, we need to define the material. EDEM™ software offers the user the option of both selecting the powder material properties at first (see *Figure 4.1*) and defining the particle size distribution and particle shape (see *Figure 4.2*).

As seen in *Figure 4.1*, the Poisson's ratio (ν) of alumina is inserted, equal to 0.3 [71], as well as the solid's bulk density (ρ), equal to 3820 Kg/m^3 [71], and the shear modulus (G), equal to $1 \cdot 10^7$ Pa. Let it be clear that it is possible to insert either the shear or Young's modulus (E) value, since the other one is calculated by the first one and the Poisson ratio, by the *Equation (4.1)*.

$$E = 2G \cdot (1 + 2\nu) \Leftrightarrow G = \frac{E}{2 \cdot (1 + 2\nu)} \qquad (4.1)$$

EDEM^{TM} software tutorials suggest that an initial value of G around $1 \cdot 10^7$ Pa is used, since using the actual value drastically affects the timestep, rendering it extremely small, thus making the simulation non-viable timewise. In general, the suggested value of G for EDEM^{TM} simulations, according to the supporting educational material provided by Altair^{TM}, ranges between $1 \cdot 10^6$ Pa and $1 \cdot 10^9$ Pa. In DEM simulations, it is common practice to use lower shear modulus ratios for particle materials compared to the actual shear modulus value of the real-world material.

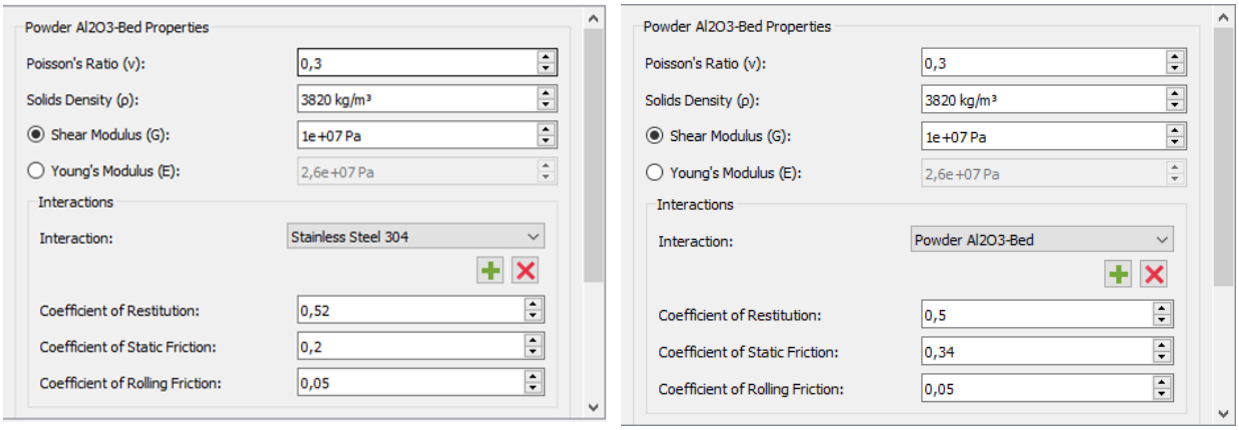

Figure 4.1: Powder material properties and interactions adjustment in the EDEM software.

However, before running the whole set of simulations, it is of paramount importance to examine how the selected shear modulus value affects both the timestep, hence the total time of the simulations, and the accuracy of the results. Zhang et al. (2020) selected a value of 3 GPa ($3 \cdot 10^9$ Pa) for their simulations [71], which is outside the suggested range by the EDEM^{TM} tutorials. However, this value is still two orders of magnitude below its actual value, which is approximately 150 GPa [183], [184], [185]. After running shear cell tests to define the interparticle interactions as well as the interactions between particles and wall, i.e., the coefficients of restitution, static and rolling friction,

they ran cross checking simulations/experiments of the angle of avalanche and angle of repose tests, finding that the angles were deviating by only +1.1% and +1.6% respectively. This result validated the realistic behaviour of the powder particles within the simulation environment. However, Chen et al. (2017) [186] examined by how many orders of magnitude it is possible to decrease the Young's modulus without affecting the simulation's results for a powder mixing experiment in a rolling drum, which is very similar to the angle of avalanche test. In essence, due to the *Equation (4.1)*, if the Poisson ratio is constant, then E and G are linearly related. Hence, a decrement of E by n orders of magnitude will result in a decrement of G by n orders of magnitude and vice versa. Chen et al. proved that, when E varied between the real-world value, E_0, and the value $0.001E_0$, the simulation results were comparable and closely resembled the real experiment, both in results of avalanche angle, as well as in terms of mixing mechanics and powder behaviour. However, when the E value was set to $0.0007E_0$, and for all values below that, the angle of avalanche was reduced by approximately 15% (from 33° to 28°) and, due to the reduce of shearing forces, the mixing rate was decreased [186]. However, the type of experiment (drum mixing of powder) relies much more heavily on shear forces, compared to the powder recoating of a bed via a doctor blade. Fouda et al. (2019) studied powder spreading of a mono-sized Ti6Al4V powder via a doctor blade. The calibration of the simulation was again performed via cross-checking simulation and experimental results of an angle of repose test. They also studied the shear modulus range of 1MPa to 100 MPa. Given that the real-world shear modulus of Ti6Al4V (G_0) is approximately equal to 42.5 GPa, 1 MPa is equal to $2.2 \cdot 10^{-5}G_0$ and 100 MPa is equal to $2.2 \cdot 10^{-3}G_0$, representing a decrement of 5 and 3 orders of magnitude respectively. The differences that the variance of the shear modulus imposed onto the powder kinematics were minimal, so a value of 1 MPa was selected to maximize the timestep and minimize the simulation time.

The author of the current work reached the same conclusion after evaluating powder spreading of the same trial that was carried out thrice, one with a shear modulus value of 10 MPa ($6.6 \cdot 10^{-5}G_0$), the second one with a shear modulus of 150 MPa ($10^{-3}G_0$) and the third with the actual value of 150 GPA (G_0). Between the first and the second trial, the powder kinematics were minimally changed, and the only quality parameter that was minorly altered was the $(h_l - h_{l,th})$, from -21.2 to -18.9 μm. Surface coverage ratio and packing density of the layer were virtually unaffected, while the surficial RMS

roughness of the layer changed minimally. In general, the results can be seen in *Table 4.2*. In the parentheses, the reader can check the deviation of the quality criteria with regard to the third trial, in which the real-world value of the shear modulus of the powder material was used.

Table 4.2: Layer quality for various shear ratio values. The settings used were the ones used for the trial #9 of the Taguchi L27 array for powder spreading, i.e., $U_{tr} = 0.01\ m/sec$, $f_{vib} = 2000\ Hz$, $A_{vib} = 5\ \mu m$ and $\theta_{rel} = 5^o$.

TRIAL #	$G\ (Pa)$	$\lvert h_l - h_{th} \rvert\ (\mu m)$	*SCR* (%)	$S_q - RMS\ (\mu m)$	*PD* (% *of BD*)
1	$1 \cdot 10^7$	21.5 (+18.8%)	99.3 (−0.1%)	16.4 (+10%)	67.8 (+0.6%)
2	$1.5 \cdot 10^8$	18.9 (+4.4%)	99.4 (≡)	15.8 (+6%)	67.4 (≡)
3	$1.5 \cdot 10^{11}$	18.1	99.4	14.9	67.4

In order for the DEM simulation to run in a stable manner, the critical time step is calculated using the Rayleigh time step [187], as follows (*Equation (4.2)*).

$$\Delta t_c = \frac{\pi \cdot r_{min}}{\beta} \sqrt{\frac{\rho}{G}} \qquad (4.2)$$

Where r_{min} is the minimum particle radius found in the simulation's domain [188], [189], ρ is the bulk density of the powder, G is the shear modulus of the powder's material and β can be approximated by *Equation (4.3)* [190], [191], with ν being the Poisson ratio of the material of the powder.

$$\beta = 0.8766 + 0.163\nu \qquad (4.3)$$

As seen in *Figure 4.2(c)* and *(d)*, the author has set the minimum particle radius at $r_{min} = 2.5\mu m$, in order to not allow very small particles to enforce a very small timestep and to prevent the powder from displaying an extremely cohesive behaviour. Similarly, the author has set the maximum particle diameter at $D_{max} = 75\mu m$, which is 25% smaller than the theoretical layer thickness $h_{l,th}$, since particles with a diameter approximately equal to the vertical distance between the doctor blade and the substrate would make the surface quality to drastically deteriorate [8]. After calculating the critical timestep between the three trials, the *Table 4.3* is presented.

In *Table 4.3*, both the critical timestep and the total simulation time of the three trials are presented. It is important to note that EDEM™ offers the capability of NVIDIA™ CUDA computing. Graphics card programming drastically decreases the simulation

time for problems that are compatible with parallel computing. In the case of DEM simulations, it is possible to run the calculations for multiple powder particles in a parallel architecture. This capability was enabled, so, for simple CPU-based computing, the simulation times would get exponentially higher as the number of particles increased.

Table 4.3: Calculated timesteps for various shear ratio values.

TRIAL #	$r_{min}\ (\mu m)$	$\rho\left(\frac{Kg}{m^3}\right)$	ν	β	$G\ (Pa)$	Δt_c (nsec)	$t_{sim}(h)$
1	2.5	3820	0.3	0.9255	10^7	165.861	2.5
2	2.5	3820	0.3	0.9255	$1.5 \cdot 10^8$	42.825	25
3	2.5	3820	0.3	0.9255	$1.5 \cdot 10^{11}$	1.354	168

By decreasing the shear modulus by three orders of magnitude compared to its real-world value, the simulation ran at around one tenth $\left({}^1/_{10}\right)$ of the time, from 168 hours to only 15 hours, while the only quality criteria that were minimally affected were the surface layer thickness deviation and the surface root mean square roughness, which were increased by 4.4% and 6% respectively. By a further decrease of the shear modulus by another order of magnitude, again the only quality criteria that were affected were the surface layer thickness deviation and the surface root mean square roughness, which were increased by a further 14.4% and 4% respectively, with the percentages calculated as a fraction of their values in the real-world G simulation (trial #3).

It can be safely deduced that, in order for the simulations to run fast enough to complete the 27 simulations of the Taguchi design in a reasonable amount of time, the smallest value of the shear modulus must be selected. The deviation can only be considered significant in the case of the layer thickness (18.8%), but not at such a level to justify running simulations at 12 $(25/2.5)$ or 67 $(168/2.5)$ times the simulation time necessary for the lowest tested shear modulus. Even so, the study remains "on the safe side", because, by decreasing the shear modulus, the quality of the layer seems to deteriorate. If the surface quality is considered acceptable by the 10 MPa shear modulus value, then the layer produced by the real-world shear modulus value will be of higher quality, rendering it acceptable as well.

4.2 Particle Size Distribution

Since the powder selected was spherical alumina, in the EDEM software a uniform spherical shape was selected for all particles. Hence, there was no need to import a 3D template via SEM scans of the powder particles, which would make the simulation slower. When it comes to the size, some Excel spreadsheet calculations were carried out in order to examine which kind of distribution best fits the three PSD numbers (D_{10}, D_{50} and D_{90}) provided by the powder manufacturer.

a

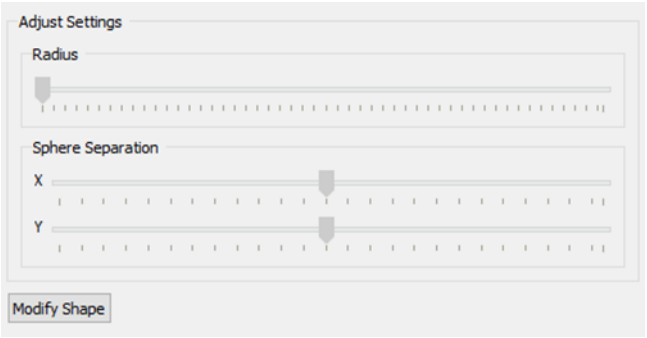

b

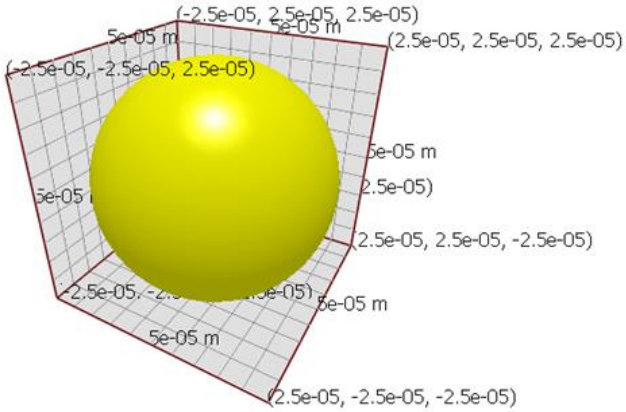

c

Edit Contact Radius

	Name	Position X (m)	Position Y (m)	Position Z (m)	Physical Radius (m)	Contact Radius (m)
0	sphere 0	0	0	0	2.5e-05	2.6e-05

d

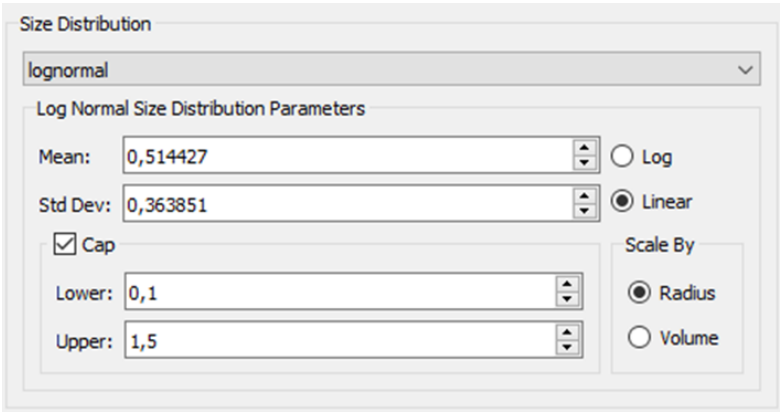

Figure 4.2: ***(a)*** Setting initial settings for spherical particle; ***(b)*** particle depiction; ***(c)*** Sphere geometrical data; ***(d)*** particle size distribution selection and parametrization.

In many studies, a lognormal distribution is used to approximate the particle size distribution of a given powder, however, no method of defining the lognormal

distribution parameters based on the aforementioned powder PSD specifications has been documented.

Initially, a lognormal distribution is being defined as follows:

Let Z be a standard normal variable, i.e., a variable that follows a normal (Gaussian) distribution, and $\mu \in (-\infty, +\infty)$, $\sigma > 0$ be two real numbers. Then, the distribution of the variable

$$X = e^{\mu+\sigma Z}$$

is called the log-normal distribution with parameters μ and σ. It must be emphasized that these parameters are the expected value (or mean) and standard deviation respectively of the variable's natural logarithm, and not of the variable X itself. The mean and the standard deviation of the variable X, which follows a lognormal distribution, are given by the *Equations (4.4)* and *(4.5)* respectively.

$$\mu_X = \sqrt{e^{2\mu+\sigma^2}} \tag{4.4}$$

$$\sigma_X = \sqrt{{\mu_X}^2\left(e^{\sigma^2} - 1\right)} \tag{4.5}$$

And, inversely

$$\mu = \ln\left(\frac{{\mu_X}^2}{\sqrt{{\mu_X}^2 + {\sigma_X}^2}}\right) \tag{4.6}$$

$$\sigma^2 = \ln\left(1 + \frac{{\sigma_X}^2}{{\mu_X}^2}\right) \tag{4.7}$$

The probability density function $f_X(x)$ and cumulative distribution function $F_X(x)$ of a lognormal distribution are given in *Equations (4.8)* and *(4.9)* respectively.

$$f_X(x) = \frac{1}{x\sigma\sqrt{2\pi}} \exp\left(-\frac{(lnx - \mu)^2}{2\sigma^2}\right) \tag{4.8}$$

$$F_X(x) = \frac{1}{2}\left[1 + erf\left(\frac{lnx - \mu}{\sigma\sqrt{2}}\right)\right] \tag{4.9}$$

Where erf is the error function, see *Equation (4.10)*

$$erf(z) = \frac{2}{\sqrt{\pi}} \int_0^z e^{-t^2} dt \qquad (4.10)$$

Solving the following system of the *Equations (4.11), (4.12)* and *(4.13)*

$$\left\{ \begin{matrix} D_{90} = 47.5 \\ D_{50} = 21 \\ D_{10} = 8.2 \end{matrix} \right\} \Leftrightarrow \left\{ \begin{matrix} F_X(47.5) = 0.9 \\ F_X(21) = 0.5 \\ F_X(8.2) = 0.1 \end{matrix} \right\} \qquad \begin{matrix} (4.11) \\ (4.12) \\ (4.13) \end{matrix}$$

(4.12) and *(4.13)* are used to calculate μ and σ, using *(4.9)*. The result is

$$\left\{ \begin{matrix} \mu = 3.0445 \\ \sigma = 0.7338 \end{matrix} \right\} \qquad \begin{matrix} (4.14) \\ (4.15) \end{matrix}$$

While *(4.11)* is used in order to validate that the approximation is a good fit.

$$F_X(47.5) = \frac{1}{2}\left[1 + erf\left(\frac{ln47.5 - 3.0445}{0.7338 \cdot \sqrt{2}}\right)\right] = 0.867 \cong 0.9$$

With a deviation of

$$\frac{0.867 - 0.9}{0.9} \cdot 100\% = -3.7\%$$

Using *(4.14)* and *(4.15)*, *Equation (4.9)* turns into

$$(4.9) \overset{(4.14),(4.15)}{\Longleftrightarrow} F_X(x) = \frac{1}{2}\left[1 + erf\left(\frac{lnx - 3.0445}{0.7338 \cdot \sqrt{2}}\right)\right] \qquad (4.16)$$

So, to calculate D_{90}, E*quation (4.16)* gives

$$F_X(x) = 0.9 \Rightarrow erf\left(\frac{lnx - 3.0445}{0.7338 \cdot \sqrt{2}}\right) = 0.8 \Rightarrow \frac{lnx - 3.0445}{0.7338 \cdot \sqrt{2}} = 0.9062 \Rightarrow$$

$$x = 53.78 \cong 47.5$$

With a deviation of

$$\frac{53.78 - 47.5}{47.5} \cdot 100\% = +13.2\%$$

In order to define the lognormal distribution in the EDEM software, the user has to insert the μ_X and σ_X values, which are calculated by using *Equations (4.4)* and *(4.5)*.

$$(4.4) \overset{(4.14),(4.15)}{\Longrightarrow} \mu_X = 27.488 \qquad (4.17)$$

$$(4.5) \xrightarrow{(4.17),(4.15)} \sigma_X = 23.216 \tag{4.18}$$

The software demands that the values the user feeds as input are normalized, i.e., divided by the average diameter of the particle that is selected, which is 50μm (see *Figure 4.2(c)*, field "Physical Radius"). Hence, the values the user needs to insert are

$$\frac{\mu_X}{D_{ave}} = \frac{27.488}{50} = 0.549758 \tag{4.19}$$

$$\frac{\sigma_X}{D_{ave}} = \frac{23.216}{50} = 0.464323 \tag{4.20}$$

These values are used as input in "Mean" and "Std. dev" parameters of the lognormal distribution tab, see *Figure 4.2(d)*. Furthermore, in the same *Figure*, the user sets the maximum and minimum particle size caps, as a number to be multiplied with the average particle size that is set in *Figure 4.2(c)*, in the "Physical Radius" tab.

4.3 Calculation of Cohesive Forces

In *Figure 4.2(c)*, another choice is visible. It is the "Contact radius" tab. This tab must be filled with a value greater than the physical radius, and it is only used in the case where cohesive and adhesive attractive forces are to be taken into consideration.

With the term "cohesive" forces, the forces are referred to that are applied between particles of the same material, while the term "adhesive forces" refers to the forces that are applied between different materials, such as those that are developed between the particles and the doctor blade, the deposition plate, i.e., the substrate, or any other geometries of the simulation.

In the case like the ones that are examined in this work, the motion of very fine powders of particle diameter less than 100μm is not solely governed by gravitational forces, but by attractive Van Der Waals forces as well [192]. In order for the simulation to take under consideration these forces too, the contact model chosen is the "Hertz-Mindlin with JKR v2".

The general geometry of a contact between two dissimilar, unequal sized, spherical, elastic particles that are subjected to a normal force F_n can be seen in *Figure 4.3* [192]. In this Figure, a (English a) denotes the radius of the circular contact area that the two

compressed spherical particles create. $\delta_i,\ i = 1,2$, (Greek "delta") denotes the distance between the limit of each sphere with the compressed surface, had the spheres been uncompressed at the same spot as they currently are. Hence, $\delta_n = \delta_1 + \delta_2$ is the relative approach of the centroids of the two contacting spheres.

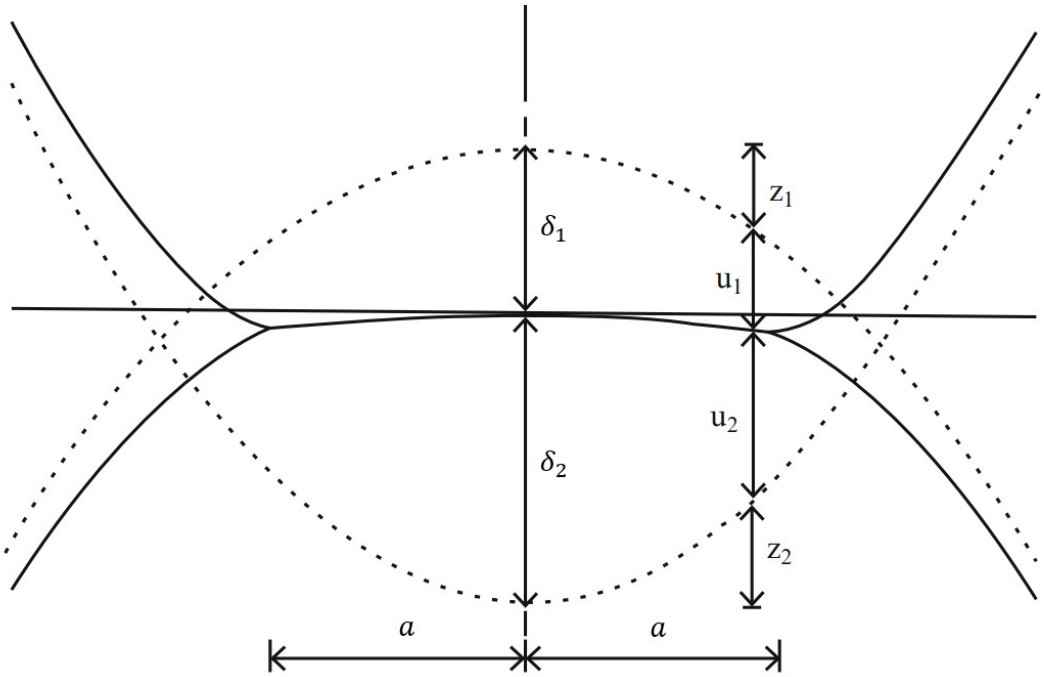

Figure 4.3: Contact of two dissimilar, unequal sized, spherical, elastic particles, subjected to a normal force. Description of each particle's deformation [192].

The relative approach between the spheres is positive when the spheres are in contact and compressed against each other, i.e., when the distance between their centres is smaller than the sum of their two radii, and negative when the distance between the centres of the two spheres is larger compared to the sum of their radii.

If the case described examines the elastic, non-adhesive contact between two dissimilar, unequal sized, spherical, elastic particles, subjected to a normal force, then the analysis is as follows:

The pressure distribution that exists within this circular contact area is denoted by the *Equation (4.21)*.

$$p(r) = p_0 \left[1 - \left(\frac{r}{a}\right)^2\right]^{\frac{1}{2}} \qquad (4.21)$$

While the sphere displacements (from their original point had the contact not existed) over the contact area, by *Equation (4.22)*.

$$u_i(r) = \frac{\pi p_0 (1 - v_i)^2}{4aE_i}(2a^2 - r^2) \tag{4.22}$$

Where E_i and v_i are the Young's modulus and Poisson ratio of each sphere.

Based on *Figure 4.3*, *Equation (4.23)* gives:

$$u_1(r) + u_2(r) = \delta_n - \left(\frac{r^2}{2R^*}\right) \tag{4.23}$$

Where R^* denotes the relative radius of curvature of the surface and is given by *Equation (4.24)*

$$\frac{1}{R^*} = \frac{1}{R_1} + \frac{1}{R_2} \tag{4.24}$$

$$(4.23) \xrightarrow{(4.22)} \left(\frac{\pi p_0}{4aE^*}\right)(2a^2 - r^2) = \delta_n - \left(\frac{r^2}{2R^*}\right) \tag{4.25}$$

Where E^* denotes the relative contact compliance and is given by *Equation (4.26)*

$$\frac{1}{E^*} = \frac{(1 - {\nu_1}^2)}{E_1} + \frac{(1 - {\nu_2}^2)}{E_2} \tag{4.26}$$

So, the relative approach is given as

$$(4.25) \xrightarrow{r=0} \delta_n = \frac{\pi p_0 a}{2E^*} \tag{4.27}$$

And the radius of the contact area, as follows:

$$(4.26) \xrightarrow{(4.27),\ r=a} a = \frac{\pi p_0 R^*}{2E^*} \tag{4.28}$$

And the normal force is given by

$$F_n = \int_0^a p(r) 2\pi r dr = \frac{2}{3} p_0 \pi a^2 \tag{4.29}$$

So, the equivalent equations for δ_n and a are

$$(4.27) \xrightarrow{(4.29),\ a^2 = R^* \delta_n} a^3 = \frac{3F_n R^*}{4E^*} \tag{4.30}$$

$$(4.28) \xrightarrow{(4.29),\ a^2 = R^* \delta_n} {\delta_n}^3 = \frac{9{F_n}^2}{16 R^* {E^*}^2} \tag{4.31}$$

So, by rearranging Equation *(4.30)*,

$$(4.30) \Rightarrow F_n = \frac{4}{3} E^* \left(R^* {\delta_n}^3 \right)^{1/2} \quad (4.32)$$

Which makes it possible to calculate the normal stiffness of the contact as follows:

$$k_n = \frac{dF_n}{d\delta_n} = 2E^* (R^* \delta_n)^{1/2} = 2E^* a \quad (4.33)$$

The above analysis (Hertz-Mindlin model [193], [194], [192]) is very useful in the case when researchers do not want to evaluate any plastic deformation inflicted on the particles and, at the same time, the particles are above a certain size limit, commonly above 50 μm [192], in order for the cohesive and adhesive forces to be negligible compared to the gravitational ones, hence of no effect to the result of the simulation. However, in the case that is examined in this study, where the minimum particle diameter is at 5 μm, i.e., an order of magnitude smaller compared to the limit where cohesive forces are of no value, it is imperative that they are included in the model, so there is a need to adjust the analysis that is presented above.

There is a multitude of mechanisms by which microscopic particles may adhere to each other. In the case of relatively strong bonds, it may be solid, cemented or glued by a viscous liquid. Weaker bonds may be provided by pendular liquid bridges, Van der Waals forces, electrostatics or electro-magnetic fields [192]. In this work, however, there is no presence of viscous liquid or moisture that could create liquid bonds. Electrostatic charge is ignored, since the minimum particle diameter is at 5 microns, which is not at the nanoscale, where the forces due to electrostatic charges begin to surpass gravitational forces. Even though, some electrostatic charge can be developed, either via contact between the insulator (aluminum oxide) with the substrate (stainless steel plate), or via contact of particles of alumina with each other, granted they are of dissimilar size [195], they would be negligible due to the rather large average size of the powder sample used. Furthermore, it is stated in literature that, even in the case of a fluidized bed of alumina particles, the charge of alumina dust is relatively neutral [196]. Hence, in the case of powder deposition, where much smaller excitation of the particles is performed, the charges developed will be even more insignificant. In a similar manner, electro-magnetic fields are not present, so, the only factor to be taken

under consideration are the Van Den Waals forces. Furthermore, no plastic deformation of the particles or the geometries is to be taken under consideration in this work, since the materials are of very high hardness and they collide with each other at relatively low speeds, resulting in no permanent deformations.

There are two different models that describe the behaviour of auto-adhesive particles due to Van der Waals forces, the JKR (Johnson-Kendall-Roberts) model [197] and the DMT (Derjaguin-Muller-Toporov) model [198].

A brief explanation of the JKR model follows below:

The general relationship between normalized normal force and normalized relative particle approach in JKR model is given by the *Equation (4.34)*. Normal force F_n^{JKR} is normalized by dividing it by the pull-off force, F_{po}, and relative approach δ_n is normalized by dividing it by the relative approach at tear-off moment δ_{to}.

$$\frac{\delta_n}{\delta_{to}} = \frac{3\left(\frac{F_n^{JKR}}{F_{po}}\right) + 2 + 2\left(1 + \frac{F_n^{JKR}}{F_{po}}\right)^{1/2}}{3^{2/3}\left[\frac{F_n^{JKR}}{F_{po}} + 2 + 2\left(1 + \frac{F_n^{JKR}}{F_{po}}\right)^{1/2}\right]^{1/3}}, \frac{F_n^{JKR}}{F_{po}} \geq -1 \qquad (4.34)$$

With F_{po} being the maximum tensile force required to break the contact among the two particles (i.e., the "pull-off force"). The pull-off force for the JKR model is given by *Equation (4.35)*

$$F_{po} = \frac{3}{2}\pi R^* \Gamma \qquad (4.35)$$

And δ_{to} is the relative approach at tear-off moment, given by *Equation (4.36)*

$$\delta_{to} = \left(\frac{3{F_{po}}^2}{16R^*{E^*}^2}\right)^{1/3} \qquad (4.36)$$

JKR model gives the *Equation (4.37)* and *Equation (4.38)* for the normal force F_n^{JKR} and relative approach δ_n respectively as functions of the contact patch radius, a.

$$F_n^{JKR} = \frac{4E^* a^3}{3R^*} - (8\pi E^* \Gamma a^3)^{1/2} \qquad (4.37)$$

$$\delta_n = \frac{a^2}{R^*} - \left(\frac{2\pi\Gamma a}{E^*}\right)^{1/2} \tag{4.38}$$

The radius of the contact patch between the two spheres at the moment of equilibrium is defined as a_0, and given by *Equation (4.39).*

$$(4.37) \xrightarrow{F_n^{JKR}=0, a>0} a_0 = \sqrt[3]{\frac{9\pi\Gamma R^{*2}}{2E^*}} \tag{4.39}$$

The letter order of *Figure 4.4(b)* from A to F shows how a contact is described. Initially, at point A, the two particles are not in contact, zero force is exerted to them by each other, and there is a negative relative approach. As the two particles approach each other, they eventually reach point B, where the particles are infinitesimally before contact. The relative approach is zero, meaning that the distance between the spheres' centres is approximately equal to the sum of the two radii, yet the force remains zero. However, once the contact is achieved (point C), which is checked in the simulation via the physical radii of the two particles, the relative approach and the normalized approach become exactly equal to zero (*Equation (4.40)*)

$$\frac{\delta_{n,C}}{\delta_{to}} = 0 \tag{4.40}$$

And the force immediately drops to a value of (*Equation (4.41)*)

$$(4.34) \xrightarrow{(4.40)} \frac{F_{n,C}^{JKR}}{F_{po}} = -\frac{8}{9} \tag{4.41}$$

At the point of contact (Point 3 of *Figure 4.4(a)*/Point C of *Figure 4.4(b)*) the following equation also applies for the radius of the contact patch:

$$(4.38) \xrightarrow{\delta_{n,C}=0,(4.39)} \frac{a_C}{a_0} = \left(\frac{2}{3}\right)^{2/3} \tag{4.42}$$

Then, the loading stage begins, when the two spheres deform elastically, compressing against each other as *Figure 4.3* demonstrates. During this stage, eventually the two particles achieve a state of equilibrium, i.e., a state where the normal force exerted on each other is zero (point 4 of *Figure 4.4(a)*), as described in *Equation (4.43)*.

$$\frac{F_{n,EQ}^{JKR}}{F_{po}} = 0 \tag{4.43}$$

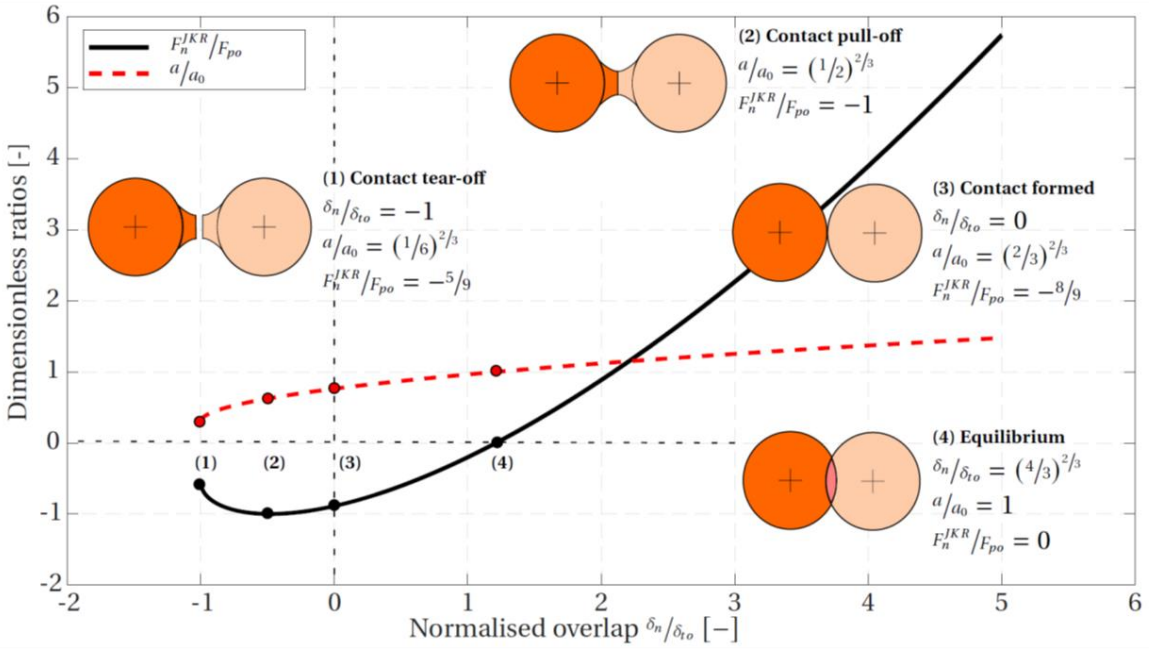

a

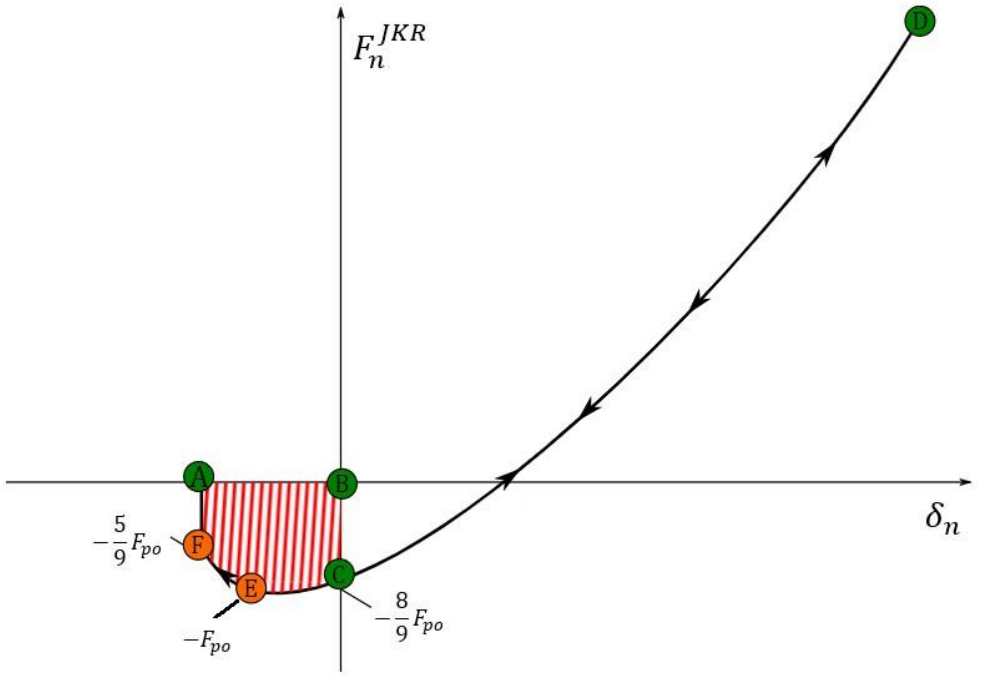

b

Figure 4.4: ***(a)*** Explanation of the 4 critical moments of the JKR contact model for adhesive, elastic, contacts (Contact, equilibrium, pull-off, tear-off) [199]; ***(b)*** Visual depiction of the work of adhesion between the two surfaces and order of contact evolution [200].

At the equilibrium point, the following equations apply

$$(4.34) \xrightarrow{(4.43)} \frac{\delta_{n,EQ}}{\delta_{to}} = \left(\frac{4}{3}\right)^{2/3} \tag{4.44}$$

$$\frac{a_{EQ}}{a_0} = 1 \tag{4.45}$$

After equilibrium, the loading continues, but the compression is now decelerated instead of accelerated, since the force is now positive, which means that the two spheres are now being repelled and the forces exerted on them via their own behaviour as non-linear springs are surpassing the attracting Van der Waals forces. Eventually, the deceleration forces the compression to reach a maximum point, which is point D of *Figure 4.4(b)*.

Then, since there is assumed that no plastic deformation exists, the relative approach begins to become smaller, as the spheres begin to accelerate towards the opposite direction, with their centres distancing themselves from each other. The force versus relative approach diagram follows the same curve, but towards the opposite direction. This is the unloading stage, where the stored elastic energy becomes kinetic energy. As soon as the relative approach becomes zero again, at point 3 or C of *Figure 4.4(a)* or *Figure 4.4(b)* respectively, all the work done during the loading stage is recovered.

However, since the two bodies are still in cohesive contact, further work needs to be done in order for them to be separated. This work, termed W_{adh} is given by the area that is highlighted in red, in *Figure 4.4(b)*. Initially, the relative approach begins to take negative values, and the "bottleneck" effect appears. Eventually, at the "pull-off" point (2 or E point in *Figure 4.4(a)* or *Figure 4.4(b)* respectively), the force takes a maximum negative value, and the following equations apply:

$$\frac{F_{n,E}^{JKR}}{F_{po}} = -1 \tag{4.46}$$

$$(4.34) \xrightarrow{(4.46)} \frac{\delta_{po}}{\delta_{to}} = -\left(\frac{1}{3}\right)^{2/3} \tag{4.47}$$

$$(4.37) \xrightarrow{F_{n,E}^{JKR} = -F_{po}, (4.35), (4.39)} \frac{a_{po}}{a_0} = \left(\frac{1}{2}\right)^{2/3} \tag{4.48}$$

If the system is load-controlled, then the situation becomes unstable at the pull-off point described above. However, particle system simulations are always displacement-

driven, hence the bond breaks at the tear-off point (point 1 or F of *Figure 4.4(a)* or *Figure 4.4(b)* respectively) [201]. At tear-off point, the following equations apply:

$$\frac{\delta_{n,F}}{\delta_{to}} = -1 \tag{4.49}$$

It should be noted that the range of the *Equation (4.34)* is $\frac{\delta_n}{\delta_{to}} \geq \frac{\delta_{po}}{\delta_{to}} = -\left(\frac{1}{3}\right)^{2/3} \cong -0.481$, so it is impossible to use that *Equation* to calculate points of the JKR diagram that are between the pull-off and the tear-off points.

$$\frac{F_{n,to}^{JKR}}{F_{po}} = -\frac{5}{9} \tag{4.50}$$

$$\frac{a_{to}}{a_0} = \left(\frac{1}{6}\right)^{2/3} \tag{4.51}$$

Finally, the extra work of adhesion necessary to break the contact is given by *Equation (4.52)*:

$$W_{adh} = \int_{\delta_n=0}^{\delta_n=\delta_{to}} F_n^{JKR}(\delta_n)d\delta_n = \int_{a=a_C}^{a=a_{to}} F_n^{JKR}(a)\frac{d\delta_n}{da}da \tag{4.52}$$

Based on *(4.37)*, *(4.38), (4.39), (4.42)* and *(4.51)*, *Equation (4.52)* gives:

$$W_{adh} = \int_{a=\left(\frac{2}{3}\right)^{2/3}\cdot\sqrt[3]{\frac{9\pi\Gamma R^{*2}}{2E^*}}}^{a=\left(\frac{1}{6}\right)^{2/3}\cdot\sqrt[3]{\frac{9\pi\Gamma R^{*2}}{2E^*}}} \left[\frac{4E^*a^3}{3R^*} - (8\pi E^*\Gamma a^3)^{1/2}\right]\cdot\left[\frac{2a}{R^*} - \left(\frac{2\pi\Gamma}{4E^*a}\right)^{1/2}\right]da \Rightarrow$$

$$\Rightarrow W_{adh} = \frac{8E^*}{15R^{*2}}({a_{to}}^5 - {a_C}^5) - \frac{4\sqrt{2\pi\Gamma E^*}}{3R^*}\left({a_{to}}^{7/2} - {a_C}^{7/2}\right) + \pi\Gamma({a_{to}}^2 - {a_C}^2) \tag{4.53}$$

With

$$a_{to} = \left(\frac{1}{6}\right)^{2/3}\cdot\sqrt[3]{\frac{9\pi\Gamma R^{*2}}{2E^*}} \qquad \text{and} \qquad a_C = \left(\frac{2}{3}\right)^{2/3}\cdot\sqrt[3]{\frac{9\pi\Gamma R^{*2}}{2E^*}}$$

After explaining the mechanics behind the JKR model, the justification on why this was the selected contact model will follow.

Even though scientists initially believed that the two models (JKR and DMT) were competitive with each other, they soon began to believe that they are limits to a range

of solutions that are governed by the non-dimensional, Tabor parameter μ, which is shown in *Equation (4.54)* [192]. Grierson et al. (2005) [202] state that "Tabor's parameter is physically equivalent to the ratio between the normal elastic deformation caused by adhesion (i.e., in the absence of applied load) and the spatial range of the adhesion forces themselves."

$$\mu = \left(\frac{R^* \Gamma^2}{E^{*2} {z_0}^3}\right)^{1/3} \tag{4.54}$$

In *Equation (4.54)*, z_0 is the equilibrium separation in the Lennard-Jones potential, Γ is the work of adhesion, which is given as

$$\Gamma = \gamma_1 + \gamma_2 - \gamma_{12} \tag{4.55}$$

Where γ_1 and γ_2 are the surface energies of the two contacting bodies and γ_{12} is the interface energy. In the case where two particles of the same material are in contact with each other, the interface energy is zero, and *Equation (4.55)* gives $\Gamma = 2\gamma$, since $\gamma_1 = \gamma_2 = \gamma$.

There are many different opinions regarding the areas of the Tabor parameter values and which contact adhesion model is applicable within each area. Thornton [192] suggests that in general, for $\mu < 0.1$, the DMT model is suitable, while for $\mu > 5$ the JKR theory is preferrable. For the values that lay in the area in-between, Maugis (1992) has developed an analytic approach [203], the Maugis-Dugdale (MD) approach, however it is analytical, hence much more complicated than the two aforementioned models. Nevertheless, it has been proven that the Maugis approach is accurate in all areas of the Tabor parameter [204], while JKR and DMT are the MD approximations at high and low Tabor parameter's values respectively. Greenwood (1997), after comparing the effect of the Tabor parameter on the agreement between Maugis-Dugdale's analytical model and JKR/DMT model predictions, states that, for values of $\mu \geq 3$, the JKR theory is a good approximation of the actual radius of contact, defined as the location of the maximum tensile stress. The shapes and pressure distributions are also in close agreement with the ones predicted by JKR-theory [205]. Greenwood also proves that the DMT theory is "wrong in theory and in practice" (Greenwood, 2017) [205]. Instead, the Bradley-Derjaguin *Equation (4.56)* describes accurately how the tensile load varies with regard to the separation. *Equation (4.56)* is accurate for all

values of μ for large positive separations and is even accurate for negative separations, for small values of μ [205].

$$T(\delta_n) = 2\pi R^* \Gamma \left[\frac{4}{3}\left(\frac{z_0}{\delta_n}\right)^2 - \frac{1}{3}\left(\frac{z_0}{\delta_n}\right)^8\right] \quad (4.56)$$

This is why, from this moment on, in this work, the author will not refer to DMT, but to the Bradley-Derjaguin model, for small values of the Tabor parameter. The MD model implementation in a DEM simulation would drastically increase the simulation time, since the method involves much more equations and mathematical calculations. In general, the JKR model is applied for large diameter, more compliant materials (smaller Young's modulus), while the DMT model is preferrable for smaller bodies of more rigid materials (larger Young's modulus) [204]. In order to examine which model to choose, it was necessary to calculate the Tabor parameter values for the particles of a-alumina, as follows:

The surface energy of amorphous alumina (a-Al_2O_3) is $\gamma_{a-Al_2O_3} = 0.97 \pm 0.04 \frac{J}{m^2}$ [206]. However, this value refers to nanoparticles of diameters between 2-5 nm, and is valid for surface areas greater than 370 m^2/g. The diagram shown in *Figure 4.5* shows how the surface area of spherical alumina particles changes with the change in the particle's diameter. It is known that the surface energy depends on particle size, with the general consensus being that it decreases with the decrease in particle size [207]. This is justified, since the number of next neighbors of surface atoms reduces with decreasing particle size [207]. Tepesch et al. (2000) calculated the surface energy of stoichiometric (1-Al-terminated) amorphous alumina (a-Al_2O_3) as $\gamma_{a-Al_2O_3} = 2.13 \frac{J}{m^2}$ [208]. This surface is the most stable expression of a-alumina. Indeed, this value comes in accordance with the rule of thumb that as the particle size increases, the surface energy increases as well. Hence, for two contacting particles of a-alumina, $\Gamma \cong 4.26 \frac{J}{m^2}$.

R^* and E^* are calculated by the *Equations (4.24)* and *(4.26)* respectively, replacing $E_1 = E_2 = E$ and $\nu_1 = \nu_2 = \nu$, hence taking

$$R^* = \frac{R_1 R_2}{R_1 + R_2} \quad (4.57)$$

$$E^* = \frac{E}{2(1-\nu^2)} \tag{4.58}$$

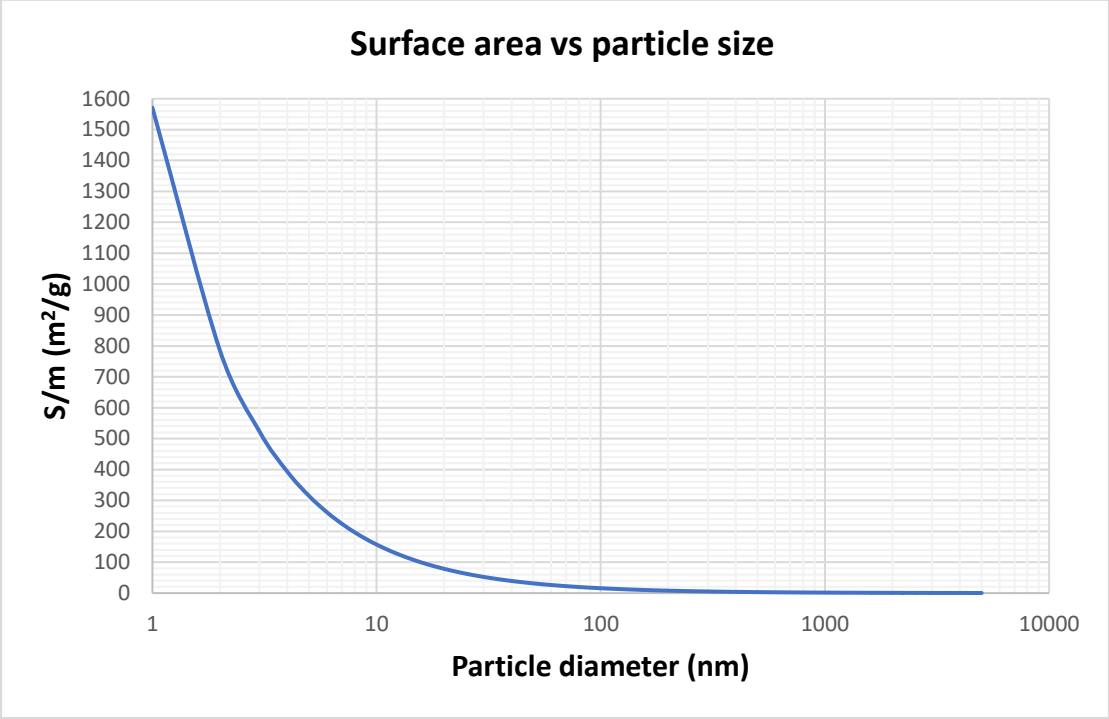

Figure 4.5: Surface area vs particle diameter plot for spherical a-alumina particles.

Finally, the equilibrium separation in the Lennard-Jones potential for a-Al_2O_3 is $z_{0_{a-Al_2O_3}} = 5.1\ \text{Å} = 5.1 \cdot 10^{-10}\ m$ [209]. The diagram of the *Figure 4.6* shows how the Tabor parameter value varies with the diameter of the two spherical a-alumina particles in contact. Let it be noted that the shear modulus is adjusted to $1.29 \cdot 10^{11}\ Pa$, so that, combined with a Poisson ratio of 0.3, the Young's modulus is the maximum within the limit provided in [185], i.e., 413 GPa.

It can be assumed that the Tabor parameter μ increases with the increase of the particle size. If the first among the two particles in contact has a diameter of 5 μm, then the Tabor parameter values range between 1.492 and 1.840 for the second particle's diameter being 5 and 75 μm respectively. If the first particle's diameter is 75 μm, however, the Tabor parameter values range between 1.840 and 3.681 for the second particle's diameter being 5 and 75 μm respectively.

Greenwood [205] suggests that, as the Tabor parameter increases, the pull-off force, i.e., the force needed to separate two spheres decreases steadily from the Bradley value $(2\pi R^* \Gamma)$ towards the JKR value $\left(\frac{3}{2}\pi R^* \Gamma\right)$. For $\mu \geq 3$, the JKR model is accurate [210],

for $2 \leq \mu \leq 3$ the force-separation curves resemble a hybrid of the JKR approach for positive and marginally negative approach values, and Bradley curve for large negative separations, while for $\mu \leq 0.2$ they approximate the Bradley curve in the tensile region.

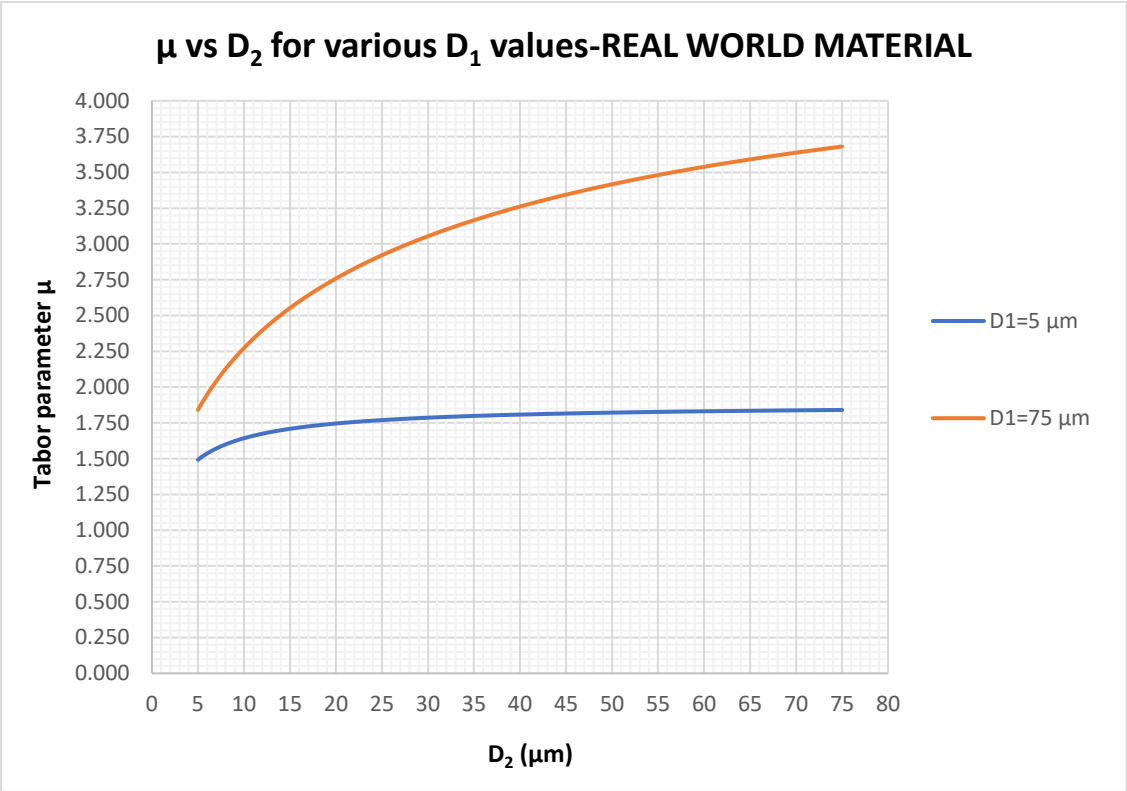

Figure 4.6: Tabor parameter curve vs the second particle's diameter, for the two extreme values of the first article's diameter.

Judging by *Figure 4.6*, it can be deduced that, for the real-world material, almost all contacts of the larger particles (around 60-75 μm diameter) would be able to be modelled via JKR or at least hybrid JKR, as Greenwood suggests for $\mu \geq 2$ values. However, for smaller particles (around 5-15 μm diameter), the Bradley-Derjaguin *Equation (4.56)* or even the analytic MD approach would be better. The MD approach would render the simulation much slower, however, the Bradley-Derjaguin and hybrid JKR models would be beneficial in areas where the JKR seems to deviate significantly from the analytical solution of the adhesive elastic contact problem.

In the trial runs that were performed in this study, in order to determine which shear modulus value would be used in the simulations, the shear modulus and, thus, the Young's modulus was varied from its actual value to a value 4 orders of magnitude smaller. The Tabor parameter's value increases with the decrease of the relative modulus of elasticity (E^*) taking it to larger values by 3 orders of magnitude. Hence,

the selection of the "Hertz-Mindlin with JKR v2" model in the EDEM software is perfectly justified.

In *Figure 4.2(c)*, there is a field termed "Contact radius". This variable will be from this point on be called $R_{c,EDEM}$, and is given by the *Equation (4.59)*.

$$R_{c,EDEM} \geq R_{particle} + |\delta_{to}| \tag{4.59}$$

Where $R_{particle}$ refers to the average particle radius, as given in the field "Physical Radius" of *Figure 4.2(c)* and δ_{to} is the relative approach of the two particles in contact (both of $R_{particle}$ radius) at which the contact breaks, with "to" standing for "tear-off". The relative approach at tear-off moment is given by *Equation (4.60)* [192].

$$\delta_{to} = \left(\frac{3{F_{po}}^2}{16R^*E^{*2}}\right)^{1/3} \tag{4.60}$$

With F_{po} being the maximum tensile force required to break the contact among the two particles (i.e., the "pull-off force"), given by *Equations (4.61)* and *(4.62)* for the JKR and Bradley (or DMT) model respectively [192].

$$F_{po}^{JKR} = \frac{3}{2}\pi R^*\Gamma \tag{4.61}$$

$$F_{po}^{Bradley} = 2\pi R^*\Gamma \tag{4.62}$$

Finally, *Equation (4.60)*, after replacing by *Equations (4.61)*, *(4.57)* and *(4.58)* takes the form of the *Equation (4.63)*:

$$\delta_{to} = \sqrt[3]{\frac{16.655R_1R_2\Gamma^2(1-\nu^2)^2}{(R_1+R_2)E^2}} \tag{4.63}$$

And, for $R_1 = R_2 = R_{ave} = 25\mu m$, *(4.63)* is written as:

$$\delta_{to} = \sqrt[3]{\frac{8.327R_{ave}\Gamma^2(1-\nu^2)^2}{E^2}} \tag{4.64}$$

So, *Table 4.4* is created, as follows:

Table 4.4: Calculated relative approach and Tabor parameter for different shear modulus values.

CASE	G (Pa)	ν	E (Pa)	E^* (Pa)	R_{ave} (μm)	R^* (μm)	$\Gamma\left(\frac{J}{m^2}\right)$	z_0 (Å)	δ_{to} (μm)	μ
$SIM-1$	$1\cdot10^7$	0.3	$3.2\cdot10^7$	$1.76\cdot10^7$	25	12.5	4.26	5.1	1.451	1768.56
$SIM-2$	$1.5\cdot10^8$	0.3	$4.8\cdot10^8$	$2.64\cdot10^8$	25	12.5	4.26	5.1	0.239	290.78
$RW-3$	$1.29\cdot10^{11}$	0.3	$4.13\cdot10^{11}$	$2.27\cdot10^{11}$	25	12.5	4.26	5.1	0.003	3.22

Searching through literature and EDEM software tutorials, it remains unclear and, to the author's knowledge, untested, whether the contact radius setting has to be chosen based on the real-world material's shear modulus value or based on the shear modulus value that is set within the simulation environment in order for the timestep to be increased. Hence, three cases were compared, in order to examine the differences. By examining the Tabor parameter for each case, it is noticeable that, the higher the particle's stiffness, the smaller its relative approach at bond breakage moment. Indeed, when the material becomes less compliant and loses its elasticity, indicated by the increase of 4 orders of magnitude in Young's modulus, the Tabor parameter decreases by 3 orders of magnitude, from 1768.56 to 3.22, while the respective approach at bond breakage also decreases from around 1.5μm to around 3nm.

It is important to clarify that EDEM's contact radius does not examine whether two particles, or a particle and a body in the simulation, have approached each other enough in order for adhesive/cohesive forces to facilitate. This is a common misconception that needs to be clarified. In order for adhesive/cohesive forces to apply, two particles or a particle and a geometry need to come into physical contact first. This check happens via the physical radii of the two bodies. However, the contact radius creates a zone around each particle where negative approach is possible. As the two particles collide, they demonstrate simultaneously their compliance/elasticity and their cohesion. Their momentum creates a collision force and they behave like springs, initially with a positive approach, where they decelerate as they deform more and more. However, this collision is less "violent" and they decelerate slower than they would if the cohesive forces had not been present, since they now get attracted to each other due to Van der Waals forces. Eventually, the approach will stop increasing and it will decrease again, however, when it becomes zero, the particles will not separate, but the "bottleneck effect" will develop, since the particles will remain in contact due to the cohesive forces,

and further work is required in order to create two new, separated surfaces. *Figure 4.4* explains the stages of a contact between two particles. The larger EDEM's contact radius is, the larger the negative approach it will allow, hence the larger the "zone of influence" each particle will create around it, within which, attracting adhesive forces will act. Hence, the larger the EDEM's contact radius, the more cohesive the behaviour the powder will exhibit. The real-world material is much stiffer and less cohesive compared to the one in the simulations. For the simulations, the value of the contact radius is 26μm, which would be valid in the case where the relative approach at bond breakage would be 1μm. This was selected in order to round it down from the 26.451 value it should have had based on the simulation-set value for the material's shear ratio. This makes the material exhibit a behaviour closer to reality. However, scaling it down any further would cause a large deviation from the calculated value, which would create an unrealistic material of very low relative approach at bond breakage despite its very high elasticity. Furthermore, by setting the difference between the physical and contact radii of the average particle at 1μm, the simulation is easily scalable, while the increased cohesion makes this a study "on the safe side", since, if the suggested system can counter the simulation material's cohesion, the real-world material will be much easier to spread evenly.

It is of some interest to examine the fluctuation of the particles' behaviour in the simulation with regard to their real-world behaviour. *Table 4.5* is filled for this reason.

Table 4.5: The relation of parameter values between the real-world and the simulation-defined material. In parentheses, it is stated how this parameter affects the powder's behaviour compared to its counterpart.

	REAL-WORLD PARTICLES	***SIMULATION PARTICLES***
Young's modulus	↑ (less elasticity)	↓ (more elasticity)
Tabor's parameter	<5 (less elasticity)	>100 (more elasticity)
Suitable model for F_{po}	Bradley ($2\pi R^{*}\Gamma$) (more cohesion)	JKR $\left(\frac{3}{2}\pi R^{*}\Gamma\right)$ (less cohesion)
Relative approach at bond breakage $\delta_{to}(\mu m)$	3nm (less cohesion)	1451nm (more cohesion)

As seen in *Table 4.5*, the real-world material demonstrates higher stiffness and less compliance, thanks to its higher Young's modulus. This is also reflected on the calculated Tabor parameter for each case. The most suitable model to describe the real-

world particles would be the Bradley pull-off force model, while the simulation implements a JKR pull-off force, which is 25% lower. This means that, despite their higher rigidity, which is translated to shorter collisions of smaller deformations and sharper force profiles during contact for the real-world particles, these demand a 25% larger pull-off force in order to escape from cohesive forces by their neighbouring particles, which slightly compensates for the less cohesive behaviour they demonstrate, which is also visible by examining the relative approach at bond breakage.

In order to provide a better understanding on the magnitude of the cohesive forces, let us examine the simple problem of two spherical particles on a normal, central collision, where one of them, which from now on will be named "Particle 1" is space-locked, i.e., stationary and immovable. This means that it is kept at the same place while the one colliding onto it, from now on called "Particle 2", is experiencing all the momentum effects by the collision.

At the moment just before the collision, particle 1 is stationary, i.e., $u_{1,before} = 0$, while particle 2 is approaching it at a speed $u_{2,before} > 0$. After the collision, particle 1 remains at the same position, still stationary, so $u_{1,after} = 0$, while particle 2 is moving away from particle 1, at a speed of $u_{2,after} > 0$. As explained before, JKR model suggests an initial contact, then a loading stage, followed by an unloading stage. When the unloading stage reaches point 3 or C of *Figure 4.4(a)* or *Figure 4.4(b)* respectively, i.e., the point of zero relative approach, all the work done during the loading stage is recovered, since there is no plastic deformation. The work of adhesion consumed in order for the moving particle to escape from the adhesive pull of the other particle is the difference between the kinetic energy of the system before the collision and after the bond is torn-off.

$$E_{before} = E_{after} \Rightarrow \frac{1}{2} m_2 {u_{2,before}}^2 = \frac{1}{2} m_2 {u_{2,after}}^2 + W_{adh} \Rightarrow$$

$$u_{2,after} = \sqrt{\frac{1}{m_2}\left(m_2 {u_{2,before}}^2 - 2W_{adh}\right)} \qquad (4.65)$$

Where the work of adhesion is given by *Equation (4.53)*.

In order for the particles to break their adhesive bond, particle 2 has to have a $u_{2,before}$ greater than a certain threshold, otherwise the two particles remain bonded adhesively

with each other. This threshold is calculated by ensuring that the quantity $\frac{1}{m_2}(m_2 {u_{2,before}}^2 - 2W_{adh})$ is positive. Hence, the criterion is

$$\frac{1}{m_2}(m_2 {u_{2,before}}^2 - 2W_{adh}) \geq 0 \Rightarrow u_{2,before} \geq \sqrt{\frac{2W_{adh}}{m_2}} \qquad (4.66)$$

So, the escape velocity is defined as

$$u_{esc} = \sqrt{\frac{2W_{adh}}{m_2}} \qquad (4.67)$$

Three different cases are examined, using the maximum (D_{max}), minimum (D_{min}) and mean (D_{50}) diameter based on the particle size distribution, as it was defined previously:

a) Particle 1: $D_1 = D_{max}$ =75 μm/Particle 2: D_2=5-75 μm
b) Particle 1: $D_1 = D_{50}$=21 μm/Particle 2: D_2=5-75 μm
c) Particle 1: $D_1 = D_{min}$ =5 μm/Particle 2: D_2=5-75 μm

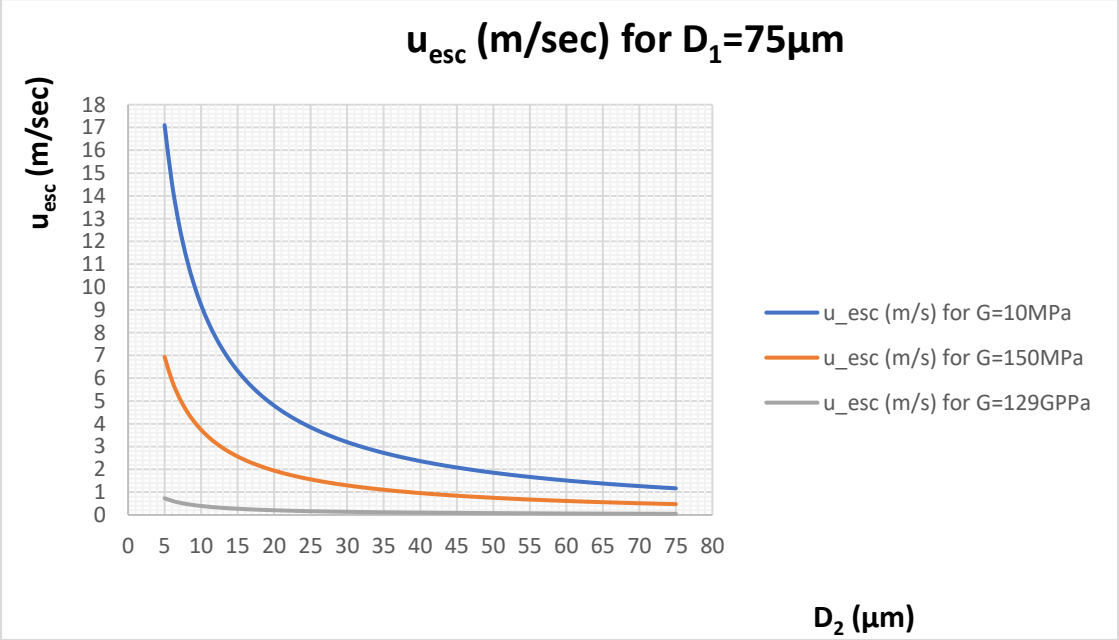

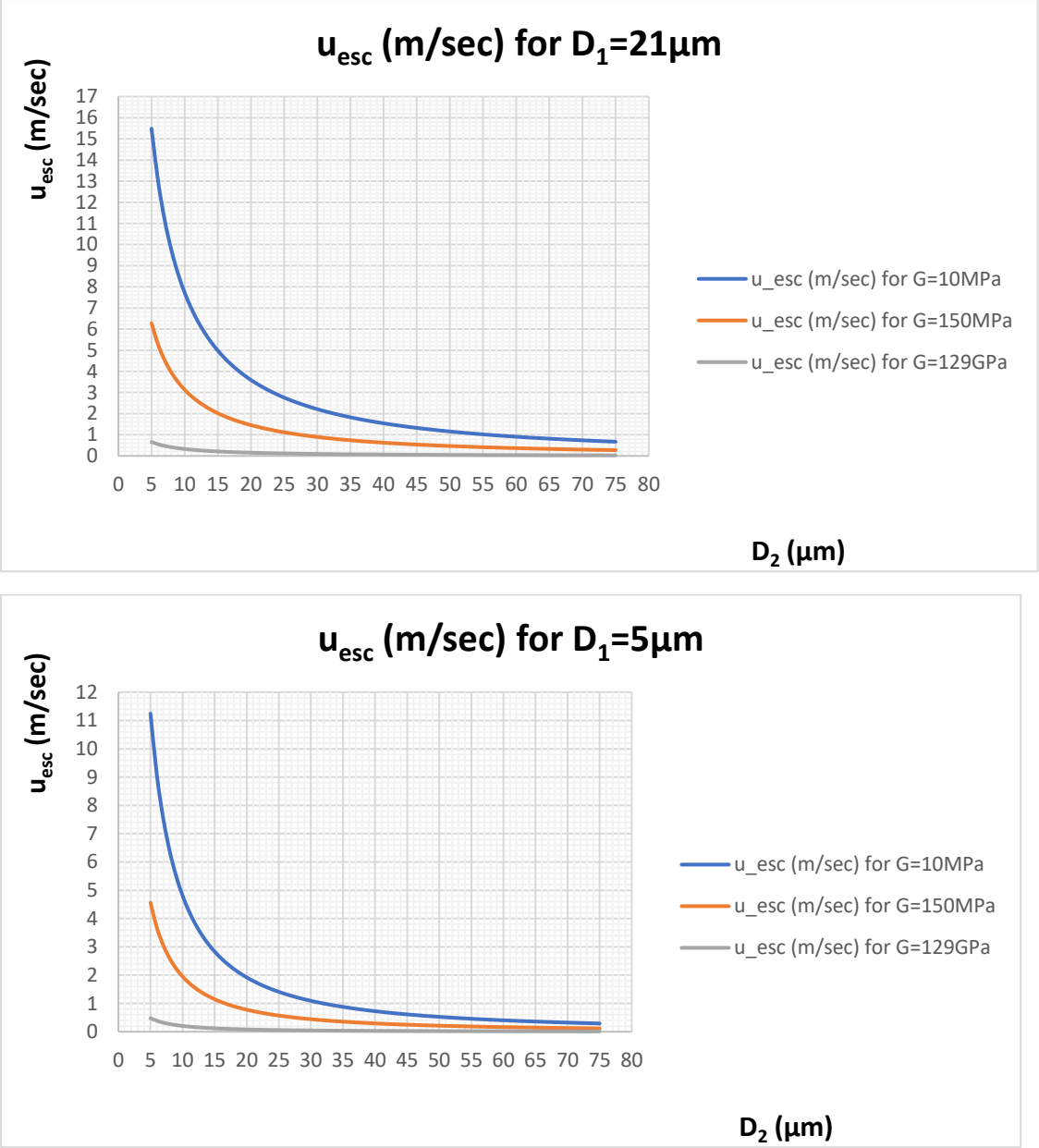

Figure 4.7: Escape velocity for 3 different diameters of the space-locked particle versus the diameter of the colliding particle. Each plot features 3 different curves, each one for a different value of the shear modulus.

Judging by the graphs of *Figure 4.7*, it is evident that, for a defined, constant diameter of the space-locked particle, the larger the diameter of the colliding particle, the easier it is for it to escape from the adhesive pull between the two. Furthermore, the curve moves lower as the shear modulus, hence the Young's modulus as well, increases. This means that, particles of a higher stiffness (due to higher Young's modulus), escape more easily from the adhesive bond.

Following the previous analysis, the simulations will follow the Hertz-Mindlin with JKR model, which was explained above. The model is designed to simulate the particles' behaviour under elastic, adhesive interactions.

4.4 Simulation Geometry and Simulation Description

The powder spreading simulation features 6 physical bodies and a virtual shape, necessary to use as a powder factory. The 6 physical bodies are the substrate onto which the powder is deposited, the doctor blade which performs the powder spreading, and 4 metal plates that serve as the left, right, back and front border of the powder layer. These geometrical borders create a square sample area with a side of 1mm. The height of the back and front border plates is equal to the theoretical layer thickness, i.e., 100μm, while that of the right and left border plates is equal to 1mm (see *Figure 4.8*).

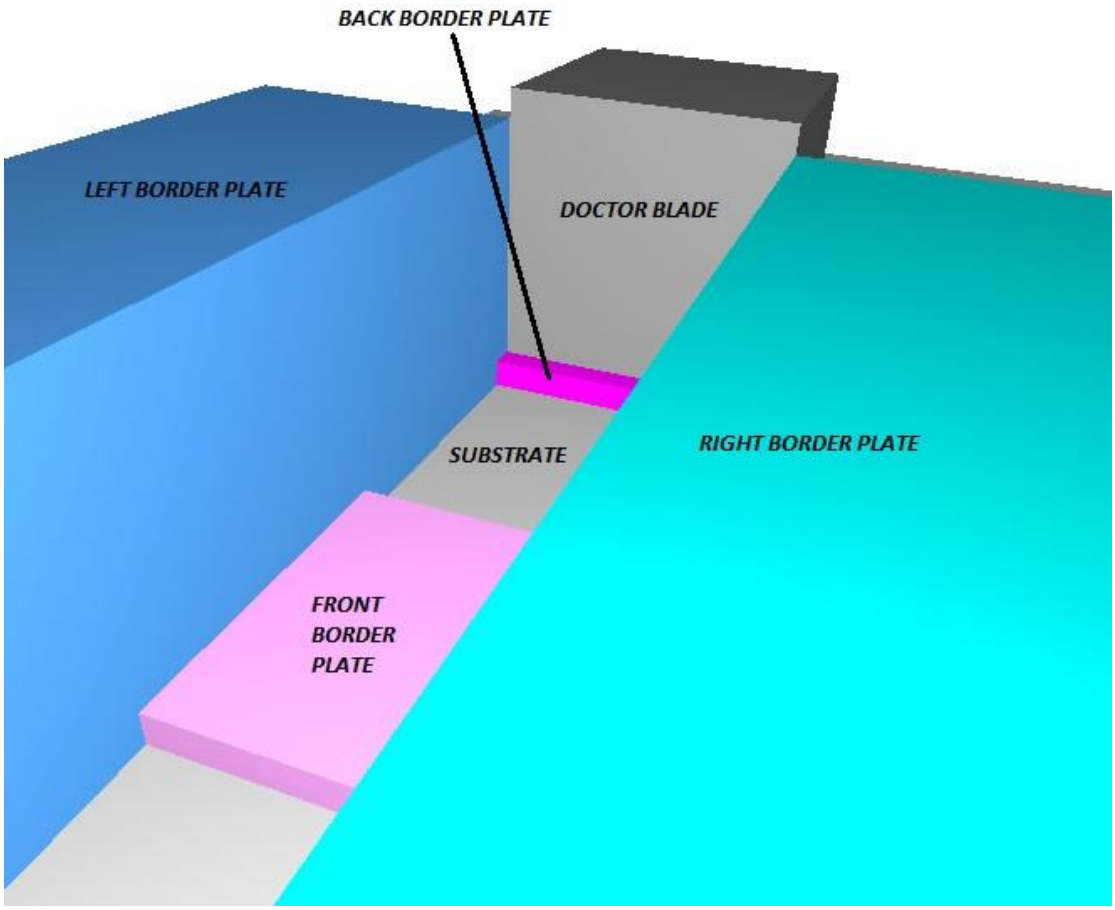

Figure 4.8: The physical bodies of the powder spreading simulation: ***(a)*** Light gray-Substrate-fabrication platform; ***(b)*** Dark gray-Doctor blade; ***(c)*** Cyan-Right Border plate; ***(d)*** Blue-Left border plate; ***(e)*** Magenta-Back border plate; ***(f)*** Pink-Front border plate.

Above the sample square there is a virtual cube of 1mm side, which functions as the powder factory (see *Figure 4.9*). The simulation is set to populate the area inside this virtual cube with spherical powder particles of a diameter that follows the lognormal distribution that was described in previous sections. This area is simultaneously populated for all particles at the start of the simulation, the sole constraint being that the particles must not be in physical contact with each other at the moment of their generation.

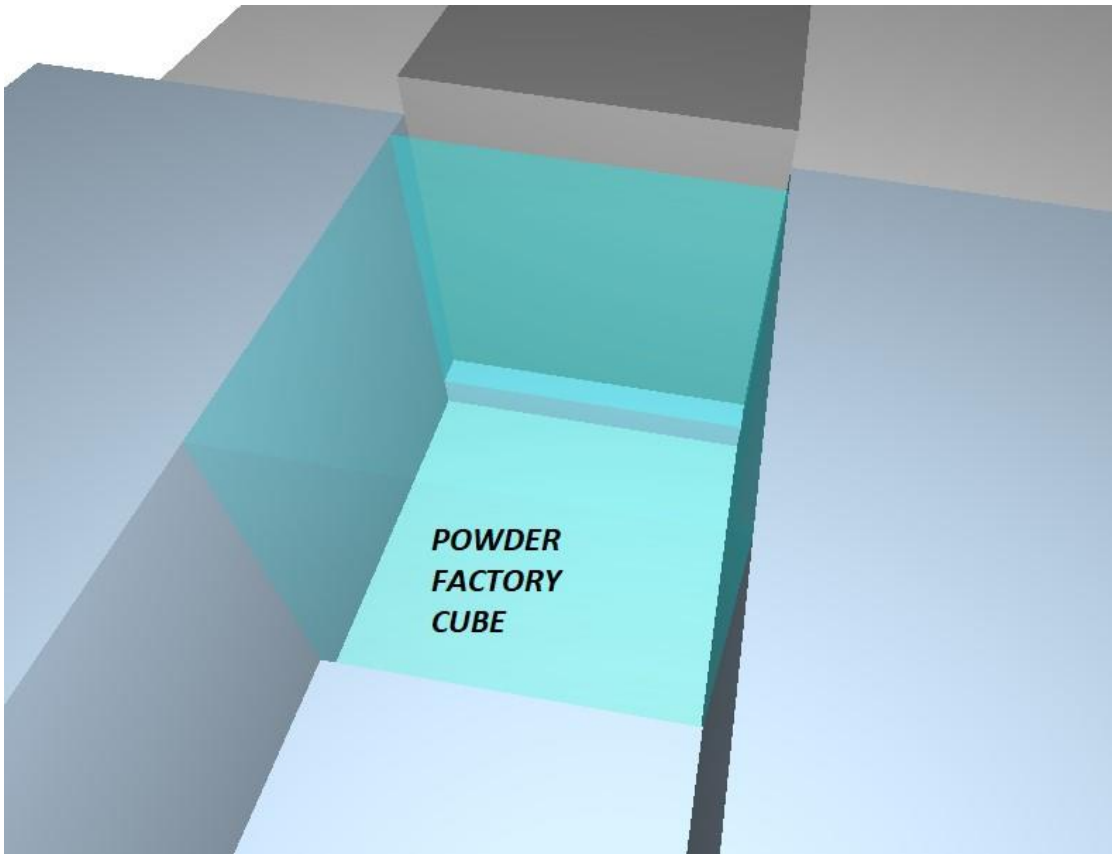

Figure 4.9: Semi-transparent cyan cube, which functions as a powder factory.

Then, the particles are left to drop vertically onto the sample square under the influence of gravity, creating a slope in front of the doctor blade that will perform the deposition (see *Figure 4.10*).

As the *Figure 4.10* depicts, all the particles are created simultaneously. No physical contacts between any two particles exist at the moment of particle generation. Then, the particles free-fall onto the substrate, filling the space over the sample square.

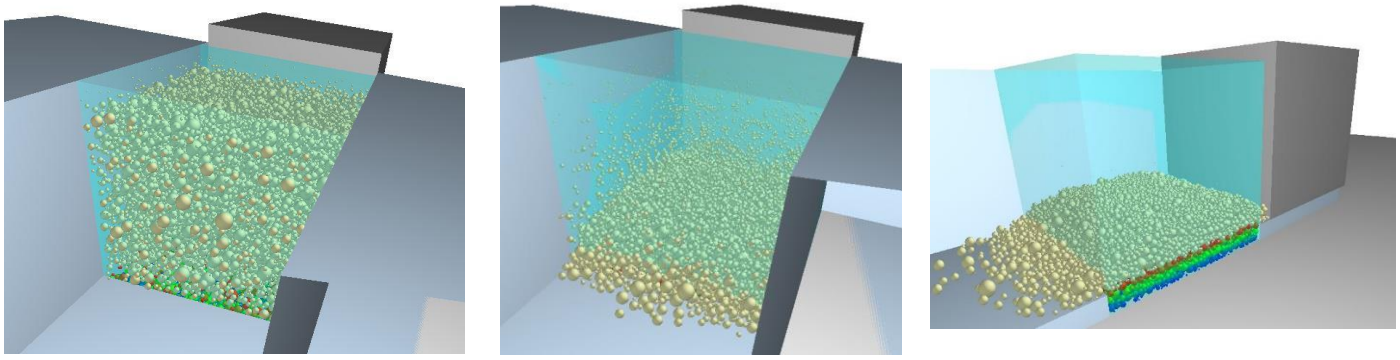

Figure 4.10: (Left) Simultaneous powder particle generation; (Middle) Particles free-fall onto the substrate; (Right) Particles' free fall is complete. The slope has been created- deposition is ready to begin.

The smaller particles fall slower compared to larger ones, due to the effect of air drag. The simulation enables natural gravity, with $\vec{g} = -9.81\hat{k}\ {}^{m}/_{sec^2}$ and Schiller-Naumann drag model [211], [212], the air's characteristics being:

$$\rho_{air} = 1.225\ {}^{Kg}/_{m^3}$$
$$\nu_{air} = 1.81 \cdot 10^{-5} Pa \cdot sec$$
$$\overrightarrow{u_{air}} = 0\hat{\imath} + 0\hat{\jmath} + 0\hat{k}$$
$$scale = 1$$

where ν_{air} is the kinematic viscosity of the air, $\overrightarrow{u_{air}}$ is the velocity of the air, indicating that in this case there is no air flow that would affect the motion of the particles, and "scale=1" means that the amount of drag applied to each particle is the full amount with regard to its size, and not a fraction of it.

For the simulations, the material of the physical bodies is Stainless Steel 304, its properties being [213]:

$$\rho_{St.304} = 8000\ {}^{Kg}/_{m^3}$$
$$\nu_{St.304} = 0.275$$
$$G_{St.304} = 6.23 \cdot 10^{10}\ Pa = 62.3\ GPa$$
$$E_{St.304} = 1.93 \cdot 10^{11}\ Pa = 193\ GPa$$

The powder material properties and the powder-powder and powder-geometry interaction coefficients have been set as shown in *Section 4.1* (*Figure 4.1*).

After the slope has been created and the particles are all frozen, i.e., at a status of negligible kinetic energy, the doctor blade is ready to perform the spreading process. The spreading consists of a superposition of two motions; a linear translational motion with a constant speed along the axis of deposition (x-axis) and a vertical (along z-axis)

vibrational motion, i.e., a sinusoidal oscillation of constant frequency and amplitude throughout the deposition process.

In order for the vertical sinusoidal oscillation to be performed between the positions $z_{down} = h_{l,th}$ (where $h_{l,th}$ is the theoretical layer thickness, i.e., the vertical distance between the substrate and the spreading plane that the blade creates) and $z_{up} = h_{l,th} + 2A_{vib}$ (where A_{vib} is the amplitude of the vibration), in the simulation, first there is a vertical offsetting motion of the blade, which moves the blade upwards along the z-axis by a displacement of $+A_{vib}$. As shown in *Figure 4.11*, the offsetting happens via a linear motion with constant speed along the vertical axis. In the figure, offsetting motion has a duration of $\Delta t = 0.005\ sec$, and speed of $u_{off} = 0.001\ m/sec$, leading to an offset displacement of $\Delta z_{off} = 5\ \mu m$.

After this step is complete, the vibration is set, considering the current position of the blade along the z-axis as the starting point of the oscillation. Simultaneously with the vibration start, the translational motion starts as well. *Figure 4.12* and *Figure 4.13* show the setup of the two motions that, by the principle of superposition, lead to the powder spreading process.

As seen in *Figure 4.12*, for this vibration the frequency is set to $f_{vib} = 2000\ Hz$ and the amplitude to $A_{vib} = 5\ \mu m$.

Similarly, as seen in *Figure 4.13*, the spreading speed is constant, and set to $u_{tr} = 0.01\ m/sec$. The duration of the translational motion is set in order for the blade to pass above the sample square and past it to a safe distance, ensuring that, at the end of the simulation, there are no remaining disturbances to the deposited layer by the blade, and at the same time, that the layer has had enough time for the particles to reach a "frozen" status, i.e., a condition of very low kinetic energy, very close to been completely motionless. After this time estimation is performed for the translational motion, the same duration is set for the vibrational motion.

After these steps and setups are completed, the simulation is ready to run and compute the results for the current trial of powder deposition.

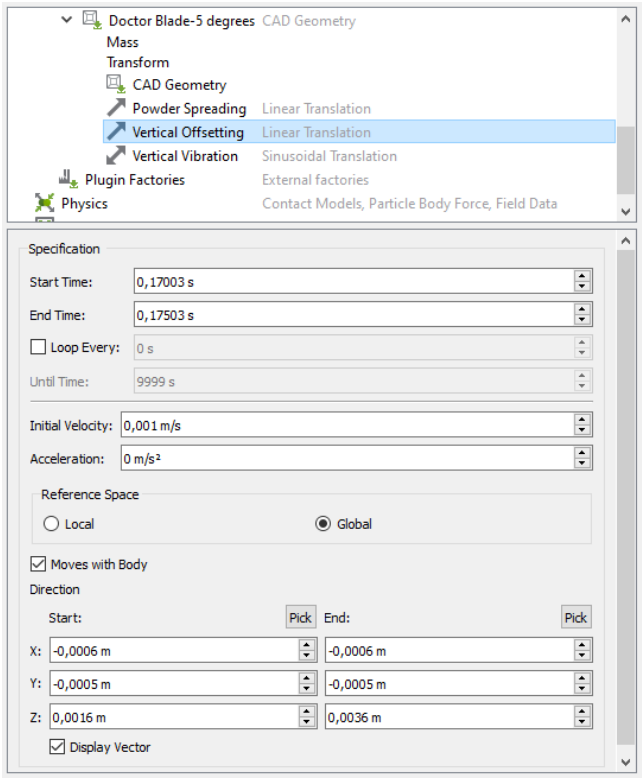

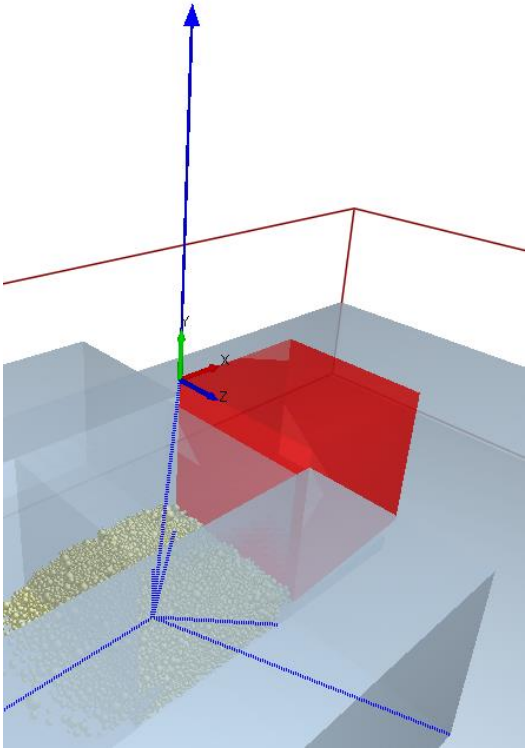

Figure 4.11: (Left) Motion setup for the offsetting; (Right) The axis of the offsetting is displayed via the long blue vector.

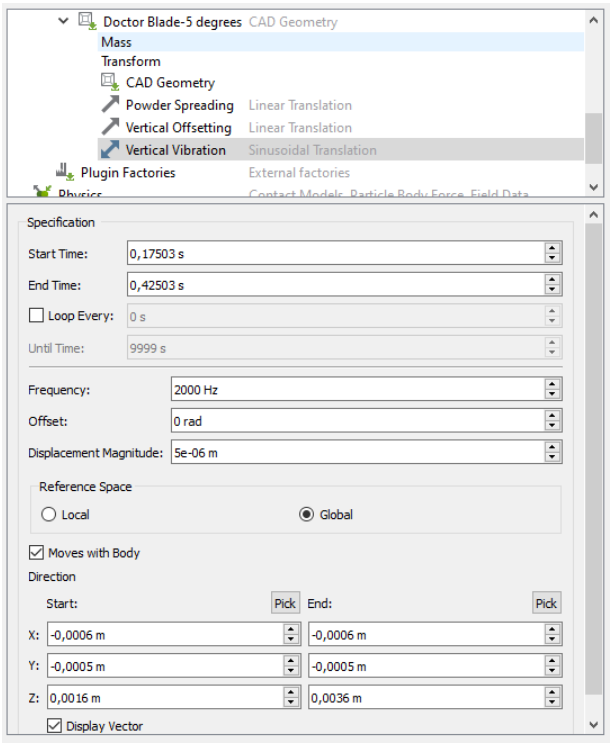

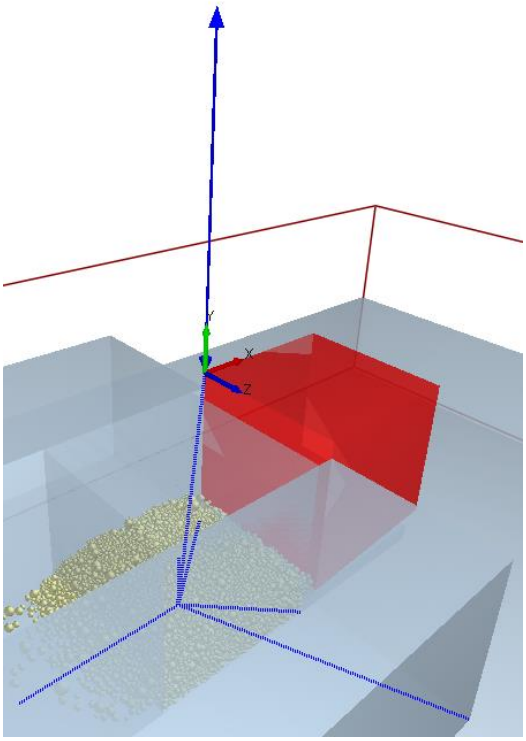

Figure 4.12: (Left) Motion setup for the sinusoidal oscillation; (Right) The axis of the oscillation is displayed via the long blue vector.

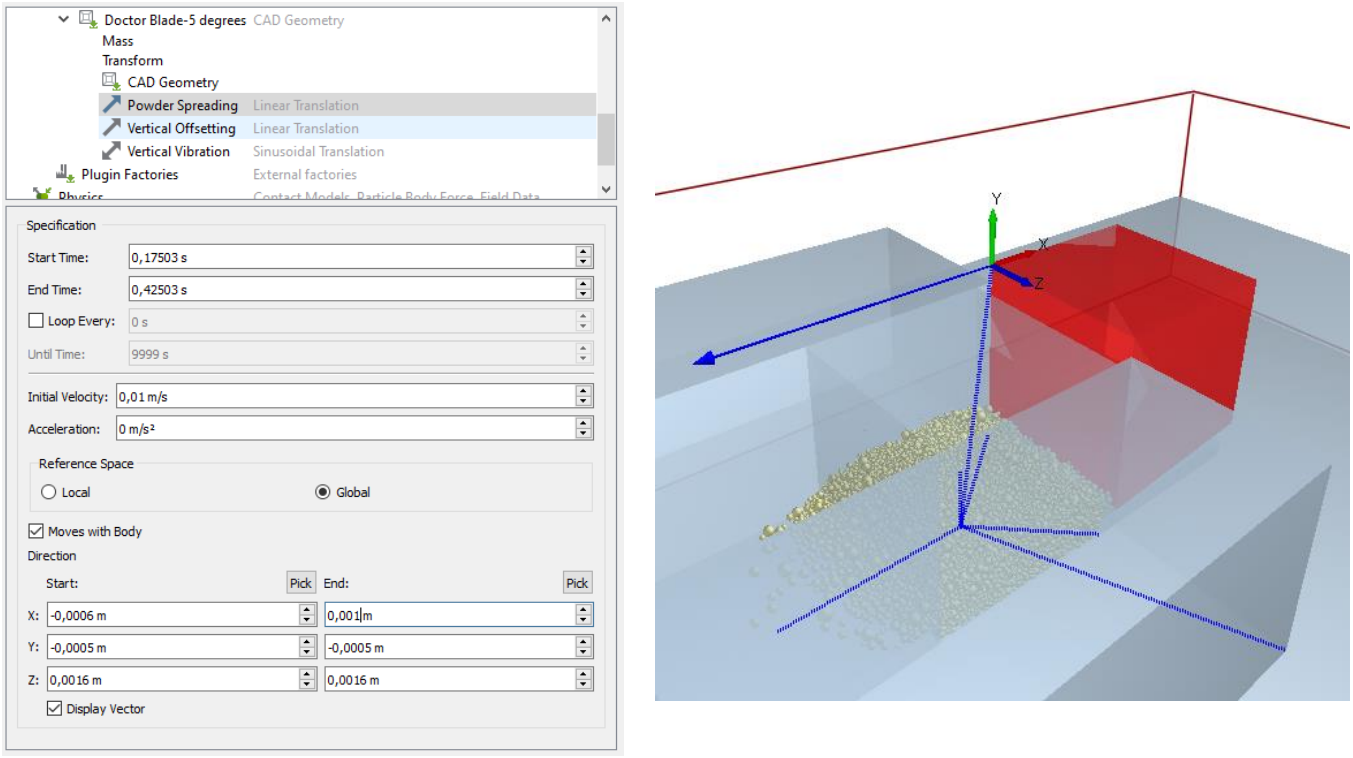

Figure 4.13: (Left) Motion setup for the translational motion of the doctor blade; (Right) The axis of the linear translation is displayed via the long blue vector.

4.5 Surface Evaluation and Quality Criteria

After the powder spreading simulation ends, the result is a square layer of (1x1) (mm x mm), with a theoretical (nominal) thickness of 0.1 mm. From the EDEM environment, it is possible to export a file containing the coordinates of the centres of the spherical particles, the particles' diameter and the particles' ID. Particle ID is a unique number for each particle, that is assigned to the particle during the particle generation stage, as it is being performed by the factory set to create the powder in the simulation. The same file contains the timestamp of the final moment of the simulation, which is the moment that corresponds to the extracted data, and the total mass of the particles that comprise the layer, in order to avoid summing the individual masses in a spreadsheet, or calculating them via their volume and density. *Table 4.6* shows the format of the data extracted by the EDEM software after the simulation of powder spreading.

Figure 4.14 is a top view of the deposited powder layer when the spreading process has been completed. The colouring of the particles happens either via their centres' Z-coordinate (*Figure 4.14(a)*), or via the particles' diameter (*Figure 4.14(b)*). Particles that are positioned higher or have a larger diameter are assigned colours of red hue, and

the ones that are positioned lower or have a smaller diameter are assigned colours of blue hue respectively, as the legend on the right side of the figure explains.

Table 4.6: Structure of the exported EDEM file for the particles constituting the layer of the simulation trials.

Particle ID	*Diameter*	X_{centre}	Y_{centre}	Z_{centre}
1	1.39E-05	-0.0001	-0.00017	0.000507
3	1.98E-05	-0.00038	-0.0002	0.000531
⋮	⋮	⋮	⋮	⋮
20609	3.51E-05	-0.00013	-0.00035	0.000531

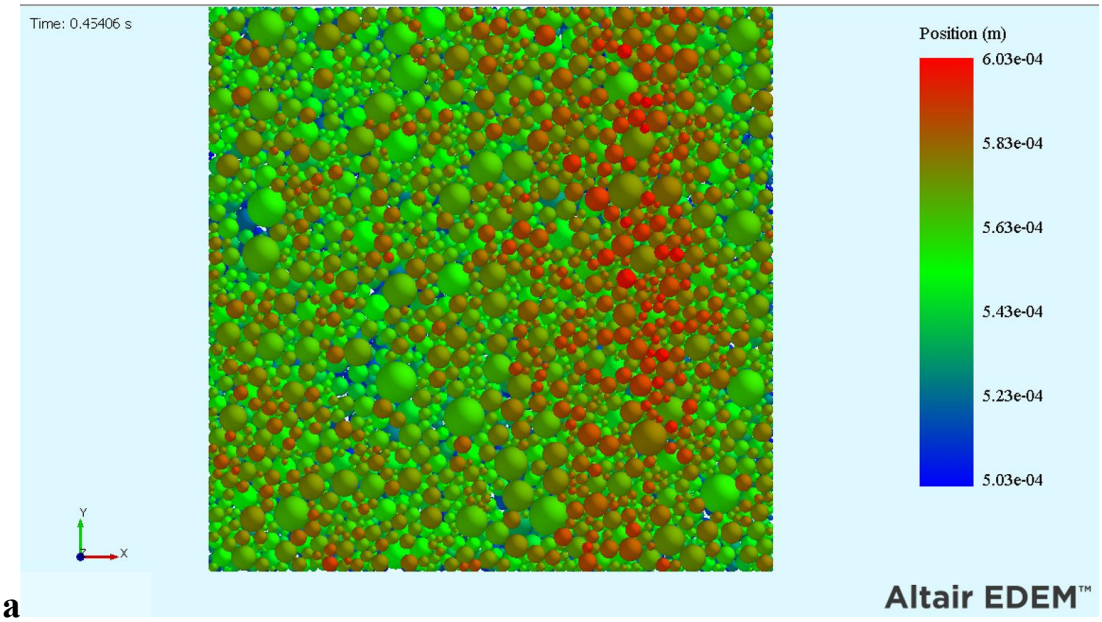

a

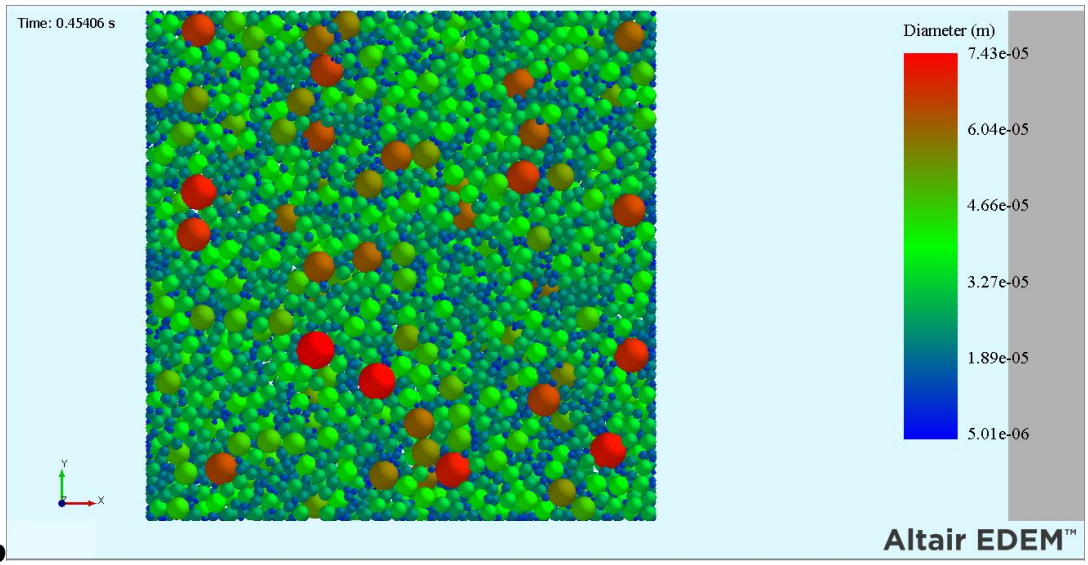

b

Figure 4.14*:** Sample top view of the deposited powder layer, with colouring of the particles via: ***(a) vertical position; ***(b)*** diameter.

The layer as exported by the EDEM environment is a file in the form described by *Table 4.6*. However, the file exported includes the data of every particle that constitutes the layer. This means that, in order to calculate the actual layer thickness, it is necessary to find a way to mathematically define only the points that constitute the top of the exported layer. To do this, the following methodology is proposed.

Initially, a grid is defined within the 1x1 (mm x mm) square within which the powder is located. The grid has an x-step of 1μm and a y-step of 1μm too. The grid size was selected so that it is 5 times smaller than the smallest powder particle (5-micron diameter). It could have been even smaller, but testing proved that it does not affect the results, however it vastly increases computational time and even causes overflow in some cases.

$$\Delta x = 1\ \mu m \tag{4.68}$$

$$\Delta y = 1\ \mu m \tag{4.69}$$

This means that the square has 1001 x-values and 1001 y-values, the respective lines intersecting each other, developing a grid of n_{nodes}= 1,002,001 "nodes". Each node has an abscissa $x_{i,j}, i = 1, 2, \dots, n_x = 1001, j = 1, 2, \dots, n_y = 1001$ and an ordinate $y_{i,j}, i = 1, 2, \dots, n_x = 1001, j = 1, 2, \dots, n_y = 1001$. The range of the abscissa and the ordinate of the nodes is defined so that the start of the coordinate system is positioned at the centre of the square. So, the general form of the nodes coordinates is given by *Equation (4.70)*.

$$\begin{Bmatrix} x_{i,j}, i = 1, 2, \dots, 1001, j = 1, 2, \dots, 1001, x_{i,j} \in [-500, 500] \\ y_{ij}, i = 1, 2, \dots, 1001, j = 1, 2, \dots, 1001, y_{i,j} \in [-500, 500] \\ z_{i,j} = 0 \end{Bmatrix} \tag{4.70}$$

With the coordinate unit being the μm.

From each node a vertical "ray" can be cast, in the form of a line, with an equation

$$\begin{Bmatrix} x = x_{i,j} \\ y = y_{i,j} \\ z \in R \end{Bmatrix} \tag{4.71}$$

This vertical line intersects some particles of the layer. In order to calculate the layer points, a c-code script compares the z-coordinates of all the intersection points of each "ray" with the particles and keeps the one with the highest z-coordinate. If a "ray" has no intersections with any particles, then the layer point that refers to this node is the node itself, i.e., the z-coordinate of the layer point is set to zero. The C-code script that

calculates the top-surface of the powder layer can be found in *Section 8.3* (*Appendix C-POWDER LAYER CALCULATION*). The code needs 5 preset files in order to calculate results. These files contain the particle data of the layer, i.e., the particles' ID ("PARTICLE_ID.txt"), their diameter ("PARTICLE_DIAMETER.txt"), and the x, y and z coordinates of the centre of each particle ("PARTICLE_X.txt", "PARTICLE_Y.txt" and "PARTICLE_Z.txt" respectively). The code opens the files, reads the data, which are in columns within each file and then proceeds to calculate one layer point for each node. The coordinates of the layer point are stored in "Surface_points_calculated_XYZ_coordinates_columns.txt".

The code works in a very simple way, explained via the flowchart of *Figure 4.15*. For each node, it examines whether the distance between the vertical projection of the centre of a particle onto the node plane ($z = 0$) and the node is smaller, equal to, or larger compared to the radius of the particle under-examination. If this distance is smaller than the radius, then the "ray" has two intersection points with the particle. If it is equal to the radius, it has one intersection point with the sphere, i.e., the contact point, and, if this distance is larger than the radius, then there are no intersections between the ray and the particle's sphere. After the intersection points are calculated for all the particles of the layer for the "ray" cast from one node, the one with the largest z-coordinate is stored into a new .txt file. This value is the layer height at the node $\left(z_{LAYER_{i,j}}\right)$. Then, the code moves to the next node and repeats the process. The final result is a cloud of points that comprise the layer's top surface.

The spatial equation that gives the spherical particles' surface is

$$(x - x_C)^2 + (y - y_C)^2 + (z - z_C)^2 = \left(\frac{D_{particle}}{2}\right)^2 \qquad (4.72)$$

where x_C, y_C, z_C are the coordinates of the centre of the particle and $D_{particle}$ is the particle's diameter.

The "ray"-particle intersection height at the (i,j) node for the k^{th} particle can be calculated by replacing *(4.71)* into *(4.72)*, taking:

$$z_{int_{k-(i,j)}} = z_{C_k} \pm \sqrt{\left(\frac{D_{k-particle}}{2}\right)^2 - \left(x_{i,j} - x_{C_k}\right)^2 - \left(y_{i,j} - y_{C_k}\right)^2} \qquad (4.73)$$

which is defined for a particle only if the quantity that is below the square root sign is non-negative, i.e., if the distance check explained before is successful. Let us note that $k = 1, 2, \dots, n_{particles}$.

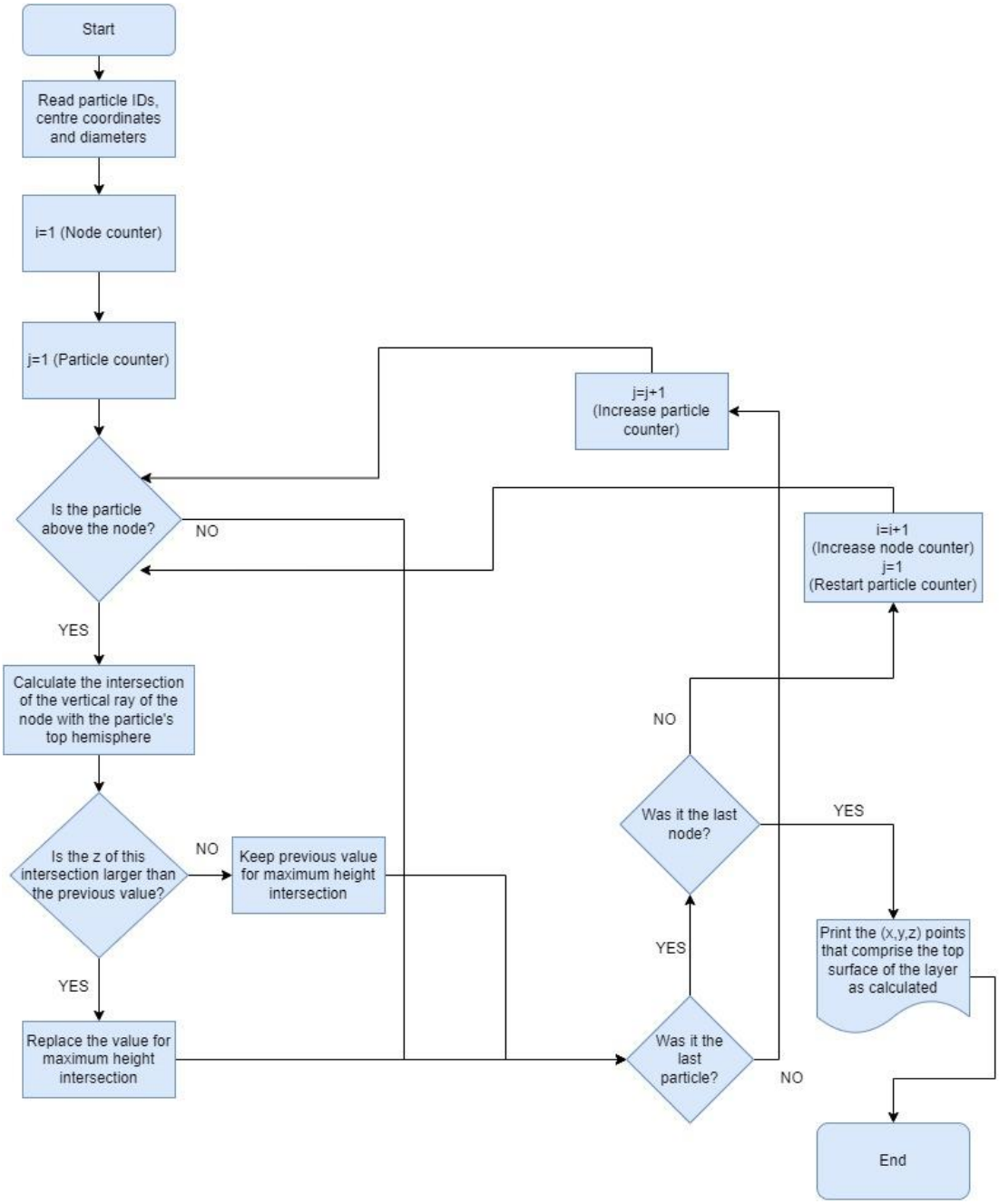

Figure 4.15: Flowchart of the top-surface layer calculation code.

After obtaining the points that define the layer's top surface $\left(x_{i,j}, y_{i,j}, z_{LAYER_{i,j}}\right)$, the next step is to actually quantify the layer's quality for the SLS/SLM process standards. In order to evaluate the surface produced by each trial, a few surface quality criteria are necessary. For this, four quality criteria are defined, namely the Layer Thickness

Deviation (LTD), Surface Coverage Ratio (SCR), Root-mean-Square Surface Roughness (S_q-RMS) and True Packing Density (PD or PD_{tr}). These criteria will be examined in the following Sections.

4.5.1 Actual to Theoretical Layer Thickness Deviation LTD and |LTD| (μm)

First of all, it is important to examine how closely the actual layer thickness approaches the theoretical layer thickness, which corresponds to the vertical distance between the substrate's surface and the plane that the lower edge of the doctor blade creates as it moves horizontally along the x-axis. In most studies it is assumed that the vertical displacement of the fabrication piston is equal to the layer height. However, this is not the case. The actual layer height is always slightly smaller, due to interparticle cohesive and particle-recoater adhesive phenomena. The impact of these phenomena varies as basic spreading parameters such as the recoater's translational speed or the layer height are altered.

Based on the points stored in the "Surface_points_calculated_XYZ_coordinates_ columns.txt" file, the actual layer thickness is calculated as the average value of the height of all the nodes. Therefore:

$$h_l = \frac{1}{n_{nodes}} \sum_{i=1}^{n_x} \sum_{j=1}^{n_y} z_{LAYER_{i,j}} \tag{4.74}$$

And the deviation between actual and theoretical layer thickness is given by

$$(LTD) = \left(h_l - h_{l,th}\right) = \left(\frac{1}{n_{nodes}} \sum_{i=1}^{n_x} \sum_{j=1}^{n_y} z_{LAYER_{i,j}} \right) - h_{l,th} \tag{4.75}$$

$$|LTD| = \left|h_l - h_{l,th}\right| = \left| \left(\frac{1}{n_{nodes}} \sum_{i=1}^{n_x} \sum_{j=1}^{n_y} z_{LAYER_{i,j}} \right) - h_{l,th} \right| \tag{4.76}$$

The actual layer thickness corresponds to the mean plane of the powder layer surface. This means that the mean plane of the under-examination powder layer surface is described by $z = h_l$. In order to calculate roughness and other surficial parameters, as will be shown in *Section 4.5.3*, a new Z ("capital-z") height variable is defined, which

corresponds to the mean plane of the layer $z = h_l$, instead of the reference plane $z = 0$. So, from now on:

$$Z_{i,j} = z_{LAYER_{i,j}} - h_l \tag{4.77}$$

4.5.2 Surface Coverage Ratio SCR (%)

If the layer is viewed from above, i.e., when the top view of the layer is examined, it is possible that it is fully covered by powder. However, there is also the possibility that some areas of the sample square have not been covered, making it possible for the examiner to see the substrate. *Figure 4.16* shows in black circles certain layer defects. In optimum deposition, the gaps are filled with smaller-sized particles, leaving absolutely no uncovered areas. Practically, researchers aim to minimize these coverage defects.

These uncovered areas might be the outcome of a larger particle or a particle agglomerate getting dragged along the surface, or getting pushed at such a high speed that its inertia enables it to keep moving for a longer than the desirable distance after losing contact with the recoater, causing a gap behind it. In order to have a high-quality layer, it is of paramount importance that there are as fewer uncovered nodes as possible. An "uncovered node" is a node for which the c-code described above has returned a zero number of "ray"-particle intersections, meaning that this node has zero particles located above it. The surface coverage ratio (SCR) is calculated by dividing the number of uncovered nodes to the total number of nodes within the sample square (*Equation (4.78)*).

$$SCR(\%) = \left(\frac{n_{uncovered}}{n_{nodes}}\right) \cdot 100\% \tag{4.78}$$

The maximum value that SCR can take is 100%, in which case, perfect coverage is achieved. Practically, as estimated by the examination of the layer samples developed by the 27 spreading trials that comprise the Taguchi DoE, if a layer coverage is below 98.5%, the layer quality is considered to be unacceptable for SLS/SLM processes. It has been noticed that the general surface quality generally deteriorates drastically when the SCR reaches values equal to or even lower than 98.5%.

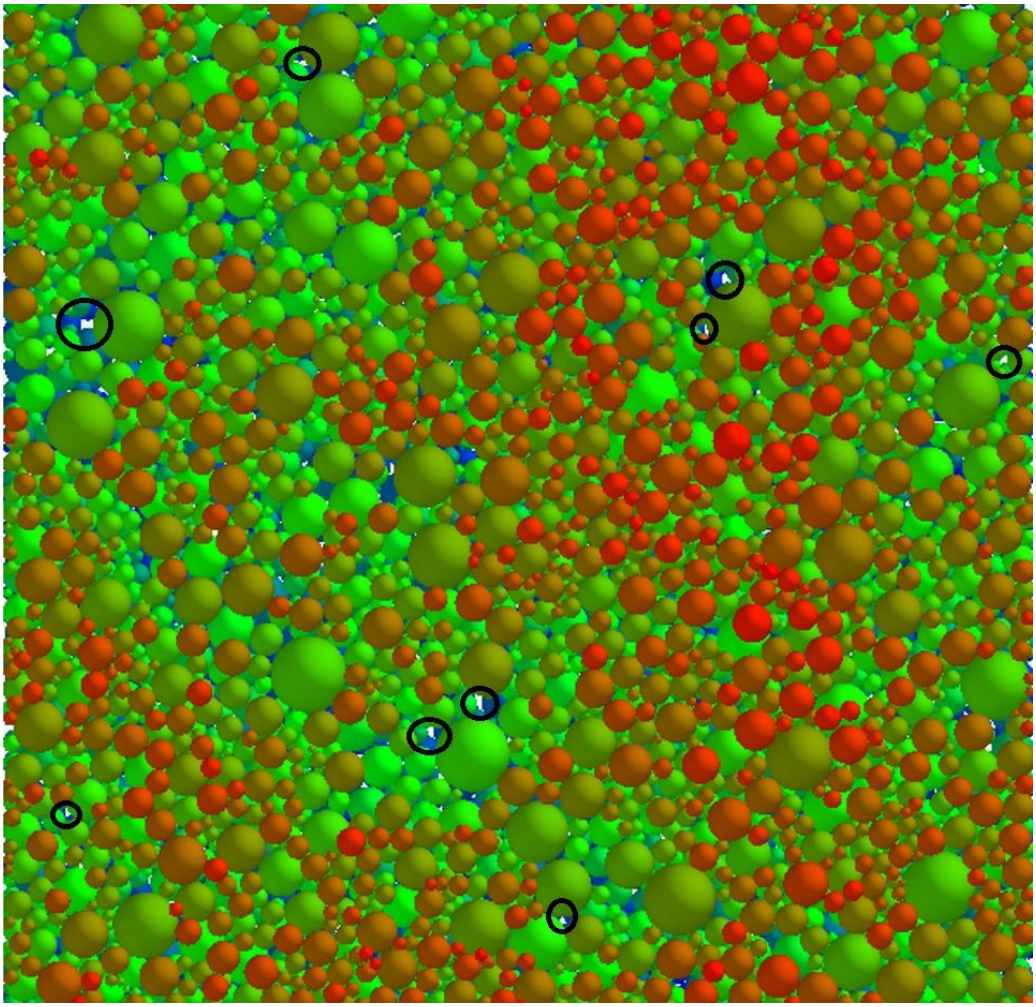

Figure 4.16: In black circles, uncovered areas where the substrate is visible, denoting coverage defects.

4.5.3 Root-Mean-Square Surface Roughness S_q-RMS (μm)

Surface roughness of the calculated top surface of the powder layer is very important to the quality of the finished product, as it has already been explained in previous chapters (see *Chapter 2*). Deep valleys or high peeks are detrimental to the quality, since they can be inherited to the next layers, even affecting the dimensional accuracy of a part. It is common practice to extract profiles from the deposited layer via methods such as white light scanning [103] it order to evaluate the surface roughness via its two-dimensional definition. However, by this method, it is possible to omit examining profiles where significant defects are present and suggest that a layer is of higher quality than it actually is. To address this issue, areal (instead of the profile) method is suggested in this work for calculating the surficial root mean square roughness of the surface as a metric known for its statistical importance.

The parameters R_q and S_q (see *Figure 4.17*) are two of the most widely used parameters and are also referred to as the RMS values. They correspond to the standard deviation of the height distribution. Furthermore, they generate reliable statistics and enable stable results since they are not significantly influenced by scratches, contamination, and measurement noise.

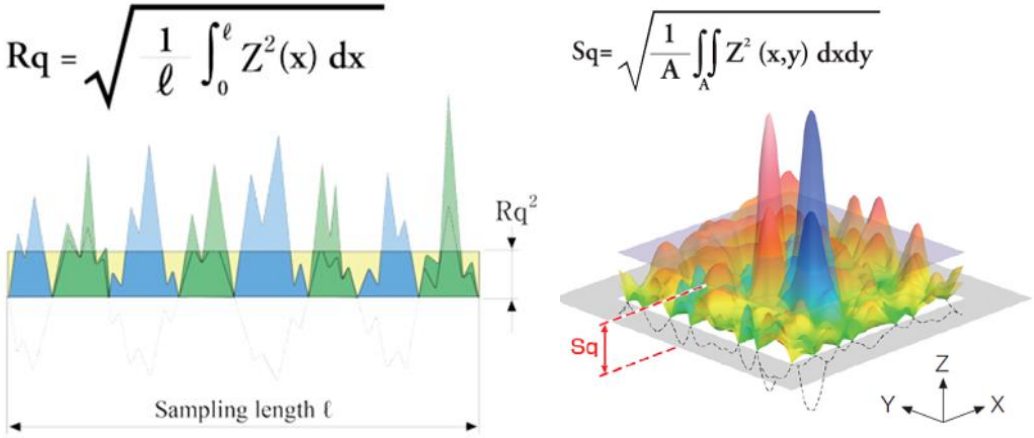

Figure 4.17: The profile (left) and areal (right) method for calculating the root mean square (RMS) roughness of a surface [214].

The equation used to calculate the areal RMS surface roughness of the layer is

$$S_q = \sqrt{\frac{1}{A}\iint_A Z^2(x,y)dxdy} \qquad (4.79)$$

where A is the sample area (in the case examined in this work, $A = 1\mu m^2$) and $Z(x,y)$ is the equation that gives the top surface of the powder layer in analytical form, as denoted in *Equation (4.77)*. It is of paramount importance to note that, in order to calculate any surficial parameters that will be mentioned from now on, the height $Z(x,y)$ that denotes the top surface of the layer refers to the mean plane of the surface, i.e., to the plane $z = h_l$, h_l being defined by *Equation (4.74)*. So, in the entire *Chapter 4*, wherever the term Z is encountered, it refers for clarity to $(z_{LAYER} - h_l)$. However, it is not possible to formulate an analytical equation to describe the top surface of the powder layer. Instead, it has been defined as a cloud of points via the coordinates of these points. Hence, the *Equation (4.79)* must be solved numerically.

The integral $I = \iint_A Z^2(x,y)dxdy$ is the volume between the surface $Z^2(x,y)$ and the plane $Z = 0$. Hence, the first step towards its calculation is to raise the z-coordinates of the points that exist in the "Surface_points_calculated_XYZ_coordinates_columns.txt"

file to the second power. The result is a column of points with coordinates $P_{i,j}\left(x_{i,j}, y_{i,j}, {Z_{i,j}}^2\right)$. The integral I represents the volume between the surface described by the points P and the plane $Z = 0$. This volume can be divided to many smaller volumes, each one of them with a square base of 1μm, since both Δx and Δy are equal to 1μm. It is possible to use the trapezoid rule to numerically calculate each one of these infinitesimal volumes. The geometrical shape which is correlated to this infinitesimal volume is a truncated right rectangular prism with square base. More specifically, it is a prism with a square base, with a 1micron side, however the four vertical edges are of various lengths (or heights), see *Figure 4.18*.

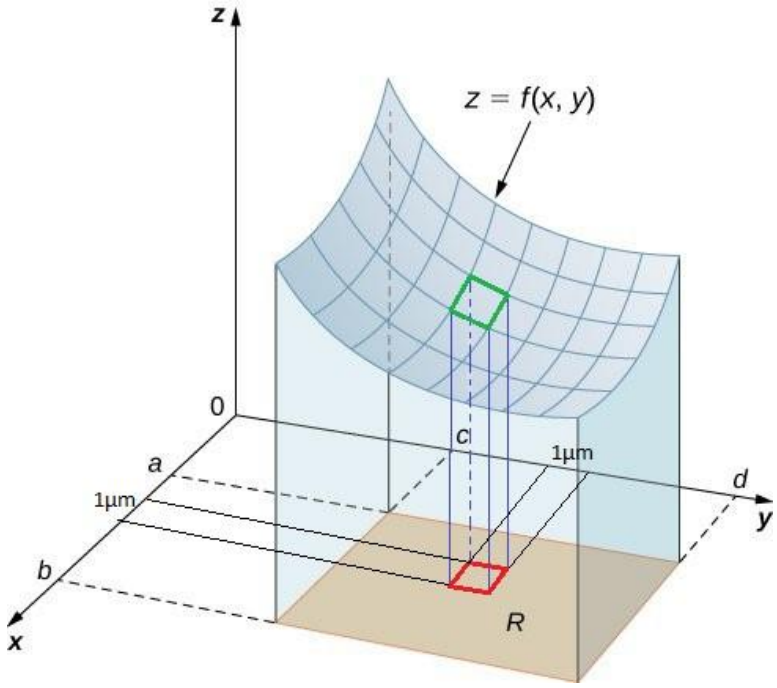

Figure 4.18: Infinitesimal prism visualization.

A random infinitesimal square will be the one defined by the nodes

$$N_{i,j}\left(x_{i,j}, y_{i,j}\right)$$
$$N_{i+1,j}\left(x_{i+1,j}, y_{i+1,j}\right)$$
$$N_{i+1,j+1}\left(x_{i+1,j+1}, y_{i+1,j+1}\right)$$
$$N_{i,j+1}\left(x_{i,j+1}, y_{i,j+1}\right)$$

These nodes refer respectively to the following top surface points of the powder layer;

$$P_{i,j}\left(x_{i,j}, y_{i,j}, {Z_{i,j}}^2\right)$$
$$P_{i+1,j}\left(x_{i+1,j}, y_{i+1,j}, {Z_{i+1,j}}^2\right)$$
$$P_{i+1,j+1}\left(x_{i+1,j+1}, y_{i+1,j+1}, {Z_{i+1,j+1}}^2\right)$$
$$P_{i,j+1}\left(x_{i,j+1}, y_{i,j+1}, {Z_{i,j+1}}^2\right)$$

Then, to calculate the volume secluded between the 4 nodes ($N_{i,j}$, $N_{i+1,j}$, $N_{i+1,j+1}$, $N_{i,j+1}$) and the 4 points ($P_{i,j}$, $P_{i+1,j}$, $P_{i+1,j+1}$, $P_{i,j+1}$), we have:

$$\Delta V_{Z^2} = \int_{y=y_j}^{y=y_{j+1}} \left(\int_{x=x_i}^{x=x_{i+1}} Z^2(x,y)dx \right) dy = \int_{y=y_j}^{y=y_{j+1}} \left[\frac{\Delta x \cdot \left(Z^2(x_{i+1},y) + Z^2(x_i,y) \right)}{2} \right] dy =$$

$$= \frac{\Delta x}{2} \cdot \int_{y=y_j}^{y=y_{j+1}} \left[\left(Z^2(x_{i+1},y) + Z^2(x_i,y) \right) \right] dy =$$

$$= \frac{\Delta x}{2} \cdot \left\{ \frac{\Delta y \cdot \left[Z^2(x_{i+1},y_{j+1}) + Z^2(x_i,y_{j+1}) \right] + \left[Z^2(x_{i+1},y_j) + Z^2(x_i,y_j) \right]}{2} \right\} =$$

$$= \frac{\Delta x \cdot \Delta y}{4} \cdot \left[Z^2(x_{i+1},y_{j+1}) + Z^2(x_i,y_{j+1}) + Z^2(x_{i+1},y_j) + Z^2(x_i,y_j) \right] =$$

$$= \frac{\Delta x \cdot \Delta y}{4} \cdot \left(Z_{i+1,j+1}^2 + Z_{i,j+1}^2 + Z_{i+1,j}^2 + Z_{i,j}^2 \right) \Rightarrow$$

$$\Delta V_{Z^2} = \frac{\Delta x \cdot \Delta y}{4} \cdot \sum_{n=j}^{j+1} \sum_{m=i}^{i+1} Z_{m,n}^2 \qquad (4.80)$$

So, the volume of every truncated right rectangular square-base prism is equal to the sum of the heights of the 4 vertical edges, multiplied by the steps along the x and y axis, and divided by 4. Hence, in order to calculate the total volume between the surface defined by the points $P_{i,j}$ and the $z = 0$ plane, the volume of every infinitesimal prism has to be added.

If a node is located at one of the 4 corners of the sample square, the only infinitesimal prism it is part of is the one located at the corner of the sample square. However, if a node is located onto one of the four edges of the square sample, it is part to two different infinitesimal prisms, hence it contributes twice to the total volume. Finally, if a node is interior to the sample square, i.e., it does not belong to neither an edge nor a corner of the sample square, then it belongs to four different infinitesimal prisms, contributing four times to the total volume.

Hence;

$$V_{Z^2} = \frac{\Delta x \cdot \Delta y}{4} \cdot \left\{ \left[Z_{1,1}^2 + Z_{n_x,1}^2 + Z_{n_x,n_y}^2 + Z_{1,n_y}^2 \right] + 2\left(\sum_{j=2}^{n_y-1} Z_{1,j}^2 + \sum_{j=2}^{n_y-1} Z_{n_x,j}^2 + \sum_{i=2}^{n_x-1} Z_{i,1}^2 + \sum_{i=2}^{n_x-1} Z_{i,n_y}^2 \right) + 4\left(\sum_{j=2}^{n_y-1} \sum_{i=2}^{n_x-1} Z_{i,j}^2 \right) \right\} \quad (4.81)$$

And, after this calculation, the RMS aerial surficial roughness of the surface is given by *Equation (4.82)*, as:

$$S_q = \sqrt{\frac{1}{A} V_{Z^2}} \quad (4.82)$$

By the same method used to calculate the S_q, it is possible to calculate other areal surficial parameters, such as the arithmetical mean height (S_a), the skewness (Ssk) and the kurtosis (Sku), by using the following equations:

$$S_a = \frac{1}{A} \iint_A |Z(x,y)| dxdy \quad (4.83)$$

$$Ssk = \frac{1}{{S_q}^3} \left[\frac{1}{A} \iint_A Z^3(x,y) dxdy \right] \quad (4.84)$$

$$Sku = \frac{1}{{S_q}^4} \left[\frac{1}{A} \iint_A Z^4(x,y) dxdy \right] \quad (4.85)$$

In order to use *Equations (4.83)*, *(4.84)* and *(4.85)*, the double integrals are calculated by using the *Equation (4.81)* and replacing $Z_{i,j}^2$ with $|Z_{i,j}|$, $Z_{i,j}^3$ and $Z_{i,j}^4$ respectively. *Figure 4.19* shows the physical representation of these surficial parameters.

The arithmetic mean height (S_a-measured in μm) and the root mean square roughness (S_q-measured in μm) are quite similar quantities, representing the mean of the average height difference for the average plane and the standard deviation of the height distribution. They both are not heavily impacted by dents, scratches, contamination and measurement noise, and generate reliable statistics.

$$Sa = \frac{1}{A}\iint_A |Z(x,y)|\,dxdy$$

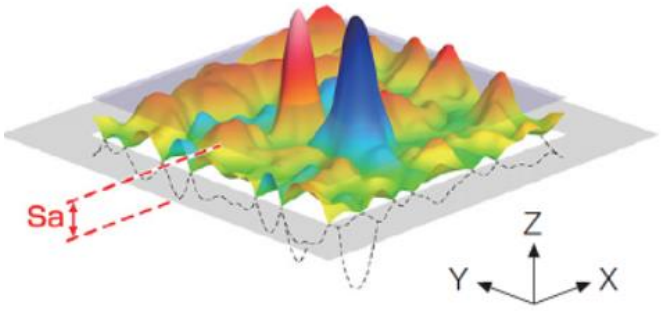

$$Ssk = \frac{1}{Sq^3}\left(\frac{1}{A}\iint_A Z^3(x,y)\,dxdy\right)$$

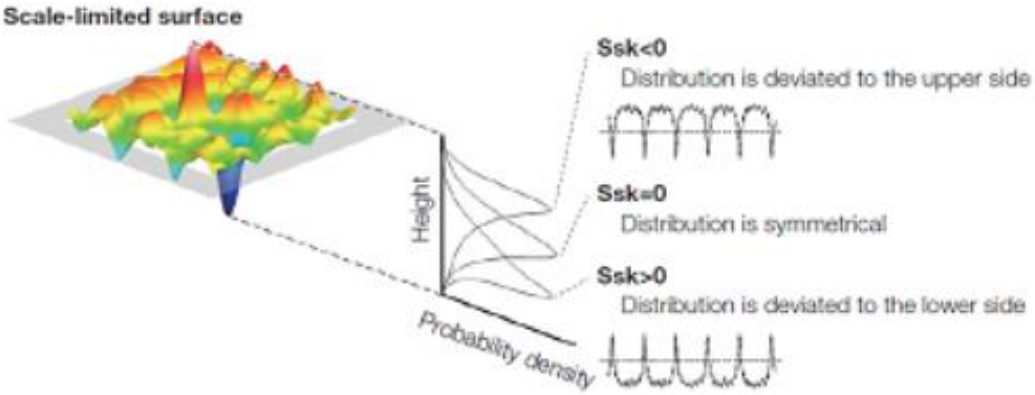

$$Sku = \frac{1}{Sq^4}\left(\frac{1}{A}\iint_A Z^4(x,y)\,dxdy\right)$$

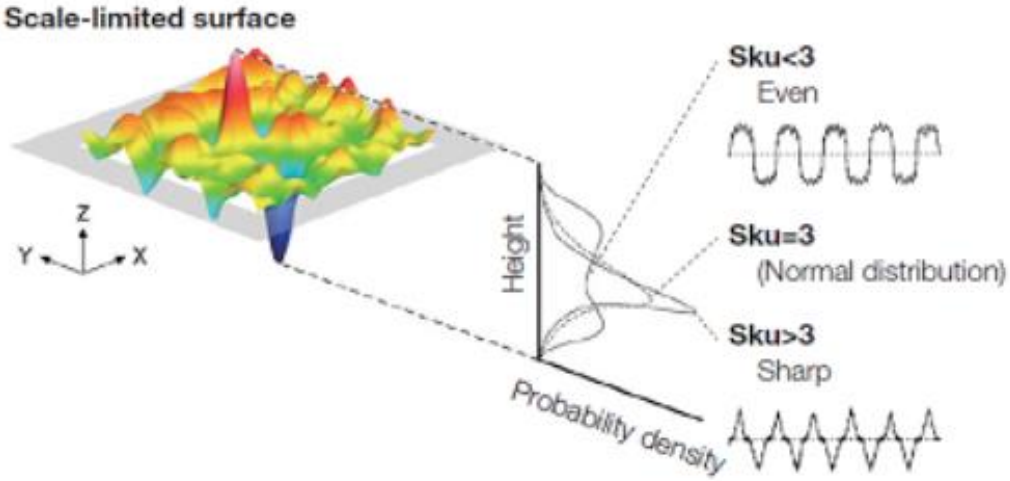

Figure 4.19: (Top) S_a; (Middle) Ssk; (Bottom) Sku [214].

Skewness (Ssk-unitless parameter) represents the degree of symmetry of the surface heights about the mean plane. Skewness' sign indicates the peak or valley predominance of a surface. More specifically, negative skewness values indicate that the distribution is deviated upwards, hence the surface presents deep valleys while the areas that are above the mean plane are smoother and more even. Similarly, positive skewness values indicate a distribution deviated downwards, i.e., a surface with very high peak structures, where the areas below the mean plane are smoother and less steep.

Kurtosis (Sku-unitless parameter) is used to evaluate sharpness in the height distribution. More specifically, Sku indicates the presence of inordinately high peaks/deep valleys (Sku>3) or lack thereof (Sku<3) making up the texture. If the surface heights are normally distributed (i.e., bell curve) then Ssk is 0 and Sku is 3. Surfaces described as gradually varying, free of extreme peaks or valley features, will tend to have Sku <3 [215].

Skewness is useful when it comes to monitoring the effect of wear on a surface (e.g. evaluating the abrasion and oil sump of lubricants for slide planes), while kurtosis is a good way of spotting the presence of either peak or valley defects which may occur on a surface [216], [214].

There are more surficial parameters that might be useful, like the peak-to-valley roughness (S_z), the maximum peak height (S_p) and the maximum peak depth (S_v), however, they mostly identify the magnitude of the largest defects of the surface and fail to examine the consistency and evenness of the surface, which the metrics described above examine more accurately.

4.5.4 True Packing Density PD (%)

The packing density, also termed compaction ratio, is very important to measure, since it is directly connected to the finished parts' density and microhardness, as explained in previous chapters.

In many works, packing density is calculated by dividing the mass of a layer by the theoretical volume of the layer. This means that, the volume of the layer is calculated by simply multiplying its border dimensions along the three axes, x, y and z [217], [218]. However, as it has been already mentioned in this Section, the actual layer height is different than the theoretical layer height, i.e., the vertical downwards displacement

of the fabrication piston of the SLS/SLM machine. Hence, this might be an indicator of how well the powder layer is "filled", but it is not an actual indicator of how well the powder particles themselves have been arranged within the layer, in order to increase their individual coordination numbers, and minimize the air gaps between them. In this work, the true packing density is calculated, by dividing the mass of the deposited powder in the layer by the actual layer thickness, which refers to the mean line of the surficial roughness profile that refers to the layer's surface. Then, the percentage is calculated by dividing the true packing density by the bulk density of the material of the powder.

$$PD\left({}^{Kg}/_{m^3}\right) = \frac{m_{LAYER}}{V_{LAYER}} = \frac{1}{V_Z}\sum_{i=1}^{n_{particles}} m_{particle,i} \quad (4.86)$$

$$PD(\%) = \left(\frac{PD\left({}^{Kg}/_{m^3}\right)}{\rho_{powder,BULK}}\right)\cdot 100\% \quad (4.87)$$

Where V_Z is calculated using the *Equation (4.81)* and replacing every $Z_{i,j}^2$ variable with $Z_{i,j}$.

4.6 Taguchi Design for Spreading

The Taguchi DoE is a statistical tool widely used for reaching to conclusions when it comes to the effect of various factors on the result of an experiment, with regard to some quality criterion that is set beforehand. The number of factors and the number of each factor's levels leads to the selection of an orthogonal array (OA) suitable to accommodate all the necessary combinations of the factors' levels in order to reach to solid outcomes [219].

Four variables are being examined, namely:

1. *Translational speed of the doctor blade* along the deposition (x) axis (u_{tr}). This variable was examined at three levels:
    a) 0.01 m/sec
    b) 0.05 m/sec
    c) 0.1 m/sec

These levels were selected according to the powder deposition speed standards that currently apply to the industrial SLS/SLM machines. These were validated in both the prototype SLS/SLM powder deposition system designed [59], [103] as well as via cross-checking of the translational speed of the powder deposition system of the industrial SLM machine of the Laboratory of Manufacturing Engineering of the School of Mechanical Engineering of NTUA (Z-rapid iSLM280).

2. *Vibrational frequency of the doctor blade* along the vertical (z) axis (f_{vib}). This variable was examined at three levels:
    a) 500 Hz
    b) 1000 Hz
    c) 2000 Hz

    The frequencies selected were relatively low compared to, say, ultrasound frequencies, since, the higher the frequency, the smaller the timestep of the simulation. Furthermore, the purpose of the simulations was to examine whether a low-frequency-vibrating doctor blade is preferable compared to powder spreading without any vibration applied on the doctor blade, which is the common way in which powder is being deposited in industrial SLS/SLM machines. It is important to note that there has been preliminary testing of the powder deposition via doctor blade recoater without vibration, since almost every commercial SLS/SLM machine features powder deposition systems that do not oscillate the recoater. The preliminary testing examined the deposited layer's quality for a flat doctor blade that does not vibrate, at two different translational speed levels, 0.1 and 0.01 m/sec. The results can be seen in *Figure 4.20*. *Figure 4.20* and the cross-check between it and the respective results if the blade gets vibrated (see *Figure 4.31*) prove that vibration can enhance the powder layer quality in terms of homogeneity and evenness.

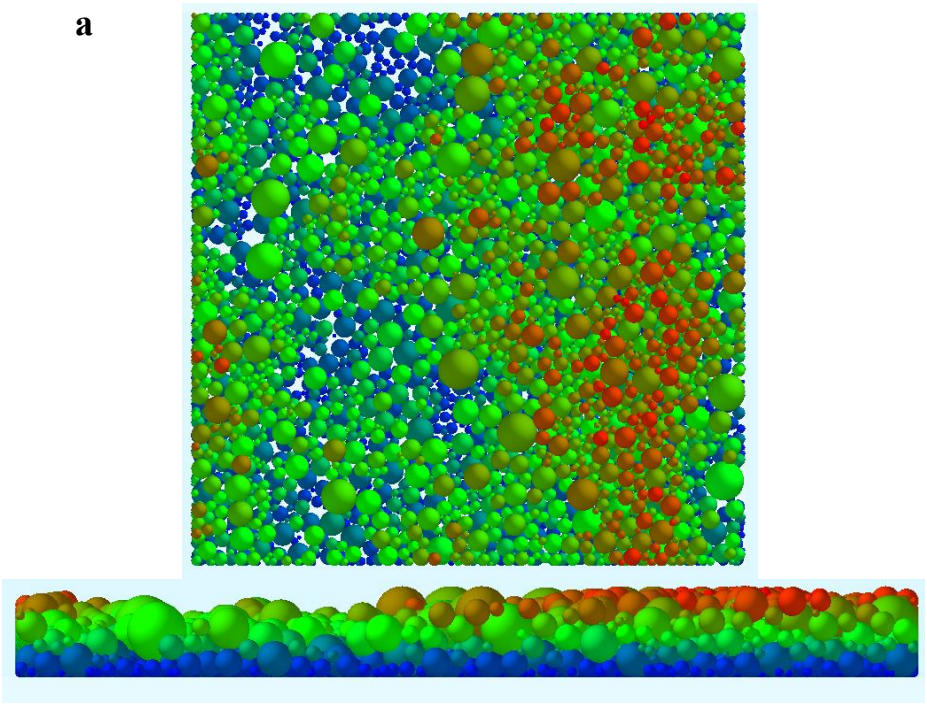

Figure 4.20: Powder deposition example with a non-vibrating doctor blade. Deposition speed of 0.08 m/sec, as the one used in commercial machines.

3. *Vibrational amplitude of the doctor blade* along the vertical (z) axis (A_{vib}). This variable was examined at three levels:
    a) 1 μm
    b) 2.5 μm
    c) 5 μm

    The amplitude values were selected in such a way that they are equal or less to the minimum powder particle diameter (5 μm). With this assumption, it is impossible to create a gap between the doctor blade and the back border plate large enough to allow powder particles to escape behind the doctor blade as the deposition process gets initiated.

4. *Angle of relief of the doctor blade* (θ_{rel}). The geometry of the doctor blade is presented in *Figure 4.21*. The doctor blade used in the simulations has a quasi-cubic design of 1mm-side. Its only feature differentiating it from a cube is its angle of relief which starts after a 100μm backwards horizontal flat area that is implemented in order for the vertical vibration to create a compaction effect on the powder. Had this horizontal area not existed, in the 5 and 10-degree doctor

blades, the compaction of the layer via vibration would be impossible, since the spreading would be manifested via a single edge of the blade. Furthermore, this would render the simulation non-realistic, since no sharpened blades are used for powder deposition. The size of 100μm for this feature was selected by comparison to the largest allowed particle diameter, which is set to 100 microns via the EDEM simulation environment. This variable was examined at three levels:

a) 0^o
b) 5^o
c) 10^o

The angles of relief were selected in a way that resembles the relatively thick, commercially available, doctor blades. The geometry of the doctor blades' profiles, as described in *Figure 4.21*, shows that, as the angle increases, the secondary contact surface between the blade and the particles decreases. The primary contact surface is defined as the vertical doctor blade's surface that forces the powder slope to move towards the direction of the translational velocity vector. The secondary contact surface is defined as the area that applies vertical pressure via vibration onto the powder layer, i.e., the 100μm-wide strip and the fraction of the inclined surface behind this strip that interacts with the particles via the vibrational and adhesive forces. When the relief angle equals to 0^o, the secondary contact area is equal to the entire 1 mm^2 of doctor blade bottom area, while, when the relief angle increases, the secondary contact area decreases to 0.1 mm^2 plus the decreasing contact zone of the inclined surface within which compressive and adhesive forces are applied between the blade and the particles.

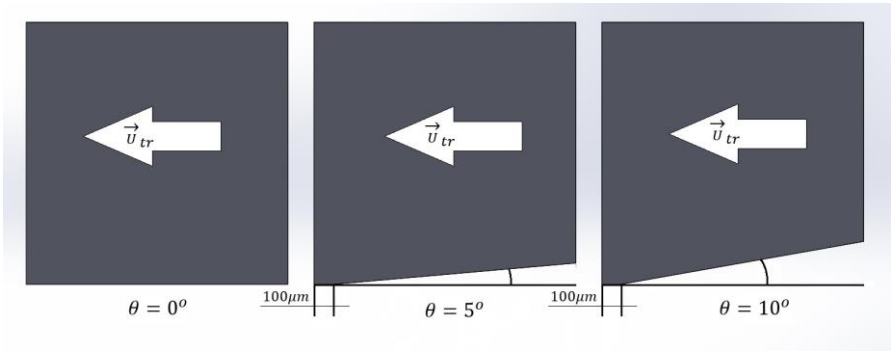

Figure 4.21: Side view of the doctor blade. Depiction of the angle of relief and the geometrical characteristics of the powder spreading front.

The goal will be to optimize the response of the quality criteria, simultaneously. However, this is not a trivial feat, since each of the four responses are individually optimized at different levels. This work presents an attempt to find global optimum levels of the variables being examined for all of the quality criteria, in order to achieve the best possible outcome. Initially, each of the four responses is examined separately.

Table 4.7 presents the setup of the experiments in an L27 orthogonal array for the Taguchi design of the powder spreading simulations. The L27 provides the capability of examining 3 interactions, which is enough for this case study. Examining more interactions would overcomplicate the design and lead to a number of trials comparable to the full factorial design. The quality criteria are the 4 criteria described in the previous Section, namely layer thickness deviation, layer root mean square roughness, layer true packing density and layer surface coverage ratio. The quality loss function is the lower the better for LTD and RMS and the higher the better for SCR and PD. Furthermore, S_a, Ssk and Sku are also being presented, since useful observations can be made through them.

4.7 Results

Results are shown on *Figure 4.22* and *Figure 4.23* referring to means and SNR respectively. The means plot depicts the average response for each combination of control factor levels, while the SNR plot depicts the ratio of the mean (signal) to the standard deviation (noise). This means that the means plot shows the average performance, while the SNR plot shows the variance from the design. In addition, ANOVA results are shown in *Table 4.8*, *Table 4.9* and *Table 4.10* for the LTD, SCR and RMS respectively.

Judging by *Figure 4.22* and *Figure 4.23*, it is easily deduced that none of the four factors has a statistically important impact on the true packing density of the layer. Packing density ranges from 66.8% (minimum, trials #11 and #13) to 68.4% (maximum, trial #1), while the number in the means plot varies between roughly 67% and 67.7%. Indeed, the powder's compressing mechanism relies mostly on gravity, since, even the vibrating blade, only momentarily pushes the layer downwards, and then moves upwards again. The blade vibrates having its lowest point at the theoretical layer thickness, meaning that it does not compress the layer below the actual layer thickness

level. However, the theoretical packing density, i.e., the density of the layer calculated via the powder mass within the layer divided by the theoretical volume of the layer, varies in an inversely proportional manner compared to the layer thickness deviation. To sum up with, the true packing density will not be examined as a quality criterion from this point on, since it was proven that the four factors do not have any substantial effect on it.

Table 4.7: L27 Orthogonal array of the Taguchi DoE for powder spreading. The results are presented as well.

#	$u_{tr}\left(\frac{m}{sec}\right)$	f_{vib} (Hz)	A_{vib} (μm)	θ_{rel} $(deg.)$	$(h_l - h_{th})$ (μm)	$\lvert h_l - h_{th} \rvert$ (μm)	SCR (%)	S_q (μm)	PD (%)	S_a (μm)	Ssk	Sku
1	**0.01**	**500**	**1.0**	**0**	-29.0	29.0	98.9	19.9	68.4	15.5	-0.672	3.889
2	**0.01**	**500**	**2.5**	**5**	-26.0	26.0	99.1	17.9	68.0	13.6	-0.906	4.852
3	**0.01**	**500**	**5.0**	**10**	-21.2	21.2	99.3	17.4	67.1	13.0	-1.179	5.572
4	**0.01**	**1000**	**1.0**	**5**	-26.7	26.7	99.1	18.1	67.6	13.8	-0.956	4.741
5	**0.01**	**1000**	**2.5**	**10**	-24.3	24.3	99.0	18.0	67.4	13.5	-1.351	5.626
6	**0.01**	**1000**	**5.0**	**0**	-22.2	22.2	99.3	16.1	68.0	12.1	-1.515	6.403
7	**0.01**	**2000**	**1.0**	**10**	-23.8	23.8	99.0	17.9	67.0	13.6	-1.338	5.570
8	**0.01**	**2000**	**2.5**	**0**	-23.0	23.0	99.1	17.0	67.8	12.8	-1.503	6.075
9	**0.01**	**2000**	**5.0**	**5**	-21.5	21.5	99.3	16.4	67.8	12.3	-1.431	6.232
10	**0.05**	**500**	**1.0**	**5**	-36.6	36.6	97.7	21.6	67.2	17.0	-0.685	3.347
11	**0.05**	**500**	**2.5**	**10**	-34.9	34.9	97.7	22.4	66.8	17.6	-0.577	3.362
12	**0.05**	**500**	**5.0**	**0**	-31.7	31.7	98.6	18.8	67.5	14.6	-1.042	4.358
13	**0.05**	**1000**	**1.0**	**10**	-36.9	36.9	97.9	20.4	66.8	16.1	-0.811	3.602
14	**0.05**	**1000**	**2.5**	**0**	-33.8	33.8	98.5	19.2	67.0	15.0	-0.926	3.993
15	**0.05**	**1000**	**5.0**	**5**	-32.1	32.1	98.4	19.9	67.1	15.5	-0.898	3.993
16	**0.05**	**2000**	**1.0**	**0**	-35.0	35.0	98.1	20.2	67.1	15.9	-0.869	3.698
17	**0.05**	**2000**	**2.5**	**5**	-32.4	32.4	98.6	19.2	67.1	14.9	-0.962	4.116
18	**0.05**	**2000**	**5.0**	**10**	-32.2	32.2	98.5	20.0	67.1	15.5	-0.815	3.956
19	**0.10**	**500**	**1.0**	**10**	-40.8	40.8	97.0	22.8	67.3	18.2	-0.399	3.051
20	**0.10**	**500**	**2.5**	**0**	-41.2	41.2	96.9	21.8	67.9	17.4	-0.597	3.059
21	**0.10**	**500**	**5.0**	**5**	-36.9	36.9	97.5	22.0	67.0	17.3	-0.596	3.310
22	**0.10**	**1000**	**1.0**	**0**	-41.4	41.4	97.0	21.7	67.6	17.3	-0.633	3.063
23	**0.10**	**1000**	**2.5**	**5**	-40.7	40.7	96.1	24.9	67.4	20.1	-0.323	2.732
24	**0.10**	**1000**	**5.0**	**10**	-37.0	37.0	94.9	28.7	66.9	22.9	-0.224	2.753
25	**0.10**	**2000**	**1.0**	**5**	-40.2	40.2	97.3	21.3	67.3	17.0	-0.622	3.169
26	**0.10**	**2000**	**2.5**	**10**	-41.1	41.1	97.3	22.5	67.5	18.0	-0.335	2.940
27	**0.10**	**2000**	**5.0**	**0**	-40.2	40.2	97.2	21.3	67.5	16.8	-0.558	3.604

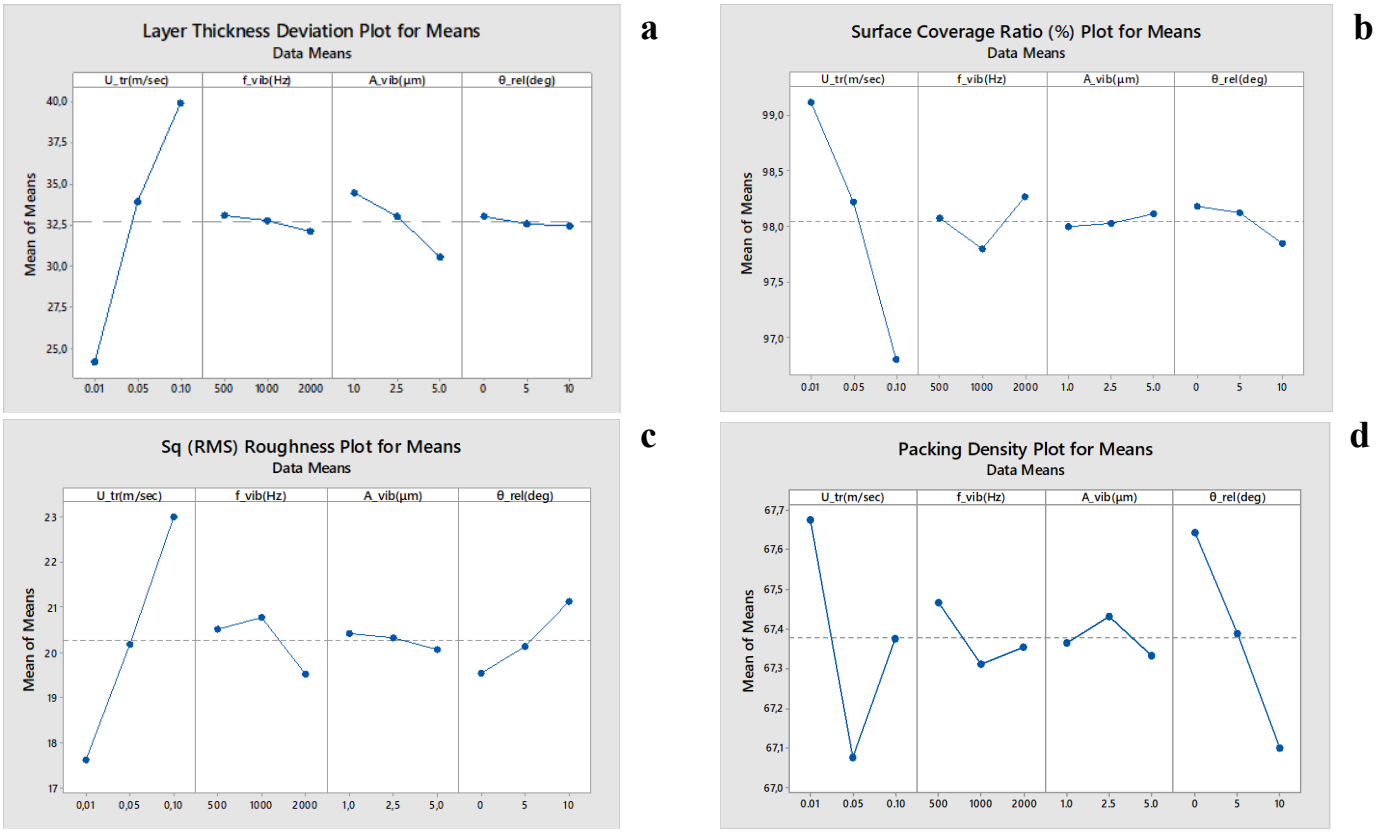

Figure 4.22: Means plots of the four quality criteria of the powder spreading Taguchi analysis; ***(a)*** LTD; ***(b)*** SCR; ***(c)*** RMS; ***(d)*** PD.

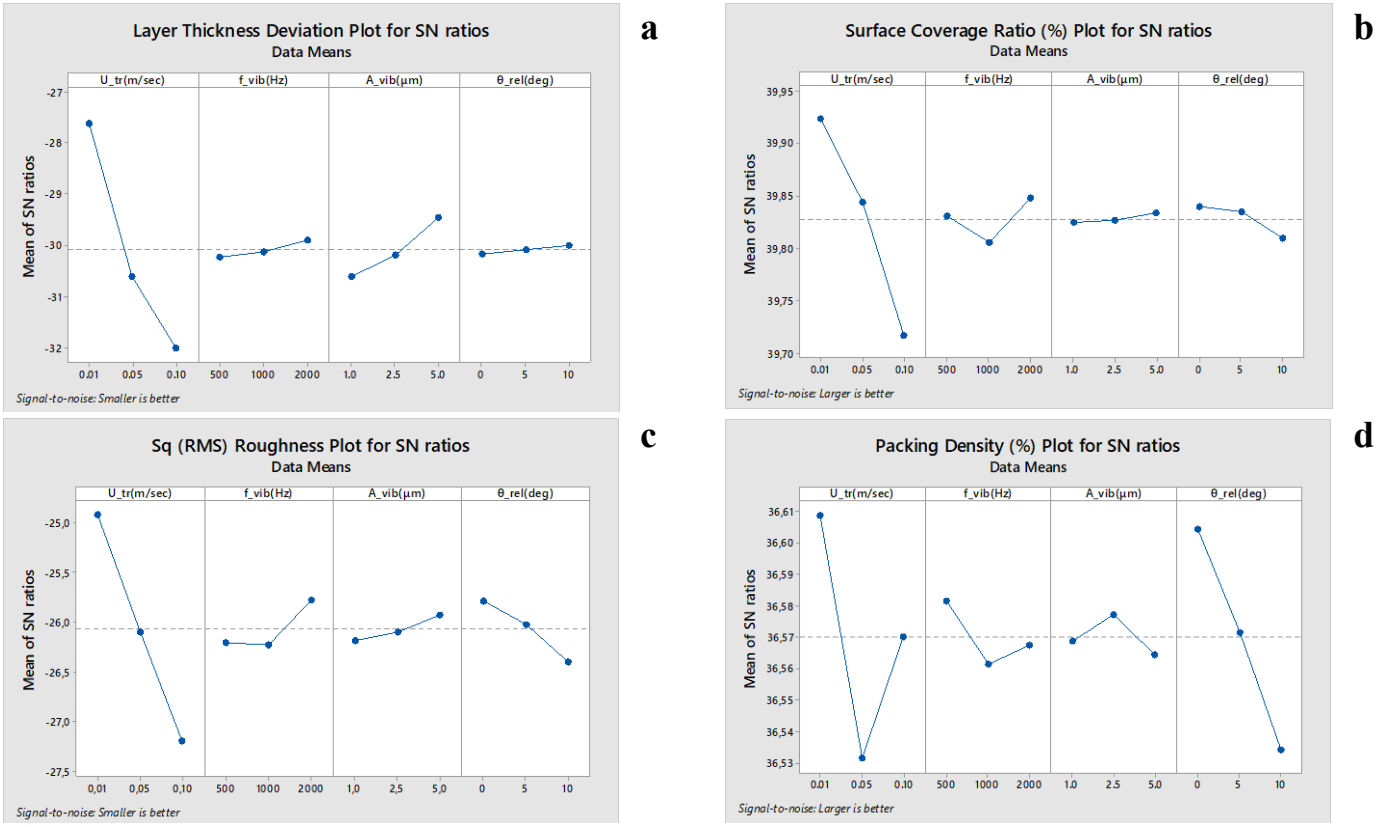

Figure 4.23: Signal-to-Noise ratios plots of the four quality criteria of the powder spreading Taguchi analysis; ***(a)*** LTD; ***(b)*** SCR; ***(c)*** RMS; ***(d)*** PD.

4.7.1 LTD Results

Referring to *Table 4.8*, the layer thickness deviation $|h_l - h_{th}|$ is primarily affected by the blade's translational speed, and, to a much lesser extent, by the amplitude of the blade's vibration. It is clear that, the smaller the doctor blade's translational speed, the more the actual layer thickness approaches the theoretical layer thickness. Similarly, the larger the amplitude of the vibration, the smaller the layer thickness deviation. The frequency of vibration and the blade's angle of relief demonstrate weak influence on layer thickness deviation, as can be seen in the "Contribution" column of *Table 4.8*.

Table 4.8: Analysis of Variance (ANOVA) for layer thickness deviation.

Source	DoF	SeqSS	Contribution	Adj SS	Adj MS	F-value	P-value
Regression	7	1182.59	94.68%	1182.59	168.941	48.33	0.000
U_{tr} (m/sec)	1	1092.82	87.49%	65.78	65.783	18.82	0.000
f_{vib} (Hz)	1	4.51	0.36%	14.28	14.284	4.09	0.058
A_{vib} (µm)	1	71.25	5.70%	37.67	37.668	10.78	0.004
θ_{rel} (deg)	1	1.56	0.12%	0.65	0.653	0.19	0.670
U_{tr} (m/sec) *f_{vib} (Hz)	1	9.77	0.78%	9.77	9.772	2.80	0.111
U_{tr} (m/sec) *A_{vib} (µm)	1	2.66	0.21%	2.66	2.659	0.76	0.394
U_{tr} (m/sec) *θ_{rel} (deg)	1	0.01	0.00%	0.01	0.014	0.00	0.950
Error	19	66.42	5.32%	66.42	3.496		
Total	26	1249.01	100.00%				

The ANOVA for the layer thickness deviation (*Table 4.8*) shows that the spreading speed dictates the layer thickness deviation by 87.49%, while the amplitude of vibration contributes by 5.70%. The contribution of the other two factors (frequency of vibration and blade's angle of relief) is negligible, at 0.36% and 0.12% respectively. The same can be said for the interaction between the factors. The only interactions examined are the interactions between the blade's speed and the other factors, since it is obviously the most impactful factor. As can be seen in *Figure 4.24*, the translational speed of the blade and the amplitude of the vibration have relatively parallel lines, which means that they demonstrate low degree of interaction, which is traceable only at higher speeds. The same can be said for the interaction between the blade speed and its vibration frequency. They demonstrate no interaction at low and middle speed levels, however, at larger speed values it becomes more beneficial to maintain a low frequency, while at low and middle speeds it is the other way around. When it comes to the blade's angle

of relief, the interaction between that and the blade's speed reveals that, at low and high speeds sharper blades with large angle of relief perform better, however, at middle speeds, the optimum performance is that of the flat-bottomed blade.

The regression equation of the layer thickness deviation is given by *Equation (4.88)*;

$$|h_l - h_{th}| = 29.78 + 126.8u_{tr} - 0.00205f_{vib} - 1.26A_{vib} - 0.067\theta_{rel} + 0.0262u_{tr}f_{vib} + 5.17u_{tr}A_{vib} + 0.15u_{tr}\theta_{rel} \quad (4.88)$$

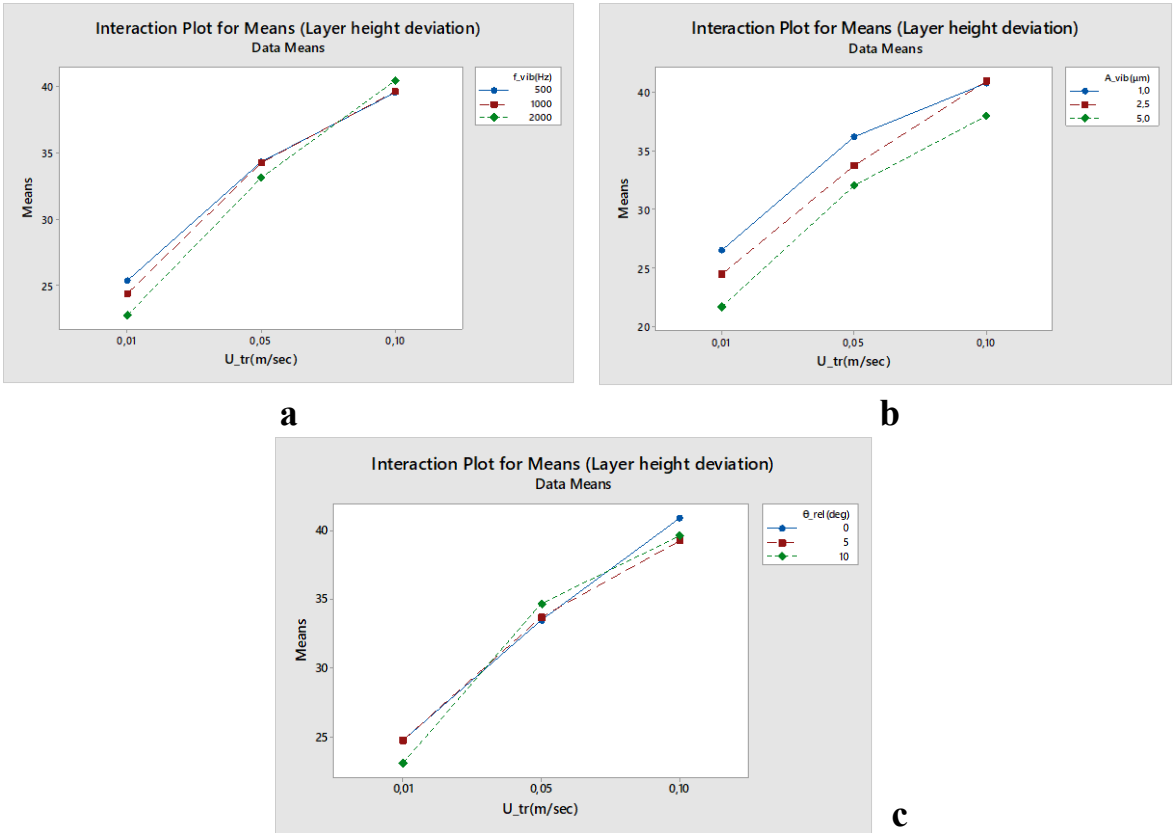

Figure 4.24: Interaction plots for means of the layer thickness deviation; ***(a)*** u_{tr}-f_{vib}; ***(b)*** u_{tr}-A_{vib}; ***(c)*** u_{tr}-θ_{rel}.

The optimum level combination is the following:

$$\begin{Bmatrix} u_{tr} = 0.01\,m/sec \\ f_{vib} = 2000\,Hz \\ A_{vib} = 5\,\mu m \\ \theta_{rel} = 10^o \end{Bmatrix}$$

Which, according to the *Equation (4.88)*, gives the optimum layer thickness deviation of

$$|h_l - h_{th}|_{opt} = 20.8\,\mu m$$

After running a cross-checking simulation with the optimum parameter levels, validation of the expected layer thickness deviation was achieved, the resulting value being

$$|h_l - h_{th}|_{opt,sim} = 20.4\ \mu m$$

having a (-) 1.9% deviation from the expected value of 20.8 μm, which is less than the error of the regression equation, as calculated by the ANOVA (5.32%).

4.7.2 SCR Results

In terms of the surface coverage ratio, *Figure 4.22* and *Figure 4.23* show that it is, similarly to layer thickness deviation, primarily influenced by the spreading speed (78.44% contribution, *Table 4.9*). Again, an increase in the spreading speed comes with a decrease of the surface coverage ratio, meaning that the layer quality deteriorates.

Table 4.9: Analysis of Variance (ANOVA) for surface coverage ratio.

Source	DoF	Seq SS	Contribution	Adj SS	Adj MS	F-value	P-value
Regression	7	264.644	84.48%	264.644	378.063	14.77	0.000
U_{tr} (m/sec)	1	245.720	78.44%	13.689	136.885	5.35	0.032
f_{vib} (Hz)	1	0.3201	1.02%	0.0051	0.00512	0.02	0.889
A_{vib} (μm)	1	0.0581	0.19%	0.6210	0.62098	2.43	0.136
θ_{rel} (deg)	1	0.5000	1.60%	0.0021	0.00213	0.01	0.928
U_{tr} (m/sec) *f_{vib} (Hz)	1	0.0922	0.29%	0.0922	0.09218	0.36	0.556
U_{tr} (m/sec) *A_{vib} (μm)	1	0.6259	2.00%	0.6259	0.62591	2.45	0.134
U_{tr} (m/sec) *θ_{rel} (deg)	1	0.2961	0.95%	0.2961	0.29611	1.16	0.296
Error	19	48.630	15.52%	48.630	0.25595		
Total	26	313.274	100.00%				

By *Table 4.9*, it is made clear that the frequency and amplitude of vibration, as well as the blade's angle of relief, play a small role (1.02%, 0.19% and 1.60% respectively) in terms of surface coverage ratio. However, as seen in *Figure 4.25*, it can be noticed that, when it comes to the spreading speed-angle of relief pair, there is negligible interaction, the flat-bottomed blades showing better results at all speeds. However, for both the pairs spreading speed-vibrating frequency and spreading speed-vibrating amplitude, it is only at low and middle speeds that there is no interaction and the surface coverage is affected positively with higher frequency and amplitude. Contrariwise, at greater spreading

speed values this trend gets completely reversed in terms of amplitude and, smaller amplitudes give better coverage ratios at maximum speed. In terms of frequency, middle frequency levels inflict a drastic deterioration in terms of surface coverage at maximum spreading speed, leading to the conclusion that the natural frequency of the system is located at approximately 1000 Hz.

The regression equation of the surface coverage ratio is given by *Equation (4.89)*;

$$SCR(\%) = 98.907 - 18.29u_{tr} + 0.000039f_{vib} + 0.162A_{vib} + 0.0038\theta_{rel} + 0.00254u_{tr}f_{vib} - 2.51u_{tr}A_{vib} - 0.697u_{tr}\theta_{rel} \quad (4.89)$$

The optimum level combination is the following:

$$\begin{Bmatrix} u_{tr} = 0.01\,m/sec \\ f_{vib} = 2000\,Hz \\ A_{vib} = 5\,\mu m \\ \theta_{rel} = 0^o \end{Bmatrix}$$

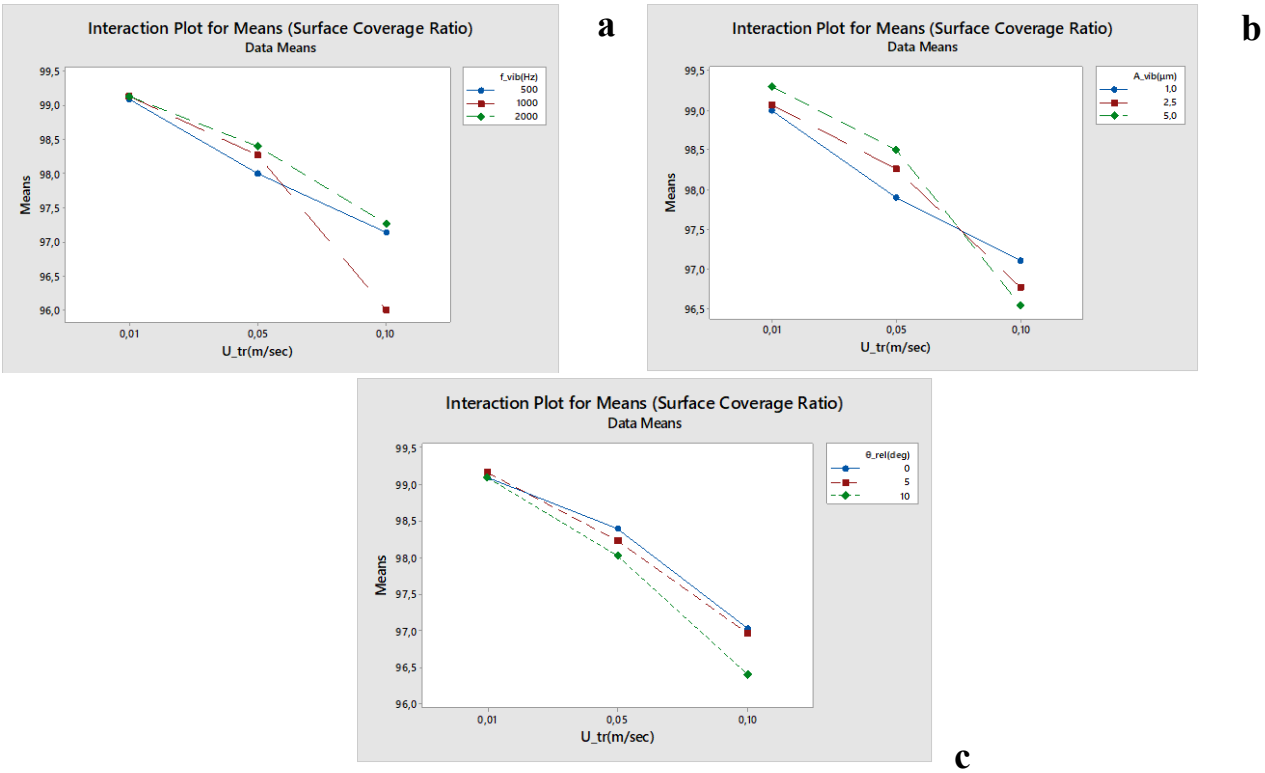

Figure 4.25: Interaction plots for means of the surface coverage ratio; ***(a)*** u_{tr}-f_{vib}; ***(b)*** u_{tr}-A_{vib}; ***(c)*** u_{tr}-θ_{rel}.

Which, according to the *Equation (4.89)*, gives the optimum surface coverage ratio of

$$SCR_{opt} = 99.54\%$$

After running a cross-checking simulation with the optimum parameter levels, validation of the expected surface coverage ratio was achieved, with the value being

$$SCR_{opt,sim} = 99.3\%$$

having a (-) 0.2% deviation from the expected value of 99.54%, which is less than the error of the regression equation, as calculated by the ANOVA (15.52%). The error of the regression is higher than 10%, probably because of the high inherent complexity of the process. However, this is not enough to harm the credibility of the results, as shown in the calculated deviation between the simulation and the expected regression value.

4.7.3 S_q-RMS Results

The plot for the means of the S_q (RMS surficial roughness) shows that, in agreement with the previous quality parameters, the smaller the spreading speed, the smaller the roughness, hence the better the surface quality. In spite of the previous quality parameters, who were affected minimally by the angle of relief, surface roughness seems to be affected more by it. Flatter blades tend to create smoother surfaces, probably due to the increased contact zone between them and the surface. Again, high frequency and amplitude levels show better results in terms of surface roughness.

Table 4.10: Analysis of Variance (ANOVA) for surficial RMS roughness.

Source	*DoF*	*Seq SS*	*Contribution*	*Adj SS*	*Adj MS*	*F-value*	*P-value*
Regression	7	166.032	84.33%	166.032	237.188	14.60	0.000
U_{tr} (m/sec)	1	129.530	65.79%	0.514	0.5136	0.32	0.580
f_{vib} (Hz)	1	5.696	2.89%	1.853	18.529	1.14	0.299
A_{vib} (μm)	1	0.632	0.32%	11.329	113.287	6.97	0.016
θ_{rel} (deg)	1	11.045	5.61%	0.050	0.0504	0.03	0.862
U_{tr} (m/sec) *f_{vib} (Hz)	1	0.000	0.00%	0.000	0.0000	0.00	0.996
U_{tr} (m/sec) *A_{vib} (μm)	1	12.539	6.37%	12.539	125.390	7.72	0.012
U_{tr} (m/sec) *θ_{rel} (deg)	1	6.590	3.35%	6.590	65.902	4.06	0.058
Error	19	30.860	15.67%	30.860	16.242		
Total	26	196.892	100.00%				

The spreading speed is again the prevalent affecting factor (65.79%), however, as seen in *Table 4.10* (ANOVA for RMS), the angle of relief and the frequency of vibration are also important (5.61% and 2.89% contribution respectively). Additionally, while the amplitude does not seem to have a strong influence on the response (0.32%), its interaction with the spreading speed is quite significant (6.37%).

In *Figure 4.26*, it is interesting to note that, even though at low spreading speed the effect of different angle of relief is negligible on the RMS response, as the speed increases, the worse the results that are achieved via sharper blades, in terms of produced surface roughness. Furthermore, while in the area between low and medium speeds there seems to be no interaction between speed and vibrating frequency, or between speed and vibrating amplitude, this trend changes between medium and high-speed levels. Interestingly, while at low and medium speeds it is beneficial to apply a high vibrating amplitude, at high spreading speed it is the other way around and it is more beneficial to opt for a lower vibrating amplitude value. This is possibly due to the high amount of kinetic energy fed towards the particles, amount which surpasses a threshold and leads to a more unstable behaviour of the powder bed, leading to more surficial defects.

The regression equation of the surficial RMS roughness is given by *Equation (4.90)*;

$$S_q = 20.02 + 11.2u_{tr} - 0.000739f_{vib} - 0.691A_{vib} - 0.019\theta_{rel} + 0.0001u_{tr}f_{vib} + 11.22u_{tr}A_{vib} + 3.29u_{tr}\theta_{rel} \quad (4.90)$$

The optimum level combination is the following:

$$\begin{Bmatrix} u_{tr} = 0.01\, m/sec \\ f_{vib} = 2000\, Hz \\ A_{vib} = 5\, \mu m \\ \theta_{rel} = 0^o \end{Bmatrix}$$

Which, according to the *Equation (4.90)*, gives the optimum surficial RMS roughness of

$$S_{q_{opt}} = 15.8\, \mu m$$

After running a cross-checking simulation with the optimum parameter levels, validation of the expected surficial RMS roughness was achieved, with the value being

$$S_{q_{opt,sim}} = 15.7\, \mu m$$

having a (-) 0.6% deviation from the expected value of 15.8 μm, which is less than the error of the regression equation, as calculated by the ANOVA (15.67%). Again, the error might be surpassing 10% due to the complexity of the process, however, this is not

enough to negatively affect the credibility of the experiment and the validity of the extracted results and conclusions.

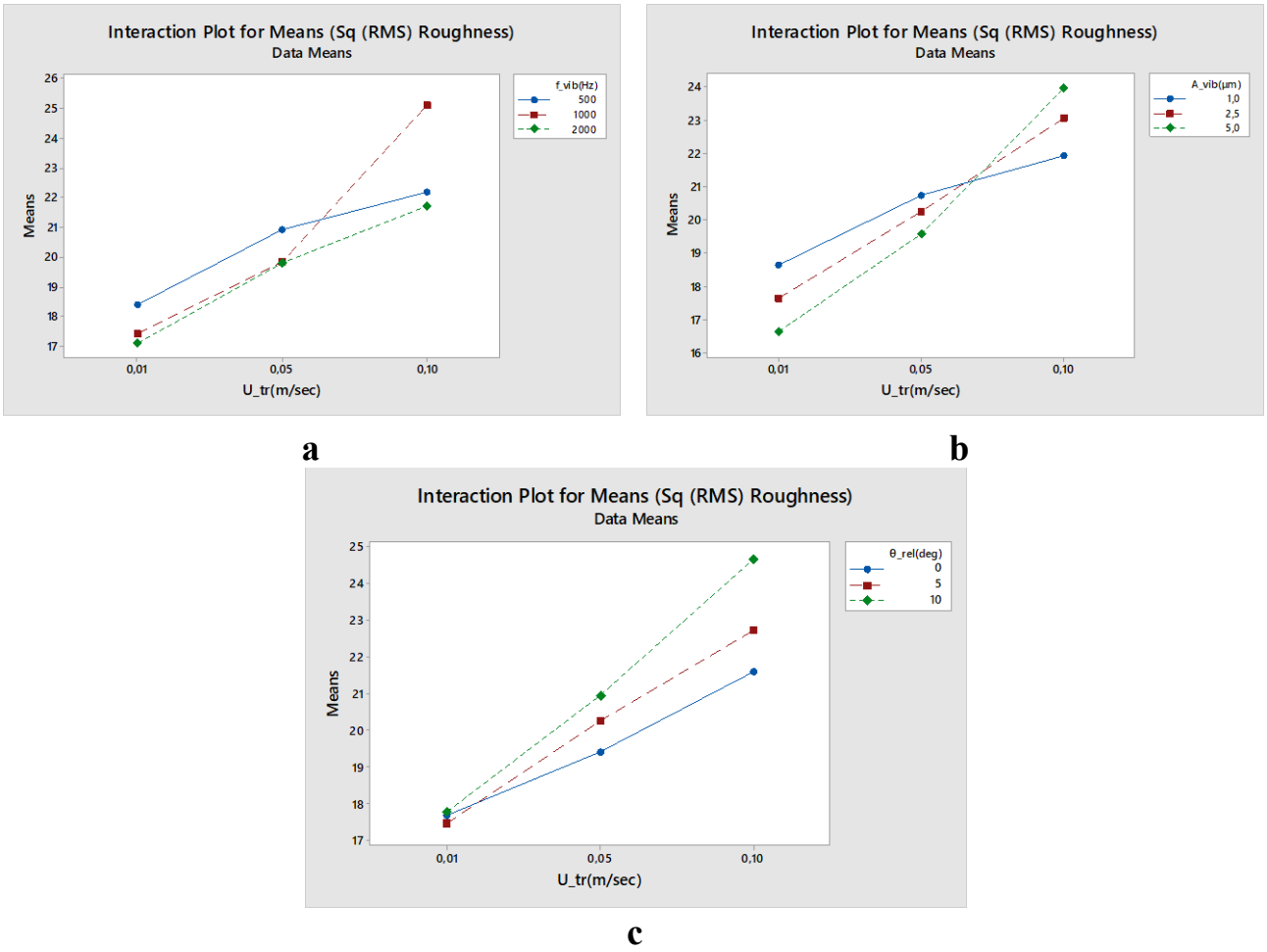

Figure 4.26: Interaction plots for means of the surficial RMS roughness; ***(a)*** u_{tr}-f_{vib}; ***(b)*** u_{tr}-A_{vib}; ***(c)*** u_{tr}-θ_{rel}.

4.8 Discussion

A general conclusion is that, in the case where it is absolutely necessary to vastly increase the spreading speed, the negative outcome in terms of RMS and SCR can be compensated to some extent by opting for flat-bottomed blades instead of sharp ones and reducing the vibration amplitude, while maintaining a high vibrating frequency. This does lead to slightly larger layer thickness deviation, but this is more easily countered via adjusting the downwards motion of the fabrication piston, i.e., the theoretical thickness of the layer, while a poor SCR and RMS value signal important surficial defects that can be inherited to the next layers.

In general, the optimum set of parameters for all the three quality criteria is by ¾ the same (referring to u_{tr}, f_{vib} and A_{vib}), at

$$\begin{Bmatrix} u_{tr} = 0.01\,m/sec \\ f_{vib} = 2000\,Hz \\ A_{vib} = 5\,\mu m \end{Bmatrix}$$

with the observation that a flat-bottomed blade promotes optimum SCR and RMS, while a sharp blade promotes a better LTD, compromising the other two, as shown in *Table 4.11*.

Table 4.11: Performance comparison of optimum LTD vs optimum SCR/RMS spreading settings.

OPTIMUM	u_{tr} (m/sec)	f_{vib} (Hz)	A_{vib} (μm)	θ_{rel} (deg)	LTD_{reg} (LTD_{sim})	SCR_{reg} (SCR_{sim})	$S_{q_{reg}}$ $\left(S_{q_{sim}}\right)$	Ssk_{sim}	Sku_{sim}
LTD	0.01	2000	5	10	20.8 (20.4)	99.51 (99.29)	15.9 (16.5)	-1.412	6.304
SCR	0.01	2000	5	0	21.4 (22.1)	99.54 (99.33)	15.8 (15.7)	-1.543	6.530
RMS	0.01	2000	5	0	21.4 (22.1)	99.54 (99.33)	15.8 (15.7)	-1.543	6.530

(**Note:** Reg stands for "regression", while sim for "simulation".)

Since the method of simultaneous optimization of various quality criteria is very tough and does not always point with clarity towards a certain optimum solution, this work features an attempt to use surficial skewness and kurtosis as equivalent indicators of surface quality.

Initially, in order to evaluate all quality criteria simultaneously, LTD, SCR and RMS are normalized so that the values they take are between 0 and 1 for all the 27 trials of the Taguchi DoE. Then, a weighted means of these is calculated, using optimized weights, as can be seen in *Table 4.12* and

Table 4.13. These weighted means are calculated by summing normalized LTD, normalized RMS and normalized (100-SCR) values, in order for all of them to optimize the process when minimized. However, the connection between these weighted means and the experiment is performed via plotting the weighted means vs the Ssk and Sku

values, since it is the general observation that the trials' performance is becoming better the smaller (negative) Ssk and the larger (positive) Sku values become.

By examining *Table 4.7* closely, we observe that the kurtosis of all the trials has a negative value, which is to be expected, since the top surfaces of the spherical particles create surfaces that feature smoother, rounder peaks and deeper, sharper valleys, with a distribution that deviates to the upper side. Furthermore, almost all the trials feature kurtosis values larger than 3 (except for trials #23 and #24), which is also expected, since it is indicating the presence of inordinately deep valleys, since, as mentioned already, the peaks are quite even, shaped like top hemispheres.

After arranging the lines of *Table 4.7* by ascending order for (i) Ssk and (ii) Sku, we plot the three quality criteria versus Ssk and Sku respectively, in *Figure 4.27* and *Figure 4.28*. The skewness plot reveals a clear trend. As the layer's quality deteriorates (increase of LTD and RMS, decrease of SCR), the value of skewness tends to become larger, approaching zero from the negative side. Similarly, the kurtosis plot reveals a similar trend. As the layer's quality deteriorates (increase of LTD and RMS, decrease of SCR), the value of kurtosis tends to become smaller, approaching zero from the positive side. The two aforementioned figures provide the linear approximation of the three quality criteria graphs versus Ssk and Sku, with their equations and R^2.

While it has become obvious that, in general, smaller negative skewness values and larger positive kurtosis values indicate better layer surface quality by correlation to all three quality criteria used, it is necessary to find a rule that connects these three criteria to the two surficial dimensionless parameters. For this, it is safe to assume that each dimensionless parameter is linearly connected to a weighted means of the three quality criteria, as shown in *Equations (4.91)* and *(4.92)*.

$$WM_{Ssk} = w_{|LTD|_n - Ssk} \cdot |LTD|_n + w_{(100-SCR)_n - Ssk} \cdot (100 - SCR)_n + w_{S_{q_n} - Ssk} \cdot S_{q_n} \qquad (4.91)$$

$$WM_{Sku} = w_{|LTD|_n - Sku} \cdot |LTD|_n + w_{(100-SCR)_n - Sku} \cdot (100 - SCR)_n + w_{S_{q_n} - Sku} \cdot S_{q_n} \qquad (4.92)$$

We can algorithmically make combinations of the three weights, having as a given that their sum must always be equal to 1, aiming to develop a curve, the linear approximation of which has the best fit among all the possible curves that we can create by altering the weight combination. The best fit is the one with the highest R^2 value, i.e., the one which best approximates a line.

Table 4.12: L27 Orthogonal array of the Taguchi DoE for powder spreading. The results are presented as well. Lines sorted by ascending Ssk value.

#	u_{tr} $\left(\frac{m}{sec}\right)$	f_{vib} (Hz)	A_{vib} (μm)	θ_{rel} $(deg.)$	$\lvert h_l - h_{th} \rvert$ (μm)	$(100 - SCR)$ (%)	S_q (μm)	LTD_n	$(100 - SCR)_n$	S_{q_n}	WM	Ssk	Sku
6	**0.01**	**1000**	**5**	**0**	22.2	0.7	16.1	0.050	0.000	0.000	0.017	-1.515	6.403
8	**0.01**	**2000**	**2.5**	**0**	23	0.9	17	0.089	0.045	0.071	0.076	-1.503	6.075
9	**0.01**	**2000**	**5**	**5**	21.5	0.7	16.4	0.015	0.000	0.024	0.019	-1.431	6.232
5	**0.01**	**1000**	**2.5**	**10**	24.3	1	18	0.153	0.068	0.151	0.148	-1.351	5.626
7	**0.01**	**2000**	**1**	**10**	23.8	1	17.9	0.129	0.068	0.143	0.134	-1.338	5.57
3	**0.01**	**500**	**5**	**10**	21.2	0.7	17.4	0.000	0.000	0.103	0.062	-1.179	5.572
12	**0.05**	**500**	**5**	**0**	31.7	1.4	18.8	0.520	0.159	0.214	0.318	-1.042	4.358
17	**0.05**	**2000**	**2.5**	**5**	32.4	1.4	19.2	0.554	0.159	0.246	0.350	-0.962	4.116
4	**0.01**	**1000**	**1**	**5**	26.7	0.9	18.1	0.272	0.045	0.159	0.193	-0.956	4.741
14	**0.05**	**1000**	**2.5**	**0**	33.8	1.5	19.2	0.624	0.182	0.246	0.375	-0.926	3.993
2	**0.01**	**500**	**2.5**	**5**	26	0.9	17.9	0.238	0.045	0.143	0.171	-0.906	4.852
15	**0.05**	**1000**	**5**	**5**	32.1	1.6	19.9	0.540	0.205	0.302	0.380	-0.898	3.993
16	**0.05**	**2000**	**1**	**0**	35	1.9	20.2	0.683	0.273	0.325	0.448	-0.869	3.698
18	**0.05**	**2000**	**5**	**10**	32.2	1.5	20	0.545	0.182	0.310	0.385	-0.815	3.956
13	**0.05**	**1000**	**1**	**10**	36.9	2.1	20.4	0.777	0.318	0.341	0.493	-0.811	3.602
10	**0.05**	**500**	**1**	**5**	36.6	2.3	21.6	0.762	0.364	0.437	0.547	-0.685	3.347
1	**0.01**	**500**	**1**	**0**	29	1.1	19.9	0.386	0.091	0.302	0.321	-0.672	3.889
22	**0.1**	**1000**	**1**	**0**	41.4	3	21.7	1.000	0.523	0.444	0.643	-0.633	3.063
25	**0.1**	**2000**	**1**	**5**	40.2	2.7	21.3	0.941	0.455	0.413	0.600	-0.622	3.169
20	**0.1**	**500**	**2.5**	**0**	41.2	3.1	21.8	0.990	0.545	0.452	0.645	-0.597	3.059
21	**0.1**	**500**	**5**	**5**	36.9	2.5	22	0.777	0.409	0.468	0.573	-0.596	3.31
11	**0.05**	**500**	**2.5**	**10**	34.9	2.3	22.4	0.678	0.364	0.500	0.556	-0.577	3.362
27	**0.1**	**2000**	**5**	**0**	40.2	2.8	21.3	0.941	0.477	0.413	0.601	-0.558	3.604
19	**0.1**	**500**	**1**	**10**	40.8	3	22.8	0.970	0.523	0.532	0.685	-0.399	3.051
26	**0.1**	**2000**	**2.5**	**10**	41.1	2.7	22.5	0.985	0.455	0.508	0.672	-0.335	2.94
23	**0.1**	**1000**	**2.5**	**5**	40.7	3.9	24.9	0.965	0.727	0.698	0.793	-0.323	2.732
24	**0.1**	**1000**	**5**	**10**	37	5.1	28.7	0.782	1.000	1.000	0.924	-0.224	2.753

The algorithm has a 0.05 step and uses this to increase and decrease the weights for each iteration. Then, it calculates the points of the curve and finally uses the least-squares linear approximation to calculate the linear fit and the R^2 value. The weight combination that leads to the best linear approximation are the following:

$$\begin{Bmatrix} w_{LTD-Ssk} = 0.35 \\ w_{SCR-Ssk} = 0.05 \\ w_{RMS-Ssk} = 0.60 \end{Bmatrix} \qquad WM_{Ssk} = 0.6449 \cdot Ssk + 0.9549 \qquad R^2 = 0.8869$$

$$\begin{Bmatrix} w_{LTD-Sku} = 0.40 \\ w_{SCR-Sku} = 0.20 \\ w_{RMS-Sku} = 0.40 \end{Bmatrix} \qquad WM_{Sku} = -0.1497 \cdot Sku + 1.1224 \qquad R^2 = 0.9499$$

Table 4.13: L27 Orthogonal array of the Taguchi DoE for powder spreading. The results are presented as well. Lines sorted by ascending Sku value.

#	u_{tr} $\left(\frac{m}{sec}\right)$	f_{vib} (Hz)	A_{vib} (μm)	θ_{rel} $(deg.)$	$\lvert h_l - h_{th} \rvert$ (μm)	$100 - SCR$ (%)	S_q (μm)	LTD_n	$(100 - SCR)_n$	S_{q_n}	WM	Ssk	Sku
23	**0.1**	**1000**	**2.5**	**5**	40.7	3.9	24.9	0.965	0.727	0.698	0.811	-0.323	2.732
24	**0.1**	**1000**	**5**	**10**	37	5.1	28.7	0.782	0.000	1.000	0.713	-0.224	2.753
26	**0.1**	**2000**	**2.5**	**10**	41.1	2.7	22.5	0.985	0.545	0.508	0.706	-0.335	2.94
19	**0.1**	**500**	**1**	**10**	40.8	3	22.8	0.970	0.477	0.532	0.696	-0.399	3.051
20	**0.1**	**500**	**2.5**	**0**	41.2	3.1	21.8	0.990	0.455	0.452	0.668	-0.597	3.059
22	**0.1**	**1000**	**1**	**0**	41.4	3	21.7	1.000	0.477	0.444	0.673	-0.633	3.063
25	**0.1**	**2000**	**1**	**5**	40.2	2.7	21.3	0.941	0.545	0.413	0.650	-0.622	3.169
21	**0.1**	**500**	**5**	**5**	36.9	2.5	22	0.777	0.591	0.468	0.616	-0.596	3.31
10	**0.05**	**500**	**1**	**5**	36.6	2.3	21.6	0.762	0.636	0.437	0.607	-0.685	3.347
11	**0.05**	**500**	**2.5**	**10**	34.9	2.3	22.4	0.678	0.636	0.500	0.599	-0.577	3.362
13	**0.05**	**1000**	**1**	**10**	36.9	2.1	20.4	0.777	0.682	0.341	0.584	-0.811	3.602
27	**0.1**	**2000**	**5**	**0**	40.2	2.8	21.3	0.941	0.523	0.413	0.646	-0.558	3.604
16	**0.05**	**2000**	**1**	**0**	35	1.9	20.2	0.683	0.727	0.325	0.549	-0.869	3.698
1	**0.01**	**500**	**1**	**0**	29	1.1	19.9	0.386	0.909	0.302	0.457	-0.672	3.889
18	**0.05**	**2000**	**5**	**10**	32.2	1.5	20	0.545	0.818	0.310	0.505	-0.815	3.956
14	**0.05**	**1000**	**2.5**	**0**	33.8	1.5	19.2	0.624	0.818	0.246	0.512	-0.926	3.993
15	**0.05**	**1000**	**5**	**5**	32.1	1.6	19.9	0.540	0.795	0.302	0.496	-0.898	3.993
17	**0.05**	**2000**	**2.5**	**5**	32.4	1.4	19.2	0.554	0.841	0.246	0.488	-0.962	4.116
12	**0.05**	**500**	**5**	**0**	31.7	1.4	18.8	0.520	0.841	0.214	0.462	-1.042	4.358
4	**0.01**	**1000**	**1**	**5**	26.7	0.9	18.1	0.272	0.955	0.159	0.363	-0.956	4.741
2	**0.01**	**500**	**2.5**	**5**	26	0.9	17.9	0.238	0.955	0.143	0.343	-0.906	4.852
7	**0.01**	**2000**	**1**	**10**	23.8	1	17.9	0.129	0.932	0.143	0.295	-1.338	5.57
3	**0.01**	**500**	**5**	**10**	21.2	0.7	17.4	0.000	1.000	0.103	0.241	-1.179	5.572
5	**0.01**	**1000**	**2.5**	**10**	24.3	1	18	0.153	0.932	0.151	0.308	-1.351	5.626
8	**0.01**	**2000**	**2.5**	**0**	23	0.9	17	0.089	0.955	0.071	0.255	-1.503	6.075
9	**0.01**	**2000**	**5**	**5**	21.5	0.7	16.4	0.015	1.000	0.024	0.215	-1.431	6.232
6	**0.01**	**1000**	**5**	**0**	22.2	0.7	16.1	0.050	1.000	0.000	0.220	-1.515	6.403

The line depicting the weighted mean of the quality criteria versus Ssk is an increasing function of Ssk, see *Figure 4.29*. Since the quality of the deposited layer deteriorates with increasing (negative) Ssk values, it is safe to come to the conclusion that, the smaller the quantity $(0.35 \cdot LTD + 0.05 \cdot SCR + 0.60 \cdot RMS)$, the better the quality of the layer, according to Ssk.

Similarly, the line depicting the weighted mean of the quality criteria versus Sku is a decreasing function of Sku, see *Figure 4.30*. Since the quality of the deposited layer deteriorates with decreasing (positive) Sku values, it is safe to come to the conclusion

that, the smaller the quantity $(0.40 \cdot LTD + 0.20 \cdot SCR + 0.40 \cdot RMS)$, the better the quality of the layer, according to Sku.

Both Ssk and Sku lead to very similar observations with regard to the weighted mean of LTD, SCR and RMS that needs to be minimized in order to optimize the layer's quality. The weights calculated are very similar to the quality criteria importance that an expert on the field of additive manufacturing would assign to them. Surface coverage ratio is the least important, since it detects the extent to which large surface defects exist within the layer. Such defects can be caused by the dragging of an agglomerate along the surface, creating a line that leaves the substrate visible, drastically decreasing the SCR. However, such defects are easily avoidable via implementing proper sieving of the powder prior to recoating. Despite the possibility of such defects being catastrophic for the surface quality, since they are usually inherited from layer to layer and cause serious defects in the geometrical accuracy or even the feature geometry of the finished part, the easiness in their avoidance renders them quite uncommon. That is why it is assigned the lowest weight, at 0.05 and 0.2 for Ssk and Sku evaluation respectively.

Secondly, the layer thickness deviation shows how lower the mean line of the layer's surface is compared to the plane of the theoretical layer thickness. This value is important, since it is directly connected to the theoretical packing density of the layer, as is calculated in most works. Despite being important, it is easily countered by adjusting (increasing) appropriately the theoretical layer thickness by increasing the vertical downwards displacement of the fabrication piston, in order to achieve the desired actual layer height. Hence, it is assigned a medium weight, at 0.35-0.4 for Ssk and Sku evaluation respectively.

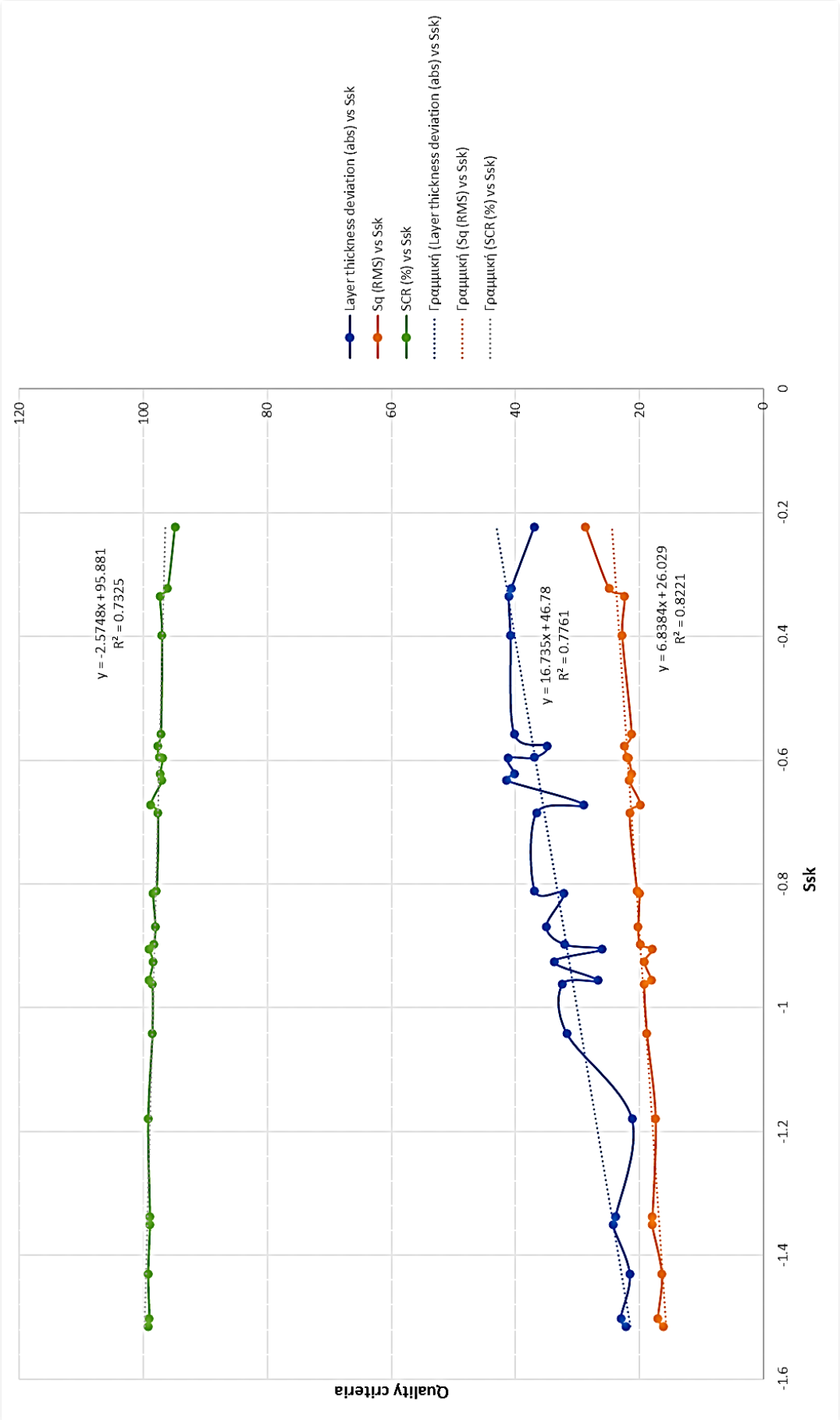

Figure 4.27: Quality criteria vs Ssk.

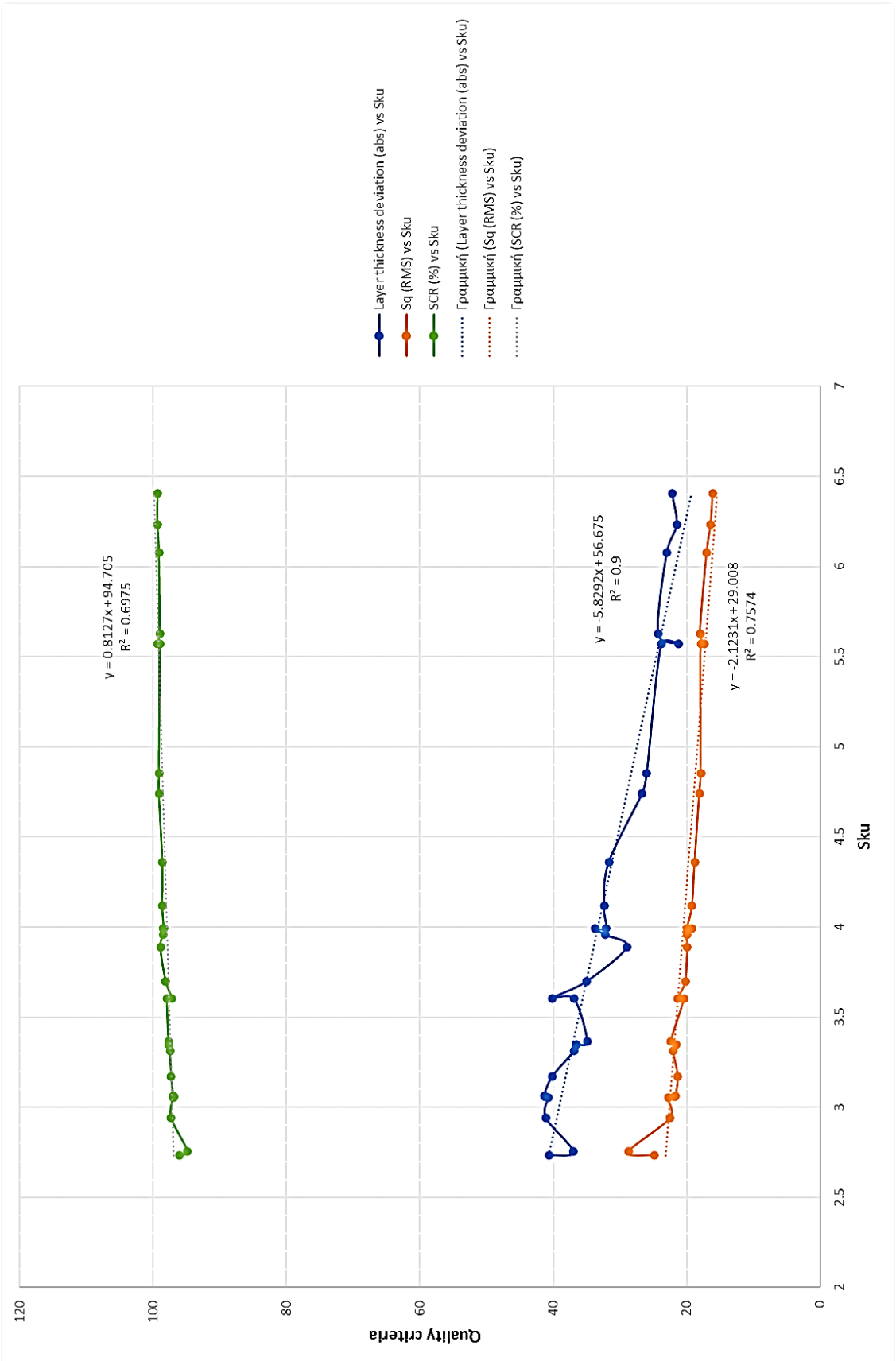

Figure 4.28: Quality criteria vs Sku.

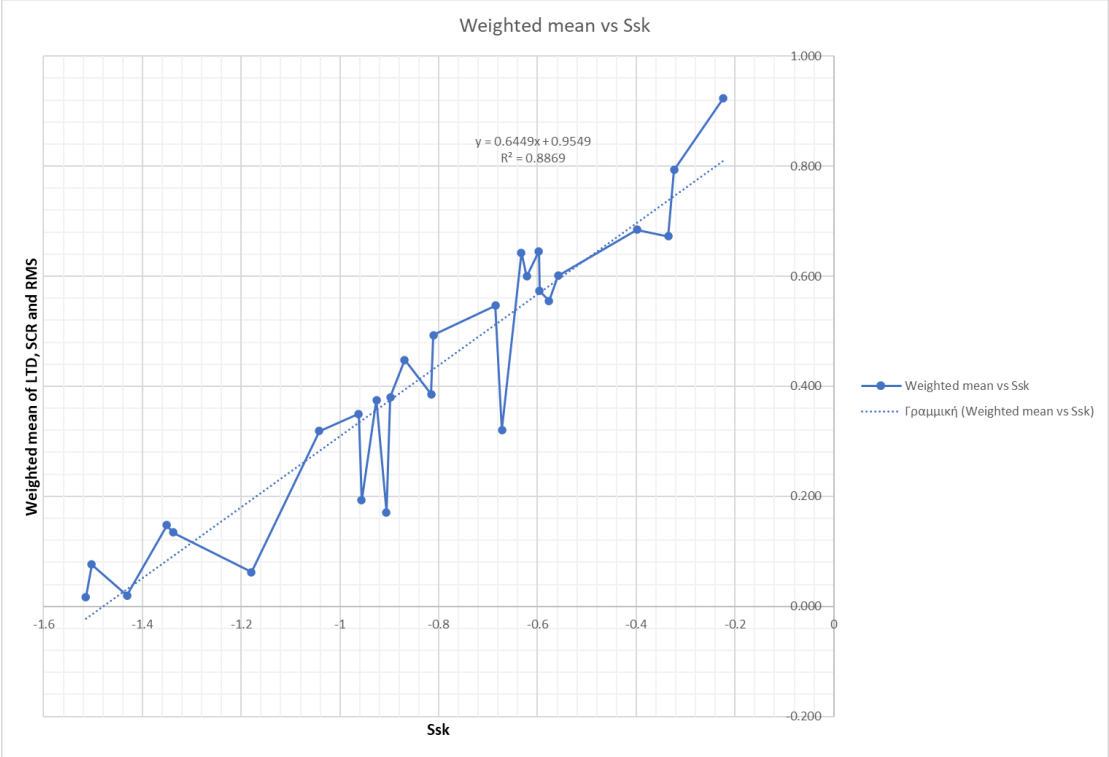

Figure 4.29: Weighted mean of LTD, SCR and RMS (weights 0.35, 0.05 and 0.60 respectively) versus Ssk.

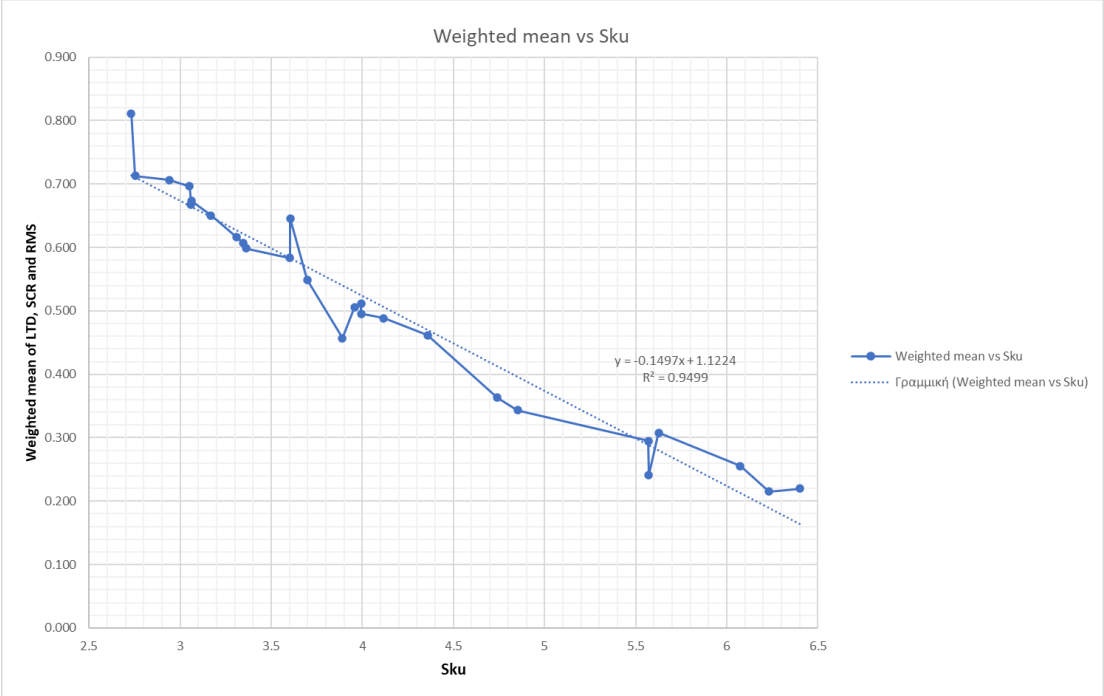

Figure 4.30: Weighted mean of LTD, SCR and RMS (weights 0.4, 0.2 and 0.4 respectively) versus Sku.

Finally, the RMS roughness is an indicator of the deposited layer's evenness and homogeneity. This shows whether the finished surface of the part will have a high or low roughness value. A high layer RMS roughness value cannot lead to serious inherited defects throughout the layers; however, it can affect the surface quality of the finished part, making it necessary to be post-processed in order for it to become ready for use. Furthermore, the RMS surface roughness is the most consistent quality criteria, as it will identify without fail large areas where the layer's surface is below or above the mean line, identifying intense spreading fluctuations during the powder-recoater interaction. Hence, it is assigned the highest weight, at 0.6 and 0.4 for Ssk and Sku evaluation respectively.

In conclusion, the empirical approach of the method is in agreement to the calculated analytical results after the statistical analysis. Ssk and Sku can be solely used in conjunction with weighted means of the three quality criteria in order to examine the general quality of the layer. Examining Ssk or Sku is equivalent to examining a weighted mean of the three quality criteria, namely layer thickness deviation (LTD), surface coverage ratio (SCR) and root mean square surficial roughness of the layer (RMS). The weights are in good agreement to the ones that would have been chosen by experts of the field. By the validation simulations run to check the validity of the regression equations, we take the values of *Table 4.11*. Both Ssk and Sku values are indicating that the optimum parameter level combination for the SCR and RMS values leads to a higher layer quality than the one created from the parameter combination that optimizes LTD. Hence, the optimum parameter level combination is:

$$\begin{Bmatrix} u_{tr} = 0.01\,m/sec \\ f_{vib} = 2000\,Hz \\ A_{vib} = 5\,\mu m \\ \theta_{rel} = 0^{o} \end{Bmatrix}$$

As proof of the vibration's positive effect on the spreading outcome, a comparison between the calculated Taguchi optimum level combination with a trial where the optimum translational speed and angle of relief are chosen, but are combined with no vibration. The visual comparison is provided in *Figure 4.31*, while the *Table 4.14* provides the quality indicators comparison between the produced layers.

Table 4.14: No vibration vs vibration performance.

	u_{tr} (m/sec)	f_{vib} (Hz)	A_{vib} (μm)	θ_{rel} (deg)	LTD_{reg} (LTD_{sim})	SCR_{reg} (SCR_{sim})	$S_{q_{reg}}$ $\left(S_{q_{sim}}\right)$	Ssk_{sim}	Sku_{sim}
NO VIB.	0.01	0	0	0	- (28.9)	- (98.56)	- (20.9)	-0.716	3.962
OPTIMUM	0.01	2000	5	0	21.4 (22.1)	99.54 (99.33)	15.8 (15.7)	-1.543	6.530

(Note: Reg stands for "regression", while sim for "simulation". The zero-vibration trial can't have regression values calculated, since this level was not included in the Taguchi design.)

It is obvious that the optimum level combination calculated by the Taguchi analysis is superior compared to its equivalent zero-vibration trial in every quality criterion, including the Ssk and Sku ones, which function as general layer quality indicators as explained above. Furthermore, by examining the top views of the deposited layer, it is evident that the zero-vibration layer features multiple surface defects, as the SCR has already showed. These defects are located behind generally larger particles, revealing the detrimental effect that the dragging of large particles has to the layer quality. Vibration tends to alleviate the dragging of large particles and agglomerates, or even break down agglomerates to an extent, leading to fewer large defect areas.

It is clear that, in the zero-vibration trial, the height of the particles shows more randomness, and many particles are over the theoretical layer height, as shown in the legend on the right-hand side of the image. Contrariwise, in the optimum Taguchi analysis trial, the particles have a very uniform height, with the colour showing much less deviation, while the top of most particles are just touching the theoretical layer height, as seen clearly in the side view of each layer as well. The positive effect of vibration, in combination with the fact that the layer's theoretical packing density increases with applied vibration, which solely derives from a decrease of the layer thickness deviation and not by the increased packing of the particles, which is proven to be negligible, come in agreement with the findings in [220], who proved these via DEM simulations for both a vibrating roller and a vibrating doctor blade as the recoating mechanism.

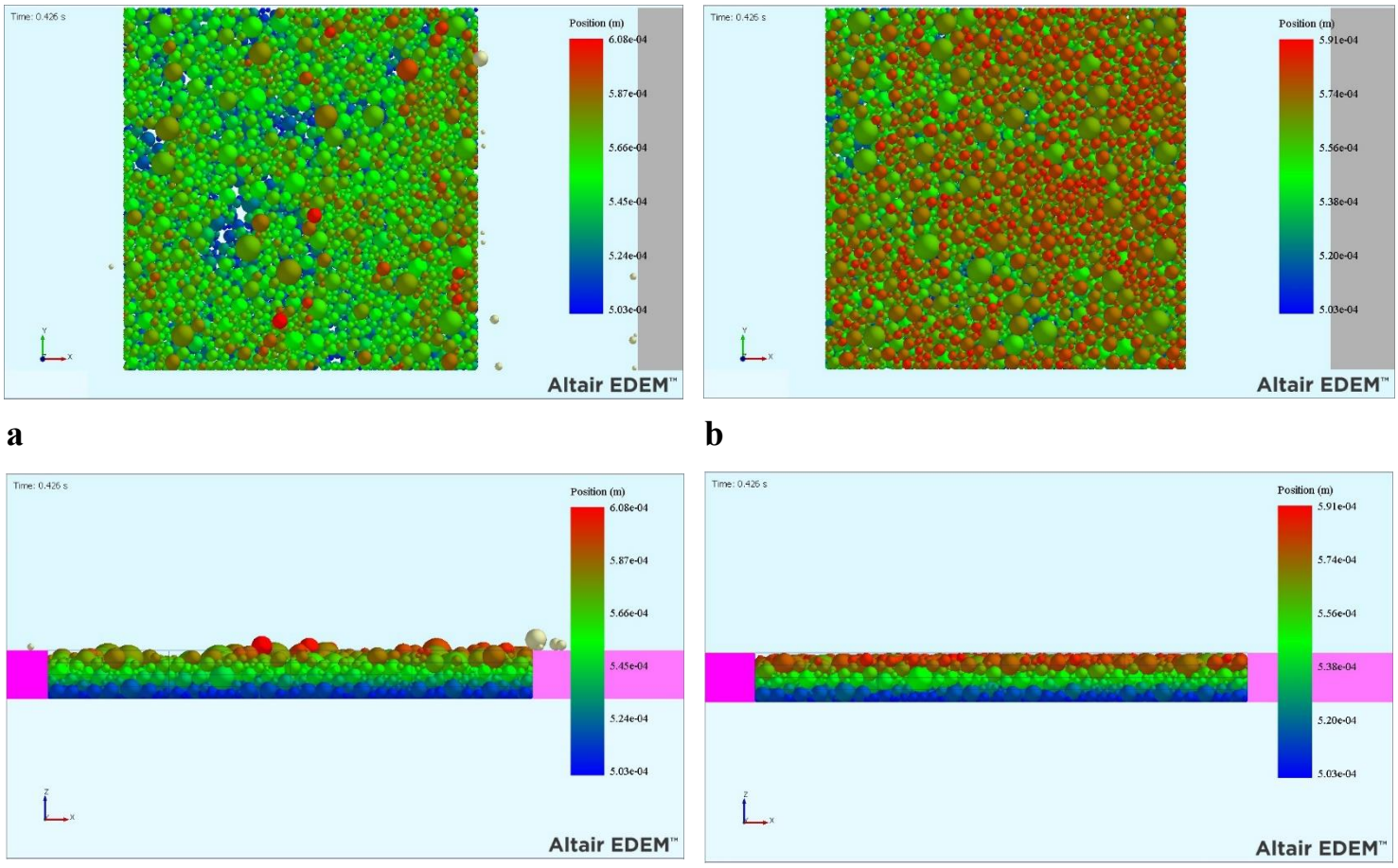

a **b**

c **d**

Figure 4.31: Layer quality comparison ***(a)*** No vibration (top view); ***(b)*** With vibration-optimum combination of Taguchi analysis (top view); ***(c)*** No vibration (side view); ***(d)*** With vibration-optimum combination of Taguchi analysis (side view) (Note: Magenta: Back border plate; Pink: Front border plate).

Since it has been proven that Ssk and Sku serve as general layer quality indicators, it is necessary to run a regression analysis to estimate these indicators based on the spreading parameters. *Table 4.15* and *Table 4.16* provide the analysis, while *Equations (4.93)* and *(4.94)* provide the regression equations.

$$|Ssk| = 0.587 - 0.90u_{tr} + 0.000295f_{vib} + 0.1455A_{vib} + 0.0112\theta_{rel} - 0.00318u_{tr}f_{vib} - 1.222u_{tr}A_{vib} - 0.00901A_{vib}\theta_{rel} \quad (4.93)$$

$$Sku = 3.498 - 9.95u_{tr} + 0.000656f_{vib} + 0.4665A_{vib} + 0.0582\theta_{rel} - 0.00613u_{tr}f_{vib} - 3.07u_{tr}A_{vib} - 0.0273A_{vib}\theta_{rel} \quad (4.94)$$

The regression equations above were calculated in order to minimize the error of the ANOVA. More specifically, the interactions were selected to maximize the sum of the

contribution column of the ANOVA table, hence minimizing the error of the regression equation.

Table 4.15: Analysis of Variance (ANOVA) for skewness in powder spreading.

Source	DoF	Seq SS	Contribution	Adj SS	Adj MS	F-value	P-value
Regression	7	314.077	90.74%	314.077	0.448681	26.61	0.000
U_{tr} (m/sec)	1	238.472	68.90%	0.00401	0.004008	0.24	0.631
f_{vib} (Hz)	1	0.16578	4.79%	0.29422	0.294217	17.45	0.001
A_{vib} (µm)	1	0.09149	2.64%	0.33803	0.338033	20.05	0.000
θ_{rel} (deg)	1	0.09188	2.65%	0.01437	0.014371	0.85	0.367
U_{tr} (m/sec) *f_{vib} (Hz)	1	0.15900	4.59%	0.14302	0.143016	8.48	0.009
U_{tr} (m/sec) *A_{vib} (µm)	1	0.14879	4.30%	0.14879	0.148786	8.82	0.008
U_{tr} (m/sec) *θ_{rel} (deg)	1	0.09911	2.86%	0.09911	0.099110	5.88	0.025
Error	19	0.32040	9.26%	0.32040	0.016863		
Total	26	346.117	100.00%				

Table 4.16: Analysis of Variance (ANOVA) for kurtosis in powder spreading.

Source	DoF	Seq SS	Contribution	Adj SS	Adj MS	F-value	P-value
Regression	7	301.817	91.23%	301.817	43.117	28.25	0.000
U_{tr} (m/sec)	1	243.774	73.69%	0.4860	0.4860	3.18	0.090
f_{vib} (Hz)	1	11.329	3.42%	14.524	14.524	9.52	0.006
A_{vib} (µm)	1	20.368	6.16%	34.737	34.737	22.76	0.000
θ_{rel} (deg)	1	0.1624	0.49%	0.3852	0.3852	2.52	0.129
U_{tr} (m/sec) *f_{vib} (Hz)	1	0.6266	1.89%	0.5332	0.5332	3.49	0.077
U_{tr} (m/sec) *A_{vib} (µm)	1	0.9391	2.84%	0.9391	0.9391	6.15	0.023
A_{vib} (µm) *θ_{rel} (deg)	1	0.9064	2.74%	0.9064	0.9064	5.94	0.025
Error	19	28.999	8.77%	28.999	0.1526		
Total	26	330.816	100.00%				

By using the regression equations, we find that, indeed, the optimum level parameter combination is the one seen in *Table 4.14*, i.e., the combination

$$\begin{Bmatrix} u_{tr} = 0.01\,m/sec \\ f_{vib} = 2000\,Hz \\ A_{vib} = 5\,\mu m \\ \theta_{rel} = 0^{o} \end{Bmatrix}$$

The regression optimum skewness and kurtosis values are calculated as:

$$Ssk_{opt,reg} = -1.771$$

$$Sku_{opt,reg} = 6.766$$

The simulation-calculated optimum Ssk and Sku values are the following

$$Ssk_{opt,sim} = -1.543$$

$$Sku_{opt,sim} = 6.530$$

The deviation between the simulation-calculated optimum values and the regression-calculated ones is (-) 12.9% and (-) 3.5% for skewness and kurtosis respectively. Kurtosis value is within the 8.77% error predicted by the ANOVA, while skewness is slightly exceeding the 9.26% predicted by the ANOVA. However, this is not a very important error, even though it is indicative of the fact that kurtosis might be a more reliable indicator of layer quality.

5 *Powder Sieving Simulations*

Sieving is a process that, to the knowledge of the author, has not been adequately investigated, or modelled via DEM simulations for implementation in layer deposition for PBF processes. It is vastly important, since it can limit the number of agglomerates and oversized particles in the layer, both of which can significantly decrease the layer's quality after its spreading. Sieving can also break down agglomerates via its vibrational motion, leading to higher powder economy.

In order to deposit the correct amount of powder on exactly the right area, this work suggests the sieving of powder over the desired area as a first step before a doctor blade (or roller) takes over, or even as a method of recoater-less powder deposition, if calibrated properly. It is proven that, with doctor blades or roller spreaders, the smaller particles are compressed and deposited faster, at the start of the layer, while, as the spreader moves towards the end of the layer, the larger particles are dragged along by the spreader [8], [96], [99], leading to a difference in terms of particle size distribution along the layer itself, effect known as powder segregation. However, this is a problem only in the case a feeding piston is used. If the powder is sprinkled evenly onto the surface from above via a vibrating sieve, and the spreader is then used only to flatten the top of the produced layer, then this problem is countered [59], [137]. However, since this is another step adding to the total manufacturing time, it is necessary to optimize sieving and make it as efficient as possible. For this reason, a Taguchi DoE is used in this Chapter.

Let us note that, powder material properties, particle size distribution and cohesion/adhesion determination methods are exactly as those applied in the simulations concerning the powder spreading process in *Chapter 4*, hence the reader is referred to pertinent *Sections 4.1* to *4.3*.

5.1 Simulation Geometry and Simulation Description

The powder sieving simulation features seven (7) bodies. These are the deposition plate, the four borders that define the area in which the sieved powder is dropping (front, back, left and right border), the sieve and the sieve's blocker, which is a plate that blocks the bottom of the sieve's apertures, so that the powder in the sieve begins to drop only when the blocking plate slides out of the way. The borders create a square sample area with a side of 1 mm. The height of the border plates is also equal to 1 mm, while the thickness of the blocker plate is equal to 100 μm (see *Figure 5.1*).

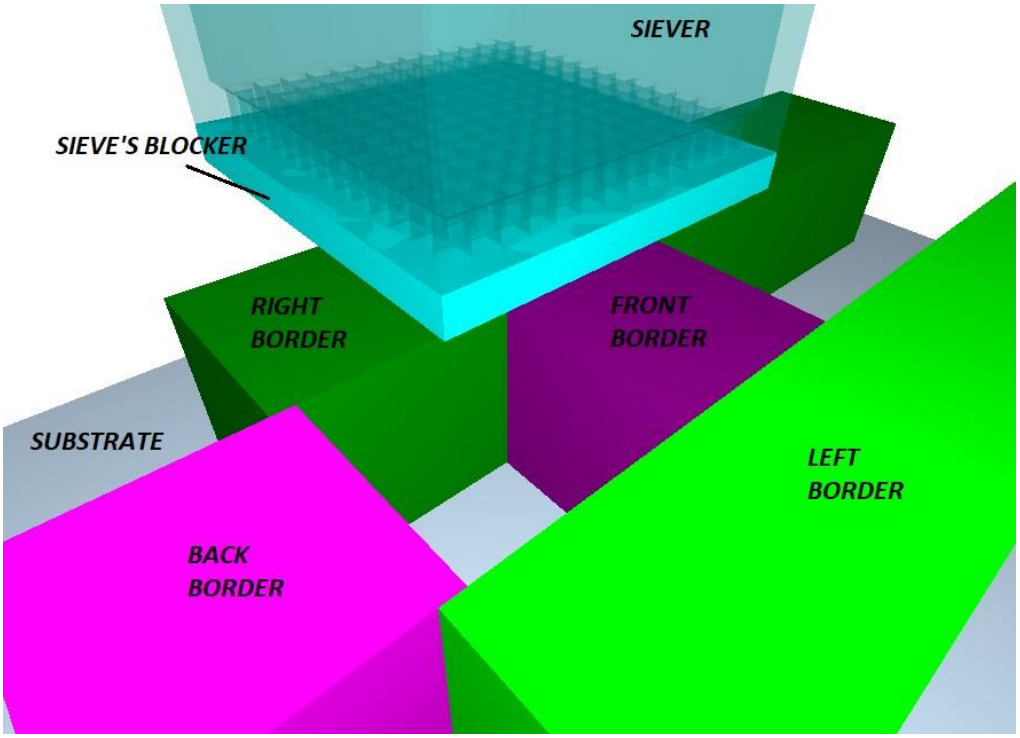

Figure 5.1: The physical bodies of the powder sieving simulation.

There is also a virtual body, necessary to use as a powder factory. This has a shape of a 1-mm-side cuboid, enveloped within the sieve, so that when it is activated, powder instantaneously fills the sieve (see *Figure 5.2*). Its height varies, depending on the trial of the Taguchi DoE, as will be explained in the next Section. The steps of the sieving process can be seen in *Figure 5.3*.

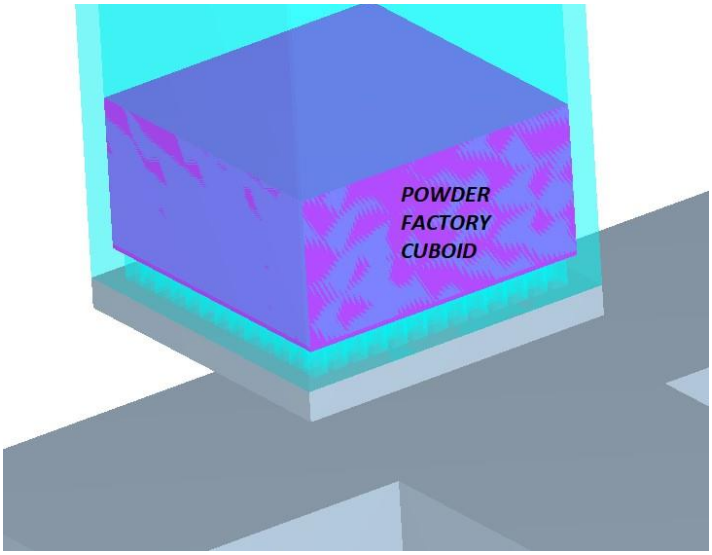

Figure 5.2: Sieving powder factory.

Similar to the spreading simulation, the sieving simulation begins by populating the virtual body of the cuboid that functions as a factory. All powder particles are created simultaneously, at the beginning moment of the simulation, by populating the powder factory cuboid (*Figure 5.2*) in such a way that inter-particle physical contact is avoided until no other particles can fit into the said virtual body. Then, they are free-falling inside the sieve, while the sieve's blocking plate is right beneath the sieve, preventing any particles from falling onto the substrate. The free-falling particles partially occupy the sieve's ducts, while eventually clogging them up. When the particles reach a very low kinetic energy value, which the simulation environment recognizes as motionless condition ("frozen" particles), the blocking plate slides to the sieve's side, releasing the sieve's apertures and enabling the particles to freely fall onto the substrate (see *Figure 5.4*).

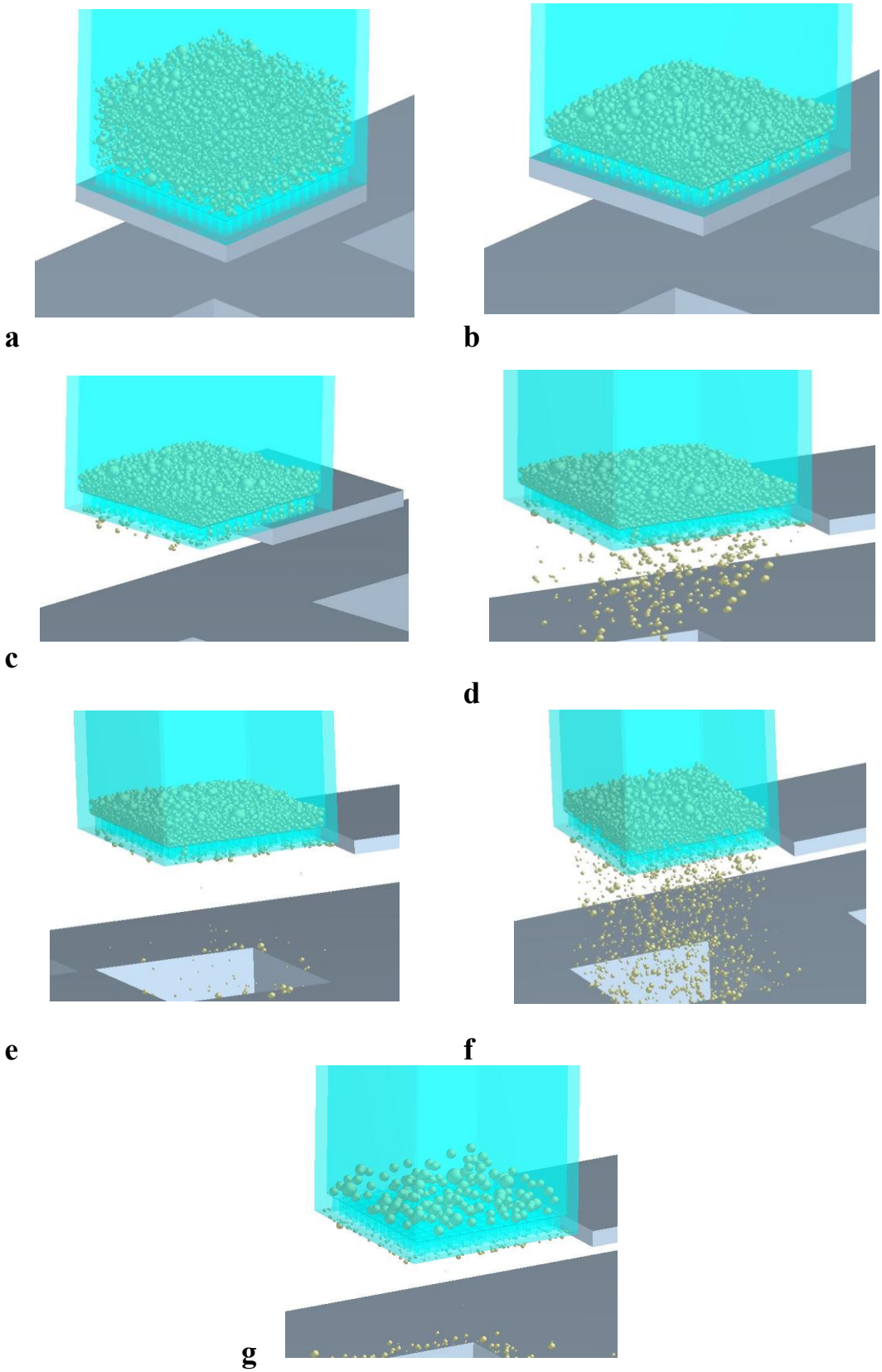

Figure 5.3: Sieving simulation steps; ***(a)*** Powder generation; ***(b)*** Particles resting motionless with blocked sieve; ***(c)*** Sieve's blocking plate retracts; ***(d)*** Initial "cloud" of particles drops; ***(e)*** Sieve's ducts are clogged - no more particles will drop unless the sieve vibrates; ***(f)*** Normal sieving operation; ***(g)*** Powder segregation completed.

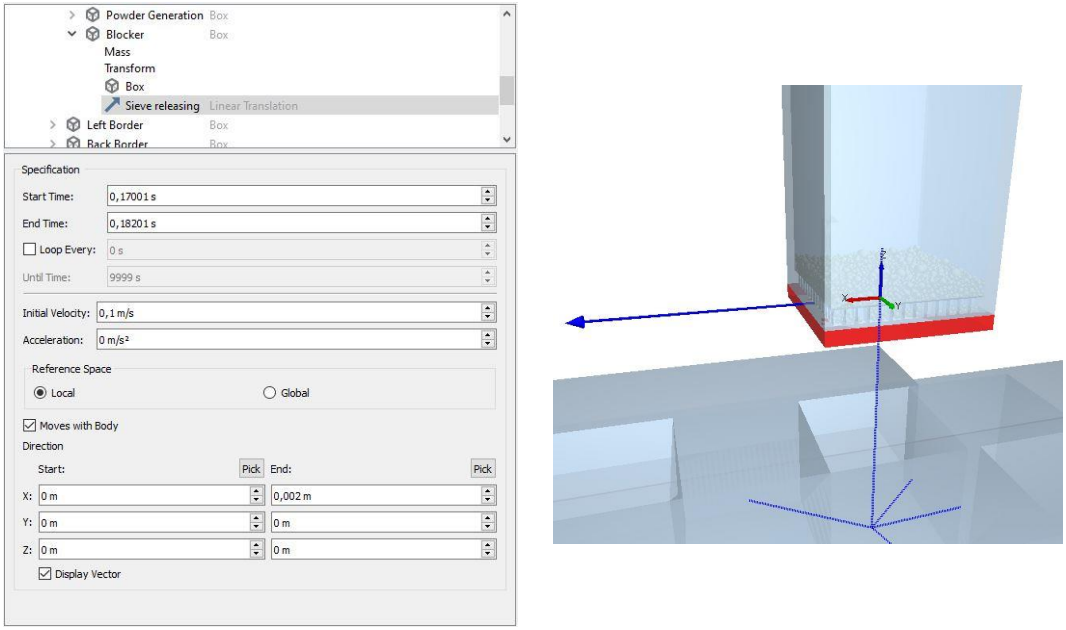

Figure 5.4: Sieve releasing setup; (Left) Motion setup for the retraction of the sieve's blocking plate; (Right) The axis of the motion is displayed via blue vector.

Once the blocker has reached its place on the side of the sieve, the sieve begins vibrating vertically, with an amplitude and frequency defined by the Taguchi DoE (see next Section).

Similar to the spreading simulation, the model features natural gravity, Schiller-Naumann drag model with the same air properties as seen in previous Section. All the physical bodies are made of Stainless Steel 304.

The sieving simulation is only completed when no more particles in the sieve remain that are physically possible to pass through the sieve's ducts, i.e., when the only particles remaining in the sieve have a size larger than the sieve's aperture. In *Figure 5.5* the settings for the sieve's vibration can be seen.

After the simulation is complete, data is extracted concerning the total mass of the particles that have passed through the sieve over time and the particle size distribution of the particles that remain in the sieve over time. Specific quality criteria for the Taguchi DoE can be defined that use this data. The next Section covers these criteria.

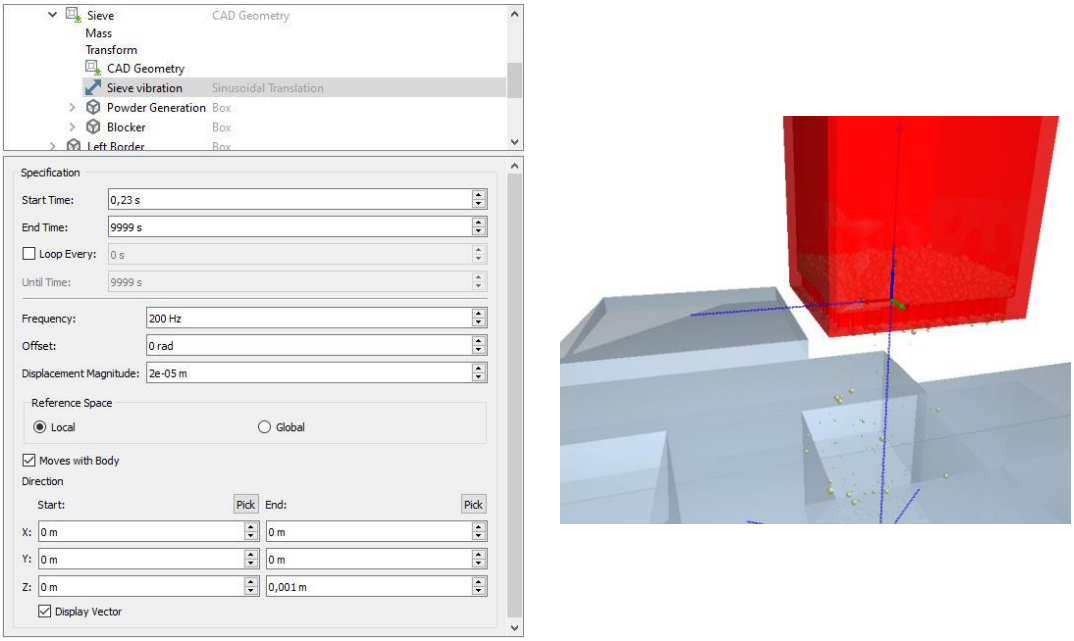

Figure 5.5: Sieving vibration setup; (Left) Motion setup for the sinusoidal oscillation of the sieve; (Right) The axis of the oscillation is displayed via blue vector.

5.2 Sieving Phase Identification and Quality Criteria

The sieving process is optimized according to four quality criteria namely: powder mass flow, total powder mass sieved during linearity, sieving duration of linearity and linearity end size ratio (LESR). These criteria will be defined and explained in the following Sub-sections.

5.2.1 Powder Mass Flow During Linearity Q (mg/sec)

First of all, it is very important that the mass flow through the sieve is constant, to easily adjust the amount of powder that will be deposited onto a specific surface indirectly by adjusting the sieving duration. Linearity is desired during the process, meaning that, the mass sieved and the time should be connected via a linear equation. The general form of the sieved mass versus time curve can be seen in *Figure 5.6*.

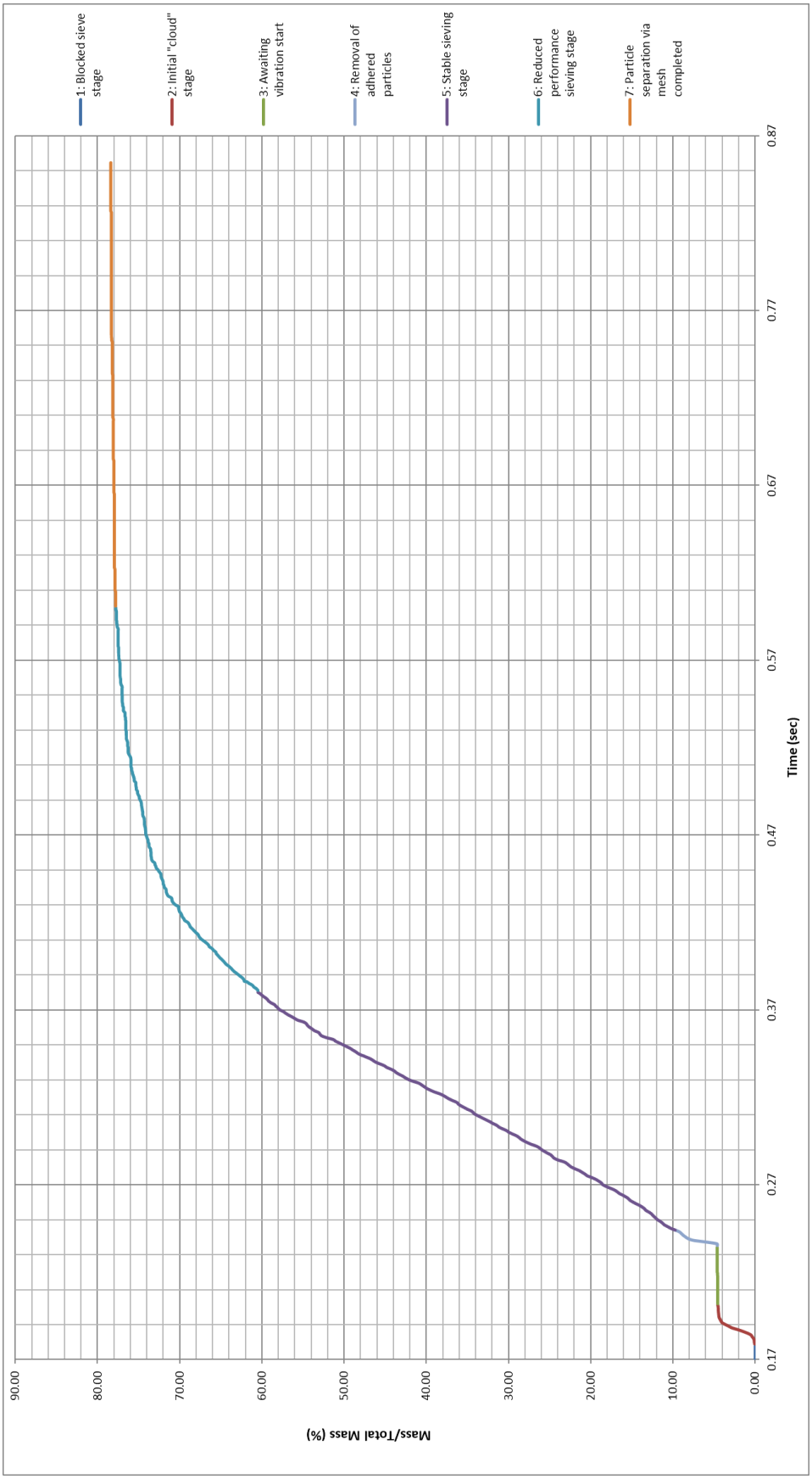

Figure 5.6: Sieved mass vs time curve. The plot refers to Trial #1 from the sieving Taguchi DoE.

As seen in the plot, seven (7) sieving stages can be identified denoted by different colours.

1. During Stage 1, the sieve is blocked by the blocking plate, hence the powder particles are ‘frozen’ inside the sieve. However, during the powder generation and the particles’ free fall until this frozen status is achieved, some particles managed to enter the sieve’s ducts before the latter got clogged up by the Van der Waals forces acting between the particles.
2. When the blocker plate is retracted, the particles that were filling the sieve’s ducts are falling onto the substrate, creating an initial “cloud” (Stage 2).
3. Subsequently, after these particles fall, no more particles can travel through the ducts and onto the substrate while the sieve remains motionless. This is Stage 3, where the sieve is awaiting the vibration in order for the sieving to begin. During that stage, many small particles are hanging from the bottom of the sieve, due to the microscopic adhesive forces that exceed gravity.
4. When the vibration begins, at the very first oscillation, these freely hanging particles drop onto the substrate, creating a second “cloud” of particles. This is Stage 4.
5. Next, providing that the vibration is of sufficient frequency and amplitude to enforce the stirring of the powder in the sieve and facilitate the unclogging of the ducts, the powder begins to pass through the sieve and fall onto the substrate at a steady flow rate. This is Stage 5, where the desired linearity is achieved. During this stage, less and less of the finer particles remain in the sieve, while the larger ones tend to remain in the sieve, since they cannot pass through the ducts as easily.
6. Eventually, the flow rate decreases and the linearity of the stable sieve stage is lost, as the sieving process enters Stage 6. In Stage 6, the sieving continues, even though its performance is decreased. During this stage, the particles that pass through the ducts are infinitesimally smaller compared to the sieve’s apertures. This continues until the powder is completely separated and the only particles remaining in the sieve are the ones of size larger than the aperture’s size.

7. Stage 7 follows, where no more particles pass through the sieve, and the powder segregation has been completed.

The linearity is desired and ensured in the experiments by assuming a minimum R^2 value of 0.995 (99.5%). This value was selected by visual inspection of the curve's shape. It was observed that, at the timestamp when the R^2 value exceeded 99.5%, Stage 5 (Stable sieving stage) had already ended and the graph had entered Stage 6 (Reduced performance sieving stage), see *Figure 5.6*. Hence, this value was selected by trial-and-error, in order to consistently locate the ending of the stable sieving stage as accurately as possible. However, whether a large or small mass flow is desired depends on the application.

In the case of multi-material deposition, where, for each layer, there are multiple sieving procedures to be performed (please refer to *Chapter 6* for more details), it is imperative that mass flow during linearity is maximized, in order for the process to be as time-efficient as possible. However, in the case where sieving is used to spread powder evenly, and create layers that are PBF-ready without the use of a recoater, it is of more use for the powder sieving to be performed slowly, in a controlled and homogeneous manner, with tolerably low mass flow rates.

Furthermore, when sieving gets past the stable phase and into Stage 6 and even Stage 7, the mass flow of the powder that passes through the sieve drastically decreases, while the average size of the deposited particles increases. This means that, at the lowest areas of the layer the smallest and medium-sized particles are located, while at the top areas of the layer the large particles become more and more, as proven by *Figure 5.7*. This shows the average height of the centre of the particles in the sieving-produced layer for different particle diameter classes. The larger the particles, the higher their position in the layer, both by particle's centre and particle's bottom evaluation.

This creates problems in all cases, since, if the layer is to be subsequently flattened by a recoating mechanism, the large particles that rest at the top of the layer will be dragged along it, reaching high kinetic energy status due to their direct contact with the recoater, leading to surficial defects. If the created layer by the sieving is to be immediately fused by a laser beam, then the large particles resting at the top will cause surficial defects of the sintered/melted part and can even create large-sized spatter in the case of SLM. "The larger the particles, the higher likelihood to partially melt and adhere to particles

near the part border thus causing a higher surface roughness of the finished part" (Ali et. al, 2019) [221]. Hence, maintaining a constant powder mass flow throughout the sieving process will ensure that the particle size distribution will be as even as possible with regard to the layer height, which will lead to high quality finished parts with homogeneous density and mechanical properties.

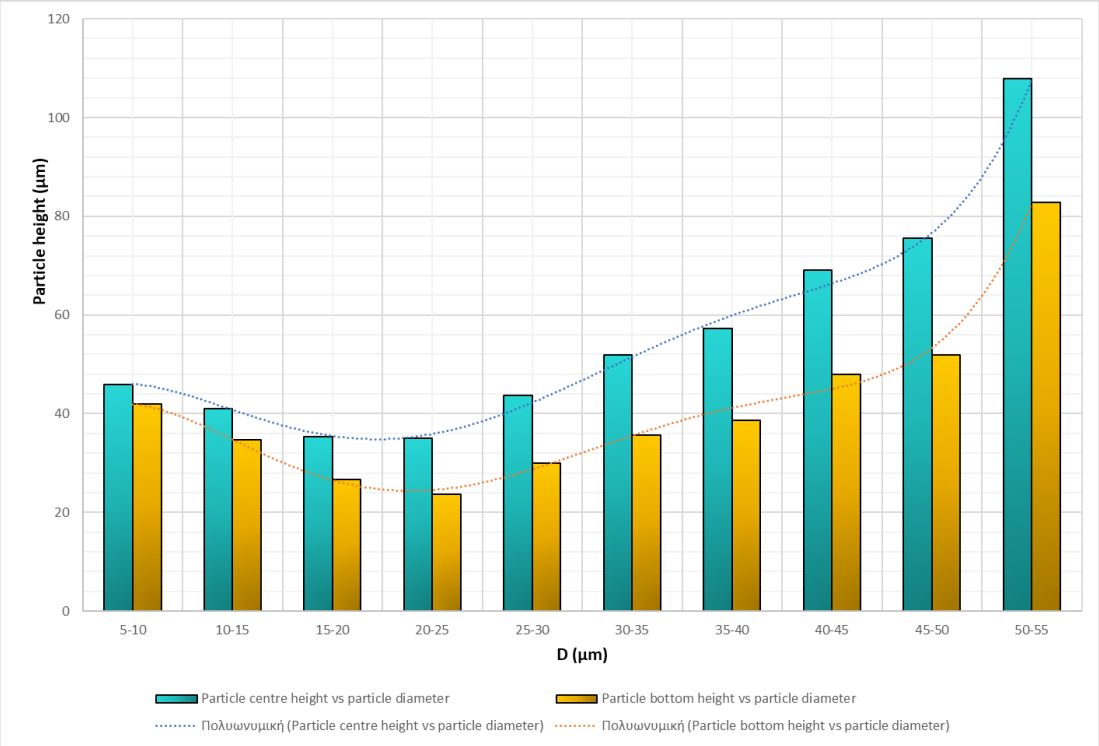

Figure 5.7: Particle position's height vs particle diameter in sieved layer; The plot refers to Trial #1 from the sieving Taguchi DoE.

5.2.2 Total Powder Mass Sieved During Linearity m (mg)

It is important to ensure that, for the layer that needs to be deposited, a sufficient amount of powder has been sieved onto the surface. In order to do this, it is necessary to maximize the mass of powder that passes through the sieve during its stable phase, i.e., during the linear mass flow stage compared to the other phases. In the case where a recoater will flatten out the surface after the sieving finishes, this amount of powder needs to be larger with regard to the powder amount that will constitute the finished layer, since the scraping of the top of the layer unavoidably expels some material from the surface.

5.2.3 In-Sieve Linearity End Size Ratio LESR (D_{90}/A.S.)

It is imperative to identify when the sieve needs to be emptied and refilled, or when it is needed to top it up with raw powder without emptying it. In order to do this, "linearity end size ratio" is introduced. The linearity end size ratio (LESR) indicates the ratio of the D_{90} of the particles that remain in the sieve at the moment when linearity ends, divided by the aperture size of the sieve ducts, see *Equation (5.1)*. D_{90} is selected since it gives an estimation of the average diameter of the coarse particles, rather than D_{10} and D_{50} which correspond to the average diameter of fine and the average particle size of the sample respectively. The flow rate depends on the percentage of the coarse particles within the sample, justifying this selection. D_{90} is divided by the aperture size in order to provide a normalized parameter.

$$LESR = \frac{D_{90\ (in-sieve,at\ lin.end)}}{A.S.} \qquad (5.1)$$

LESR connects the particle size distribution of the particles in-sieve to the moment when the sieving's linear behaviour ends. Hence, LESR is an indication of the degree of the achieved segregation of the powder sample at the end of the linear sieving stage. It is useful to identify how the sieving parameters interact with this quantity, in order to identify when it is necessary to refill or empty the sieve. Evaluating this leads to powder economy, since, at higher LESR values (close to, or even larger than 1) the vast majority of the particles that remain in-sieve at linearity-end are the ones that physically cannot pass through the apertures of the sieve, so the remaining powder can be disposed of and the sieve can be refilled with a new powder batch.

Note that refilling the sieve at linearity-stop moment without emptying the remaining powder might have negligible effect on powder kinematics if it is done a few times, but it can vastly alter the initial particle size distribution when done multiple times, as the large particles from each refilling batch add up, moving the distribution to the right side. It is strongly suggested that the remaining powder is emptied after every sieving, or, for time efficiency, at least after depositing each layer completely (in multi-material deposition).

5.2.4 Sieving Linearity Duration t_{lin} (sec)

As mentioned earlier, depending on the nature of the process, it is important to define the duration of the linear phase of sieving, since, in some cases a longer linear phase with smaller mass flow is preferable, and in others a shorter linear phase with larger mass flow is the way to go.

However, this criterion is directly connected to the first two criteria (mass flow Q and total mass m), since, in linearity, *Equation (5.2)* applies:

$$Q = \frac{m}{t_{lin}} \qquad (5.2)$$

meaning that it is only necessary to examine two out of these three parameters to adequately define the sieving process and its behaviour during its linear, stable phase.

5.3 Taguchi Design for Sieving

Four process variables are being examined, namely:

1. *Vibrational frequency of the sieve* at the vertical direction, f_{vib} *(Hz)*. This variable was examined in three levels:
   a) 200 Hz
   b) 350 Hz
   c) 500 Hz

   These frequencies were selected to be much lower compared to ultrasound sieving, since, at very high frequencies the continuous offering of very high energy values to the powder leads to an excessive fugacity of the particles, which form a "micro-suspended" state on the sieve [222]. In order to examine this, a very large domain in combination with sealed sieves would be necessary, to prevent the particles from escaping the sieve. The levels selected are quite easily achieved by mechanical means. The minimum level (200 Hz) was selected after preliminary simulations showed that frequencies below 150 Hz were unable to facilitate the necessary stirring of the powder to perform the sieving. In these cases, the sieve would oscillate vertically and carry the powder along with it, leaving the particles motionless with regard to the sieve.

2. *Vibrational amplitude of the sieve*, A_{vib} *(μm)*. This variable was examined in three levels:
   a) 20 μm
   b) 35 μm
   c) 50 μm

   These values were selected by preliminary trials. It was demonstrated that amplitudes smaller than 10 μm were unable to facilitate the necessary stirring of the powder, while amplitudes larger than 70 μm would cause the powder to escape the 2 mm high sieve, hence leaving the domain of the simulation. These limits must be checked prior to simulations for different powder materials and particle size distributions, since the cohesive forces will be affected and different excitation levels will be necessary to induce stirring.

3. *Sieve ducts' taper angle*, θ_{tap} *(degrees)*. This variable was examined in three levels:
   a) 1^o
   b) 4^o
   c) 7^o

   The sieve is open at the top, rectangular, with square apertures. The side of the sieve is 1 mm and its height is 2 mm (referring to sieve interior dimensions-sieve volume capacity is 2 mm^3). The thickness of the sieve is 100 μm and kept constant for all the simulations. However, the ducts are shaped as inverted tapers, meaning that the aperture diverges (i.e., aperture area increases) while moving downwards (see *Figure 5.8*). This variable aims to examine whether the adhesive forces and the clogging of the ducts by powder particles differ with various taper values. The values chosen were in agreement with industrial manufacturing standards [223].

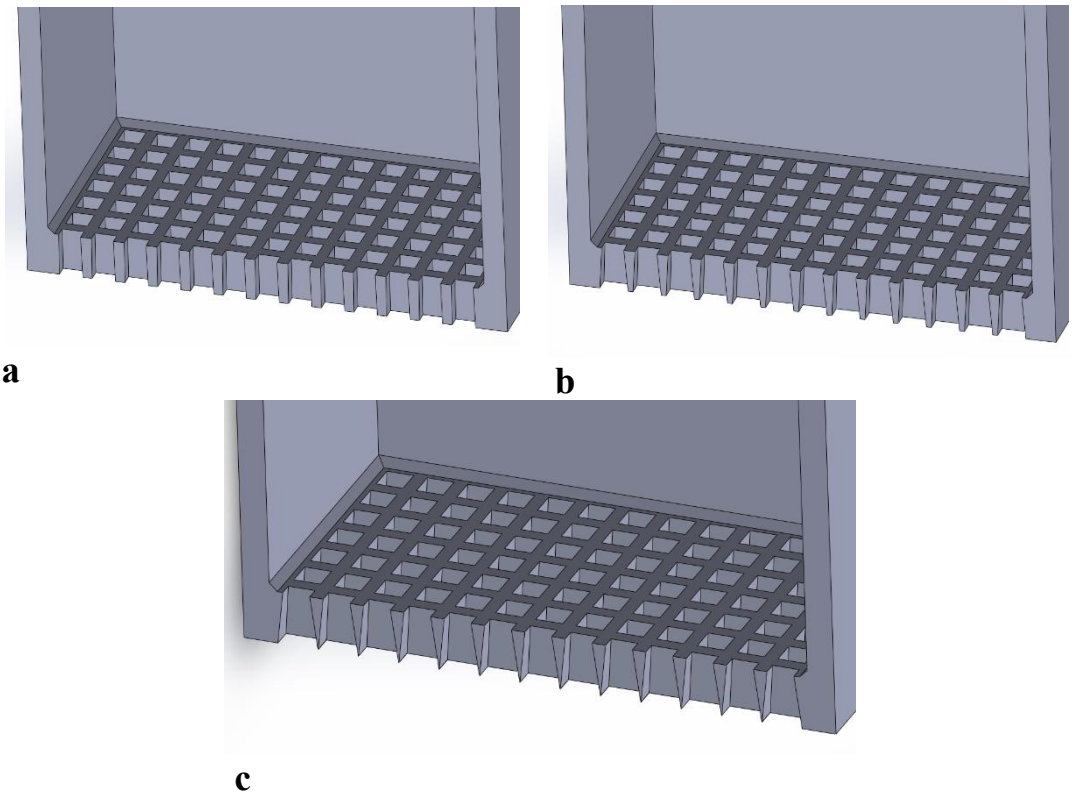

Figure 5.8: Section cut view of the square-aperture sieves with different taper angle ***(a)*** 1°; ***(b)*** 4°; ***(c)*** 7°.

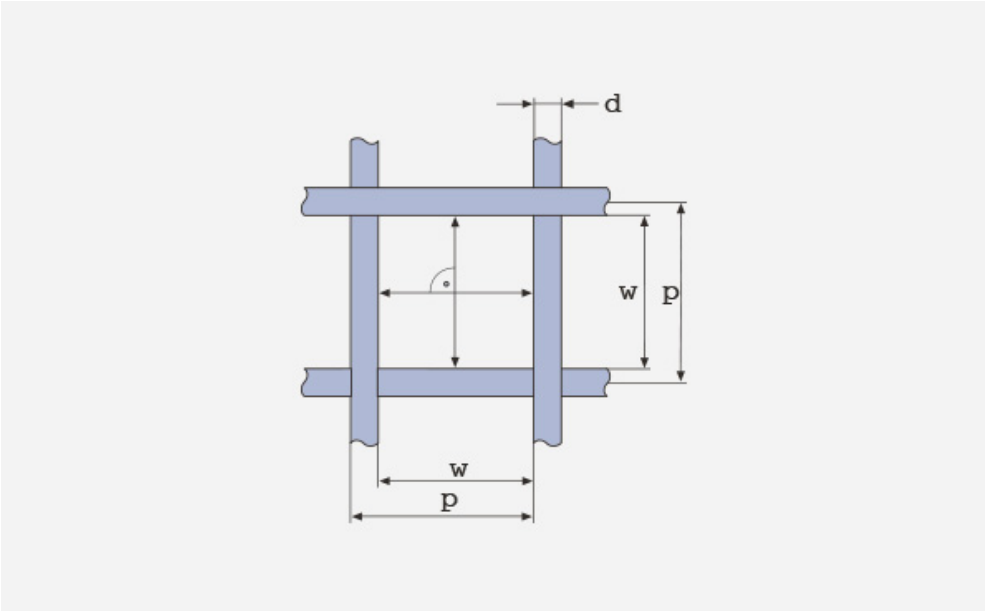

Figure 5.9: Square-aperture mesh geometry; d-wire diameter or aperture distance; w-aperture width; p-mesh pitch.

To be more specific, the sieving plate is designed by the process of electroforming a thin, 100 μm-thick metal sheet to create inverted taper-shaped apertures throughout the sheet. The geometry of the square mesh is described in

Figure 5.9. The figure refers to woven wire mesh, but the same terminology and definitions apply to a sheet form mesh as well [224]. The sieve used in the simulations is designed to be a 325 mesh (325 lines/inch) with an aperture width of 50 μm (w=50 μm) and a mesh pitch of 78.2 μm (p=78.2 μm). This means that the distance between two consecutive apertures is equal to d=p-w⇒ d=28.2 μm. The calculations are in accordance with the specifications provided in [223], as can be seen in *Table 5.1*.

There is also the possibility of having hexagonal (honeycomb) or circular (round) apertures. Possible differences in their behaviour will be examined with regard to the Taguchi-defined optimum levels for the square-aperture sieve, for economy in computation time since sieving simulations are costly.

Table 5.1: Mesh specs of the selected square-aperture sieve.

Lines (Line/inch)	Mesh pitch (μm)	Maximum sheet size (mm)	Aperture accuracy guaranteed area		Min. to Max. aperture size (μm)
325	78.2	380	±2	≤Φ180	8-62
			±4	≤Φ300	

4. *Box factory height*, h_{bf} *(mm)*. This variable was examined in three levels:
   a) 0.5 mm
   b) 1.0 mm
   c) 1.5 mm

   This variable determines the amount of the powder that fills the sieve at the beginning of the simulation. As more and more powder particles are stacked into the sieve, the height of the powder stack increases. This means that more particles are stacked onto the ones that are positioned right above the ducts, transferring their weight onto them. Hence, a stronger vibrational excitation will be necessary to facilitate the stirring of the powder that is needed for the sieving to be performed. This variable aims to examine how much powder can be fed into the sieve before the stacked weight of the powder particles prevent the sieving from being performed in an acceptably consistent and fast manner. These levels were selected to be in agreement with the selected sieve height (2 mm) corresponding to the 25%, 50% and 75% of the height of the sieve.

5.4 Taguchi DoE Results

Table 5.2 presents the L27 Taguchi orthogonal array for the powder sieving process and the results concerning the four defined criteria. The results are also presented in *Figure 5.10* and *Figure 5.11*.

***Table 5.2*:** L27 Taguchi DoE orthogonal array for powder sieving including results.

TRIAL #	F_{vib} (Hz)	A_{vib} (μm)	θ_{tap} (deg.)	h_{bf} (mm)	Q (mg/sec)	m (mg)	LESR	t_{lin} (sec)
1	**200**	**20**	**1**	**0.5**	1.141	0.183	1.190	0.171
2	**200**	**20**	**4**	**1.0**	0.888	0.238	0.886	0.271
3	**200**	**20**	**7**	**1.5**	0.900	0.218	0.760	0.243
4	**200**	**35**	**1**	**1.0**	0.844	0.429	1.243	0.523
5	**200**	**35**	**4**	**1.5**	0.737	0.659	1.298	0.923
6	**200**	**35**	**7**	**0.5**	1.082	0.152	1.056	0.145
7	**200**	**50**	**1**	**1.5**	0.576	0.296	0.829	0.501
8	**200**	**50**	**4**	**0.5**	0.750	0.110	0.915	0.147
9	**200**	**50**	**7**	**1.0**	0.673	0.341	1.112	0.523
10	**350**	**20**	**1**	**1.0**	0.771	0.427	1.242	0.578
11	**350**	**20**	**4**	**1.5**	0.584	0.664	1.331	1.183
12	**350**	**20**	**7**	**0.5**	1.075	0.146	1.041	0.140
13	**350**	**35**	**1**	**1.5**	0.404	0.566	1.179	1.388
14	**350**	**35**	**4**	**0.5**	0.594	0.102	0.932	0.176
15	**350**	**35**	**7**	**1.0**	0.536	0.334	1.111	0.640
16	**350**	**50**	**1**	**0.5**	0.372	0.083	0.914	0.233
17	**350**	**50**	**4**	**1.0**	0.334	0.269	1.039	0.811
18	**350**	**50**	**7**	**1.5**	0.307	0.462	1.072	1.525
19	**500**	**20**	**1**	**1.5**	0.408	0.648	1.304	1.622
20	**500**	**20**	**4**	**0.5**	0.983	0.111	0.910	0.115
21	**500**	**20**	**7**	**1.0**	0.696	0.359	1.140	0.535
22	**500**	**35**	**1**	**0.5**	0.496	0.076	0.880	0.159
23	**500**	**35**	**4**	**1.0**	0.421	0.282	1.051	0.681
24	**500**	**35**	**7**	**1.5**	0.338	0.522	1.128	1.523
25	**500**	**50**	**1**	**1.0**	0.278	0.265	0.991	0.969
26	**500**	**50**	**4**	**1.5**	0.239	0.452	1.042	2.025
27	**500**	**50**	**7**	**0.5**	0.347	0.065	0.847	0.205

Judging by *Figure 5.10*, initially it becomes obvious that, the total mass of powder that passes through the sieve during the stable phase increases with an increase in the box factory height. The effect of the other three variables is negligible compared to h_{bf}. It seems that the optimum is to have a small taper angle and a medium frequency and amplitude as vibration settings. However, in terms of mass flow, the fastest sieving process is performed by implementing low vibrational frequency and amplitude, a large

taper angle and the minimum box factory height level. This proves that, the fuller the sieve gets, the more the sieving process gets slowed down, since the stacked-up weight of the powder particles prevents the adequate vibrational stirring. The combination of the two aforementioned observations comes in agreement with the plot for the time duration of the linear stage of sieving. Indeed, the larger the vibrational frequency and amplitude and the larger the box factory height, the longer the duration of the linear stage of sieving. Hence, in order to make it a time-efficient process, low frequencies and amplitudes must be selected and the sieve should be filled with the smallest amount of powder possible, while, if a smooth, long-lasting sieving process is desired, the sieve should be filled with plenty of powder and high frequency and amplitude levels should be chosen. Finally, LESR attains maximum value for medium frequency and amplitude levels, small taper angle and high box factory height levels.

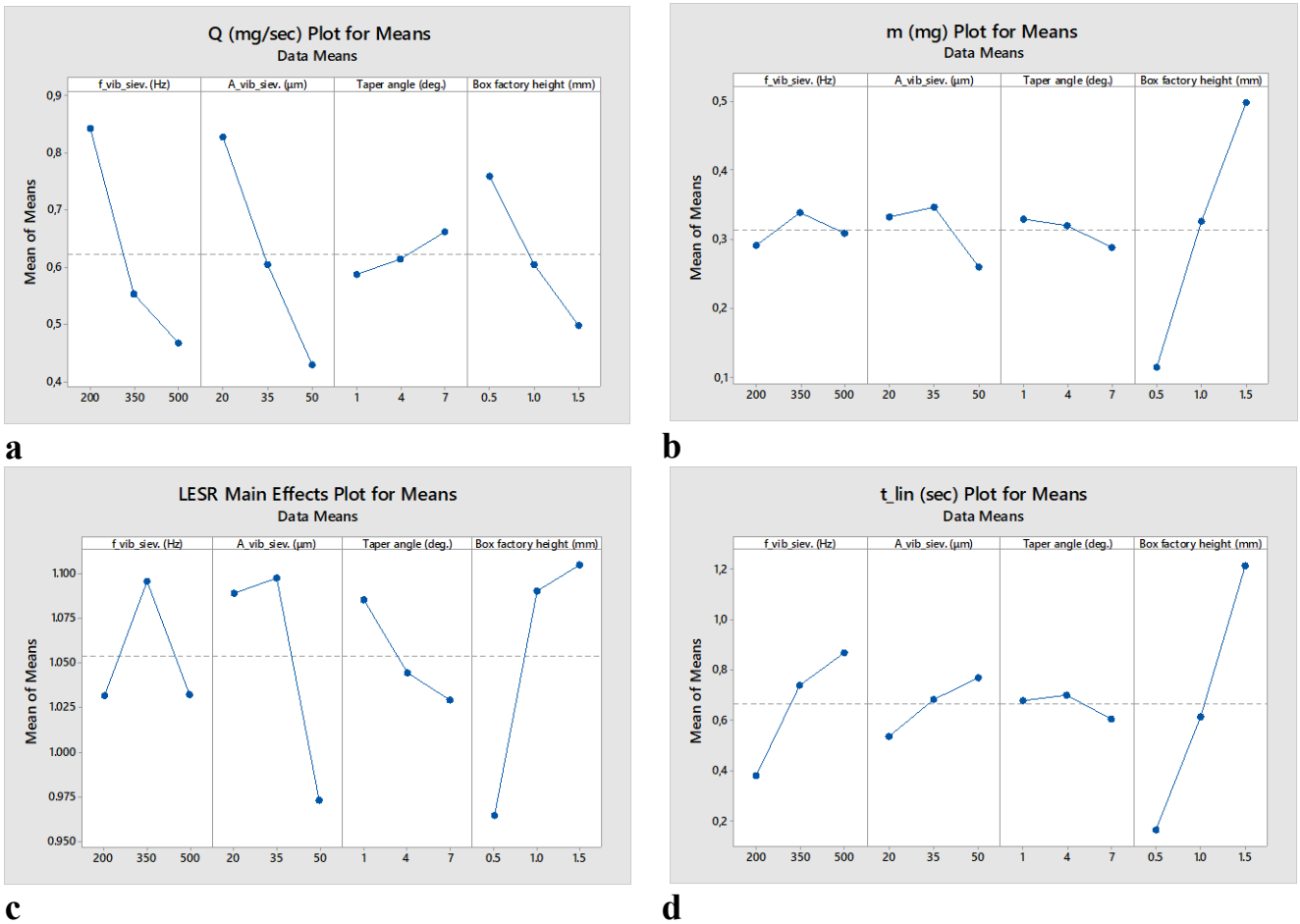

***Figure 5.10*:** Means plots of the four quality criteria of the powder sieving Taguchi analysis.

The higher the LESR value at the end of linearity, the higher powder economy is achieved, since it is strongly suggested that the sieve gets emptied and refilled at the end of each sieving pass, in order for a uniform particle size distribution to be achieved in the deposited layer(s) and/or sublayers. A smaller taper angle could mean that the adhesive forces are stronger in the ducts, since the particles are closer to the duct wall throughout their travel from the top to the bottom of the aperture. This would promote faster clogging of the ducts, leading to the ending of the linearity phase and to a slower, non-linear sieving rate.

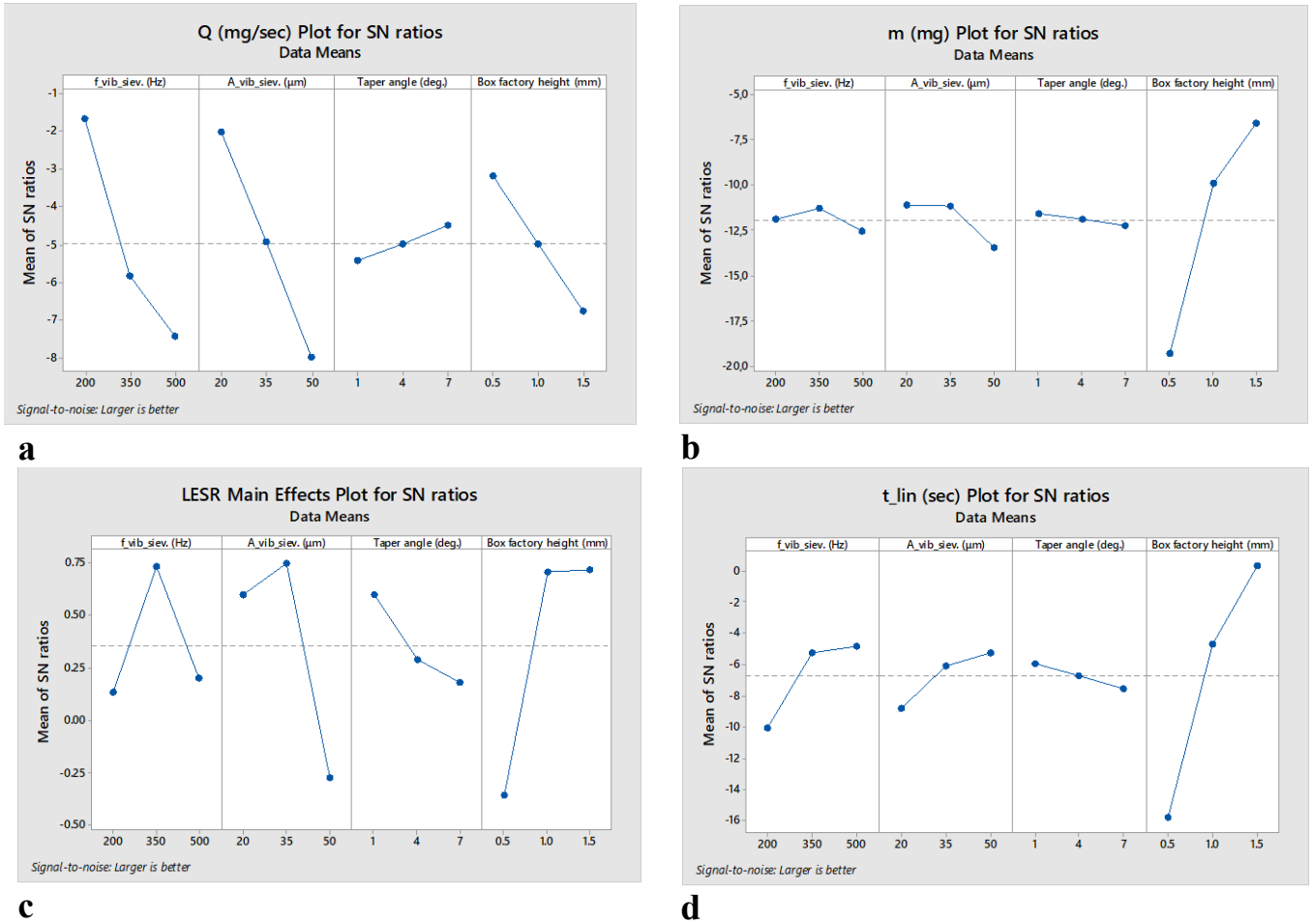

***Figure 5.11*:** Signal-to-noise ratio plots of the four quality criteria of the powder sieving Taguchi analysis.

5.4.1 Total Mass in Linearity (m) Results

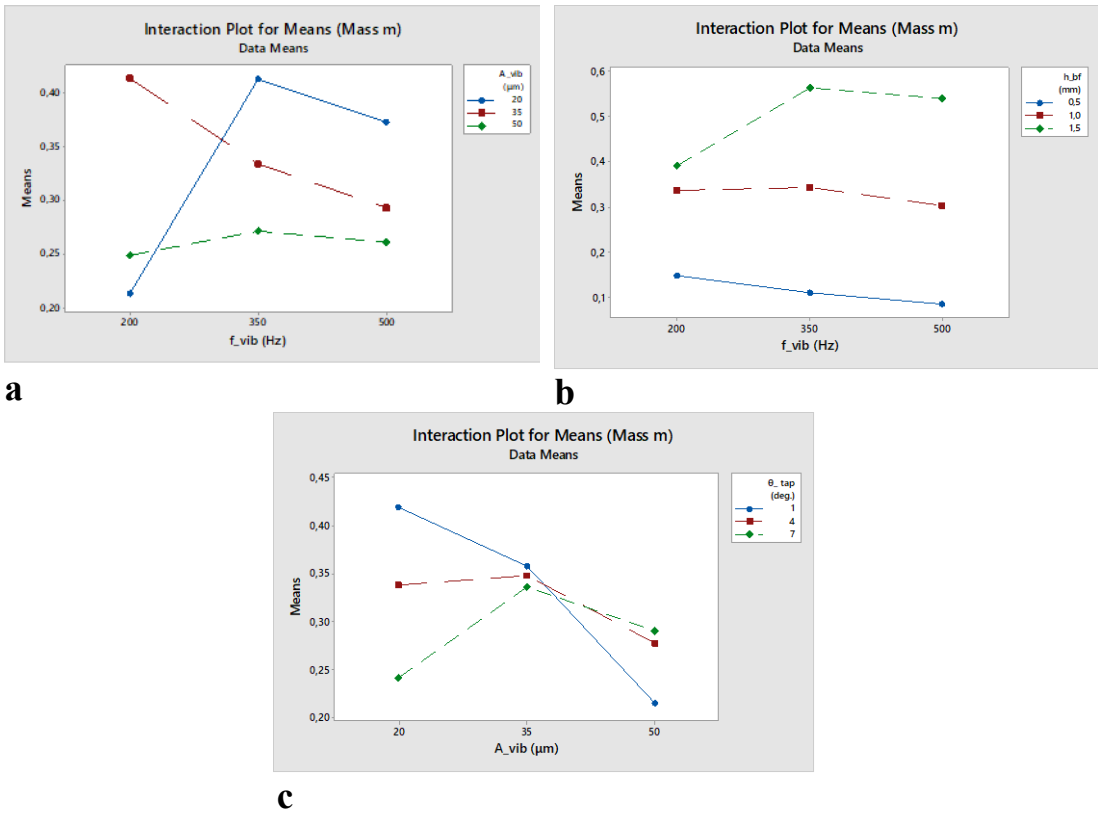

***Figure 5.12*:** Interaction plots for means of the total sieved mass during the linear sieving stage.

As seen in *Figure 5.12*, the box factory height and vibrating frequency feature relatively parallel lines, meaning that there is small interaction between them. However, this is not the case for the other two interactions. The frequency-amplitude interaction graph shows that, at the smallest frequency level, both high and small amplitude levels have similar, relatively bad, results. However, a medium amplitude level corresponds to vastly improved results, indicating that a resonance frequency is being approached. However, for medium and high frequency levels, the lowest amplitude gives the best results. Furthermore, when it comes to the amplitude-taper angle interaction, even for low amplitudes, the smaller the taper angle, the better the results, this trend is completely reversed for larger amplitude levels. This potentially derives from the fact that high amplitudes lead to higher reverse bouncing of the particles that are already positioned inside the ducts during the downwards motion of the sieve's oscillation. This leads to more intense clogging phenomena in the narrower ducts, while the wider ones can easily get unclogged during the upwards motion of the sieve.

Table 5.3 shows that the box factory height dominates the response of mass sieved in linearity, at 72.09%. Interestingly, the interactions contribute more than the other factors do on themselves.

Table 5.3: Analysis of Variance (ANOVA) for total mass sieved in linearity.

Source	DF	Seq SS	Contribution	Adj SS	Adj MS	F-Value	P-Value
Regression	7	0.779953	84.58%	0.779953	0.111422	14.89	0.000
f_{vib} (Hz)	1	0.001318	0.14%	0.000243	0.000243	0.03	0.859
A_{vib} (µm)	1	0.023544	2.55%	0.000646	0.000646	0.09	0.772
θ_{tap} (deg.)	1	0.007771	0.84%	0.038923	0.038923	5.20	0.034
h_{bf} (mm)	1	0.664705	72.09%	0.017935	0.017935	2.40	0.138
f_{vib} (Hz) *A_{vib} (µm)	1	0.016428	1.78%	0.016428	0.016428	2.20	0.155
f_{vib} (Hz) *h_{bf} (mm)	1	0.034347	3.72%	0.018180	0.018180	2.43	0.136
A_{vib} (µm) *θ_{tap} (deg.)	1	0.031840	3.45%	0.031840	0.031840	4.26	0.053
Error	19	0.142149	15.42%	0.142149	0.007482		
Total	26	0.922102	100.00%				

Equation (5.3) shows the regression of the total mass sieved in linearity.

$$\begin{aligned} m = {} & 0.173 + 0.000097 f_{vib} - 0.00138 A_{vib} - 0.0483 \theta_{tap} + 0.197 h_{bf} \\ & - 0.000016 f_{vib} A_{vib} + 0.000536 f_{vib} h_{bf} \\ & + 0.001182 A_{vib} \theta_{tap} \end{aligned} \qquad (5.3)$$

The optimum level combination maximizing the mass sieved in linearity is as follows:

$$\begin{Bmatrix} f_{vib} = 500\ Hz \\ A_{vib} = 20\ \mu m \\ \theta_{tap} = 1^{o} \\ h_{bf} = 1.5\ mm \end{Bmatrix}$$

which, according to *Equation (5.3)*, gives the optimum sieved mass amount as

$$m_{opt} = 0.701\ mg$$

After running a cross-checking simulation with the optimum parameter levels, validation of the expected sieved mass amount was achieved, the value being

$$m_{opt,sim} = 0.648\ mg$$

having a (-) 7.6% deviation from the expected value of 0.701 mg, which is less than the error of the regression equation, as calculated by ANOVA (15.42%).

Note in *Table 5.2* that trials #5 and #11 show a higher mass value than the estimated optimum one (i.e., 0.659 and 0.664 mg respectively). This happens because of the error

of the regression. However, since the deviation between these values is less than 2.5%, it is safe to keep the calculated by the regression optimum parameter level.

5.4.2 Linearity Mass Flow Rate (Q) Results

Table 5.4 shows that the vibration frequency and amplitude have a high impact on the flow rate, with a 33.49% and 37.25% contribution respectively. The box factory height follows, at 16.10%. There is a strong influence of the interaction between amplitude and box factory height, at 4.04%.

***Table 5.4*:** Analysis of Variance (ANOVA) for the mass flow during linearity.

Source	DF	Seq SS	Contribution	Adj SS	Adj MS	F-Value	P-Value
Regression	7	176.532	92.86%	176.532	0.252189	35.32	0.000
f_{vib} (Hz)	1	0.63657	33.49%	0.03887	0.038869	5.44	0.031
A_{vib} (µm)	1	0.70805	37.25%	0.11374	0.113745	15.93	0.001
θ_{tap} (deg.)	1	0.02449	1.29%	0.01715	0.017145	2.40	0.138
h_{bf} (mm)	1	0.30602	16.10%	0.12230	0.122304	17.13	0.001
f_{vib} (Hz) *A_{vib} (µm)	1	0.00715	0.38%	0.00386	0.003864	0.54	0.471
A_{vib} (µm) *h_{bf} (mm)	1	0.07680	4.04%	0.07680	0.076800	10.75	0.004
θ_{tap} (deg.) * h_{bf} (mm)	1	0.00623	0.33%	0.00623	0.006230	0.87	0.362
Error	19	0.13568	7.14%	0.13568	0.007141		
Total	26	190.100	100.00%				

Equation (5.4) shows the regression of the mass flow of the linear sieving stage.

$$Q = 1.944 - 0.000965 f_{vib} - 0.02101 A_{vib} + 0.028 \theta_{tap} - 0.571 h_{bf} - 0.000008 f_{vib} A_{vib} + 0.01067 A_{vib} h_{bf} - 0.0157 \theta_{tap} h_{bf} \quad (5.4)$$

The optimum level combination maximizing mass flow of the linear stage is as follows:

$$\begin{Bmatrix} f_{vib} = 200\ Hz \\ A_{vib} = 20\ \mu m \\ \theta_{tap} = 7^{o} \\ h_{bf} = 0.5\ mm \end{Bmatrix}$$

which, according to the *Equation (5.4)*, gives the optimum mass flow of

$$Q_{opt} = 1.261\ mg/sec$$

After running a cross-checking simulation with the optimum parameter levels, validation of the expected mass flow was achieved, the value being:

$$Q_{opt,sim} = 1.181\ mg/sec$$

having a (-) 6.3% deviation from the expected value of 1.164 mg/sec, which is less than the error of the regression equation calculated by ANOVA (7.14%).

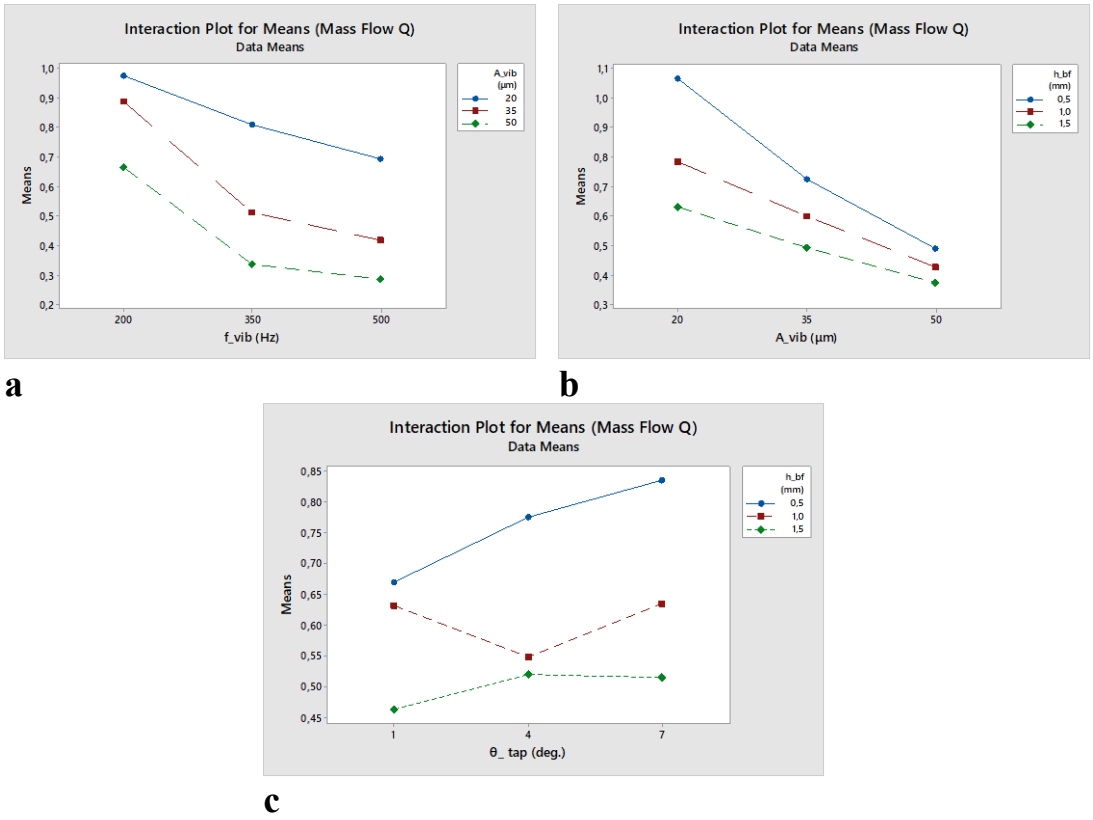

***Figure 5.13*:** Interaction plots for means of the mass flow during linear sieving stage.

The interactions plot for the mass flow, see *Figure 5.13*, shows that there is minimal interaction between the parameters, since the lines are relatively parallel in all three graphs.

5.4.3 Linearity Duration (t_{lin}) Results

Table 5.5 shows that the box factory height (primarily) and the vibration frequency (secondarily) have a high impact on the duration of sieving linearity, with 62.75% and 13.55% contribution respectively. Their interaction also demonstrates a high influence, at 12.84%. The contribution of the other parameters and interactions is insignificant, so it is safe to state that the frequency and the amount of raw powder fed into the sieve are the factors that largely determine the duration linear sieving phase.

Equation (5.5) shows the regression of the time duration of the linear stage.

$$t = 0.707 - 0.001914 f_{vib} - 0.01061 A_{vib} - 0.0905 \theta_{tap} - 0.518 h_{bf} + 0.003539 f_{vib} h_{bf} + 0.002235 A_{vib} \theta_{tap} + 0.00938 A_{vib} h_{bf} \quad (5.5)$$

***Table 5.5*:** Analysis of Variance (ANOVA) for the total duration of linear sieving stage.

Source	DF	Seq SS	Contribution	Adj SS	Adj MS	F-Value	P-Value
Regression	7	747.360	94.69%	747.360	106.766	48.40	0.000
f_{vib} (Hz)	1	106.921	13.55%	0.20059	0.20059	9.09	0.007
A_{vib} (μm)	1	0.24059	3.05%	0.04630	0.04630	2.10	0.164
θ_{tap} (deg.)	1	0.02457	0.31%	0.13670	0.13670	6.20	0.022
h_{bf} (mm)	1	495.285	62.75%	0.06750	0.06750	3.06	0.096
f_{vib} (Hz) *h_{bf} (mm)	1	101.326	12.84%	0.79268	0.79268	35.93	0.000
A_{vib} (μm) *θ_{tap} (deg.)	1	0.11375	1.44%	0.11375	0.11375	5.16	0.035
A_{vib} (μm) *h_{bf} (mm)	1	0.05936	0.75%	0.05936	0.05936	2.69	0.117
Error	19	0.41913	5.31%	0.41913	0.02206		
Total	26	789.272	100.00%				

The level combination that maximizes the duration of linearity is as follows:

$$\begin{Bmatrix} f_{vib} = 500\ Hz \\ A_{vib} = 50\ \mu m \\ \theta_{tap} = 7^o \\ h_{bf} = 1.5\ mm \end{Bmatrix}$$

which, according to *Equation (5.5)*, gives the maximum steady sieving duration of

$$t_{max} = 1.948\ sec$$

After running a cross-checking simulation with the previous parameter levels, validation of the expected maximum linearity duration was achieved, the value being:

$$t_{max,sim} = 1.905\ sec$$

having a (-) 2.2% deviation from the expected value of 1.948 sec, which is smaller than the error of the regression equation calculated by ANOVA (5.31%).

Again, there is a trial, namely #26 that has a larger linearity duration, at 2.025 sec. However, this deviation (+4%) is smaller than the regression's error, so it can be safely assumed that the correct parameter combination has been selected. These deviations show that there are more parameters that possibly affect the sieving time that have not been taken into consideration, however the deviation from the expected error is reasonably small to make it acceptable.

It can be noted that, based on the interaction plots in *Figure 5.14*, the amplitude and the amount of powder fed into the sieve do not seem to have any significant interaction,

while, on the contrary, amplitude and taper angle interaction seems to be more important as the lines intersect each other on the interaction plot.

Finally, as the vibrating frequency increases, the more powder is fed into the sieve, the longer the steady phase will last. If the minimum level of powder is fed into the sieve, the steady phase will last approximately the same regardless of the frequency variation, while, at medium and high box factory height levels, the linearity duration increases with the increase in frequency, the slope increasing as the initial raw powder amount is increased.

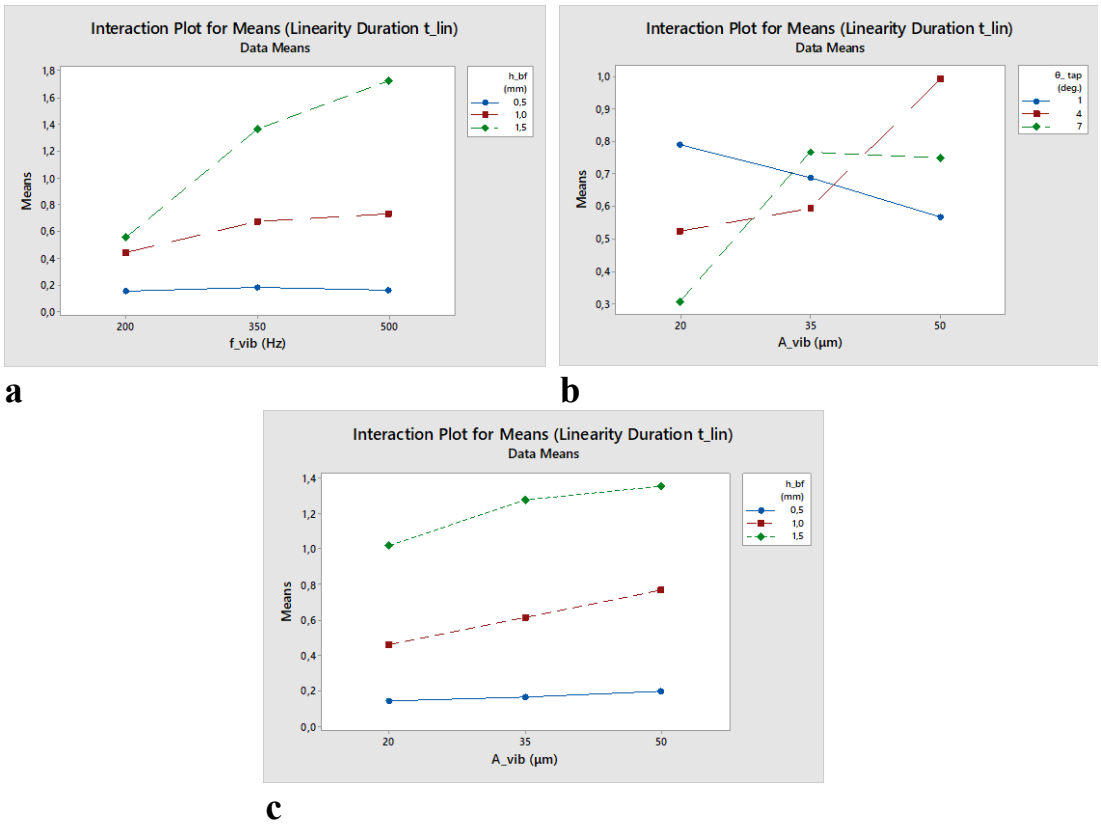

***Figure 5.14*:** Interaction plots for means of the duration of the linear sieving stage.

5.4.4 LESR Results

Finally, no safe conclusions can be extracted by the ANOVA regarding the LESR parameter, since the minimum error of the regression is equal to 46.25%. This clearly indicates that the process is more complex and more variables that are not considered here play a role on the response of this quality criterion. The results can be seen in *Table 5.6*.

***Table 5.6*:** Analysis of Variance for the LESR parameter at the end of the linearity stage.

Source	DF	Seq SS	Contribution	Adj SS	Adj MS	F-Value	P-Value
Regression	7	0.344655	53.75%	0.344655	0.049236	3.15	0.022
f_{vib} (Hz)	1	0.000001	0.00%	0.003211	0.003211	0.21	0.655
A_{vib} (µm)	1	0.060436	9.43%	0.00511	0.00511	0.33	0.574
θ_{tap} (deg.)	1	0.014168	2.21%	0.071888	0.071888	4.61	0.045
h_{bf} (mm)	1	0.08792	13.71%	0.020017	0.020017	1.28	0.272
f_{vib} (Hz) *A_{vib} (µm)	1	0.020336	3.17%	0.020336	0.020336	1.3	0.268
f_{vib} (Hz) *h_{bf} (mm)	1	0.10286	16.04%	0.062422	0.062422	4	0.06
A_{vib} (µm) *θ_{tap} (deg.)	1	0.058934	9.19%	0.058934	0.058934	3.78	0.067
Error	19	0.296567	46.25%	0.296567	0.015609		
Total	26	0.641223	100.00%				

However, the interaction plots for the LESR parameters provide some interesting insight. Given that the higher the LESR value, the more complete segregation of the power sample is achieved, it is observed that, higher initial powder level in the sieve demands higher sieving frequency, see *Figure 5.15a*. The lowest powder level achieves very low segregation at high frequencies and the LESR value increases at lower frequencies.

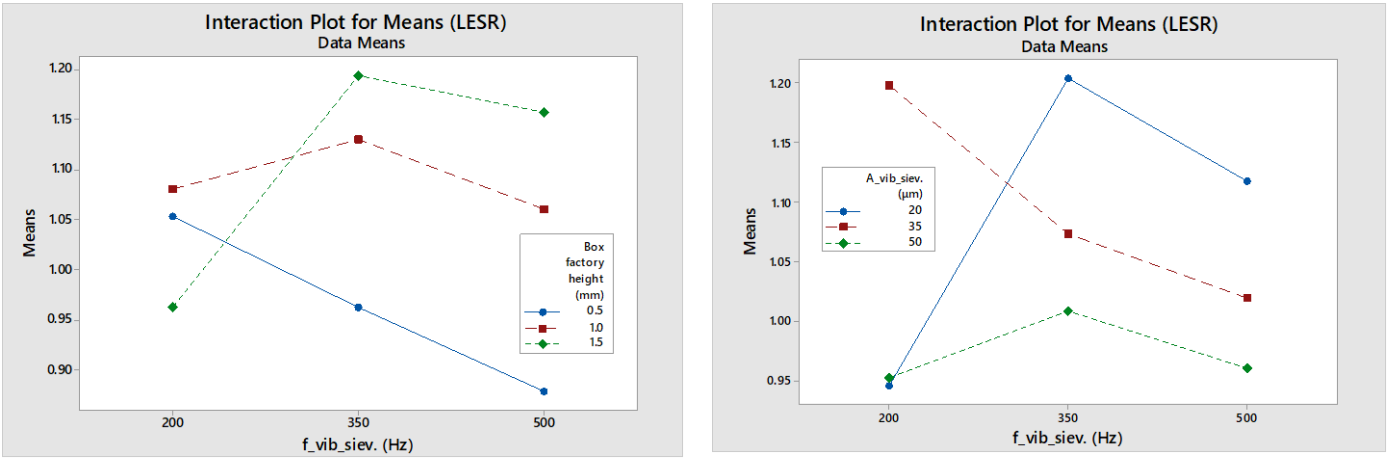

a **b**

Figure 5.15*:** LESR interaction graphs: ***(a) f_{vib}-h_{bf}; ***(b)*** f_{vib}- A_{vib}.

The highest powder level achieves poor segregation via the smallest frequency level, the highest via the middle level and an acceptable level at high frequency of vibration. The middle powder level achieves the highest segregation level via middle frequencies, while high and low frequencies have similar results. In addition, high and middle

frequencies function better in terms of the achieved LESR value the lower the vibrating amplitude gets. However, low frequencies only function well in combination with middle levels of amplitude, see *Figure 5.15b*.

Figure 5.10c shows that LESR at the end of linearity stage generally takes values very close to 1, in the range between 0.95 and 1.1.

In the literature it can be noted that dry sieving is possible for powder of average diameters as small as 30 μm [225], [226]. However, as proven in this work, dry sieving can work for smaller particles with minimal aperture blinding, as long as sufficient vibration is provided to counter the adhesive and cohesive forces and break down the agglomerates. Of course, this only applies up to a limit, since particle diameter in the simulations in this work was at minimum 5 μm, and on the average 21 μm, i.e., not a lot smaller compared to the 30 μm limit that is encountered in literature, so the results come in agreement with the technological limitations of the method. It should be taken under consideration, that the vibration frequencies selected were larger compared to the common ones used (200, 350 and 500 Hz instead of the commonly used 10-50 Hz of industrial sifting machines [227]) in order to avoid aperture clogging without drastically increasing the powder fugacity, which happens in ultrasonic frequencies (approx. 36000 Hz) [222].

As mentioned earlier, in the case of sieving as a preparatory step to powder deposition via a recoating mechanism, such as a doctor blade or a counter-rotating roller, it is imperative that the powder amount necessary is sieved as fast as possible to minimize the total manufacturing time. In this case, sieving only functions as a method to prevent agglomerates and large powder particles from being deposited in the layer.

However, it is possible that sieving can function as powder spreading mechanism. In that case, it is imperative that the powder deposition is slow and controllable, since it needs to stop exactly at the right moment, i.e., when the thickness of the layer is the desired one. In this work, we will examine the deposited layer quality for layers produced solely by sieving, and they will be compared in terms of quality to the optimized layers with and without blade vibration that were calculated in the previous chapter.

5.5 Aperture Shape Evaluation

In order to evaluate the impact of the aperture shape (square, hexagonal or circular) on the aforementioned sieving performance criteria, it is decided that, for time economy, the shape effect will only be examined on the three optimum sieving parameter sets, i.e., the one that maximizes mass flow, the one that maximizes sieved mass and the one that maximizes duration of the linear sieving stage.

The ideal sieving sets of parameter levels are the following, see *Table 5.7*.

***Table 5.7*:** Ideal sieving parameter sets based on different quality criteria.

Maximum mass sieved in linearity	Maximum mass flow in linearity	Maximum linearity duration
$(\boldsymbol{\Sigma_1})$: $\begin{cases} \boldsymbol{f_{vib} = 500\ Hz} \\ \boldsymbol{A_{vib} = 20\ \mu m} \\ \boldsymbol{\theta_{tap} = 1^o} \\ \boldsymbol{h_{bf} = 1.5\ mm} \end{cases}$	$(\boldsymbol{\Sigma_2})$: $\begin{cases} \boldsymbol{f_{vib} = 200\ Hz} \\ \boldsymbol{A_{vib} = 20\ \mu m} \\ \boldsymbol{\theta_{tap} = 7^o} \\ \boldsymbol{h_{bf} = 0.5\ mm} \end{cases}$	$(\boldsymbol{\Sigma_3})$: $\begin{cases} \boldsymbol{f_{vib} = 500\ Hz} \\ \boldsymbol{A_{vib} = 50\ \mu m} \\ \boldsymbol{\theta_{tap} = 7^o} \\ \boldsymbol{h_{bf} = 1.5\ mm} \end{cases}$

In order to examine solely the shape effect, the designed (regular) hexagonal aperture (see *Figure 5.16*) has a distance between facing edges equal to the side of the square aperture (50 μm). This leads to a side equal to 28.868 μm. Similarly, the circular aperture's diameter (see *Figure 5.17*) is equal to the side of the square aperture. In this way, it is ensured that all the designed sieves allow particles of the same maximum size to pass through their ducts.

***Table 5.8*:** Active sieving area for different aperture-shaped sieves.

	# of Apertures N_a	Characteristic dimension	Aperture area formula	Aperture area (mm^2)	Total aperture area (mm^2)
Square	169	Side: $a_s = 50\ \mu m$	$A_s = {a_s}^2$	$2.5 \cdot 10^{-3}$	0.4225
Hexagonal	188	Side: $a_h = 28.868\ \mu m$	$A_h = \frac{3\sqrt{3}}{2} {a_h}^2$	$2.17 \cdot 10^{-3}$	0.4080 (-3.4%)
Circular	188	Diameter: $D_c = 50\ \mu m$	$A_c = \pi \left(\frac{D_c}{2}\right)^2$	$1.963 \cdot 10^{-3}$	0.3690 (-12.7%)

An alternative design would be to opt for apertures of different shape, but define their characteristic dimension by ensuring that the apertures maintain a constant surface area.

However, in powder deposition for PBF-ready layers, it is of paramount importance to control the maximum particle diameter, and ensure that it is smaller than the theoretical layer thickness. Hence, the author opted for the aperture design method that provides accurate particle size "filtering".

Additionally, the distance between neighbouring apertures is kept the same regardless of the aperture's shape. A constant inter-aperture distance was selected in order to maintain the same amount of interference between neighbouring apertures among all the different sieve designs. Decreasing the distance would increase the interference by neighbouring apertures and vice versa. This way, the calculated aperture-to-total area ratio is 42.25% for the square aperture sieve, 40.8% for the hexagonal-aperture sieve and 36.9% for the circular-aperture sieve, given that the total surface area of the sieve is equal to 1 mm^2. The details of this calculation can be seen in *Table 5.8*.

Figure 5.16 and *Figure 5.17* show the geometry of the sieves used in the simulations.

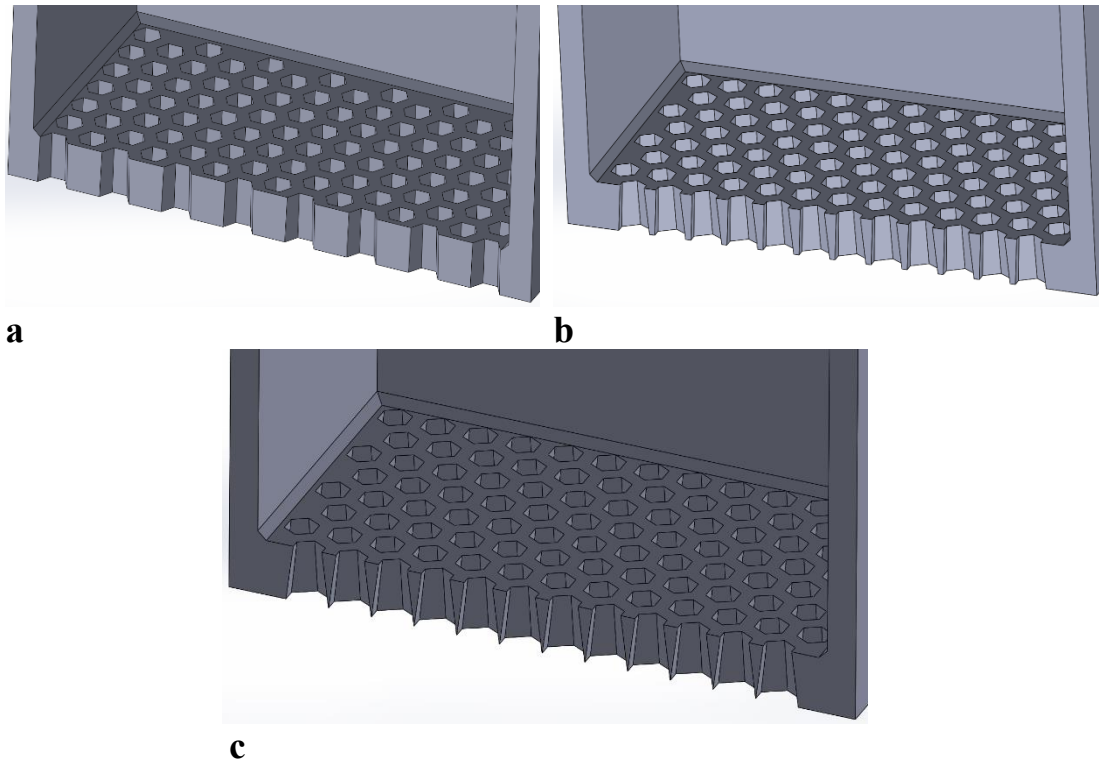

Figure 5.16*:** Section cut view of the hexagonal-aperture sieves. Sieve thickness is 100 μm. Inverted taper angle: ***(a) 1°; ***(b)*** 4°; ***(c)*** 7°.

If a spherical particle of 50 μm diameter would try to pass through the defined apertures, in the case of the square aperture, it would have 4 contact points to it, in the case of the

hexagon the contact points would be 6, while in the case of the circular aperture, the particle would make full contact with the top edge of the aperture.

The more the contact points, the more intense the friction phenomena when the particle attempts to pass through the aperture. Hence, the circular apertures would not allow the larger particles to pass. A particle size distribution of the powder in the deposited layer slightly moved towards the left would be expected as we move from square towards hexagonal and circular aperture sieves. For the same reason, the LESR of the powder inside the sieve at the end of linearity would slightly decrease, as some smaller particles with diameter slightly smaller than 50 μm will find it tougher to pass through the hexagonal and circular apertures. The mass sieved and the mass flow are expected to decrease as well.

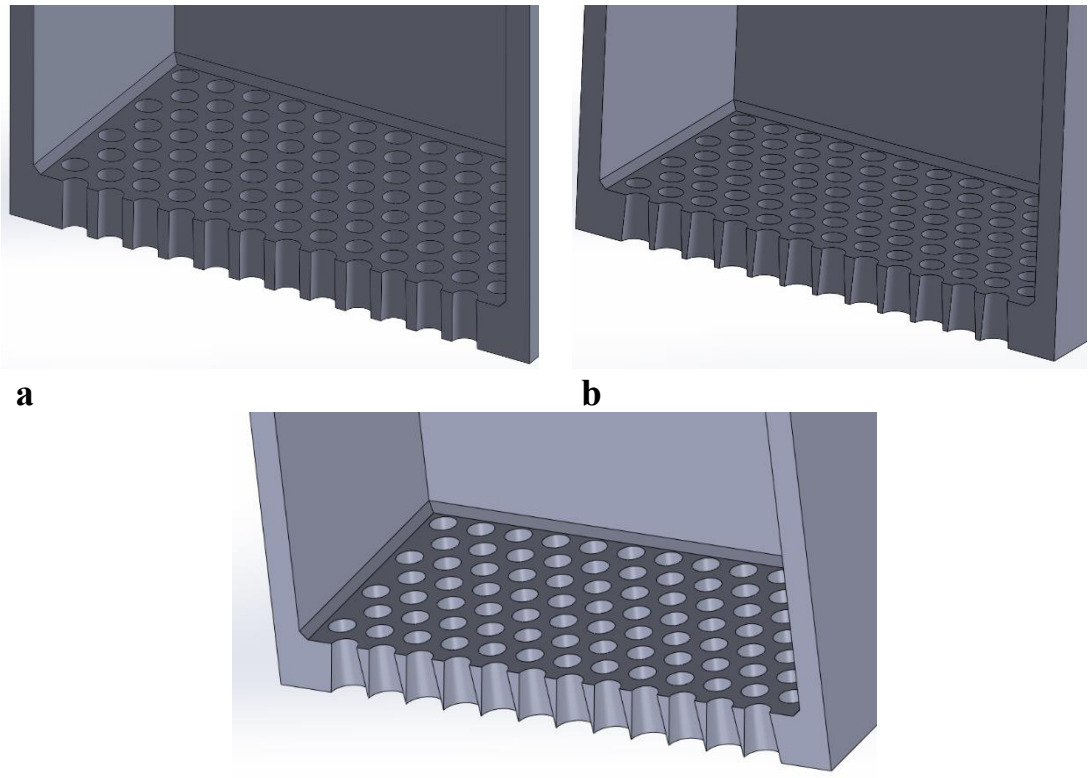

Figure 5.17*:** Section cut view of the circular-aperture sieves. Sieve thickness is 100 μm. Inverted taper angle: ***(a) 1°; ***(b)*** 4°; ***(c)*** 7°.

In *Table 5.9*, the main quality indicators for the sieving process are compared for different aperture shape on the three trials with parameter combinations that maximize sieved mass, mass flow and linearity duration. These were calculated after running sieving DEM simulations using the variable level sets of *Table 5.9*. The percentages are

calculated with regard to the respective value of the same parameter set for the square aperture. The following observations can be made.

***Table 5.9*:** Aperture shape effect comparison.

TRIAL	TRIAL SETTINGS	APERTURE TYPE	Q (mg/sec)	m (mg)	LESR	t_{lin} (sec)	Q_n (Q/N_a) [mg/(sec·aperture)]
Σ_1 (max m)	(Σ_1): $\begin{cases} f_{vib} = 500\ Hz \\ A_{vib} = 20\ \mu m \\ \theta_{tap} = 1^o \\ h_{bf} = 1.5\ mm \end{cases}$	***SQUARE***	0.408	0.648	1.304	1.622	0.002414
		HEXAGONAL	0.468 (+14.7%)	0.636 (-1.9%)	1.334 (+2.3%)	1.405 (-13.4%)	0.002489
		CIRCULAR	0.435 (+6.6%)	0.661 (+2.0%)	1.303 (-0.8%)	1.595 (-1.7%)	0.002314
Σ_2 (max Q)	(Σ_2): $\begin{cases} f_{vib} = 200\ Hz \\ A_{vib} = 20\ \mu m \\ \theta_{tap} = 7^o \\ h_{bf} = 0.5\ mm \end{cases}$	***SQUARE***	1.121	0.193	1.177	0.185	0.006633
		HEXAGONAL	1.150 (+2.6%)	0.180 (-6.7%)	1.192 (+1.3%)	0.165 (-10.8%)	0.006117
		CIRCULAR	1.089 (-2.9%)	0.194 (-0.5%)	1.194 (+1.4%)	0.185 (≡)	0.005793
Σ_3 (max t_{lin})	(Σ_3): $\begin{cases} f_{vib} = 500\ Hz \\ A_{vib} = 50\ \mu m \\ \theta_{tap} = 7^o \\ h_{bf} = 1.5\ mm \end{cases}$	***SQUARE***	0.226	0.426	1.045	1.905	0.001337
		HEXAGONAL	0.207 (-8.4%)	0.431 (+1.2%)	1.020 (-2.4%)	2.113 (+10.9%)	0.001101
		CIRCULAR	0.193 (-14.6%)	0.355 (-16.7%)	0.978 (-6.4%)	1.845 (-3.1%)	0.001027

In the case of maximizing powder mass that has passed through the sieve in linearity, the mass itself remains relatively unchanged, at approximately 0.636-0.661 mg. The same applies for LESR, at 1.303-1.334. However, the linearity duration decreases by 13.4% in the square-to-hexagonal transition and then returns to a similar value to the one of the square-aperture for the circular-aperture trial. Of course, since the mass is relatively stable, the opposite with regard to the linearity duration applies for the mass flow. This contradicts the expected result that was stated above. The experiment indicates that there is no strong statistical difference between the square-aperture and circular-aperture sieve performance (see *Table 5.9*), as can be judged by the percentages provided, but the hexagonal-sieve performance shows higher mass flow and decreased linearity duration.

In the case of maximizing the powder flow of the linear phase of sieving, no statistically important differences can be observed in any of the set quality indicators, namely mass flow, mass, linearity duration and LESR. Any variances among these can be attributed to slight differences during the powder generation phase, as the particles are generated randomly by a lognormal distribution as explained in the powder spreading-relevant chapter of this work. The powder generation happens again at the start of each trial and

differences of approximately 2.9% in total powder mass have been observed between the three trials of the mass flow-maximizing set.

In the case of maximizing the duration of linearity, when moving from a square-aperture sieve to a hexagonal-aperture sieve, the mass flow decreases by 8.4%. However, the total mass sieved remains almost the same, as well as the LESR. This means that, the decreased mass flow is the only factor affecting the duration of linearity, which is increased by 10.9%. However, the total aperture area of the hexagonal-aperture sieve is only 3.4% smaller with regard to the one of the square-aperture sieve. This means that the decrease of the mass flow would be expected up to a 3.4% and the remaining 5% can be attributed to the decreased passing probability for the larger particles to pass through the sieve ducts. When we move from the hexagonal to the circular aperture sieve, the mass flow further decreases by another 6.2% with regard to the square one. However, in this case, the linearity duration also decreases with regard to the square one by 3.1%. This is attributed to the fact that, when linearity stops, the LESR value is 6.4% lower compared to the square sieve. This makes the total mass sieved also decrease by 16.7%, while hexagonal sieve allowed approximately the same mass as the square one. Hence, the more the aperture shape deviates from the square shape and moves towards regular polygons of an increasing number of sides, at first the mass sieved does not get affected and the only values affected are the mass flow and linearity duration, but after a critical number of sides this trend seizes to exist and the LESR value decreases, causing even the duration of linearity to decrease.

The differences in the observations between the three trials clearly show that the aperture shape is an important factor that demonstrates interaction with the 4 variables of the experiment.

The last column of *Table 5.9* provides an important insight. If the mass flow becomes normalized by the number of apertures for each sieving trial, then it becomes clear that, regardless of the sieving variable levels, as we move from the square towards the circular apertures, the mass flow per aperture decreases. This comes in complete agreement with the prediction, since

i. It is increasingly difficult for borderline passing particles (i.e., particles of 50 μm diameter) to penetrate the apertures and move through them, and

ii. Square apertures, while a borderline passing particle passes through them, leave some space at the corners for fine particles to pass. This space becomes smaller for hexagonal apertures and becomes non-existent for circular apertures.

Hence, for sieves that possess apertures that correspond to borderline passing particles of the same size, it is important to increase the number of apertures while moving from square aperture shape towards the circular aperture shape in order to achieve the same mass flow.

5.6 Sieved Layer Quality

It is very important to examine whether controlled sieving is able to produce PBF-appropriate layers of powder, since this would be a very time-efficient powder deposition method that would promote powder economy. In order to do this, the same Taguchi DoE as the one used in *Section 5.3* is used, however, the quality criteria will be the ones used in the spreading Taguchi DoE, i.e., LTD, SCR, PD and RMS-roughness, see *Chapter 4.5*. The deposited layer will be considered ready for evaluation at the precise moment when the mass inside the sample square will be equal to the optimum spread layer mass via a doctor blade (SCR-RMS), i.e., equal to 0.205 mg. By comparing the true packing density of the spread layers created for the spreading Taguchi DoE in *Chapter 4.6* to the true packing density values of *Table 5.10*, it becomes obvious that it remains stable regardless of the deposition method (with doctor blade recoater, or recoater-less, via sieving). Hence, the actual layer thickness is expected to be similar by maintaining a stable total layer mass, at 0.205 mg. The design and results of the Taguchi DoE for the powder deposition via sieving can be seen in *Table 5.10*. The levels of the sieving variables were kept the same as they were set in *Section 5.3*, in order to make consistent observations which connect sieving performance criteria to deposited layer quality.

After proving in *Chapter 4* that skewness (Ssk) and kurtosis (Sku) are general layer surface quality indicators that take under consideration LTD, SCR and RMS roughness, these two quantities will be used to evaluate the quality of the powder layers created via sieving.

The layers developed have negative skewness, since the spherical powder particles create distributions that deviate to the upper side with regard to the mean line. The

developed surfaces are also typically leptokurtic, i.e., with a kurtosis value larger than 3, since the only sharpness of the profile is developed by the valleys, which are steeper and narrower the higher the layer quality is. The steeper and narrower the valleys, the higher the Sku value. Furthermore, the flatter and larger the "plateaus" of the surface, the smaller the (negative) Ssk value. This means that, the more packed the particles are on the top of the layer, the flatter the plateaus will appear to be, and the smaller the (negative) surface skewness value. *Figure 4.19* provides a visual explanation of Ssk and Sku parameters [214].

***Table 5.10*:** L27 Orthogonal array of the Taguchi DoE for powder deposition via sieving. The results are presented as well.

TRIAL #	F_{vib} (Hz)	A_{vib} (μm)	θ_{tap} (deg.)	h_{bf} (mm)	(LTD) (μm)	SCR (%)	S_q (μm)	PD_{tr} (%)	PD_{th} (%)	S_a (μm)	Ssk	Sku
1	**200**	**20**	**1**	**0.5**	-21.0	99.3	19.0	67.8	53.7	14.8	-0.788	4.269
2	**200**	**20**	**4**	**1.0**	-20.2	99.3	18.2	67.5	54.0	14.0	-0.786	4.583
3	**200**	**20**	**7**	**1.5**	-20.5	99.3	18.1	67.4	53.7	14.1	-0.794	4.571
4	**200**	**35**	**1**	**1.0**	-20.4	99.3	18.5	67.3	53.7	14.5	-0.745	4.312
5	**200**	**35**	**4**	**1.5**	-20.7	99.3	18.7	67.4	53.5	14.5	-0.747	4.338
6	**200**	**35**	**7**	**0.5**	-21.3	99.3	18.5	68.1	53.7	14.5	-0.732	4.293
7	**200**	**50**	**1**	**1.5**	-20.6	99.4	18.1	67.5	53.7	14.1	-0.682	4.372
8	**200**	**50**	**4**	**0.5**	-21.4	99.3	19.2	68.1	53.7	15.1	-0.650	3.948
9	**200**	**50**	**7**	**1.0**	-20.3	99.4	17.4	67.4	53.8	13.4	-0.800	4.719
10	**350**	**20**	**1**	**1.0**	-20.4	99.4	18.4	67.6	53.9	14.2	-0.834	4.476
11	**350**	**20**	**4**	**1.5**	-19.9	99.4	18.1	67.4	54.0	14.0	-0.770	4.499
12	**350**	**20**	**7**	**0.5**	-19.8	99.4	19.9	67.9	54.6	15.5	-0.400	3.884
13	**350**	**35**	**1**	**1.5**	-20.2	99.3	17.9	67.4	53.9	13.8	-0.832	4.666
14	**350**	**35**	**4**	**0.5**	-20.5	99.3	20.5	68.3	54.4	16.1	-0.455	3.701
15	**350**	**35**	**7**	**1.0**	-20.6	99.4	17.0	67.5	53.7	13.1	-0.809	4.924
16	**350**	**50**	**1**	**0.5**	-22.0	99.3	21.4	68.4	53.4	17.0	-0.482	3.385
17	**350**	**50**	**4**	**1.0**	-19.9	99.4	16.4	67.0	53.8	12.6	-0.864	5.165
18	**350**	**50**	**7**	**1.5**	-20.5	99.3	18.0	67.4	53.7	13.9	-0.873	4.643
19	**500**	**20**	**1**	**1.5**	-20.7	99.3	19.0	67.8	53.8	14.8	-0.784	4.286
20	**500**	**20**	**4**	**0.5**	-19.8	99.3	20.1	67.9	54.6	15.7	-0.421	3.896
21	**500**	**20**	**7**	**1.0**	-20.3	99.3	18.1	67.6	54.0	14.1	-0.802	4.517
22	**500**	**35**	**1**	**0.5**	-21.8	99.3	21.0	68.5	53.6	16.5	-0.536	3.559
23	**500**	**35**	**4**	**1.0**	-19.9	99.4	17.0	66.9	53.7	13.1	-0.851	4.965
24	**500**	**35**	**7**	**1.5**	-20.5	99.4	17.4	67.4	53.7	13.5	-0.865	4.792
25	**500**	**50**	**1**	**1.0**	-20.0	99.5	16.2	67.0	53.7	12.5	-0.839	5.074
26	**500**	**50**	**4**	**1.5**	-20.0	99.4	16.2	67.1	53.8	12.4	-0.951	5.550
27	**500**	**50**	**7**	**0.5**	-29.6	99.2	20.3	68.7	48.5	16.1	-0.430	3.316

Note that, since all skewness values are negative, as imposed by the spherical particle geometry, the ANOVA table and regression equations below refer to the absolute value

of skewness, for easiness of calculation. *Table 5.11* and *Table 5.12* show how much the sieving parameters contribute to the kurtosis and skewness values of the layer that is produced via powder sieving.

***Table 5.11*:** Analysis of Variance (ANOVA) for the kurtosis (Sku) value of the sieving-produced layer.

Source	DF	Seq SS	Contribution	Adj SS	Adj MS	F-Value	P-Value
Regression	7	486.145	63.86%	486.145	0.69449	4.80	0.003
f_{vib} (Hz)	1	0.01681	0.22%	0.75909	0.75909	5.24	0.034
A_{vib} (µm)	1	0.07880	1.04%	0.55630	0.55630	3.84	0.065
θ_{tap} (deg.)	1	0.08820	1.16%	0.08820	0.08820	0.61	0.445
h_{bf} (mm)	1	309.673	40.68%	0.49812	0.49812	3.44	0.079
f_{vib} (Hz) *A_{vib} (µm)	1	0.22005	2.89%	0.22005	0.22005	1.52	0.233
f_{vib} (Hz) *h_{bf} (mm)	1	0.79362	10.43%	0.79362	0.79362	5.48	0.030
A_{vib} (µm) *h_{bf} (mm)	1	0.56724	7.45%	0.56724	0.56724	3.92	0.062
Error	19	275.095	36.14%	275.095	0.14479		
Total	26	761.240	100.00%				

***Table 5.12*:** Analysis of Variance (ANOVA) for the absolute value of skewness (|Ssk|) value of the sieving-produced layer.

Source	DF	Seq SS	Contribution	Adj SS	Adj MS	F-Value	P-Value
Regression	7	0.461942	69.81%	0.461942	0.065992	6.28	0.001
f_{vib} (Hz)	1	0.003335	0.50%	0.094560	0.094560	8.99	0.007
A_{vib} (µm)	1	0.002048	0.31%	0.001111	0.001111	0.11	0.749
θ_{tap} (deg.)	1	0.000016	0.00%	0.018258	0.018258	1.74	0.203
h_{bf} (mm)	1	0.321068	48.52%	0.025997	0.025997	2.47	0.132
f_{vib} (Hz) *h_{bf} (mm)	1	0.112133	16.95%	0.094761	0.094761	9.01	0.007
A_{vib} (µm) *θ_{tap} (deg.)	1	0.004302	0.65%	0.004302	0.004302	0.41	0.530
θ_{tap} (deg.) *h_{bf} (mm)	1	0.019040	2.88%	0.019040	0.019040	1.81	0.194
Error	19	0.199767	30.19%	0.199767	0.010514		
Total	26	0.661709	100.00%				

The *Equations (5.6)* and *(5.7)* show the regression of the kurtosis and skewness of the sieving-produced layer respectively.

$$Sku = 6.2 - 0.00533f_{vib} - 0.0456A_{vib} + 0.0233\theta_{tap} - 1.385h_{bf} + 0.00006f_{vib}A_{vib} + 0.00343f_{vib}h_{bf} + 0.029A_{vib}h_{bf} \quad (5.6)$$

$$|Ssk| = 1.059 - 0.001314f_{vib} - 0.00103A_{vib} - 0.0421\theta_{tap} - 0.267h_{bf} + 0.001224f_{vib}h_{bf} + 0.000435A_{vib}\theta_{tap} + 0.0266\theta_{tap}h_{bf} \quad (5.7)$$

The optimum level combination to maximize both the kurtosis and the skewness of the layer is the following:

$$\begin{Bmatrix} f_{vib} = 500\ Hz \\ A_{vib} = 50\ \mu m \\ \theta_{tap} = 7^o \\ h_{bf} = 1.5\ mm \end{Bmatrix}$$

which, according to the *Equations (5.6)* and *(5.7)*, gives the optimum values of skewness and kurtosis as follows:

$$Sku_{opt} = 5.588$$

$$Ssk_{opt} = -1.005$$

After running a cross-checking simulation with the optimum parameter levels, validation of the expected kurtosis and skewness was achieved, the values being

$$Sku_{opt,sim} = 5.161$$

$$Ssk_{opt,sim} = -0.838$$

Kurtosis has a (-) 7.6% deviation from the expected value, which is less than the error of the regression equation, as calculated by ANOVA (36.14%). Similarly, skewness has a (-) 16.6% deviation from the expected value, which is less than the error of the regression equation, as calculated by the ANOVA (30.19%). Let us note that, the errors of the regression equations are quite large, since there are probably more parameters affecting the layer quality on top of the ones that are examined in this work. To elaborate, this error might be attributed to two factors. Firstly, the left, right, bottom and top border plate bodies of the simulation create a square ring shape of slightly reduced layer thickness near the edges of the square sample, which might affect the skewness and kurtosis differently for each trial, since the width of this square ring depends on the speed at which the particles descend after sliding past the sieve's apertures. Secondly, the layer data for layer sample evaluation are taken at the simulation moment during

which the mass goal of 0.205 mg is achieved. However, some particles are bouncing out of the frame of calculation at this moment, which could cause slight variation in Ssk and Sku, based on the velocity of these particles. Finally, for the last trial (#27), the mass goal could not be physically reached, causing an extreme value that affects the error of the regressions. However, the regression-calculated values of Sku and Ssk proved to be quite close to their simulation-calculated values.

Despite the accuracy of the estimation, by checking *Table 5.10*, it becomes obvious that TRIAL #26 has better values for both skewness and kurtosis compared to the regression-calculated optimum ones. More specifically, it has

$$Sku_{\#26,sim} = 5.550 \qquad Ssk_{\#26,sim} = -0.951$$

By a quick-check in the regression equations, it is proven that the parameter level combination

$$\begin{Bmatrix} f_{vib} = 500\ Hz \\ A_{vib} = 50\ \mu m \\ \theta_{tap} = 4^{o} \\ h_{bf} = 1.5\ mm \end{Bmatrix}$$

that corresponds to TRIAL #26 is the second-best parameter combination according to the regression equations, with

$$Sku_{\#26,reg} = 5.518 \qquad Ssk_{\#26,reg} = -0.946$$

The simulation kurtosis and skewness values of TRIAL #26 only have a (+) 0.6% and (+) 0.5% deviation from their regression-calculated values. The regression-calculated optimum values differ because of the high regression error. Hence, the accepted level combination that produces the best layer via sieving will be the parameter combination of TRIAL #26.

In *Table 5.13*, a comparison of powder deposition via doctor blade-based spreading and controlled sieving is presented. From this, it can be deduced that, despite the fact that sieving-facilitated powder deposition leads to a layer quality inferior to the one achieved via a vibrated doctor blade recoater, the layer quality however is superior to the one achieved by a non-vibrated doctor blade recoater. This is a particularly important observation, since most industrial powder deposition systems designed for PBF do not employ a vibrating doctor blade, but a simple one moving only linearly over the substrate, parallel to the fabrication piston. In this case, it would be better to

simply use a vibrating sieve, since by controlling properly the vibration frequency, amplitude and powder level inside it, a better surface quality would be achieved, at much lower deposition time. The visual representation of the layers described in *Table 5.13* can be seen in *Figure 5.18*.

***Table 5.13*:** Recoater spreading vs sieving-produced layer comparison.

	u_{tr} (m/sec)	f_{vib} (Hz)	A_{vib} (μm)	θ_{rel} (deg)	LTD_{reg} (LTD_{sim})	SCR_{reg} (SCR_{sim})	$S_{q_{reg}}$ $(S_{q_{sim}})$	Ssk_{reg} (Ssk_{sim})	Sku_{reg} (Sku_{sim})
DOCTOR BLADE - NO-VIB.	0.01	0	0	0	- (28.9)	- (98.56)	- (20.9)	- (-0.716)	- (3.962)
VIB. DOCTOR BLADE - OPTIMUM	0.01	2000	5	0	21.4 (22.1)	99.54 (99.33)	15.8 (15.7)	-1.771 (-1.543)	6.766 (6.530)
	f_{vib} (Hz)	A_{vib} (μm)	θ_{tap} (deg)	h_{bf} (mm)	LTD_{sim}	SCR_{sim}	$S_{q_{sim}}$	Ssk_{reg} (Ssk_{sim})	Sku_{reg} (Sku_{sim})
SIEVING - OPTIMUM SKU-SSK	500	50	4	1.5	20.0	99.47	16.2	-0.946 (-0.951)	5.518 (5.550)

(**Note:** 'reg' stands for "regression", while 'sim' for "simulation". The zero-vibration trial cannot have regression values calculated, since this level was not included in the Taguchi design.)

In general, the quality of the deposited layers via sieving largely depends on depositing the necessary powder mass during linearity, i.e., before the small particles become largely depleted and the mass flow becomes a lot smaller. In general, all trials that have a powder factory height of 0.5 mm have powder mass deposited in linearity smaller than the necessary 0.205 mg (see *Table 5.2*). This means that, in order to deposit the necessary amount of powder, we would need to keep sieving during the non-linear sieving stage. This would lead to sprinkling the top of the layer with particles of larger diameter, leading to higher peaks. This would potentially decrease the LTD, since many particles would exceed the desired height that is defined by the theoretical layer thickness, but the surface roughness would increase. Furthermore, the kurtosis value would decrease, since the sharpness of the surface would also decrease. The valleys would get wider and the plateaus not that extended, alleviating the leptokurtic surface

element. The skewness would increase (in negative values), since the surface would not deviate to the top side that much anymore.

In *Table 5.14* a comparison is made between the sieved layer's quality for the different control factor combination cases as examined via Ssk, Sku and the relation between the linearity duration and the time needed to deposit the necessary powder mass (0.205 mg) with the linearity mass flow of each trial.

Judging by the *Table 5.14*, it becomes obvious how, to obtain the best sieved powder layer quality, it is imperative to ensure that the duration of the linear sieving stage, in combination with the linearity mass flow are capable of providing the necessary powder mass before the ending of the linear stage. In order to ensure that a good quality layer is deposited via sieving, the user must select sieving parameters that ensure a sieved mass during linearity greater than the mass of the ideal spread layer via a vibrating doctor blade.

In the previous chapters, the author assumed that slower sieving can be beneficial in order to develop good quality, PBF-ready powder layers without the need for levelling them via a recoating mechanism. This assumption has been confirmed, since, sieving parameter combinations that promote longer linearity duration are in general connected to better deposited layer quality, as seen in *Table 5.14*.

The last two columns of *Table 5.14* compare the quality of the examined layer to the one achieved by powder spreading with a non-vibrating doctor blade (see *Table 5.13*). In 7 out of the 9 trials using a powder factory height of 0.5 mm, the result by both Ssk and Sku evaluation is worse than the one achieved by a non-vibrating doctor blade recoater. The only trials of an h_{bf}=0.5 mm that provided an acceptable layer quality were trials #1 and #6, in which the low powder level was paired with a low level of vibrating frequency, combination that provides the highest powder mass during linearity for this h_{bf} level. However, the necessary mass was still not reached, even by a small amount, so the setting combination would not be acceptable either. In conclusion, in order to produce layers comparable to the ones via non-vibrating doctor blades, it is necessary to feed the sieve with enough powder, but ensure it is oscillated at a proper level to facilitate the motion of the particles and prevent clogging. Furthermore, time adjustment of the vibration and blocking-unblocking the bottom part of the sieve via a

plate at the correct timing is of paramount importance to achieve the desired layer height.

***Table 5.14*:** Linearity importance of sieving on the produced layer quality; Red signals the worst performance trials while green the trials with the best results.

TRIAL #	F_{vib} (Hz)	A_{vib} (μm)	θ_{tap} (deg.)	h_{bf} (mm)	Q (mg/sec)	m (mg)	t_{lin} (sec)	$t_{0.205}$	t_{lin}-$t_{0.205}$	m-m_{des}	Ssk	Sku	Ssk-$Ssk_{DB\text{-}No\text{-}vib}$	Sku-$Sku_{DB\text{-}No\text{-}vib}$
1	**200**	**20**	**1**	**0.5**	1.141	0.183	0.171	0.180	-0.009	-0.022	-0.788	4.269	-0.072	0.307
2	**200**	**20**	**4**	**1**	0.888	0.238	0.271	0.231	0.040	0.033	-0.786	4.583	-0.070	0.621
3	**200**	**20**	**7**	**1.5**	0.9	0.218	0.243	0.228	0.015	0.013	-0.794	4.571	-0.078	0.609
4	**200**	**35**	**1**	**1**	0.844	0.429	0.523	0.243	0.280	0.224	-0.745	4.312	-0.029	0.350
5	**200**	**35**	**4**	**1.5**	0.737	0.659	0.923	0.278	0.645	0.454	-0.747	4.338	-0.031	0.376
6	**200**	**35**	**7**	**0.5**	1.082	0.152	0.145	0.189	-0.044	-0.053	-0.732	4.293	-0.016	0.331
7	**200**	**50**	**1**	**1.5**	0.576	0.296	0.501	0.356	0.145	0.091	-0.682	4.372	0.034	0.410
8	**200**	**50**	**4**	**0.5**	0.75	0.11	0.147	0.273	-0.126	-0.095	-0.650	3.948	0.066	-0.014
9	**200**	**50**	**7**	**1**	0.673	0.341	0.523	0.305	0.218	0.136	-0.800	4.719	-0.084	0.757
10	**350**	**20**	**1**	**1**	0.771	0.427	0.578	0.266	0.312	0.222	-0.834	4.476	-0.118	0.514
11	**350**	**20**	**4**	**1.5**	0.584	0.664	1.183	0.351	0.832	0.459	-0.770	4.499	-0.054	0.537
12	**350**	**20**	**7**	**0.5**	1.075	0.146	0.14	0.191	-0.051	-0.059	-0.400	3.884	0.316	-0.078
13	**350**	**35**	**1**	**1.5**	0.404	0.566	1.388	0.507	0.881	0.361	-0.832	4.666	-0.116	0.704
14	**350**	**35**	**4**	**0.5**	0.594	0.102	0.176	0.345	-0.169	-0.103	-0.455	3.701	0.261	-0.261
15	**350**	**35**	**7**	**1**	0.536	0.334	0.64	0.382	0.258	0.129	-0.809	4.924	-0.093	0.962
16	**350**	**50**	**1**	**0.5**	0.372	0.083	0.233	0.551	-0.318	-0.122	-0.482	3.385	0.234	-0.577
17	**350**	**50**	**4**	**1**	0.334	0.269	0.811	0.614	0.197	0.064	-0.864	5.165	-0.148	1.203
18	**350**	**50**	**7**	**1.5**	0.307	0.462	1.525	0.668	0.857	0.257	-0.873	4.643	-0.157	0.681
19	**500**	**20**	**1**	**1.5**	0.408	0.648	1.622	0.502	1.120	0.443	-0.784	4.286	-0.068	0.324
20	**500**	**20**	**4**	**0.5**	0.983	0.111	0.115	0.209	-0.094	-0.094	-0.421	3.896	0.295	-0.066
21	**500**	**20**	**7**	**1**	0.696	0.359	0.535	0.295	0.240	0.154	-0.802	4.517	-0.086	0.555
22	**500**	**35**	**1**	**0.5**	0.496	0.076	0.159	0.413	-0.254	-0.129	-0.536	3.559	0.180	-0.403
23	**500**	**35**	**4**	**1**	0.421	0.282	0.681	0.487	0.194	0.077	-0.851	4.965	-0.135	1.003
24	**500**	**35**	**7**	**1.5**	0.338	0.522	1.523	0.607	0.916	0.317	-0.865	4.792	-0.149	0.830
25	**500**	**50**	**1**	**1**	0.278	0.265	0.969	0.737	0.232	0.06	-0.839	5.074	-0.123	1.112
26	**500**	**50**	**4**	**1.5**	0.239	0.452	2.025	0.858	1.167	0.247	-0.951	5.550	-0.235	1.588
27	**500**	**50**	**7**	**0.5**	0.347	0.065	0.205	0.591	-0.386	-0.14	-0.430	3.316	0.286	-0.646

In order to ensure that the minimum necessary powder amount is provided, the total mass of the particles that can physically pass through the sieve ducts can be calculated, via the particle size distribution of the powder and the total powder mass fed into the sieve.

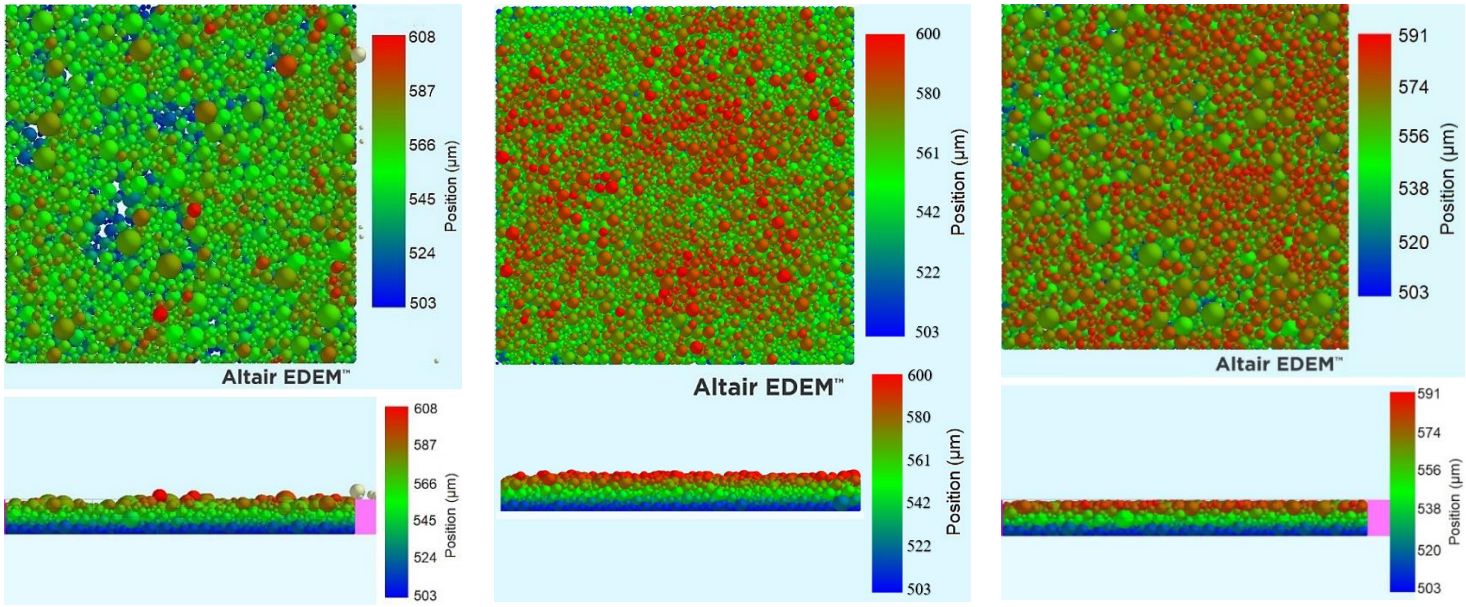

a **b** **c**

Figure 5.18: Visual comparison of the optimum layers developed by; ***(a)*** vibration-less doctor blade; ***(b)*** controlled sieving; ***(c)*** vibrated doctor blade.

In order to estimate the layer quality, the average rating of their Ssk and their Sku value is calculated, the highest rating (100%) being assigned to the best layer and the lowest (0%) to the worst layer. The results, along with the values of every quality criterion described are shown in *Table 5.15*. The results are shown in increasing order of average rating of the ones that were calculated for Ssk and Sku.

Table 5.15 helps reach to the following conclusions:

1. Trials with larger (t_{lin}-$t_{0.205}$) and (m-m_{des}) values are superior in terms of quality. Hence, trials with h_{bf}=0.5 mm are the least promising, unless they feature low sieve excitation levels (f_{vib}=200 Hz and A_{vib}=20 or 35 µm), see trials #6 and #1). Inversely, trials with h_{bf}=1.5 or 1 mm and low sieve excitation levels (f_{vib}=200 Hz and A_{vib}=20 or 35 µm) create layers of average quality, compared to the ones of the same initial powder amount (h_{bf}=1.5 or 1 mm) combined with high sieve excitation levels (f_{vib}=500 or 350 Hz and A_{vib}=50 or 35 µm).

2. In continuation from 1, the optimum layers are the ones developed by the sieving combination that promote the highest mass sieved in linearity combined with the lowest mass flow, meaning that indeed the slower the sieving rate, the better the sieved deposited layer quality.

3. SCR remains practically unchanged for every trial (99.3±0.1 % for the sample of the 27 trials), indicating that the coverage ratio is an intrinsic property of the sieving method in terms of sieving deposition.

Table 5.15: Layer quality for each trial by increasing order. Colour code added for every quality criterion.

TRIAL #	F_{vib} (Hz)	A_{vib} (μm)	θ_{tap} (deg.)	h_{bf} (mm)	t_{lin}-$t_{0.205}$ (sec)	m-m_{des} (mg)	LTD (μm)	SCR (%)	S_q (μm)	PD_{tr} (%)	Ssk-$Ssk_{DB\text{-}No\text{-}vib}$	Sku-$Sku_{DB\text{-}No\text{-}vib}$	Rating (%)
27	500	50	7	0.5	-0.386	-0.14	-29.6	99.2	20.3	68.7	0.286	-0.646	2.7
16	350	50	1	0.5	-0.318	-0.122	-22	99.3	21.4	68.4	0.234	-0.577	9.0
12	350	20	7	0.5	-0.051	-0.059	-19.8	99.4	19.9	67.9	0.316	-0.078	12.7
14	350	35	4	0.5	-0.169	-0.103	-20.5	99.3	20.5	68.3	0.261	-0.261	13.6
20	500	20	4	0.5	-0.094	-0.094	-19.8	99.3	20.1	67.9	0.295	-0.066	14.9
22	500	35	1	0.5	-0.254	-0.129	-21.8	99.3	21	68.5	0.18	-0.403	17.8
8	200	50	4	0.5	-0.126	-0.095	-21.4	99.3	19.2	68.1	0.066	-0.014	36.8
7	200	50	1	1.5	0.145	0.091	-20.6	99.4	18.1	67.5	0.034	0.41	49.2
6	200	35	7	0.5	-0.044	-0.053	-21.3	99.3	18.5	68.1	-0.016	0.331	52.0
4	200	35	1	1	0.28	0.224	-20.4	99.3	18.5	67.3	-0.029	0.35	53.6
5	200	35	4	1.5	0.645	0.454	-20.7	99.3	18.7	67.4	-0.031	0.376	54.4
1	200	20	1	0.5	-0.009	-0.022	-21	99.3	19	67.8	-0.072	0.307	56.5
19	500	20	1	1.5	1.12	0.443	-20.7	99.3	19	67.8	-0.068	0.324	56.6
11	350	20	4	1.5	0.832	0.459	-19.9	99.4	18.1	67.4	-0.054	0.537	60.1
21	500	20	7	1	0.24	0.154	-20.3	99.3	18.1	67.6	-0.086	0.555	63.4
2	200	20	4	1	0.04	0.033	-20.2	99.3	18.2	67.5	-0.07	0.621	63.4
3	200	20	7	1.5	0.015	0.013	-20.5	99.3	18.1	67.4	-0.078	0.609	63.8
10	350	20	1	1	0.312	0.222	-20.4	99.4	18.4	67.6	-0.118	0.514	65.3
9	200	50	7	1	0.218	0.136	-20.3	99.4	17.4	67.4	-0.084	0.757	67.7
13	350	35	1	1.5	0.881	0.361	-20.2	99.3	17.9	67.4	-0.116	0.704	69.4
18	350	50	7	1.5	0.857	0.257	-20.5	99.3	18	67.4	-0.157	0.681	72.6
15	350	35	7	1	0.258	0.129	-20.6	99.4	17	67.5	-0.093	0.962	73.1
24	500	35	7	1.5	0.916	0.317	-20.5	99.4	17.4	67.4	-0.149	0.83	75.2
23	500	35	4	1	0.194	0.077	-19.9	99.4	17	66.9	-0.135	1.003	77.8
25	500	50	1	1	0.232	0.06	-20	99.5	16.2	67	-0.123	1.112	79.2
17	350	50	4	1	0.197	0.064	-19.9	99.4	16.4	67	-0.148	1.203	83.5
26	500	50	4	1.5	1.167	0.247	-20	99.4	16.2	67.1	-0.235	1.588	100.0
AVERAGE					-	-	-20.8	99.3	18.5	67.6	-0.007	0.434	-
STANDARD DEVIATION					-	-	1.8	0.1	1.4	0.5	-	-	-
STANDARD DEVIATION (%)					-	-	8.8	0.1	7.6	0.7	-	-	-

4. True packing density remains practically unchanged for every trial (67.6±0.5 % for the sample of the 27 trials), as was expected. However, slight changes indicate the opposite trend to the expected one, i.e., higher true packing density for the lower quality layers. This can be again explained by the presence of oversized particles on top of the layer. The oversized particles occupy a large space, leading to a slight increase of the true packing density, as it was defined in *Section 4.5.4*.

5. In certain trials (#12 and #20), the LTD value appears to indicate towards a higher layer quality, even though the other criteria point towards the opposite. This is, as explained previously, due to the fact that the average height is heavily influenced by extreme values. In both these trials, in order to sieve the desired powder mass (0.205 mg), sieving had to continue past the end of the linear stage. This caused the accumulation of oversized particles on the top of the layer, creating high peaks that decrease the |LTD| value, but simultaneously deteriorate the layer quality, as depicted by S_q.
6. Sku and Ssk again prove themselves to be accurate layer quality indicators, capable of identifying whether an increase in LTD (decrease in |LTD|), like in trials #12 and #20, points towards an actual or false layer quality increase.

5.7 Sieving Deposition Duration

The time needed for sieving would be equal to 0.858 sec, since

$$t_{siev} = \frac{m_{opt}}{Q_{\#26}} = \frac{0.205\ mg}{0.239\ mg/sec} = 0.858\ sec < t_{lin,\#26} = 2.025\ sec$$

The total time necessary for completing the deposition of a layer would include the sieving time and the sieve reloading and vibrational powder flattening time. The sieve would be reloaded by a vertical silo above it, as described in *Section 3.4.1* [59], [137]. A rolling dispensing cylinder would ensure that the necessary powder amount would be accurately fed into the sieve, while the sieve would be blocked by a plate positioned right below it, being in contact with it to seal the apertures. The rolling dispenser described in the aforementioned sources features a helical-patterned row of blind, hemi-spherical apertures, which trap the powder and feed it into the sieve. Each hemi-spherical aperture has a diameter of 9 mm. The cylinder features 19 apertures. The capacity of each aperture is calculated as

$$V_{ap} = \frac{1}{2} \cdot \left(\frac{4}{3}\pi R^3\right) = 191\ mm^3$$

Given that the true packing density of the powder is approximately equal to 67.5%, the pure powder volume of each aperture is given by

$$V_{powder,ap} = 0.675 \cdot V_{ap} = 129\ mm^3$$

And, since the density of a-alumina is equal to 3820 Kg/m^3=3.82 mg/mm^3, the powder mass inside a single aperture is given by

$$m_{powder,ap} = \rho_{a-Al_2O_3} \cdot V_{powder,ap} = 492\ mg$$

The mass per mm^2 of deposited layer necessary is 0.205 mg. The active length of the dispensing roller (i.e., the distance that encompasses every dispensing aperture) is 200 mm. For a sample surface of 200 mm x 200 mm (40000 mm^2), the deposited layer would consist of 8200 mg. However, for this to happen, the powder level inside the sieve should correspond to a powder box factory height of 1.5 mm. Allowing for the powder to rest after its generation, this would lead to a settled powder height equal to 410 μm = 0.41 mm (see *Table 6.2*). For a powder level of 0.41 mm with horizontal dimensions of 200 mm x 200 mm and a true packing density of 67.5%, the actual powder volume is equal to

$$V_{pow,total} = 0.675 \cdot (200 \cdot 200 \cdot 0.41)\ mm^3 = 11070\ mm^3$$

Which corresponds to total powder mass of

$$m_{pow,total} = \rho_{a-Al_2O_3} \cdot V_{pow,total} = 42287\ mg$$

This powder mass corresponds to a certain number of dispensing roller apertures, equal to

$$N_{DR,ap} = \frac{m_{pow,total}}{m_{powder,ap}} \cong 85.931$$

Which corresponds to (85.931/19) ≅ 4.523 revolutions.

Hence, it is easily understood that, in order to dispense the necessary amount of powder, the designed cylindrical dispenser would have to perform 4.523 revolutions, which, at a speed of 60 RPM would take only 4.523 secs. An alternative would be to include more helixes to the same cylinder. The cylinder has a diameter of 39 mm, meaning that, its circumference is equal to 2πR ≅ 122.5 mm, which can accommodate at maximum 13 helixes, since (cylinder circumference)/(aperture diameter) = (122.5/9) = 13.61. By adding three more helixes, the necessary time would drop to (4.523/4) ≅ 1.13 sec which is an acceptable time, since this could easily be performed during the selective laser solidifying (sintering/melting) of the previous layer.

The surface flattening of the in-sieve powder while the sieve is blocked is necessary to ensure a homogeneous powder level in the sieve and guarantee homogeneous sieving

throughout the sieve's surface. This could be done by applying vibration on the sieve while the powder is being dispensed, so this would not increase the total time necessary for the deposition of a single layer at all.

Additionally, the sieve loading could be performed while the laser beam performs the melting/sintering of the previous layer, which only lasts for approximately 2 seconds, depending on part size and complexity, as well as to machine settings such as scan speed and hatch spacing. This means that the only time when the loading would act as a delay to the process would be the deposition of the first layer, as long as the user ensures that the loading is performed faster compared to the laser scanning time of the layer.

The data used can be seen in *Table 5.16* below.

***Table 5.16*:** Trial #26 sieving data.

TRIAL #	F_{vib} (Hz)	A_{vib} (μm)	θ_{tap} (deg.)	h_{bf} (mm)	Q (mg/sec)	m (mg)	LESR	t_{lin} (sec)
26	**500**	**50**	**4**	**1.5**	0.239	0.452	0.788	2.025

6 *Multi-material Powder Deposition*

Multi-material deposition is defined as the deposition of a powder layer where the type of powder applied by the recoating system may vary, based on the coordinates of the powder bed's position onto which the powder is applied. Alternatively, simply phrased, in multi-material deposition, a mosaic-patterned layer of various different kinds of powders should be able to be created. Multi-material powder layer deposition remains a generally unresolved issue in the field of powder based (PB) additive manufacturing (AM) processes and the most significant challenge of multi-material PBF-LB manufacturing.

Multi-material AM is mainly limited to layers of alternating material, whether it being completely different materials or a mixture of powders of two specific materials at varying percentages, in order to create functionally graded components. However, it is quite often that engineers are presented with the need to create parts made from more than one different material combined, where it is impossible to create the different material features by simply altering the material between layers. So, the need to produce accurate, consistent multi-material layers of powders is of paramount importance.

In literature there have been some attempts of multi-material Powder Bed Fusion. A commercial dual material powder deposition system has been produced by Aerosint™ [228]. This system is based on deposition in a line-by-line pattern via a dual cylinder system that, in combination with electronics, controls the powder flow [229]. To be more specific, patterning drums deposit fine powder voxels without contact with the layer, in a line-at-once manner [228]. Even though the suggested system is comparably fast to simple roller/doctor blade uni-material powder recoaters, it is ambiguous whether it is possible to create a substantially and consistently even powder layer in terms of layer surface roughness and powder packing density. Also, in order to add a new material, it is necessary to add another cylinder, further complicating the design. Furthermore, the accuracy of the borders between the uni-material subareas has not been examined and determined. Finally, the details of the system have not been made

available to the scientific community, since it is a prototype and the company maintains all copyrights.

Another attempt has been made by Fraunhofer IGCV [230]. Their method is based on depositing layers of different powder types sequentially. Initially, a complete layer of the first powder type (Type A) is deposited (layer N) and selective consolidation of the first powder is achieved. Then, controlled vacuum pumping removes the non-consolidated powder of the first type. Then, a layer of the second powder type (Type B) is deposited and selectively consolidated too, (layer N). The non-consolidated powder of the second type remains to serve as support for the next layer (layer N+1) and the process is repeated. Despite the accuracy of the process, the accurate removal of only the last layer is not yet achievable by the current state-of-the-art and the process is time-consuming, since it takes double the time uni-material deposition would take. Furthermore, the consolidated parts of the first powder type might have protrusions, which, if they come into contact with the recoater, could possibly damage it or insert dimensional inaccuracy to the finished part [231]. The fact that multi-material powder deposition has not been implemented yet, even though the combination of different materials in objects to optimize mechanical and other properties has been happening in various other manufacturing methods proves the necessity to develop a robust, accurate and universal method to spread a powder layer of a number of different powder types and of any desired geometrical pattern, while ensuring that the produced layer complies to certain quality criteria.

It has been proven (see *Chapter 2*) that powder homogeneity is a very important factor that affects the quality of the finished part in Selective Laser Sintering (SLS) and Selective Laser Melting (SLM). The powder deposition methods have been identified and categorized and statistical analysis was used, namely AHP, to determine which method is the most efficient overall for uni-material powder deposition, i.e. deposition of powder where one layer fully consists of one type of powder, for SLS/SLM [137]. The most efficient and widely accepted process was shown to be a rolling cylinder and/or a doctor blade in various pattern combinations (termed “mechanical powder deposition”) [137]. However, even though this method is adequate, simple, easily controllable and provides satisfactory results for uni-material powder deposition, it is very impractical for multi-material deposition. This is due to friction between the recoater and the different kinds of powder unavoidably leading to unwanted mixing of

the powders and distortion of the boundaries between the uni-material subareas of the layer. Electrostatic deposition remains a concept, however it is non-applicable for metallic powders, while other alternatives that have been examined, such as ultrasound nozzle arrays are very slow in terms of deposition speed and require extremely good fine tuning and control of the vibrational stimuli that will be applied on each nozzle. Furthermore, it is extremely difficult to perfectly isolate the nozzles between each other, thus not excluding the possibility of accidentally stimulating neighbouring nozzles and depositing the wrong amount or kind of powder onto the wrong position of the powder bed. Finally, nozzles can deposit very fine powders with very good accuracy in terms of quantity and position, however the resulting layer's compaction level and surface roughness does not match the standards achieved by a roller/doctor blade recoating system.

Next, a multi-material powder deposition system is suggested relying on the principle of a contour gauge and a mathematically defined surface segmentation method. A slicing software is used in order to provide the powder layer sections and to assign powder types to certain positions, based on the coordinates of the powder bed.

6.1 Geometrical Definition of the Problem

6.1.1 Step 1: Slicer Data

The slicing software performs the slicing of the 3D model of the designed part (in CAD form, such as: SWD, STL, IGES, etc. format) by using subsequent horizontal layers at a distance equal to the actual layer thickness. Based on the difference between nominal (also termed as theoretical) and actual layer thickness (see *Chapter 2*), the slicing software determines the effective layer thickness of the deposited powder layer, and, subsequently, based on coordinates, which spot (or voxel) of the powder bed will be covered by which type of powder. The powder bed is a downwards moving fabrication piston or table, and the bottom left corner of it is the coordinate origin. In order to determine effectively where each powder type will be deposited, the slicing software must create uni-material areas and identify the borders between them. The slicer data also includes the number of the different powder types used and arranged in an array

(PT) by order of appearance, see *Equation (6.1)*, after the border curves are numbered (see *Section 6.1.2*). The number of the different powder types used is denoted by $n_{p.t.}$.

$$PT = \begin{bmatrix} PT_1 & PT_2 & \cdots & PT_k & \cdots & PT_{n_{p.t.}} \end{bmatrix}^T \quad (6.1)$$

In *Figure 6.1*, a dual material surface (left) and a triple material surface (right) are presented. This difference affects the deposition process in terms of subarea segmentation and spreading order, as will be explained in detail in the next Sections.

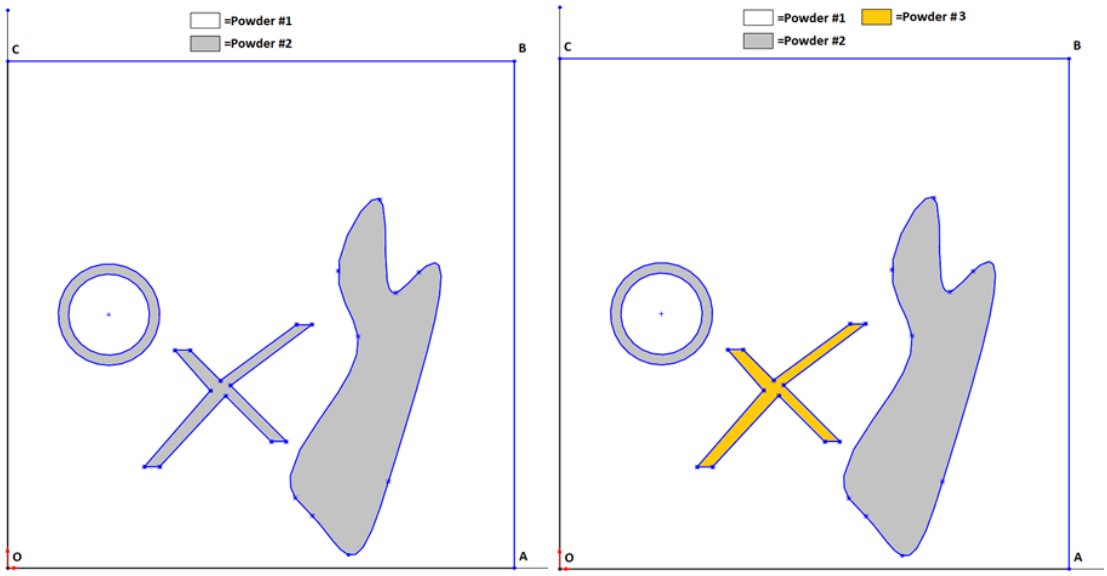

***Figure 6.1*:** Typical multi-material layer examples; (Left) A dual powder layer (Right) A triple powder layer.

6.1.2 Step 2: Identification, Definition and Numbering of Border Curves

The term "border curve" defines every closed curve where powders of different materials come in contact within the layer, including the outer borders of the powder bed [$(OABC)$ rectangle, see *Figure 6.2*]. Border curves are by definition closed curves. Because of this fact, there is no single $x = f(y)$ function to represent one border curve. Each border curve can be represented in the software by either a number of $x = f(y)$ functions, or by a number of points via the coordinates of each point that belongs to the curve. Each one of these two representations has advantages and disadvantages regarding the suggested surface segmentation method. A function is much more precise, but a closed curve cannot be interpreted as a simple function, so there is a need to divide

it into more functions. On the contrary, points lack in accuracy in depicting a curve, however it is easier to treat a border line as a matrix of x and y coordinates and solve the surface segmentation equations numerically, without having to divide the curve into subfunctions.

The way of defining a border curve (the ith curve) by point coordinates can be seen in *Equation (6.2)*.

$$BC_i: \begin{bmatrix} x_1 & x_2 & \cdots & x_k & \cdots & x_{N_{p_i}} \\ y_1 & y_2 & \cdots & y_k & \cdots & y_{N_{p_i}} \end{bmatrix}^T \quad (6.2)$$

where N_{p_i} is the number of the points of the (ith) curve.

Each border curve is a closed curve, so it can be enveloped in a rectangular box. The box $(OABC)$ denoting the border of the powder bed is defined by the points, see *Figure 6.2*:

$$O(0,0)$$
$$A(x_{max}, 0)$$
$$B(x_{max}, y_{max})$$
$$C(0, y_{max})$$

the dimensions of the powder bed being defined as x_{max}, y_{max}. In the following analysis and example, a square powder bed of 100 mm side is assumed ($x_{max} = y_{max} = 100\, mm$). This box is by default the first border box of the layer. All subsequent boxes are identified and numbered by scanning of the area with a vertical line $x = x_0$ that starts at the $x_0 = 0$ position and ends at the $x_0 = x_{max}$ position. A border curve gets identified when the scanning vertical line intersects or comes into contact with one.

The numbering of the border curves begins from the left of the x-axis. The first border encountered by the vertical $x = x_0$ scanning line as it scans the $(OABC)$ border is named “Border 2”, the next one “Border 3”, etc.

In the case that the vertical scanning line will encounter two border curves simultaneously (at the same $x = x_0$ coordinate), these border lines are numbered starting with the one with the smallest $y = y_0$ value of encounter as the $(OABC)$ border gets scanned by the horizontal $y = y_0$ line, in an upwards scan. However, it is also possible that two border curves are encountered by the vertical scanning line at exactly

the same point. These special cases and the numbering rule followed are explained in *Figure 6.5*. Three cases are identified:

1. *Case 1:* Same x_0 of encounter, but different y_0. Numbering starts from the smallest y_0 value.
2. *Case 2:* Same x_0 and y_0 value of encounter. The numbering starts with the border curve that gets intersected at a lower y_0 value when the vertical scanning line moves at $x=x_0+dx$.
3. *Case 3:* Same as in Case 2, but with nested (i.e., multi-material) features.

As a general and universal rule, the border curves that are positioned closer to the axes (x=0 primarily and y=0 secondarily) are numbered prior to the ones positioned further from the axes. At the end of the border curve numbering process, we end up having N_b border curves. Two border curves might be in contact with each other, but it is impossible to intersect each other.

Each border curve must be a closed curve, so that it defines a "feature", i.e., a smaller area within the $(OABC)$ border box. A feature is defined as a uni-material or multi-material area that is enveloped by a border curve. Note that a multi-material feature nests further features, which can also be multi-material. By contrast, a uni-material feature cannot nest any features by definition. A feature, in accordance to the constraint that applies to border curves, can possibly be nested within another one or be in contact with another one. A case of a uni-material feature is the one defined by border 4 or the one defined by border 5, see *Figure 6.2*. A case of a multi-material feature is the one defined by border 2, see *Figure 6.2*. Each border line and, subsequently, each feature, gets enveloped in a box, see *Figure 6.2*. The slicing software is responsible for assigning a material to each uni-material feature. It should be noted that material type is assigned to multi-material features as well, since there are areas within a multi-material feature that do not belong to a certain uni-material feature (i.e., they are not enveloped by a closed border curve). This can be depicted by the points of the circular ring that is defined by Border Curves 2 and 3, see *Figure 6.2*. These points belong to Feature 2, but not to Feature 3. Hence, they do not belong to a uni-material feature, however, they, too, must be covered by a powder material. That's why a material is assigned to Feature 2 as well, despite it being multi-material.

Figure 6.2 depicts the numbering of the 5 border curves of the pattern introduced in *Figure 6.1*. Each border curve is encompassed in a Box, that is assigned the same number as the one that identifies the border curve. Each box is defined by its limits (i.e., the corner coordinates) as follows:

For the i^{th} box:

$$x_{i,L} \rightarrow x_{i,R}$$

$$y_{i,D} \rightarrow y_{i,U}$$

Where (L, R, D and U) stand for (Left, Right, Down and Up) respectively. *Figure 6.3* depicts the limit coordinates of the border boxes.

In general, the algebraic definition of a border curve is more accurate, since the curve depiction accuracy does not depend on the distance between the points which are connected via linear segments in the numerical method. However, it is far more difficult to define every border curve via algebraic equations, since, most of the times, the equations used will be very complex, such as b-splines or Bezier curves, which drastically increases the computational time, as the equations that need to be solved in order to develop the fronts (see next chapter) are much more complicated.

The point-based depiction of border curves provides easily solvable equations, in the form of intersecting linear equations, in order to define the fronts, while it is also much easier to extract data in numeric form via any slicing of 3D/2D CAD software.

This is the reason why the numerical depiction of border curves was selected in this work.

An order of complexity n_{com} is defined for every feature. For uni-material features, this is equal to 1, while, for multi-material features, this is equal to the number of nested features within the outer feature (n_{nested}), plus one.

$$n_{com} = n_{nested} + 1$$

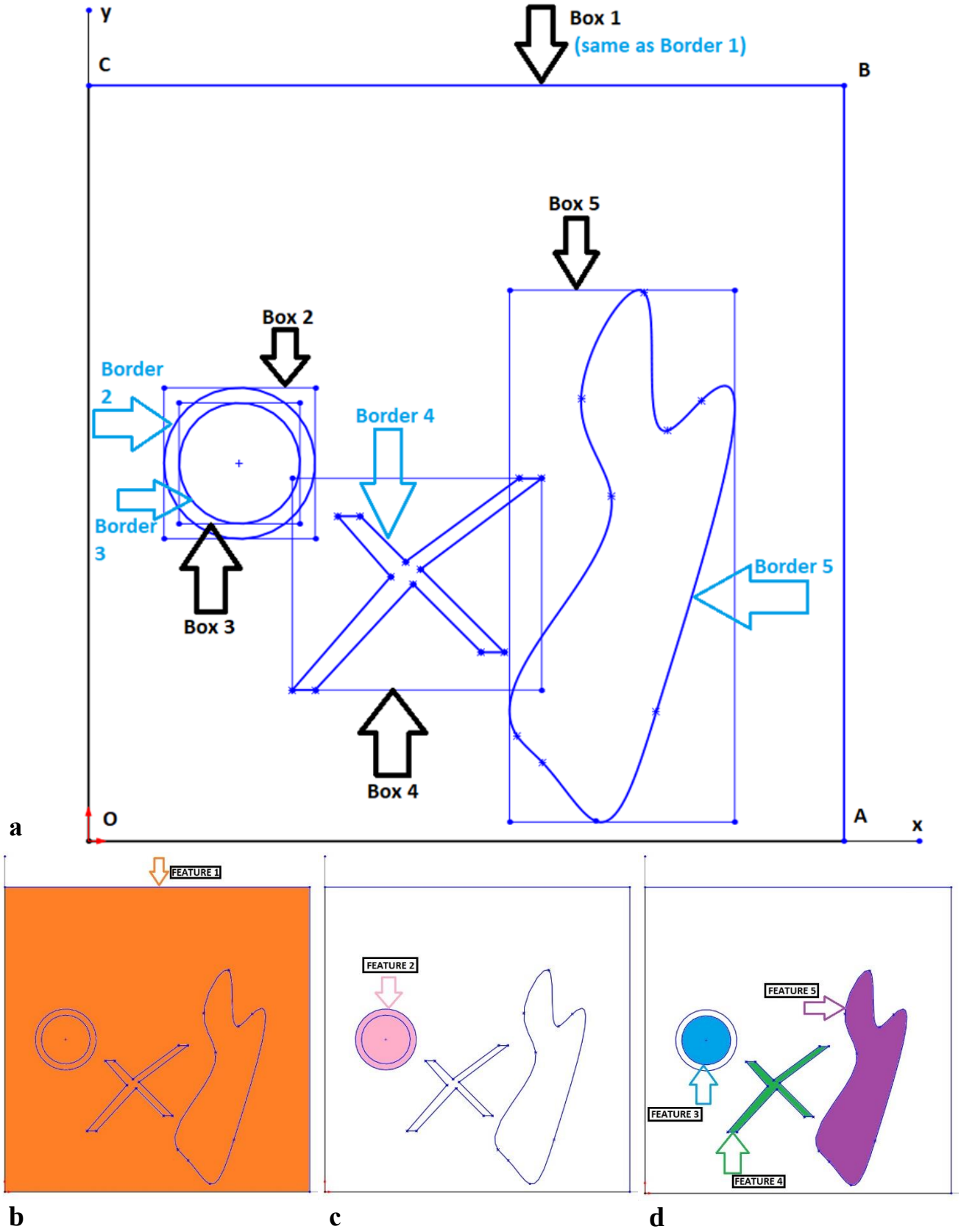

Figure 6.2*: *(a) Border curve numbering and definition of surrounding limit boxes; ***(b)-(c)*** multi-material features of the pattern; ***(d)*** uni-material features of the pattern.

So, the order of complexity of the 2nd feature of *Figure 6.2* is 2, because feature 2 nests feature 3, while the complexity of features 3, 4 and 5 is 1, because neither of these features have any nested features. Let us note that, it is possible that a box nests another one, but the respective features both have a complexity order of 1. In *Figure 6.4*, Box 1 nests box 2, but both features 1 and 2 are uni-material features (i.e., they both have an order of complexity equal to 1). This happens because feature 1 does not nest feature 2. If a feature is multi-material, its box nests other boxes too, however, it is possible that a uni-material feature's box nests other boxes as well. Furthermore, a multi-material feature might nest other multi-material or uni-material features.

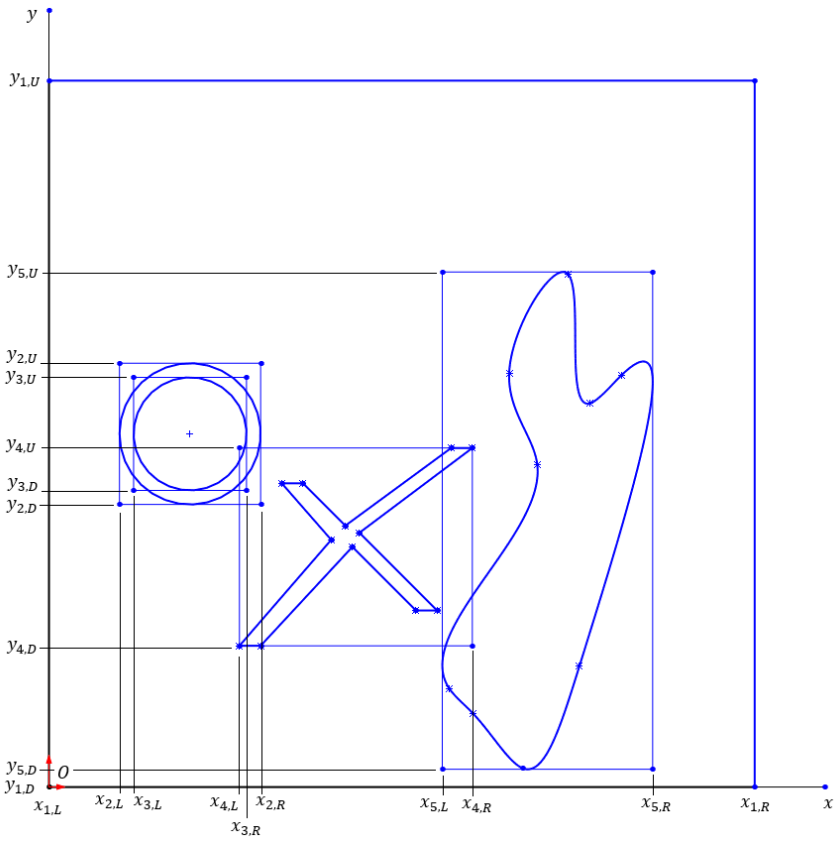

***Figure 6.3*:** Border box limit coordinates.

After the boxes have been defined and numbered, the powder type array is completed, by order of appearance, as shown in the two examples of *Figure 6.2*.

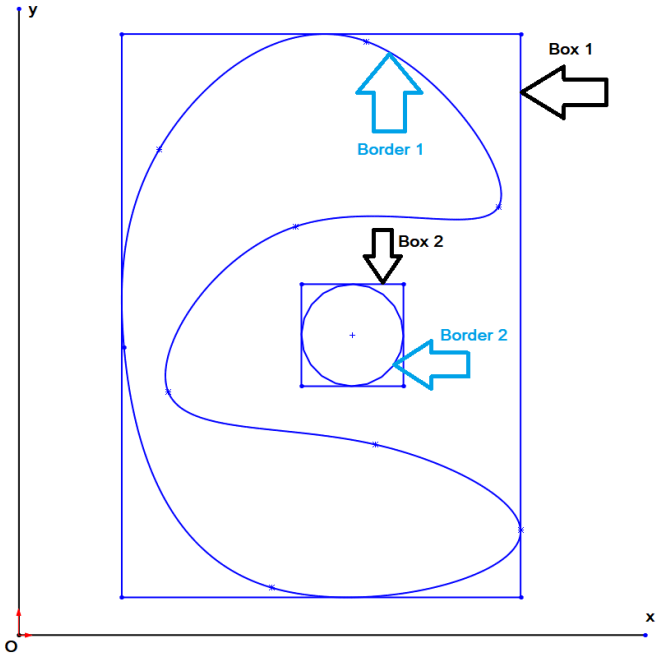

***Figure 6.4*:** Special case of feature complexity.

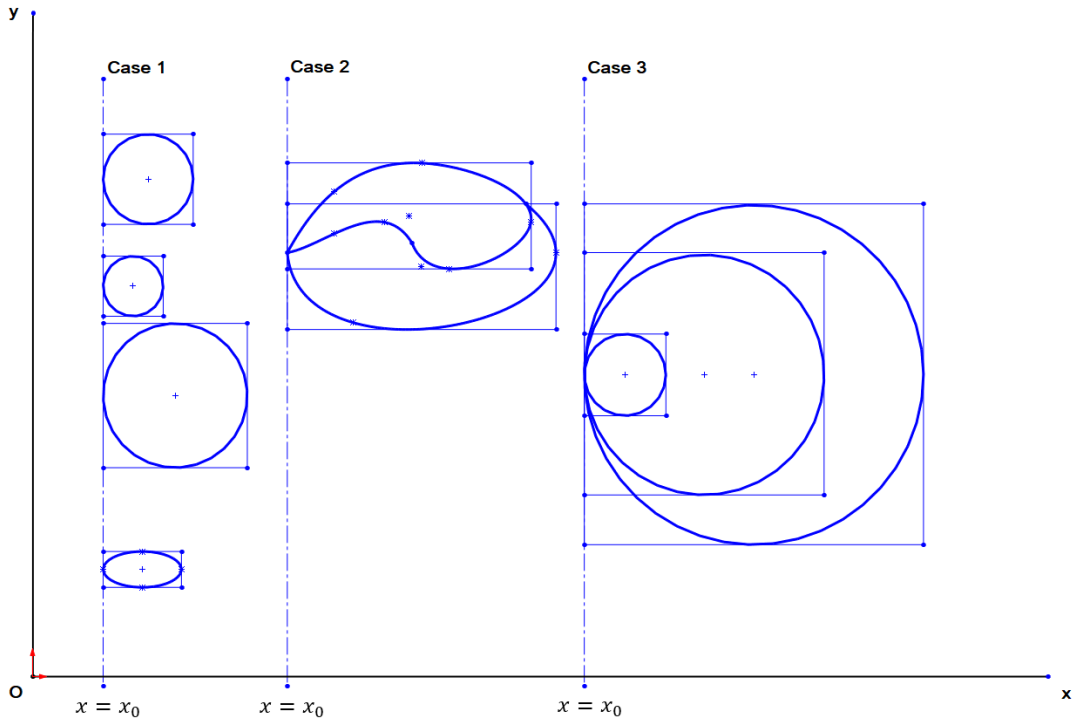

***Figure 6.5*:** Special cases of border curve numbering.

6.1.3 Step 3: Left and Right Front Development (X-Axis Segmentation)

As an essential step in the method, specific uni-material subareas need to be isolated. These subareas are not to be confused with features. A feature is the area encompassed by a border curve and it might be uni-material or multi-material. The subareas that are defined by this step of the method are strictly uni-material and are encompassed by sections of multiple border curves. The isolation of these uni-material sub-areas happens via two "fronts", namely the left and the right front. In order to develop these fronts, the assumption that all border curves behave as opaque walls, hence impenetrable by light, is made. For the initialization of the method, the first left front is defined as the line (AOCB), see *Figure 6.2*. We assume that every point of the left front casts a light ray, parallel to the Ox axis, extending towards the right-hand side. Each light ray moves only through the 1st powder type, till it meets an opaque surface, i.e., till it "collides" onto a feature. At that point, the light ray stops. The locus of these points defines the 'right front'.

In the second iteration, the first iteration's right front now becomes the second iteration's left front. The light rays are cast from the new left front. Again, the light rays work in exactly the same way as in the previous iteration, but now they only move freely through the 2nd powder type. The other powder types are considered "opaque" and do not allow the light rays to be transmitted through them. The light rays again stop when they intersect a feature, defining a point of the second iteration's right front. The process continues, till the entire surface is covered.

The third iteration is conducted in the same way, but it allows the transmission of light rays through the 3rd powder type, if it exists. If only two powder types exist, then the third iteration again allows the light ray transmission through the 1st powder type. The maximum number of iterations is equal to the number of different powder types ($n_{p.t.}$) multiplied by the maximum number of intersections (n_{max_int}) a horizontal line ($y=y_0$, $y_0 \in [0, y_{max}]$) can have with the border curves.

This process will be termed "x-axis surface segmentation" from now on. The left and right front of each iteration isolate a uni-material subarea which will be covered by the pre-assigned powder type before moving to isolate the next uni-material subarea. The comparison between *Figure 6.6* and *Figure 6.7* demonstrate how the x-axis surface

segmentation differs between a dual and a triple-material pattern, even when the geometrical features of the layer are identical. *Figure 6.6* shows every step of the dual material x-axis surface segmentation of the pattern shown in *Figure 6.1(Left)*. The 1st powder type is depicted with green colour, while the 2nd powder type with purple. *Figure 6.7* shows every step of the triple material x-axis surface segmentation of the pattern shown in *Figure 6.1(Right)*. The 1st powder type is depicted with green colour, the 2nd powder type with purple and the 3rd powder type with blue. In both *Figure 6.6* and *Figure 6.7* the powder that is being deposited in the current step is depicted with deeper shades, while the powder that has been deposited in previous steps is depicted with lighter shades.

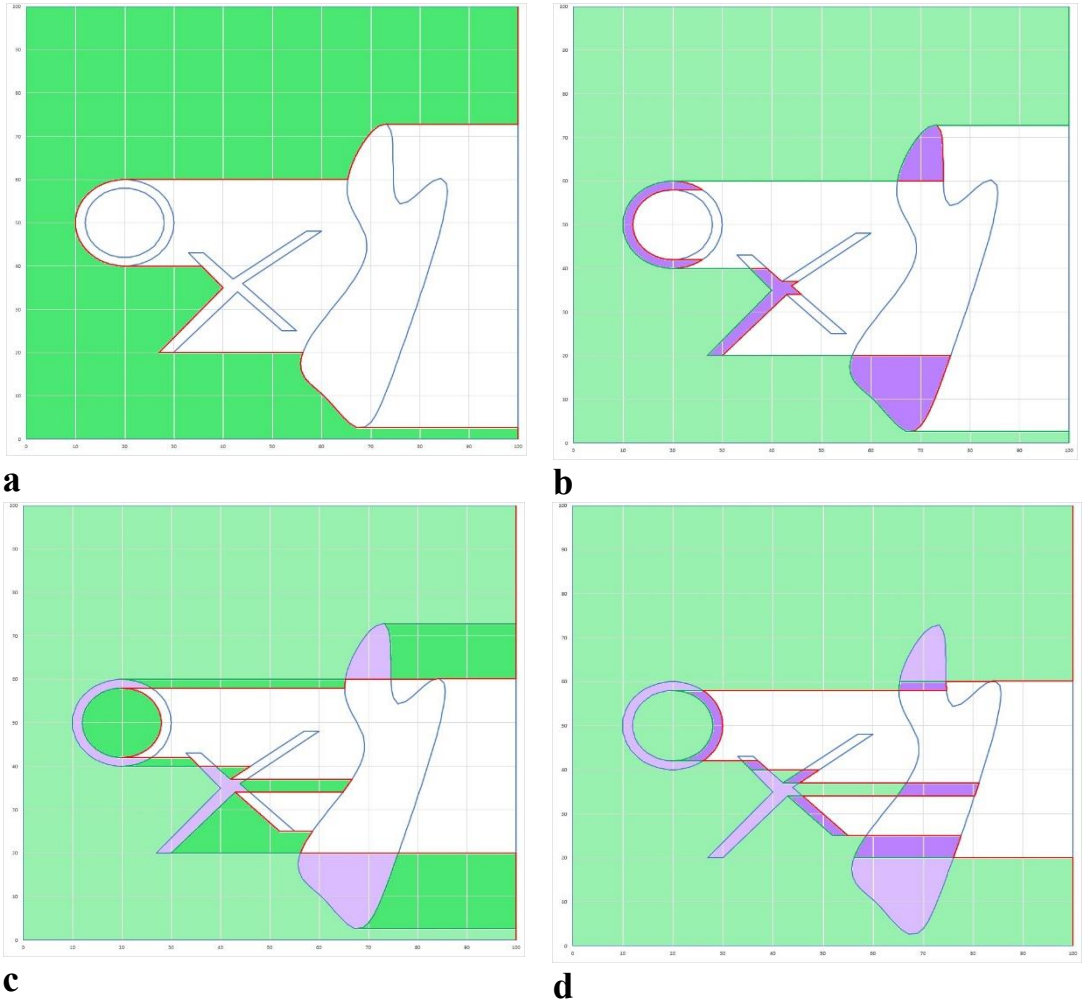

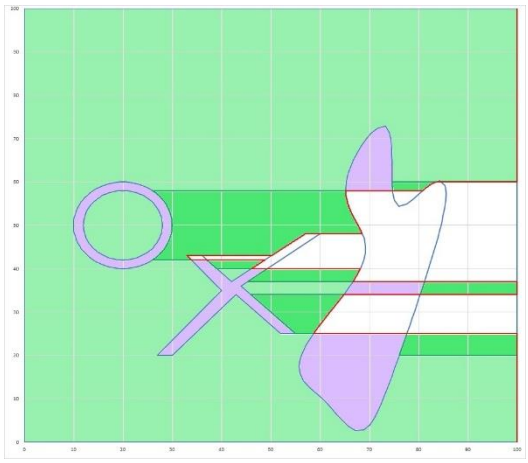

e

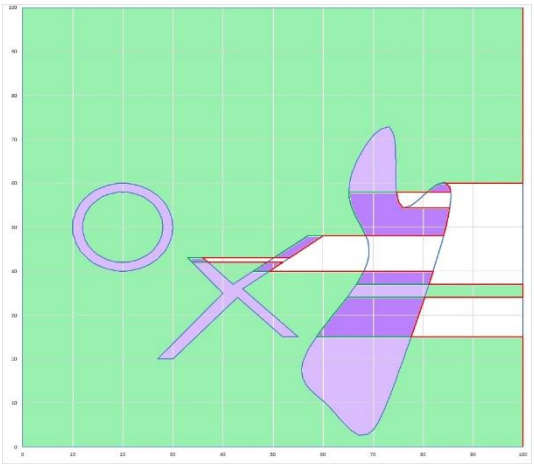

f

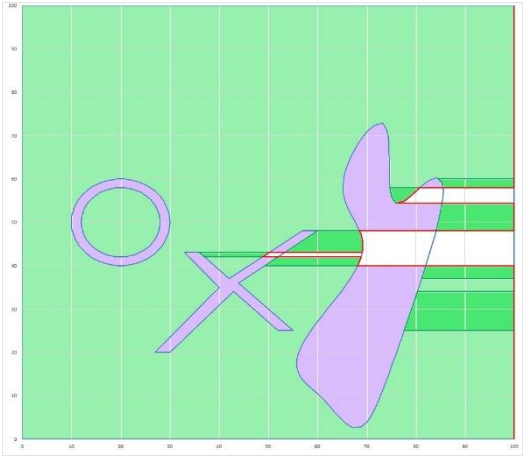

g

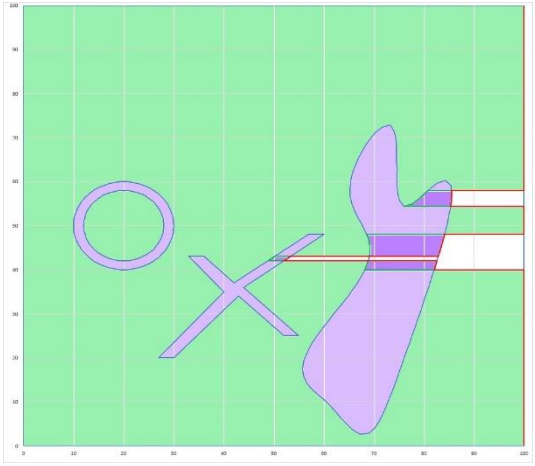

h

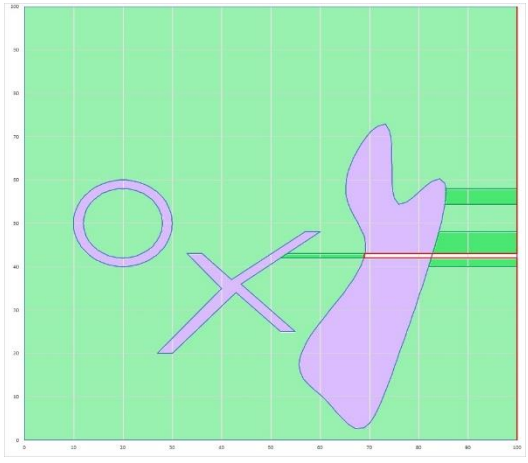

i

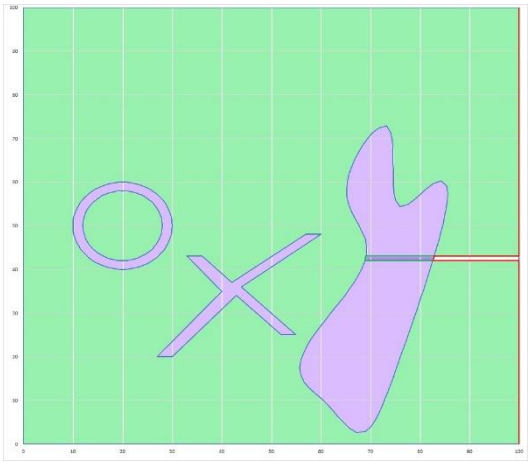

j

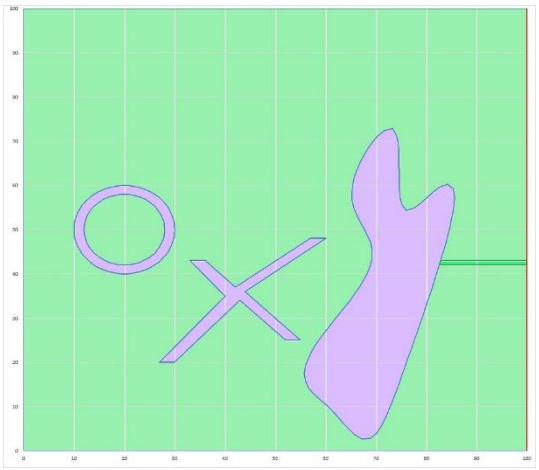

k

Figure 6.6*:** Dual material x-axis surface segmentation example; ***(a)-(k): iterations of the method.

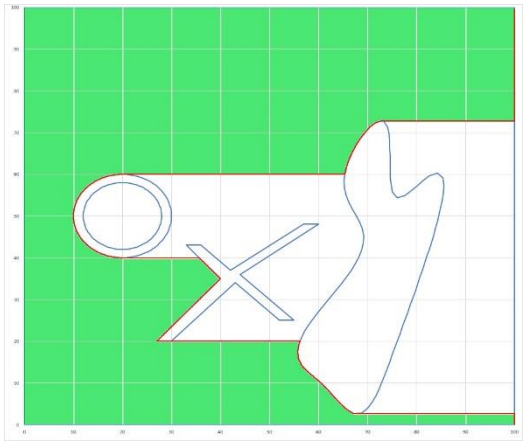

a

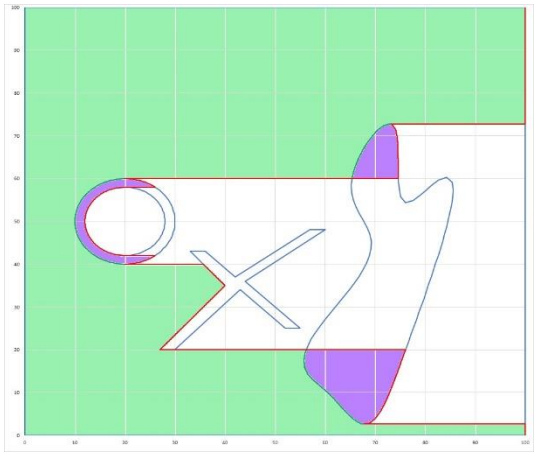

b

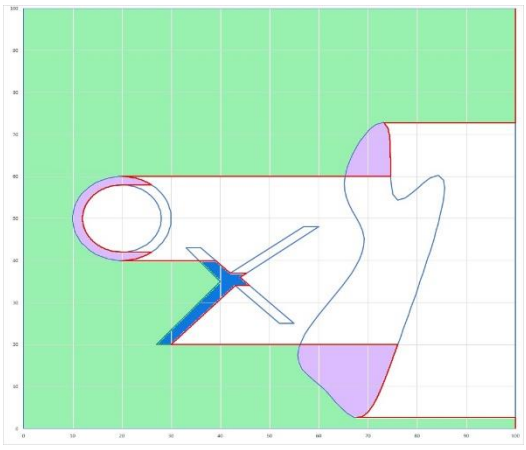

c

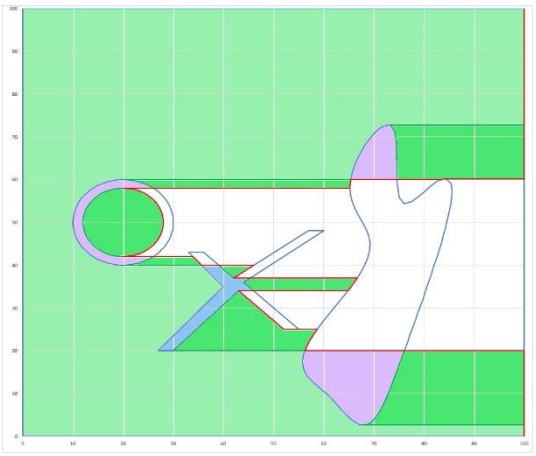

d

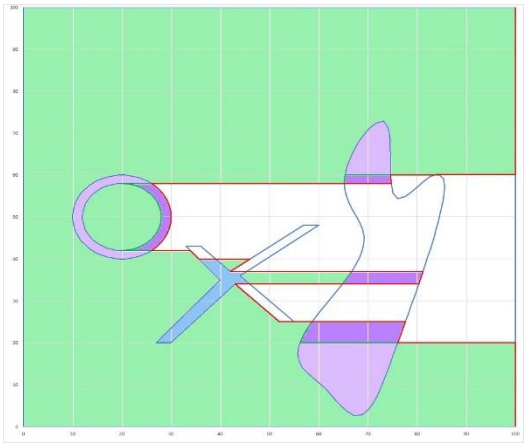

e

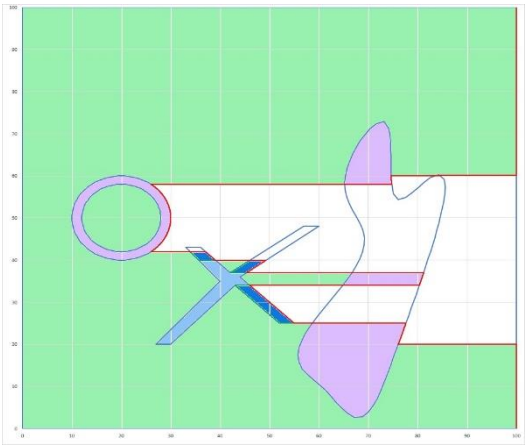

f

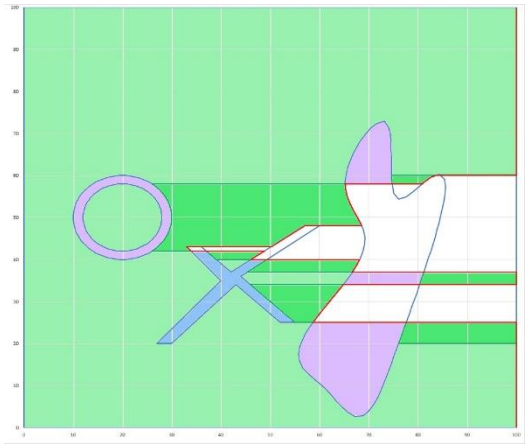

g

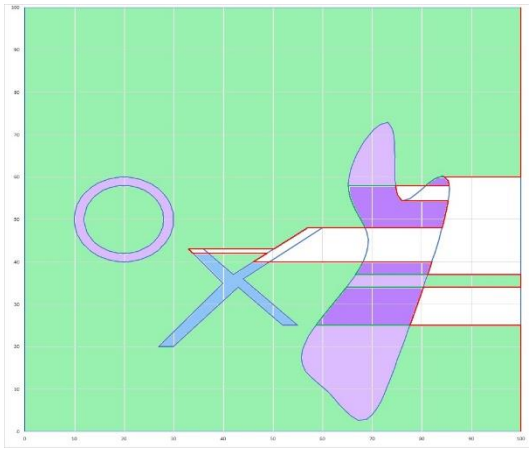

h

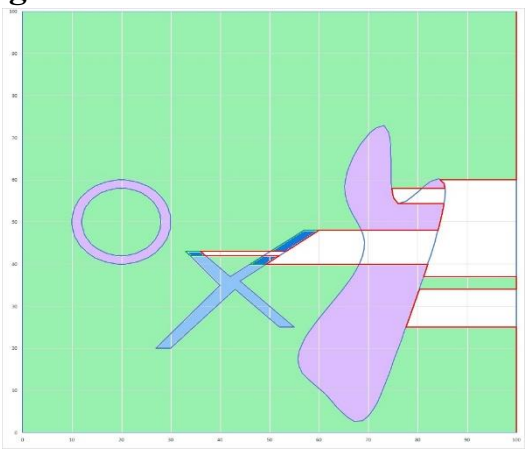

i

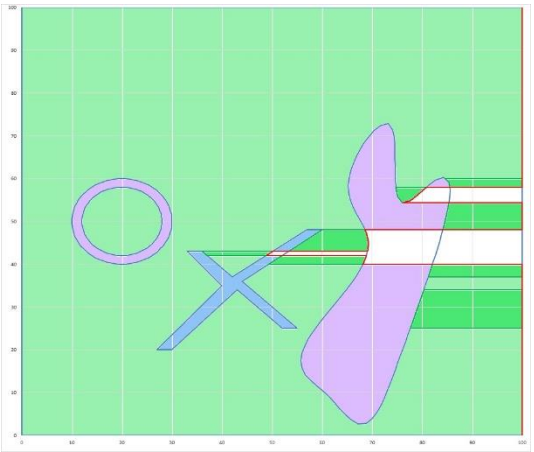

j

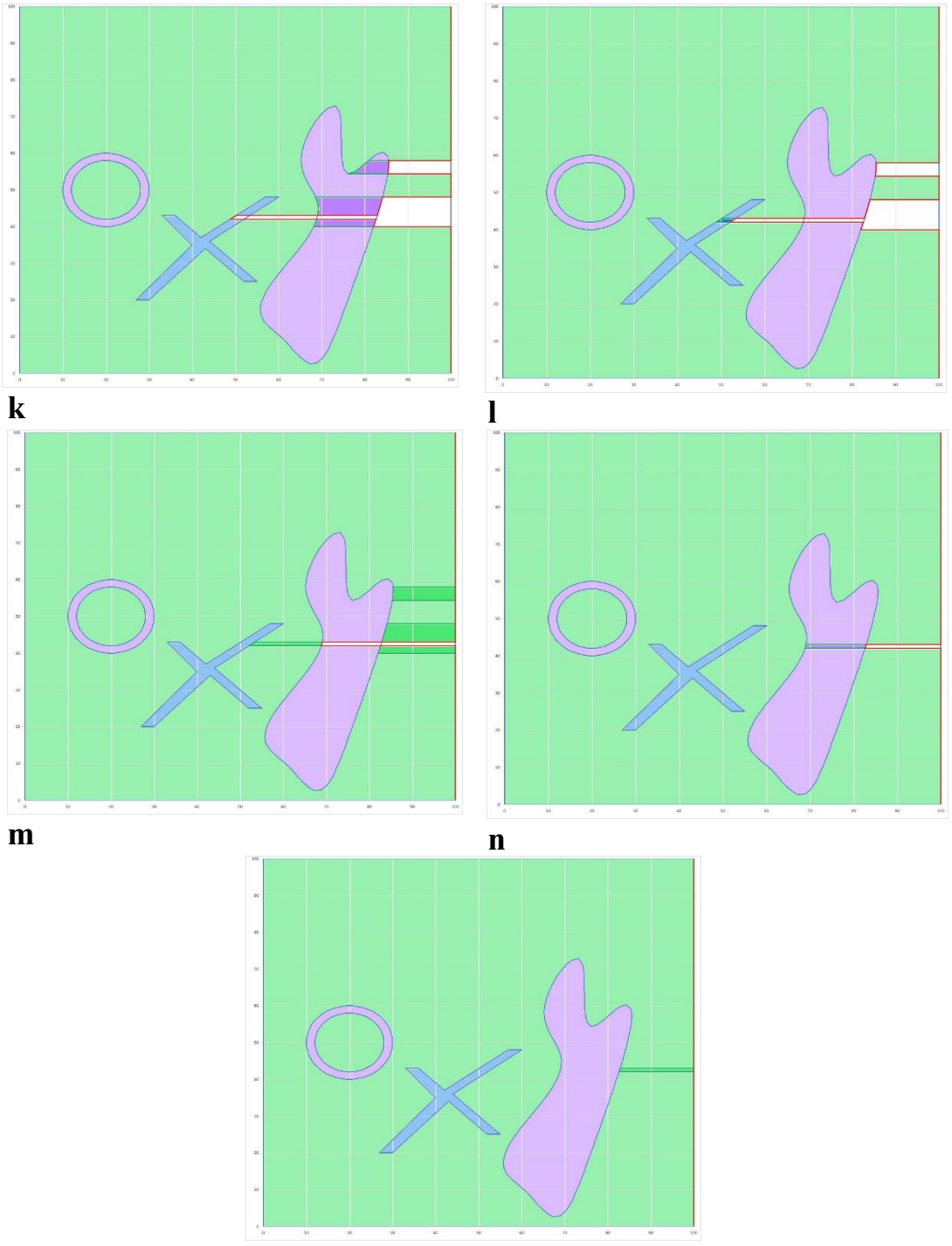

Figure 6.7*:** Triple material x-axis surface segmentation example; ***(a)-(o): iterations of the method.

In both *Figure 6.6* and *Figure 6.7*, the left fronts are depicted with green colour and the right fronts with red colour. The areas where the left and right front coincide are visualized with red colour as well.

The development of the left and right front for each step of the x-axis segmentation process is carried out by a two-part C-code that can be found in *Sections 8.4* and *8.5*

(*Appendices D* and *E*). The code of *Appendix D* (*Section 8.4*) is presented by the flowchart of *Figure 6.8*. It initially solves the problem of finding the intersections of the border curves with every horizontal "light ray" $y = y_0, y_0 \in [y_{1,D}, y_{1,U}]$ and stores them in a file which will be opened by the code in *Appendix E* (*Section 8.5*), which is responsible for sorting these intersection points into left and right fronts based on the material distribution within the layer that is defined inside the program by the user. The code of *Appendix E* (*Section 8.5*) is presented by the flowchart of *Figure 6.9*.

6.1.3.1 Intersection Calculating Code

The code of *Appendix D* (*Section 8.4*) is presented by the flowchart of *Figure 6.8*.

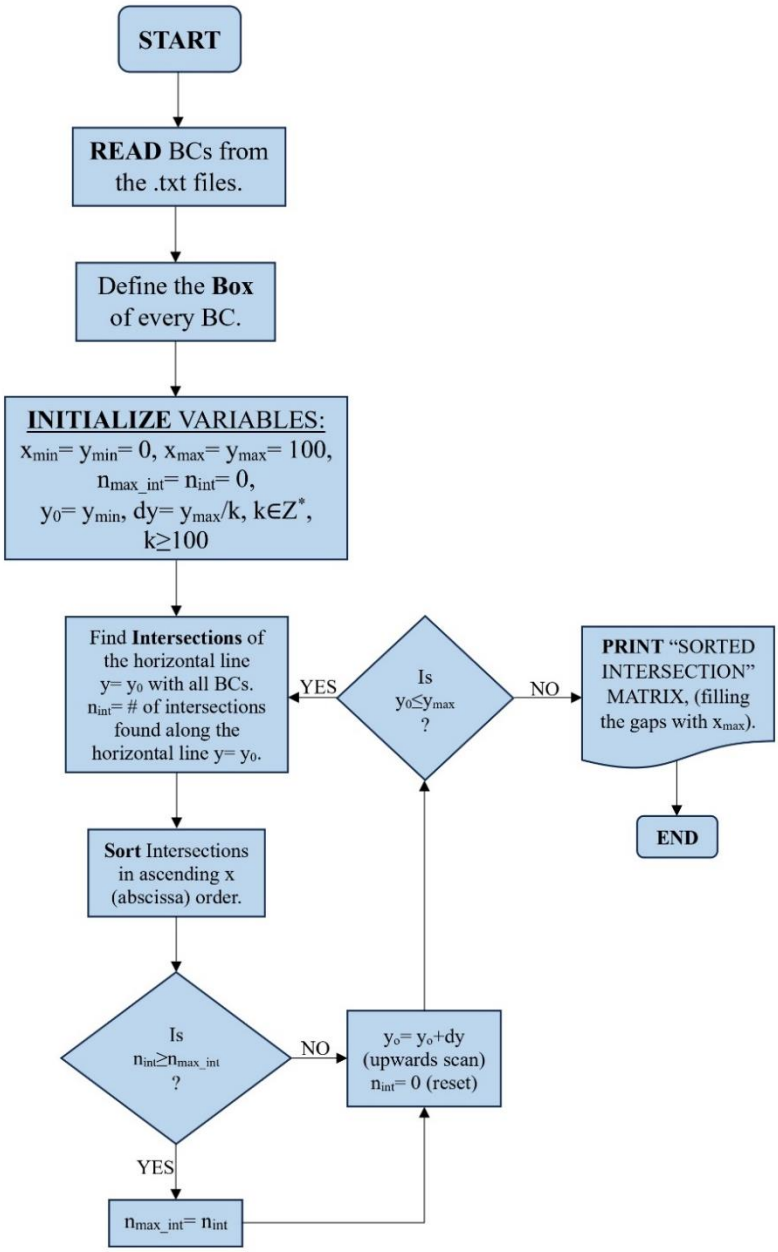

Figure 6.8: Flowchart of the C-code of Appendix D.

The *Appendix D* (*Section 8.4*) code's function is the following. The code opens the N_b .txt files that contain the coordinates of the points of each border curve. After reading and storing these data in arrays, the code calculates the maximums and minimums of each border curve, in order to define the $x_{i,L}$, $x_{i,R}$, $y_{i,D}$ and $y_{i,U}$ values. After this, the code enters a loop where the y axis is scanned upwards. The code calculates and stores the coordinates of the intersection points between every $y = y_0$, $y_0 \in [y_{1,D}, y_{1,U}]$ horizontal line with every border curve. If two consecutive points of the i[th] border curve are the $A(x_j, y_j)$ and $B(x_{j+1}, y_{j+1})$, then they are connected by a linear segment, the equation of which is given as

$$(\varepsilon_{AB}): y = \frac{y_{j+1} - y_j}{x_{j+1} - x_j} x + \frac{y_j x_{j+1} - y_{j+1} x_j}{x_{j+1} - x_j}$$

The intersection points are calculated by solving the following system.

$$(\Sigma_1): \begin{Bmatrix} y = y_0 \\ y = \frac{y_{j+1} - y_j}{x_{j+1} - x_j} x + \frac{y_j x_{j+1} - y_{j+1} x_j}{x_{j+1} - x_j} \end{Bmatrix}$$

However, in order for the horizontal line $y = y_0$ to intersect the linear segment (AB), it is necessary that the following equation applies:

$$(y_j - y_0)(y_{j+1} - y_0) < 0$$

In that case, the intersection point is given as

$$\Gamma_{int} \left(\frac{x_{j+1} - x_j}{y_{j+1} - y_j} y_0 + \frac{y_{j+1} x_j - y_j x_{j+1}}{y_{j+1} - y_j}, y_0 \right)$$

Table 6.1: The structure of "SORTED INTERSECTIONS" matrix.

y	Int_1	Int_2	$\cdots$	Int_k	$\cdots$	$Int_{n_{max\_int}}$
$\mathbf{0}$	$Int_1(0)$	$Int_2(0)$	$\cdots$	$Int_k(0)$	$\cdots$	$Int_{n_{max\_int}}(0)$
$\boldsymbol{dy}$	$Int_1(dy)$	$Int_2(dy)$	$\cdots$	$Int_k(dy)$	$\cdots$	$Int_{n_{max\_int}}(dy)$
$\mathbf{2}\boldsymbol{dy}$	$Int_1(2dy)$	$Int_2(2dy)$	$\cdots$	$Int_k(2dy)$	$\cdots$	$Int_{n_{max\_int}}(2dy)$
$\vdots$	$\vdots$	$\vdots$	$\ddots$	$\vdots$	$\ddots$	$\vdots$
$\boldsymbol{jdy}$	$Int_1(jdy)$	$Int_2(jdy)$	$\cdots$	$Int_k(jdy)$	$\cdots$	$Int_{n_{max\_int}}(jdy)$
$\vdots$	$\vdots$	$\vdots$	$\ddots$	$\vdots$	$\ddots$	$\vdots$
$\boldsymbol{y_{max}}$	$Int_1(y_{max})$	$Int_2(y_{max})$	$\cdots$	$Int_k(y_{max})$	$\cdots$	$Int_{n_{max\_int}}(y_{max})$

The code uses checks to include intersections which might coincide with a point of the border curve as well. After all the intersections with all the border curves are calculated at a certain ordinate value y_0, these are sorted by increasing abscissa value. Then, the code moves onto the next ordinate value $y_0 + dy$ and repeats the process. The intersections are then stored into a .txt file in order to be opened by the code of *Appendix E* (*Section 8.5*), which is responsible for their sorting into fronts, based on the material of each uni-material area of the layer. This file contains a matrix called "SORTED INTERSECTIONS", the structure of which can be seen in *Table 6.1*.

6.1.3.2 Front Developing Code

The code of *Appendix E* (*Section 8.5*) is presented by the flowchart of *Figure 6.9*.

Initially, it assigns a material to each border curve. As explained previously, each border curve defines a closed area, inside which there might be only one or more materials, depending on the complexity n_{com} of the curve. In the given pattern of the example (see *Figure 6.1, Figure 6.2* and *Figure 6.3*) the border curves 3, 4 and 5 have a complexity of 1 and the 2nd border curve a complexity of 2. Finally, the border curve 1 has a complexity of 5. It is easy to assign a material to the border curves that have a complexity of 1, however, it is slightly more complicated for border curves of a higher order of complexity. The border curve 2 is a circle which nests completely the border curve 3, which is a circle of a smaller radius.

The two circles have no common points, i.e., they are not contacting with each other, so the material assigned to the 2nd border curve is the one that is in contact internally to it, i.e., material #2 (in both *Figure 6.1(Left)* and *Figure 6.1(Right)* examples-dual and triple material deposition respectively). In general, the materials (i.e., the powder types PT) assigned to each border curve $\left(PT_{BC_k}, k \in [1, N_b]\right)$ are stored in an array named MAT, as shown in the *Equation (6.3)*.

$$\begin{aligned} MAT &= \left[PT_{BC_1} \quad PT_{BC_2} \quad \cdots \quad PT_{BC_k} \quad \cdots \quad PT_{BC_{N_b}}\right]^T \\ &= \left[PT_1 \quad PT_{BC_2} \quad \cdots \quad PT_{BC_k} \quad \cdots \quad PT_{BC_{N_b}}\right]^T \end{aligned} \tag{6.3}$$

By definition, as mentioned earlier, material #1 is assigned to the BC1 and material #2 to the BC2. So, in the case of dual deposition (*Figure 6.1(Left)*) the array of materials assigned to the border curves is

$$MAT_{dual} = [PT_1 \quad PT_2 \quad PT_1 \quad PT_2 \quad PT_2]^T$$

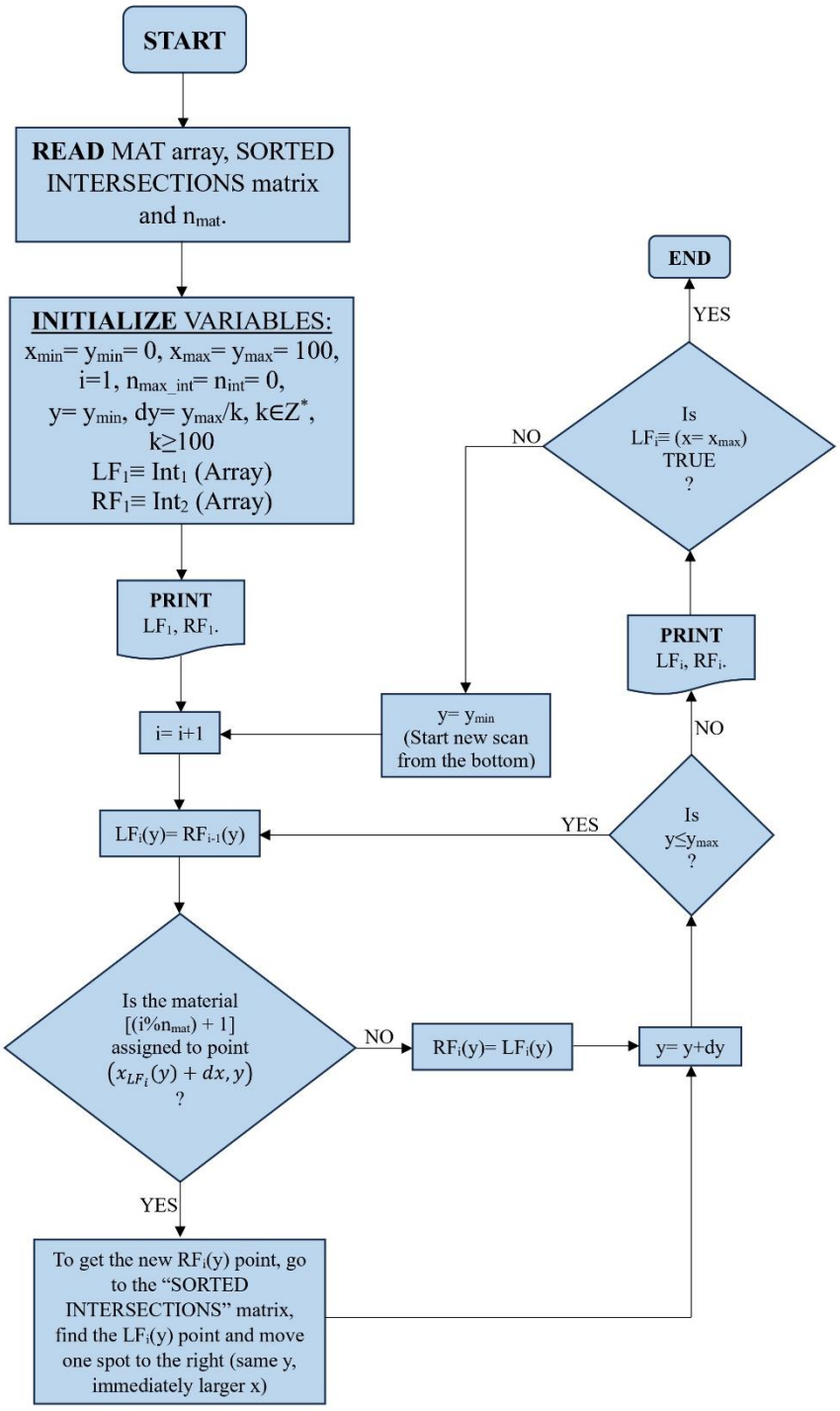

Figure 6.9: Flowchart of the C-code of Appendix E.

While the array of materials assigned to the border curve for the triple material example (*Figure 6.1(Right)*) is

$$MAT_{triple} = [PT_1 \quad PT_2 \quad PT_1 \quad PT_3 \quad PT_2]^T$$

After assigning materials to each border curve, the code begins an iteration from the first to the last powder type. During each iteration a uni-material area that only consists of the respective powder type is created by two "fronts", a left and a right front. So, in the first iteration, powder type 1 is deposited in the uni-material area that is defined by the left front #1 (LF1) and the right front #1 (RF1), in the second iteration, powder type 2 is deposited in the uni-material area defined by the left front #2 (LF2) and the right front #2 (RF2) and so on, until the layer is complete.

The LF1 is, by definition, the left vertical line of the BC1, while the RF1 is the locus of the second intersections in every ordinate value $y_0 \in [y_{1,D}, y_{1,U}]$. By definition, the left front of each iteration coincides with the right front of the previous one, so

$$LF_i \equiv RF_{i-1}$$

The new right front, RF2, is developed by examining the locus of the points that are located infinitesimally close to the right-hand side of the LF2. At each ordinate value $y_0 \in [y_{1,D}, y_{1,U}]$, the code moves each point of the LF2 towards the right by a small value dx. Then, the point $\Delta\left(x_{LF_2}(y_0) + dx, y_0\right)$ is examined. If this point is internal to a uni-material area that is assigned the material #2, then the RF2 gets assigned the next intersection of the y_0 ordinate. Otherwise, if this point is internal to a uni-material area of any other material, which is not to be deposited during this iteration of the process, then RF2 is assigned the same point the LF2 is assigned at this specific ordinate value y_0. This procedure is termed "internality check". In order to be performed, it is necessary to examine which border curve the point Δ is internal to, in order to assign a material to it. The "ray casting algorithm", deriving by the Jordan curve theorem, is used for this purpose [232].

This is a very common problem in computational geometry, aiming to examine whether a point is inside, outside, or on the boundary of a polygon. For simplicity reasons, in this work a point on the boundary is consider internal to the border curve and it is assigned the same material as the material of the border curve that is described. The ray-casting algorithm defines a linear "ray" that starts from the point that is under examination and moves infinitely towards a random, but fixed, direction on the plane of the polygon. This ray may or may not intersect the edge of the polygon. If it intersects the edge of the polygon an odd number of times, then the point is internal to the polygon, while, if it intersects the edge of the polygon an even number of times, the

point is external to the polygon. This is why this algorithm is also known as the "crossing number" or the "even–odd rule" algorithm.

It is possible that a point is internal to more than one border curves. By definition, every point is internal to BC1. If a point is internal to more than one border curves, then we consider it internal to the innermost border curve. For example, the centre of the circle that is the BC2 (see *Figure 6.1, Figure 6.2* and *Figure 6.3*) is internal to BC2. However, it is also internal to BC3. Hence, it is considered internal to BC3 and it is assigned the powder type that is assigned to BC3.

The code of *Appendix E* (*Section 8.5*) uses the ray that starts from the point that is under examination and connects it to the origin of the coordinate system O(0,0). Let the point that is under examination and internality check be $\Delta(x_\Delta, y_\Delta)$, following the terminology used above. The ray that begins from Δ towards the O(0,0) is given by

$$(\varepsilon_{\Delta O}): y = \frac{y_\Delta}{x_\Delta} x$$

To examine whether Δ is internal or external to a border curve, say BCi (the ith border curve), the code calculates every intersection between BCi and $\varepsilon_{\Delta O}$, by solving the following system.

$$(\Sigma_2): \begin{Bmatrix} y = \dfrac{y_\Delta}{x_\Delta} x \\ y = \dfrac{y_{j+1} - y_j}{x_{j+1} - x_j} x + \dfrac{y_j x_{j+1} - y_{j+1} x_j}{x_{j+1} - x_j} \end{Bmatrix}$$

Given that two consecutive points of the ith border curve are the $A(x_j, y_j)$ and $B(x_{j+1}, y_{j+1})$, as stated earlier. Since, by definition, x and y are non-negative, i.e., the layer is located in the first quadrant, and the (ΔO) ray starts from Δ and moves only towards lower x and y values, the only acceptable solutions of the system are the ones with

$$\begin{gathered} 0 \le x_{sol} \le x_\Delta \\ \text{and} \\ 0 \le y_{sol} \le y_\Delta \end{gathered} \qquad (6.4)$$

If a solution is detected and the ray-intersection criterion, see *Equation (6.4)*, does not apply, it means that the solution lies on the side of the (ΔO) line that stretches to +∞, hence it is not taken into consideration for the internality check.

After the code completes the internality check, it assigns the correct material to the examined point, and, if the assigned material is the one that is to be deposited during the current iteration, then the new right front point that is selected for the current y_0 ordinate value is the next one of the stored intersections calculated by solving the (Σ_1) system, by increasing abscissa value (see *Table 6.1*). In any other case, the new right front point remains the same as it was during the previous iteration of the code. In this way, the code manages to implement the "opaque wall" method that was described in previous Sections.

The code finishes only when, after some iteration, the new right front coincides with the vertical line $x = x_{1,R}$, i.e., the right limit of BC1.

6.2 Physical Implementation - Testing Apparatus Development

After defining the way in which one multi-material area will be divided into several uni-material areas, in order for the deposition to be performed sequentially it is necessary to define the assembly and the geometry of the apparatus that will be responsible for performing the area segmentation. As mentioned in *Section 6.1*, this method is based on the function of contour gauges. A contour gauge (also known as profile gauge) is a tool for recording the cross-sectional shape of a surface. It consists of an array of very thin "blades" made of metal or plastic, which are kept parallel with each other by a frame, which also maintains them on the same plane. By independently sliding parallel alongside each other when pressed on an object, in a perpendicular direction with regard to the frame, it is possible to replicate and copy the shape of the said object. Such devices are commonly used in carpentry and DIY projects. *Figure 6.10* demonstrates some typical examples of contour gauge usage and gives general instructions on how it is commonly used to replicate shapes.

After the x-axis surface segmentation (see previous Section) is completed, each and every one of the uni-material sub-areas that got defined must be sequentially covered by the predetermined powder types. In order for the powder to only be deposited onto the sub-area defined, a system must be developed that will physically isolate the sub-area with acceptable accuracy and repeatability. The proposed design features a dual contour gauge, as can be seen in *Figure 6.11*. It consists of two arrays of thin blades

that can slide parallel with and independently of each other, along the x axis of the powder bed. One array is positioned on the left-hand side of the surface of the fabrication table, and the other one on the right-hand side of the table, the blade fronts facing inwards, towards the center of the powder bed, see *Figure 6.11*. Each blade of the gauges can move separately and is positioned at the predetermined x-coordinate by a micro-stepper motor that pushes it to its place via a probe-tip, or a simple rack-and-pinion method. Once a blade is pushed to its position, it gets prevented from moving backwards via a linear ratchet, which features very fine teeth, in order for the backlash error to be minimized. It is also possible to avoid unwanted movement of each blade by simply applying holding torque onto it via the motor that initially positioned it at the predesignated spot. This holding torque is the most viable solution, since it can be applied during any moment that the blade's spontaneous motion would be unwanted, regardless of the motion's direction, as is the case in the linear ratchet-based solution.

Figure 6.10: Typical contour gauge usage; (Above) Examples of replicating the cross-section of objects; (Below) Instructions of proper usage.

It becomes clear that, by using a dual contour gauge assembly as shown in the *Figure 6.11*, any uni-material areas developed via the x-axis segmentation method described in the previous Section can be isolated. The blades need to be sufficiently thin with regard to both the size of the layer and the size of the features that must be created on the layer.

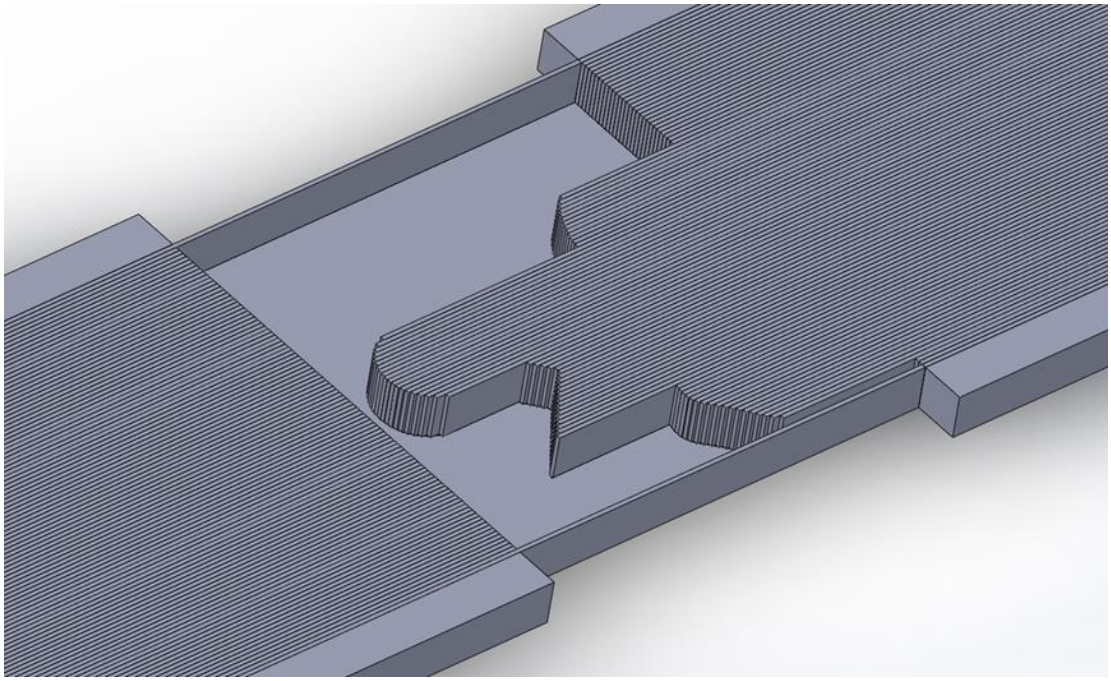

a

b

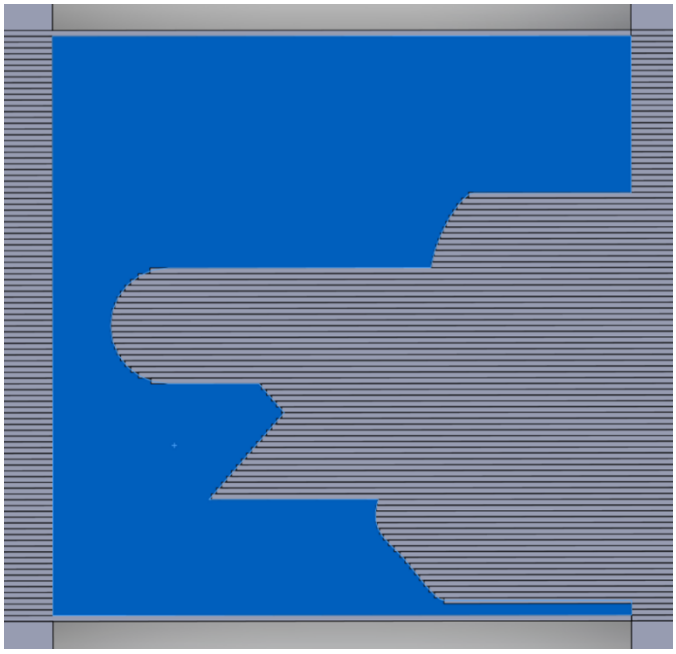

***Figure 6.11*:** Dual contour gauge blade arrangement. The left and right front are created by proper positioning of each blade of the two contour gauges. In this instance, the subarea shown in *Figure 6.6(a)* and *Figure 6.7(a)* is isolated.

The designed apparatus, see *Figure 6.12* has two commercial contour gauges placed facing each other and secured onto an aluminum plate. Four bolts function as spacers between the bottom of the contour gauge blades and the deposition plate. By turning the bolts by 360^{o} clockwise, the contour assembly gets lifted vertically by a distance equal to the step of the bolts' thread. These bolts can also be used to ensure that the

contour gauge assembly is parallel to the deposition plate, ensuring an even powder layer thickness.

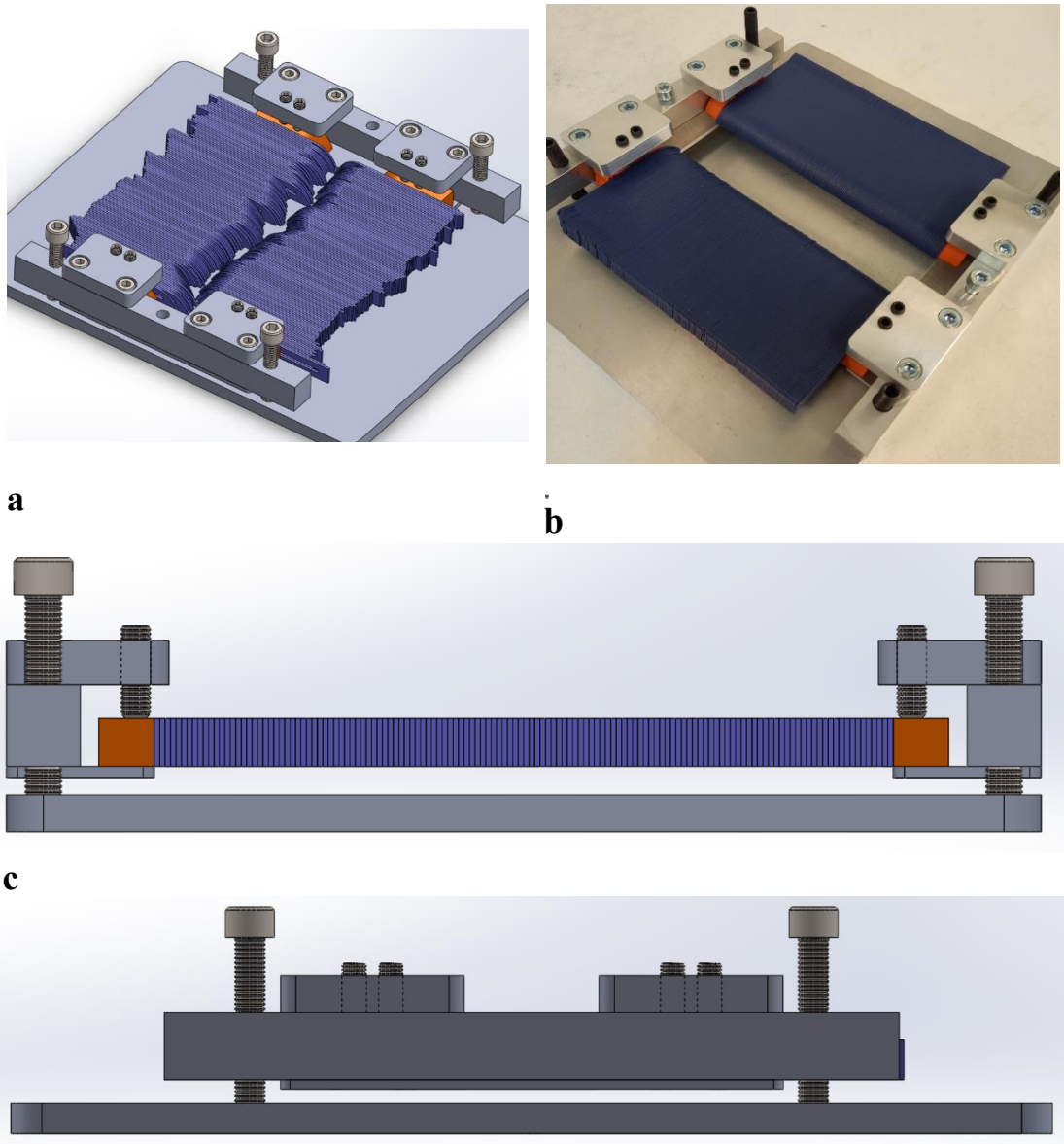

Figure 6.12: Photo and 3D CAD (SolidWorks™) drawings of the multi-material deposition apparatus; ***(a)*** CAD isometric view; ***(b)*** Photo of the manufactured apparatus; ***(c)*** Left side view; ***(d)*** Front view.

For the apparatus that was designed, the blades had a thickness (t_b) of 1mm, however, the verification of the design was also tested via simulation, in order to identify possible design flaws and examine ways to counter potential problems to optimize the finished layer's quality. The multi-material powder spreading verification via simulation will be covered in the next chapter.

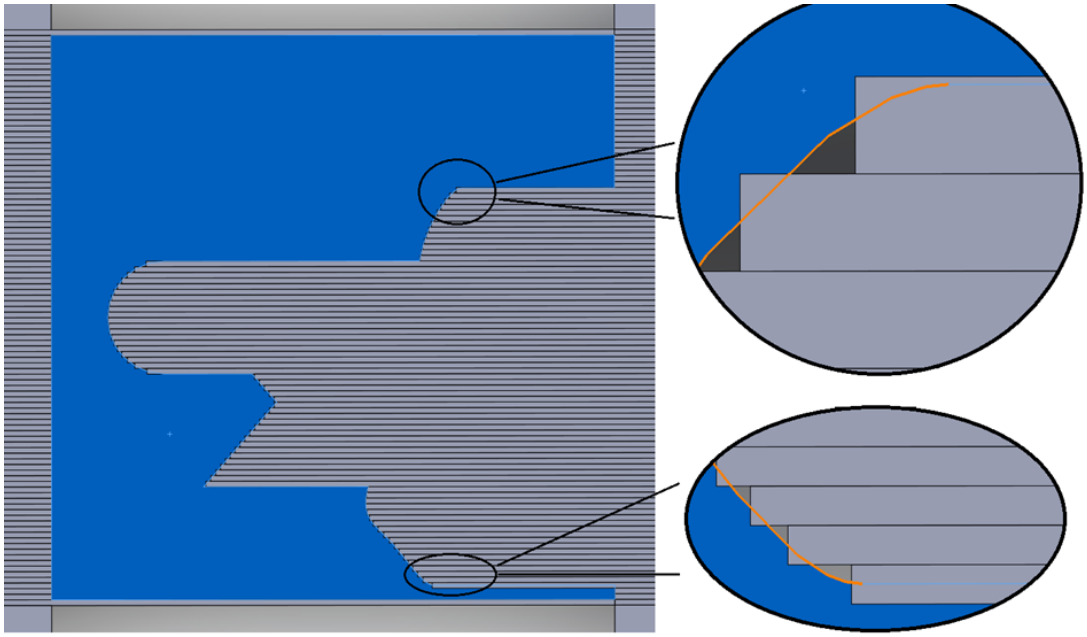

Figure 6.13: Blade thickness-induced error during x-axis segmentation.

Since all the blades have the same thickness and the features that need to be designed within the layer do not necessarily have a width equal to an integer multiple of the blades' thickness, some error is inserted in the representation of the layer's border curves. Additionally, since all the blades are rectangular, the border curves are approximated by vertical and horizontal linear segments. The vertical ones, i.e., the ones along the y-axis, are always equal in length to the blade thickness, while the horizontal ones, i.e., the ones along the x-axis, do not have a fixed length, since their length depends on the border curve that the contour gauge blades aim to approximate. These effects are visualized in *Figure 6.13*.

In order to eliminate this error, it is possible to further divide the uni-material subarea shown in *Figure 6.13*, using a process termed "y-axis segmentation".

The subarea of *Figure 6.13*, that has been defined by the x-axis segmentation process, has seven horizontal lines, as shown in *Figure 6.14*. These horizontal lines further divide it into six new subareas, which are shown in *Figure 6.14* by different colouring, starting from the lowest one (red) and moving to the highest one with regard to its y-value (dark blue).

The y-axis segmentation is introduced in order to ensure accuracy of deposition in the "important horizontal" lines. In *Figure 6.14*, the area has been separated via horizontal lines. The top and the bottom horizontal lines belong to the Box 1 (see *Figure 6.3*),

which makes them the borders of the powder bed. It is common practice to position the under-building part's centre near the centre of the powder bed, to avoid proximity of its walls to the borders of the powder bed. This is because the powder bed quality is drastically reduced in that area. So, the bottom (1st) and top (7th) horizontal lines are named "non-important" horizontal lines for the current y-axis segmentation, and the other ones (2nd through 6th) are named "important". This means that, the inserted approximation error is acceptable in the 1st and 7th lines, but it is not tolerated in the middle horizontal lines.

However, this error is avoided by giving the left and right blade array the possibility to move controllably along the y-axis, parallel to the powder bed, in order to adjust their positioning. The left blade array is responsible for limiting the bottom and left side of each subarea of the y-axis segmentation, while the right blade array limits the right and top side of the area that is to be covered with powder.

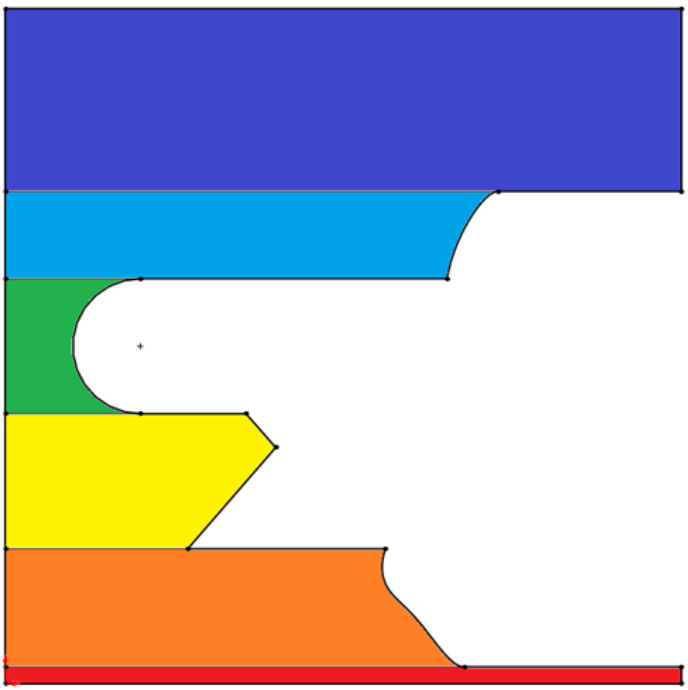

a

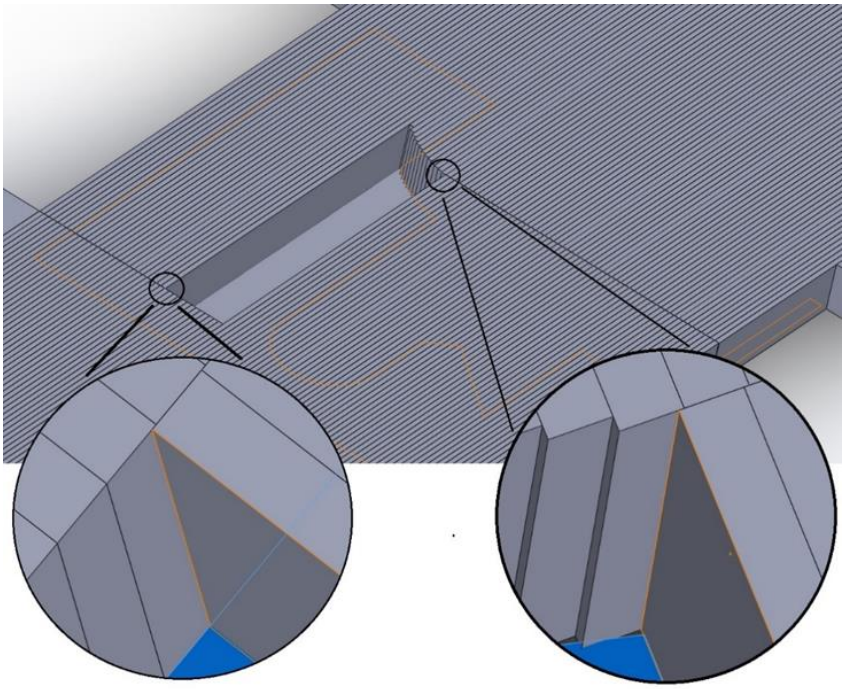

b

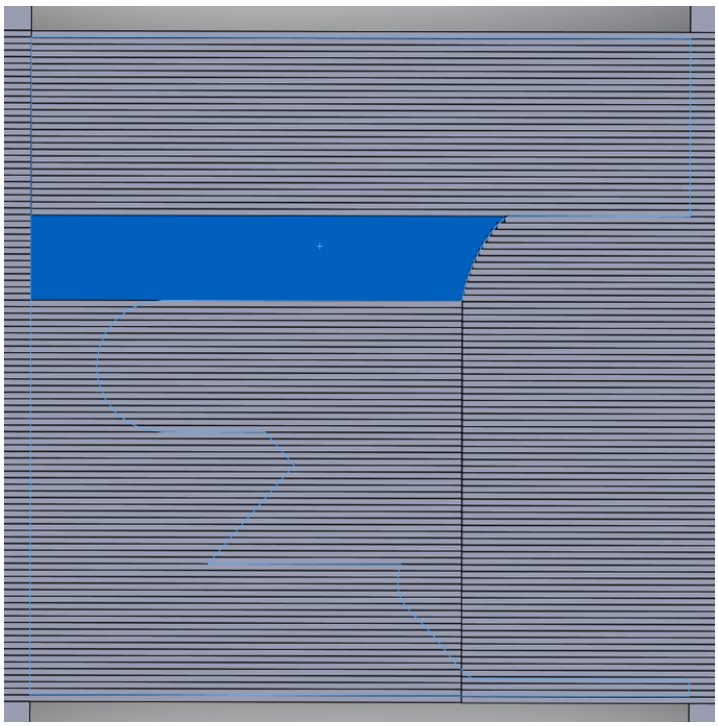

c

Figure 6.14: Y-axis segmentation; ***(a)*** y-axis segmentation of the subarea shown in *Figure 6.13*, ***(b)*** Left and right blade array positioning for coverage of the 5th subarea (light blue) of the y-axis segmentation shown in *Figure 6.14(a)*; ***(c)*** Top view of the isolated 5th subarea (light blue) of the y-axis segmentation shown in *Figure 6.14(a)*.

In this case, if a user judges that accuracy of the said feature is vastly important, the possibility to proceed to y-axis segmentation after the x-axis segmentation is provided. This would, however, create 6 uni-material subareas out of the 1 uni-material subarea defined in *Figure 6.11*, increasing the powder deposition time by approximately 6 times.

In the author's estimation, the accuracy gained like this does not compensate the manufacturing time lost, hence the experiment and simulation that follow will only perform the x-axis segmentation of a surface.

The manufactured apparatus for multi-material deposition facilitates the deposition of one or more layers on top of each other in steps as follows:

1. The two contour gauges are placed at the desired height by manually turning the four bolts at the four corners of the assembly. The height is equal to the theoretical layer thickness. The thickness of the first layer is at minimum equal to 1 mm, since the plate that is contacting on the bottom of the contour gauges has a 1 mm thickness. The following layers can have any value of theoretical thickness the user chooses, by turning the bolts as desired based on the thread's pitch.
2. The blades of the left and right contour gauges are positioned to the proper x-coordinates manually or, for reasons of accuracy and productivity, via a motorized rack-and-pinion system that is capable of transferring motion to each blade individually.
3. The powder is sieved manually above the apparatus, till an adequate amount of powder has filled the first uni-material subarea of the layer. Sieving-based deposition is possible; however, a controlled sieving apparatus is necessary. This is why for this experiment the layer recoating was performed by the contour gauge blades.
4. The left contour gauge moves towards the right front, and the blades function as the powder recoater. The excess powder amount that remains trapped between the two contour gauges gets removed via a small vacuum cleaner (e.g. one used for computer keyboard cleaning) and a brush while the two blade arrays are in contact. The powder removal needs to be performed carefully, in order to not disturb the deposited layer.
5. The right contour gauge is repositioned to develop the new right front and the cycle 'sieving-spreading-excess powder removal' is repeated.
6. Step 5 is repeated until the whole layer has been completed.

The identified flaws of the proposed apparatus design are two; firstly, the two contour gauges are at the same height. This means that, during the spreading step, there is no right limit for the powder, which means that the powder can create a slope that will

move to the right of the pre-designated border during its spreading. This inserts some unwanted error to the final limit between the uni-material areas. Secondly, the excess powder amount gets accumulated on the top of the two blade arrays, in the small V-shaped space that is created between them, while the blades of the left and right contour gauge are in contact, see *Figure 6.15(i)* and *(l)*. The removal of this powder must be performed manually, or automatically by employing a powder suction method that is strong enough to ensure the removal of the excess powder, yet delicate enough to guarantee that the deposited layer will not be affected.

Furthermore, the friction between the blades increases the more the holding bolts get tightened, which means that a golden means must be achieved, ensuring that the contour gauges are secured in place, yet not tightened too much, rendering the blades unmovable, or too stiff to slide. Additionally, there are some design challenges for turning this concept into a fully-functioning, automated powder deposition machine. The blades need to be able to slide independently from each other. However, the motion of a blade is possible to cause a slight displacement of the blades next to it, due to friction. Hence, the friction between the blades must be minimized. Also, since the blades will be about 1 mm thick, it is quite challenging to develop a system where each blade will be connected to a different actuator. Micro-motors could solve this issue. The motors' holding torque will be also necessary to ensure that the blades will hold their position while other, neighbouring blades are still in motion, allowing for larger friction levels between the blades.

Figure 6.15 presents the stages of the powder deposition experiment using the presented apparatus, and the finished powder layer result.

a

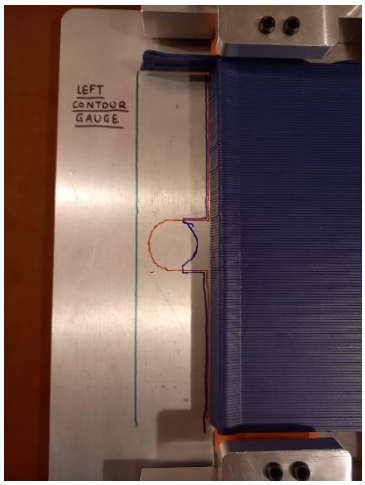
LEFT
CONTOUR
GAUGE

b

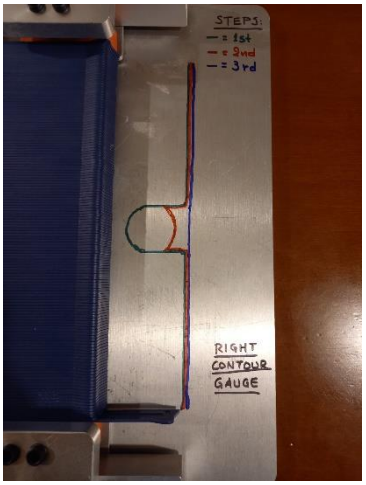
STEPS:
— = 1st
— = 2nd
— = 3rd
RIGHT
CONTOUR
GAUGE

c

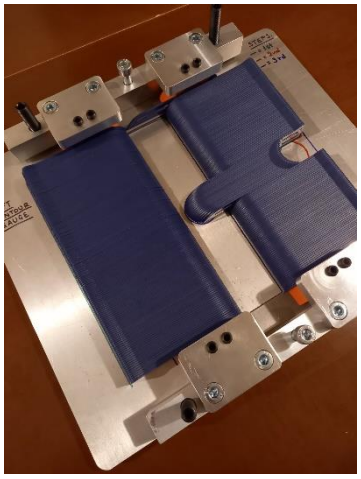

d


STEPS:
— = 1st
— = 2nd
— = 3rd
LEFT
CONTOUR
GAUGE
RIGHT
CONTOUR
GAUGE

e

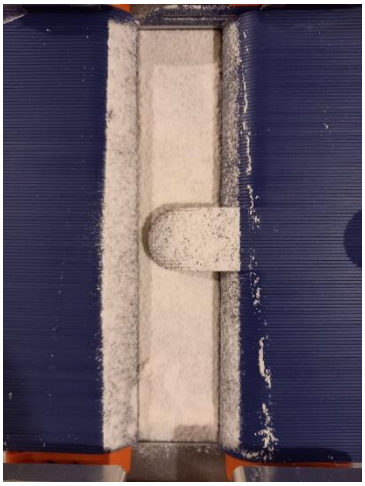

f

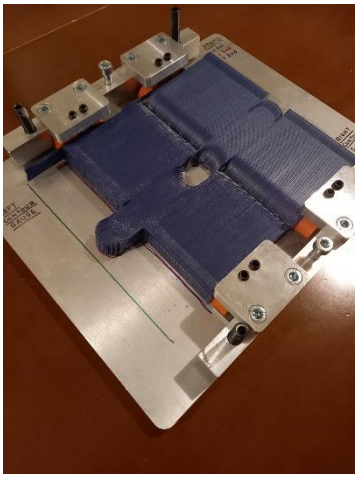

g

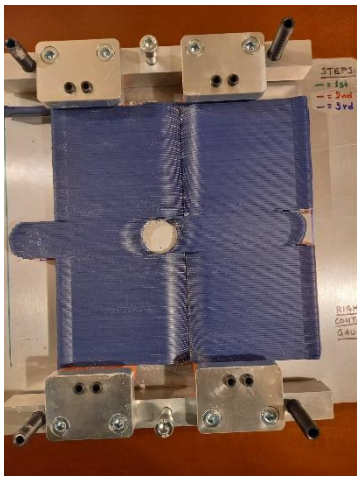
STEPS:
— = 1st
— = 2nd
— = 3rd

h

i

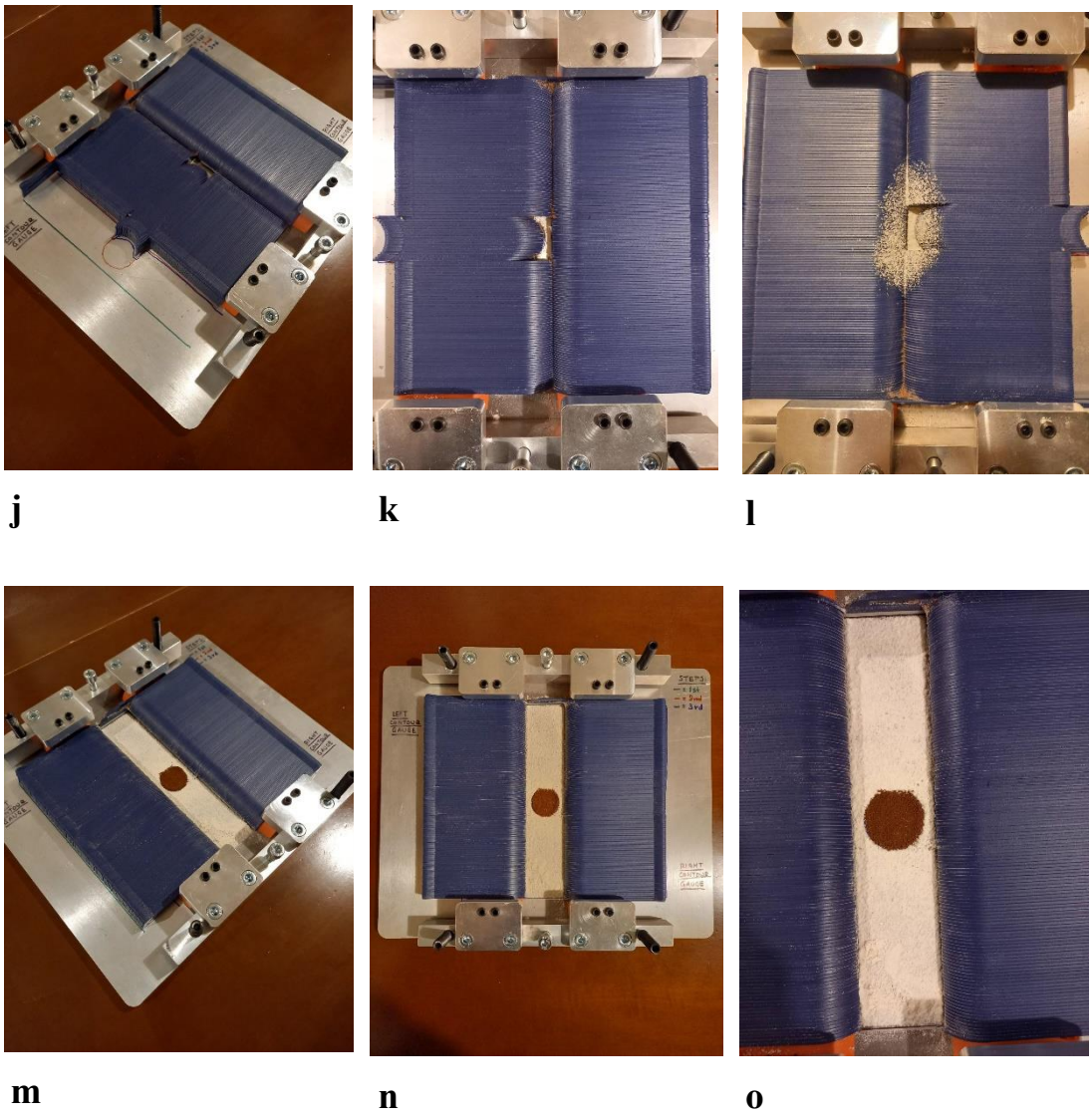

Figure 6.15: Multi-material deposition experiment. The pattern used is similar to the one seen in *Figure 6.18*. ***(a-b-c)*** Border curves and left-right fronts on the deposition plate; ***(d-e-f)*** Step 1 of the deposition; ***(g-h-i)*** Step 2 of the deposition; ***(j-k-l)*** Step 3 of the deposition; ***(m-n-o)*** Final layer. The border curves are depicted accurately.

The x-y dimensions of the layer are 40 mm and 200 mm and the centre of the circular border curve was the middle of the rectangular layer, i.e., point C(20 mm, 100 mm). The diameter of the circular border curve was 30 mm.

The verification of the approximation of the border curves in the deposited layer via the experimental jig was performed via Hough Circle Transform [233]. Hough Circle Transform is a method for image circle detection. It can identify both the centre and the radius of a circle. More specifically, the Hough Transform is a feature extraction technique used in image analysis, computer vision, and digital image processing. Its goal is to find imperfect instances of objects within a certain class of shapes by a voting

procedure. The classic Hough Transform was originally developed to identify lines in the image, but it can also be used to detect other shapes, such as circles or ellipses [234], [235].

By using the Hough Circle Transformation on a photo of the deposited multi-material layer, namely *Figure 6.15(n)* it is possible to identify the circular pattern of the deposited surface and compare it to the centre coordinates and radius of the border curve it derives from. It is important that the photograph is taken from a position directly above the surface. Ideally, the lens axis should pass from the centre of the circular pattern. However, since the centre's coordinates are to be estimated, this is only possible by visual approximation. This positioning helps minimize errors deriving from perspective. The photo was taken using a lens of the following specifications: 48 MP resolution, f/2.0 aperture size, 26 mm focal length (wide), 1/2.0" sensor size, 0.8 μm pixel size, PDAF (phase detection auto-focus). Despite the fact that the lens used was a wide-angle lens, the photo was taken from a focal distance of 500 mm, therefore the circular feature only occupies 8% and 6% of the photo's length and height respectively. This renders distortion of the circular feature of the photo minimal.

The result of the Python-code [233] used can be seen in *Figure 6.16*. The pixel-to-mm scale can be calculated by measuring the pixel distance between opposing blades, which is equal to 40 mm by design. It is important that this measurement is performed for opposing blades near the centre of the covered area and close to the circular pattern, to minimize the perspective-induced error. It was calculated that 40 mm correspond to 245 pixels. Hence, the scale is Ratio = 0.163 mm/px.

The diameter of the circle is equal to 2·92=184 px. Hence, the diameter of the circle is equal to

$$D_{mm} = Ratio \cdot D_{px} \cong 30.041\ mm$$

which is only by 0.14% larger than the diameter of the circular border curve. To calculate the centre's coordinates, the four distances by the edges of the area of deposition are calculated as: $d_{vertical\text{-}top} \cong 97.633$ mm, $d_{vertical\text{-}bottom} \cong 96.163$ mm, $d_{horizontal\text{-}left} \cong 20.735$ mm and $d_{horizontal\text{-}right} \cong 18.776$ mm.

These are the absolute values. It can be noticed that the sums of the vertical and horizontal distances are smaller compared to the y-length and x-length of the layer, i.e.,

200 mm and 40 mm respectively. This can be attributed to perspective error introduced by the camera. This error can be taken into account as follows:

$$x_C = \frac{d_{horizontal-left}}{\left(d_{horizontal-left} + d_{horizontal-right}\right)} \cdot 40\ mm = 20.992\ mm$$

$$y_C = \frac{d_{vertical-bottom}}{\left(d_{vertical-bottom} + d_{vertical-top}\right)} \cdot 200\ mm = 99.241\ mm$$

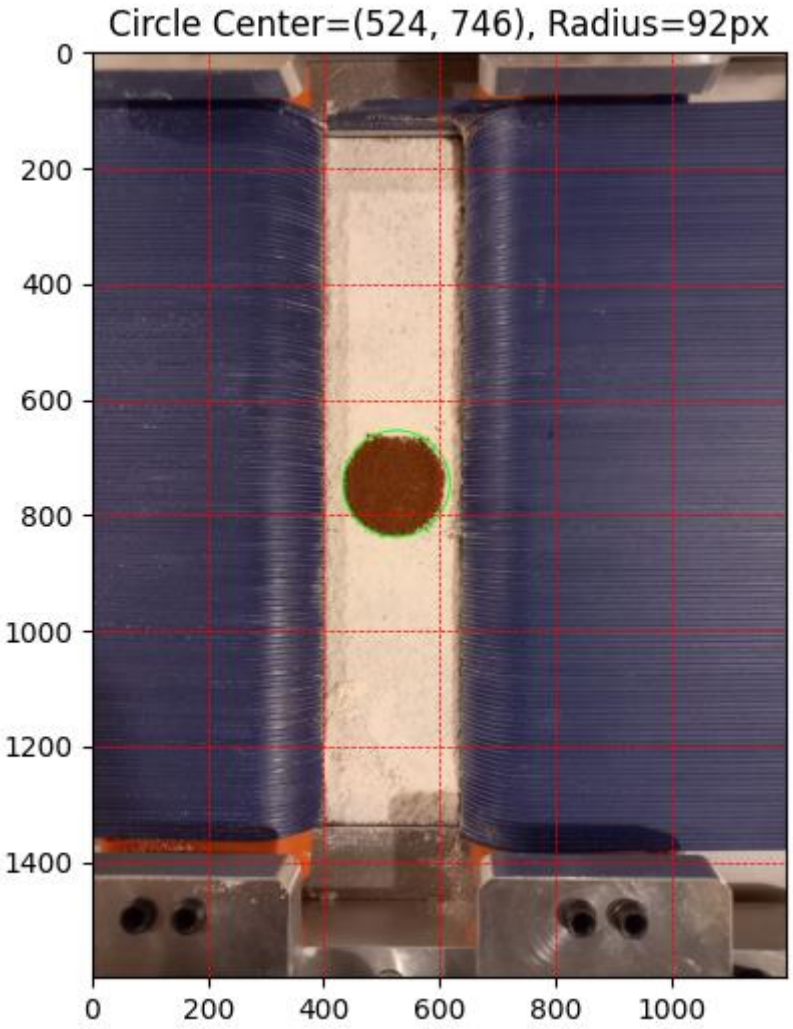

Figure 6.16: Circular pattern identification via Hough Circle Transform.

With the O(0,0) being positioned at the bottom left point of the rectangular layer.

It can be noticed that the centre's abscissa and ordinate deviate by (+) 4.96% and (-) 0.8% from the expected values (20 mm and 100 mm respectively), as these were defined by the circular border curve. These deviations can be attributed to multiple errors, such as the camera positioning, which could be off-centre or slightly rotated,

introducing image deformations. Image resolution could also introduce some error. Additionally, the blades were positioned to each point in such a way that the midpoint of the blade's front would intersect the border curve, possibly affecting the circle's diameter and centre coordinates. However, these deviations are not prohibitive and the method looks quite promising, especially after considering that the experimental jig provides neither optimum blade shape, nor optimized spreading parameters, which will be examined via DEM simulation in *Section 6.3*.

6.3 Design Optimization - Simulation Using the Suggested Design

In order to counter the addressed flaws, the dual contour gauge system was designed again. The design that will be presented will be explained in detail. Finally, the optimized design will be used for a multi-material powder spreading simulation, to examine the result and estimate possible errors of the method.

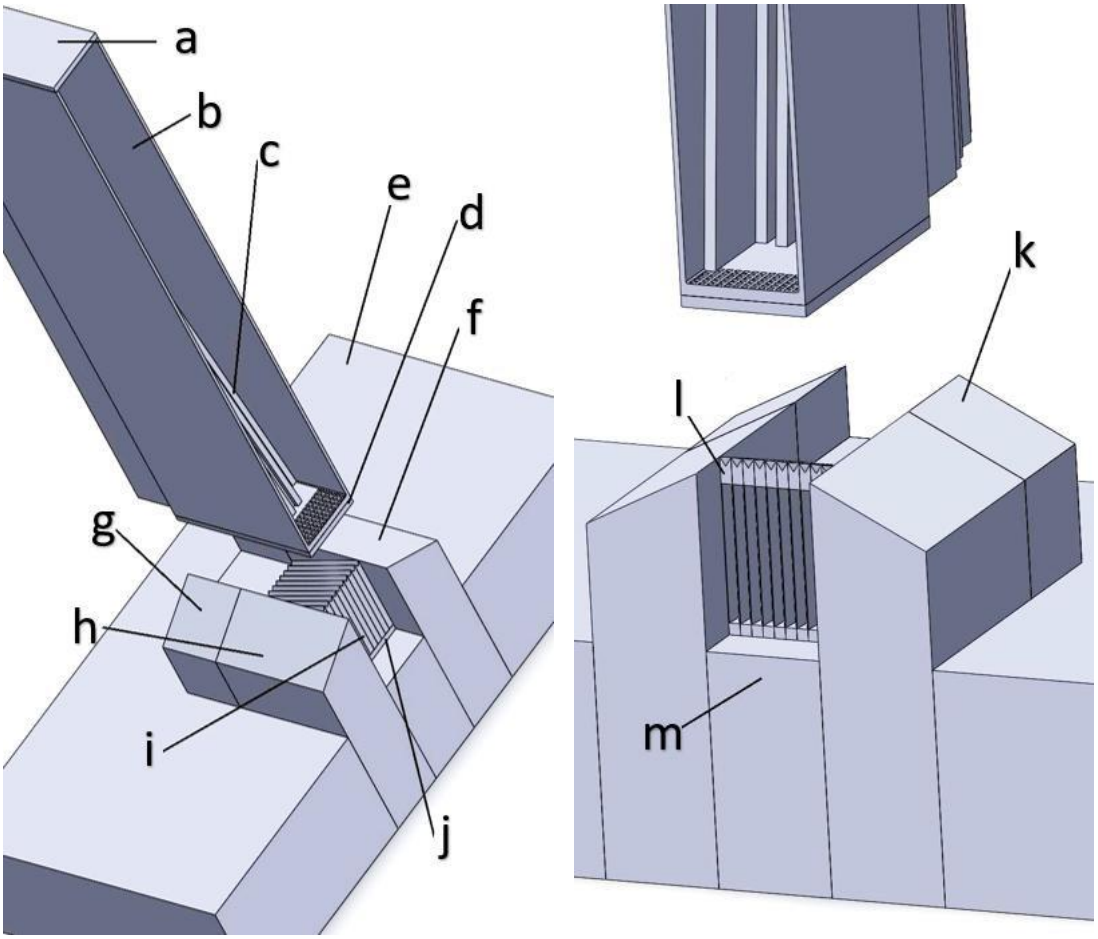

Figure 6.17: Left and right hand-side section views of the 3D CAD (SolidWorks^{TM}) drawings of the multi-material powder deposition system assembly.

The design features, see *Figure 6.17*:

a. 1 sieve sealing cap
b. 1 Π-shaped sieve
c. 20 sieve limiting inclined blades (10 left and 10 right)
d. 1 sieve blocking plate
e. 1 powder deposition plate
f. 1 top powder limiting block
g. 1 left blade limiting block
h. 1 bottom powder limiting block
i. 10 powder spreading blades (left contour gauge)
j. 1 left powder limiting block
k. 1 right blade limiting block
l. 10 hollow blades (right contour gauge)
m. 1 right powder limiting block

The powder deposition plate envelops the 2 (left and right) blade limiting blocks as well as the 4 (left, right, top and bottom) powder limiting blocks. All six limiting blocks function as pistons sliding vertically with regard to the top surface of the powder deposition plate. This ensures that the system has the ability to spread new layers over the previous layers of powder, by simply raising all the pistons, as well as the left and right contour gauge of blades vertically by the desired theoretical layer thickness.

The 10 powder spreading blades have a 0^o relief angle ($\theta_{rel}=0^o$), since this was proven to be the optimum level for optimized layer quality. Both the powder spreading and the hollow blades have an outward inclination ensuring that the powder which drops on them instead of inside the uni-material subarea during the sieving process will slide outwards and will not contaminate the next uni-material area during the repositioning of the blades into the new left and right fronts. The hollow blades are hollow throughout their length, and their floor is slightly inclined outwards. This facilitates ducts, whose purpose is to drive the excess powder away from the layer. The motion of the spreading blades during the spreading process forces the excess powder through these ducts of the hollow blades. Thus, an even layer is created and powder economy is promoted, since the excess powder can easily be collected and recycled. The height of the hollow blades' floor at their left-hand side (the side which creates the right front) is 100 μm, equal to the theoretical layer thickness, and it gets reduced slightly towards their right,

free edge. During spreading, the spreading blades are 100 μm higher than the hollow blades, in order to create the top surface of the new layer. The spreading speed is equal to u_{tr}=0.01 m/sec and the vertical vibration of the spreading blades has an amplitude of A_{vib}=5 μm and a frequency of f_{vib}=2000 Hz, since these are the optimum spreading parameter levels as calculated by the Taguchi method described in *Chapter 5*.

Each blade has a thickness (t_b) of 100 μm. The 10 blades have a combined thickness of 1 mm. The area that will be covered in the simulation is a square of 1mm x 1mm, with a theoretical thickness of 100 μm, same to the sample right rectangular prism that was used in the powder spreading Taguchi experiments. The layer pattern that will be used in the simulation will be a circle of 0.3 mm radius. The approximation of the circle via the blades and the x-axis segmentation can be seen in *Figure 6.18*. The staircase effect is visible, however, given that the circular feature is comparable in size with the blade thickness, this is to be expected. This effect is much less obvious in larger features, which are at least 2 orders of magnitude larger than the blade thickness (i.e., features of approximately 10 mm size along the y-axis, compared to the 0.1 mm of blade thickness). In the said Figure, with light colours (green and orange) the uni-material areas that have been covered in previous steps are depicted. Similarly, with bright colours (green and orange) we depict the uni-material area that is to be covered during the current step of the segmentation.

The sieve is Π-shaped, so that it gets sealed via the two contour gauges of inwards-inclined blades. These blades have also a 100 μm thickness, and they are designed to completely replicate the shape of the uni-material area that is to be covered and is left uncovered via the spreading and hollow blades. This promotes powder economy, since the powder is sieved directly onto the desired uni-material area. If this were not the case, a large amount of powder would drop onto the outwards-inclined spreading and hollow blade contour gauges and slide via their outward-inclined surfaces outside of the layer, potentially getting contaminated by a different type of powder, rendering it unusable. The sieving parameters were selected in such a way that the process provides the necessary powder mass during sieving linearity at the fastest possible rate. Furthermore, the sieve's blades have an inwards inclination of 82°, which reduces the compressive force of the powder during the repositioning of the blades. Had this not been the case, the increased compressive force would increase the possibility for agglomerate forming, making the sieve clogging phenomena more intense and

ultimately reducing the mass flow of the powder during the linear sieving stage, or even reducing the duration of the linearity phase.

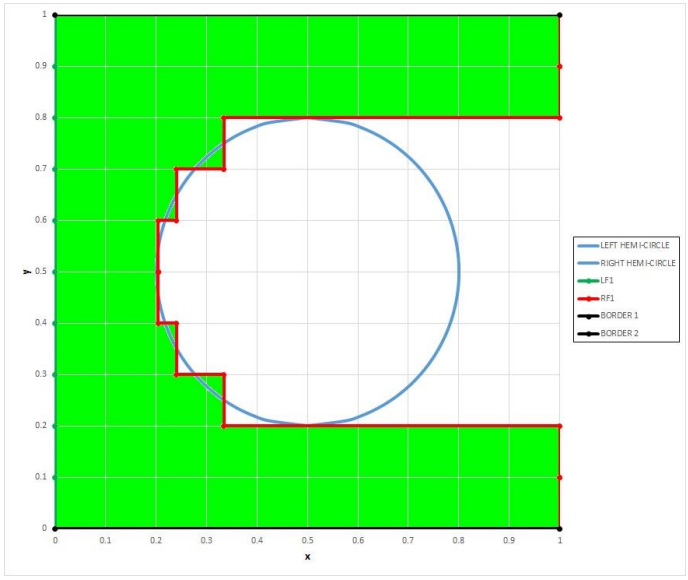

a

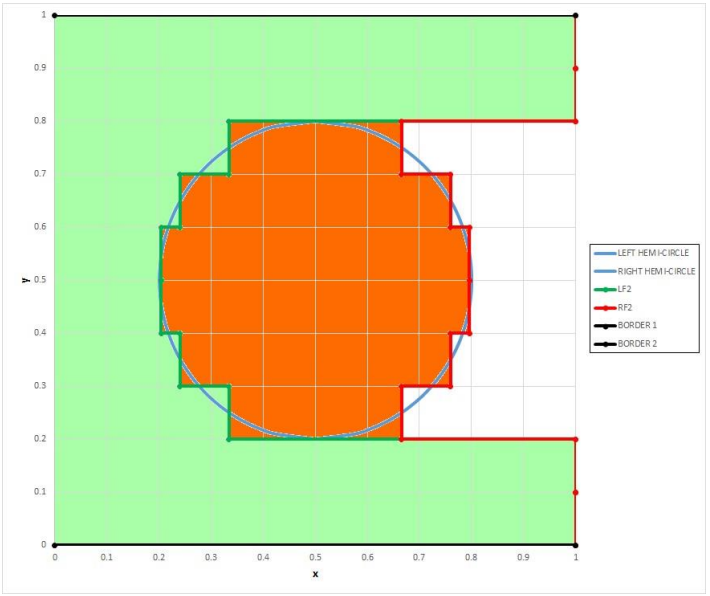

b

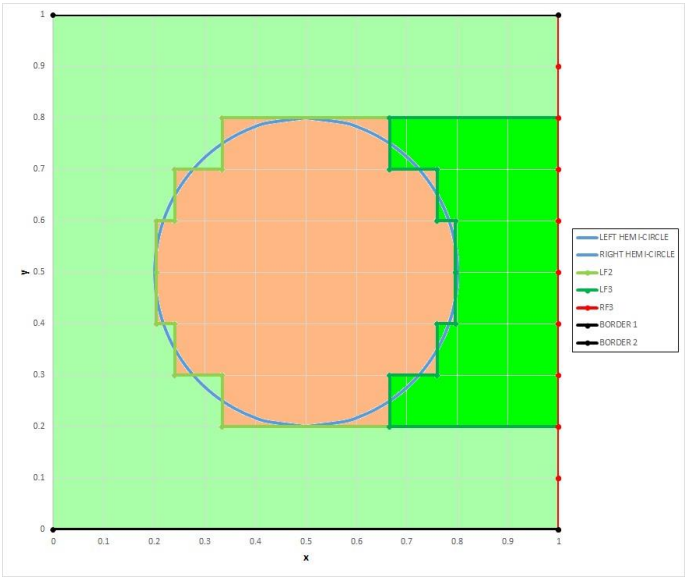

c

Figure 6.18: X-axis segmentation of the circular pattern used for the simulation; ***(a)*** Step 1; ***(b)*** Step 2; ***(c)*** Step 3 of the segmentation.

Let us assume that the level of the settled powder inside the sieve at some random sieve's inclined blades positioning is equal to h_{packed}. There are 10 blade couples, each one created by the left and right sieve's blade that face each other. Every one of these blade couples creates a volume V_i, i=1 to 10, the shape of which is an extruded trapezoid of a small base equal to b_i and a large base equal to B_i, i=1 to 10. The height of every

extruded trapezoid is equal to h_{packed}. The extruded thickness of the trapezoid is equal to the blade thickness, t_b (equal to 100 μm). Hence, the *Equation (6.5)* applies:

$$V_i = \left[\frac{(B_i + b_i)h_{packed}}{2}\right] t_b \qquad (6.5)$$

So, the total volume occupied by the settled powder inside the sieve is equal to

$$V_{packed} = \sum_{i=1}^{10} V_i = \frac{h_{packed} t_b}{2} \sum_{i=1}^{10} (B_i + b_i)$$

The angle of inclination of the sieve's blades is equal to θ=82°. So, the large base is given by

$$B_i = b_i + \frac{2h_{packed}}{tan\theta}$$

Finally, by replacing, the total volume occupied by the settled powder inside the sieve is given by the *Equation (6.6)*.

$$V_{packed} = h_{packed} t_b \left(\frac{10h_{packed}}{tan\theta} + \sum_{i=1}^{10} b_i\right) \qquad (6.6)$$

The sieving Taguchi experiments revealed that the higher the powder level in the sieve, the smaller the flow rate during the linearity of the sieving process. By reducing the space occupied by powder inside the sieve during the repositioning of the sieve's blades, the level of the powder would rise, which would decrease the flow rate during the sieving process. For this reason, the initial level should be equal to the one created in the orthogonal rectangular sieve of 1 mm x 1 mm used in the sieving Taguchi experiments by a cubic 1 mm side 'powder factory'. This means that, the rectangular powder factory responsible for the powder generation should have a height different than 1 mm, which must be calculated. It cannot be said whether it must be higher or shorter than 1 mm, since; a) the blades are inclined inwards instead of having vertical wall, and b) a part of the sieve's active surface is now covered. In order to calculate the desired factory height, a simple volume conservation method is used.

For the orthogonal rectangular sieve of 1 mm x 1 mm square base used in the sieving Taguchi experiments, the factory height took 3 possible values, i.e., 0.5, 1.0 and 1.5 mm. After the powder settled down inside the sieve while the sieve was blocked and stationary, the level of the powder was measured in the simulations. Furthermore, the

total volume and the total mass of the powder particles inside the sieve were exported by the DEM simulation software as well. Results are shown in *Table 6.2*.

Table 6.2: Comparison between powder mass, powder volume, settled powder level and theoretical packing density of the powder inside the Taguchi sieving experiment sieve for the different powder factory height levels.

$h_{bf}\ (mm)$	$m_{prt,TOTAL}\ (mg)$	$V_{prt,TOTAL}\ (mm^3)$	$h_{packed}\ (\mu m)$	$PD_{th}\ (\%)$
0.5	0.3083	0.0807	147	54.898
1.0	0.6184	0.1619	290	55.828
1.5	0.9056	0.2371	410	57.829

Referring to *Table 6.2*, it becomes clear that the particles' total mass, the particles' total volume and the settled powder level in the sieve are all quantities that are linearly connected to the height of the powder factory. The theoretical packing density column of the Table is calculated as the ratio between the total volume of the powder particles divided by the volume of the rectangular prism defined by the base of the sieve and the level of the settled powder $\left(V_{packed-Taguchi} = abh_{packed}\right)$, where a, b are the sides of the Taguchi-used sieve's base, and are both equal to 1 mm.

$$PD_{th} = \frac{V_{prt,TOTAL}}{V_{packed}} \tag{6.7}$$

It can be noticed that the theoretical packing density remains approximately the same, regardless of the powder factory height, see *Table 6.2*. This was expected, since the powder's settling down is promoted solely by gravitational forces. The result had the blocked sieve been vibrated a few times would be different. The average theoretical packing density is calculated as the average of the three values of *Table 6.2*, so we take $PD_{th,ave} = 56.185\%$.

The sieve features square apertures with a 4° inverted taper angle (θ_{tap}). It has been proven that a larger taper angle increases the powder mass flow rate, see *Figure 5.10(a)*. Simultaneously, however, it decreases the total powder mass sieved during the linear sieving stage. So, it was decided to opt for the middle level of taper angle, in order to render it a non-factor during the selection of the other three parameters.

To calculate the necessary powder mass, the optimum deposited layer from the spreading Taguchi experiments was used. The total mass of the optimum layer produced in the spreading Taguchi experiments was 0.205 mg (see *Table 4.14* for the layer

characteristics). By using the deposited mass of that layer, it was deduced that it is necessary to achieve a sieving performance equivalent to the one achieved in the Taguchi sieving experiments that used an h_{bf} level of 1 mm. The performance achieved by h_{bf}=0.5 mm does not provide the necessary powder mass during linearity regardless of what the level of the other sieving parameters is, while the one achieved by h_{bf}=1.5 mm drastically decreases Q (mg/sec) of the linear sieving stage, slowing down the entire process. However, in order to achieve sieving performance identical to the one achieved in the Taguchi sieving experiment with h_{bf}=1.0 mm, it is necessary to achieve the same settled powder level inside the sieve assembly, as compared to the one achieved inside the sieve used in the Taguchi-oriented simulation, i.e., h_{packed}=290 μm (see *Table 6.2*). Since the geometry of the sieve's blades here, in combination with the altering blade position create a totally different geometry, a different h_{bf} value needs to be used (granted that the factory retains its rectangular prism shape- same base square, with a 1 mm side, but with a different height).

Table 6.3: Powder factory height calculation in the multi-material simulation stages.

	h_{packed} (mm)	$\sum_{i=1}^{10} b_i$ (mm)	V_{packed} (mm^3)	$V_{prt,TOTAL}$ (mm^3)	$m_{prt,TOTAL}$ (mg)	h_{bf} (mm)
STEP 1 (→)	0.29	5.557	0.1729	0.0972	0.371	**0.599**
STEP 2 (→)	0.29	2.886	0.0955	0.0536	0.205	**0.321**
STEP 3 (→)	0.29	1.557	0.0569	0.0320	0.123	**0.183**

In order to maintain a 290 μm packed powder level inside the sieve at the start of every sieving step, the volume of the packed powder is calculated by using *Equation (6.6)*. The sum of the b_i for every step is calculated by the horizontal, along the x-axis distances of the blades that face each other, at their lowermost point. Then, by assuming a constant theoretical packing density value of 56.185%, the total volume of the powder particles is calculated. Then, by linear interpolation between the h_{bf} and the $V_{prt,TOTAL}$ columns of *Table 6.2*, the necessary height of the powder factory is calculated. Let us note that, the width and length of the powder factory are both equal to 1 mm. Despite the fact that Step 1 and Step 3 are to be performed by the same sieve and the same powder type, had we added the necessary heights of the respective factories to fill Sieve #1, we would end up with much higher h_{packed} with regard to the desired 0.29 mm for both Step 1 and Step 3, leading to different sieving performance in terms of flow rate,

mass sieved and linearity duration. Hence, after Step 1 is completed, the sieve gets emptied and refilled with the new cuboid's box factory height being equal to 0.183, as shown in *Table 6.3*. So, the final values in order to provide the sieves with the appropriate amount of powder are the following:

$$\boldsymbol{h_{bf-SIEVE\ \#1\ (Step\ 1)}} = 0.599\ mm$$

$$\boldsymbol{h_{bf-SIEVE\ \#2\ (Step\ 2)}} = 0.321\ mm$$

$$\boldsymbol{h_{bf-SIEVE\ \#1\ (Step\ 3)}} = 0.183\ mm$$

For reasons of simplicity, both materials of the simulation will be alumina particles as in the spreading and sieving Taguchi simulations (see *Chapter 4* for powder specs and simulation data), since, in order to use a different material, we should again run another Taguchi spreading and sieving DoE to optimize its spreading and sieving process, which is not the point of this work. The first material, i.e., the one which will be used to cover the uni-material areas of step 1 and step 3 (green colour of *Figure 6.18*) will be fed into sieve subassembly #1, while the second material, i.e., the one used to cover the uni-material area of step 2 (orange colour of *Figure 6.18*) will be fed into sieve subassembly #2.

We have already explained why a 4^o taper angle sieve and a 1mm-equivalent powder factory height were selected. For these parameter levels and by using the regression equations (*Equations (5.3)*, *(5.4)* and *(5.5)*), the mass during linearity, the mass flow in linearity and the duration of linearity were calculated for every level combination of vibrating frequency and amplitude. The goal was to provide sufficient powder mass to cover every uni-material area, at the fastest possible rate, while ensuring that this happens without having to continue the sieving process after the linearity stage of the sieving was completed. By using an Excel spreadsheet, the optimum sieving combination of parameters was determined to be the following:

$$\begin{Bmatrix} f_{vib} = 200\ Hz \\ A_{vib} = 20\ \mu m \\ \theta_{tap} = 4^o \\ h_{bf} = 1.0\ mm \end{Bmatrix}$$

Which provided the following results

$$\begin{Bmatrix} m_{lin}(h_{bf} = 1.0) = 0.3064\ mg \\ Q_{lin}(h_{bf} = 1.0) = 0.9904\ mg/sec \\ t_{lin}(h_{bf} = 1.0) = 0.3062\ sec \end{Bmatrix}$$

In this trial of the sieving-Taguchi DoE, we can define a critical linearity mass ratio, LMR_{cr}, as follows:

$$LMR_{cr} = \frac{m_{lin}}{m_{prt,TOTAL}} \tag{6.8}$$

The LMR_{cr} is a characteristic of the sieving performance at certain powder level, taper angle and sieve vibration conditions. For the sieving conditions of our choice, and by the data provided in *Table 6.2*,

$$LMR_{cr} = \frac{0.3064}{0.6184} = 0.495$$

The mass powder content of each uni-material surface is given by the mass of the optimum spread layer (m_{opt}=0.205 mg) multiplied by the ratio of the uni-material surface area divided by the surface of the optimum spread layer (A_{opt}=1 mm^2). This amount is also multiplied by a safety factor to calculate the powder mass that was sieved, since, in order to spread the powder, it is necessary to sprinkle more powder over the uni-material subarea and "scrape" the excess powder via the doctor blade recoater. Furthermore, during sieving, some powder will not end up in the desired area, but will slide outwards over the outwards-inclined spreading or hollow blades, or the top and bottom powder blocking blocks. Hence, a safety factor greater than 1 is necessary, to ensure that sufficient powder will end up into the desired place.

$$m_{spread\_step-i} = \left(\frac{A_{step-i}}{A_{opt}}\right) m_{opt}$$

$$S_f = \frac{m_{sieved\_step-i}}{m_{spread\_step-i}} > 1$$

Similarly, since the sieve's active sieving area is being restricted by another dual contour gauge system which perfectly copies the uni-material area that is to be covered, the mass flow rate is given by

$$Q_{step-i} = \left(\frac{A_{step-i}}{A_{opt}}\right) Q_{lin}$$

The maximum powder mass sieved during the linear sieving phase at each step is given by multiplying the total powder mass by the LMR_{cr} that was calculated above, i.e., by using *Equation (6.8)* for each step of the process. The safety factor is then calculated,

as well as the time necessary for the sieving of each step to be completed. The results are presented in *Table 6.4*. The calculated safety factors for the suggested powder factory heights given in *Table 6.3* indicate that the factories designed provide a sufficient powder amount for the deposition of a good quality layer, since all of them are above 1.5.

Table 6.4: Calculated sieving duration and sieved mass for each step of the simulation.

	Surface (mm^2)	Spread mass (mg)	Maximum sieved mass (in linearity) (mg)	Safety factor (SF)	Q (mg/sec)	t (sec)
Optimum layer (SCR-RMS)	1	0.205	0.3064	1.495	0.9904	0.3062
Step 1 (Material #1)	0.522	0.107	0.184	1.720	0.5173	0.356
Step 2 (Material #2)	0.322	0.066	0.102	1.545	0.3189	0.320
Step 3 (Material #1)	0.156	0.032	0.061	1.906	0.1542	0.396

Having defined the spreading conditions, as well as having calculated the factory dimensions and the sieving durations and conditions, the simulation can run according to the following steps:

1. Activating powder factory #1 inside sieve #1 (material #1).
2. Contour gauge positioning for Step 1 (both spreading-hollow blades and sieve #1's inclined blades).
3. Unblocking sieve #1 and vibrating the sieve #1 subassembly for 0.356 secs.
4. Re-blocking sieve #1 and spreading with spreading blades.
5. Switching sieve #1 with sieve #2-positioning it above the sample square and repeating points 1-4 for Step 2, i.e. factory #2 inside sieve #2 (material #2) with vibration time 0.320 sec.
6. During 5, sieve #1 gets emptied and refilled with powder factory #3 (no time is wasted due to the overlap of actions).
7. Switching sieve #2 with sieve #1-positioning it above the sample square and repeating points 1-4 for Step 3, with vibration time 0.396 sec.

The blade repositioning at each step is performed at the coordinates pertinent to the step that is underway. The finished results are visible in *Figure 6.19*, which provides section cuts with planes parallel to the deposition plate at various height percentages of the deposited layer.

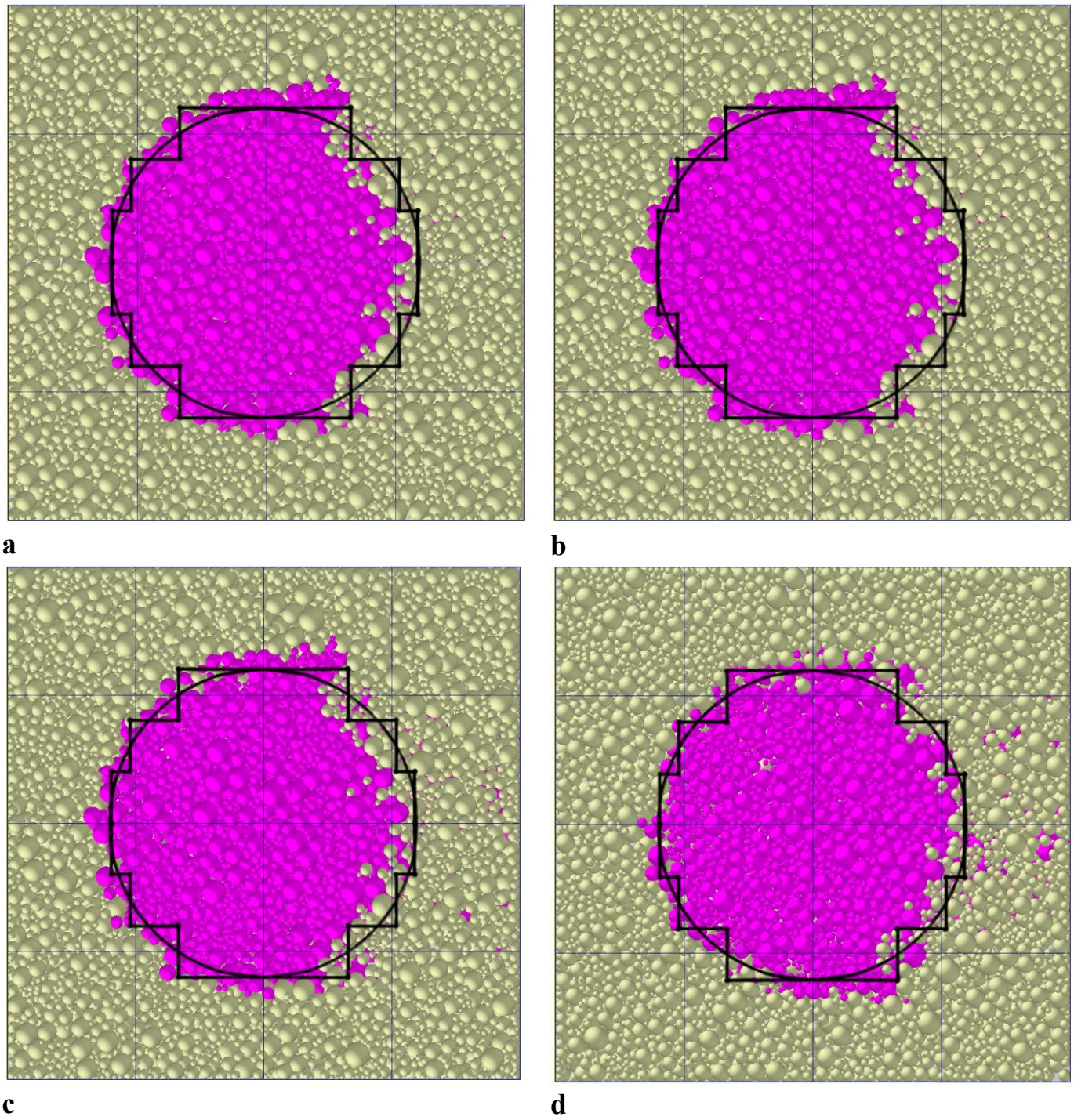

a **b**

c **d**

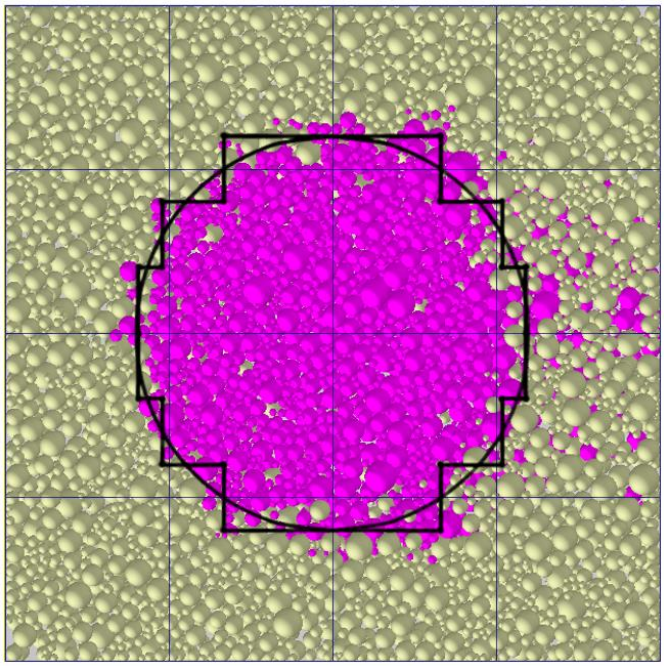

e

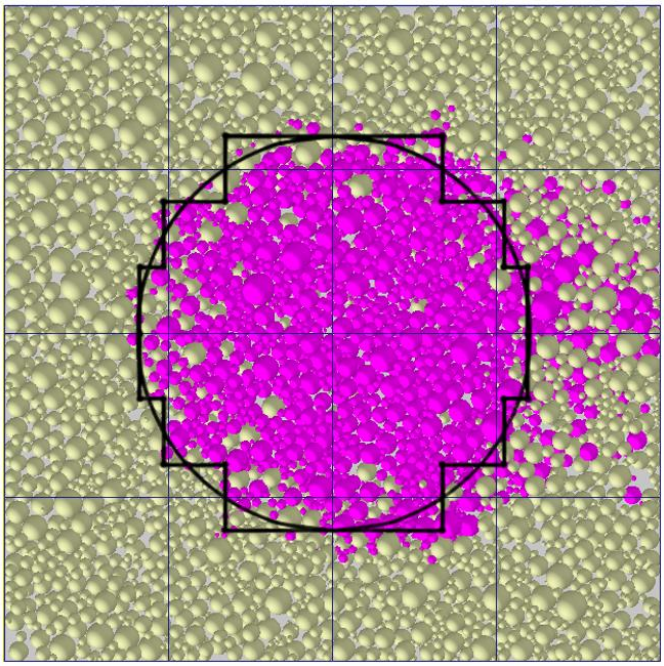

f

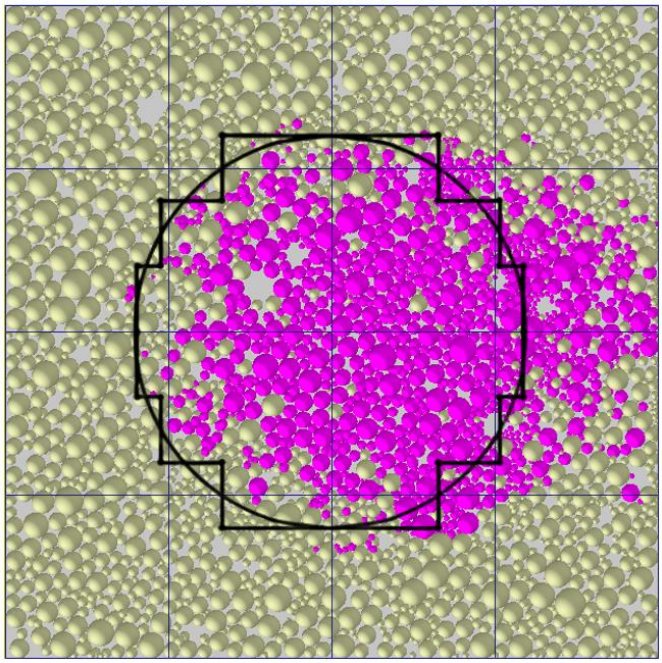

g

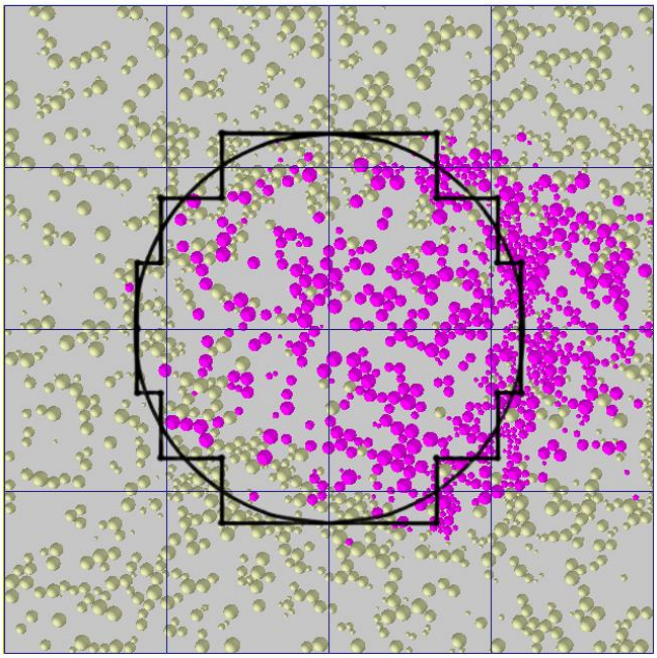

h

Figure 6.19: Section views of the finished spread layer by the suggested multi-material powder deposition method at different height percentages of the finished layer; ***(a)*** 100%; ***(b)*** 87.5%; ***(c)*** 75%; ***(d)*** 62.5%; ***(e)*** 50%; ***(f)*** 37.5%; ***(g)*** 25%; ***(h)*** 12.5%.

Material #1 is depicted with light yellow, while material #2 is depicted with magenta colour. The pictures also depict the circle and the uni-material area borders as defined by the edges of the blades that created the left and right fronts for every step of the process. This was done in order to compare the expected borders of the uni-material areas with the actual ones after the powder deposition. In *Figure 6.19*, it becomes

obvious that the structured borders between the different materials are in good agreement to the preset ones. This is especially obvious in the high sections of the layer, i.e., the ones closer to the top surface of the layer. For the 100%, 87.5% and 75% sections (*a*, *b* and *c subfigures*) there is some error, as the circular patters seems to be slightly offset to the left with regard to the preset borders that are shown in black lines. From this point on, this error will be termed top-section-left-hand side error (T-L error). In the first two section views, the linear infiltration (dx_{inf}) of the magenta powder inside the first uni-material area (at the left semi-circle of the circular border curve) reaches a value of approximately 25 μm along the x-axis, while the infiltration of the yellow powder inside the second uni-material area (at the right semi-circle of the circular border curve) reaches a value of approximately 45 μm along the x-axis. These values were visually estimated, by reference to the grid inserted in the Figures depicting the section views.

In the 62.5% and 50% (*d* and *e*), this error has vanished and the circular pattern is in perfect agreement with the desired borders. However, as we move towards the lower section cuts, i.e., the ones closer to the substrate, there seems to be some error, as the circular pattern is offset towards the right with regard to the black border curves. At first, in the 37.5% section view (*f*), there only seems to be some particles infiltrating their right-hand side neighbouring uni-material area, while this effect gets more prominent in the 25% and 12.5% (*g* and *h* respectively). From now on this will be termed bottom-section-right hand side error (B-R error). In the last two section views, the infiltration of the yellow powder inside the circle (at the left semi-circle of the circular border curve) reaches a value of approximately 175 μm along the x-axis, while the infiltration of the magenta powder inside the third uni-material area (at the right semi-circle of the circular border curve) reaches a value of approximately 200 μm along the x-axis.

Both the T-L error and the B-R error have a common cause. After the spreading of a uni-material area is complete, the hollow blades get repositioned by moving towards the right-hand side of the sample square, in order to free and present the next uni-material area over which the next powder is to be sieved. During this motion the right-hand side of the already deposited uni-material area, which is being held vertical by the hollow blades, collapses under gravity forces, forming a slope. This motion is similar to the one made by the powder in the angle of repose experiment.

Zhang et al. (2020) calculated and cross-checked the experimental and simulation-defined angle of repose of the powder used in this work to be equal to 25.8° and 26.2° respectively [71]. By assuming that the angle of repose is equal to 26.2°, which is the value the simulation should answer to, the calculated infiltration of the slope should be equal to

$$dx_{inf-B-R} = \frac{h_{l,th}}{\tan(26.2^o)} = \frac{100\ \mu m}{\tan(26.2^o)} = 203\ \mu m$$

This value is almost the same as the one shown in the section views for the magenta powder infiltration inside the third uni-material area. However, the yellow powder infiltration in the second uni-material area was slightly smaller. This difference may be explained by the following observation. The relative position of the hollow blades with regard to the deposited uni-material area may be enhancing or alleviating the sloping effect. When the hollow blades move from the first to the second right front, releasing the first uni-material area, the blades with the smallest and largest y-value (ordinates) are positioned at larger x-values (abscissae), so their motion does not propel powder particles more to the right via friction forces during the blade repositioning. However, this is not the case when the hollow blades get repositioned from the second to the third right front, hence releasing the second uni-material area. In that case, the innermost blades are the ones at the largest abscissae, while the outermost blades the ones at the smaller abscissae. Hence, during their repositioning, the outermost hollow blades will apply frictional forces onto the powder that is in contact to their side at a slightly smaller or larger ordinate value, if the said blade is above or below the y=0.5 mm value. This will increase the horizontal infiltration displacement of the powder, enhancing the phenomenon.

This easily explains the B-R error. The T-L error is created during the sieving of the next uni-material area. The powder that is entering the next uni-material area penetrates the gap that is left at the top of the slope by the powder of the previous uni-material area during the hollow blades' repositioning process. This explains why the T-L error is less intense compared to the B-R error.

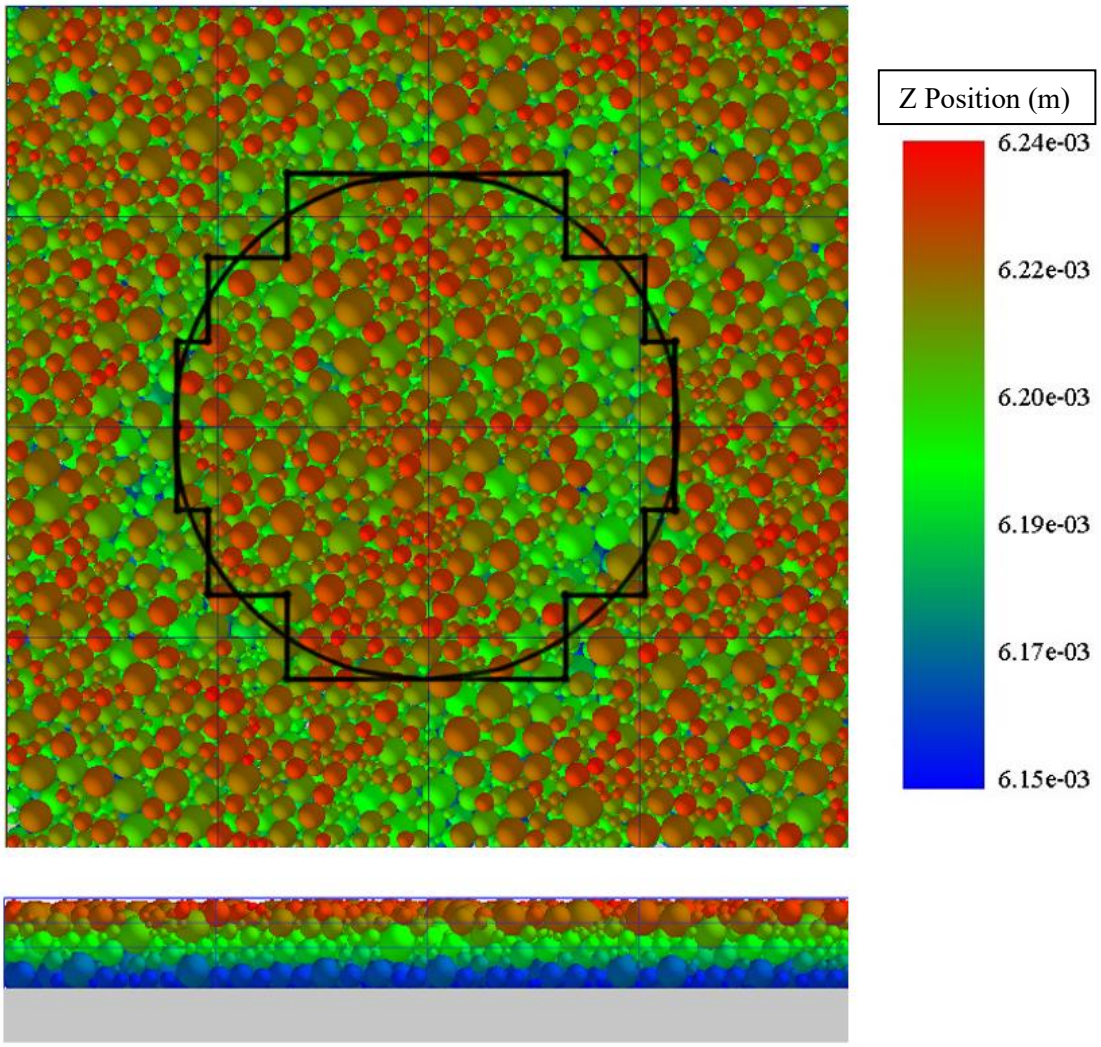

Figure 6.20: Top and side views of the multi-material layer deposited with the suggested method.

It is of paramount importance to note that, both the T-L and the B-R errors are solely dependent on powder rheological properties, i.e., the angle of repose, and their linear infiltration value depends only on the theoretical layer thickness. This means that, although for small features, such as a circle of a 0.3 mm radius, the T-L and (especially) the B-R error seems to be significant, the same absolute value of error will remain regardless of the size of the feature, as long as the same powder type and layer thickness is used. This level of error is indicative of the suggested method's capabilities, since, in the case of the design of a cube of 10 mm side, the error would be equal to 2%, and only at 25% of the depth of each layer, since the B-R error only appears in the 12.5% and 25% section views.

It is suggested that, in order for this method to be applied, methods to minimize linear infiltration should be studied. In general, every factor affecting powder flowability can

potentially affect the linear infiltration, since the angle of repose would be affected. For example, the larger the mean size of the powder the smaller the linear infiltration would be, till it becomes practically zero, when the layer consists only of particles of diameter equal to the theoretical layer thickness, since at that case no particles are stacked on top of each other. However, a very fine powder could also show a decreased linear infiltration, due to the increased interparticle cohesion.

It is possible that this would slightly increase the local roughness of the inter-material interface of the developed objects, however whether this would affect the post-solidification adhesion between the different material areas is to be investigated.

Table 6.5: Multi-material vs optimum uni-material doctor-blade deposited layer; (Reg: "regression"; sim: "simulation").

	u_{tr} (m/sec)	f_{vib} (Hz)	A_{vib} (μm)	θ_{rel} (deg)	LTD_{reg} (LTD_{sim})	SCR_{reg} (SCR_{sim})	$S_{q_{reg}}$ $\left(S_{q_{sim}}\right)$	Ssk_{sim}	Sku_{sim}
MULTI-MATERIAL	0.01	2000	5	0	- (21.6)	- (99.50)	- (13.9)	-1.440	6.907
UNI-MATERIAL OPTIMUM	0.01	2000	5	0	21.4 (22.1)	99.54 (99.33)	15.8 (15.7)	-1.543	6.530

Table 6.5 in combination with *Figure 6.20* shows how the multi-material layer spread is compared to the optimum uni-material layer, as this was established by the spreading Taguchi DoE of *Chapter 4*. It can be seen that the layer thickness deviation of the multi-material layer is at 21.6 μm, the surface coverage ratio is at 99.5% and the root mean square roughness at 13.9 μm, all being very close to the values of the optimum spread uni-material surface layer. The multi-material powder deposition trial cannot have regression values calculated, since its process is completely different compared to the trials included in the Taguchi design. Furthermore, the quality indicators of skewness (Ssk) and kurtosis (Sku) are also very close to the ones of the optimum uni-material layer, proving that the sequential powder spreading and the sloping phenomenon described before do not impact the quality of the finished surface negatively.

The breaking down of sub-process duration for the simulation can be seen in *Table 6.6*:

Table 6.6: Multi-material deposition process duration; The real-life adjusted duration refers to the same multi-material layer pattern as the one examined in the current simulation, but in a 100:1 scale (i.e., 100 times larger than the simulation one).

	Stage	In-sim duration (sec)	Real-life adjusted duration (sec)
1	Filling sieve #1	0.1	0.5
2	Blade positioning-Step 1	0.01	0.1
3	Sieving-Step 1	0.356	0.356
4	Spreading-Step 1	0.1	10
5	Sieve switch	0.1	1
6	Filling sieve #2	0.1	0.5
7	Blade positioning-Step 2	0.01	0.1
8	Sieving-Step 2	0.320	0.320
9	Spreading-Step 2	0.06	6
10	Sieve switch	0.1	1
11	Blade positioning-Step 3	0.01	0.1
12	Sieving-Step 3	0.396	0.396
13	Spreading-Step 3	0.035	3.5
TOTAL		**1.697**	**23.872**

In order to estimate what the adjusted duration in an actual multi-material powder deposition process would be, it is necessary to point out that the sieving durations are not surface-related. The sieve's surface will cover the entire surface of the layer that is to be deposited, and the powder level in the sieve will be adjusted according to the guidelines provided in this chapter to ensure that sieving times will remain the same. However, the blade positioning, spreading and sieve switch times will be much larger, considering that the moving parts will have to travel much larger distances in order for a real mechanism to cover a surface which will be, e.g., 100 times larger compared to the 1 mm-side sample square that is examined in this simulation. Especially in the case of spreading process, increasing the speed will cause deterioration of the surface quality, as was proved by the Taguchi spreading DoE. However, it is still possible to compensate slightly for this by adjusting other spreading parameters, as was indicated in the *Chapter 4*. Still, in the case of sieve switching or blade positioning, it is possible to significantly increase the speed, as these moves have no effect on the deposited layer quality.

To make an estimation of the time necessary to complete the multi-material powder deposition of a 100 mm (i.e., 10 cm) side square layer of 100 μm thickness with the

same pattern as in the simulation (circular border curve of 30 mm radius), the following calculations are made:

The powder spreading time is multiplied by 100, since the length along the deposition (x) axis is multiplied by 100 (from 1 to 100 mm), while the spreading blades' feed remains the same. The sieving time remains constant, since the only parameter that changes is the dimensions of the sieve, which does not affect the sieving duration. Blade positioning time (for the right contour gauge hollow blades and both the sieves' left and right inclined blades) and sieve switch time are increased ten-fold, as an estimation made by the author, despite the distances necessary to be covered are multiplied by 100, since the blades' speed and sieve translational speed can be increased with regard to the simulation. This is because they do not affect the quality of the deposited surface. The only exception is the right hollow blades, which should accelerate slowly after a uni-material subarea is covered, in order to avoid increasing the linear infiltration value due to adhesion with powder particles. However, once their vertical wall is separated from the particles, the hollow blades can reach high velocity values without any impact on the deposited layer's quality. Finally, the sieve-filling time, which includes powder vibrational flattening in the sealed sieve prior to sieving is increased five-fold, as an estimation by the author. This is because the method suggested in *Sections 3.4.1* and *5.7*, based on a powder doser drum with hollow apertures is highly customizable (cylinder diameter, number and diameter of blind apertures, number of helixes, rotational speed of the drum during dosing) in order to achieve the desired filling time. However, sieve-filling and sieve-blade repositioning are steps that can be performed during the deposition of the previous subarea, or during the solidification of the previous layer, hence they are not delaying the total part manufacturing time.

The final estimation is a time of approximately 24 seconds for a single layer. The same size of a uni-material layer would be optimally spread in a time of approximately 11 seconds (sieve filling, sieving and spreading with a speed of 0.01 m/sec).

To sum up with, in the relatively simple case studied, the duration of the two-material powder spreading process is about double of the uni-material counterpart. However, this is expected to increase very considerably with the complexity of the multi-material layer and the multitude of its uni-material features. It is suggested that new slicing algorithms are developed to keep the multi-material layer complexity to a minimum or break down complex multi-material designs to more than one, simpler multi-material

components which are to be assembled in order to both reduce the number of components and keep the manufacturing time within acceptable limits. Proper part positioning in the 3D domain is also necessary, in order to simplify the border curves in each layer and minimize the number of uni-material sub-layers within each layer. New studies should focus on identifying the necessary features of components that should be built via multi-material PBF and select the ones which would create the most benefits without sacrificing beyond tolerance manufacturing time.

7 Conclusions

7.1 Achievements and Limitations

In addition to the detailed discussion of the findings provided in each individual chapter of this Thesis, a summary of the issues that were successfully dealt with in this work as a whole and the pertinent limitations is provided next.

The first issue that was addressed was the lack of an extended literature review based on powder spreading for PBF-based AM. The presented literature review is well-rounded, up-to-date, and it follows a sequential connection between powder spreading process parameters, powder layer quality indicators (PLQIs) combined with ways to monitor them, and finished part quality indicators (FPQIs). This way, researchers and members of the industry can easily connect potential changes in the powder recoating process to changes in the quality of the finished part. The information is easily accessible, since it is provided in the form of tables. However, quantification of the effect of powder spreading parameter changes to certain finished part quality criteria remains a necessity, as the connections made are mostly qualitative and experiments need to be run to fine-tune spreading process parameters with regard to the desirable finished part's mechanical properties.

The second issue that was addressed was the lack of comparison among powder spreading methods as well as lack of a method to optimize the development of a powder deposition system (PDS). The Analytic Hierarchy Process (AHP) was used to deal with this issue in a systematic, statistically robust and flexible way. The powder deposition methods identified in literature were: mechanical deposition, electrostatic deposition (or magnetic for ferromagnetic powders), aerosol assisted spray deposition (AASD), tower nozzle deposition and vibrational/ultrasound deposition. The criteria used for their comparison were: need for calibration, ease of automation and control for universal application, simplicity of process, quality of deposited surface, spreading speed, manufacturing cost and ease of manufacturing. Mechanical deposition has proven to be the optimum method for powder spreading, mostly thanks to its ability to

spread layers fast in combination with its high controllability and good deposited layer quality. The design of a prototype PDS was, again via AHP, compared to common commercial PDS, built for PBF machines. The comparison was performed in two parts; (i) the powder dosing/sieving group comparison and (ii) the powder recoating group comparison. The first one highlighted the necessity for prior sieving of the powder for agglomeration and large particle filtering. Furthermore, the vertical silo paired with an indented dosing cylinder as a storage and feeding method outperforms the commonly used feeding piston, which does not promote powder size distribution control, agglomeration filtering, powder economy or the ability to easily install powder quality sensors and applications (e.g., temperature and humidity sensors, powder stirrer, etc.). The second comparison showed the superiority of a combined, height-adjustable doctor blade and roller recoating system. The doctor blade moving prior to the roller maintains constant the height of the powder slope in front of the roller, hence keeping a constant pressure throughout the spreading. This leads to homogeneous packing density throughout the layer. The doctor blade on its own fails to apply high levels of compression, leaving relatively low packing density layers, while the roller on its own leads to layers that are highly compressed at first and less compressed as the roller moves, due to the powder slope decreasing and the fact that the smaller particles are deposited first, leaving the larger ones to be spread at the right-most parts of the layers, the deposition being performed from left to right. The suggested design can also support sieving-only deposition during the spreading for enhanced powder economy and better particle distribution control.

The third issue addressed was the connection between powder spreading parameters and the quality of the deposited layer. This was studied by DEM-based simulation, Taguchi DoE and ANOVA. Powder spreading was modelled via vertical doctor blades with different values of angle of relief at various recoating speeds and vertical vibration of the doctor blade at various amplitude and frequency levels. The powder layer quality was examined by layer thickness deviation (LTD), surface coverage ratio (SCR), surface layer RMS roughness (S_q) and true packing density (PD_{tr}). The difference between true packing density, which solely takes under consideration the coordination number of all the particles, and the theoretical packing density, which considers the theoretical layer thickness as a way to calculate the volume of the layer, was shown. It was proven that using a very low shear ratio value (G), approximately 3-4 orders of

magnitude smaller to the real-world value, leads to results on the safe side, with slightly worse powder layer quality, but at computational time up to 12 times less. Cross-examination between simulation and experimental results for angle of repose and angle of avalanche tests ensured the realistic rheological behaviour of the powder. True packing density was found to be constant regardless of the spreading parameter levels. Furthermore, recoating speed was proven to be the most impactful parameter for layer quality in terms of every quality criterion. The effect of vibration was proven to be beneficial, as it creates more level layers, with smaller roughness and layer thickness deviation. Especially at relatively low recoating speed, which improves the layer quality, larger vibrating frequency (2000 Hz) was found to have the optimum effect. Additionally, weighed means of the three quality criteria (namely; LTD, SCR and S_q) were plotted versus the skewness (Ssk) and kurtosis (Sku) values for each one of the Taguchi trials. The weights were calculated to establish the best linear approximation by least-squares. It was proven that Ssk and Sku can serve as equivalent surface layer quality criteria. This makes it possible for researchers to only evaluate one surficial layer parameter to estimate the deposited layer quality, hence making the process of surface layer evaluation significantly easier. However, this should also be tested for experimentally-spread layers via 3D scanning of the layer. In addition, simulations only examined spherical particles, so non-spherical ones should also be examined to check whether Ssk and Sku can serve as surface layer indicators regardless of particle shape geometry.

The fourth issue addressed was suitability of powder sieving as an alternative to doctor blades for powder deposition. The same powder model was used again with DEM simulation, Taguchi DoE and ANOVA. The sieving parameters examined were the powder fed into the sieve, the vertical vibration amplitude and frequency and the inverse taper angle of the sieve's apertures. The effect of the aforementioned parameters was examined during the steady phase, i.e., the stage during which the sieving process demonstrates stable mass flow. The duration of the steady phase, the powder mass sieved during the steady phase and the steady phase mass flow were evaluated. The results proved that the total mass in linearity and the duration of linearity are affected almost solely by the amount of powder fed into the sieve, i.e., by the powder level in the sieve. The higher the powder level, the longer the duration and the total powder mass sieved during the stable sieving phase. This effect is accentuated by high

vibrational frequency. However, the mass flow seems to depend more heavily on the vibrational amplitude and frequency (almost equally for each one) and less on the powder level in the sieve. Smaller amplitude leads to higher mass flow, the effect being accentuated by smaller frequency and smaller powder level in the sieve. Then, the quality of the powder layer created by controlled sieving was evaluated for each of the Taguchi DoE trials by measuring Ssk and Sku. It was proven that, by controlled sieving it is possible to deposit PBF-ready layers of higher quality compared to the ones deposited via vibration-less doctor blade. By ensuring properly controlled vibration of the sieve and adequacy of the mass that will be deposited during the sieving stable phase for the desired layer thickness, PBF-ready layers can be created. This minimizes spreading time, since sieving only happens 'momentarily' for the layer thicknesses desired in PBF processes. However, mechanical limitations exist, since proper equipment needs to be developed to eliminate noise interference (e.g., noise caused by the motor vibrations that are transferred to the sieve through the parts of the assembly that are in contact with each other) and ensure that the direction, the amplitude and frequency of the vibration are achieved with accuracy.

The fifth issue addressed in this work was the notable lack of various multi-material powder deposition methods. A method based on the dual contour gauge design was developed and it was mathematically defined and coded. The multi-material layer was separated into several uni-material sub-layers, each of which could be isolated via a different positioning of the blades of each one of the contour gauges. Then, powder could be sieved onto the isolated sub-layer by using proper sieving parameters, as these were defined in the sieving simulations previously. The powder layer is either deposited solely via sieving, or the left contour gauge blades function as doctor blades. During repositioning of the latter for the isolation of the next uni-material sub-layer, the recoating and expelling of the excess powder are performed, using the optimized spreading parameters that were defined in the spreading simulations previously. A validation proof-of-concept experiment was performed both via DEM simulation and via an in-house built experimental jig. Both tests indicated that the borders of the deposited patterns and the layer surface quality are acceptable. This process may provide researchers and the industry with a novel way of multi-material deposition. However, highly complex layers or many materials drastically increase the deposition

time. Furthermore, an automated device needs to be designed and manufactured, which, given the complexity of the design and the multitude of the blades, is not a trivial feat.

7.2 Future Work

The high level of complexity of powder deposition for the preparation of PBF-ready uni-material and multi-material layers makes it impossible to cover every aspect in a single thesis; hence, the following suggestions for future work are made.

At first, the literature review uncovered the need to develop more methods of monitoring the powder deposited layer quality online, with non-destructive methods. Especially there are no ways of monitoring true packing density during or right after the layer deposition by the powder deposition system. For instance, methods based on light reflectivity of the powder may be examined, since, the denser the layer, the less light escapes from a beam dropping vertically onto the layer. In addition, researchers need to quantify the relation between powder spreading parameters to PLQIs and, ultimately, to FPQIs, since the qualitative analysis provided only gives the general guidelines, but it is not enough to actually optimize part development in terms of mechanical properties.

Furthermore, it is of paramount importance to design and manufacture powder deposition systems that implement controllable vibration onto the recoating method (roller or doctor blade). For instance, vibration via ultra-sonication seems promising, as long as only the recoater receives the excitation and the previous layers remain intact, which would be a challenging feat. Alternatively, simple mechanical vibrations enforced via high-speed motors paired with cams of the desired dimensions might also be worth examining, especially for vibration amplitudes larger than the ones examined in this work. Developing systems that accurately control the direction, frequency and amplitude of vibration is a necessity for achieving the sieving deposition, which could be a breakthrough, as it will drastically reduce part manufacturing time for the PBF processes.

Leveraging DEM simulation, it would be beneficial to examine the effect of vibration on a roller recoater and compare it to the performance of the vibrated doctor blade. Additionally, particle shapes of increased angularity could be examined, in order to check whether the surficial skewness and kurtosis of the layer can serve as equivalent

layer quality indicators, since the different particle shape would affect the surficial parameters in ways that cannot be predicted or estimated without running the said simulations. Finally, examination of actual powder layers should be performed and the results should be connected to the simulations. 3D white light scanning is a suitable non-destructive method for layer quality evaluation, since it provides a point cloud of the top surface of the layer.

Finally, in order to actually develop multi-material layers using the method introduced in this work, the described system should be designed in a way that provides automated and accurate motion and positioning of every element of the assembly, which, given its complexity, will be challenging. In order to minimize the part production time, developing new software to optimize the part positioning within the build chamber in order to simplify the border curve patterns is imperative, so that the number of uni-material sub-layers is minimized. Furthermore, hybrid multi-material powder deposition methods could be developed. Combining the dual contour gauge method with vibrating nozzle methods could alleviate the limitations of each method, since the former could be used to spread large uni-material areas fast, while the latter could be implemented to accelerate the deposition of small areas, creating the small features of the mosaic pattern, simplifying the x-axis segmentation process.

7.3 Publications Stemming from this Thesis

- Chapter 2:
  1. P. Avrampos and G.-C. Vosniakos, “A review of powder deposition in additive manufacturing by powder bed fusion,” *J. Manuf. Process.*, vol. 74, pp. 332–352, Feb. 2022, doi: 10.1016/j.jmapro.2021.12.021.
- Chapter 3:
  1. P. Avrampos and G.-C. Vosniakos, “A prototype powder deposition system for an open Selective Laser Sintering machine,” *Procedia Manuf.*, vol. 51, pp. 755–762, 2020, doi: 10.1016/j.promfg.2020.10.106.
  2. P. Avrampos, “Optimized development of a prototype Selective Laser Sintering powder recoating system via Analytic Hierarchy Process,” *Int. J. Exp. Des. Process Optim.*, vol. 1, no. 1, p. XX, 2023, doi: 10.1504/IJEDPO.2023.10059808.
  3. S. Pasalopoulos, P. Avrampos, and G.-C. Vosniakos, “Surface quality evaluation of non-sintered powder layers in Selective Laser Sintering by 3D scanning,” *Procedia Manuf.*, vol. 51, no. 2019, pp. 748–754, 2020, doi: 10.1016/j.promfg.2020.10.105.
- Chapter 4:
  1. P. Avrampos and G.-C. Vosniakos, “A Study on Powder Spreading

Quality in Powder Bed Fusion Processes Using Discrete Element Method Simulation," *J. Manuf. Mater. Process.*, vol. 8, no. 3, p. 101, May 2024, doi: 10.3390/jmmp8030101.

- Chapter 5:
  1. P. Avrampos and G.-C. Vosniakos, "A Simulation Study on Sieving as a Powder Deposition Method in Powder Bed Fusion Processes," *Materials (Basel).*, vol. 17, no. 14, p. 3382, Jul. 2024, doi: 10.3390/ma17143382.
- Chapter 6:
  1. P. Avrampos and G.-C. Vosniakos, "A Novel Method of Depositing Multi-material Powder Layers for Powder Bed Fusion Processes," (under review).

8 *Appendices*

8.1 Appendix A: Bill of Materials of Prototype PRS (screws, nuts and washers are not included)

Code	Description	Qty	Material	M/B*
	Powder Hopper/Doser Subassembly	**1**		
1	Powder tank	1	Al 6061	M
2	Doser cylinder tube	1	Al 6061	M
3	Doser drum cylinder	1	Al 6061	M
4	Doser cylinder housing	2	Al 6061	M
5	Doser powder seal	1	Ertalon PA6	M
6	Powder tank level indicator	1	Polystyrene	M
7	Motor mounting bracket	1	Cast iron	M
8	Doser mounting bracket	1	Cast iron	M
9	GT2 20T timing pulley	1	Al 6061	B
10	GT2 60T timing pulley	1	Al 6061	B
11	GT2 320mm timing belt	1	GFRP Neoprene	B
17	Compression springs D_i=6.5mm d_w=0.5mm n=13 L_o=20mm	6	Inox 302	B
22	AFBMA 20.1 - 15 x 35 x 11 (d_i x d_o x t) Ball Bearings	2	SAE 52100 St	B
23	42BYGHW804 (NEMA 17) *Wantai Motors* Stepper Motor (Doser)	1	(multiple)	B
	Siever subassembly	**1**		
24	Connecting arms	2	Cast iron	M
25	Siever top bearing plate	1	Al 6061	M
26	Siever bottom bearing plate	1	Al 6061	M
27	Siever connecting rod	1	Al 6061	M
28	Siever cam	1	Cast iron	M
29	Siever cam axle	1	Cast iron	M
30	Siever spacer	1	Cast iron	M
31	Siever middle axle	1	Cast iron	M
32	Siever connecting part	1	Al 6061	M
33	Siever rod spacer	2	Cast iron	M

34	Siever rod D=8mm	1	Inox 302	B
35	Siever tank	1	Al 6061	M
36	Interchangeable mesh	1	Carbon steel	B
37	Siever motor mounting bracket	1	Cast iron	M
38	GT2 20T timing pulley	1	Al 6061	B
39	GT2 40T timing pulley	3	Al 6061	B
40	GT2 200mm timing belt	1	GFRP Neoprene	B
41	Tipper connecting part	1	Al 6061	M
42	Tipper belt tensioning plate	1	Al 6061	M
43	Tipper motor mounting bracket	1	Cast iron	M
44	GT2 320mm timing belt	1	GFRP Neoprene	B
45	Brass bushings 6 x 12 x 10(d_i x d_o x t)	2	Brass	B
46	Horizontal axis brackets SHF8	2	Al 6061	B
47	ISO radial ball bearings (15 x 24 x 5) (d_i x d_o x t)	2	SAE 52100 St	B
48	ISO radial ball bearings (8 x 22 x 7) (d_i x d_o x t)	2	SAE 52100 St	B
49	ISO radial ball bearings (8 x 16 x 5) (d_i x d_o x t)	2	SAE 52100 St	B
50	57BYGH420 (NEMA 23) *Wantai Motors* Stepper Motor (Siever)	1	(multiple)	B
51	57BYGH420 (NEMA 23) *Wantai Motors* Stepper Motor (Tipper)	1	(multiple)	B
	Doctor blade subassembly	**1**		
65	Doctor blade	1	inox 302	B
66	Starrett V1212MXRL Micrometer, 25-50mm, 1 μm resolution	2	(multiple)	B
67	Doctor blade securing cylinder	1	Al 6061	M
68	Micrometer height adjusting rods	2	Cast iron	M
69	Doctor blade z-inclination controlling plates	2	Al 6061	M
70	Micrometer holders	2	Al 6061	M
71	Micrometer cylinder junctions	2	Polystyrene	M
72	Micrometer cylinder junction spheres	2	Inox 302	B
73	Compression springs D_i=11mm, d_w=0.75mm, n=10, L_o=45mm	2	Inox 302	B
	Recoating cylinder (roller) subassembly	**1**		
82	Roller D=22mm	1	Inox 302	B
83	Roller housing	2	Al 6061	M
84	Roller gantry plate	1	Al 6061	M
85	Roller gantry side cable rail (Left)	1	Al 6061	M
86	Roller gantry side cable rail (Right)	1	Al 6061	M
87	Linear bearing platform MGN12CH	4	(multiple)	B

88	Roller motor mounting bracket	1	Al 6061	M
89	GT2 40T timing pulley	2	Al 6061	B
90	GT2 200mm timing belt	1	GFRP Neoprene	B
91	AFBMA 18.1.3.1 - 10 x 14 x 12 mm (d_i x d_o x t) Needle Roller Bearings	2	SAE 52100 St	B
99	42BYGHW804 (NEMA 17) *Wantai Motors* Stepper Motor (Roller)	1	(multiple)	B
	Linear motion system	**1**		
100	MGN 12H Rails	2	(multiple)	B
101	57BYGH420 (NEMA 23) *Wantai Motors* Stepper Motor	1	(multiple)	B
102	Lead screw-nut block	1	Inox 302	B
103	Linear motor mounting bracket	1	Al 6061	M
107	Roller gantry plate-Lead screw nut's connector	1	Al 6061	M

*M/B: made/bought

8.2 Appendix B: Arduino™ UNO Code for PRS Control

```
/*
- SECOND APPROACH IN SYSTEM HANDLING.
- Dosers are activated by the same pin.
- System will be executed only once.
- Somehow PMAC should reset the system (TX input?).
- Debouncing is the function with which switches acquire a steady response.
*/

// SYSTEM INITIALIZATION.

#include <AccelStepper.h>

/* Initialize Xaxis stepper motor pins and properties of the motor. */
/* Arduino Pin assignment. */
/* Purple (DRV8825) Top Right Driver. */
#define Xaxis_pindir 2
#define Xaxis_pinstep 3
#define sleep_Xaxis 8
/* Xaxis stepper motor property settings. */
#define stepsPerRev_Xaxis 200
#define Xaxis_speed 750
#define Xaxis_acc 40000

/* Initialize Doser Drum stepper motor pins and properties of the motor. */
/* Arduino Pin assignment. */
/* Red (Big Easy Driver) Bottom Left Driver. */
#define dd_pindir 4
#define dd_pinstep 5
#define sleep_dd 19
/* Doser Drum stepper motor property settings. */
#define dd_speed 1500
#define dd_acc 1000

/* Initialize Roller stepper motor pins and properties of the motor. */
/* Arduino Pin assignment. */
/* Red (Big Easy Driver) Top Left Driver. */
#define roller_pindir 7
#define roller_pinstep 6
#define sleep_roller 18
/* Roller stepper motor property settings. */
#define roller_speed 4000

/* Initialize Sieve Tipper stepper motor pins and properties of the motor. */
/* Arduino Pin assignment. */
/* Green (A4988) Top Left Driver. */
#define tipper_pindir 12
#define tipper_pinstep 11
#define sleep_tipper 13
/* Tipper stepper motor property settings. */
#define tipper_speed 500
#define tipper_acc 65000
#define stepsPerRev_tipper 2000

/* Initialize Sieve's palindromic motion's stepper motor pins. */
/* Arduino Pin assignment. */
/* Red (Big Easy Driver) Middle Left Driver. */
#define siever_pindir 9
#define siever_pinstep 10
#define sleep_siever 17
/* Siever stepper motor property settings. */
#define siever_speed 10000
#define siever_acc 40000
#define stepsPerRev_siever 3200

/* Define the Arduino pins of the switches of the Powder Deposition System (PDS). */
#define switch_Xaxis 14 // Left border switch for Xaxis stepper motor motion. A0-HIGH
when Open (NC).
#define enc_lin 16      // Linear encoder for Xaxis stepper motor motion. A2-HIGH when
Open (NC).

/* Define global variables for the amount of void loop() execution times and linear
encoder position identification. */
```

```
int execute=HIGH ;               // Execute program when HIGH, stop execution while
LOW.
int lin_count=0;                // Counts how many times linear encoder changes value.
int lin_prev=HIGH,lin_now=HIGH; // Show the previous and current state of the linear
encoder's switch, respectively.

/* Initialization of stepper motors driving via the AccelStepper library. */
AccelStepper Xaxis(AccelStepper::DRIVER,Xaxis_pinstep,Xaxis_pindir); //
(steps,direction).
AccelStepper dd(AccelStepper::DRIVER,dd_pinstep, dd_pindir);
AccelStepper roller(AccelStepper::DRIVER,roller_pinstep,roller_pindir);
AccelStepper siever(AccelStepper::DRIVER,siever_pinstep,siever_pindir);
AccelStepper tipper(AccelStepper::DRIVER,tipper_pinstep,tipper_pindir);

// SYSTEM SETUP (To be executed only once, at the start of the SLS printing process).

void setup() {

/* Starting serial to screen monitor the program. */
 Serial.begin(9600);
 Serial.println("entered setup");

/* Set Xaxis stepper motor initial settings. */
Xaxis.setMaxSpeed(Xaxis_speed);   // Setting maximum Speed.
Xaxis.setAcceleration(Xaxis_acc); // Setting Acceleration.
Xaxis.setEnablePin(sleep_Xaxis);  // Setting Enable Pin.

/* Set Doser Drum stepper motor initial settings. */
dd.setMaxSpeed(dd_speed);   // Setting maximum Speed.
dd.setAcceleration(dd_acc); // Setting Acceleration.
dd.setEnablePin(sleep_dd);  // Setting Enable Pin.

/* Set Roller stepper motor initial settings. */
roller.setMaxSpeed(8000);          // Setting maximum Speed.
roller.setAcceleration(100);       // Setting Acceleration.
roller.setEnablePin(sleep_roller); // Setting Enable Pin.

/* Set Siever stepper motor initial settings. */
siever.setMaxSpeed(siever_speed);   // Setting maximum Speed.
siever.setAcceleration(siever_acc); // Setting Acceleration.
siever.setEnablePin(sleep_siever);  // Setting Enable Pin.

/* Set Tipper stepper motor initial settings. */
tipper.setMaxSpeed(tipper_speed);   // Setting maximum Speed.
tipper.setAcceleration(tipper_acc); // Setting Acceleration.
tipper.setEnablePin(sleep_tipper);  // Setting Enable Pin.

/* Initialization of switches. */
pinMode(switch_Xaxis,INPUT); // Left border switch of Xaxis.

/* Bringing table into starting position (left). */
tipper.disableOutputs();
roller.disableOutputs();
siever.disableOutputs();
dd.disableOutputs();
Xaxis.enableOutputs();       // Enable the driving outputs of Xaxis stepper motor.
Xaxis.setSpeed(Xaxis_speed); // Set the speed of Xaxis stepper motor.

// Serial.println("System Initialization process begin");
while (digitalRead(switch_Xaxis)==HIGH){
  Xaxis.runSpeed();               // Move powder deposition system to the left (Xaxis
<---) till the left border switch is pressed.
}
Xaxis.setPinsInverted(1,0,0);      // Change Xaxis moving direction from left to right
by inverting the rotation direction of Xaxis stepper motor.
myMove(Xaxis,2*stepsPerRev_Xaxis); // Move Xaxis to the right slightly, so that left
border switch gets released again.
Xaxis.disableOutputs();
delay(2000); // Delay for 2000 msec = 2 sec.
Xaxis.enableOutputs();
Xaxis.setSpeed(Xaxis_speed);       // The setSpeed() function must be used after every
myMove() function call.
while (lin_count<1 && digitalRead(switch_Xaxis)==HIGH){ // While linear encoder click
counter is less than 1 and the left border switch is released, enter the loop.
  Xaxis.runSpeed();
  lin_now=digitalRead(enc_lin);    // Read the linear encoder switch current status.
```

```
  if (lin_now!=lin_prev){          // Compare current to previous linear encoder switch
status.
    lin_count++;                   // If status has changed, increase the linear
encoder click number.
    debounce(Xaxis,Xaxis_speed);   // Debouncing via slight motion of the motor to the
same direction (?? Is it really necessary at this point ??).
    }
  lin_prev=lin_now; // Update the previous linear encoder status.
  }
lin_count=0;        // Zero the total linear encoder click count [This variable will be
used in void loop()].
}

// MAIN PROGRAM LOOP (To be executed every time the PMAC requests, in communication
with the other subsystems of the SLS machine).

void loop(){
  Serial.print("Just entered void loop:\n");
//  Serial.print(lin_count);
while (execute==HIGH)
{
//  Serial.println("Just entered while (execute==HIGH) loop:\n");
//  Serial.print(lin_count,"\n");
//  Serial.print(lin_prev, "\n");
//  Serial.print(lin_now, "\n");

Xaxis.disableOutputs(); // Temporarily disable Xaxis stepper motor's driving.
dd.enableOutputs();     // Enable the driving outputs of Doser Drum's stepper motor.

/* Doser Drum dispenses the powder dosage via its rotation. */
dd.setSpeed(dd_speed);
myMove(dd,20000);
dd.disableOutputs();
delay(200);

/* Xaxis to move till the powder sieve initializing position */
Xaxis.enableOutputs();

while (lin_count<=2 &&digitalRead(switch_Xaxis)==HIGH){
  Xaxis.runSpeed();
  lin_now=digitalRead(enc_lin);
  if (lin_now!=lin_prev){
    lin_count++;
    debounce(Xaxis,Xaxis_speed);
//    Serial.print(lin_count);
//    Serial.print(lin_prev, "\n");
//    Serial.print(lin_now, "\n");
  }
}
lin_prev=lin_now;
Xaxis.disableOutputs();
delay(1000);

/* When the Xaxis reaches the predifined position (climbing of second 'hill' of linear
encoder), begin the Roller and the Sieve's stepper motors' movement. */
// Serial.println("laying powder");
Xaxis.enableOutputs();
roller.enableOutputs();
siever.enableOutputs();
roller.setPinsInverted(1,0,0);
Xaxis.setSpeed(Xaxis_speed);
roller.setSpeed(roller_speed);
siever.setSpeed(siever_speed);

/* Powder deposition - simultaneous Xaxis, Roller and Sieve's palindromic movements. */
while (lin_count<=6 &&digitalRead(switch_Xaxis)==HIGH){

  while (lin_count==3){
    Xaxis.runSpeed();
    roller.runSpeed();
    siever.runSpeed();
    lin_now=digitalRead(enc_lin);
    Serial.println(lin_now);
    if (lin_now!=lin_prev){
      lin_count++;
      debounce2(Xaxis,roller,Xaxis_speed,roller_speed);
//      Serial.print(lin_count,"\n");
```

```
//      Serial.print(lin_prev, "\n");
//      Serial.print(lin_now, "\n");
    }
     lin_prev=lin_now;
  }
  siever.disableOutputs();

  while(lin_count>=4 && lin_count<=5){
    Xaxis.runSpeed();
    roller.runSpeed();
    lin_now=digitalRead(enc_lin);
    if (lin_now!=lin_prev){
      lin_count++;
      debounce2(Xaxis,roller,Xaxis_speed,roller_speed);
    }
    lin_prev=lin_now;
  }

  if(lin_count==6){
    Xaxis.disableOutputs();
    roller.disableOutputs();
    tipper.enableOutputs();
    tipper.setPinsInverted(1,0,0);
    myMove(tipper,200);
    delay(200);
    tipper.setPinsInverted(0,0,0);
    tipper.setSpeed(tipper_speed);
    myMove(tipper,199);
  }

  tipper.disableOutputs();
  break;
}

lin_count=0;

delay(2000); //TIPPER FUNCTION-TO BE PERFECTED, not to be performed in every loop
(trials to finalise it).

/* Powder deposition system returns to its starting position (Left). */
Xaxis.enableOutputs();
roller.enableOutputs();
Xaxis.setPinsInverted(0,0,0);
roller.setPinsInverted(0,0,0);
myMove(Xaxis,2*stepsPerRev_Xaxis);
Xaxis.setSpeed(Xaxis_speed);
roller.setSpeed(roller_speed);

while (lin_count<=5 &&digitalRead(switch_Xaxis)==HIGH){
  Xaxis.runSpeed();
  roller.runSpeed();
  lin_now=digitalRead(enc_lin);
  if (lin_now!=lin_prev){
    lin_count++;
    debounce2(Xaxis,roller,Xaxis_speed,roller_speed);
    }
  lin_prev=lin_now;
  }
lin_count=0;
delay(1000);
Xaxis.setPinsInverted(1,0,0);
Xaxis.disableOutputs();
roller.disableOutputs();
execute=LOW;
  }
}

void myMove (AccelStepper&myStepper,int steps)
{
myStepper.move(steps);
// Serial.println("moving");
while (myStepper.distanceToGo()){
  // if(myStepper==&tipper){
  //
  myStepper.run();
  }
}
```

```
void debounce (AccelStepper&myStepper,int stepperSpeed)
{
int temp=0;
float coef=0.;
if (&myStepper==&Xaxis){
  coef=0.5;
  }
else if (&myStepper==&roller){
  coef=1/8;
  }
else{
 coef=0.3;
  }

myStepper.setSpeed(stepperSpeed);
while (temp<coef*stepperSpeed){
  myStepper.runSpeed();
  temp++;
  }
}

void debounce2 (AccelStepper&myStepper1,AccelStepper&myStepper2, int stepperSpeed1,int
stepperSpeed2)
{
int temp=0;
myStepper1.setSpeed(stepperSpeed1);
myStepper2.setSpeed(stepperSpeed2);
while (temp<500){
  myStepper1.runSpeed();
  myStepper2.runSpeed();
  temp++;
  }
}
```

8.3 Appendix C: Powder Layer Points Calculation

```
/* POWDER LAYER EVALUATION-LAYER SURFACE POINTS ACQUISITION */
#include <stdio.h>
#include <stdlib.h>
#include <math.h>
#define N_particles_max 100000
int main()
{

/* Open the already created .txt files that contain the particle data - center
coordinates and diameters. These coordinates are extracted by EDEM software post-
simulation */
/* The .txt files must be located in the same folder as the c code and its .exe post-
compilation file */
/* All lengths are measured in micrometers (μm) */

    FILE* ptr1 = fopen("PARTICLE_ID.txt", "r");
    if (ptr1 == NULL)
  {
        printf("no such file.");
        return 0;
     }

    FILE* ptr2 = fopen("PARTICLE_DIAMETER.txt", "r");
    if (ptr2 == NULL)
  {
        printf("no such file.");
        return 0;
    }

    FILE* ptr3 = fopen("PARTICLE_X.txt", "r");
    if (ptr3 == NULL)
  {
        printf("no such file.");
        return 0;
     }

    FILE* ptr4 = fopen("PARTICLE_Y.txt", "r");
    if (ptr4 == NULL)
  {
        printf("no such file.");
        return 0;
     }

    FILE* ptr5 = fopen("PARTICLE_Z.txt", "r");
    if (ptr5 == NULL)
  {
        printf("no such file.");
        return 0;
     }

    int i;
    int prt_ID[N_particles_max];
    float prt_D[N_particles_max], prt_X[N_particles_max], prt_Y[N_particles_max],
prt_Z[N_particles_max];

/* Read particle center coordinates, diameter and ID from the .txt files and store
them in the respective arrays */

  int N_ID, N_D, N_X, N_Y, N_Z;

  i=0;
  while(fscanf(ptr1, "%d\n",&prt_ID[i])!=EOF)
  {
    i=i+1;
  }
  N_ID=i;

  i=0;
  while(fscanf(ptr2, "%f\n",&prt_D[i])!=EOF)
  {
    i=i+1;
  }
```

```
  N_D=i;

  i=0;
  while(fscanf(ptr3, "%f\n",&prt_X[i])!=EOF)
  {
    i=i+1;
  }
  N_X=i;

  i=0;
  while(fscanf(ptr4, "%f\n",&prt_Y[i])!=EOF)
  {
    i=i+1;
  }
  N_Y=i;

  i=0;
  while(fscanf(ptr5, "%f\n",&prt_Z[i])!=EOF)
  {
    i=i+1;
  }
  N_Z=i;

/* Check that the particle data are stored correctly via screen display */
  int N_prt;

  if( (N_ID==N_D) && (N_ID==N_X) && (N_ID=N_Y) && (N_ID=N_Z) )
  {
//   printf("All N_values are equal to %d.\n", N_ID);
    N_prt=N_ID;
  }
  else
  {
    printf("Error at file reading.\n");
  }

/* Initialize grid x and y values */
/* Calculate limits in excel, then enter here to reduce computing time */

  float x_min = -500;
  float y_min = -500;
  float z_min = 502.5;
  float D_min = 5;
  float x_max = 500;
  float y_max = 500;
  float z_max = 597.4;
  float D_max = 71.3;
  float z_substrate = 500;

  float x, y;
  float dx=1;   /* X-step */
  float dy=1;   /* Y-step */
  float distance;
  float z_temp;
  float sp_Z;

  sp_Z = z_substrate;
/* DEBUG */

//  printf("A/a\tParticle ID\tDiameter\tX\t\tY\t\tZ\n", i+1, prt_ID[i], prt_D[i],
prt_X[i], prt_Y[i], prt_Z[i]);

//  for(i=0;i<N_prt;i++)
//  {
//    printf("%d\t%d\t\t%f\t%f\t%f\t%f\n", i+1, prt_ID[i], prt_D[i], prt_X[i],
prt_Y[i], prt_Z[i]);
//  }

  int sp_cnt=0;   /* sp stands for surface points */

  const char* fileName = "Surface_points_calculated_XYZ_coordinates_grid";
  const char* fileType = ".txt";
  char name_buffer[512];
  FILE* f = NULL;
  sprintf(name_buffer,"%s%s", fileName, fileType);
  f = fopen(name_buffer,"w");
```

```
  const char* fileName2 = "Surface_points_calculated_XYZ_coordinates_columns";
  const char* fileType2 = ".txt";
  char name_buffer2[512];
  FILE* f2 = NULL;
  sprintf(name_buffer2,"%s%s", fileName2, fileType2);
  f2 = fopen(name_buffer2,"w");

  for(x=x_min ; x<=x_max ; x+=dx)
  {
    for(y=y_min ; y<=y_max ; y+=dy)
    {
//     printf("(%f,%f)\n", x, y);

      for(i=0 ; i<N_prt ; i++)
      {
        distance = ((x-prt_X[i])*(x-prt_X[i])) + ((y-prt_Y[i])*(y-prt_Y[i]));

        if( distance < (prt_D[i]/2)*(prt_D[i]/2) )
        {
          z_temp = prt_Z[i] + sqrt( (prt_D[i]/2)*(prt_D[i]/2) - (x-prt_X[i])*(x-
prt_X[i]) - (y-prt_Y[i])*(y-prt_Y[i]) );

          if( z_temp>sp_Z )
          {
            sp_Z=z_temp;
          }

        }
        else if( fabs(distance - (prt_D[i]/2)*(prt_D[i]/2)) <= 0.00001 )
        {
          z_temp = prt_Z[i];

          if(z_temp>sp_Z)
          {
            sp_Z=z_temp;
          }

        }
      }

      fprintf(f2, "%f\t%f\t%f\n", x, y, sp_Z);
      fprintf(f, "%f ", y);
      sp_cnt++;
           sp_Z = z_substrate;

    }
    fprintf(f, "\n");

  }

    return 0;
}
```

8.4 Appendix D: X-axis Segmentation / Intersection Calculation and Sorting

```
/* MULTIMATERIAL POWDER LAYER SEGMENTATION-FRONT DEVELOPMENT */
#include <stdio.h>
#include <stdlib.h>
#include <math.h>
#define Nbc 101   /* NUMBER OF POINTS WITH WHICH EACH BORDER CURVE IS DEPICTED */
#define Nfmax 10^6   /* MAXIMUM NUMBER OF POINTS OF EACH FRONT */

int main()
{

/* Open the already created .txt files that contain the border point coordinates.
These coordinates are extracted y Solidworks section cuts of slicing softwares */
/* The .txt files must be located in the same folder as the c code and its .exe post-
compilation file */
/* WARNING: MIGHT NEED TO COMMENT OUT OR ADD LINES, IN CASE OF MORE OR LESS BORDER
CURVES */

    FILE* ptr1 = fopen("BORDER1.txt", "r");
    if (ptr1 == NULL)
  {
        printf("no such file.");
        return 0;
    }

  FILE* ptr2 = fopen("BORDER2.txt", "r");
    if (ptr2 == NULL)
  {
        printf("no such file.");
        return 0;
    }

    FILE* ptr3 = fopen("BORDER3.txt", "r");
    if (ptr3 == NULL)
  {
        printf("no such file.");
        return 0;
    }

  FILE* ptr4 = fopen("BORDER4.txt", "r");
    if (ptr4 == NULL)
  {
        printf("no such file.");
        return 0;
    }

    FILE* ptr5 = fopen("BORDER5.txt", "r");
    if (ptr5 == NULL)
  {
        printf("no such file.");
        return 0;
    }

    int i;

/*  Insert as many border curves as they exist in the multimaterial layer that is to
be deposited by simply adding lines */
/*  WARNING: MIGHT NEED TO COMMENT OUT OR ADD LINES, IN CASE OF MORE OR LESS BORDER
CURVES  */

    float xborder1[Nbc],yborder1[Nbc];
    float xborder2[Nbc],yborder2[Nbc];
    float xborder3[Nbc],yborder3[Nbc];
    float xborder4[Nbc],yborder4[Nbc];
    float xborder5[Nbc],yborder5[Nbc];

/*  Read border curve coordinates from the .txt files and store them in the
respective arrays */
/*  WARNING: MIGHT NEED TO COMMENT OUT OR ADD LINES, IN CASE OF MORE OR LESS BORDER
CURVES  */
```

```
  int N1, N2, N3, N4, N5;

  i=0;
  while(fscanf(ptr1, "%f%f\n",&xborder1[i],&yborder1[i])!=EOF)
  {
    i=i+1;
  }
  N1=i;

  i=0;
  while(fscanf(ptr2, "%f%f\n",&xborder2[i],&yborder2[i])!=EOF)
  {
    i=i+1;
  }
  N2=i;

  i=0;
  while(fscanf(ptr3, "%f%f\n",&xborder3[i],&yborder3[i])!=EOF)
  {
    i=i+1;
  }
  N3=i;

  i=0;
  while(fscanf(ptr4, "%f%f\n",&xborder4[i],&yborder4[i])!=EOF)
  {
    i=i+1;
  }
  N4=i;

  i=0;
  while(fscanf(ptr5, "%f%f\n",&xborder5[i],&yborder5[i])!=EOF)
  {
    i=i+1;
  }
  N5=i;

/* Close the BC files again */

  fclose(ptr1);
  fclose(ptr2);
  fclose(ptr3);
  fclose(ptr4);
  fclose(ptr5);

/* Check that the border curves are stored correctly via screen display */

//  for(i=0;i<N5;i++){
//    printf("%d\t%f\t%f\n",i+1,xborder5[i],yborder5[i]);
//  }

/* Front creation (Left Front (LF) represents the left array of blades-Right Front
(RF) represents the right array of blades of the area segmentation method) */

  float y, dy;

/* Find the size (along the y-axis) of the powder layer, along with the maximum and
minimum values of the y-arrays of each border curve */
/*  WARNING: MIGHT NEED TO COMMENT OUT OR ADD LINES, IN CASE OF MORE OR LESS BORDER
CURVES  */

  float y_1U, y_2U, y_3U, y_4U, y_5U;   /* Define the upper limits (maximum y-
coordinates) of the 5 border curves */
  float y_1D, y_2D, y_3D, y_4D, y_5D;   /* Define the lower limits (minimum y-
coordinates) of the 5 border curves */
  float temp_y_max, temp_y_min;   /* Define the temporary helper-variables */
  int placeholder_1U[10], placeholder_2U[10], placeholder_3U[10], placeholder_4U[10],
placeholder_5U[10];  /* Define the placeholders for the position of the maximum y-
value of the array */
  int placeholder_1D[10], placeholder_2D[10], placeholder_3D[10], placeholder_4D[10],
placeholder_5D[10];  /* Define the placeholders for the position of the minimum y-
value of the array */

  temp_y_max=yborder1[0];  /* Initialize maximum value */
  temp_y_min=yborder1[0];  /* Initialize minimum value */

  for(i=0;i<10;i++)
```

```
  {
    placeholder_1U[i]=0;   /* Initialize maximum value's position in the array */
    placeholder_1D[i]=0;   /* Initialize minimum value's position in the array */
  }

  int number_of_max_1, number_of_min_1;
  number_of_max_1=0;
  number_of_min_1=0;

  for (i = 1; i < N1; i++)
  {
      if (yborder1[i] > temp_y_max)
    {
      temp_y_max = yborder1[i];
      }
      if (yborder1[i] < temp_y_min)
    {
        temp_y_min = yborder1[i];
    }
    }
  y_1U=temp_y_max;
  y_1D=temp_y_min;



//  Finding the position of the maximums and minimums of the BC1

  for (i = 0; i < N1; i++)
  {
    if(fabs(yborder1[i]-y_1U)<0.00001)
    {
      number_of_max_1++;
      placeholder_1U[number_of_max_1-1]=i;
    }

    if(fabs(yborder1[i]-y_1D)<0.00001)
    {
      number_of_min_1++;
      placeholder_1D[number_of_min_1-1]=i;
    }
  }

  for(i=0;i<number_of_max_1;i++)
  {
    printf("#%d max of BC1 is the point (%f,%f)\n", i+1, xborder1[placeholder_1U[i]],
y_1U);
  }

  for(i=0;i<number_of_min_1;i++)
  {
    printf("#%d min of BC1 is the point (%f,%f)\n", i+1, xborder1[placeholder_1D[i]],
y_1D);
  }



  temp_y_max=yborder2[0];  /* Initialize maximum value */
  temp_y_min=yborder2[0];  /* Initialize minimum value */

  for(i=0;i<10;i++)
  {
    placeholder_2U[i]=0;   /* Initialize maximum value's position in the array */
    placeholder_2D[i]=0;   /* Initialize minimum value's position in the array */
  }

  int number_of_max_2, number_of_min_2;
  number_of_max_2=0;
  number_of_min_2=0;

  for (i = 1; i < N2; i++)
  {
      if (yborder2[i] > temp_y_max)
    {
      temp_y_max = yborder2[i];
      }
      if (yborder2[i] < temp_y_min)
    {
```

```
       temp_y_min = yborder2[i];
    }
    }
  y_2U=temp_y_max;
  y_2D=temp_y_min;


//  Finding the position of the maximums and minimums of the BC2

  for (i = 0; i < N2; i++)
  {
    if(fabs(yborder2[i]-y_2U)<0.00001)
    {
      number_of_max_2++;
      placeholder_2U[number_of_max_2-1]=i;
    }

    if(fabs(yborder2[i]-y_2D)<0.00001)
    {
      number_of_min_2++;
      placeholder_2D[number_of_min_2-1]=i;
    }
  }

  for(i=0;i<number_of_max_2;i++)
  {
    printf("#%d max of BC2 is the point (%f,%f)\n", i+1, xborder2[placeholder_2U[i]],
y_2U);
  }

  for(i=0;i<number_of_min_2;i++)
  {
    printf("#%d min of BC2 is the point (%f,%f)\n", i+1, xborder2[placeholder_2D[i]],
y_2D);
  }



  temp_y_max=yborder3[0];  /* Initialize maximum value */
  temp_y_min=yborder3[0];  /* Initialize minimum value */

  for(i=0;i<10;i++)
  {
    placeholder_3U[i]=0;   /* Initialize maximum value's position in the array */
    placeholder_3D[i]=0;   /* Initialize minimum value's position in the array */
  }

  int number_of_max_3, number_of_min_3;
  number_of_max_3=0;
  number_of_min_3=0;

  for (i = 1; i < N3; i++)
  {
      if (yborder3[i] > temp_y_max)
    {
      temp_y_max = yborder3[i];
      }
      if (yborder3[i] < temp_y_min)
    {
       temp_y_min = yborder3[i];
    }
    }
  y_3U=temp_y_max;
  y_3D=temp_y_min;


//  Finding the position of the maximums and minimums of the BC3

  for (i = 0; i < N3; i++)
  {
    if(fabs(yborder3[i]-y_3U)<0.00001)
    {
      number_of_max_3++;
      placeholder_3U[number_of_max_3-1]=i;
    }
```

```
    if(fabs(yborder3[i]-y_3D)<0.00001)
    {
      number_of_min_3++;
      placeholder_3D[number_of_min_3-1]=i;
    }
  }

  for(i=0;i<number_of_max_3;i++)
  {
    printf("#%d max of BC3 is the point (%f,%f)\n", i+1, xborder3[placeholder_3U[i]],
y_3U);
  }

  for(i=0;i<number_of_min_3;i++)
  {
    printf("#%d min of BC3 is the point (%f,%f)\n", i+1, xborder3[placeholder_3D[i]],
y_3D);
  }



  temp_y_max=yborder4[0];  /* Initialize maximum value */
  temp_y_min=yborder4[0];  /* Initialize minimum value */

  for(i=0;i<10;i++)
  {
    placeholder_4U[i]=0;   /* Initialize maximum value's position in the array */
    placeholder_4D[i]=0;   /* Initialize minimum value's position in the array */
  }

  int number_of_max_4, number_of_min_4;
  number_of_max_4=0;
  number_of_min_4=0;

  for (i = 1; i < N4; i++)
  {
      if (yborder4[i] > temp_y_max)
    {
      temp_y_max = yborder4[i];
      }
      if (yborder4[i] < temp_y_min)
    {
        temp_y_min = yborder4[i];
    }
  }
  y_4U=temp_y_max;
  y_4D=temp_y_min;



// Finding the position of the maximums and minimums of the BC4

  for (i = 0; i < N4; i++)
  {
    if(fabs(yborder4[i]-y_4U)<0.00001)
    {
      number_of_max_4++;
      placeholder_4U[number_of_max_4-1]=i;
    }

    if(fabs(yborder4[i]-y_4D)<0.00001)
    {
      number_of_min_4++;
      placeholder_4D[number_of_min_4-1]=i;
    }
  }

  for(i=0;i<number_of_max_4;i++)
  {
    printf("#%d max of BC4 is the point (%f,%f)\n", i+1, xborder4[placeholder_4U[i]],
y_4U);
  }

  for(i=0;i<number_of_min_4;i++)
  {
```

```
    printf("#%d min of BC4 is the point (%f,%f)\n", i+1, xborder4[placeholder_4D[i]],
y_4D);
  }



  temp_y_max=yborder5[0];  /* Initialize maximum value */
  temp_y_min=yborder5[0];  /* Initialize minimum value */

  for(i=0;i<10;i++)
  {
    placeholder_5U[i]=0;   /* Initialize maximum value's position in the array */
    placeholder_5D[i]=0;   /* Initialize minimum value's position in the array */
  }

  int number_of_max_5, number_of_min_5;
  number_of_max_5=0;
  number_of_min_5=0;

  for (i = 1; i < N5; i++)
  {
      if (yborder5[i] > temp_y_max)
    {
      temp_y_max = yborder5[i];
      }
      if (yborder5[i] < temp_y_min)
    {
       temp_y_min = yborder5[i];
    }
    }
  y_5U=temp_y_max;
  y_5D=temp_y_min;



//  Finding the position of the maximums and minimums of the BC5

  for (i = 0; i < N5; i++)
  {
    if(fabs(yborder5[i]-y_5U)<0.00001)
    {
      number_of_max_5++;
      placeholder_5U[number_of_max_5-1]=i;
    }

    if(fabs(yborder5[i]-y_5D)<0.00001)
    {
      number_of_min_5++;
      placeholder_5D[number_of_min_5-1]=i;
    }
  }

  for(i=0;i<number_of_max_5;i++)
  {
    printf("#%d max of BC5 is the point (%f,%f)\n", i+1, xborder5[placeholder_5U[i]],
y_5U);
  }

  for(i=0;i<number_of_min_5;i++)
  {
    printf("#%d min of BC5 is the point (%f,%f)\n", i+1, xborder5[placeholder_5D[i]],
y_5D);
  }



//  printf("%f\n",y_1U);
//  printf("%f\n",y_1D);

/* DEFINE THE Y AND DY VALUES FOR THE SCANNING OF THE POWDER LAYER */

  y=0;
  dy=y_1U/1000;
    int max_int_count_total=0;
  float X_INT_COMPLETE[30000], Y_INT_COMPLETE[30000];
  int BC_INT_IND_COMPLETE[30000];
```

```
  int cumsum_int_at_cur_y[30000];   /* Stores the cumulative sum of intersections of
all the border curves until a certain y value */
  int big_loop_counter=0;
  int int_count_total[30000];
  cumsum_int_at_cur_y[0]=0;


  for(y=0;y<=y_1U;y=y+dy)
  {
    /* FIND THE INTERSECTIONS OF THE Y=Y_CURRENT HORIZONTAL SCANNING LINE WITH THE BC1
*/

    y=round(10*y)/10;   /* Eliminating the rounding error for more accurate results */

    big_loop_counter++;

    float x_int_1[50], y_int_1[50];
    int intersections_count_1=0;

    if( (y>y_1D) && (y<y_1U) )
    {
      for(i=0;i<N1-1;i++)
      {
        if(fabs(yborder1[i]-y)<0.00001)
        {
          intersections_count_1++;
          if(i>0 && i<N1-1 && (yborder1[i-1]-yborder1[i])*(yborder1[i]-
yborder1[i+1])<0)     /* Searching for local extremes (minimums and maximums) */
          {
            x_int_1[intersections_count_1-1]=xborder1[i]-0.001;
            y_int_1[intersections_count_1-1]=y;
            intersections_count_1++;
            x_int_1[intersections_count_1-1]=xborder1[i]+0.001;  /* Duplicating the
extreme */
            y_int_1[intersections_count_1-1]=y;
          }
          else
          {
            x_int_1[intersections_count_1-1]=xborder1[i];
            y_int_1[intersections_count_1-1]=y;
          }
        }
        else if((yborder1[i]-y)*(yborder1[i+1]-y)<0)
        {
          intersections_count_1++;
          if(xborder1[i]!=xborder1[i+1])
          {
            y_int_1[intersections_count_1-1]=y;
            x_int_1[intersections_count_1-1]=y*(xborder1[i+1]-
xborder1[i])/(yborder1[i+1]-yborder1[i])+(yborder1[i+1]*xborder1[i]-
yborder1[i]*xborder1[i+1])/(yborder1[i+1]-yborder1[i]);    /* Linear interpolation */
          }
          else
          {
            x_int_1[intersections_count_1-1]=xborder1[i];
            y_int_1[intersections_count_1-1]=y;
          }
        }
      }
    }
    else if(fabs(y-y_1D)<=0.00001)
    {
      for(i=0;i<N1-1;i++)
      {
//        printf("%f\t%f\t%f\n", y, yborder1[i], fabs(y-yborder1[i]));
        float kappa=fabs(y-yborder1[i]);
        if(kappa<=0.00001)
        {
          intersections_count_1++;
          if(i>0 && i<N1-1 && (yborder1[i-1]-yborder1[i])*(yborder1[i]-
yborder1[i+1])<0)   /* Absolute minimum of BC1 */
          {
            x_int_1[intersections_count_1-1]=xborder1[i]-0.001;
            y_int_1[intersections_count_1-1]=y;
            intersections_count_1++;
            x_int_1[intersections_count_1-1]=xborder1[i]+0.001;  /* Duplicate point */
            y_int_1[intersections_count_1-1]=y;
```

```
         }
         else
         {
           x_int_1[intersections_count_1-1]=xborder1[i];
           y_int_1[intersections_count_1-1]=y;
         }
       }
     }
   }
   else if(fabs(y-y_1U)<=0.00001)
   {
     for(i=0;i<N1-1;i++)
     {
       if(fabs(y-yborder1[i])<=0.00001)
       {
         intersections_count_1++;
         if(i>0 && i<N1-1 && (yborder1[i-1]-yborder1[i])*(yborder1[i]-
yborder1[i+1])<0)   /* Absolute maximum of BC1 */
         {
           x_int_1[intersections_count_1-1]=xborder1[i]-0.001;
           y_int_1[intersections_count_1-1]=y;
           intersections_count_1++;
           x_int_1[intersections_count_1-1]=xborder1[i]+0.001;  /* Duplicate point */
           y_int_1[intersections_count_1-1]=y;
         }
         else
         {
           x_int_1[intersections_count_1-1]=xborder1[i];
           y_int_1[intersections_count_1-1]=y;
         }
       }
     }
   }
   else
   {
     printf("No intersections of the 1st border curve exist at y=%f\n",y);
   }

   printf("The 1st border curve has %d intersection(s) at y=%f\n",
intersections_count_1, y);

   /* FIND THE INTERSECTIONS OF THE Y=Y_CURRENT HORIZONTAL SCANNING LINE WITH THE BC2
*/

   float x_int_2[50], y_int_2[50];
   int intersections_count_2=0;

   if( (y>y_2D) && (y<y_2U) )
   {
     for(i=0;i<N2-1;i++)
     {
       if(fabs(yborder2[i]-y)<0.00001)
       {
         intersections_count_2++;
         if(i>0 && i<N2-1 && (yborder2[i-1]-yborder2[i])*(yborder2[i]-
yborder2[i+1])<0)   /* Searching for local extremes in BC2 */
         {
           x_int_2[intersections_count_2-1]=xborder2[i];//-0.001;
           y_int_2[intersections_count_2-1]=y;
         //  intersections_count_2++;
         //  x_int_2[intersections_count_2-1]=xborder2[i]+0.001;  /* Duplicating the
extreme */
         //  y_int_2[intersections_count_2-1]=y;
         }
         else
         {
           x_int_2[intersections_count_2-1]=xborder2[i];
           y_int_2[intersections_count_2-1]=y;
         }
       }
       else if( (yborder2[i]-y)*(yborder2[i+1]-y)<0 )
       {
         intersections_count_2++;
         if(xborder2[i]!=xborder2[i+1])
         {
           y_int_2[intersections_count_2-1]=y;
```

```
          x_int_2[intersections_count_2-1]=y*(xborder2[i+1]-
xborder2[i])/(yborder2[i+1]-yborder2[i])+(yborder2[i+1]*xborder2[i]-
yborder2[i]*xborder2[i+1])/(yborder2[i+1]-yborder2[i]);    /* Linear interpolation */
         }
         else
         {
          x_int_2[intersections_count_2-1]=xborder2[i];
          y_int_2[intersections_count_2-1]=y;
         }
       }
     }
   }
   else if(fabs(y-y_2D)<=0.00001)
   {
     for(i=0;i<N2-1;i++)
     {
     //  printf("%f\t%f\t%f\n", y, yborder2[i], fabs(y-yborder2[i]));
       float kappa=fabs(y-yborder2[i]);
       if(kappa<=0.00001)
       {
         intersections_count_2++;
         if(i>0 && i<N2-1 && (yborder2[i-1]-yborder2[i])*(yborder2[i]-
yborder2[i+1])<0)   /* Absolute minimum of BC2 */
         {
          x_int_2[intersections_count_2-1]=xborder2[i];//-0.001;
          y_int_2[intersections_count_2-1]=y;
         //  intersections_count_2++;
         //  x_int_2[intersections_count_2-1]=xborder2[i]+0.001;  /* Duplicating the
extreme */
         //  y_int_2[intersections_count_2-1]=y;
         }
         else
         {
          x_int_2[intersections_count_2-1]=xborder2[i];
          y_int_2[intersections_count_2-1]=y;
         }
       }
     }
   }
   else if(fabs(y-y_2U)<=0.00001)
   {
     for(i=0;i<N2-1;i++)
     {
       if(fabs(y-yborder2[i])<=0.00001)
       {
         intersections_count_2++;
         if(i>0 && i<N2-1 && (yborder2[i-1]-yborder2[i])*(yborder2[i]-
yborder2[i+1])<0)   /* Absolute maximum of BC2 */
         {
          x_int_2[intersections_count_2-1]=xborder2[i];//-0.001;
          y_int_2[intersections_count_2-1]=y;
         //  intersections_count_2++;
         //  x_int_2[intersections_count_2-1]=xborder2[i]+0.001;  /* Duplicating the
extreme */
         //  y_int_2[intersections_count_2-1]=y;
         }
         else
         {
          x_int_2[intersections_count_2-1]=xborder2[i];
          y_int_2[intersections_count_2-1]=y;
         }
       }
     }
   }
   else
   {
     printf("No intersections of the 2nd border curve exist at y=%f\n",y);
   }

   printf("The 2nd border curve has %d intersection(s) at y=%f\n",
intersections_count_2, y);

   /* FIND THE INTERSECTIONS OF THE Y=Y_CURRENT HORIZONTAL SCANNING LINE WITH THE BC3
*/

   float x_int_3[50], y_int_3[50];
   int intersections_count_3=0;
```

```
    if( (y>y_3D) && (y<y_3U) )
    {
      for(i=0;i<N3-1;i++)
      {
        if(fabs(yborder3[i]-y)<0.00001)
        {
          intersections_count_3++;
          if(i>0 && i<N3-1 && (yborder3[i-1]-yborder3[i])*(yborder3[i]-
yborder3[i+1])<0)   /* Searching for local extremes in BC3 */
          {
            x_int_3[intersections_count_3-1]=xborder3[i];//-0.001;
            y_int_3[intersections_count_3-1]=y;
          //  intersections_count_3++;
          //  x_int_3[intersections_count_3-1]=xborder3[i]+0.001;  /* Duplicating the
extreme */
          //  y_int_3[intersections_count_3-1]=y;
          }
          else
          {
            x_int_3[intersections_count_3-1]=xborder3[i];
            y_int_3[intersections_count_3-1]=y;
          }
        }
        else if( (yborder3[i]-y)*(yborder3[i+1]-y)<0)
        {
          intersections_count_3++;
          if(xborder3[i]!=xborder3[i+1])
          {
            y_int_3[intersections_count_3-1]=y;
            x_int_3[intersections_count_3-1]=y*(xborder3[i+1]-
xborder3[i])/(yborder3[i+1]-yborder3[i])+(yborder3[i+1]*xborder3[i]-
yborder3[i]*xborder3[i+1])/(yborder3[i+1]-yborder3[i]);    /* Linear interpolation */
          }
          else
          {
            x_int_3[intersections_count_3-1]=xborder3[i];
            y_int_3[intersections_count_3-1]=y;
          }
        }
      }
    }
    else if(fabs(y-y_3D)<=0.00001)
    {
      for(i=0;i<N3-1;i++)
      {
      //  printf("%f\t%f\t%f\n", y, yborder3[i], fabs(y-yborder3[i]));
        float kappa=fabs(y-yborder3[i]);
        if(kappa<=0.00001)
        {
          intersections_count_3++;
          if(i>0 && i<N3-1 && (yborder3[i-1]-yborder3[i])*(yborder3[i]-
yborder3[i+1])<0)   /* Absolute minimum of BC3 */
          {
            x_int_3[intersections_count_3-1]=xborder3[i];//-0.001;
            y_int_3[intersections_count_3-1]=y;
          //  intersections_count_3++;
          //  x_int_3[intersections_count_3-1]=xborder3[i]+0.001;  /* Duplicating the
extreme */
          //  y_int_3[intersections_count_3-1]=y;
          }
          else
          {
            x_int_3[intersections_count_3-1]=xborder3[i];
            y_int_3[intersections_count_3-1]=y;
          }
        }
      }
    }
    else if(fabs(y-y_3U)<=0.00001)
    {
      for(i=0;i<N3-1;i++)
      {
        if(fabs(y-yborder3[i])<=0.00001)
        {
          intersections_count_3++;
```

```
         if(i>0 && i<N3-1 && (yborder3[i-1]-yborder3[i])*(yborder3[i]-
yborder3[i+1])<0)   /* Absolute maximum of BC3 */
         {
           x_int_3[intersections_count_3-1]=xborder3[i];//-0.001;
           y_int_3[intersections_count_3-1]=y;
         //  intersections_count_3++;
         //  x_int_3[intersections_count_3-1]=xborder3[i]+0.001;  /* Duplicating the
extreme */
         //  y_int_3[intersections_count_3-1]=y;
         }
         else
         {
           x_int_3[intersections_count_3-1]=xborder3[i];
           y_int_3[intersections_count_3-1]=y;
         }
       }
     }
   }
   else
   {
     printf("No intersections of the 3rd border curve exist at y=%f\n",y);
   }

   printf("The 3rd border curve has %d intersection(s) at y=%f\n",
intersections_count_3, y);

   /* FIND THE INTERSECTIONS OF THE Y=Y_CURRENT HORIZONTAL SCANNING LINE WITH THE BC4
*/

   float x_int_4[50], y_int_4[50];
   int intersections_count_4=0;

   if( (y>y_4D) && (y<y_4U) )
   {
     for(i=0;i<N4-1;i++)
     {
       if(fabs(yborder4[i]-y)<0.00001)
       {
         intersections_count_4++;
         if(i>0 && i<N4-1 && (yborder4[i-1]-yborder4[i])*(yborder4[i]-
yborder4[i+1])<0)   /* Searching for local extremes in BC4 */
         {
           x_int_4[intersections_count_4-1]=xborder4[i];//-0.001;
           y_int_4[intersections_count_4-1]=y;
         //  intersections_count_4++;
         //  x_int_4[intersections_count_4-1]=xborder4[i]+0.001;  /* Duplicating the
extreme */
         //  y_int_4[intersections_count_4-1]=y;
         }
         else
         {
           x_int_4[intersections_count_4-1]=xborder4[i];
           y_int_4[intersections_count_4-1]=y;
         }
       }
       else if( (yborder4[i]-y)*(yborder4[i+1]-y)<0)
       {
         intersections_count_4++;
         if(xborder4[i]!=xborder4[i+1])
         {
           y_int_4[intersections_count_4-1]=y;
           x_int_4[intersections_count_4-1]=y*(xborder4[i+1]-
xborder4[i])/(yborder4[i+1]-yborder4[i])+(yborder4[i+1]*xborder4[i]-
yborder4[i]*xborder4[i+1])/(yborder4[i+1]-yborder4[i]);    /* Linear interpolation */
         }
         else
         {
           x_int_4[intersections_count_4-1]=xborder4[i];
           y_int_4[intersections_count_4-1]=y;
         }
       }
     }
   }
   else if(fabs(y-y_4D)<=0.00001)
   {
     for(i=0;i<N4-1;i++)
     {
```

```
     //  printf("%f\t%f\t%f\n", y, yborder4[i], fabs(y-yborder4[i]));
       float kappa=fabs(y-yborder4[i]);
       if(kappa<=0.00001)
       {
         intersections_count_4++;
         if(i>0 && i<N4-1 && (yborder4[i-1]-yborder4[i])*(yborder4[i]-
yborder4[i+1])<0)   /* Absolute minimum of BC4 */
         {
           x_int_4[intersections_count_4-1]=xborder4[i];//-0.001;
           y_int_4[intersections_count_4-1]=y;
         //  intersections_count_4++;
         //  x_int_4[intersections_count_4-1]=xborder4[i]+0.001;  /* Duplicating the
extreme */
         //  y_int_4[intersections_count_4-1]=y;
         }
         else
         {
           x_int_4[intersections_count_4-1]=xborder4[i];
           y_int_4[intersections_count_4-1]=y;
         }
       }
     }
    }
    else if(fabs(y-y_4U)<=0.00001)
    {
      for(i=0;i<N4-1;i++)
      {
        if(fabs(y-yborder4[i])<=0.00001)
        {
          intersections_count_4++;
          if(i>0 && i<N4-1 && (yborder4[i-1]-yborder4[i])*(yborder4[i]-
yborder4[i+1])<0)   /* Absolute maximum of BC4 */
          {
            x_int_4[intersections_count_4-1]=xborder4[i];//-0.001;
            y_int_4[intersections_count_4-1]=y;
          //  intersections_count_4++;
          //  x_int_4[intersections_count_4-1]=xborder4[i]+0.001;  /* Duplicating the
extreme */
          //  y_int_4[intersections_count_4-1]=y;
          }
          else
          {
            x_int_4[intersections_count_4-1]=xborder4[i];
            y_int_4[intersections_count_4-1]=y;
          }
        }
      }
    }
    else
    {
      printf("No intersections of the 4th border curve exist at y=%f\n",y);
    }

    printf("The 4th border curve has %d intersection(s) at y=%f\n",
intersections_count_4, y);

    /* FIND THE INTERSECTIONS OF THE Y=Y_CURRENT HORIZONTAL SCANNING LINE WITH THE BC5
*/

    float x_int_5[50], y_int_5[50];
    int intersections_count_5=0;

    if( (y>y_5D) && (y<y_5U) )
    {
      for(i=0;i<N5-1;i++)
      {
        if(fabs(yborder5[i]-y)<0.00001)
        {
          intersections_count_5++;
          if(i>0 && i<N5-1 && (yborder5[i-1]-yborder5[i])*(yborder5[i]-
yborder5[i+1])<0)   /* Searching for local extremes in BC5 */
          {
            x_int_5[intersections_count_5-1]=xborder5[i]-0.001;
            y_int_5[intersections_count_5-1]=y;
            intersections_count_5++;
            x_int_5[intersections_count_5-1]=xborder5[i]+0.001;  /* Duplicating the
extreme */
```

```
          y_int_5[intersections_count_5-1]=y;
         }
         else
         {
          x_int_5[intersections_count_5-1]=xborder5[i];
          y_int_5[intersections_count_5-1]=y;
         }
       }
       else if( (yborder5[i]-y)*(yborder5[i+1]-y)<0)
       {
         intersections_count_5++;
         if(xborder5[i]!=xborder5[i+1])
         {
          y_int_5[intersections_count_5-1]=y;
          x_int_5[intersections_count_5-1]=y*(xborder5[i+1]-
xborder5[i])/(yborder5[i+1]-yborder5[i])+(yborder5[i+1]*xborder5[i]-
yborder5[i]*xborder5[i+1])/(yborder5[i+1]-yborder5[i]);    /* Linear interpolation */
         }
         else
         {
          x_int_5[intersections_count_5-1]=xborder5[i];
          y_int_5[intersections_count_5-1]=y;
         }
       }
     }
   }
   else if(fabs(y-y_5D)<=0.00001)
   {
     for(i=0;i<N5-1;i++)
     {
     //  printf("%f\t%f\t%f\n", y, yborder5[i], fabs(y-yborder5[i]));
       float kappa=fabs(y-yborder5[i]);
       if(kappa<=0.00001)
       {
         intersections_count_5++;
         if(i>0 && i<N5-1 && (yborder5[i-1]-yborder5[i])*(yborder5[i]-
yborder5[i+1])<0)   /* Absolute minimum of BC5 */
         {
          x_int_5[intersections_count_5-1]=xborder5[i]-0.001;
          y_int_5[intersections_count_5-1]=y;
          intersections_count_5++;
          x_int_5[intersections_count_5-1]=xborder5[i]+0.001;  /* Duplicating the
extreme */
          y_int_5[intersections_count_5-1]=y;
         }
         else
         {
          x_int_5[intersections_count_5-1]=xborder5[i];
          y_int_5[intersections_count_5-1]=y;
         }
       }
     }
   }
   else if(fabs(y-y_5U)<=0.00001)
   {
     for(i=0;i<N5-1;i++)
     {
       if(fabs(y-yborder5[i])<=0.00001)
       {
         intersections_count_5++;
         if(i>0 && i<N5-1 && (yborder5[i-1]-yborder5[i])*(yborder5[i]-
yborder5[i+1])<0)   /* Absolute maximum of BC5 */
         {
          x_int_5[intersections_count_5-1]=xborder5[i]-0.001;
          y_int_5[intersections_count_5-1]=y;
          intersections_count_5++;
          x_int_5[intersections_count_5-1]=xborder5[i]+0.001;  /* Duplicating the
extreme */
          y_int_5[intersections_count_5-1]=y;
         }
         else
         {
          x_int_5[intersections_count_5-1]=xborder5[i];
          y_int_5[intersections_count_5-1]=y;
         }
       }
     }
```

```
    }
    else
    {
      printf("No intersections of the 5th border curve exist at y=%f\n",y);
    }

    printf("The 5th border curve has %d intersection(s) at y=%f\n",
intersections_count_5, y);

    /* Fill arrays with all intersections-create array of indicators-to which BC each
intersection belongs */

    float x_int_ALL[50], y_int_ALL[50];  /* arrays that contain all intersections */
    int BC_int_ind[50];  /* Indicator array-if an intersection belongs to BC1, then
it has value of 1, if it belongs to BC2, it has a value of 2, etc. */

    for(i=0;i<intersections_count_1;i++)
    {
      x_int_ALL[i]=x_int_1[i];
      y_int_ALL[i]=y_int_1[i];
      BC_int_ind[i]=1;
    }

    for(i=intersections_count_1;i<intersections_count_1+intersections_count_2;i++)
    {
      x_int_ALL[i]=x_int_2[i-intersections_count_1];
      y_int_ALL[i]=y_int_2[i-intersections_count_1];
      BC_int_ind[i]=2;
    }


  for(i=intersections_count_1+intersections_count_2;i<intersections_count_1+intersect
ions_count_2+intersections_count_3;i++)
    {
      x_int_ALL[i]=x_int_3[i-intersections_count_1-intersections_count_2];
      y_int_ALL[i]=y_int_3[i-intersections_count_1-intersections_count_2];
      BC_int_ind[i]=3;
    }


  for(i=intersections_count_1+intersections_count_2+intersections_count_3;i<intersect
ions_count_1+intersections_count_2+intersections_count_3+intersections_count_4;i++)
    {
      x_int_ALL[i]=x_int_4[i-intersections_count_1-intersections_count_2-
intersections_count_3];
      y_int_ALL[i]=y_int_4[i-intersections_count_1-intersections_count_2-
intersections_count_3];
      BC_int_ind[i]=4;
    }


  for(i=intersections_count_1+intersections_count_2+intersections_count_3+intersectio
ns_count_4;i<intersections_count_1+intersections_count_2+intersections_count_3+inters
ections_count_4+intersections_count_5;i++)
    {
      x_int_ALL[i]=x_int_5[i-intersections_count_1-intersections_count_2-
intersections_count_3-intersections_count_4];
      y_int_ALL[i]=y_int_5[i-intersections_count_1-intersections_count_2-
intersections_count_3-intersections_count_4];
      BC_int_ind[i]=5;
    }

    /* Intersection array sorting in ascending x-coordinate order */

      float temp_sort_x;
      int temp_sort_ind;
      int j;


  int_count_total[big_loop_counter]=intersections_count_1+intersections_count_2+inter
sections_count_3+intersections_count_4+intersections_count_5;
      cumsum_int_at_cur_y[big_loop_counter]=cumsum_int_at_cur_y[big_loop_counter-
1]+int_count_total[big_loop_counter];


      if(max_int_count_total<int_count_total[big_loop_counter])
      {
```

```
       max_int_count_total=int_count_total[big_loop_counter];
       printf("The current maximum intersection number is %d and first occurs at
y=%f\n", max_int_count_total, y);
     }



         for (i = 0; i < int_count_total[big_loop_counter]; ++i)
         {
             for (j = i + 1; j < int_count_total[big_loop_counter]; ++j)
             {
                 if (x_int_ALL[i] > x_int_ALL[j])
                 {
                     temp_sort_x =  x_int_ALL[i];
                     temp_sort_ind = BC_int_ind[i];
                     x_int_ALL[i] = x_int_ALL[j];
                     BC_int_ind[i] = BC_int_ind[j];
                     x_int_ALL[j] = temp_sort_x;
                     BC_int_ind[j] = temp_sort_ind;
                 }
             }
         }

   int help=0;
   for(i=cumsum_int_at_cur_y[big_loop_counter-
1];i<cumsum_int_at_cur_y[big_loop_counter];i++)
   {

       X_INT_COMPLETE[i]=x_int_ALL[help];
       Y_INT_COMPLETE[i]=y_int_ALL[help];
       BC_INT_IND_COMPLETE[i]=BC_int_ind[help];
       help++;
   }

   for (i = 0; i < int_count_total[big_loop_counter]; ++i)
   {
     printf("#%d intersection: The #%d border curve's (BC%d) has an intersection at
the point (%f,%f)\n", i+1, BC_int_ind[i], BC_int_ind[i], x_int_ALL[i], y_int_ALL[i]);

   }
 }

 for(i=0;i<big_loop_counter;i++)
 {
   printf("At y=%f, there are %d intersections, raising the cumulative sum of
intersections to the number of %d\n", i*dy,
int_count_total[i+1],cumsum_int_at_cur_y[i+1]);
 }

/* FITTING THE INTERSECTIONS INTO FRONTS */

 int internal_int_counter=1;
 int local_counter[10000];

 for(i=0;i<cumsum_int_at_cur_y[big_loop_counter];i++)
 {
   if(i==0)
   {
     printf("#%d intersection: The #%d border curve's (BC%d) has an intersection (the
#%d intersection at y=%f) at the point (%f,%f)\n", i+1, BC_INT_IND_COMPLETE[i],
BC_INT_IND_COMPLETE[i], internal_int_counter, Y_INT_COMPLETE[i], X_INT_COMPLETE[i],
Y_INT_COMPLETE[i]);
     local_counter[i]=internal_int_counter;
   }
   else if(fabs(Y_INT_COMPLETE[i]-Y_INT_COMPLETE[i-1])<=0.00001)
   {
     internal_int_counter++;
     printf("#%d intersection: The #%d border curve's (BC%d) has an intersection (the
#%d intersection at y=%f) at the point (%f,%f)\n", i+1, BC_INT_IND_COMPLETE[i],
BC_INT_IND_COMPLETE[i], internal_int_counter, Y_INT_COMPLETE[i], X_INT_COMPLETE[i],
Y_INT_COMPLETE[i]);
     local_counter[i]=internal_int_counter;
   }
   else
   {
```

```
     printf("#%d intersection: The #%d border curve's (BC%d) has an intersection (the
#1 intersection at y=%f) at the point (%f,%f)\n", i+1, BC_INT_IND_COMPLETE[i],
BC_INT_IND_COMPLETE[i], Y_INT_COMPLETE[i], X_INT_COMPLETE[i], Y_INT_COMPLETE[i]);
     internal_int_counter=1;
     local_counter[i]=internal_int_counter;
   }
  }

// printf("A/A\tX_inters.\tY_inters.\tLoc.int.count\t BC\n");
//
// for(i=0;i<cumsum_int_at_cur_y[big_loop_counter];i++)
// {
//   printf("%d\t%f\t%f\t%d\t\t %d\n", i+1, X_INT_COMPLETE[i], Y_INT_COMPLETE[i],
local_counter[i], BC_INT_IND_COMPLETE[i]);
// }

  printf("The maximum number of intersections is %d.\n", max_int_count_total);

/* Add duplicates for local minimums or maximums */



/* Add the necessary points (X_1R,y_current) in the X_INT_COMPLETE and Y_INT_COMPLETE
arrays */

  int m;
  int added_points=0;
  float X_INT_COMPLETE_FINAL[20000], Y_INT_COMPLETE_FINAL[20000];
  int BC_INT_IND_COMPLETE_FINAL[20000], local_counter_FINAL[20000];

  for(i=0;i<cumsum_int_at_cur_y[big_loop_counter];i++)
  {
     if(fabs(X_INT_COMPLETE[i]-100)<0.00001 && local_counter[i]<max_int_count_total)
     {
       X_INT_COMPLETE_FINAL[i+added_points]=X_INT_COMPLETE[i];
       Y_INT_COMPLETE_FINAL[i+added_points]=Y_INT_COMPLETE[i];
       BC_INT_IND_COMPLETE_FINAL[i+added_points]=BC_INT_IND_COMPLETE[i];
       local_counter_FINAL[i+added_points]=local_counter[i];

       for(m=local_counter[i]+1;m<=max_int_count_total;m++)
       {
         added_points++;
         X_INT_COMPLETE_FINAL[i+added_points]=100;
         Y_INT_COMPLETE_FINAL[i+added_points]=Y_INT_COMPLETE[i];
         BC_INT_IND_COMPLETE_FINAL[i+added_points]=1;
         local_counter_FINAL[i+added_points]=m;
       }
     }
     else
     {
       X_INT_COMPLETE_FINAL[i+added_points]=X_INT_COMPLETE[i];
       Y_INT_COMPLETE_FINAL[i+added_points]=Y_INT_COMPLETE[i];
       BC_INT_IND_COMPLETE_FINAL[i+added_points]=BC_INT_IND_COMPLETE[i];
       local_counter_FINAL[i+added_points]=local_counter[i];
     }
  }

// printf("-------------------------------------------------------------------------------
-------------------------------------------------\n");
// printf("A/A\tX_inters.\tY_inters.\tLoc.int.count\t BC\n");
//
// for(i=0;i<cumsum_int_at_cur_y[big_loop_counter]+added_points;i++)
// {
//   printf("%d\t%f\t%f\t%d\t\t %d\n", i+1, X_INT_COMPLETE_FINAL[i],
Y_INT_COMPLETE_FINAL[i], local_counter_FINAL[i], BC_INT_IND_COMPLETE_FINAL[i]);
// }

/* OPEN THE .TXT FILES THAT WILL CONTAIN THE COORDINATES OF THE FRONTS. */
/* THE NUMBER OF FRONTS IS AT MOST EQUAL TO THE NUMBER OF MAXIMUM INTERSECTIONS AT
SOME Y MULTIPLIED BY THE NUMBER OF MATERIALS ON THE LAYER MINUS 1 */
/* (MAX # FRONTS)=(max_int_count_total)*(# MATERIALS - 1) */

  const char* fileName1 = "Intersection_#";
  const char* fileType = ".txt";
  char buffer1[50];
```

```
  FILE* f1 = NULL;

  int j;

/* Print points into files based on the order of intersections at each y */

  float x_sol, y_sol;
  int loc_cnt_sol, BC_ind_sol;
  float distance, distance_min;;
  distance_min=1000;
  distance=1100;
  int n, j_prev;

  for(i=0;i<max_int_count_total;i++)
  {
    for(j=0;j<cumsum_int_at_cur_y[big_loop_counter]+added_points;j++)
    {
      if(j==0)
      {
        sprintf(buffer1,"%s%d%s",fileName1,i+1,fileType);
        f1 = fopen(buffer1,"w");
      }

      if(local_counter_FINAL[j]==i+1)
      {
        if( (j>1 && j<(cumsum_int_at_cur_y[big_loop_counter]+added_points-1) &&
X_INT_COMPLETE_FINAL[j]-X_INT_COMPLETE_FINAL[j_prev]<-2.5) /* || (j>0 &&
BC_INT_IND_COMPLETE_FINAL[j]!=BC_INT_IND_COMPLETE_FINAL[j_prev] &&
X_INT_COMPLETE_FINAL[j]<X_INT_COMPLETE_FINAL[j_prev]) */ )
        {
          for(n=0;n<12;n++)
          {
            distance = (X_INT_COMPLETE_FINAL[j_prev]-X_INT_COMPLETE_FINAL[j-
local_counter_FINAL[j]+(n+1)])*(X_INT_COMPLETE_FINAL[j_prev]-X_INT_COMPLETE_FINAL[j-
local_counter_FINAL[j]+(n+1)])+(Y_INT_COMPLETE_FINAL[j_prev]-Y_INT_COMPLETE_FINAL[j-
local_counter_FINAL[j]+(n+1)])*(Y_INT_COMPLETE_FINAL[j_prev]-Y_INT_COMPLETE_FINAL[j-
local_counter_FINAL[j]+(n+1)]);

            if(distance<=distance_min)
            {
              x_sol=X_INT_COMPLETE_FINAL[j-local_counter_FINAL[j]+(n+1)];
              y_sol=Y_INT_COMPLETE_FINAL[j-local_counter_FINAL[j]+(n+1)];
              loc_cnt_sol=local_counter_FINAL[j-local_counter_FINAL[j]+(n+1)];
              BC_ind_sol=BC_INT_IND_COMPLETE_FINAL[j-local_counter_FINAL[j]+(n+1)];
              distance_min=distance;
            }
          }

          fprintf(f1, "%f\t%f\t%d\t%d\n", x_sol, y_sol, loc_cnt_sol, BC_ind_sol);
          fprintf(f1, "%f\t%f\t%d\t%d\n", X_INT_COMPLETE_FINAL[j],
Y_INT_COMPLETE_FINAL[j], local_counter_FINAL[j], BC_INT_IND_COMPLETE_FINAL[j]);
        }
        else if( (j>1 && j<(cumsum_int_at_cur_y[big_loop_counter]+added_points-1) &&
X_INT_COMPLETE_FINAL[j]-X_INT_COMPLETE_FINAL[j_prev]>2.5 ) /*|| (j>0 &&
BC_INT_IND_COMPLETE_FINAL[j]!=temp_BC &&
X_INT_COMPLETE_FINAL[j]>X_INT_COMPLETE_FINAL[j-1]) */ )
        {
          for(n=0;n<12;n++)
          {
            distance = (X_INT_COMPLETE_FINAL[j]-X_INT_COMPLETE_FINAL[j-
local_counter_FINAL[j]-n])*(X_INT_COMPLETE_FINAL[j]-X_INT_COMPLETE_FINAL[j-
local_counter_FINAL[j]-n])+(Y_INT_COMPLETE_FINAL[j]-Y_INT_COMPLETE_FINAL[j-
local_counter_FINAL[j]-n])*(Y_INT_COMPLETE_FINAL[j]-Y_INT_COMPLETE_FINAL[j-
local_counter_FINAL[j]-n]);

            if(distance<=distance_min)
            {
              x_sol=X_INT_COMPLETE_FINAL[j-local_counter_FINAL[j]-n];
              y_sol=Y_INT_COMPLETE_FINAL[j-local_counter_FINAL[j]-n];
              loc_cnt_sol=local_counter_FINAL[j-local_counter_FINAL[j]-n];
              BC_ind_sol=BC_INT_IND_COMPLETE_FINAL[j-local_counter_FINAL[j]-n];
              distance_min=distance;
            }
          }

          fprintf(f1, "%f\t%f\t%d\t%d\n", x_sol, y_sol, loc_cnt_sol, BC_ind_sol);
```

```
         fprintf(f1, "%f\t%f\t%d\t%d\n", X_INT_COMPLETE_FINAL[j],
Y_INT_COMPLETE_FINAL[j], local_counter_FINAL[j], BC_INT_IND_COMPLETE_FINAL[j]);
       }
       else
       {
         fprintf(f1, "%f\t%f\t%d\t%d\n", X_INT_COMPLETE_FINAL[j],
Y_INT_COMPLETE_FINAL[j], local_counter_FINAL[j], BC_INT_IND_COMPLETE_FINAL[j]);

       }

       j_prev=j;
       distance_min=1100;
     }
   }
   fclose(f1);
  }

/* ------------------------------------------------------------------------------------
------------------------------------------------------------------------------- */

/* PRINT FILE FOR THE FRONT-CREATING PROGRAM TO RUN */

  const char* fileName2 = "All_intersections";
  char buffer2[50];

  FILE* f2 = NULL;
  sprintf(buffer2,"%s%s", fileName2, fileType);
  f2 = fopen(buffer2,"w");

  for(j=0;j<cumsum_int_at_cur_y[big_loop_counter]+added_points;j++)
  {
    fprintf(f2, "%d\t%f\t%f\t%d\t%d\n", j, X_INT_COMPLETE_FINAL[j],
Y_INT_COMPLETE_FINAL[j], local_counter_FINAL[j], BC_INT_IND_COMPLETE_FINAL[j]);
  }

/* ------------------------------------------------------------------------------------
------------------------------------------------------------------------------- */

  return 0;
}
```

8.5 Appendix E: X-axis Segmentation / Front Development

```
/* ASSIGNING MATERIAL TO POINT-CHECKING FOR INTERNALITY-EXTERNALITY */
#include <stdio.h>
#include <stdlib.h>
#include <math.h>
#define Nbc 101 /* NUMBER OF POINTS WITH WHICH EACH BORDER CURVE IS DEPICTED */

int main()
{

/* Open the already created .txt files that contain the border point coordinates. These
coordinates are extracted by Solidworks section cuts of slicing software. */
/* The .txt files must be located in the same folder as the c code and its .exe post-
compilation file */
/* WARNING: MIGHT NEED TO COMMENT OUT OR ADD LINES, IN CASE OF MORE OR LESS BORDER
CURVES */

    FILE* ptr1 = fopen("BORDER1.txt", "r");
    if (ptr1 == NULL)
  {
        printf("no such file.");
        return 0;
    }

  FILE* ptr2 = fopen("BORDER2.txt", "r");
    if (ptr2 == NULL)
  {
        printf("no such file.");
        return 0;
    }

    FILE* ptr3 = fopen("BORDER3.txt", "r");
    if (ptr3 == NULL)
  {
        printf("no such file.");
        return 0;
    }

  FILE* ptr4 = fopen("BORDER4.txt", "r");
    if (ptr4 == NULL)
  {
        printf("no such file.");
        return 0;
    }

    FILE* ptr5 = fopen("BORDER5.txt", "r");
    if (ptr5 == NULL)
  {
        printf("no such file.");
        return 0;
    }

    FILE* ptr6 = fopen("All_intersections.txt", "r");
    if (ptr6 == NULL)
  {
        printf("no such file.");
        return 0;
    }

    int i;

/* Insert as many border curves as they exist in the multimaterial layer that is to be
deposited by simply adding lines */
/* WARNING: MIGHT NEED TO COMMENT OUT OR ADD LINES, IN CASE OF MORE OR LESS BORDER
CURVES */

    float xborder1[Nbc],yborder1[Nbc];
    float xborder2[Nbc],yborder2[Nbc];
    float xborder3[Nbc],yborder3[Nbc];
    float xborder4[Nbc],yborder4[Nbc];
```

```
    float xborder5[Nbc],yborder5[Nbc];
    float x[15000], y[15000];
    int local_counter[15000], BC_indicator[15000], placeholder[15000];

/* Read border curve coordinates from the .txt files and store them in the respective
arrays */
/* WARNING: MIGHT NEED TO COMMENT OUT OR ADD LINES, IN CASE OF MORE OR LESS BORDER
CURVES */

  int N1, N2, N3, N4, N5, num_of_int;

  i=0;
  while(fscanf(ptr1, "%f%f\n",&xborder1[i],&yborder1[i])!=EOF)
  {
    i=i+1;
  }
  N1=i;

  i=0;
  while(fscanf(ptr2, "%f%f\n",&xborder2[i],&yborder2[i])!=EOF)
  {
    i=i+1;
  }
  N2=i;

  i=0;
  while(fscanf(ptr3, "%f%f\n",&xborder3[i],&yborder3[i])!=EOF)
  {
    i=i+1;
  }
  N3=i;

  i=0;
  while(fscanf(ptr4, "%f%f\n",&xborder4[i],&yborder4[i])!=EOF)
  {
    i=i+1;
  }
  N4=i;

  i=0;
  while(fscanf(ptr5, "%f%f\n",&xborder5[i],&yborder5[i])!=EOF)
  {
    i=i+1;
  }
  N5=i;

  i=0;
  while(fscanf(ptr6, "%d%f%f%d%d\n", &placeholder[i], &x[i], &y[i], &local_counter[i],
&BC_indicator[i])!=EOF)
  {
    i=i+1;
  }
  num_of_int=i;

/* Measure the number of horizontal lines, i.e. the (y_1,U/dy) */

  int num_of_hor_lines=0;
  float y_counter;

  for(y_counter=0;y_counter<=100;y_counter+=0.1)
  {
    num_of_hor_lines++;
  }

//  printf("The number of horizontal y=y0 lines is %d.\n", num_of_hor_lines);       /*
Debug line */

/* Check that the border curves are stored correctly via screen display */

//  for(i=0;i<N5;i++){                                /* Debug line */
//    printf("%d\t%f\t%f\n",i+1,xborder5[i],yborder5[i]);               /* Debug line */
//  }                                        /* Debug line */

/* Find the maximum number of intersections with a horizontal y=y0 line. */

  int max_int_count_total;
```

```
  max_int_count_total = local_counter[0];

  for (i = 1; i < num_of_int; ++i)
  {
      if (max_int_count_total < local_counter[i])
    {
       max_int_count_total = local_counter[i];
      }
  }

//  printf("Number of intersections per horizontal line is %d\n", max_int_count_total);
  /* Debug line */

/* ASSIGN MATERIAL TO EACH BORDER CURVE AND FIND THE NUMBER OF MATERIALS IN THE LAYER
*/

  int num_of_materials;
  int assigned_material;
  int mat_BC[5];

  mat_BC[0]=1; /* Material #1 is assigned to the BC1 - ALWAYS */
  mat_BC[1]=2; /* Material #2 is assigned to the BC2 - ALWAYS */
  mat_BC[2]=1; /* Material #1 is assigned to the BC3 */
  mat_BC[3]=3; /* Material #3 is assigned to the BC4 */
  mat_BC[4]=2; /* Material #2 is assigned to the BC5 */

  num_of_materials=mat_BC[0];

  for (i = 0; i < 5; i++)
  {
      if (mat_BC[i]>=num_of_materials)
    {
       num_of_materials=mat_BC[i];   /* The number of materials in the layer is equal
to the maximum value of the array mat_BC[] */
      }
  }

/* ENTER THE COORDINATES OF THE POINT THAT IS TO BE EXAMINED-ASSIGN MATERIAL TYPE TO IT
*/

  float x_A, y_A;
//  x_A=46.7;       /* Debug line */
//  y_A=36.8;       /* Debug line */
  float dx=0.13;

/* DEFINE THE ARRAYS TO STORE THE COORDINATES OF THE INTERSECTIONS OF THE BORDER CURVES
WITH THE OA RAY - FOR INTERNALITY CHECKS */

  float x_int_temp, y_int_temp;
  float x_int[50], y_int[50];
  int intersections_count_2=0;
  int intersections_count_3=0;
  int intersections_count_4=0;
  int intersections_count_5=0;

/* DEFINE INTERNALITY AND EXTERNALITY INDICES */

  int int_index_1, int_index_2, int_index_3, int_index_4, int_index_5; /* The internal
index of an internal point is 1, and the internal index of an external point equals to
0 */
  int_index_1=1;                          /* Always, by default, as the BC1 is the
orthogonal rectange area that envelops the entire layer */

  int ext_index[5];

/* DEFINE SWITCHES TO CHECK WHETHER A POINT IS DIRECTLY ONTO A BORDER CURVE */

  int switch_1=0;
  int switch_2=0;
  int switch_3=0;
  int switch_4=0;
  int switch_5=0;

/* ------------------------------------------------------------------------------------
------------------------------------------------------------------------------------
---------------------------------------------------------- */
```

```
/* Develop the first two fronts LF0 and RF0 */

  FILE* f1 = NULL;
  FILE* f2 = NULL;

  char buffer1[50];
  char buffer2[50];

  const char* fileName1 = "LF_#";
  const char* fileName2 = "RF_#";
  const char* fileType = ".txt";

  sprintf(buffer1,"%s%d%s", fileName1, 0, fileType);
  f1 = fopen(buffer1,"w");
  sprintf(buffer2,"%s%d%s", fileName2, 0, fileType);
  f2 = fopen(buffer2,"w");

  float x_sol, y_sol;
  int loc_cnt_sol, BC_ind_sol;
  int placeholderRF_sol;
  float distance, distance_min;
  distance_min=1000;
  int n, j_prev, j, k1;
  k1=0;

/* Creating LF0 */

  float xLF[2000], yLF[2000];
  int LCLF[2000], BCLF[2000], placeholderLF[2000];   /* Placeholder stores the
position that the selected point has within the x and y array that contains all the
intersections */

/* Creating RF0 */

  float xRF[2000], yRF[2000];
  int LCRF[2000], BCRF[2000], placeholderRF[2000];

/* LF0 AND RF0 COINCIDE, AND THEY ARE THE VERTICAL x=x_1,L=0 LINE */

  for(i=0;i<num_of_int;i++)
  {
    if(local_counter[i]==1)
    {
      k1++;
      xLF[k1-1]=x[i];
      yLF[k1-1]=y[i];
      LCLF[k1-1]=local_counter[i];
      BCLF[k1-1]=BC_indicator[i];
      placeholderLF[k1-1]=i;
      fprintf(f1, "%d\t%d\t%f\t%f\t%d\t%d\n", k1-1, i, x[i], y[i], local_counter[i],
BC_indicator[i]);

      xRF[k1-1]=x[i];
      yRF[k1-1]=y[i];
      LCRF[k1-1]=local_counter[i];
      BCRF[k1-1]=BC_indicator[i];
      placeholderRF[k1-1]=i;
      fprintf(f2, "%d\t%d\t%f\t%f\t%d\t%d\n", k1-1, i, x[i], y[i], local_counter[i],
BC_indicator[i]);
    }
  }

  fclose(f1);
  fclose(f2);

/* We will now create the new front couples (i.e. LF1-RF1, LF2-RF2, etc.) */

  int FLC=0;  /* Stands for Front Loop Counter. It counts the number of the DO...WHILE
loop iteration */
  int switcheroo=0;
  int all_equal;
  int previous_RF_elements;
  previous_RF_elements=k1;
  k1=0;        /* k1 counter will be used to count the elements of the new Right Front
inside the DO...WHILE Loop */
```

```
  do
  {
    /* Opening the files that will contain the data of the new Left Front and Right
Front */

    FILE* f3 = NULL;
    FILE* f4 = NULL;

    sprintf(buffer1,"%s%d%s", fileName1, FLC+1, fileType);
    f3 = fopen(buffer1,"w");
    sprintf(buffer2,"%s%d%s", fileName2, FLC+1, fileType);
    f4 = fopen(buffer2,"w");

    /* The new Left Front is the previous Right Front, hence the previous_RF_elements
is equal to the new_LF_elements */

    for(i=0;i<previous_RF_elements;i++)
    {
      xLF[i]=xRF[i];
      yLF[i]=yRF[i];
      LCLF[i]=LCRF[i];
      BCLF[i]=BCRF[i];
      placeholderLF[i]=placeholderRF[i];
      fprintf(f3, "%d\t%d\t%f\t%f\t%d\t%d\n", i, placeholderLF[i], xLF[i], yLF[i],
LCLF[i], BCLF[i]);
    }

    fclose(f3);

    /* Creating the new Right Front */

    for(j=0;j<previous_RF_elements;j++)
    {
      if(fabs(yLF[j])<0.001)
      {
        k1++;
        xRF[k1-1]=100;
        yRF[k1-1]=yLF[j];

        if(LCLF[j]<max_int_count_total)
        {
          LCRF[k1-1]=LCLF[j]+1;
          placeholderRF[k1-1]=placeholderLF[j]+1;
        }
        else
        {
          LCRF[k1-1]=max_int_count_total;
          placeholderRF[k1-1]=max_int_count_total;
        }

        BCRF[k1-1]=1;

        fprintf(f4, "%d\t%d\t%d\t%f\t%f\t%d\t%d\n", j, k1-1, placeholderRF[k1-1],
xRF[k1-1], yRF[k1-1], LCRF[k1-1], BCRF[k1-1]);

      }
      else if(fabs(xLF[j]-100)<0.001)
      {
        k1++;
        xRF[k1-1]=xLF[j];
        yRF[k1-1]=yLF[j];

        if(LCLF[j]<max_int_count_total)
        {
          LCRF[k1-1]=LCLF[j]+1;
        }
        else
        {
          LCRF[k1-1]=max_int_count_total;
        }

        if( (placeholderLF[j]+1) % max_int_count_total != 0 )
        {
          placeholderRF[k1-1]=placeholderLF[j]+1;
        }
        else
```

```
       {
         placeholderRF[k1-1]=placeholderLF[j];
       }

       BCRF[k1-1]=1;

       fprintf(f4, "%d\t%d\t%d\t%f\t%f\t%d\t%d\n", j, k1-1, placeholderRF[k1-1],
xRF[k1-1], yRF[k1-1], LCRF[k1-1], BCRF[k1-1]);
     }
     else
     {
       x_A=x[placeholderLF[j]+1]-dx;
       y_A=y[placeholderLF[j]+1];


       /*
################################################################################
################################################################################
#################################### */
       /* ############################################ INTERNALITY CHECK WITHIN THE
DO...WHILE LOOP
################################################################################
################################### */

          /* BC1 */

          /* LOCATE THE A POINT WITH REGARD TO THE BC1 BORDER CURVE */

          /* DEFINE WHAT HAPPENS IN BORDER CONDITIONS, I.E. WHEN THE POINT WE EVALUATE
IS ON THE BC1 BORDER CURVE */


            for(i=0;i<N1;i++)
            {
              if(fabs(x_A-xborder1[i])<=0.00001 && fabs(y_A-yborder1[i])<=0.00001)   /*
If the A point happens to coincide with a point of the BC. */
              {
                switch_1=1;     /* The A point is on the BC. */
                break;
              }
              else if(i<N1-1 && fabs(x_A-xborder1[i])<=0.00001 && fabs(x_A-
xborder1[i+1])<=0.00001 && (y_A-yborder1[i])*(y_A-yborder1[i+1])<0)  /* If the A point
happens to be on the vertical linear segment that is defined by the i-th and (i+1)th
point of the BC. */
              {
                switch_1=1;     /* The A point is on the BC. */
                break;
              }
              else if(i<N1-1 && fabs(y_A-yborder1[i])<=0.00001 && fabs(y_A-
yborder1[i+1])<=0.00001  && (x_A-xborder1[i])*(x_A-xborder1[i+1])<0)   /* If the A
point happens to be on the horizontal linear segment that is defined by the i-th and
(i+1)th point of the BC. */
              {
                switch_1=1;     /* The A point is on the BC. */
                break;
              }
              else if(i<N1-1 && fabs(-y_A+(yborder1[i]*xborder1[i+1]-
yborder1[i+1]*xborder1[i])/(xborder1[i+1]-xborder1[i])+x_A*(yborder1[i+1]-
yborder1[i])/(xborder1[i+1]-xborder1[i]))<=0.00001 && (y_A-yborder1[i])*(y_A-
yborder1[i+1])<0) /* If the A point happens to be on the random inclined linear segment
that is defined by the i-th and (i+1)th point of the BC. */
              {
                switch_1=1;     /* The A point is on the BC. */
                break;
              }
              else
              {
                switch_1=0;   /* The A point is not on the BC. */
              }
            }

            if(switch_1==1)
            {
              printf("The A(%f,%f) point is located exactly onto the 1st Border Curve
(BC1).\n", x_A, y_A);
            }
            else
```

```
            {
              printf("The A(%f,%f) point is internal to the 1st Border Curve
(BC1).\n", x_A, y_A);  /* By default, a point is either internal to, or located exactly
onto the BC1. */
            }

          /* ------------------------------------------------------------------------
------------------------------------------------------------------------------------
---------------------------------------------------------------------- */

          /* BC2 */

            /* DEFINE WHAT HAPPENS IN BORDER CONDITIONS, I.E. WHEN THE POINT WE
EVALUATE IS ON THE BC2 BORDER CURVE */


            for(i=0;i<N2;i++)
            {
              if(fabs(x_A-xborder2[i])<=0.00001 && fabs(y_A-yborder2[i])<=0.00001)   /*
If the A point happens to coincide with a point of the BC. */
               {
                 switch_2=1;     /* The A point is on the BC. */
                 break;
               }
              else if(i<N2-1 && fabs(x_A-xborder2[i])<=0.00001 && fabs(x_A-
xborder2[i+1])<=0.00001 && (y_A-yborder2[i])*(y_A-yborder2[i+1])<0)  /* If the A point
happens to be on the vertical linear segment that is defined by the i-th and (i+1)th
point of the BC. */
               {
                 switch_2=1;     /* The A point is on the BC. */
                 break;
               }
              else if(i<N2-1 && fabs(y_A-yborder2[i])<=0.00001 && fabs(y_A-
yborder2[i+1])<=0.00001 && (x_A-xborder2[i])*(x_A-xborder2[i+1])<0)  /* If the A point
happens to be on the horizontal linear segment that is defined by the i-th and (i+1)th
point of the BC. */
               {
                 switch_2=1;     /* The A point is on the BC. */
                 break;
               }
              else if(i<N2-1 && fabs(-y_A+(yborder2[i]*xborder2[i+1]-
yborder2[i+1]*xborder2[i])/(xborder2[i+1]-xborder2[i])+x_A*(yborder2[i+1]-
yborder2[i])/(xborder2[i+1]-xborder2[i]))<=0.00001 && (y_A-yborder2[i])*(y_A-
yborder2[i+1])<0) /* If the A point happens to be on the random inclined linear segment
that is defined by the i-th and (i+1)th point of the BC. */
               {
                 switch_2=1;     /* The A point is on the BC. */
                 break;
               }
              else
               {
                 switch_2=0;   /* The A point is not on the BC. */
               }
            }

          /* LOCATE THE INTERSECTIONS OF THE OA RAY WITH THE BC2 BORDER CURVE, TO
ESTABLISH INTERNALITY OR EXTERNALITY */

            if(switch_2==0)
            {
              for(i=0;i<N2-1;i++)
              {
                if(fabs(xborder2[i]-xborder2[i+1])<=0.00001)  /* In case the i-th and
(i+1)-th points of the BC have the same x. */
                 {
                   x_int_temp=xborder2[i];
                   y_int_temp=(y_A/x_A)*xborder2[i];

                   if( ((yborder2[i]-y_int_temp)*(yborder2[i+1]-y_int_temp)<0) &&
(y_int_temp<y_A) )
                    {
                      intersections_count_2++;
                      x_int[intersections_count_2-1]=x_int_temp;
                      y_int[intersections_count_2-1]=y_int_temp;
                    }
                 }
```

```
                else if(fabs(yborder2[i]-yborder2[i+1])<=0.00001)  /* In case the i-th
and (i+1)-th points of the BC have the same y. */
                {
                  x_int_temp=(x_A/y_A)*yborder2[i];
                  y_int_temp=yborder2[i];

                  if( ((xborder2[i]-x_int_temp)*(xborder2[i+1]-x_int_temp)<0) &&
(x_int_temp<x_A) )
                   {
                     intersections_count_2++;
                     x_int[intersections_count_2-1]=x_int_temp;
                     y_int[intersections_count_2-1]=y_int_temp;
                   }
                }
                else if(fabs((y_A/x_A)-(yborder2[i]/xborder2[i]))<0.00001 &&
yborder2[i]<y_A)     /* In case any points of the BC happen to belong exactly onto the
OA ray */
                {
                  intersections_count_2++;
                  x_int_temp=xborder2[i];
                  y_int_temp=yborder2[i];
                  x_int[intersections_count_2-1]=x_int_temp;
                  y_int[intersections_count_2-1]=y_int_temp;
                }
                else
                {
                  x_int_temp=(yborder2[i]*xborder2[i+1]-
yborder2[i+1]*xborder2[i])/(xborder2[i+1]-xborder2[i])*(1/((y_A/x_A)-((yborder2[i+1]-
yborder2[i])/(xborder2[i+1]-xborder2[i]))));
                  y_int_temp=(y_A/x_A)*x_int_temp;

                  if( ((yborder2[i]-y_int_temp)*(yborder2[i+1]-y_int_temp)<0) &&
(y_int_temp<y_A) )
                   {
                     intersections_count_2++;
                     x_int[intersections_count_2-1]=x_int_temp;
                     y_int[intersections_count_2-1]=y_int_temp;
                   }
                }
              }
            }

            if(switch_2==1)
            {
          //   printf("The A(%f,%f) point is located exactly onto the 2nd Border Curve
(BC2).\n", x_A, y_A);
            }
            else
            {
              printf("The 2nd Border Curve (BC2) has %d intersections with the OA ray
casted from the A(%f,%f) point towards the O(0,0) point.\n", intersections_count_2,
x_A, y_A);
            }

            for(i=0;i<intersections_count_2;i++)
            {
              printf("BC2's #%d intersection with the OA ray is the (%f,%f) point.\n",
i+1, x_int[i], y_int[i]);
            }

          /* IF THERE IS AN ODD NUMBER OF INTERSECTIONS, A IS INTERNAL, IF THERE IS AN
EVEN ONE, IT IS EXTERNAL TO THE BORDER CURVE */

            if(switch_2==1)
            {
              printf("The A(%f,%f) point is exactly onto the 2nd Border Curve
(BC2).\n", x_A, y_A);
              int_index_2=1;    /* Being onto a BC counts as being an internal point to
it. */
            }
            else if(switch_2==0 && intersections_count_2 % 2 == 0)
            {
              printf("The A(%f,%f) point is external to the 2nd Border Curve
(BC2).\n", x_A, y_A);
              int_index_2=0;
            }
            else if (switch_2==0 && intersections_count_2 % 2 == 1)
```

```
            {
              printf("The A(%f,%f) point is internal to the 2nd Border Curve
(BC2).\n", x_A, y_A);
              int_index_2=1;
            }

            intersections_count_2=0;

          /* ------------------------------------------------------------------------
------------------------------------------------------------------------------------
------------------------------------------------------------------------ */

          /* BC3 */

            /* DEFINE WHAT HAPPENS IN BORDER CONDITIONS, I.E. WHEN THE POINT WE
EVALUATE IS ON THE BC3 BORDER CURVE */


            for(i=0;i<N3;i++)
            {
              if(fabs(x_A-xborder3[i])<=0.00001 && fabs(y_A-yborder3[i])<=0.00001)   /*
If the A point happens to coincide with a point of the BC. */
               {
                 switch_3=1;     /* The A point is on the BC. */
                 break;
               }
               else if(i<N3-1 && fabs(x_A-xborder3[i])<=0.00001 && fabs(x_A-
xborder3[i+1])<=0.00001 && (y_A-yborder3[i])*(y_A-yborder3[i+1])<0)  /* If the A point
happens to be on the vertical linear segment that is defined by the i-th and (i+1)th
point of the BC. */
               {
                 switch_3=1;     /* The A point is on the BC. */
                 break;
               }
               else if(i<N3-1 && fabs(y_A-yborder3[i])<=0.00001 && fabs(y_A-
yborder3[i+1])<=0.00001 && (x_A-xborder3[i])*(x_A-xborder3[i+1])<0)  /* If the A point
happens to be on the horizontal linear segment that is defined by the i-th and (i+1)th
point of the BC. */
               {
                 switch_3=1;     /* The A point is on the BC. */
                 break;
               }
               else if(i<N3-1 && fabs(-y_A+(yborder3[i]*xborder3[i+1]-
yborder3[i+1]*xborder3[i])/(xborder3[i+1]-xborder3[i])+x_A*(yborder3[i+1]-
yborder3[i])/(xborder3[i+1]-xborder3[i]))<=0.00001 && (y_A-yborder3[i])*(y_A-
yborder3[i+1])<0) /* If the A point happens to be on the random inclined linear segment
that is defined by the i-th and (i+1)th point of the BC. */
               {
                 switch_3=1;     /* The A point is on the BC. */
                 break;
               }
               else
               {
                 switch_3=0;   /* The A point is not on the BC. */
               }
            }

          /* LOCATE THE INTERSECTIONS OF THE OA RAY WITH THE BC3 BORDER CURVE, TO
ESTABLISH INTERNALITY OR EXTERNALITY */

            if(switch_3==0)
            {
              for(i=0;i<N3-1;i++)
              {
                if(fabs(xborder3[i]-xborder3[i+1])<=0.00001)  /* In case the i-th and
(i+1)-th points of the BC have the same x. */
                 {
                   x_int_temp=xborder3[i];
                   y_int_temp=(y_A/x_A)*xborder3[i];

                   if( ((yborder3[i]-y_int_temp)*(yborder3[i+1]-y_int_temp)<0) &&
(y_int_temp<y_A) )
                    {
                      intersections_count_3++;
                      x_int[intersections_count_3-1]=x_int_temp;
                      y_int[intersections_count_3-1]=y_int_temp;
                    }
```

```
                }
                else if(fabs(yborder3[i]-yborder3[i+1])<=0.00001)   /* In case the i-th
and (i+1)-th points of the BC have the same y. */
                {
                  x_int_temp=(x_A/y_A)*yborder3[i];
                  y_int_temp=yborder3[i];

                  if( ((xborder3[i]-x_int_temp)*(xborder3[i+1]-x_int_temp)<0) &&
(x_int_temp<x_A) )
                   {
                     intersections_count_3++;
                     x_int[intersections_count_3-1]=x_int_temp;
                     y_int[intersections_count_3-1]=y_int_temp;
                   }
                }
                else if(fabs((y_A/x_A)-(yborder3[i]/xborder3[i]))<0.00001  &&
yborder3[i]<y_A)     /* In case any points of the BC happen to belong exactly onto the
OA ray */
                {
                  intersections_count_3++;
                  x_int_temp=xborder3[i];
                  y_int_temp=yborder3[i];
                  x_int[intersections_count_3-1]=x_int_temp;
                  y_int[intersections_count_3-1]=y_int_temp;
                }
                else
                {
                  x_int_temp=(yborder3[i]*xborder3[i+1]-
yborder3[i+1]*xborder3[i])/(xborder3[i+1]-xborder3[i])*(1/((y_A/x_A)-((yborder3[i+1]-
yborder3[i])/(xborder3[i+1]-xborder3[i]))));
                  y_int_temp=(y_A/x_A)*x_int_temp;

                  if( ((yborder3[i]-y_int_temp)*(yborder3[i+1]-y_int_temp)<0) &&
(y_int_temp<y_A) )
                   {
                     intersections_count_3++;
                     x_int[intersections_count_3-1]=x_int_temp;
                     y_int[intersections_count_3-1]=y_int_temp;
                   }
                }
              }
            }

            if(switch_3==1)
            {
          //   printf("The A(%f,%f) point is located exactly onto the 3rd Border Curve
(BC3).\n", x_A, y_A);
            }
            else
            {
              printf("The 3rd Border Curve (BC3) has %d intersections with the OA ray
casted from the A(%f,%f) point towards the O(0,0) point.\n", intersections_count_3,
x_A, y_A);
            }

            for(i=0;i<intersections_count_3;i++)
            {
              printf("BC3's #%d intersection with the OA ray is the (%f,%f) point.\n",
i+1, x_int[i], y_int[i]);
            }

          /* IF THERE IS AN ODD NUMBER OF INTERSECTIONS, A IS INTERNAL, IF THERE IS AN
EVEN ONE, IT IS EXTERNAL TO THE BORDER CURVE */

            if(switch_3==1)
            {
              printf("The A(%f,%f) point is exactly onto the 3rd Border Curve
(BC3).\n", x_A, y_A);
              int_index_3=1;    /* Being onto a BC counts as being an internal point to
it. */
            }
            else if(switch_3==0 && intersections_count_3 % 2 == 0)
            {
              printf("The A(%f,%f) point is external to the 3rd Border Curve
(BC3).\n", x_A, y_A);
              int_index_3=0;
            }
```

```
            else if (switch_3==0 && intersections_count_3 % 2 == 1)
            {
              printf("The A(%f,%f) point is internal to the 3rd Border Curve
(BC3).\n", x_A, y_A);
              int_index_3=1;
            }

            intersections_count_3=0;

          /* ------------------------------------------------------------------------
------------------------------------------------------------------------------------
------------------------------------------------------------------------ */

          /* BC4 */

            /* DEFINE WHAT HAPPENS IN BORDER CONDITIONS, I.E. WHEN THE POINT WE
EVALUATE IS ON THE BC4 BORDER CURVE */


            for(i=0;i<N4;i++)
            {
              if(fabs(x_A-xborder4[i])<=0.00001 && fabs(y_A-yborder4[i])<=0.00001)   /*
If the A point happens to coincide with a point of the BC. */
               {
                 switch_4=1;     /* The A point is on the BC. */
                 break;
               }
              else if(i<N4-1 && fabs(x_A-xborder4[i])<=0.00001 && fabs(x_A-
xborder4[i+1])<=0.00001 && (y_A-yborder4[i])*(y_A-yborder4[i+1])<0)  /* If the A point
happens to be on the vertical linear segment that is defined by the i-th and (i+1)th
point of the BC. */
               {
                 switch_4=1;     /* The A point is on the BC. */
                 break;
               }
              else if(i<N4-1 && fabs(y_A-yborder4[i])<=0.00001 && fabs(y_A-
yborder4[i+1])<=0.00001 && (x_A-xborder4[i])*(x_A-xborder4[i+1])<0)  /* If the A point
happens to be on the horizontal linear segment that is defined by the i-th and (i+1)th
point of the BC. */
               {
                 switch_4=1;     /* The A point is on the BC. */
                 break;
               }
              else if(i<N4-1 && fabs(-y_A+(yborder4[i]*xborder4[i+1]-
yborder4[i+1]*xborder4[i])/(xborder4[i+1]-xborder4[i])+x_A*(yborder4[i+1]-
yborder4[i])/(xborder4[i+1]-xborder4[i]))<=0.00001 && (y_A-yborder4[i])*(y_A-
yborder4[i+1])<0) /* If the A point happens to be on the random inclined linear segment
that is defined by the i-th and (i+1)th point of the BC. */
               {
                 switch_4=1;     /* The A point is on the BC. */
                 break;
               }
              else
               {
                 switch_4=0;   /* The A point is not on the BC. */
               }
            }

          /* LOCATE THE INTERSECTIONS OF THE OA RAY WITH THE BC4 BORDER CURVE, TO
ESTABLISH INTERNALITY OR EXTERNALITY */

            if(switch_4==0)
            {
              for(i=0;i<N4-1;i++)
              {
                if(fabs(xborder4[i]-xborder4[i+1])<=0.00001)  /* In case the i-th and
(i+1)-th points of the BC have the same x. */
                 {
                   x_int_temp=xborder4[i];
                   y_int_temp=(y_A/x_A)*xborder4[i];

                   if( ((yborder4[i]-y_int_temp)*(yborder4[i+1]-y_int_temp)<0) &&
(y_int_temp<y_A) )
                    {
                      intersections_count_4++;
                      x_int[intersections_count_4-1]=x_int_temp;
                      y_int[intersections_count_4-1]=y_int_temp;
```

```
                }
              }
              else if(fabs(yborder4[i]-yborder4[i+1])<=0.00001)  /* In case the i-th
and (i+1)-th points of the BC have the same y. */
              {
                x_int_temp=(x_A/y_A)*yborder4[i];
                y_int_temp=yborder4[i];

                if( ((xborder4[i]-x_int_temp)*(xborder4[i+1]-x_int_temp)<0) &&
(x_int_temp<x_A) )
                {
                  intersections_count_4++;
                  x_int[intersections_count_4-1]=x_int_temp;
                  y_int[intersections_count_4-1]=y_int_temp;
                }
              }
              else if(fabs((y_A/x_A)-(yborder4[i]/xborder4[i]))<0.00001 &&
yborder4[i]<y_A)     /* In case any points of the BC happen to belong exactly onto the
OA ray */
              {
                intersections_count_4++;
                x_int_temp=xborder4[i];
                y_int_temp=yborder4[i];
                x_int[intersections_count_4-1]=x_int_temp;
                y_int[intersections_count_4-1]=y_int_temp;
              }
              else
              {
                x_int_temp=(yborder4[i]*xborder4[i+1]-
yborder4[i+1]*xborder4[i])/(xborder4[i+1]-xborder4[i])*(1/((y_A/x_A)-((yborder4[i+1]-
yborder4[i])/(xborder4[i+1]-xborder4[i]))));
                y_int_temp=(y_A/x_A)*x_int_temp;

                if( ((yborder4[i]-y_int_temp)*(yborder4[i+1]-y_int_temp)<0) &&
(y_int_temp<y_A) )
                {
                  intersections_count_4++;
                  x_int[intersections_count_4-1]=x_int_temp;
                  y_int[intersections_count_4-1]=y_int_temp;
                }
              }
            }
          }

          if(switch_4==1)
          {
        //   printf("The A(%f,%f) point is located exactly onto the 4th Border Curve
(BC4).\n", x_A, y_A);
          }
          else
          {
            printf("The 4th Border Curve (BC4) has %d intersections with the OA ray
casted from the A(%f,%f) point towards the O(0,0) point.\n", intersections_count_4,
x_A, y_A);
          }

          for(i=0;i<intersections_count_4;i++)
          {
            printf("BC4's #%d intersection with the OA ray is the (%f,%f) point.\n",
i+1, x_int[i], y_int[i]);
          }

        /* IF THERE IS AN ODD NUMBER OF INTERSECTIONS, A IS INTERNAL, IF THERE IS AN
EVEN ONE, IT IS EXTERNAL TO THE BORDER CURVE */

          if(switch_4==1)
          {
            printf("The A(%f,%f) point is exactly onto the 4th Border Curve
(BC4).\n", x_A, y_A);
            int_index_4=1;    /* Being onto a BC counts as being an internal point to
it. */
          }
          else if(switch_4==0 && intersections_count_4 % 2 == 0)
          {
            printf("The A(%f,%f) point is external to the 4th Border Curve
(BC4).\n", x_A, y_A);
            int_index_4=0;
```

```
            }
            else if (switch_4==0 && intersections_count_4 % 2 == 1)
            {
              printf("The A(%f,%f) point is internal to the 3rd Border Curve
(BC3).\n", x_A, y_A);
              int_index_4=1;
            }

            intersections_count_4=0;

          /* ------------------------------------------------------------------------
------------------------------------------------------------------------------------
------------------------------------------------------------------------ */

          /* BC5 */

            /* DEFINE WHAT HAPPENS IN BORDER CONDITIONS, I.E. WHEN THE POINT WE
EVALUATE IS ON THE BC5 BORDER CURVE */


            for(i=0;i<N5;i++)
            {
              if(fabs(x_A-xborder5[i])<=0.00001 && fabs(y_A-yborder5[i])<=0.00001)   /*
If the A point happens to coincide with a point of the BC. */
               {
                 switch_5=1;     /* The A point is on the BC. */
                 break;
               }
              else if(i<N5-1 && fabs(x_A-xborder5[i])<=0.00001 && fabs(x_A-
xborder5[i+1])<=0.00001 && (y_A-yborder5[i])*(y_A-yborder5[i+1])<0)  /* If the A point
happens to be on the vertical linear segment that is defined by the i-th and (i+1)th
point of the BC. */
               {
                 switch_5=1;     /* The A point is on the BC. */
                 break;
               }
              else if(i<N5-1 && fabs(y_A-yborder5[i])<=0.00001 && fabs(y_A-
yborder5[i+1])<=0.00001 && (x_A-xborder5[i])*(x_A-xborder5[i+1])<0)  /* If the A point
happens to be on the horizontal linear segment that is defined by the i-th and (i+1)th
point of the BC. */
               {
                 switch_5=1;     /* The A point is on the BC. */
                 break;
               }
              else if(i<N5-1 && fabs(-y_A+(yborder5[i]*xborder5[i+1]-
yborder5[i+1]*xborder5[i])/(xborder5[i+1]-xborder5[i])+x_A*(yborder5[i+1]-
yborder5[i])/(xborder5[i+1]-xborder5[i]))<=0.00001 && (y_A-yborder5[i])*(y_A-
yborder5[i+1])<0) /* If the A point happens to be on the random inclined linear segment
that is defined by the i-th and (i+1)th point of the BC. */
               {
                 switch_5=1;     /* The A point is on the BC. */
                 break;
               }
              else
               {
                 switch_5=0;   /* The A point is not on the BC. */
               }
            }

          /* LOCATE THE INTERSECTIONS OF THE OA RAY WITH THE BC5 BORDER CURVE, TO
ESTABLISH INTERNALITY OR EXTERNALITY */

            if(switch_5==0)
            {
              for(i=0;i<N5-1;i++)
              {
                if(fabs(xborder5[i]-xborder5[i+1])<=0.00001)  /* In case the i-th and
(i+1)-th points of the BC have the same x. */
                {
                  x_int_temp=xborder5[i];
                  y_int_temp=(y_A/x_A)*xborder5[i];

                  if( ((yborder5[i]-y_int_temp)*(yborder5[i+1]-y_int_temp)<0) &&
(y_int_temp<y_A) )
                   {
                     intersections_count_5++;
                     x_int[intersections_count_5-1]=x_int_temp;
```

```
                    y_int[intersections_count_5-1]=y_int_temp;
                  }
                }
                else if(fabs(yborder5[i]-yborder5[i+1])<=0.00001)  /* In case the i-th
and (i+1)-th points of the BC have the same y. */
                {
                  x_int_temp=(x_A/y_A)*yborder5[i];
                  y_int_temp=yborder5[i];

                  if( ((xborder5[i]-x_int_temp)*(xborder5[i+1]-x_int_temp)<0) &&
(x_int_temp<x_A) )
                  {
                    intersections_count_5++;
                    x_int[intersections_count_5-1]=x_int_temp;
                    y_int[intersections_count_5-1]=y_int_temp;
                  }
                }
                else if(fabs((y_A/x_A)-(yborder5[i]/xborder5[i]))<0.00001 &&
yborder5[i]<y_A)     /* In case any points of the BC happen to belong exactly onto the
OA ray */
                {
                  intersections_count_5++;
                  x_int_temp=xborder5[i];
                  y_int_temp=yborder5[i];
                  x_int[intersections_count_5-1]=x_int_temp;
                  y_int[intersections_count_5-1]=y_int_temp;
                }
                else
                {
                  x_int_temp=(yborder5[i]*xborder5[i+1]-
yborder5[i+1]*xborder5[i])/(xborder5[i+1]-xborder5[i])*(1/((y_A/x_A)-((yborder5[i+1]-
yborder5[i])/(xborder5[i+1]-xborder5[i]))));
                  y_int_temp=(y_A/x_A)*x_int_temp;

                  if( ((yborder5[i]-y_int_temp)*(yborder5[i+1]-y_int_temp)<0) &&
(y_int_temp<y_A) )
                  {
                    intersections_count_5++;
                    x_int[intersections_count_5-1]=x_int_temp;
                    y_int[intersections_count_5-1]=y_int_temp;
                  }
                }
              }
            }

            if(switch_5==1)
            {
          //   printf("The A(%f,%f) point is located exactly onto the 5th Border Curve
(BC5).\n", x_A, y_A);
            }
            else
            {
              printf("The 5th Border Curve (BC5) has %d intersections with the OA ray
casted from the A(%f,%f) point towards the O(0,0) point.\n", intersections_count_5,
x_A, y_A);
            }

            for(i=0;i<intersections_count_5;i++)
            {
              printf("BC5's #%d intersection with the OA ray is the (%f,%f) point.\n",
i+1, x_int[i], y_int[i]);
            }

          /* IF THERE IS AN ODD NUMBER OF INTERSECTIONS, A IS INTERNAL, IF THERE IS AN
EVEN ONE, IT IS EXTERNAL TO THE BORDER CURVE */

            if(switch_5==1)
            {
              printf("The A(%f,%f) point is exactly onto the 5th Border Curve
(BC5).\n", x_A, y_A);
              int_index_5=1;    /* Being onto a BC counts as being an internal point to
it. */
            }
            else if(switch_5==0 && intersections_count_5 % 2 == 0)
            {
              printf("The A(%f,%f) point is external to the 5th Border Curve
(BC5).\n", x_A, y_A);
```

```
              int_index_5=0;
            }
            else if (switch_5==0 && intersections_count_5 % 2 == 1)
            {
              printf("The A(%f,%f) point is internal to the 5th Border Curve
(BC5).\n", x_A, y_A);
              int_index_5=1;
            }

            intersections_count_5=0;

          /* ------------------------------------------------------------------------
------------------------------------------------------------------------------------
------------------------------------------------------------------- */

          /* MATERIAL ASSIGNMENT OF THE A POINT BASED ON THE CALCULATED INTERNALITY
INDICES */


            ext_index[0]=!int_index_1;
            ext_index[1]=!int_index_2;
            ext_index[2]=!int_index_3;
            ext_index[3]=!int_index_4;
            ext_index[4]=!int_index_5;


            if(ext_index[1]*ext_index[2]*ext_index[3]*ext_index[4]==1)
            {
              assigned_material=mat_BC[0];
              printf("The A(%f,%f) point is only internal to the 1st Border Curve
(BC1). Its material is material #%d.\n", x_A, y_A, mat_BC[0]);
            }
            else if(ext_index[4]==0)
            {
              assigned_material=mat_BC[4];
              printf("The innermost Border Curve to which the A(%f,%f) point is
internal to is the 5th Border Curve (BC5). Its material is material #%d.\n", x_A, y_A,
mat_BC[4]);
            }
            else if( ext_index[4]==1 && ext_index[3]==0 )
            {
              assigned_material=mat_BC[3];
              printf("The innermost Border Curve to which the A(%f,%f) point is
internal to is the 4th Border Curve (BC4). Its material is material #%d.\n", x_A, y_A,
mat_BC[3]);
            }
            else if( ext_index[3]==1 && ext_index[2]==0 )
            {
              assigned_material=mat_BC[2];
              printf("The innermost Border Curve to which the A(%f,%f) point is
internal to is the 3rd Border Curve (BC3). Its material is material #%d.\n", x_A, y_A,
mat_BC[2]);
            }
            else if( ext_index[2]==1 && ext_index[1]==0 )
            {
              assigned_material=mat_BC[1];
              printf("The innermost Border Curve to which the A(%f,%f) point is
internal to is the 2nd Border Curve (BC2). Its material is material #%d.\n", x_A, y_A,
mat_BC[1]);
            }
            printf("%d assigned material number\n", assigned_material);

            if( assigned_material == (FLC % num_of_materials)+1 )
            {


              if( (j>1 && x[placeholderLF[j]+1]-xRF[k1-1]<-2.5) )
              {
                distance_min=1100;
                for(n= placeholderLF[j]+1-local_counter[placeholderLF[j]] ;
n<placeholderLF[j]+1-local_counter[placeholderLF[j]] + max_int_count_total ; n++)
                {
                  distance = (xRF[k1-1]-x[n])*(xRF[k1-1]-x[n])+(yRF[k1-1]-
y[n])*(yRF[k1-1]-y[n]);

                  if(distance<=distance_min)
                  {
```

```
                    x_sol=x[n];
                    y_sol=y[n];
                    loc_cnt_sol=local_counter[n];
                    BC_ind_sol=BC_indicator[n];
                    placeholderRF_sol=n;
                    distance_min=distance;
                   }
                  }

                  k1++;
                  xRF[k1-1]=x_sol;
                  yRF[k1-1]=y_sol;
                  LCRF[k1-1]=loc_cnt_sol;
                  BCRF[k1-1]=BC_ind_sol;
                  placeholderRF[k1-1]=placeholderRF_sol;
                  fprintf(f4, "%d\t%d\t%d\t%f\t%f\t%d\t%d\n", j, k1-1, placeholderRF[k1-
1], xRF[k1-1], yRF[k1-1], LCRF[k1-1], BCRF[k1-1]);
                 }
                 else if( (j>1 && j<previous_RF_elements-1 && x[placeholderLF[j]+1]-
xRF[k1-1]>2.5) )
                 {
                   distance_min=1100;
                   for(n= placeholderLF[j-1]-((placeholderLF[j-1]) % max_int_count_total)
; n<placeholderLF[j-1]-((placeholderLF[j-1]) % max_int_count_total)+max_int_count_total
; n++)
                   {
                    distance = (x[placeholderLF[j]+1]-x[n])*(x[placeholderLF[j]+1]-
x[n])+(y[placeholderLF[j]+1]-y[n])*(y[placeholderLF[j]+1]-y[n]);

                    if(distance<=distance_min)
                    {
                      x_sol=x[n];
                      y_sol=y[n];
                      loc_cnt_sol=local_counter[n];
                      BC_ind_sol=BC_indicator[n];
                      placeholderRF_sol=n;
                      distance_min=distance;
                    }
                   }

                   k1++;
                   xRF[k1-1]=x_sol;
                   yRF[k1-1]=y_sol;
                   LCRF[k1-1]=loc_cnt_sol;
                   BCRF[k1-1]=BC_ind_sol;
                   placeholderRF[k1-1]=placeholderRF_sol;
                   fprintf(f4, "%d\t%d\t%d\t%f\t%f\t%d\t%d\n", j, k1-1, placeholderRF[k1-
1], xRF[k1-1], yRF[k1-1], LCRF[k1-1], BCRF[k1-1]);
                 }



                k1++;
                xRF[k1-1]=x[placeholderLF[j]+1];
                yRF[k1-1]=y[placeholderLF[j]+1];
                LCRF[k1-1]=local_counter[placeholderLF[j]+1];
                BCRF[k1-1]=BC_indicator[placeholderLF[j]+1];
                placeholderRF[k1-1]=placeholderLF[j]+1;
                printf("why-1\n");

                fprintf(f4, "%d\t%d\t%d\t%f\t%f\t%d\t%d\n", j, k1-1, placeholderRF[k1-
1], xRF[k1-1], yRF[k1-1], LCRF[k1-1], BCRF[k1-1]);
               }
               else
               {
                 k1++;
                 xRF[k1-1]=xLF[j];
                 yRF[k1-1]=yLF[j];
                 LCRF[k1-1]=LCLF[j];
                 BCRF[k1-1]=BCLF[j];
                 placeholderRF[k1-1]=placeholderLF[j];

                 printf("why-2\n");
                 fprintf(f4, "%d\t%d\t%d\t%f\t%f\t%d\t%d\n", j, k1-1, placeholderRF[k1-
1], xRF[k1-1], yRF[k1-1], LCRF[k1-1], BCRF[k1-1]);
               }
```

```
       /*
##########################################################################################
##########################################################################################
##################################### */
       /*
##########################################################################################
##########################################################################################
##################################### */
     }
    }

    previous_RF_elements=k1;
    k1=0;

    fclose(f3);
    fclose(f4);


    /* Check if the new RF coincides with the x=x_1,R=100 vertical line. If it does,
switch=1, and the DO...WHILE loop ends. */

    /* Checking if the new Left Front is coincident with the x=x_1,R=100 vertical line,
in order to stop the DO...WHILE loop */

    for(i=0;i<previous_RF_elements-1;i++)
    {
      if(fabs(xRF[i]-xRF[i+1])>0.001)
      {
        switcheroo=0;   /* If at least two elements are not the same with each other,
then there is no chance that LF_new coincides with the x=100 line, so front_switch=0 */
        all_equal=0;
        break;
      }
      else
      {
        all_equal=1;
      }
    }

    if(all_equal==1 && fabs(xLF[0]-100)<0.001)
    {
      switcheroo=1;   /* If all elements are equal and one of them equals to 100, then
the LF coincides with the x=100 line, so front_switch=1 */
    }

    if(switcheroo==0)
    {
      printf("The new RF is not the x=x_1,R=100 yet, there must be a new
iteration.\n");     // Debug line
    }
    else
    {
      printf("The new RF is coincident with the x=x_1,R=100 yet, the loop will now
stop.\n");   // Debug line
    }

    FLC++;

  }while(switcheroo==0);

  return 0;
}
```

9 Bibliography

[1] A. Savini and G. G. Savini, “A short history of 3D printing, a technological revolution just started,” in *2015 ICOHTEC/IEEE International History of High-Technologies and their Socio-Cultural Contexts Conference (HISTELCON)*, Aug. 2015, pp. 1–8. doi: 10.1109/HISTELCON.2015.7307314.

[2] ISO/ASTM, “ISO/ASTM 52900:2021(en) Additive manufacturing — General principles — Fundamentals and vocabulary,” 2021. https://www.iso.org/obp/ui/#iso:std:iso-astm:52900:ed-2:v1:en (accessed Apr. 29, 2024).

[3] A. Mahmood, T. Akram, H. Chen, and S. Chen, “On the Evolution of Additive Manufacturing (3D/4D Printing) Technologies: Materials, Applications, and Challenges,” *Polymers (Basel).*, vol. 14, no. 21, p. 4698, Nov. 2022, doi: 10.3390/polym14214698.

[4] S. Pratheesh Kumar, S. Elangovan, R. Mohanraj, and J. R. Ramakrishna, “Review on the evolution and technology of State-of-the-Art metal additive manufacturing processes,” *Mater. Today Proc.*, vol. 46, pp. 7907–7920, 2021, doi: 10.1016/j.matpr.2021.02.567.

[5] A. K. Kushwaha *et al.*, “Powder bed fusion–based additive manufacturing: SLS, SLM, SHS, and DMLS,” in *Tribology of Additively Manufactured Materials*, P. Kumar, M. Misra, and P. L. B. T.-T. of A. M. M. Menezes, Eds. Elsevier, 2022, pp. 1–37. doi: 10.1016/B978-0-12-821328-5.00001-9.

[6] X. Zhang and F. Liou, “Introduction to additive manufacturing,” in *Additive Manufacturing*, J. Pou, A. Riveiro, and J. P. B. T.-A. M. Davim, Eds. Elsevier, 2021, pp. 1–31. doi: 10.1016/B978-0-12-818411-0.00009-4.

[7] A. B. Peters *et al.*, “Selective laser sintering in reactive atmospheres: Towards in-situ synthesis of net-shaped carbide and nitride ceramics,” *Addit. Manuf.*, vol. 45, p. 102052, Sep. 2021, doi: 10.1016/j.addma.2021.102052.

[8] P. Avrampos and G.-C. Vosniakos, “A review of powder deposition in additive manufacturing by powder bed fusion,” *J. Manuf. Process.*, vol. 74, pp. 332–352, Feb. 2022, doi: 10.1016/j.jmapro.2021.12.021.

[9] D. Gu, “Introduction,” in *Laser Additive Manufacturing of High-Performance Materials*, D. Gu, Ed. Berlin, Heidelberg: Springer Berlin Heidelberg, 2015, pp. 1–13. doi: 10.1007/978-3-662-46089-4_1.

[10] F. Tjellesen and A. Hartmann, “Methods and apparatus for the manufacture of three-dimensional objects,” WO2020115492A1, 2019

[11] C. Körner, “Additive manufacturing of metallic components by selective electron beam melting — a review,” *Int. Mater. Rev.*, vol. 61, no. 5, pp. 361–377, Jul. 2016, doi: 10.1080/09506608.2016.1176289.

[12] N. Hopkinson and E. Poonjolai, “High Speed Sintering-Early Research into a New Rapid Manufacturing Process,” *Solid Free. Fabr. Symp.*, Jan. 2004.

[13] G. E. Muniz, “Additive Manufacturing in FP7 and Horizon 2020, Report from the EC Workshop on Additive Manufacturing,” Brussels, 2014. [Online]. Available: https://op.europa.eu/o/opportal-service/download-handler?identifier=6aeec19c-265f-11e7-ab65-01aa75ed71a1&format=pdf&language=en&productionSystem=cellar&part

[14] A. Purvis, “The Gartner 2017 report on 3D Printing,” *3dnatives*, 2017. https://www.3dnatives.com/en/gartner-2017-3d-printing080820174/ (accessed Apr. 17, 2024).

[15] C. Valdivieso, “Gartner Hype Cycle 2019: 3D Printing Predictions,” *3dnatives*, 2019. https://www.3dnatives.com/en/gartner-hype-cycle-3dprintingpredictions-150120194/ (accessed Apr. 19, 2024).

[16] T. Wohlers, R. I. Campbell, O. Diegel, J. Kowen, N. Mostow, and I. Fidan, “Wohlers Report 2022: 3D Printing and Additive Manufacturing Global State of the Industry,” Fort Collins, Colo., Washington, DC, 2022. [Online]. Available: https://wohlersassociates.com/product/wohlers-report-2022/

[17] T. D. Ngo, A. Kashani, G. Imbalzano, K. T. Q. Nguyen, and D. Hui, “Additive manufacturing (3D printing): A review of materials, methods, applications and challenges,” *Compos. Part B Eng.*, vol. 143, pp. 172–196, Jun. 2018, doi: 10.1016/j.compositesb.2018.02.012.

[18] M. Baumers, C. Tuck, and R. Hague, “Selective heat sintering versus laser sintering: comparison of deposition rate, process energy consumption and cost performance,” in *SFF proceedings*, 2015, pp. 109–121. [Online]. Available: http://utw10945.utweb.utexas.edu/sites/default/files/2015/2015-9-Baumers.pdf

[19] B. Utela, D. Storti, R. Anderson, and M. Ganter, “A review of process development steps for new material systems in three dimensional printing (3DP),” *J. Manuf. Process.*, vol. 10, no. 2, pp. 96–104, Jul. 2008, doi: 10.1016/j.jmapro.2009.03.002.

[20] A. Mostafaei *et al.*, “Binder jet 3D printing—Process parameters, materials, properties, modeling, and challenges,” *Prog. Mater. Sci.*, vol. 119, p. 100707, 2021, doi: https://doi.org/10.1016/j.pmatsci.2020.100707.

[21] S. Barui, A. K. Panda, S. Naskar, R. Kuppuraj, S. Basu, and B. Basu, “3D inkjet printing of biomaterials with strength reliability and cytocompatibility: Quantitative process strategy for Ti-6Al-4V,” *Biomaterials*, vol. 213, p. 119212, Aug. 2019, doi: 10.1016/j.biomaterials.2019.05.023.

[22] S. K. Tiwari, S. Pande, S. Agrawal, and S. M. Bobade, “Selection of selective laser sintering materials for different applications,” *Rapid Prototyp. J.*, vol. 21, no. 6, pp. 630–648, Oct. 2015, doi: 10.1108/RPJ-03-2013-0027.

[23] S. Singh, S. Ramakrishna, and R. Singh, “Material issues in additive manufacturing: A review,” *J. Manuf. Process.*, vol. 25, pp. 185–200, Jan. 2017, doi: 10.1016/j.jmapro.2016.11.006.

[24] I. Ferretto, D. Kim, N. M. Della Ventura, M. Shahverdi, W. Lee, and C. Leinenbach, “Laser powder bed fusion of a Fe–Mn–Si shape memory alloy,” *Addit. Manuf.*, vol. 46, p. 102071, Oct. 2021, doi: 10.1016/j.addma.2021.102071.

[25] F. Rouzé l′Alzit *et al.*, “Powder bed laser sintering of copper-doped hydroxyapatite: Numerical and experimental parametric analysis,” *Addit. Manuf.*, vol. 46, p. 102044, Oct. 2021, doi: 10.1016/j.addma.2021.102044.

[26] T. Ullsperger *et al.*, “Ultra-short pulsed laser powder bed fusion of Al-Si alloys: Impact of pulse duration and energy in comparison to continuous wave excitation,”

Addit. Manuf., vol. 46, p. 102085, Oct. 2021, doi: 10.1016/j.addma.2021.102085.

[27] S. Pramanik, L. Tasche, K.-P. Hoyer, and M. Schaper, "Investigating the microstructure of an additively manufactured FeCo alloy: an electron microscopy study," *Addit. Manuf.*, vol. 46, p. 102087, Oct. 2021, doi: 10.1016/j.addma.2021.102087.

[28] G. Soundarapandiyan *et al.*, "The effects of powder reuse on the mechanical response of electron beam additively manufactured Ti6Al4V parts," *Addit. Manuf.*, vol. 46, p. 102101, Oct. 2021, doi: 10.1016/j.addma.2021.102101.

[29] B. H. Bae, J. W. Lee, J. M. Cha, I.-W. Kim, H.-D. Jung, and C.-B. Yoon, "Preliminary Characterization of Glass/Alumina Composite Using Laser Powder Bed Fusion (L-PBF) Additive Manufacturing," *Materials (Basel).*, vol. 13, no. 9, p. 2156, May 2020, doi: 10.3390/ma13092156.

[30] X. Wang, O. Sanchez-Mata, S. E. Atabay, J. A. Muñiz-Lerma, M. Attarian Shandiz, and M. Brochu, "Crystallographic orientation dependence of Charpy impact behaviours in stainless steel 316L fabricated by laser powder bed fusion," *Addit. Manuf.*, vol. 46, p. 102104, Oct. 2021, doi: 10.1016/j.addma.2021.102104.

[31] D. Sofia, R. Chirone, P. Lettieri, D. Barletta, and M. Poletto, "Selective laser sintering of ceramic powders with bimodal particle size distribution," *Chem. Eng. Res. Des.*, vol. 136, pp. 536–547, Aug. 2018, doi: 10.1016/j.cherd.2018.06.008.

[32] D. Sofia, D. Barletta, and M. Poletto, "Laser sintering process of ceramic powders: The effect of particle size on the mechanical properties of sintered layers," *Addit. Manuf.*, vol. 23, pp. 215–224, Oct. 2018, doi: 10.1016/j.addma.2018.08.012.

[33] G. Ziółkowski, K. Gruber, E. Tokarczyk, R. Roszak, and M. Ziegenhorn, "X-ray Computed Tomography for the ex-situ mechanical testing and simulation of additively manufactured IN718 samples," *Addit. Manuf.*, vol. 45, p. 102070, Sep. 2021, doi: 10.1016/j.addma.2021.102070.

[34] H. Gu, Z. Bashir, and L. Yang, "The re-usability of heat-exposed poly (ethylene terephthalate) powder for laser sintering," *Addit. Manuf.*, vol. 28, pp. 194–204, Aug. 2019, doi: 10.1016/j.addma.2019.05.004.

[35] P. Tan, F. Shen, W. S. Tey, and K. Zhou, "A numerical study on the packing quality of fibre/polymer composite powder for powder bed fusion additive manufacturing," *Virtual Phys. Prototyp.*, vol. 16, no. sup1, pp. S1–S18, Sep. 2021, doi: 10.1080/17452759.2021.1922965.

[36] V. V Popov, A. Katz-Demyanetz, A. Garkun, and M. Bamberger, "The effect of powder recycling on the mechanical properties and microstructure of electron beam melted Ti-6Al-4 V specimens," *Addit. Manuf.*, vol. 22, pp. 834–843, Aug. 2018, doi: 10.1016/j.addma.2018.06.003.

[37] H. P. Tang, M. Qian, N. Liu, X. Z. Zhang, G. Y. Yang, and J. Wang, "Effect of Powder Reuse Times on Additive Manufacturing of Ti-6Al-4V by Selective Electron Beam Melting," *JOM*, vol. 67, no. 3, pp. 555–563, 2015, doi: 10.1007/s11837-015-1300-4.

[38] S. Ghods *et al.*, "Electron beam additive manufacturing of Ti6Al4V: Evolution of powder morphology and part microstructure with powder reuse," *Materialia*, vol. 9, p. 100631, Mar. 2020, doi: 10.1016/j.mtla.2020.100631.

[39] J.-P. Kruth and G. Levy, "Survey of Materials and Material Issues in Rapid Manufacturing by SLS/SLM," 2009. [Online]. Available:

https://lirias.kuleuven.be/retrieve/78845

[40] D. Bourell *et al.*, “Materials for additive manufacturing,” *CIRP Ann.*, vol. 66, no. 2, pp. 659–681, 2017, doi: 10.1016/j.cirp.2017.05.009.

[41] D. K. Leigh and D. Bourell, “Powder Bed Fusion of Polymers,” in *Additive Manufacturing Processes*, ASM International, 2020, pp. 52–57. doi: 10.31399/asm.hb.v24.a0006543.

[42] Z. Chen *et al.*, “3D printing of ceramics: A review,” *J. Eur. Ceram. Soc.*, vol. 39, no. 4, pp. 661–687, Apr. 2019, doi: 10.1016/j.jeurceramsoc.2018.11.013.

[43] L. Yang and H. Miyanaji, “CERAMIC ADDITIVE MANUFACTURING : A REVIEW OF CURRENT STATUS AND CHALLENGES,” in *Solid Freeform Fabrication 2017: Proceedings of the 28th Annual International*, 2017, pp. 652–679.

[44] S. L. Sing *et al.*, “Direct selective laser sintering and melting of ceramics: a review,” *Rapid Prototyp. J.*, vol. 23, no. 3, pp. 611–623, Apr. 2017, doi: 10.1108/RPJ-11-2015-0178.

[45] Y. Zhang *et al.*, “Additive Manufacturing of Metallic Materials: A Review,” *J. Mater. Eng. Perform.*, vol. 27, no. 1, pp. 1–13, Jan. 2018, doi: 10.1007/s11665-017-2747-y.

[46] M. Puttegowda, S. M. Rangappa, M. Jawaid, P. Shivanna, Y. Basavegowda, and N. Saba, “Potential of natural/synthetic hybrid composites for aerospace applications,” in *Sustainable Composites for Aerospace Applications*, M. Jawaid and M. B. T.-S. C. for A. A. Thariq, Eds. Elsevier, 2018, pp. 315–351. doi: 10.1016/B978-0-08-102131-6.00021-9.

[47] I. Shishkovsky, N. Kakovkina, and V. Scherbakov, “Fabrication of heat-resisting nickel composite gradient structures with TiC nano additive during powder bed fusion process,” *Procedia CIRP*, vol. 74, pp. 68–71, 2018, doi: https://doi.org/10.1016/j.procir.2018.08.032.

[48] Y.-H. Chueh, X. Zhang, C. Wei, Z. Sun, and L. Li, “Additive Manufacturing of Polymer-Metal/Ceramic Functionally Graded Composite Components via Multiple Material Laser Powder Bed Fusion,” *J. Manuf. Sci. Eng.*, vol. 142, no. 5, May 2020, doi: 10.1115/1.4046594.

[49] X. Zhang, Y. Chueh, C. Wei, Z. Sun, J. Yan, and L. Li, “Additive manufacturing of three-dimensional metal-glass functionally gradient material components by laser powder bed fusion with in situ powder mixing,” *Addit. Manuf.*, vol. 33, p. 101113, May 2020, doi: 10.1016/j.addma.2020.101113.

[50] “Biomaterials,” *Elsevier*, 2021. https://www.journals.elsevier.com/biomaterials (accessed Jul. 16, 2021).

[51] A. Hudecki, G. Kiryczyński, and M. J. Łos, “Biomaterials, Definition, Overview,” in *Stem Cells and Biomaterials for Regenerative Medicine*, M. J. Łos, A. Hudecki, and E. B. T.-S. C. and B. for R. M. Wiecheć, Eds. Elsevier, 2019, pp. 85–98. doi: 10.1016/B978-0-12-812258-7.00007-1.

[52] A. Nouri, A. Rohani Shirvan, Y. Li, and C. Wen, “Additive manufacturing of metallic and polymeric load-bearing biomaterials using laser powder bed fusion: A review,” *J. Mater. Sci. Technol.*, vol. 94, pp. 196–215, Dec. 2021, doi: 10.1016/j.jmst.2021.03.058.

[53] S. Bose, D. Ke, H. Sahasrabudhe, and A. Bandyopadhyay, “Additive manufacturing of biomaterials,” *Prog. Mater. Sci.*, vol. 93, pp. 45–111, Apr. 2018, doi: 10.1016/j.pmatsci.2017.08.003.

[54] W. S. W. Harun, M. S. I. N. Kamariah, N. Muhamad, S. A. C. Ghani, F. Ahmad, and Z. Mohamed, “A review of powder additive manufacturing processes for metallic biomaterials,” *Powder Technol.*, vol. 327, pp. 128–151, Mar. 2018, doi: 10.1016/j.powtec.2017.12.058.

[55] S. D. Dobson and T. L. Starr, “Powder characterization and part density for powder bed fusion of 17-4 PH stainless steel,” *Rapid Prototyp. J.*, vol. 27, no. 1, pp. 53–58, Jan. 2021, doi: 10.1108/RPJ-01-2020-0023.

[56] N. P. Karapatis, G. Egger, P. Gygax, and R. Glardon, “Optimization of powder layer density in selective laser sintering,” in *Proceedings of the 9th Annual International Solid Freeform Fabrication Symposium, Austin, Texas*, 1999, pp. 255–264. doi: https://doi.org/10.26153/TSW%2F746.

[57] A. Spierings and G. Levy, “Comparison of density of stainless steel 316 L parts produced with selective laser melting using different powder grades,” 2009.

[58] S. E. Brika, M. Letenneur, C. A. Dion, and V. Brailovski, “Influence of particle morphology and size distribution on the powder flowability and laser powder bed fusion manufacturability of Ti-6Al-4V alloy,” *Addit. Manuf.*, vol. 31, p. 100929, Jan. 2020, doi: 10.1016/j.addma.2019.100929.

[59] P. Avrampos and G.-C. Vosniakos, “A prototype powder deposition system for an open Selective Laser Sintering machine,” *Procedia Manuf.*, vol. 51, pp. 755–762, 2020, doi: 10.1016/j.promfg.2020.10.106.

[60] J. S. Weaver *et al.*, “The effects of particle size distribution on the rheological properties of the powder and the mechanical properties of additively manufactured 17-4 PH stainless steel,” *Addit. Manuf.*, vol. 39, p. 101851, Mar. 2021, doi: 10.1016/j.addma.2021.101851.

[61] A. T. Sutton, C. S. Kriewall, M. C. Leu, and J. W. Newkirk, “Powder characterisation techniques and effects of powder characteristics on part properties in powder-bed fusion processes,” *Virtual Phys. Prototyp.*, vol. 12, no. 1, pp. 3–29, Jan. 2017, doi: 10.1080/17452759.2016.1250605.

[62] I. Cruz-Matías *et al.*, “Sphericity and roundness computation for particles using the extreme vertices model,” *J. Comput. Sci.*, vol. 30, pp. 28–40, Jan. 2019, doi: 10.1016/j.jocs.2018.11.005.

[63] D. Schiochet Nasato and T. Pöschel, “Influence of particle shape in additive manufacturing: Discrete element simulations of polyamide 11 and polyamide 12,” *Addit. Manuf.*, vol. 36, p. 101421, Dec. 2020, doi: 10.1016/j.addma.2020.101421.

[64] S. Haeri, “Optimisation of blade type spreaders for powder bed preparation in Additive Manufacturing using DEM simulations,” *Powder Technol.*, vol. 321, pp. 94–104, 2017, doi: https://doi.org/10.1016/j.powtec.2017.08.011.

[65] S. Shamsdini, M. H. Ghoncheh, and M. Mohammadi, “Effect of recoater-blade type on the mechanical properties and microstructure of additively manufactured maraging steels,” *Mater. Sci. Eng. A*, vol. 812, p. 141104, Apr. 2021, doi: 10.1016/j.msea.2021.141104.

[66] M. Daňa, I. Zetková, and P. Hanzl, “The Influence of a Ceramic Recoater Blade on 3D Printing using Direct Metal Laser Sintering,” *Manuf. Technol.*, vol. 19, no. 1, pp. 23–28, Feb. 2019, doi: 10.21062/ujep/239.2019/a/1213-2489/MT/19/1/23.

[67] M. Wohlfart, “Use-cases of different recoater configurations for DMLS®,” 2020. https://www.linkedin.com/pulse/use-cases-different-recoater-configurations-dmls-

michael-wohlfart (accessed Jul. 13, 2021).

[68] M. Y. Kayacan, K. Özsoy, B. Duman, N. Yilmaz, and M. C. Kayacan, "A study on elimination of failures resulting from layering and internal stresses in Powder Bed Fusion (PBF) additive manufacturing," *Mater. Manuf. Process.*, vol. 34, no. 13, pp. 1467–1475, Oct. 2019, doi: 10.1080/10426914.2019.1655151.

[69] "Surface Science: Categorizing Surface Energy," *3M, Science. Applied to Life*, 2021. https://www.3m.com/3M/en_US/bonding-and-assembly-us/resources/science-of-adhesion/categorizing-surface-energy/ (accessed Jul. 23, 2021).

[70] S. Haeri, Y. Wang, O. Ghita, and J. Sun, "Discrete element simulation and experimental study of powder spreading process in additive manufacturing," *Powder Technol.*, vol. 306, pp. 45–54, Jan. 2017, doi: 10.1016/j.powtec.2016.11.002.

[71] J. Zhang, Y. Tan, T. Bao, Y. Xu, X. Xiao, and S. Jiang, "Discrete Element Simulation of the Effect of Roller-Spreading Parameters on Powder-Bed Density in Additive Manufacturing," *Materials (Basel).*, vol. 13, no. 10, p. 2285, May 2020, doi: 10.3390/ma13102285.

[72] A. Budding and T. H. J. Vaneker, "New Strategies for Powder Compaction in Powder-based Rapid Prototyping Techniques," *Procedia CIRP*, vol. 6, pp. 527–532, 2013, doi: 10.1016/j.procir.2013.03.100.

[73] L. Wang, A. Yu, E. Li, H. Shen, and Z. Zhou, "Effects of spreader geometry on powder spreading process in powder bed additive manufacturing," *Powder Technol.*, vol. 384, pp. 211–222, May 2021, doi: 10.1016/j.powtec.2021.02.022.

[74] G. Jacob, C. U. Brown, and A. Donmez, "The influence of spreading metal powders with different particle size distributions on the powder bed density in laser-based powder bed fusion processes," Advanced Manufacturing Series (NIST AMS), National Institute of Standards and Technology, Gaithersburg, MD, Gaithersburg, MD, Mar. 2018. doi: 10.6028/NIST.AMS.100-17.

[75] J. F. Bredt, S. Clark, and G. Gilchrist, "Three dimensional printing material system and method," US7087109B2, 2006 [Online]. Available: https://patents.google.com/patent/US7087109B2

[76] S. Shamsdini, S. Shakerin, A. Hadadzadeh, B. S. Amirkhiz, and M. Mohammadi, "A trade-off between powder layer thickness and mechanical properties in additively manufactured maraging steels," *Mater. Sci. Eng. A*, vol. 776, p. 139041, 2020, doi: https://doi.org/10.1016/j.msea.2020.139041.

[77] M. Strømme Mattsson, P. Hedenus, G. . Niklasson, and R. Ek, "A new method of characterising liquid uptake within particles over short time periods," *Int. J. Pharm.*, vol. 199, no. 2, pp. 179–185, Apr. 2000, doi: 10.1016/S0378-5173(00)00381-1.

[78] P. Hedenus, M. Strømme Mattsson, G. . Niklasson, O. Camber, and R. Ek, "Characterisation of instantaneous water absorption properties of pharmaceutical excipients," *Int. J. Pharm.*, vol. 202, no. 1–2, pp. 141–149, Jul. 2000, doi: 10.1016/S0378-5173(00)00436-1.

[79] L.-P. Lefebvre, F. Bernier, N. Orsoni-Wiemer, C. Charbonneau, B. Alchikh-Sulaiman, and S. Yue, "Rheology of powders: assessing the robustness and impact of humidity, tribocharging, particle size and composition," *Proceeding of the EuroPM Conference*. European Powder Metallurgy Association, 2019.

[80] Freeman Technology, "Powder Rheology," 2021. https://www.freemantech.co.uk/learn/powder-rheology (accessed Jul. 15, 2021).

[81] A. Rescaglio, J. Schockmel, F. Francqui, N. Vandewalle, and G. Lumay, “How tribo-electric charges modify powder flowability,” in *Annual Transactions of The Nordic Rheology Society*, 2017, pp. 17–21. [Online]. Available: https://www.semanticscholar.org/paper/How-tribo-electric-charges-modify-powder-Rescaglio-Schockmel/aa45af6a0c1c621f84fe0b7082054338a977e81a

[82] R. Mertens, S. Dadbakhsh, J. Van Humbeeck, and J.-P. Kruth, “Application of base plate preheating during selective laser melting,” *Procedia CIRP*, vol. 74, pp. 5–11, 2018, doi: https://doi.org/10.1016/j.procir.2018.08.002.

[83] R. Mertens, B. Vrancken, N. Holmstock, Y. Kinds, J.-P. Kruth, and J. Van Humbeeck, “Influence of Powder Bed Preheating on Microstructure and Mechanical Properties of H13 Tool Steel SLM Parts,” *Phys. Procedia*, vol. 83, pp. 882–890, 2016, doi: 10.1016/j.phpro.2016.08.092.

[84] H. Ali, L. Ma, H. Ghadbeigi, and K. Mumtaz, “In-situ residual stress reduction, martensitic decomposition and mechanical properties enhancement through high temperature powder bed pre-heating of Selective Laser Melted Ti6Al4V,” *Mater. Sci. Eng. A*, vol. 695, pp. 211–220, May 2017, doi: 10.1016/j.msea.2017.04.033.

[85] X. Li and J. Dong, “Study on Curve of Pre-heating Temperature Control in Selective Laser Sintering,” in *Proceedings of the 2009 International Symposium on Web Information Systems and Applications (WISA’09)*, 2009, pp. 156–158. [Online]. Available: https://www.proquest.com/openview/2ff2fe367d06698d883499c9ad568a24/1?pq-origsite=gscholar&cbl=136089

[86] R. Casati, M. Hamidi Nasab, M. Coduri, V. Tirelli, and M. Vedani, “Effects of Platform Pre-Heating and Thermal-Treatment Strategies on Properties of AlSi10Mg Alloy Processed by Selective Laser Melting,” *Metals (Basel).*, vol. 8, no. 11, p. 954, Nov. 2018, doi: 10.3390/met8110954.

[87] C. Yan, Y. Shi, Z. Li, S. Wen, and Q. Wei, “Research on preparation and forming technology of selective laser sintering inorganic nonmetallic materials,” in *Selective Laser Sintering Additive Manufacturing Technology*, C. Yan, Y. Shi, Z. Li, S. Wen, and Q. B. T.-S. L. S. A. M. T. Wei, Eds. Elsevier, 2021, pp. 503–669. doi: 10.1016/B978-0-08-102993-0.00004-7.

[88] D. Ruggi, M. Lupo, D. Sofia, C. Barrès, D. Barletta, and M. Poletto, “Flow properties of polymeric powders for selective laser sintering,” *Powder Technol.*, vol. 370, pp. 288–297, Jun. 2020, doi: 10.1016/j.powtec.2020.05.069.

[89] M. Van den Eynde, L. Verbelen, and P. Van Puyvelde, “Influence of temperature on the flowability of polymer powders in laser sintering,” in *AIP Conference Proceedings 1914*, 2017, p. 190007. doi: 10.1063/1.5016796.

[90] D. Grossin *et al.*, “A review of additive manufacturing of ceramics by powder bed selective laser processing (sintering / melting): Calcium phosphate, silicon carbide, zirconia, alumina, and their composites,” *Open Ceram.*, vol. 5, p. 100073, Mar. 2021, doi: 10.1016/j.oceram.2021.100073.

[91] N. Hesse *et al.*, “Analysis of Tribo-Charging during Powder Spreading in Selective Laser Sintering: Assessment of Polyamide 12 Powder Ageing Effects on Charging Behavior,” *Polymers (Basel).*, vol. 11, no. 4, p. 609, Apr. 2019, doi: 10.3390/polym11040609.

[92] P. A. Kulkarni, R. J. Berry, and M. S. A. Bradley, “Review of the flowability measuring techniques for powder metallurgy industry,” *Proc. Inst. Mech. Eng. Part E J. Process Mech. Eng.*, vol. 224, no. 3, pp. 159–168, Aug. 2010, doi:

10.1243/09544089JPME299.

[93] L. I. Escano *et al.*, “Revealing particle-scale powder spreading dynamics in powder-bed-based additive manufacturing process by high-speed x-ray imaging,” *Sci. Rep.*, vol. 8, no. 1, p. 15079, Dec. 2018, doi: 10.1038/s41598-018-33376-0.

[94] C. Meier, R. Weissbach, J. Weinberg, W. A. Wall, and A. J. Hart, “Critical influences of particle size and adhesion on the powder layer uniformity in metal additive manufacturing,” *J. Mater. Process. Technol.*, vol. 266, pp. 484–501, 2019, doi: https://doi.org/10.1016/j.jmatprotec.2018.10.037.

[95] T.-P. Le, X. Wang, K. P. Davidson, J. E. Fronda, and M. Seita, “Experimental analysis of powder layer quality as a function of feedstock and recoating strategies,” *Addit. Manuf.*, vol. 39, p. 101890, Mar. 2021, doi: 10.1016/j.addma.2021.101890.

[96] R. W. Penny *et al.*, “Spatial mapping of powder layer density for metal additive manufacturing via transmission X-ray imaging,” *Addit. Manuf.*, p. 102197, Jul. 2021, doi: 10.1016/j.addma.2021.102197.

[97] Z. Xiang, M. Zhang, R. Yan, Q. Yin, and K. Zhang, “Powder-spreading dynamics and packing quality improvement for laser powder bed fusion additive manufacturing,” *Powder Technol.*, vol. 389, pp. 278–291, Sep. 2021, doi: 10.1016/j.powtec.2021.05.036.

[98] Y. Shanjani and E. Toyserkani, “Material spreading and compaction in powder-based solid freeform fabrication methods : mathematical modelling,” 2008. [Online]. Available: https://www.semanticscholar.org/paper/MATERIAL-SPREADING-AND-COMPACTION-IN-POWDER-BASED-%3A-Shanjani-Toyserkani/98cbd586ba48a7f92af0c1bf7e6be1118d2c30dd

[99] U. Ali *et al.*, “On the measurement of relative powder-bed compaction density in powder-bed additive manufacturing processes,” *Mater. Des.*, vol. 155, pp. 495–501, 2018, doi: 10.1016/j.matdes.2018.06.030.

[100] E. Wycisk, A. Solbach, S. Siddique, D. Herzog, F. Walther, and C. Emmelmann, “Effects of Defects in Laser Additive Manufactured Ti-6Al-4V on Fatigue Properties,” *Phys. Procedia*, vol. 56, pp. 371–378, 2014, doi: 10.1016/j.phpro.2014.08.120.

[101] W. Nan *et al.*, “Jamming during particle spreading in additive manufacturing,” *Powder Technol.*, vol. 338, pp. 253–262, 2018, doi: 10.1016/j.powtec.2018.07.030.

[102] M. Ahmed, M. Pasha, W. Nan, and M. Ghadiri, “A simple method for assessing powder spreadability for additive manufacturing,” *Powder Technol.*, vol. 367, pp. 671–679, 2020, doi: 10.1016/j.powtec.2020.04.033.

[103] S. Pasalopoulos, P. Avrampos, and G.-C. Vosniakos, “Surface quality evaluation of non-sintered powder layers in Selective Laser Sintering by 3D scanning,” *Procedia Manuf.*, vol. 51, no. 2019, pp. 748–754, 2020, doi: 10.1016/j.promfg.2020.10.105.

[104] M. Kalms, R. Narita, C. Thomy, F. Vollertsen, and R. B. Bergmann, “New approach to evaluate 3D laser printed parts in powder bed fusion-based additive manufacturing in-line within closed space,” *Addit. Manuf.*, vol. 26, pp. 161–165, Mar. 2019, doi: 10.1016/j.addma.2019.01.011.

[105] M. Kalms and R. B. Bergmann, “Structure function analysis of powder beds in additive manufacturing by laser beam melting,” *Addit. Manuf.*, vol. 36, no. January, p. 101396, 2020, doi: 10.1016/j.addma.2020.101396.

[106] W. Lin, D. A. Gonçalves, A. De Souza, P. Pereira, and M. Pereira, “Quality analysis method for powder deposited layers applicable to selective laser sintering and

selective laser melting processes," *J. Laser Appl.*, vol. 31, no. 2, 2019, doi: 10.2351/1.5096144.

[107] S. Beitz, R. Uerlich, T. Bokelmann, A. C. Diener, T. Vietor, and A. Kwade, "Influence of Powder Deposition on Powder Bed and Specimen Properties," *Materials (Basel).*, 2019, doi: 10.3390/ma12020297.

[108] G. Jacob, A. Donmez, J. Slotwinski, and S. Moylan, "Measurement of powder bed density in powder bed fusion additive manufacturing processes," *Meas. Sci. Technol.*, vol. 27, no. 11, p. 115601, 2016, doi: 10.1088/0957-0233/27/11/115601.

[109] J.-P. Choi *et al.*, "Evaluation of Powder Layer Density for the Selective Laser Melting (SLM) Process," *Mater. Trans.*, vol. 58, no. 2, pp. 294–297, 2017, doi: 10.2320/matertrans.M2016364.

[110] P. Lhuissier *et al.*, "In situ 3D X-ray microtomography of laser-based powder-bed fusion (L-PBF)—A feasibility study," *Addit. Manuf.*, vol. 34, p. 101271, Aug. 2020, doi: 10.1016/j.addma.2020.101271.

[111] Y. He, J. Gardy, A. Hassanpour, and A. E. Bayly, "A digital-based approach for characterising spread powder layer in additive manufacturing," *Mater. Des.*, vol. 196, p. 109102, Nov. 2020, doi: 10.1016/j.matdes.2020.109102.

[112] C. Meier, R. Weissbach, J. Weinberg, W. A. Wall, and A. John Hart, "Modeling and characterization of cohesion in fine metal powders with a focus on additive manufacturing process simulations," *Powder Technol.*, vol. 343, pp. 855–866, Feb. 2019, doi: 10.1016/j.powtec.2018.11.072.

[113] Y. Liu, L. Blunt, Z. Zhang, H. A. Rahman, F. Gao, and X. Jiang, "In-situ areal inspection of powder bed for electron beam fusion system based on fringe projection profilometry," *Addit. Manuf.*, vol. 31, p. 100940, Jan. 2020, doi: 10.1016/j.addma.2019.100940.

[114] B. Zhang, J. Ziegert, F. Farahi, and A. Davies, "In situ surface topography of laser powder bed fusion using fringe projection," *Addit. Manuf.*, vol. 12, pp. 100–107, Oct. 2016, doi: 10.1016/j.addma.2016.08.001.

[115] W. S. Land, B. Zhang, J. Ziegert, and A. Davies, "In-Situ Metrology System for Laser Powder Bed Fusion Additive Process," *Procedia Manuf.*, vol. 1, pp. 393–403, 2015, doi: 10.1016/j.promfg.2015.09.047.

[116] Z. Li *et al.*, "In Situ 3D Monitoring of Geometric Signatures in the Powder-Bed-Fusion Additive Manufacturing Process via Vision Sensing Methods," *Sensors*, vol. 18, no. 4, p. 1180, Apr. 2018, doi: 10.3390/s18041180.

[117] A. B. Spierings, N. Herres, and G. Levy, "Influence of the particle size distribution on surface quality and mechanical properties in AM steel parts," *Rapid Prototyp. J.*, vol. 17, no. 3, pp. 195–202, Apr. 2011, doi: 10.1108/13552541111124770.

[118] H. Chen, Q. Wei, Y. Zhang, F. Chen, Y. Shi, and W. Yan, "Powder-spreading mechanisms in powder-bed-based additive manufacturing: Experiments and computational modeling," *Acta Mater.*, vol. 179, pp. 158–171, Oct. 2019, doi: 10.1016/j.actamat.2019.08.030.

[119] A. AlFaify, J. Hughes, and K. Ridgway, "Controlling the porosity of 316L stainless steel parts manufactured via the powder bed fusion process," *Rapid Prototyp. J.*, vol. 25, no. 1, pp. 162–175, Jan. 2019, doi: 10.1108/RPJ-11-2017-0226.

[120] A. Leicht, M. Fischer, U. Klement, L. Nyborg, and E. Hryha, "Increasing the Productivity of Laser Powder Bed Fusion for Stainless Steel 316L through Increased

Layer Thickness," *J. Mater. Eng. Perform.*, vol. 30, no. 1, pp. 575–584, Jan. 2021, doi: 10.1007/s11665-020-05334-3.

[121] S. Ziri, A. Hor, and C. Mabru, "Effect of powder size and processing parameters on surface, density and mechanical properties of 316L elaborated by Laser Powder Bed Fusion," *ESAFORM 2021*, Apr. 2021, doi: 10.25518/esaform21.1563.

[122] M. A. Balbaa, A. Ghasemi, E. Fereiduni, M. A. Elbestawi, S. D. Jadhav, and J.-P. Kruth, "Role of powder particle size on laser powder bed fusion processability of AlSi10mg alloy," *Addit. Manuf.*, vol. 37, p. 101630, Jan. 2021, doi: 10.1016/j.addma.2020.101630.

[123] H. Nadiyadi, H. Gajera, R. Bidajwala, K. Abhisek, and K. Dave, "Effects of powder bed fusion process parameters on hardness for Inconel 718," *Mater. Today Proc.*, vol. 38, pp. 2275–2280, 2021, doi: 10.1016/j.matpr.2020.06.388.

[124] A. S. Azar, M. Reiersen, E. W. Hovig, M. M'hamdi, S. Diplas, and M. M. Pedersen, "A novel approach for enhancing the fatigue lifetime of the components processed by additive manufacturing technologies," *Rapid Prototyp. J.*, vol. 27, no. 2, pp. 256–267, Mar. 2021, doi: 10.1108/RPJ-02-2020-0030.

[125] Y. Liu, Y. Yang, S. Mai, D. Wang, and C. Song, "Investigation into spatter behavior during selective laser melting of AISI 316L stainless steel powder," *Mater. Des.*, vol. 87, pp. 797–806, 2015, doi: https://doi.org/10.1016/j.matdes.2015.08.086.

[126] J. Yin *et al.*, "Correlation between forming quality and spatter dynamics in laser powder bed fusion," *Addit. Manuf.*, vol. 31, p. 100958, 2020, doi: https://doi.org/10.1016/j.addma.2019.100958.

[127] Z. A. Young *et al.*, "Types of spatter and their features and formation mechanisms in laser powder bed fusion additive manufacturing process," *Addit. Manuf.*, vol. 36, p. 101438, Dec. 2020, doi: 10.1016/j.addma.2020.101438.

[128] D. Wang *et al.*, "Mechanisms and characteristics of spatter generation in SLM processing and its effect on the properties," *Mater. Des.*, vol. 117, no. Supplement C, pp. 121–130, 2017, doi: https://doi.org/10.1016/j.matdes.2016.12.060.

[129] S. Haeri, S. Haeri, J. Hanson, and S. Lotfian, "Analysis of radiation pressure and aerodynamic forces acting on powder grains in powder-based additive manufacturing," *Powder Technol.*, vol. 368, pp. 125–129, May 2020, doi: 10.1016/j.powtec.2020.04.031.

[130] O. Pannitz and J. T. Sehrt, "Transferability of Process Parameters in Laser Powder Bed Fusion Processes for an Energy and Cost Efficient Manufacturing," *Sustainability*, vol. 12, no. 4, p. 1565, Feb. 2020, doi: 10.3390/su12041565.

[131] Q. Guo *et al.*, "Transient dynamics of powder spattering in laser powder bed fusion additive manufacturing process revealed by in-situ high-speed high-energy x-ray imaging," *Acta Mater.*, vol. 151, pp. 169–180, Jun. 2018, doi: 10.1016/j.actamat.2018.03.036.

[132] J. L. Bartlett and X. Li, "An overview of residual stresses in metal powder bed fusion," *Addit. Manuf.*, vol. 27, pp. 131–149, May 2019, doi: 10.1016/j.addma.2019.02.020.

[133] S. Haeri, L. Benedetti, and O. Ghita, "Effects of particle elongation on the binary coalescence dynamics of powder grains for Laser Sintering applications," *Powder Technol.*, vol. 363, pp. 245–255, Mar. 2020, doi: 10.1016/j.powtec.2019.12.025.

[134] D. Sofia, D. Barletta, and M. Poletto, "Flowability of ceramic powders in the sintering

process," Dec. 2016. [Online]. Available: https://www.researchgate.net/profile/Daniele-Sofia/publication/311575774_Flowability_of_ceramic_powders_in_the_sintering_process/links/5bbec6ca299bf1010178c0c1/Flowability-of-ceramic-powders-in-the-sintering-process.pdf

[135] S. Matthes, M. Kluge, S. Jahn, and C. Emmelmann, "Factors influencing powder-properties of TiAl6V4 along the L-PBF process chain," *Prog. Addit. Manuf.*, vol. 5, no. 1, pp. 33–39, Mar. 2020, doi: 10.1007/s40964-020-00120-y.

[136] R. W. McVey, R. M. Melnychuk, J. A. Todd, and R. P. Martukanitz, "Absorption of laser irradiation in a porous powder layer," *J. Laser Appl.*, vol. 19, no. 4, pp. 214–224, Nov. 2007, doi: 10.2351/1.2756854.

[137] P. Avrampos, "Optimized development of a prototype Selective Laser Sintering powder recoating system via Analytic Hierarchy Process," *Int. J. Exp. Des. Process Optim.*, vol. 1, no. 1, p. XX, 2023, doi: 10.1504/IJEDPO.2023.10059808.

[138] C. Meier, R. Weissbach, J. Weinberg, W. A. Wall, and A. J. Hart, "1) Critical influences of particle size and adhesion on the powder layer uniformity in metal additive manufacturing," *J. Mater. Process. Technol.*, vol. 266, pp. 484–501, 2019, doi: 10.1016/j.jmatprotec.2018.10.037.

[139] S. P. Soe, "Quantitative analysis on SLS part curling using EOS P700 machine," *J. Mater. Process. Technol.*, vol. 212, no. 11, pp. 2433–2442, 2012, doi: https://doi.org/10.1016/j.jmatprotec.2012.06.012.

[140] A. G. Bailey, "The science and technology of electrostatic powder spraying, transport and coating," *J. Electrostat.*, vol. 45, no. 2, pp. 85–120, 1998, doi: https://doi.org/10.1016/S0304-3886(98)00049-7.

[141] T. Stichel *et al.*, "Electrophotographic Multilayer Powder Pattern Deposition for Additive Manufacturing," *JOM*, vol. 72, no. 3, pp. 1366–1375, 2020, doi: 10.1007/s11837-019-03965-z.

[142] E. Emeruwa, J. Jarrige, J. Mexmain, M. Billy, and K. Bouzouita, "Powder compaction with ultrasonic assistance," *J. Mater. Sci.*, vol. 25, no. 2, pp. 1459–1462, 1990, doi: 10.1007/BF00585465.

[143] O. L. Khasanov, E. S. Dvilis, V. M. Sokolov, and P. Pokholkov Yu, "Ceramic Powder Dry Compaction Under Powerful Ultrasound Action," *Key Eng. Mater.*, vol. 264–268, pp. 73–76, 2004, doi: 10.4028/www.scientific.net/KEM.264-268.73.

[144] Y. Wu and K.-L. Choy, "The microstructure of alumina coatings prepared by aerosol assisted spray deposition," *Surf. Coatings Technol.*, vol. 180–181, pp. 436–440, 2004, doi: https://doi.org/10.1016/j.surfcoat.2003.10.078.

[145] Y. Wu, J. Du, K.-L. Choy, and L. L. Hench, "Fabrication of titanium dioxide ceramics by laser sintering green layers prepared via aerosol assisted spray deposition," *Mater. Sci. Eng. A*, vol. 454–455, pp. 148–155, 2007, doi: https://doi.org/10.1016/j.msea.2006.11.077.

[146] C. Lino, R. Deepak, L. Kathleen, Y. Wenqiang, T. Alexander, and H. William, "The tower nozzle solid freeform fabrication technique," *Rapid Prototyp. J.*, vol. 16, no. 4, pp. 295–301, Jan. 2010, doi: 10.1108/13552541011049315.

[147] Z. Wang, A. Zhang, and X. Shang, "3-D Design and Numerical Simulation of Two-Phase Flow in the Laser Rapid Prototyping Coaxial Powder Delivery System," *Tsinghua Sci. Technol.*, vol. 14, pp. 200–205, 2009, doi:

https://doi.org/10.1016/S1007-0214(09)70092-6.

[148] C. Schmutzler, C. Boeker, and M. F. Zaeh, “Investigation of Deviations Caused by Powder Compaction During 3D Printing,” *Procedia CIRP*, vol. 57, pp. 698–703, 2016, doi: https://doi.org/10.1016/j.procir.2016.11.121.

[149] H. Chen, Q. Wei, Y. Zhang, F. Chen, Y. Shi, and W. Yan, “Powder-spreading mechanisms in powder-bed-based additive manufacturing: Experiments and computational modeling,” *Acta Mater.*, vol. 179, pp. 158–171, 2019, doi: https://doi.org/10.1016/j.actamat.2019.08.030.

[150] Z. Snow, R. Martukanitz, and S. Joshi, “On the development of powder spreadability metrics and feedstock requirements for powder bed fusion additive manufacturing,” *Addit. Manuf.*, vol. 28, no. April, pp. 78–86, 2019, doi: 10.1016/j.addma.2019.04.017.

[151] T. Q. Pham, T. T. Do, P. Kwon, and S. N. Foster, “Additive Manufacturing of High Performance Ferromagnetic Materials,” in *2018 IEEE Energy Conversion Congress and Exposition (ECCE)*, 2018, pp. 4303–4308. doi: 10.1109/ECCE.2018.8558245.

[152] M. L. Ang and P. J. Lloyd, “Investigation of charged particle trajectories in electrostatic powder coating systems,” *Int. J. Multiph. Flow*, vol. 13, no. 6, pp. 823–836, 1987, doi: https://doi.org/10.1016/0301-9322(87)90069-3.

[153] F. S. Ali, T. E. Base, and I. I. Inculet, “Mathematical modeling of powder paint particle trajectories in electrostatic painting,” *IEEE Trans. Ind. Appl.*, vol. 36, no. 4, pp. 992–997, 2000, doi: 10.1109/28.855952.

[154] X. Zhang, C. Wei, Y.-H. Chueh, and L. Li, “An Integrated Dual Ultrasonic Selective Powder Dispensing Platform for Three-Dimensional Printing of Multiple Material Metal/Glass Objects in Selective Laser Melting,” *J. Manuf. Sci. Eng.*, vol. 141, no. 1, Oct. 2018, doi: 10.1115/1.4041427.

[155] T. L. Saaty, “A scaling method for priorities in hierarchical structures,” *J. Math. Psychol.*, vol. 15, no. 3, pp. 234–281, 1977, doi: https://doi.org/10.1016/0022-2496(77)90033-5.

[156] R. W. Saaty, “The analytic hierarchy process—what it is and how it is used,” *Math. Model.*, vol. 9, no. 3, pp. 161–176, 1987, doi: https://doi.org/10.1016/0270-0255(87)90473-8.

[157] T. L. Saaty, “Fundamentals of the Analytic Hierarchy Process BT - The Analytic Hierarchy Process in Natural Resource and Environmental Decision Making,” D. L. Schmoldt, J. Kangas, G. A. Mendoza, and M. Pesonen, Eds. Dordrecht: Springer Netherlands, 2001, pp. 15–35. doi: 10.1007/978-94-015-9799-9_2.

[158] C. Reiff, F. Wulle, O. Riedel, S. Epple, and V. Onuseit, “On inline process control for selective laser sintering,” in *8th International Conference on Mass Customization and Personalization – Community of Europe (MCP-CE 2018)*, 2018, no. December. [Online]. Available: https://www.researchgate.net/publication/329625918_On_Inline_Process_Control_for_Selective_Laser_Sintering

[159] M. Ma, Z. Wang, M. Gao, and X. Zeng, “Layer thickness dependence of performance in high-power selective laser melting of 1Cr18Ni9Ti stainless steel,” *J. Mater. Process. Technol.*, vol. 215, pp. 142–150, 2015, doi: https://doi.org/10.1016/j.jmatprotec.2014.07.034.

[160] M. Van den Eynde, L. Verbelen, and P. Van Puyvelde, “Assessing polymer powder flow for the application of laser sintering,” *Powder Technol.*, vol. 286, pp. 151–155,

2015, doi: https://doi.org/10.1016/j.powtec.2015.08.004.

[161] V. Srivastava, S. K. Parida, and P. M. Pandey, “Surface Roughness Studies in Selective Laser Sintering of Glass filled Polyamide BT,” in *Proceedings of the 36th International MATADOR Conference*, 2010, pp. 495–499.

[162] D. L. Bourell, T. J. Watt, D. K. Leigh, and B. Fulcher, “Performance Limitations in Polymer Laser Sintering,” *Phys. Procedia*, vol. 56, pp. 147–156, 2014, doi: 10.1016/j.phpro.2014.08.157.

[163] L. Dobrzanski, A. Dobrzanska-Danikiewicz, A. Achtelik-Franczak, L. B. Dobrzański, M. Szindler, and T. Gaweł, “Porous Selective Laser Melted Ti and Ti6Al4V Materials for Medical Applications,” 2017. doi: 10.5772/65375.

[164] D. Dev Singh, T. Mahender, and A. Raji Reddy, “Powder bed fusion process: A brief review,” *Mater. Today Proc.*, 2020, doi: https://doi.org/10.1016/j.matpr.2020.08.415.

[165] 3dsourced, “Top 12 Best SLS 3D Printers 2020 (For ALL Price Ranges!),” 2020. https://3dsourced.com/3d-printers/sls-3d-printer/ (accessed Dec. 30, 2020).

[166] K. Niru, “The different SLS 3D printers on the market,” 2020. https://www.3dnatives.com/en/different-sls-3d-printers-220320184/ (accessed Dec. 30, 2020).

[167] A. Shimosaka, S. Higashihara, and J. Hidaka, “Estimation of the sieving rate of powders using computer simulation,” *Adv. Powder Technol.*, vol. 11, no. 4, pp. 487–502, 2000, doi: 10.1163/156855200750172088.

[168] T. Niino and K. Sato, “Effect of Powder Compaction in Plastic Laser Sintering Fabrication,” *20th Annu. Int. Solid Free. Fabr. Symp. SFF 2009*, pp. 193–205, Jan. 2009, [Online]. Available: http://edge.rit.edu/edge/P10551/public/SFF/SFF 2009 Proceedings/2009 SFF Papers/2009-18-Niino.pdf

[169] Eco Blade, “Eco Blade offers the finest in custom-made doctor blades.” Eco Blade, Inc., Yokohama, Japan, 2015. [Online]. Available: http://www.eco-blade.co.jp/wp-content/uploads/2014/05/2014_Catalog-e.pdf

[170] Y. Shanjani and E. Toyserkani, “Material spreading and compaction in powder-based solid freeform fabrication methods: mathematical modelling,” in *19th Annual International Solid Freeform Fabrication Symposium, SFF 2008*, 2008, pp. 399–410. [Online]. Available: https://www.semanticscholar.org/paper/MATERIAL-SPREADING-AND-COMPACTION-IN-POWDER-BASED-:-Shanjani-Toyserkani/98cbd586ba48a7f92af0c1bf7e6be1118d2c30dd#citing-papers

[171] A. Michelis, “Development of Numerical Controlled Device of Two Cartesian Motion Axes for an Additive Layered Manufacturing SLS/SLM Machine Tool.,” National Technical University of Athens, 2012. doi: http://dx.doi.org/10.26240/heal.ntua.2746.

[172] A. Bournias-Varotsis, “Powder Deposition System design for a prototype SLS/SLM machine,” National Technical University of Athens, 2013.

[173] F. Psarommatis-Giannakopoulos, “Development of a Powder Management Mechanism for an SLS/SLM Machine,” National Technical University of Athens, 2017. doi: http://dx.doi.org/10.26240/heal.ntua.6887.

[174] T. L. Saaty and L. G. Vargas, “Uncertainty and rank order in the analytic hierarchy process,” *Eur. J. Oper. Res.*, vol. 32, no. 1, pp. 107–117, Oct. 1987, doi: 10.1016/0377-2217(87)90275-X.

[175] I. Durbach, R. Lahdelma, and P. Salminen, “The analytic hierarchy process with

stochastic judgements," *Eur. J. Oper. Res.*, vol. 238, no. 2, pp. 552–559, Oct. 2014, doi: 10.1016/j.ejor.2014.03.045.

[176] E. R. Jalao, T. Wu, and D. Shunk, "A stochastic AHP decision making methodology for imprecise preferences," *Inf. Sci. (Ny).*, vol. 270, pp. 192–203, Jun. 2014, doi: 10.1016/j.ins.2014.02.077.

[177] Y. Liu, C. M. Eckert, and C. Earl, "A review of fuzzy AHP methods for decision-making with subjective judgements," *Expert Syst. Appl.*, vol. 161, p. 113738, Dec. 2020, doi: 10.1016/j.eswa.2020.113738.

[178] M. Hamka and Harjono, "Application of fuzzy preference relations method in AHP to improve judgment matrix consistency," *IOP Conf. Ser. Mater. Sci. Eng.*, vol. 821, no. 1, p. 012035, Apr. 2020, doi: 10.1088/1757-899X/821/1/012035.

[179] S. Cao, Y. Qiu, X.-F. Wei, and H.-H. Zhang, "Experimental and theoretical investigation on ultra-thin powder layering in three dimensional printing (3DP) by a novel double-smoothing mechanism," *J. Mater. Process. Technol.*, vol. 220, pp. 231–242, 2015, doi: https://doi.org/10.1016/j.jmatprotec.2015.01.016.

[180] C. Wei, H. Gu, X. Zhang, Y. Chueh, and L. Li, "Hybrid ultrasonic and mini-motor vibration-induced irregularly shaped powder delivery for multiple materials additive manufacturing," *Addit. Manuf.*, vol. 33, no. February, p. 101138, 2020, doi: 10.1016/j.addma.2020.101138.

[181] C. Wei *et al.*, "Ultrasonic material dispensing-based selective laser melting for 3D printing of metallic components and the effect of powder compression," *Addit. Manuf.*, vol. 29, p. 100818, 2019, doi: https://doi.org/10.1016/j.addma.2019.100818.

[182] P. Avrampos and G.-C. Vosniakos, "A Study on Powder Spreading Quality in Powder Bed Fusion Processes Using Discrete Element Method Simulation," *J. Manuf. Mater. Process.*, vol. 8, no. 3, p. 101, May 2024, doi: 10.3390/jmmp8030101.

[183] M. Bauccio, *ASM Engineered Materials Reference Book*, 2nd ed. ASM International, Materials Park, OH, ©1994, 1994.

[184] AZO Materials, "Alumina as a Biomaterial (99.5% Alumina)." https://www.azom.com/properties.aspx?ArticleID=105 (accessed Nov. 15, 2023).

[185] AZO Materials, "Alumina - Aluminium Oxide - Al2O3 - A Refractory Ceramic Oxide." https://www.azom.com/properties.aspx?ArticleID=52 (accessed Nov. 28, 2023).

[186] H. Chen, Y. G. Xiao, Y. L. Liu, and Y. S. Shi, "Effect of Young's modulus on DEM results regarding transverse mixing of particles within a rotating drum," *Powder Technol.*, vol. 318, pp. 507–517, Aug. 2017, doi: 10.1016/j.powtec.2017.05.047.

[187] S. J. Burns, P. T. Piiroinen, and K. J. Hanley, "Critical time step for DEM simulations of dynamic systems using a Hertzian contact model," *Int. J. Numer. Methods Eng.*, vol. 119, no. 5, pp. 432–451, Aug. 2019, doi: 10.1002/nme.6056.

[188] M. Kremmer and J. F. Favier, "A method for representing boundaries in discrete element modelling—part II: Kinematics," *Int. J. Numer. Methods Eng.*, vol. 51, no. 12, pp. 1423–1436, Aug. 2001, doi: 10.1002/nme.185.

[189] K. D. Kafui, C. Thornton, and M. J. Adams, "Discrete particle-continuum fluid modelling of gas–solid fluidised beds," *Chem. Eng. Sci.*, vol. 57, no. 13, pp. 2395–2410, Jul. 2002, doi: 10.1016/S0009-2509(02)00140-9.

[190] C. THORNTON and C. W. RANDALL, "Applications of Theoretical Contact

Mechanics to Solid Particle System Simulation," in *Micromechanics of Granular Materials*, vol. 20, M. Satake and J. T. B. T.-S. in A. M. Jenkins, Eds. Elsevier, 1988, pp. 133–142. doi: 10.1016/B978-0-444-70523-5.50023-0.

[191] Y. Li, Y. Xu, and C. Thornton, "A comparison of discrete element simulations and experiments for 'sandpiles' composed of spherical particles," *Powder Technol.*, vol. 160, no. 3, pp. 219–228, Dec. 2005, doi: 10.1016/j.powtec.2005.09.002.

[192] C. Thornton, *Granular Dynamics, Contact Mechanics and Particle System Simulations*, vol. 24. Cham: Springer International Publishing, 2015. doi: 10.1007/978-3-319-18711-2.

[193] H. Hertz, "Ueber die Berührung fester elastischer Körper.," *crll*, vol. 1882, no. 92, pp. 156–171, 1882, doi: 10.1515/crll.1882.92.156.

[194] R. D. Mindlin, "Compliance of Elastic Bodies in Contact," *J. Appl. Mech.*, vol. 16, no. 3, pp. 259–268, Sep. 1949, doi: 10.1115/1.4009973.

[195] R. Mukherjee *et al.*, "Effects of particle size on the triboelectrification phenomenon in pharmaceutical excipients: Experiments and multi-scale modeling," *Asian J. Pharm. Sci.*, vol. 11, no. 5, pp. 603–617, 2016, doi: https://doi.org/10.1016/j.ajps.2016.04.006.

[196] S. Ose, "Dusting of Alumina and Electrostatic Charging," *Part. Sci. Technol.*, vol. 21, no. 3, pp. 237–245, Jul. 2003, doi: 10.1080/02726350307483.

[197] K. L. Johnson, K. Kendall, and A. D. Roberts, "Surface energy and the contact of elastic solids," *Proc. R. Soc. London. A. Math. Phys. Sci.*, vol. 324, no. 1558, pp. 301–313, Sep. 1971, doi: 10.1098/rspa.1971.0141.

[198] B. V Derjaguin, V. M. Muller, and Y. . Toporov, "Effect of contact deformations on the adhesion of particles," *J. Colloid Interface Sci.*, vol. 53, no. 2, pp. 314–326, 1975, doi: https://doi.org/10.1016/0021-9797(75)90018-1.

[199] ITASCA, "Johnson-Kendall-Roberts (JKR) Contact Model," 2021. https://docs.itascacg.com/pfc700/common/contactmodel/jkr/doc/manual/cmjkr.html (accessed Dec. 07, 2023).

[200] A. EDEM, "The Hertz-Mindlin with JKR Version 2 model." https://2022.help.altair.com/2022.2/EDEM/Creator/Physics/Base_Models/Hertz-Mindlin_with_JKR_V2.htm (accessed Mar. 27, 2024).

[201] K. L. Johnson and J. A. Greenwood, "Adhesive Contact of Elastic Bodies: The JKR Theory," in *Encyclopedia of Tribology*, Boston, MA: Springer US, 2013, pp. 42–49. doi: 10.1007/978-0-387-92897-5_1086.

[202] D. S. Grierson, E. E. Flater, and R. W. Carpick, "Accounting for the JKR–DMT transition in adhesion and friction measurements with atomic force microscopy," *J. Adhes. Sci. Technol.*, vol. 19, no. 3–5, pp. 291–311, Jan. 2005, doi: 10.1163/1568561054352685.

[203] D. Maugis, "Adhesion of spheres: The JKR-DMT transition using a dugdale model," *J. Colloid Interface Sci.*, vol. 150, no. 1, pp. 243–269, Apr. 1992, doi: 10.1016/0021-9797(92)90285-T.

[204] X. Shi and Y.-P. Zhao, "Comparison of various adhesion contact theories and the influence of dimensionless load parameter," *J. Adhes. Sci. Technol.*, vol. 18, no. 1, pp. 55–68, Jan. 2004, doi: 10.1163/156856104322747009.

[205] J. A. Greenwood, "Adhesion of Elastic Spheres," *Proc. Math. Phys. Eng. Sci.*, vol. 453, no. 1961, pp. 1277–1297, Dec. 1997, [Online]. Available:

http://www.jstor.org/stable/53001

[206] A. H. Tavakoli *et al.*, “Amorphous Alumina Nanoparticles: Structure, Surface Energy, and Thermodynamic Phase Stability,” *J. Phys. Chem. C*, vol. 117, no. 33, pp. 17123–17130, Aug. 2013, doi: 10.1021/jp405820g.

[207] D. Vollath, F. D. Fischer, and D. Holec, “Surface energy of nanoparticles – influence of particle size and structure,” *Beilstein J. Nanotechnol.*, vol. 9, pp. 2265–2276, Aug. 2018, doi: 10.3762/bjnano.9.211.

[208] P. D. Tepesch and A. A. Quong, “First-Principles Calculations of α-Alumina (0001) Surfaces Energies with and without Hydrogen,” *Phys. status solidi*, vol. 217, no. 1, pp. 377–387, Jan. 2000, doi: 10.1002/(SICI)1521-3951(200001)217:1<377::AID-PSSB377>3.0.CO;2-B.

[209] I. Vilfan, T. Deutsch, F. Lançon, and G. Renaud, “Erratum to: ‘Structure determination of the (3×3) reconstructed α-Al2O3(0001)’ [Surf. Sci. 505 (2002) L215],” *Surf. Sci.*, vol. 529, no. 1–2, p. 281, Apr. 2003, doi: 10.1016/S0039-6028(03)00261-9.

[210] R. Spolenak, S. Gorb, H. Gao, and E. Arzt, “Effects of contact shape on the scaling of biological attachments,” *Proc. R. Soc. A Math. Phys. Eng. Sci.*, vol. 461, no. 2054, pp. 305–319, Feb. 2005, doi: 10.1098/rspa.2004.1326.

[211] L. Schiller and A. Naumann, “A Drag Coefficient Correlation,” *Zeitschrift des Vereins Dtsch. Ingenieure*, vol. 77, pp. 318–320, 1935.

[212] S. S. Karunarathne and L.-A. Tokheim, “Comparison of the influence of drag models in CFD simulation of particle mixing and segregation in a rotating cylinder,” Sep. 2017, pp. 151–156. doi: 10.3384/ecp17138151.

[213] AZO Materials, “Stainless Steel - Grade 304 (UNS S30400),” 2023. https://www.azom.com/properties.aspx?ArticleID=965 (accessed Dec. 27, 2023).

[214] OLYMPUS-IMS-EVIDENT, “Surface Roughness Measurement—Parameters,” 2023. https://www.olympus-ims.com/en/metrology/surface-roughness-measurement-portal/parameters/ (accessed Dec. 23, 2023).

[215] S. Taylor, E. C. Forrest, and B. H. Jared, “Investigating Applicability of Surface Roughness Parameters in Describing the Metallic Additive Manufacturing Process.,” 2019. [Online]. Available: https://www.osti.gov/biblio/1641526

[216] Michigan Metrology LLC, “Ssk (Skewness) and Sku (Kurtosis),” 2023. https://michmet.com/glossary-term/kurtosis/ (accessed Dec. 22, 2023).

[217] Y. M. Fouda and A. E. Bayly, “A DEM study of powder spreading in additive layer manufacturing,” *Granul. Matter*, vol. 22, no. 1, pp. 1–18, 2020, doi: 10.1007/s10035-019-0971-x.

[218] S. Wu *et al.*, “Study on powder particle behavior in powder spreading with discrete element method and its critical implications for binder jetting additive manufacturing processes,” *Virtual Phys. Prototyp.*, vol. 18, no. 1, Dec. 2023, doi: 10.1080/17452759.2022.2158877.

[219] R. Roy, *A primer on the Taguchi method*, 1st ed. New York: Society of Manufacturing Engineers, 1990. [Online]. Available: https://catalogue.nla.gov.au/Record/1852247

[220] D. Schiochet Nasato, H. Briesen, and T. Pöschel, “Influence of vibrating recoating mechanism for the deposition of powders in additive manufacturing: Discrete element simulations of polyamide 12,” *Addit. Manuf.*, vol. 48, p. 102248, Dec. 2021, doi:

10.1016/j.addma.2021.102248.

[221] U. Ali *et al.*, “Identification and characterization of spatter particles and their effect on surface roughness, density and mechanical response of 17-4 PH stainless steel laser powder-bed fusion parts,” *Mater. Sci. Eng. A*, vol. 756, pp. 98–107, May 2019, doi: 10.1016/j.msea.2019.04.026.

[222] Elcan Industries Inc., “Ultrasonic Sieving Machines: Here’s What You Should Know,” 2023. https://elcanindustries.com/blog_posts/ultrasonic-sieving-machines-heres-what-you-should-know/ (accessed May 21, 2024).

[223] Takeda Tokyo Process Service Co. Ltd., “Micro-sieves.” https://www.tkd-topro.com/english/product/microsieve/ (accessed Jan. 12, 2024).

[224] W.S.Tyler, “Terminology & Measurement Methods of Sieves,” 2024. https://wstyler.com/square-opening-wire-mesh/terminology-measurement-methods/ (accessed Jan. 12, 2024).

[225] Retsch, “Sieve Analysis: Taking a close look at quality,” 2015. https://www.retsch.com/files/8785/expert-guide-sieving.pdf (accessed Jan. 17, 2024).

[226] C. O’Callaghan, “Sifting Through Sieve Analysis,” *Innopharma Technology*, 2023. https://www.innopharmatechnology.com/news/sifting-through-sieve-analysis (accessed Jan. 17, 2024).

[227] K. Yamane, S. Ishihara, R. Soda, J. Kano, and F. Saito, “DEM Simulation of Sieving Process about Rod-like Particles,” *J. Soc. Powder Technol. Japan*, vol. 49, no. 11, pp. 818–826, 2012, doi: 10.4164/sptj.49.818.

[228] AEROSINT, “Multi-material L-PBF,” 2021. https://aerosint.com/multi-material-3d-printing-bundle/ (accessed Jan. 21, 2024).

[229] S. Diener, A. Zocca, and J. Günster, “Literature review: Methods for achieving high powder bed densities in ceramic powder bed based additive manufacturing,” *Open Ceram.*, vol. 8, p. 100191, Dec. 2021, doi: 10.1016/j.oceram.2021.100191.

[230] Fraunhofer IGCV, “3-D-Multimaterialbauteile, Projekt FORNEXTGEN,” 2018. https://www.youtube.com/watch?v=pm62sRQOUgE (accessed Jun. 11, 2024).

[231] C. Seidel, “Multi-material metal parts by Powder Bed Fusion: New application opportunities,” *Metal AM Vol 8 No. 2*, pp. 145–151, 2022. Accessed: Jun. 11, 2024. [Online]. Available: https://www.metal-am.com/articles/multi-material-metal-parts-by-powder-bed-fusion-new-application-opportunities/

[232] K. Hormann and A. Agathos, “The point in polygon problem for arbitrary polygons,” *Comput. Geom.*, vol. 20, no. 3, pp. 131–144, Nov. 2001, doi: 10.1016/S0925-7721(01)00012-8.

[233] OpenCV, “Hough Circle Transform.” https://docs.opencv.org/4.x/da/d53/tutorial_py_houghcircles.html (accessed Apr. 22, 2024).

[234] L. A. F. Fernandes and M. M. Oliveira, “A general framework for subspace detection in unordered multidimensional data,” *Pattern Recognit.*, vol. 45, no. 9, pp. 3566–3579, Sep. 2012, doi: 10.1016/j.patcog.2012.02.033.

[235] D. H. Ballard, “Generalizing the Hough transform to detect arbitrary shapes,” *Pattern Recognit.*, vol. 13, no. 2, pp. 111–122, Jan. 1981, doi: 10.1016/0031-3203(81)90009-1.